NUMERICAL STUDIES OF GASOLINE DIRECT INJECTION ENGINE PROCESSES

By

Nicholas James Beavis

BEng (Hons), MSc

A Doctoral Thesis submitted in partial fulfilment of the requirements for the award of Doctor of Philosophy of Loughborough University

2016

Loughborough University

Certificate of Originality

Thesis Access Conditions and Deposit Agreement

Students should consult the guidance notes on the electronic thesis deposit and the access conditions in the University's Code of Practice on Research Degree Programmes

Author....Nicholas Beevis.....

Title....Numerical Studies of a Coaxial Direct Injection Engine Process.....

I [Please insert name and address], "the Depositor",
would like to deposit [Please insert title of dissertation], hereafter referred to as the "Work", once it has successfully been examined in Loughborough University Institutional Repository

Status of access OPEN / ~~RESTRICTED / CONFIDENTIAL~~

Moratorium Period.....N/A.....years,
ending...../.....20.....

Status of access approved by (CAPITALS):.....

Supervisor (Signature).....S. S. Ward-Smith.....

School of.....Aero and Auto.....AAE.....

Author's Declaration *I confirm the following :*

CERTIFICATE OF ORIGINALITY
This is to certify that I am responsible for the work submitted in this thesis, that the original work is my own except as specified in acknowledgements or in footnotes, and that neither the thesis nor the original work therein has been submitted to this or any other institution for a degree

NON-EXCLUSIVE RIGHTS
The licence rights granted to Loughborough University Institutional Repository through this agreement are entirely non-exclusive and royalty free. I am free to publish the Work in its present version or future versions elsewhere. I agree that Loughborough University Institutional Repository administrators or any third party with whom Loughborough University Institutional Repository has an agreement to do so may, without changing content, convert the Work to any medium or format for the purpose of future preservation and accessibility.

DEPOSIT IN LOUGHBOROUGH UNIVERSITY INSTITUTIONAL REPOSITORY
I understand that open access work deposited in Loughborough University Institutional Repository will be accessible to a wide variety of people and institutions - including automated agents - via the World Wide Web. An electronic copy of my thesis may also be included in the British Library Electronic Theses On-line System (EThOS).
I understand that once the Work is deposited, a citation to the Work will always remain visible. Removal of the Work can be made after discussion with Loughborough University Institutional Repository, who shall make best

efforts to ensure removal of the Work from any third party with whom Loughborough University Institutional Repository has an agreement. Restricted or Confidential access material will not be available on the World Wide Web until the moratorium period has expired.

- That I am the author of the Work and have the authority to make this agreement and to hereby give Loughborough University Institutional Repository administrators the right to make available the Work in the way described above.
- That I have exercised reasonable care to ensure that the Work is original, and does not to the best of my knowledge break any UK law or infringe any third party's copyright or other Intellectual Property Right. I have read the University's guidance on third party copyright material in theses.
- The administrators of Loughborough University Institutional Repository do not hold any obligation to take legal action on behalf of the Depositor, or other rights holders, in the event of breach of Intellectual Property Rights, or any other right, in the material deposited.

The statement below shall apply to ALL copies:

This copy has been supplied on the understanding that it is copyright material and that no quotation from the thesis may be published without proper acknowledgement.

Restricted/confidential work: All access and any copying shall be strictly subject to written permission from the University Dean of School and any external sponsor, if any.

Author's signature.....Date.....29/12/17.....

user's declaration: for signature during any Moratorium period (Not Open work): *I undertake to uphold the above conditions:*			
Date	Name (CAPITALS)	Signature	Address

ABSTRACT

The GDI engine has a number of practical advantages over the more traditional port-fuel injection strategy, however a number of challenges remain the subject of continued research in an attempt to fully exploit the advantages of the GDI engine. These include complex in-cylinder flow fields and fuel-air mixing strategies, and significant temporal variation, both through an engine cycle and on a cycle-by-cycle basis. Despite advances in experimental techniques, the relative difficulty and cost of taking detailed measurements remains high, thus computational techniques are an integral part of research activities.

The research work presented in this thesis has focused on the use of detailed 3D-CFD techniques for investigating physical phenomena of the in-cylinder flow field and fuel injection process in a single cylinder GDI engine with early injection event. A detailed validation of the numerical predictions of the in-cylinder flow field using both the RANS RNG k-ε turbulence model and the Smagorinsky LES SGS turbulence model was completed with both models showing good agreement against available experimental results. A detailed validation of the numerical predictions of the fuel injection process using a Lagrangian DDM and both RANS RNG k-ε turbulence model and Smagorinsky LES SGS turbulence model was completed with both models showing excellent agreement against experimental data.

The model was then used to investigate the in-cylinder flow field and fuel injection process including research into: the three dimensional nature of the flow field; intake valve jet flapping, characterisation, causality and CCV, and whether it could account for CCV of the mixture field at spark timing; the anisotropic characteristics of the flow field using both the fluctuating velocity and turbulence intensity, including the increase in anisotropy due to the fuel injection event; the use of POD for quantitatively analysing the in-cylinder flow field; investigations into the intake valve, cylinder liner and piston crown spray plume impingement processes, including the use of a multi-component fuel surrogate and CCV of the formed liquid film; characterisation and CCV of the mixture field though the intake and compression strokes up to spark timing. Finally, the predicted turbulence characteristics were used to evaluate the resultant premixed turbulent combustion event using combustion regime diagrams.

ACKNOWLEDGEMENTS

Upon completion of this body of work, it would be inappropriate not to acknowledge the various people who have provided help and support along the way.

First I would like to thank my supervisors, Dr. Salah Ibrahim and Prof. Weeratunge Malalasekera, for their numerous helpful and insightful discussions, recommendations, support, and continual words of encouragement to help me achieve the best I can. I would like to thank Graham Wigley for his technical advice in the areas of fuel sprays and experimental techniques, and for the supply of experimental data that helped form the basis for the fuel injection mass flow rate profile.

I would like to thank a number of people at Jaguar Land Rover (JLR); Paul Dunkley for being my primary point of contact, always trying to answer my questions and requests either through his own knowledge and experience or by finding me a person within JLR who could answer the question for me; Steven Pierson for being the initial point of contact and support on the project and for providing feedback and suggestions on the numerous results shared with him; Steve Smith for the data and technical discussions regarding the thermal expansion of the valvetrain system and appropriate valve lash adjustments; Adrian Gaylard for the opportunity to present my work to someone outside of the ICE field and gain interesting insights from an alternative view point; Dave Richardson for additional technical information about the original single cylinder optical engine build that helped me to ensure the model created was an accurate representation; and the others within the CAE group who provided numerous interesting and stimulating discussions during the presentation of my work through the course of this research.

I would like to thank the numerous support persons at CD-adapco for their support in using the STAR-CD, es-ice and STAR-CCM+ codes; Karl Bass for the initial training sessions and all the subsequent support; Rohan Wanchoo for the support on various software related issues; Alex Panagoulias for always endeavouring to find an answer to my numerous questions; and Simon Fischer for the support and additional information regarding the secondary breakup models within the STAR-CD code.

I would like to thank Prof. Stefano Fontanesi for the insightful email communications on the use of LES in STAR-CD and for the suggested solver settings that helped in me achieving a stable solution.

I would like to thank JLR and the EPSRC (grant EP/K014102/1) for their financial support as part of the jointly funded Programme for Simulation Innovation.

Finally I would like to thank my family and friends for their support through this process; my mother, for always being supportive of my decisions, whatever they may be; my father, for providing the many extra words of encouragement throughout this process and in the beginning, for giving me the encouraging words to take the final decision to leave a comfortable well paid engineering job in pursuit of happiness and self-fulfilment; and Mandy, for hanging in there when I became a terrible partner during the write up of this thesis.

To all of you, and the others I've not mentioned, I offer my sincerest gratitude.

Nick Beavis

November 2016

"Nothing can resist the human will that will stake even its existence on its stated purpose"

– Benjamin Disraeli

"We always have time enough if we will but use it aright"

– Johann Wolfgang von Goethe

"We are what we repeatedly do"

– Aristotle

PUBLISHED PAPERS

Beavis, N.J., Ibrahim, S.S., and Malalasekera, W., (2015) Characteristics of GDI Engine Flow Structures. In: Leipertz, A. (ed.) *12th International Congress, Engine Combustion Processes, Current Problems and Modern Technologies, 12-13 March 2015, Ludwigsburg, Germany*. Erlangen, ESYTEC GmbH. pp. 385-396. Available from: https://dspace.lboro.ac.uk/2134/20016.

Beavis, N.J., Ibrahim, S.S., and Malalasekera, W., (2016) Numerical Simulations of a GDI Engine Flow Using LES and POD. SAE Technical Paper 2016-01-0598.

Beavis, N.J., Ibrahim, S.S. and Malasekera, W., (2016) Impingement characteristics of an early injection GDI engine: A numerical study. *International Journal of Engine Research*. Available from: doi:10.1177/1468087416663325

Beavis, N.J., Ibrahim, S.S., and Malalasekera, W., (2016) A Numerical Study of Intake Valve Jet Flapping in a GDI Engine. In: *3rd Biennial International Conference on Powertrain Modelling and Control, 7-9 September 2016, Loughborough, UK*.

Beavis, N.J., Ibrahim, S.S., and Malalasekera, W., (2016) Quantification of Flow Anisotropy and Turbulence Intensity in an Early Injection GDI Engine using LES. Accepted for presentation at: *Large-Eddy Simulation for Internal Combustion Engines, 30 November-1 December 2016, Rueil-Malmaison, France*.

Beavis, N.J., Ibrahim, S.S., and Malalasekera, W., (2017) Numerical Evaluation of Combustion Regimes in a GDI Engine. In: *Tenth Mediterranean Combustion Symposium, 17-21 September 2017, Napoli, Italy*.

Beavis, N.J., Ibrahim, S.S., and Malalasekera, W., (2017) A Numerical Study of Intake Valve Jet Flapping in a Gasoline Direct Injection Engine. Accepted for publication in: *International Journal of Powertrains*.

CONTENTS

NOMENCLATURE

LATIN SYMBOLS

A	Constant or Eigenvectors in POD decomposition
A_E	Effective valve area
A_C	Valve curtain area or cell face area
B_S	Constant in Nukiyama temperature equation
c	Cycle number
c.a.	Crank angle
C_D	Discharge coefficient
C_p	Specific heat at constant pressure
$CCV_{index_{rms,M}}$	Modal CCV RMS index
$CCV_{index_{rms,Overall}}$	Overall CCV RMS index
C_S	Smagorinsky constant
C_{ij}	Tensor coefficient in the DSM
C_k	k-equation constant
C_μ	Constant in *k*-ε model
d_p	Diameter of the droplet parcel
D	Diameter or molecular diffusivity
Da	Damköhler number
D_v	Valve head diameter
D_{10}	Arithmetic mean diameter
D_{32}	Sauter mean diameter
D_s	Spreading diameter
F	Force
Fr	Froude number
g	Acceleration due to gravity
ΔH_{vap}	Enthalpy of vapourisation
k	Kinetic energy or heat conductivity
Ka	Karlovitz number
l	Length scale or cell length

L	Characteristic length
La	Laplace number
Le	Lewis number
L_v	Valve lift
m_p	Mass of the droplet parcel
M	Turbulence resolution parameter or number of instantaneous velocity fields in POD decomposition
n	Polytropic index or total number of cycles
N	Total number of cells or Number of droplets in a given parcel or the position within the domain in a POD decomposition
Oh	Ohnesorge number
p	Pressure
q	Constant ('shape' parameter) in Rosin-Rammler distribution
Q	Heat transfer
R	Specific gas constant or ratio of connecting rod length to crank radius
Re	Reynolds number
S	Speed
$\bar{S}$	Favre-filtered strain rate tensor
$\widetilde{S_{ij}}$	Strain rate tensor
t	Time
T	Temperature
*T**	Temperature defining impingement regime in Senda impingement model
T_i	Turbulence intensity
u	Velocity or velocity in the x-axis
$\overline{u_i}$	Mean velocity component
u_i'	Fluctuating velocity component
u_l	Laminar burning velocity
v	Velocity scale or Injection velocity or Velocity in the y-axis
V	Volume
V	Characteristic velocity
w	Velocity in the z-axis
We	Weber number
x	Arbitrary distance or total number of droplets

X	Constant (‘scale’ parameter) in Rosin-Rammler distribution
z	Cutting plane in the z-axis

GREEK SYMBOLS

α	Thermal diffusivity constant
β	Droplet spreading factor
γ_c	Surface coverage ratio
Δ	Filter width
δ	Flame thickness or non-dimensional film thickness
δ_{ij}	Kronecker delta
ε	Rate of turbulence dissipation
θ	Crank angle
λ	Second viscosity or eigenvalues in POD decomposition
μ	Dynamic viscosity
μ_t	Dynamic turbulence viscosity
ρ	Density
σ	Surface tension or standard deviation
τ	Viscous stresses or characteristic time scale
τ_{ij}	SGS stresses
τ_{ij}^r	Anisotropic portion of the SGS stresses
υ_T	Kinematic turbulence viscosity
ϕ	Instantaneous flow property or Fuel-air equivalence ratio
$\bar{\phi}$	Mean component of the flow property
ϕ'	Fluctuating component of the flow property
ψ	POD modes
ω	Vorticity

SUBSCRIPTS/SUPERSCRIPTS

°	Degrees
aero	Aerodynamic
b	Burned or normal boiling
B	Boiling
c, cr, crit	Critical or cycle
cond	Conduction
C	Cyclic-average
CoV	Coefficient of variance
E	Ensemble-average
f	Fuel
HF	High frequency
i	Vector notation or i^{th} droplet parcel or i^{th} cell
k	Kolmogorov scale of turbulence
l	Liquid or laminar
L, leid	Leidenfrost
LF	Low frequency
m	Taylor or micro scale of turbulence
N	Nukiyama
P	Piston
PA	Pure Adhesion
PR	Pure Rebound
ref	Reference
res	Resolved
rms	Root mean square
sat	Saturation
sgs	Sub-grid scale
SD	Standard deviation
t	Integral scale of turbulence
T	Turbulence
u	Unburned
W	Wall

ABBREVIATIONS

ABDC	After Bottom Dead Centre
AEOI	After End of Injection
ASOI	After Start of Injection
ATDC	After Top Dead Centre
BBDC	Before Bottom Dead Centre
BDC	Bottom Dead Centre
BMEP	Brake Mean Effective Pressure
BTDC	Before Top Dead Centre
CAFE	Corporate Average Fuel Economy
CARB	California Air Resources Board
CARS	Coherent Anti-Stokes Raman Spectroscopy
CCD	Charge Coupled Device
CCSPV	Combustion Concepts for Sustainable Premium Vehicles
CCV	Cycle-to-Cycle Variability
CD	Central Differencing
CDM	Continuum Droplet Model
CFD	Computational Fluid Dynamics
CFL	Courant-Friedrichs-Lewy number
CFM	Coherent Flame Model
CHF	Critical Heat Flux
CI	Compression Ignition
CMOS	Complimentary Metal-Oxide Sensor
COP	Conformity Of Production
CoV	Coefficient of Variance
CR	Compression Ratio
CRP	Colour Ratio Pyrometry
DDM	Discrete Droplet Model
DES	Detached Eddy Simulation
DFWM	Degenerate Four-Wave Mixing
DI	Direct Injection
DNS	Direct Numerical Simulation

DSM	Dynamic Structure Model
ECFM	Extended Coherent Flame Model
EEC	European Economic Community
EGR	Exhaust Gas Recirculation
EOI	End of Injection
EPA	Environmental Protection Agency
FD	Finite Difference
FE	Finite Element
FV	Finite Volume
GDI	Gasoline Direct Injection
GHG	Green house gases
HC	Hydrocarbons
HCCI	Homogeneous Charge Compression Ignition
HCN	Hydrocyanic acid
HFS	Hybrid Forward Stepwise
HSPIV	High Speed Particle Image Velocimetry
ICE	Internal Combustion Engine
IDI	In-Direct Injection
iEGR	Internal Exhaust Gas Recirculation
IVC	Intake Valve Closing
IVO	Intake Valve Opening
JLR	Jaguar Land Rover
KH	Kevin-Helmholtz
LDA	Laser Doppler Anemometry
LED	Light Emitting Diode
LES	Large Eddy Simulation
LIF	Laser Induced Fluorescence
LISA	Linearized Instability Sheet Atomization
MARS	Monotone Advection and Reconstruction Scheme
MFB	Mass Fraction Burned
NEDC	New European Drive Cycle
NMHC	Non-methane hydrocarbons
NMOG	Non-methane organic gases

N-S	Navier-Stokes
NTC	No-Time-Counter
OEM	Original Equipment Manufacturer
PAH	Polycyclic aromatic hydrocarbons
PDA	Phase Doppler Anemometry
PDE	Partial Differential Euations
PFI	Port Fuel Injection
PISO	Pressure Implicit with Splitting of Operator
PIV	Particle Image Velocimetry
PLIF	Planar Laser Induced Fluorescence
PM	Particulate Matter
PN	Particulate Number
POD	Proper Orthogonal Decomposition
QPLIF	Quantitative Planar Laser Induced Fluorescence
RANS	Reynolds Averaged Navier-Stokes
RMS	Root Mean Square
RNG	Renormalisation Group
RSM	Reynolds Stress Model
RT	Rayleigh-Taylor
SCV	Swirl Control Valve
SGS	Sub Grid Scale
SI	Spark Ignition
SMD	Sauter Mean Diameter
SOI	Start of Injection
TAB	Taylor Analogy Break-up
TDC	Top Dead Centre
THC	Total hydrocarbons
TKE	Turbulence Kinetic Energy
UHC	Unburned Hydrocarbons
VCO	Valve Covered Orifice
VOF	Volatile Organic Fraction
WWMP	World Wide Mapping Point

LIST OF FIGURES

Chapter 1

Chapter 2

Chapter 3

Chapter 4

Chapter 5

Chapter 6

LIST OF TABLES

Chapter 1

Chapter 2

Chapter 3

Chapter 5

Chapter 6

CHAPTER 1

INTRODUCTION

"Restlessness is discontent and discontent is the first necessity of progress. Show me a thoroughly satisfied man and I will show you a failure."

– Thomas A. Edison

1.1 RESEARCH BACKGROUND AND MOTIVATION

1.1.1 Development Drivers

The purpose of this section is to present the motivations and drivers behind the continual development of the automotive internal combustion engine and more specifically the gasoline direct injection (GDI) engine.

The internal combustion engine has been a constant area of research and development since its inception in the 1860's. Its' exceptional power to weight ratio, simplicity and robustness have been key characteristics that have allowed it become very successful and find its' way into a wide range of applications. Two forms of the internal combustion engine which have seen most success are the spark-ignition (SI) engine and compression-ignition (CI) engine. It is the spark-ignition engine that is of particular interest in this work (Heywood, 1988).

A significant driver in the development of the internal combustion engine has been increasingly stringent emissions legislation. Japan was one of the first countries to impose a regulation on all sources of air pollutants under the Japanese: Air Pollution Control Act in 1968. Since then, regulatory bodies around the world have been legislating against pollutants produced by automotive vehicles. Table 1.1 illustrates the progression of emissions standards in the EU for passenger cars from Euro 1 in the year 1992, up to Euro 6 most recently implemented in September 2014.

Pollutants regulated by the European Economic Community (EEC), U.S. Environmental Protection Agency (EPA), California Air Resources Board (CARB) and Japanese Ministry regulatory bodies primarily regulate carbon monoxide, nitrous oxides, hydrocarbons and particulate emissions due to their impact on the environment and human health.

Carbon Monoxide (CO) is formed as an intermediate product of the oxidation of carbon in the fuel to carbon dioxide. This occurs due to insufficient availability of oxygen and hence is prevalent in combustion of stoichiometric or rich mixtures. Due to their typical combustion regimes, this is of particular concern for gasoline engines. Carbon monoxide is a highly toxic colourless and odourless gas that reduces the flow of oxygen in the blood stream.

Nitrous oxides (NOx) primarily compose of nitric oxide and nitrogen dioxide. Other oxides of nitrogen are also present in final exhaust species composition (e.g. N_2O) but in much smaller quantities and as such are not regulated. Nitrous oxides are formed in areas of high temperature involving chemical reactions of nitrogen and oxygen. As the temperature cools, the reaction chemistry freezes leaving significant concentrations of NOx, well above those seen than if the mixture was allowed to continue to equilibrium. Figure 1.1 illustrates the results from a nitrous oxides model proposed by Komiyama & Heywood (1973) for both early- and late-burning elements, illustrating the high temperature dependence of NOx formation and high levels present at the end of the cycle when compared to equilibrium values. Nitrous oxides act to participate in photochemical reactions which in turn lead to ozone (O_3) formation and smog. It is also a contributor to acid rain formation.

Table 1.1 – EU emissions standards for passenger cars (TransportPolicy.net, 2016)

Stage	Date	CO	HC	HC+NO_x	NO_x	PM	PN
		[g/km]					[#/km]
Compression Ignition (Diesel)							
Euro 1 †	1992.07	2.72 (3.16)	-	0.97 (1.13)	-	0.14 (0.18)	
Euro 2, IDI	1996.01	1.0	-	0.7	-	0.08	-
Euro 2, DI	1996.01[a]	1.0	-	0.9	-	0.10	-
Euro 3	2000.01	0.64	-	0.56	0.50	0.05	-
Euro 4	2005.01	0.50	-	0.30	0.25	0.025	-
Euro 5a	2009.09[b]	0.50	-	0.23	0.18	0.005[f]	-
Euro 5b	2011.09[c]	0.50	-	0.23	0.18	0.005[f]	6.0×10^{11}
Euro 6	2014.09	0.50	-	0.17	0.08	0.005[f]	6.0×10^{11}
Positive Ignition (Gasoline)							
Euro 1 †	1992.07	2.72 (3.16)	-	0.97 (1.13)	-	-	-
Euro 2	1996.01	2.2	-	0.5	-	-	-
Euro 3	2000.01	2.30	0.20	-	0.15	-	-
Euro 4	2005.01	1.0	0.10	1	0.15	-	-
Euro 5	2009.09[b]	1.0	0.1[d]	-	0.06	0.005[e,f]	-
Euro 6	2014.09	1.0	0.1[d]	-	0.06	0.005[e,f]	6.0×10^{11} [e,g]

Notes:
† Values in brackets are conformity of production (COP) limits
a. until 1999.09.30 (after that date DI engines must meet the IDI limits)
b. 2011.01 for all models
c. 2013.01 for all models
d. and NMHC = 0.068 g/km
e. applicable only to vehicles using DI engines
f. 0.0045 g/km using the PMP measurement procedure
g. 6.0×10^{12} 1/km within first three years from Euro 6 effective dates

Organic compounds, unburned or partially burned hydrocarbons (HC) emissions are regulated as either Total Hydrocarbons (THC), Non-Methane Hydrocarbons (NMHC) or Non-Methane Organic Gases (NMOG) and can arise from a number of sources including:

- Flame quenching at the combustion chamber wall
- Trapped mixture in crevice volumes later expelled during the exhaust process
- Absorption and desorption of fuel hydrocarbon components into the thin oil film on the combustion chamber walls
- Before and after the combustion process

Hydrocarbons react in the presence of oxides of nitrogen in photochemical reactions in the formation of ozone and smog. They are also considered toxic and elements are carcinogenic.

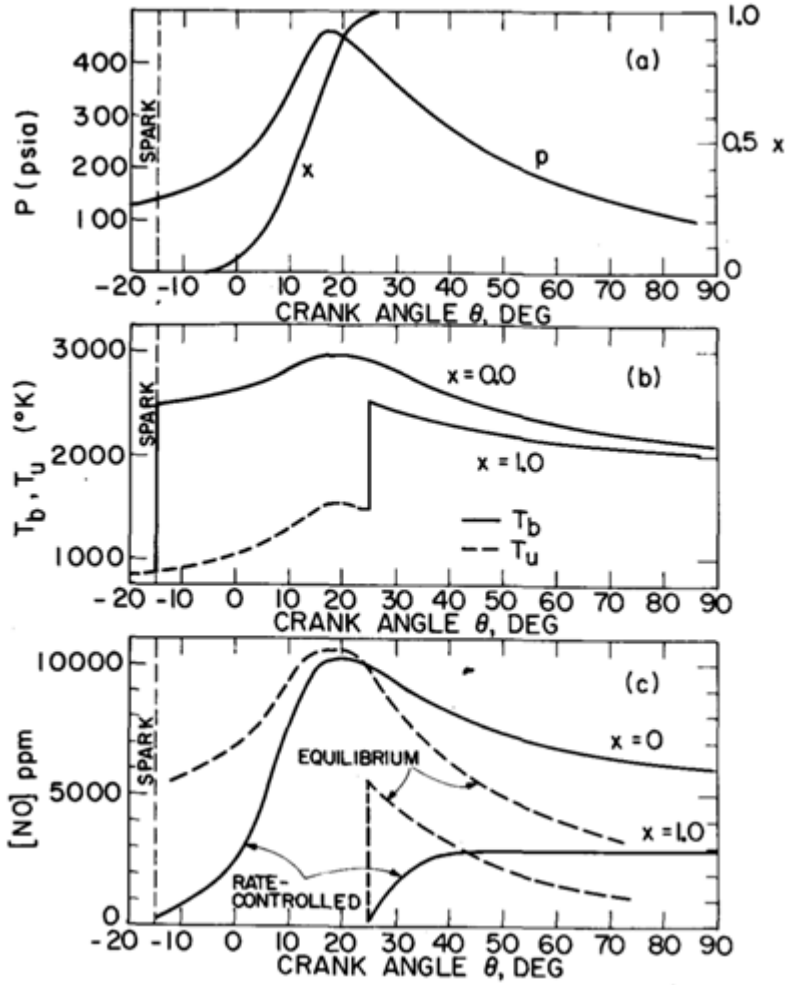

Figure 1.1 – Illustration of SI engine NO formation: (top) measured cylinder pressure and calculated mass fraction burned; (middle) calculated temperature of unburned gas T_u and burned gas T_b in early- and late-burning elements; (bottom) calculated NO concentrations in early- and late-burning elements for rate-controlled model and at equilibrium, taken from Komiyama & Heywood (1973)

Particulate matter (PM), generally consisting of combustion generated solid carbon particles, result from agglomeration or cracking and typically include a proportion of absorbed organic compound. Particulate matter pollution has been linked to harmful impact on both public health and public welfare. Environmental effects include visibility impairment due to fine particles, environmental damage due to particle settling causing increased acidity and changes in nutrient balance, aesthetic damage to stone and other materials through staining. The impact on human health is of particular concern for fine particles that are able to penetrate deep into the human lung. Numerous scientific studies have shown links between particulate matter pollution and premature death in people with heart or lung disease, nonfatal

heart attacks, irregular heartbeat, aggravated asthma, decreased lung function and increased respiratory symptoms. The introduction of direct injection to the gasoline engine and the increased flexibility of combustion strategy has meant their PM emissions are no longer insignificant (when compared to earlier Port Fuel Injection engines) and has led regulatory bodies to begin imposing emissions limits on particulate mass, and more recently particulate number, emissions (EPA, 2014b; DieselNet, 2007; USGPO, 2014b).

Carbon dioxide (CO_2) emissions are increasingly being placed in the global spotlight due to its contribution to greenhouse gases (GHG) and its association with global warming. The area of anthropogenic climate change is an area of continual research due to the tight connection between the remaining oil reserves, increases in oil demand, technology evolution and their impact on future CO_2 concentration and global mean-temperature increase (Chiari & Zecca, 2011; Höök & Tang, 2013). This has long been recognised by different governments and legislators worldwide and led to a number of legislations being enforced with a view to reducing vehicle emissions and stimulating technology development. The Corporate Average Fuel Economy (CAFE) regulations in the U.S., first enacted in 1975, require vehicle manufacturers to comply with fuel economy standards set by the Department of Transport. CAFE fuel economy valves are calculated using both city and highway test results and a weighted average of vehicle sales. In 2011, the CAFE standards were redefined, now as a function of the vehicle size (EPA, 2014a; ARB, 2012; USGPO, 2014a). In 2009 U.S. President Barack Obama proposed a new national fuel economy program to cover model year 2012 to 2016 that would increase the required average fuel economy standard from 25 miles per US gallon to 35.5 miles per U.S. gallon. In 2011, U.S. President Barack Obama announced an agreement to cover model years 2017 to 2025 that would increase the required average fuel economy standard to 54.5 miles per U.S. gallon (NHTSA, 2011). In 2009, European Union legislation adopted mandatory CO_2 emissions reduction targets. In this legislation, the maximum fleet average CO_2 for all new cars is 130g/km, being phased in between 2012 and 2015. A further fleet average CO_2 emission reduction to 95g/km is proposed for 2020 though this is yet to be approved through European Parliament and Council to become law. This European directive also provides additional credits for manufacturers producing vehicles with extremely low CO_2 emissions (<50g/km) to assist them in reducing their fleet averages (EC, 2014). The impact of the increasingly stringent CO_2 emissions standard across world markets is a significant development challenge for vehicle original equipment manufacturers (OEMs).

Another significant motivator in the development of next generation ICE's is the growing consumer requirement for fuel to power vehicles, and as a consequence for highly fuel efficient vehicles. Figure 1.2 (a) taken from Brandt, Millard-Ball, Ganser, *et al.* (2013) highlights this point by showing a prediction for the rise in energy demand for transport energy split by sector. There is a consensus amongst geologists that world production of oil will peak at some point in the future but this point in time is still of much debate. Leder & Shapiro (2008) completed a study using data from International Energy Agency, the U.S. Department of Energy, the Association for the Study of Peak Oil and Gas, and petroleum industry sources and concluded that oil production will peak within the next 5 years. Other sources, including Tsoskounoglou, Ayerides & Tritopoulou (2008), Sorrell, Speirs, Bentley, *et al.* (2010) and Brandt, Millard-Ball, Ganser, *et al.* (2013) conclude that the world peak in oil production will peak before 2040 and likely much sooner. Sorrell, Speirs, Bentley, *et al.* (2012) discusses some of the difficulties associated with predicting peak oil production and attributes it in part to how initial estimates in recoverable resources from an individual field tend to grow over time. IMechE (2013) suggests that based on current estimates of the world's main oil fields, reserves will be sufficient to meet present rates of consumption for 40 years, but consumption rates are still rising and conventional oil demand is predicted to decline around the year 2035 as shown in Figure 1.2 (b) (Brandt, Millard-Ball, Ganser, *et al.*, 2013).

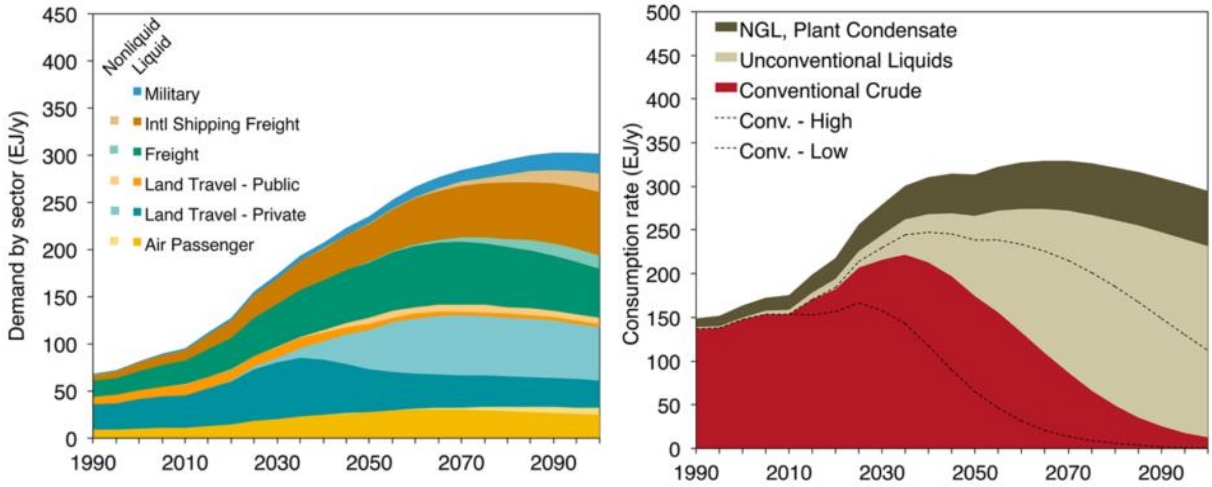

(a) (b)

Figure 1.2 – (a) Demand for transport energy and (b) Fuel consumption rate, taken from Brandt, Millard-Ball, Ganser, *et al.* (2013)

Of course, the effect of rising demand with increasing scarcity and cost of extraction of the remaining resources, acts to drive an increase in oil price and thus the cost of fuel for transportation. Based on the AA fuel price report TheAA (2014), the UK average cost of regular (95 octane) gasoline has increased from 89.4p/litre in January 2006 to 131.2p/litre in December 2013. This in turn has generated a large consumer demand for more fuel efficient vehicles.

1.1.2 Advances in GDI Engine Development

The purpose of this section is to present the development and progress of the GDI engine.

The GDI engine started life in aircraft applications. Invented by the French inventor Leon Lavavasseur in 1902 and applied in one of the first V8 aero engines (Hartmann, 2007). Post First World War, the first example of a GDI engine was the Hesselman engine in 1925 where an ultra-lean late burn injection strategy was used, with the engine started on gasoline but then switched to diesel or kerosene (Olsson, 1987; Lindh, 1992). GDI engines were used extensively during the Second World War to power high output aircraft made in Germany, the Soviet Union and the US. The first automotive application of a GDI engine was developed by Bosch and introduced by Goliath and Gutbrod in 1952 which used a high pressure injection system from a diesel engine with an intake throttle for load control. These engines are classed as ‘first generation’ GDI engines.

The energy crisis of the early 1970’s drove research into more fuel efficient engines and the development of ‘second generation’ GDI engines. One piece of research was conducted by the American Motors Corporation to develop a ‘Straticharge Continuous Fuel Injection’ (SCFI) system where the conventional SI ICE was modified to have two separate fuel systems with different injection pressures controlled as a function of the engines airflow but the engine lacked success due to mechanical fuel control problems (Peery, 1975; Weiss, 1979). In the late 1970s, a number of GDI systems were proposed including the MAN-FM system which utilised jet-wall interaction and film evaporation to achieve charge stratification and the Ford Motor Company developed ‘PROCO’ engine, a stratified-charge GDI engine utilising a high-pressure pump and spark plug positioned in the fuel spray periphery to generate stratification. The latter design was unsuccessful for a number of

reasons: electronic control technology being too immature, fuel system components too expensive, the lean combustion regime generated by the stratified-charge strategy generated high NO_x which was soon to be in-excess of the impending EPA regulations and Ford were cautious of committing to expensive technology in a V8 engine during economic instability – the late 1970s was the time of the second gas crisis in the U.S. (Time, 1979). Another development of note was the stratified charge concept that utilised a pre-chamber for injection and ignition in a relatively rich mixture where the flame then propagates into the lean mixture in the main chamber (Pischinger & Klocker, 1974). All developments up to this point had one common disadvantage; a lack of controllability of the injection strategy as a function of engine load. Unable to avoid significant piston or liner spray impingement at certain conditions, these concepts encountered significant problems including fuel dilution, increased engine out emissions and increased fuel consumption. These were unavoidable until improvements in fuel injection system technology were available.

Since the early 1990's, interest and development of the GDI engine has been reborn and with the new generation of GDI engines classed as 'third generation'. The introduction of third generation GDI engines into production has largely been led by the Japanese manufacturers of Mitsubishi, Nissan and Toyota but there are now examples of GDI technology being applied by a large number of automotive manufacturers.

Mitsubishi were the first to introduce a GDI engine into the Japanese market in 1996 in the form of a 1.8L inline-four. Figure 1.3 illustrates the three distinct combustion modes as a function of engine speed and load.

A wall-guided injection strategy was used, with the spray being directed back up towards the spark plug by the rising piston and emphasised tumble charge motion. A dual catalyst was needed to control pollutant emissions: a conventional platinum catalyst for stoichiometric operation and pure iridium catalyst for lean operation. Mitsubishi reported significant fuel economy improvements when compared to their Port Fuel Injection (PFI) engine on Japanese urban test cycle with improved power, acceleration and volumetric efficiency as a consequence of improved port design, increased compression ratio and in-cylinder charge cooling due to spray atomisation effects (Zhao, Lai & Harrington, 1999; Iwamoto, Noma, Nakayama, *et al.*, 1997).

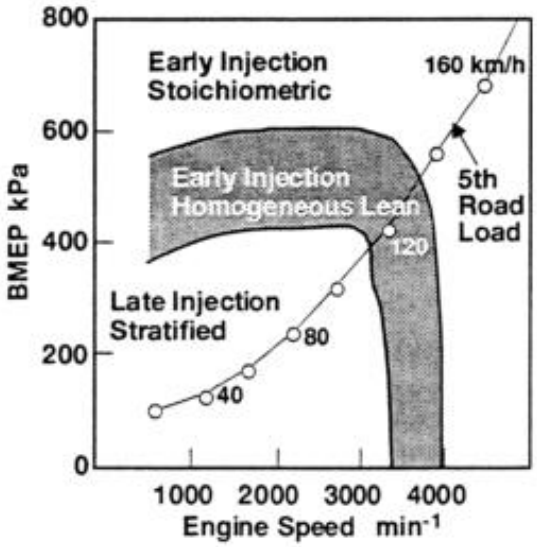

Figure 1.3 – The Mitsubishi GDI Control Map - taken from Iwamoto, Noma, Nakayama, *et al.* (1997)

Nissan were the next manufacturer to bring a GDI engine to production in the Japanese market in 1997. Utilising a similar combustion strategy to the Mitsubishi engine but with a shallow combustion bowl and swirl dominated in-cylinder charge motion. This provided improved combustion efficiency during early injection homogeneous combustion operation however does compromise the accuracy of spray targeting during late injection stratified lean operation. This was reportedly mitigated through optimised injector spray design (Zhao, Lai & Harrington, 1999).

Toyota brought a production GDI engine to the Japanese market in 1998 which was implemented in a number of vehicle models and is shown in Figure 1.4(a). Toyota also utilised a swirl dominated in-cylinder charge motion, actively controlled by a Swirl Control Valve (SCV) but employed a unique and complex piston bowl geometry for spray and mixture control. The piston bowl geometry, shown in Figure 1.4(c), comprised of three key features as depicted in Figure 1.4(b). First, an involute geometry to direct the vaporised fuel towards the spark plug. Second, an area designed as a mixture formation area positioned upstream of the spark plug. Third, a wider zone designed as the combustion space with geometry promoting rapid mixing enhanced by the port generated swirl motion. The engine also utilised variable cam phasing system on the intake valve to further enhance swirl motion at light loads (Zhao, Lai & Harrington, 1999).

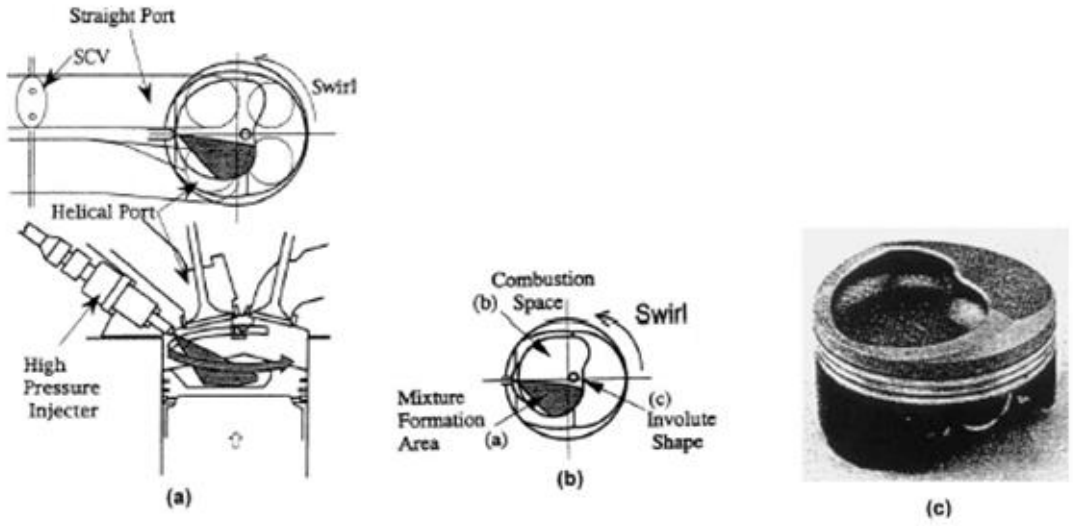

Figure 1.4 – Combustion chamber configuration of the Toyota GDI – taken from Nohira (1997)

In later years, GDI engines were brought to production by an increasing number of automotive manufacturers in Japanese, European and US markets. Companies such as Renault, VAG (including Volkswagen, Audi, and later Seat and Skoda), Ford, BMW, General Motors, Isuzu, Mazda, Mercedes-Benz, Ferrari and Jaguar Land Rover all releasing GDI engines into production in various markets and vehicle segments between 1998 to present. Technology developments have centred around injector spray characteristics (including spray pattern and injection pressure) and combustion chamber geometry and thus mixture control techniques.

The combustion operating mode of GDI engines are typically defined by the degree of in-cylinder charge stratification and the strategy used to achieve this.

Homogeneous-charge direct-injection engines tend to use a centrally mounted spark plug with centrally or side mounted injector. Fuel is injected early in the intake stroke during high levels of in-cylinder charge motion to promote mixing and obtain an almost homogenous mixture within the combustion chamber at the point of spark timing. Advantages over traditional PFI homogeneous-charge engines include:

- Eliminated transient dwell time and reduced unburned hydrocarbons as a consequence of over fuelling during transient events

- Reduced UHC during cold start due to injection into a higher pressure and temperature environment when compared to PFI where fuel is injected into low pressure and temperature environment of the intake port and back of the intake valve
- Increased power and fuel economy and reduced knock propensity as a consequence of the charge cooling effect of injecting cold fuel into the high pressure high temperature combustion chamber. The reduction in knock propensity also allows higher compression ratios to be utilised for increased in-cylinder expansion ratios or increased boosting.

Stratified-charge direct-injection engines involve creating a globally lean in-cylinder fuel-air mixture but with high levels of stratification around the spark plug at the point of ignition to ensure stable flame kernel development. To obtain charge stratification, three spray guiding methods have evolved as shown in Figure 1.5; wall-guided, air-guided and spray-guided, each driving a different combustion system design strategy.

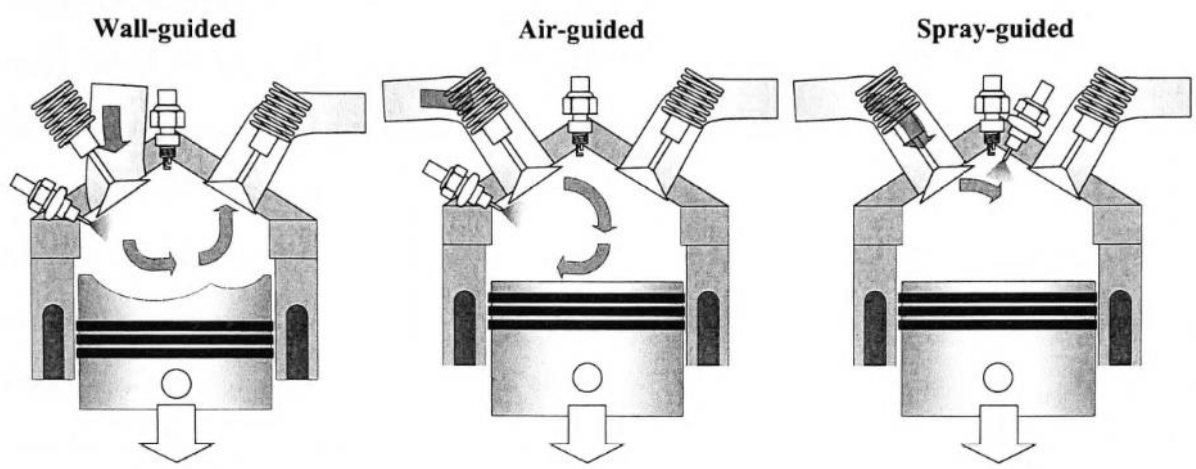

Figure 1.5 – Spray guiding strategies - taken from Ma (2006)

Some of the first stratified-charge GDI engines used wall-guiding to produce the stratified charge around the spark plug at the point of ignition timing. A heavily contoured piston bowl was used to direct the spray up towards the spark plug, with injection late in the compression stroke. As fuelling increases with load requirements, heavy piston wetting and consequential soot emissions limit stratified-charge operation. Therefore maintaining power density currently requires switching to a homogeneous stoichiometric charge operating mode at higher engine loads. The addition of a 'mixed mode' or homogeneous lean mixture operating mode is also sometimes incorporated to improve combustion stability when switching between stratified lean and homogeneous stoichiometric modes. This also provides fuel

consumption benefits associated with globally lean in-cylinder mixtures for higher speed and load ranges within the engine duty cycle.

Air-guided stratified-charge DI engines utilise a heavily induced tumble in-cylinder bulk air motion to guide the fuel spray up towards the spark plug. A contoured piston is often used, as seen in wall-guided systems, but intake port geometry tuning is also utilised to increased tumble motion and reduce fuel spray impingement on the piston.

Spray-guided stratified-charge DI engines utilise a centrally mounted injector, closely mounted to the spark plug electrodes. In this method, the spray cloud is positioned such that the fuel-air mixture at the spark plug is close to stoichiometry but with high levels of stratification away from the spark plug position. The close proximity of injector and spark plug promote a compact spray cloud that can be designed with reduced penetration, reducing the opportunity for impingement, and improved combustion phasing promoting increased burn rates and reduced cyclic variability and soot and UHC emissions. Disadvantages of the close proximity of the injector and spark plug include: high in-cylinder flow velocities (and associated fluctuations) at the spark plug, fuel impingement on spark plug electrodes and potential ignition problems, large spatial fuel-air mixture gradients drive the need for high levels of spray and in-cylinder flow-field repeatability to avoid misfire events.

The variety of spray guiding methods has also driven a number of different injector spray designs including; both inwardly and outwardly opening needle single exit pressure-swirl injectors, air-assisted pressure-swirl designs, multi-hole VCO (Valve Covered Orifice) nozzle injectors similar to those found in diesel injection systems and more recently piezo-electrically actuated outwardly opening pintle injectors.

Spray impingement in DI engines has typically been reduced by the use of increased injection pressure to produce finer, more atomised sprays. In contrast to PFI injection systems with SMD equivalent to ~120µm, GDI injectors are an order of magnitude lower in the region of ~15µm. Whilst increased injection pressure increases atomisation and reduces droplet mass, it also increases droplet velocities and hence can cause a net increase in spray momentum and still cause impingement issues. The resultant penetration is dependent on injection timing, spray characteristics and in-cylinder conditions. Further progress in reducing spray impingement has been enabled with non-symmetric spray patterns, variable injection timing and multiple injections per cycle to reduce spray penetration of each injection event.

Improvements and optimisation of the fuel system has been critical to the progress of the GDI engine.

The increasingly stringent fleet average CO_2 legislation has also driven many manufacturers to investigate coupling GDI with other technologies for further fuel efficiency improvements. GDI engines coupled with a reduction of an engine's swept volume ('downsizing') and forced induction to retain specific power output has been of significant development in Europe for a number of years now and is growing among automotive manufacturers in the US and Japanese markets. Lake, Stokes, Murphy, *et al*. (2004) of Ricardo plc produced a noteworthy paper presenting a number of turbocharging concepts applied to a GDI engine as a means of meeting future fleet average CO_2 requirements whilst controlling the octane requirement to avoid end gas autoignition or knock. The concepts included: lean operation at full load with high compression ratio (CR), cooled exhaust gas recirculation (EGR) for mixture dilution, miller cycling to reduce the effective compression ratio and dual injection strategies. Lotus Cars have also investigated spray-guided homogeneous GDI engines equipped with a fully variable valve train system as a means of reducing nitrous oxides to levels that would remove the need for a NO_x trap, hence providing compatibility with high sulphur fuels (Drake & Haworth, 2007; Zhao, Lai & Harrington, 1999).

1.1.3 Current GDI Engine Research Challenges

As discussed previously, the homogeneous GDI engine offers a number of advantages over gasoline PFI engines but still a number of research and development challenges remain in order to further exploit their advantages. The remainder of this section will provide an overview of some of the current research challenges that will be the subject of the research presented in this thesis.

1.1.3.1 Cycle-to-Cycle Variability

Cycle-to-cycle variability (CCV) in ICE's has long been a topic of research interest. Ozdor, Dulger & Sher (1994) completed a literature survey of influences on cyclic variability and

suggested that up to 10% improvement in fuel consumption would be achievable if it was possible to eliminate cyclic variability entirely. There is also a significant indirect impact whereby manufacturers have to pursue sub-optimal engine design to ensure they meet certain design requirements including: retarded timing and reduced compression ratio to avoid abnormal combustion phenomenon, lower than limit emissions output or the use of additional after-treatment systems to ensure the engine meets emissions legislation, and less aggressive combustion strategies to meet consumer drivability needs. Thus a reduction in CCV would enable an engine to operate at average running conditions that are closer to the limits of emissions legislation, allowing reductions in fuel consumption, whilst meeting or exceeding driveability requirements. The challenge lies in that the origins and relative importance of the causes of CCV are not fully understood and many are strongly coupled which provides an added level of complexity to understanding them. Ozdor, Dulger & Sher (1994) proposed that cyclic variability could be split in to four main areas:

- Mixture composition
- Cyclic cylinder charging
- Spark and spark plug
- In-cylinder mixture motion

The main causes of CCV due to the in-cylinder gas flow and mixture field can be summarised as follows from the works of Ozdor, Dulger & Sher (1994), Vermorel, Richard, Colin, *et al.* (2009) and Heywood (1988):

1.1.3.1.1 Variations in the In-Cylinder Gas Flow

Since the flow within the cylinder of an ICE is fully turbulent, the stochastic nature of turbulence means that CCV is inevitable and likely to be one of the largest sources of CCV. This also means that by nature, CCV due to flow turbulence cannot be eliminated completely, though it can be understood and minimised through engine designs that control the flow structure as closely as possible.

The turbulence intensity, particularly in the spark plug vicinity at the point of spark timing has a significant impact on the initial kernel growth rate and as a consequence the CCV (with larger time taken for kernel development exhibiting increased CCV). Increased turbulence

intensity acts to increase the kernel development due to stretching of the flame front up to a certain optimum value, dependent on the local in-cylinder conditions, whereby after excessive flame stretch causes flame quenching. The importance of the local flow scale is dependent on the mean flow conditions. With a small mean flow, any CCV in the large length scales will have a large effect on the direction of convection of the initial flame kernel. In contrast, if a significant mean flow is present and consistently convects the kernel in a particular direction, CCV in the large scale structures will have a much smaller impact and variations in the small scales will be the dominant factor in influencing the subsequent combustion process.

The mean flow velocity in the spark plug vicinity has a significant impact on the early stages of flame development. It acts to lengthen the discharge channel and increase electrical energy transferred to the flame kernel during the spark breakdown phase. It acts to convect the flame kernel away from the electrodes during the flame kernel development stage which reduces heat losses and increases the rate of flame kernel growth (Pischinger & Heywood, 1990). Whilst the initial kernel development phase only accounts for 1-2% of the total MFB, the phase contributes significantly (approximately 30%) to the total combustion cycle duration and hence CCV in the mean flow velocity in the near spark plug region can contribute significantly to the overall CCV of the combustion process. The location of the centre of the initial flame kernel also impacts the flame speed, with kernel centres closer to the centre of the combustion chamber having faster burn rates later in the cycle and centres closer to a combustion chamber wall having slower burn rates later in the cycle. Hence variations of the initial flame kernel centre due to variations in the mean flow velocity also contribute to CCV in the overall combustion process.

Since the large scale bulk gas motions are also turbulent, they are also subject to CCV and in particular, influence the breakup and atomisation processes and spatial variations in the fuel-air mixture, along with the local flow conditions in the vicinity of the spark plug at the point of ignition. The large scale flow structures of tumble, swirl or squish, are predominantly a function of the engine design, specifically the intake manifold and port geometry, valve geometry and positioning, and combustion chamber geometry, and hence it can be inferred that engine design also has a large influence on the CCV present.

1.1.3.1.2 Variations in the In-Cylinder Mixture Field

CCV due to variation in the in-cylinder mixture can be broken down into four different areas:

- The overall mixture equivalence ratio is found to influence CCV through the laminar burning speed where the fastest laminar burn speed is seen with stoichiometric mixtures. Thus any variations in overall mixture equivalence ratio from stoichiometry yield a reduction in laminar burn velocity and a subsequent increase in CCV. This is due to the magnitude of CCV in the flame development and subsequent flame propagation processes, reducing as the burning rate increases.
- Spatial variations in the local equivalence ratio, and subsequent mixture inhomogeneity, near the spark plug at the point of ignition timing will have a significant impact on initial kernel development, whereas spatial variations in mixture equivalence ratio further afield will impact the laminar flame speed during the flame propagation phase.
- CCV in the droplet breakup mechanisms and subsequent atomisation process yielding variations in the overall and local mixture equivalence ratio.
- Variations in the characteristics of fuel impingement, in terms of its likelihood, the impingement regime, and any subsequent re-introduction of droplets into the in-cylinder flow field either via surface evaporation, scraping via the piston rings or breakup over a sharp edge.

CCV in the in-cylinder mixture due to the above processes can predominantly be attributed to either variations in-cylinder flow field or in the fuel injection process itself, e.g. via variation in the level of cavitation or turbulence within the injector nozzle.

CCV in both the filling and scavenging of the cylinder is also present and acts to vary the amount of trapped mass at the start of a cycle and the residual gases that remains for the subsequent cycle. Since residual gases act as a diluent, variations in mixture equivalence ratio cause a subsequent variation in laminar burn velocity and thus CCV.

1.1.3.2 Mixture Heterogeneity

The use of mixture heterogeneity or stratified-charge DI engines have been of interest since the inception of GDI due to the potential fuel saving associated with overall lean operation and elimination of throttling losses. A number of issues with commercially viable stratified-charge GDI engines have arisen due to the characteristics of this combustion mode (Drake & Haworth, 2007; Zhao, Lai & Harrington, 1999):

- Stratified operation is typically limited to part load conditions due to increased combustion instability and smoke associated with operating at high loads and with a highly stratified mixture
- Large increases in UHC and PM when utilising a wall- or air-guided injection strategy
- High levels of combustion stability sensitivity and potential for intermittent misfires due to spray and in-cylinder flow field cyclic variability and spark plug-fuel spray geometric sensitivity.
- Fuel spray piston impingement due to the proximity of the piston at the point of injection timing, requiring careful injection strategy management and use of fast actuating injectors for multiple injection events to provide sufficient fuel quantity for engine load requirements whilst minimising spray penetration and still maintaining adequate mixture stratification.

1.2 RESEARCH OBJECTIVES

The focus of this research was to validate and then use a detailed 3D-CFD model to investigate the physical phenomena of the in-cylinder flow field and fuel injection processes in a GDI engine, with a view to furthering scientific knowledge and providing a contribution towards the solution of the current challenges in these areas.

The following bullet points provide the objectives of this research:

- Using available experimental data, complete a detailed validation of the in-cylinder flow field in a GDI engine using a detailed 3D-CFD model with both a Reynolds-

Averaged Navier-Stokes (RANS) and Large Eddy Simulation (LES) turbulence modelling approach.

- Using available experimental data, complete a detailed validation of the fuel injection process in a GDI engine modelled using a Lagrangian Discrete Droplet Model (DDM), using both a RANS and LES turbulence modelling approach.
- Investigate the characteristics of the in-cylinder flow field, including its three-dimensional nature and a number of highly transient flow structures including intake valve jet flapping.
- Investigate and characterise the in-cylinder flow field anisotropy through the intake and compression strokes up to the point of spark timing.
- Use the statistical technique of Proper Orthogonal Decomposition (POD) to quantitatively characterise the variation in turbulent flow structures through the cycle, quantify and investigate cyclic variability, and help assess the level of statistical convergence of the ensemble-average solution.
- Complete a detailed investigation of spray plume impingement on the intake valve, cylinder liner and piston crown using both a single- and multi-component fuel surrogate to investigate how numerical models can be used to accurately assess spray plume impingement and liquid film formation.
- Investigate cyclic variability of the impingement process due to continuous-phase turbulence using a DDM and LES turbulence modelling approach.
- Investigate the use of numerically derived turbulence characteristics to infer the resultant premixed turbulent combustion process using combustion regime diagrams.

1.3 THESIS STRUCTURE

Chapter 1 has presented the research background and motivation, particularly with respect to the development drivers, technological advances and research challenges of the GDI engine. It has also presented the objectives of this research.

Chapter 2 presents a literature review exploring the physical processes of the in-cylinder flow field and fuel injection processes, and the development and progression of multi-dimensional

computational fluid dynamics techniques and associated physical sub-models for modelling these processing within engines.

Chapter 3 presents the engine and numerical model. First, the chapter introduces the experimental engine, a single cylinder optical research engine that was modelled for the purpose of this research, including details of the engine configuration and operating configuration. Second, the chapter presents the numerical model and its validation against experimental results acquired from a past experimental research project. First, the sub-section presents the computational domain and methodology, and then follows with the characterisation and validation of the numerical model which is divided into two sub-sections; 1) validation with respect to the in-cylinder flow field and, 2) validation with respect to the fuel injection process. In this research both a RANS and a LES approach to modelling turbulence have been used. This allowed a decision to be made of the most appropriate modelling approach (predominantly a function of the compromise between computational fidelity and cost) for the physical process being investigated. Hence, sections on the validation of the in-cylinder flow field and the fuel injection process are further sub-divided into sections using either a RANS or LES turbulence model.

The following three chapters, *Chapters 4-6*, present the results from a number of numerical analyses using the models presented in *Chapter 3*.

Chapter 4 presents analyses into the in-cylinder flow field including investigations on flow three dimensionality, intake valve jet flapping, flow anisotropy, and the use of POD for characterising turbulent flow structures and cyclic variability.

Chapter 5 presents analyses into the fuel injection process including investigations on fuel impingement and liquid film development, mixture field characteristics, and the interactions between in-cylinder turbulence and the fuel injection event.

Chapter 6 presents analyses utilising the turbulence predictions from earlier chapters, along with turbulent premixed combustion regime diagrams, to investigate the characteristics of the resultant combustion event.

Finally, *Chapter 7* presents the conclusions from the research presented in this thesis, the contributions to scientific knowledge, and recommendations for further research in this area.

CHAPTER 2

LITERATURE REVIEW

"Imagination is more important that knowledge."

– Albert Einstein

2.1 INTRODUCTION

The GDI engine is comprised of a number of physical processes that are both complex and have high levels of interaction. The use of numerical methods to model the physical processes occurring within ICE's has been prolific since the early 1970's. Over this time, a large number of techniques have evolved, each with their own advantages and disadvantages but driven by the following factors:

- Computational cost, i.e. what are the time demands of the associated modelling tasks including pre-processing, numerical solution and post-processing
- Representativeness of the model to the physical process that is being modelled
- Our understanding of, and capability to represent, the physical process itself

For the development of models within the ICE environment, an understanding of the physical processes occurring is required. Figure 2.1 illustrates the key areas when modelling ICE's.

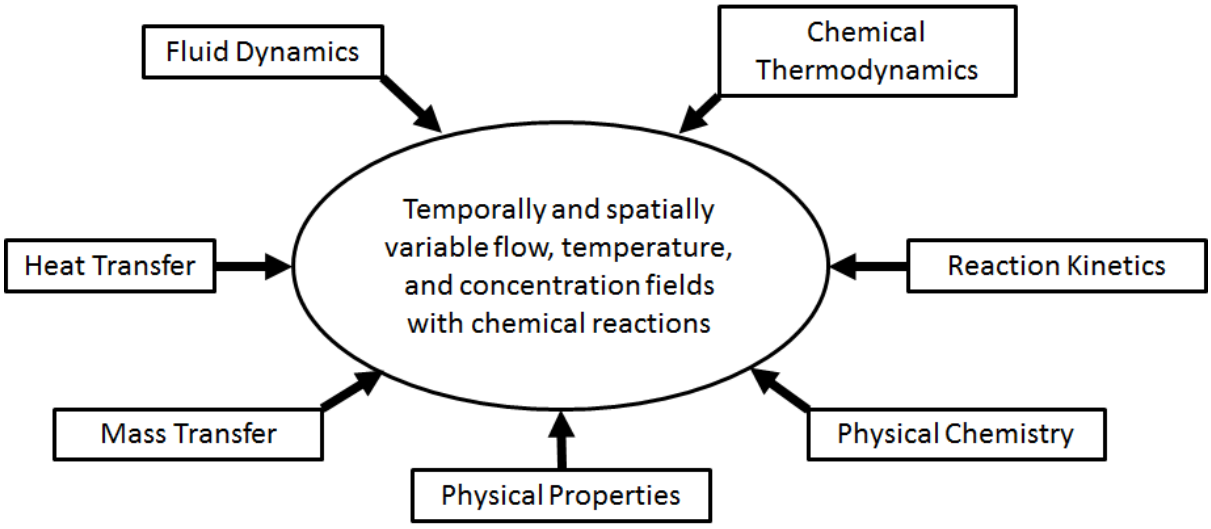

Figure 2.1 – Physical processes important for numerical simulations of ICE's - reproduced from Merker, Schwarz & Teichmann (2012)

This literature review will focus on the physical processes of the in-cylinder flow field and fuel injection processes, and the development and progression of multi-dimensional computational fluid dynamics techniques and associated physical sub-models, applied to numerically modelling them within the GDI engine.

Computational Fluid Dynamics (CFD) simulation currently represents the highest order of fidelity of the numerical tools available for modelling internal combustion engines. CFD models are based on the governing equations of fluid flow that represent the fundamental conservation laws of physics, as described below for a compressible Newtonian fluid and omitting source terms.

The *mass continuity* equation is defined by equation (2.1):

$$\frac{\partial \rho}{\partial t} + \frac{\partial (\rho u_i)}{\partial x_i} = 0 \tag{2.1}$$

The use of Newton's second law forms the *momentum equations* defined for each directional component by equation (2.2):

$$\frac{\partial(\rho u_i)}{\partial t} + \frac{\partial(\rho u_j u_i)}{\partial x_j} = -\frac{\partial p}{\partial x_i} + \frac{\partial \tau_{ij}}{\partial x_j} \tag{2.2}$$

From the first law of thermodynamics, the *energy equation* is defined by equation (2.3):

$$\frac{\partial(\rho E)}{\partial t} + \frac{\partial(\rho u_j E)}{\partial x_j} = \frac{\partial}{\partial x_j}\left(k\frac{\partial T}{\partial x_j}\right) + \frac{\partial(u_i \tau_{ij})}{\partial x_j} \tag{2.3}$$

Where E is the sum of the internal energy and the kinetic energy.

When combined with the equations of state, these governing equations, which are classified as partial differential equations (PDE's), are able to define the seven physical attributes that fully define a single phase single component fluid: pressure, temperature, density, velocity (three components) and energy.

In a viscous fluid, the momentum equations include terms to define the state of stress of a fluid element, which is defined in terms of the pressure and nine viscous stress components, six of which are independent in isotropic fluids (Schlichting, 1968). It is useful to introduce a model for the viscous stresses τ_{ij}, relating the viscous stresses to the fluid motion as a function of the local deformation rate or strain rate. In three-dimensional flows the local rate of deformation is composed of the linear deformation rate and the volumetric deformation rate. The linear deformation rate is expressed as a function of the dynamic viscosity μ and volumetric deformation rate expressed as a function of the second viscosity λ. For Newtonian fluids, the viscous stress is assumed to vary linearly with rate of strain. Employing this simplification, nine equations for the viscous stresses are formed, but is shown in tensor notation in equation (2.4), and can be substituted back into the governing equations (equations (2.2) and (2.3)), providing the so-called Navier-Stokes (N-S) equations which are the foundations of all modern CFD codes.

$$\tau_{ij} = 2\mu S_{ij} + \lambda\left(\frac{\partial u_k}{\partial x_k}\right)\delta_{ij} = 2\mu S_{ij} - \frac{2}{3}\mu\left(\frac{\partial u_k}{\partial x_k}\right)\delta_{ij} \tag{2.4}$$

Where:

The Stoke's hypothesis is used to relate λ to μ: $\lambda + \frac{2}{3}\mu = 0$

S_{ij} is the strain rate tensor, $S_{ij} = \frac{1}{2}\left(\frac{\partial u_i}{\partial x_j} + \frac{\partial u_j}{\partial x_i}\right)$

δ_{ij} is the Kronecker delta and can be equal to unity or zero as shown in equation (2.5):

$$\delta_{ij} = \begin{cases} 0 \; if \; i \neq j \\ 1 \; if \; i = j \end{cases} \tag{2.5}$$

The direct analytical solution to these PDE's produces a continuous description of the flow in space and time but due to the difficulty of solving the PDE's in this manner it is only applied to very simple flow problems. All numerical solutions rely on a grid to discretise the PDE's at discrete points in the computational domain. Whilst there are many numerical methods for solving the PDE's, three methods in particular have seen most use.

The finite difference (FD) method is the oldest technique and was among the first techniques applied to the numerical solution of PDE's, first being applied by Euler in 1968. The FD method is directly applied to the differential form of the governing equations, employing a Taylor series expansion for the discretisation of the derivatives of the flow variables. Whilst this method has obvious simplicity, it is difficult to apply to unstructured or non-Cartesian grids without introducing numerical errors and hence it is infrequently used in current applications of CFD techniques to complex geometries.

The finite volume (FV) method employs the integral form of the N-S equations and was first employed by McDonald (1971) for the simulation of 2D inviscid flows. The FV method discretises the governing equations by dividing the computational domain into a number of arbitrary control volumes. The accuracy of the spatial discretisation depends on the scheme used to evaluate the fluxes across the volume surface. The advantages of this method include ease of ensuring satisfaction of the conservation principle (since flux out of one volume must be equivalent to the flux into another volume) and its ability to be applied to unstructured and complex grids without introduction of numerical errors.

The finite element (FE) method was originally employed for structural analysis, introduced by Turner, Clough, Martin, *et al.* (1956) but it wasn't until the early 90's that the FE method begun to be used to solve the N-S equations. The FE method uses a triangular or tetrahedral grid and is thus unstructured in nature. Depending on the level of accuracy required, a number of points or nodes are defined, either at cell boundaries or within the cell itself, which

define where the PDE's are solved. The FE method has the benefit of its integral formulation and use of unstructured grids, both of which are advantageous for more complex flow problems, but the disadvantage of having a very rigorous mathematical foundation which drives a much higher computational effort. This is ultimately the reason why the FV method has seen more success in the application of N-S equations to complex flows and geometries and is the methodology used by the majority of CFD codes available today.

One of the first to develop a numerical code based on the solution of the N-S equations via the FV methods and apply it to in-cylinder conditions was Gosman and he contributed a number of papers in the late 70's and early 80's, such as Gosman & Johns (1978) and Gosman, Tsui & Watkins (1984), that are the back-bone of modern CFD codes today.

A complete review of the available solution methods is out of scope for this review but the reader is referred to the substantial amount of literature available on the schemes available for the solution of the N-S equations via the FV method.

2.2 TURBULENCE

2.2.1 Turbulence Characteristics

At low Reynolds numbers flows are quasi-laminar, but above a critical Reynolds number Re_{crit}, a series of processes take place where the flow transitions to a turbulent flow and the flow is characterised as; unsteady, random, chaotic, three dimensional, non-repeatable, exhibit intermittency in both space and time, have high levels of vorticity, and have a wide range of energy and length scales. In ICE's, the flow is highly turbulent and involves a combination of turbulent shear layers, recirculating regions and boundary layers.

Inspection of the flow structures within a turbulent flow shows rotational flow structures called turbulent eddies that exhibit a wide range of length scales. The rotational nature of the eddies generated in turbulent flows also means that significant flow mixing occurs giving cause to high coefficients of diffusion for momentum, mass and heat transfer.

Another feature of turbulent flows is the so-called energy cascade. The largest turbulent eddies interact with the mean flow and extract energy by a process called vortex stretching which arises due to distortions, as a consequence of velocity gradients present in sheared flows.

The largest eddies in the flow are limited by the size of the system boundaries itself. The characteristic velocity and length of the largest eddies are of the same order as the velocity scale and length scale of the mean flow and hence will have a similarly high Reynolds number as of the mean flow itself, indicating that large scale eddies are dominated by inertial effects and not viscous effects. The implication of this is that large eddies are effectively inviscid and angular momentum is conserved during vortex stretching. Since the angular momentum is conserved, this causes an increase in rotation rate and a reduction in cross-sectional radius thus the process causes the generation of eddies with smaller length and velocity scales. This process of vortex stretching from the mean flow is the main mechanism by which energy is provided to maintain turbulence. The smaller eddies continue to be stretched by the larger eddies and less by the mean flow and hence kinetic energy is passed down to smaller and smaller eddies, hence the term 'the energy cascade'. Since the energy acquired by the turbulent flow is at its largest when acquired by the largest eddies from the mean flow, the kinetic energy can be shown to decrease or dissipate as the wavelength of the eddies reduces. This produces the so-called energy spectrum of turbulence.

Within the energy spectrum, a number of length scales exist that characterise different aspects of the flow behaviour. Turbulent eddies responsible for the most turbulence production (and hence containing the highest energy) have a length scale called the integral length scale.

As the eddy size reduces, so does its characteristic length and characteristic velocity and hence the Reynolds number of the smallest eddies is equal to 1, where inertial and viscous forces are equal and indicate that they are dominated by viscous stresses opposed to inertial stresses as seen in the largest eddies. Turbulence of these scales is named after the Russian scientist Kolmogorov (1941) who first introduced the idea that the smallest scales of turbulence are only dependent on the fluid viscosity and the rate of dissipation. These turbulence scales dissipate energy only due to viscous effects and is converted to thermal internal energy. Turbulence at this energy level are defined by the Kolmogorov scales for length l_k, time τ_k, and velocity v_k, as shown by equations (2.6)-(2.8).

$$l_k = \left(\frac{v^3}{\varepsilon}\right)^{1/4} \tag{2.6}$$

$$\tau_k = \left(\frac{v}{\varepsilon}\right)^{1/2} \tag{2.7}$$

$$v_k = (v\varepsilon)^{1/4} \tag{2.8}$$

Where v is the kinematic viscosity and ε is the rate of turbulence energy dissipation.

Since the largest turbulence length scale is related to the turbulence producing process, the flow structure is highly anisotropic, i.e. fluctuations vary in all spatial directions and are highly dependent on the flow boundary conditions. Since the length scales for the smallest turbulence structures are only dependent on the rate of energy dissipation and viscous effects (kinematic viscosity of the fluid), any anisotropy is removed and can be considered to be isotropic, i.e. possess unity in all directions. This characteristic becomes more pronounced at high Reynolds numbers.

A third scale is often defined for characterising turbulent flow called the microscale or Taylor scale which describes turbulent eddies of intermediate size; sufficiently large to be affected by viscous action but sufficiently small that their behaviour can be expressed as a function of the rate of dissipation.

The turbulence kinetic energy per unit mass in the large scale eddies is proportional to the square of turbulence intensity. Large eddies lose a substantial fraction of energy in one turnover time l_t/u'. Hence, for a system in equilibrium, energy is dissipated from the system at the same rate as production, as denoted by equation (2.9).

$$\varepsilon \approx \frac{u'^3}{l_t} \tag{2.9}$$

Where u' is the velocity scale and l_t is the integral length scale.

Thus all of the above scales of turbulence can be linked by the following equations:

$$\frac{l_k}{l_t} \approx \left(\frac{u' l_t}{v}\right)^{-3/4} \approx Re_T^{-3/4} \tag{2.10}$$

$$\frac{\tau_k}{\tau_t} \approx Re_T^{-1/2} \tag{2.11}$$

$$\frac{v_k}{v_t} \approx Re_T^{-1/4} \tag{2.12}$$

Where Re_T is the turbulence Reynolds number

And by applying restrictions of homogenous and isotropic turbulence, an energy budget can be performed to relate integral length scale l_t and Taylor or micro length scale l_m as shown in equation (2.13), where *A* is a constant of order 1.

$$\frac{l_m}{l_t} = \left(\frac{15}{A}\right)^{1/2} Re_T^{-1/2} \tag{2.13}$$

With respect to engine flows, these approximations are reasonable at the end of compression but will not be satisfied through the intake and compression strokes.

The random nature of turbulent flows typically drives the use of statistical methods to help define the flow field. The flow property u_i is decomposed into a time-averaged mean component $\overline{u_i}$, and a fluctuating component u_i', and shown for velocity in equation (2.14).

$$u_i(t) = \bar{u}_i + u_i'(t) \tag{2.14}$$

Where the mean flow property $\bar{u}_i$ is defined as shown in equation (2.15).

$$\bar{u}_i = \frac{1}{\Delta t}\int_0^{\Delta t} u_i(t)\, dt \tag{2.15}$$

The mean flow property calculated over a number of identical experiments provides the 'ensemble-average'. The ensemble-average mean velocity in an engine environment is only a function of crank angle since it acts to average out the cyclic variation.

The spread of the fluctuating component $u_i{}'$ is described using the variance $\overline{(u_i{}')^2}$ and the root mean square (r.m.s.) $u'_{i,rms}$ as shown in equations (2.16) and (2.17) respectively. These are of particular importance due to the r.m.s. being easily calculated from experimental data and the variance of velocity fluctuations are linked to the momentum fluxes induced by turbulent eddies.

$$\overline{(u_i{}')^2} = \frac{1}{\Delta t}\int_0^{\Delta t} (u_i{}')^2 dt \tag{2.16}$$

$$u'_{i,rms} = \sqrt{\overline{(u_i{}')^2}} \tag{2.17}$$

The variance is also known as the second moment of the fluctuations and important flow structure details are contained in moments containing pairs of flow variables, e.g. second moments of the velocity components, $\overline{u'v'}$, $\overline{u'w'}$, $\overline{v'w'}$ are all non-zero due to the vortical flow structures present in turbulent flows, and the pressure-velocity moments $\overline{p'u'}$, $\overline{p'v'}$, $\overline{p'w'}$ can be linked to the diffusion of turbulent energy.

Using the variance of the velocity components, *u*, *v*, *w*, the kinetic energy per unit mass of the turbulence can be deduced as shown in equation (2.18) and the turbulence intensity T_i is found by the average of the r.m.s. velocity divided by a reference mean flow velocity as shown in equation (2.19).

$$k = \frac{1}{2}\left(\overline{u'^2} + \overline{v'^2} + \overline{w'^2}\right) \tag{2.18}$$

$$T_i = \frac{\left(\frac{2}{3}k\right)^{1/2}}{U_{ref}} \tag{2.19}$$

As mentioned above, the vortical eddy motion creates strong mixing and acts to exchange momentum and energy through the fluid. Momentum exchange causes slower moving fluid parcels to be accelerated and faster moving parcels to be decelerated which will cause additional turbulent shear stresses which are known as Reynolds stresses. The presence of other scalar gradients, e.g. temperature and species concentration, also generate fluxes across the fluid and these give rise to turbulent scalar fluxes. These additional stresses/fluxes are seen to be present when the Reynolds or velocity decomposition is applied in the Navier-Stokes equations for incompressible flow as presented earlier in Chapter 2.2.2 (Heywood, 1988; Versteeg & Malalasekera, 2007; Pope, 2000).

2.2.2 Turbulence Modelling

The modelling of turbulence within ICE's is a difficult task. Key attributes of the flow field that will influence the choice of method used to model the in-cylinder turbulence are:

- Highly anisotropic and non-homogeneous
- High Reynolds number with a wide range of time and length scales that vary throughout the simulation due to varying domain characteristic dimensions
- Highly wall bound flow field with complex boundary layer interactions with moving boundaries
- Time dependent boundary conditions

It is these attributes that are used to evaluate the suitability of a particular turbulence modelling methodology, along with computational expense and solver stability.

Flows within the laminar regime are completely described by the N-S equations but once turbulent, the flow can no longer be calculated deterministically since the minutest influence may have the largest effect; hence additional methods are required when needing to represent the effects of turbulence.

When the velocity decomposition, as shown above in equation (2.14), is applied to the mass and momentum continuity equations, we obtain the following relations shown in equations (2.20) and (2.21):

$$\frac{\partial(\rho\bar{u}_i)}{\partial x_i} = 0 \tag{2.20}$$

$$\rho\frac{\partial\bar{u}_i}{\partial t} + \rho\frac{\partial(\bar{u}_j\bar{u}_i)}{\partial x_j} = -\frac{\partial\bar{p}}{\partial x_i} + \frac{\partial\Gamma_{ij}}{\partial x_j} + \rho\frac{\partial\tau_{ij}}{\partial x_j} \tag{2.21}$$

As can be seen, these equations are of very similar form to the N-S equations but with the exception of an additional term τ_{ij}, which forms six additional terms and it is how these six terms are modelled which defines the methodology by which turbulence is modelled. In physical terms, these additional terms represent the additional stresses present in the flow as a consequence of velocity and scalar gradients caused by momentum exchange of the vertical eddy motion present in turbulent flows.

Since the flow in an engine cycle is compressed and expanded, whilst the flow velocities are low enough that density fluctuations are typically negligible, the mean density variations are not, thus mass-weighted averaging (or Favre-averaging) is also introduced. Here the instantaneous density is decomposed into a mean and fluctuating component and introduced into the N-S equations, yielding the Favre-Averaged Navier-Stokes equations.

2.2.2.1 RANS Turbulence Modelling

When the velocity decomposition is applied to the N-S equations in a Reynolds-Averaged Navier-Stokes context, the $\bar{u}_i$ term is the mean velocity component and u_i' is the fluctuating

velocity component and τ_{ij} represents the six 'Reynolds stresses'. In this class of models (with the exception of the Reynolds Stress Model – discussed briefly below), the Reynolds stresses are solved based on the assumption that there is a linear relationship between viscous stresses and Reynolds stresses, as proposed by Boussinesq in 1877 who suggested that the Reynolds stresses might be proportional to the mean rates of deformation, as shown by equation (2.22).

$$\tau_{ij} = 2\mu_t \bar{S}_{ij} - \frac{2}{3}\rho k \delta_{ij} \tag{2.22}$$

As can be seen in equation (2.22), a new term is present, the turbulence viscosity μ_t, and it is the modelling of this term, often via the use of additional transport equations, that defines the approach taken by a RANS turbulence modelling approach.

Table 2.1 identifies the most prevalent RANS turbulence models, classifying them based on the number of additional transport equations that are solved to resolve the turbulence viscosity term.

Table 2.1 – Prevalent RANS turbulence models characterised by the number of additional transport equations – reproduced from Versteeg & Malalasekera (2007)

Number of additional transport equations	**Model Name**
Zero	Mixing length model
One	Spalart-Allmaras model
Two	*k-ε* model
	k-ω model
	Algebraic stress model
Seven	Reynolds stress model

Of these models, it is the *k-ε* model (and its variants) that are the most widely used and validated within the CFD community. In the original k-ε model proposed by Launder & Spalding (1974), the turbulent viscosity μ_T is defined as shown in equation (2.23).

$$\mu_T = C_\mu \rho \frac{k^2}{\varepsilon} \tag{2.23}$$

Where C_μ is a constant, k is the turbulence kinetic energy and ε is the turbulence kinetic energy dissipation rate, both defined by individual transport equations containing five constants that through significant validation, have been standardised across a wide range of turbulent flows. It is also possible to re-write equation (2.23) based on a physical interpretation via a dimensional analysis using a velocity scale *v* and length scale *l* as shown in equation (2.24):

$$\mu_T = \rho v l \tag{2.24}$$

As can be seen from equation (2.24), the turbulence viscosity is based on a single length scale even though the flow turbulence is not homogeneous – a significant draw back of the closure approach used by the k-ε family of turbulence models.

In general the standard *k-ε* model has been shown to predict turbulent flow fields with good success in thin shear layers and recirculating flows in confined domains where Reynolds shear stresses are important. In contrast, the model has been reported to perform badly in weak shear layers (far wakes and mixing layers) of unconfined flows due to the production of turbulence kinetic energy being much less than the rate of dissipation; the *ε*-transport equation for the standard *k-ε* model assumes that production and destruction terms are proportional to production and destruction terms of the *k*-transport equation. Payri, Benajes, Margot, *et al*. (2004) investigated the in-cylinder flow field in a diesel engine using the standard *k-ε* model and reported that whilst the model offered reasonably accurate turbulence predictions, in areas of high turbulence, particularly around squish zones, turbulence was under predicted and velocity fluctuations not adequately predicted which the author attributes to the *k-ε* models poor performance in the presence of strong shear stresses.

The renormalisation group (RNG) originally proposed by Yakhot & Orszag (1986) and furthered by Yakhot, Orszag, Thangam, *et al.* (1992), extends the standard *k-ε* model by representing the effects of small scale turbulence by a random forcing function in the N-S equations. The RNG methodology then removes the small scales of motion from the N-S equations by expressing their effects as a function of larger scale motions and a modified

viscosity. The model also contains a strain-dependent correction term in the ε-equation which aims to represent the effect of mean flow distortion on the turbulence (Rodi, 1979).

Good results have been reported with the model and it is included in many CFD codes as an alternative to the standard k-ε model as it more effectively accounts for the effects of compression/expansion/rapid strain on the turbulence scales. Non-positive experiences have been reported due to the strain parameter η sensitising the RNG model to the magnitude of the strain, therefore making the effect on the dissipation rate the same regardless of the sign of the strain.

Bella, De Maio & Grimaldi (2003) evaluated the intake valve discharge coefficient at various lift values, comparing results using the standard k-ε model with the RNG k-ε model. The results showed better prediction of the discharge coefficient at low and medium lifts using the RNG k-ε model turbulence model but no comparison of turbulence quantities was offered so it is difficult to determine the reason for this. In contrast, Choi, Choi, Park, *et al.* (2003) compared the in-cylinder flow of an optical single cylinder diesel engine at 600rpm, measured using PIV, with numerical predictions using both the standard k-ε model and RNG k-ε model turbulence models and concluded that the standard k-ε model was better suited to low speed operation, though comparative results at high engine speeds to validate this suggestion were not present.

Another common addition to CFD codes is the Realizable k-ε model, developed by Shih, Liou, Sabbir, *et al.* (1994). In this model, the eddy viscosity constant is defined algebraically based on realizability constraints that prevent unrealistic values of the Reynolds stresses. The model also includes a modification to the ε-equation based on the dynamic equation of the mean vorticity fluctuation at high Reynolds numbers. The authors present good results for the model in; rotating homogeneous shear flows, boundary-free shear flows, channel flows, flat plate boundary layers with and without a pressure gradient and a backward facing step when compared with the standard k-ε model.

All models that are based on the Boussinesq assumption of isotropic eddy viscosity will poorly predict swirling flows and flows with large rapid strains that effect turbulence in a subtle manner. Secondary flows driven by anisotropic Reynolds stresses can also not be predicted adequately due to the assumptions of isotropy. This drives the consideration of more complex turbulence models in the form of: Reynolds Stress Models, Large Eddy Simulation and Detached Eddy Simulation for the modelling of in-cylinder flow fields.

The most complex of the so-called classical turbulence models is the Reynolds Stress Model (RSM); a second-moment closure model. This modelling strategy originates from Launder, Reece & Rodi (1975) where the Reynolds stresses are solved via exact transport equations, accounting for the directional effects of the Reynolds stress field. Additional work by Gibson & Launder, (1978), Speziale, Sarkar & Gatski (1991) and Craft, Launder & Suga (1996) has revolved around the modelling of the pressure-strain term due to its importance in the redistribution of energy among turbulence normal stresses and ensuring that as turbulence is driven to isotropy, the shear stresses decline. The benefits include significant improvements in the models ability to predict anisotropies in the turbulence structure but at the computational cost of needing to solve seven transport equations (rather than two as seen for the turbulence models discussed previously), greatly increasing solution run time. It is primarily this reason that has delayed the wide spread application of RSM to in-cylinder calculations. Lebrère & Dillies (1996) discusses the implementation of the RSM by Launder, Reece & Rodi (1975) into the research code KIVA-II for evaluation of the improvements in turbulence prediction against traditional two-equation turbulence models of the standard *k-ε* and RNG *k-ε* models. The author comments that while qualitatively all models provide similar results for mean quantities of turbulence through the cycle, large differences exist in turbulence anisotropy particularly during the intake stroke, in the near spark plug region towards the end of compression and in the near-wall regions. The authors also quote 30% increase in memory requirements and 50% increase in CPU time though no mention is made to the degree of parallelisation or computing technology used so in present times this information should be used carefully.

Binjuwair & Ibrahim (2013) evaluated the in-cylinder flow field of an optical single cylinder engine using both realizable *k-ε* and RSM turbulence models against experimental PIV data. Their results indicated that the realizable *k-ε* turbulence model was able to predict the qualitative trends of the turbulence kinetic energy profiles but poorly predicted the magnitude of mean and RMS fluctuating velocities. The RSM turbulence model results showed much better agreement in terms of qualitative and quantitative prediction of turbulent quantities inside the combustion chamber.

Based on the findings above, for the RANS portion of the research a variant of the RNG k-ε model will be used. This model combines the standard RNG k-ε model (Yakhot & Orszag, 1986; Yakhot, Orszag, Thangam, *et al.*, 1992) described in section 2.2.2, with additional terms not present in the standard RNG formulation to model compression and buoyancy

effects. This model was chosen due to it having a large body of research within the literature showing good predictions against experimental data, particularly in flow fields that are subject to the effects of rapid strain due to the compression and expansion of scales as seen in ICE's (Bella, De Maio & Grimaldi, 2003) but without the large increase in computational expense when using a more complex classical model like the RSM.

2.2.2.2 LES Turbulence Modelling

A large problem with RANS turbulence models is their use of a single turbulence model to represent the behaviour of a large range of turbulent motions. The LES approach solves the N-S directly for the large eddies (due to their interaction with the mean flow and geometry, and anisotropic behaviour) using space-filtered equations and only the smaller eddies (that are almost isotropic at high Reynolds numbers) are modelled.

When the velocity decomposition (equation (2.14)) is applied to the N-S equations, whilst the resultant equations take a very similar form to the RANS equations, conceptually the terms are different. In the LES context, $\bar{u}_i$ is the space-filtered velocity, u_i' is the subgrid velocity and τ_{ij} represents the sub-grid scale (SGS) stresses, which requires modelling and leads to the creation of a SGS model.

The SGS stresses are typically resolved by being related to the strain rate tensor $\bar{S}_{ij}$ using a kinematic turbulence viscosity term υ_T, via a Boussinesq or mean-gradient assumption, as shown in equation (2.25), where the isotropic portion τ_{kk} is incorporated into the filtered pressure equation, leaving only the anisotropic portion to be modelled.

$$\tau_{ij} = -2\upsilon_T \bar{S}_{ij} + \frac{1}{3}\delta_{ij}\tau_{kk} \tag{2.25}$$

With the exception of using no SGS model at all and relying on grid and numerical dissipation, the simplest SGS model is based on the work of Smagorinsky (1963) where the turbulence viscosity is defined as shown in equation (2.26).

$$\upsilon_T = (C_S\Delta)^2|\bar{S}| \tag{2.26}$$

Where C_S is the Smagorinsky constant and Δ is the filter width defined by equation (2.27).

$$\Delta = \sqrt[3]{V} \tag{2.27}$$

Where V is the cell volume of the computational grid.

The benefit of the LES SGS Smagorinsky model is that, due to it not including any additional transport equations, it is less computationally expensive. Also, since it uses a turbulence viscosity closure similar to the RANS k-ε model, initialisation is simpler and the solution stability more robust. The disadvantages of the Smagorinsky model are that the turbulence viscosity closure approach is inherently overly dissipative and the Smagorinsky constant needs adjusting for each application, which may not be known *a priori*.

An additional spatial filtering process originally suggested by Germano, Piomelli, Moin, *et al*. (1991) is often applied to the Smagorinsky SGS model where the Smagorinsky constant is obtained using the dynamic procedure, removing the need for selecting its value before starting the analysis and allowing the constant to spatially vary dependent on the local flow conditions. The disadvantages include additional computational expense incurred due to the extra filtering process and often additional averaging is needed to avoid solution instabilities.

The k-equation model, originally developed by Yoshizawa & Horiuti (1985) but later applied to engineering flows in Kim & Menon (1995), is still based on a turbulence viscosity closure approach but here the turbulence viscosity is based on the SGS turbulence kinetic energy (TKE) as defined in equation (2.28).

$$\upsilon_T = C_k \Delta \sqrt{k_{sgs}} \tag{2.28}$$

The SGS kinetic energy is obtained using an additional transport equation which has a number of physical advantages including the modelling of additional physical processes (convection, production and dissipation of the SGS kinetic energy) and the SGS kinetic energy can be used in other sub-models including droplet modelling and combustion. The disadvantages are that the additional transport equation adds additional computational

expense and due to the different formulation of the TKE, can make initialisation from RANS predictions difficult with the potential for solution instability.

More recently, the dynamic structure approach, or often called the dynamic structure model (DSM), was developed by Pomraning & Rutland (2002) and Chumakov & Rutland (2005), and instead of using a turbulence viscosity approach to resolve the SGS stresses as seen previously in equation (2.25), uses a tensor coefficient directly from the dynamic procedure as shown by equation (2.29).

$$\tau_{ij}^{s} = C_{ij} k_{sgs} \tag{2.29}$$

The advantage of this approach is that it is not purely dissipative but a balance maintained between the velocity field TKE and the SGS k-equation, and SGS kinetic energy dissipated through molecular viscosity via a viscous dissipation term. This provides a good basis for modelling the SGS kinetic energy and its application within spray and combustion sub-models but similar to the k-equation model, suffers additional computational cost due to the additional transport equation and potential for difficulties with solution initialisation.

Figure 2.2 illustrates the potential improvement in mean and fluctuating velocity prediction when using a LES turbulence modelling approach versus the RANS k-ε model when compared to experimental results.

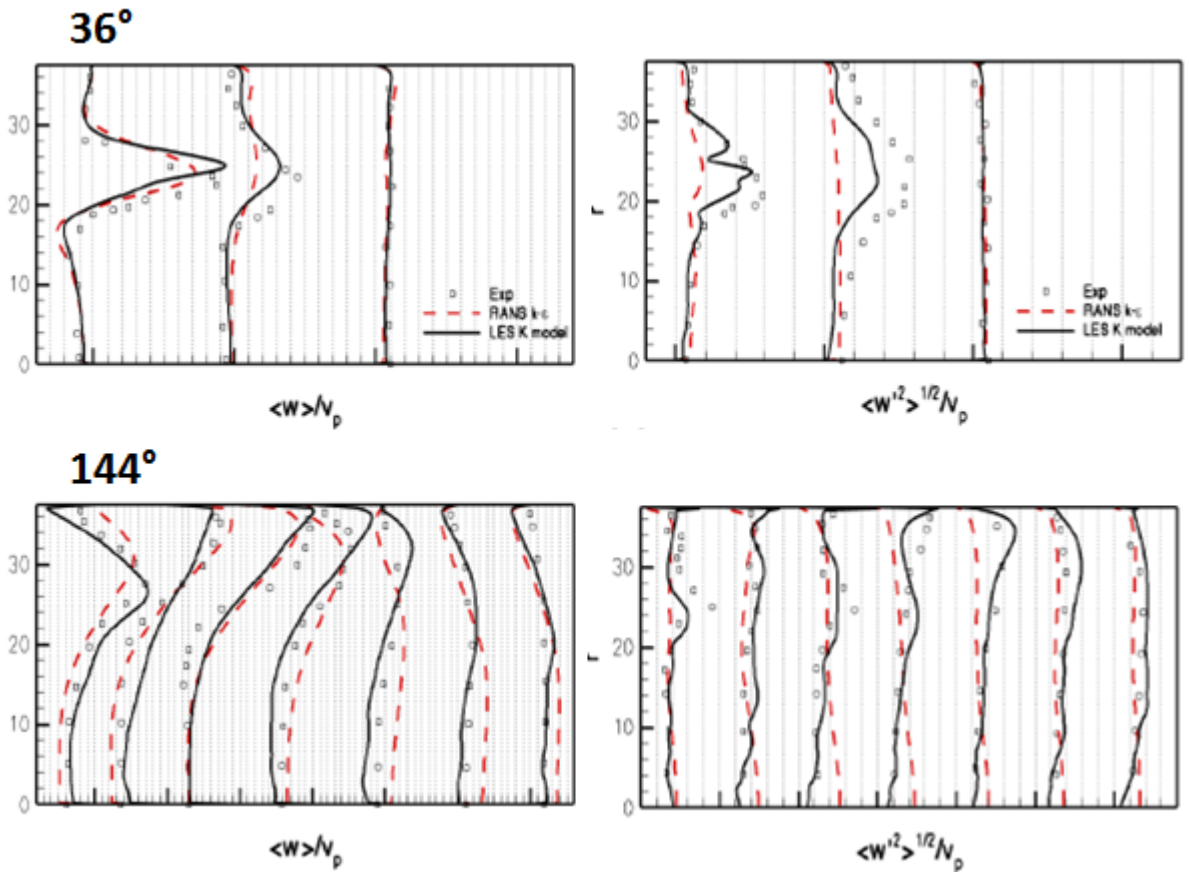

Figure 2.2 – Illustrating the improvement in mean and fluctuating velocity prediction using LES compared with a RANS technique for the same mesh and time step – reproduced from Gosman (2012)

The use of LES in industrial applications with high Reynolds numbers has been significantly less extensive than RANS approaches due to the increased computational cost associated with direct computation of large scale turbulent motions. Recent advances in computing power and the addition of LES and SGS models in a number of commercial and research CFD codes, e.g. STAR-CD (Gosman, 2012), has seen LES beginning to be applied in research institutions for the purpose of model validation and investigation into in-cylinder physical processes.

Since the turn of the century, there have been numerous examples of the application of LES to in-cylinder processes including; the investigation of in-cylinder flow fields, influences in direct injection fuel sprays, ignition and combustion cyclic variability.

The work of Colin, Ducros, Veynante, *et al.* (2000) presents the adaptation of the Extended Coherent Flame Model (ECFM) to the LES methodology. This work is continued by Richard, Colin, Vermorel, *et al.* (2007), Vermorel, Richard, Colin, *et al.* (2009) and Enaux, Granet,

Vermorel, *et al.* 2011), where the use of LES and the ECFM is applied to investigate the influence of cyclic variation on combustion variability with good success against experimental data.

Tatschl, Bogensperger, Pavlovic, *et al.* (2013), utilising commercial code AVL Fire, illustrates the application of LES to a GDI engine using the well-established Smagorinsky approach for the SGS model with a view of investigating cyclic variability and its impact on flame propagation and rate of heat release. More specifically, this example utilises a coupled 1D-3D approach, where the intake and exhaust pipework are modelled via a 1D code and provide the unsteady boundary conditions to the 3D-CFD model but no mention is made how the fluctuating components are added to the inflow boundary conditions. The fuel injection model used is the Lagrangian Discrete Droplet Model (DDM – to be discussed further in the following section) where 'the turbulent dispersion effects are assumed to be fully covered by the interaction of the droplets with the resolved LES flow field scales'. A variant of the Coherent Flame Model (CFM) adapted for use with LES is used to model combustion. The results indicate that the adopted LES approach is very capable of reflecting the degree of cyclic dispersion between different cycles.

Som & Longman (2012) have shown the improvements, both qualitatively and quantitatively, in fuel spray modelling using an LES approach with the commercial code CONVERGE for the prediction of equivalence ratio, ignition delay and soot distribution in diesel combustion. Their results show a significant improvement in the characterisation of the spray structure and ignition delay predictions as a function of ambient temperature – a sample of results are shown in Figure 2.3.

Disadvantages of the LES approach include its significant dependence on the grid size and quality and its implementation in the near wall regions where the quality of the SGS models are of significance and can be of lesser quality than a simpler RANS approach. A hybrid formulation combining both LES and RANS techniques called Detached Eddy Simulation (DES) has also been of significant interest in the CFD community. In this technique, LES is used in the main flow field but in areas where the grid size or quality is insufficient to resolve the large scale eddies the simulation switches to a RANS approach. This approach comes with its own challenges, including the effective switching between LES and RANS models but is seeing increased popularity. The application of DES to in-cylinder environment is still emerging with almost all examples of current application being to external aerodynamics.

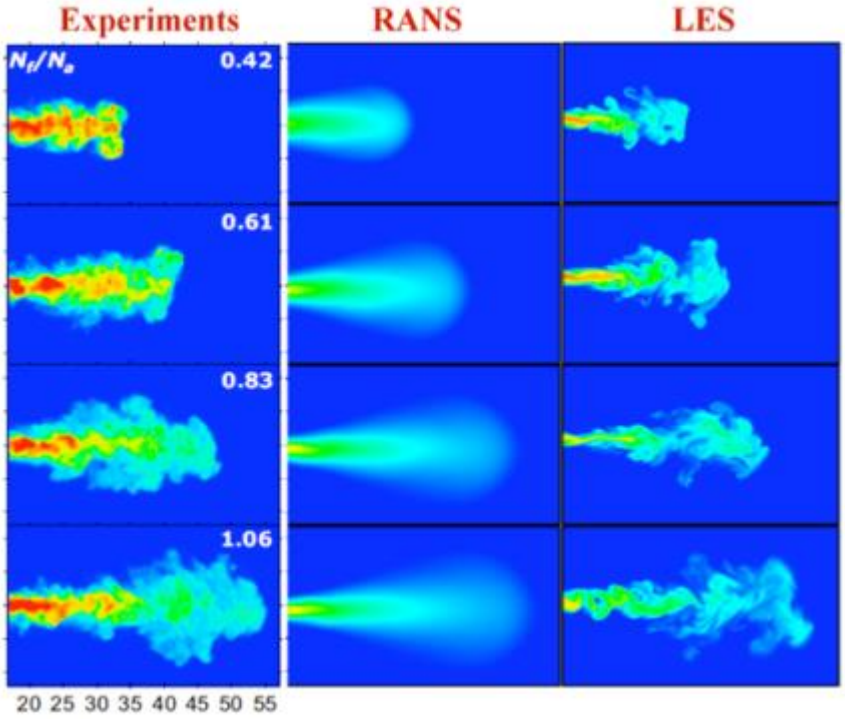

Figure 2.3 – Images comparing the instantaneous equivalence ratio calculated using RANS and LES models, against experimental data from Sandia under non-reacting conditions – taken from Som & Longman (2012)

Whilst the discussion above does not cover the extensive list of all LES SGS model variants within the literature, it does cover the most significant used within ICE research and those with a sufficient body of research to support their validity and capability of accurately predicting ICE flows.

Based on the results discussed above, the Smagorinsky SGS turbulence model was chosen to be used in this research for the following reasons:

- Well proven to provide reasonable results with adequate grid resolution and choice of Smagorinsky constant
- Easily initiated from a RANS solution
- Low computational cost due to not using an additional transport equation

A final key step in the use of the Smagorinsky SGS model for this research was in the definition of the Smagorinsky constant C_S. A number of papers were reviewed to establish an appropriate value for the Smagorinsky constant based on the characteristics of the turbulence

expected within an ICE. The works of Moureau (2004), Dugue, Gauchet & Veynante (2006) and Habchi, Devassy & Kumar (2014) quote a range for C_S^2 of 0.1 to 0.2, hence based on this a value of 0.14 (or $C_S = 0.02$) was chosen and considered appropriate for this research.

2.3 FLOW IN ENGINES

2.3.1 Intake Flow

The flow through the intake port and valve is responsible for many of the flow features generated within the cylinder.

The flow past a valve can be described by the equation for compressible flow past a restriction (derived from one-dimensional isentropic flow analysis) and real gas effects are accounted for by means of an experimentally determined discharge coefficient, C_D. The effective flow area past the valve is calculated by the product of discharge coefficient and reference area. A number of different reference areas are used when specifying valve flow but the valve curtain area, defined by equation (2.29) is one of the mostly commonly used since it varies linearly with lift, where D_v is the valve head diameter and L_v is the valve lift.

$$A_C = \pi D_v L_v \tag{2.30}$$

The flow past the intake valve can be broken down into three distinct regimes which correlate to the valve lift to diameter ratio. The different flow regions also correlate with changes in the discharge coefficient, A_E/A_C.

At very low lifts the flow is attached to the valve head and seat. As the valve lift increases the flow separates from the valve head and causes a sharp reduction in discharge coefficient. The discharge coefficient then increases with increasing lift, since the size of the separated region remains almost constant while minimum flow area increases until at high lifts the flow separates from the valve seat as well and another abrupt reduction in discharge coefficient is seen. At high engine speeds, unless the inlet valve is of sufficient size, the flow past the inlet

valve will become choked where gas velocity is limited and volumetric efficiency decreases rapidly.

Justham (2010) investigated the cyclic variability of intake valve flow using a HSDPIV system focussed on a small region along the top surface of the intake valve over a number of crank angle positions during the intake event. Results clearly show the flow initially attached to the valve head and detaching at larger lift values. It was also noted of the significant cyclic variation seen in the intake jet due to the level of turbulence present, impacting the valve lift at which the flow detaches from the valve head.

Vortices are also generated either side of the valve jet, recirculating beneath the valve head and into the upper corners of the combustion chamber as a consequence of the shear layer created between in-cylinder gas and the turbulent fast moving intake jet. These rotating vortices contribute to bulk gas motion through the intake event but break down during the compression process increasing in-cylinder turbulence levels further.

The intake valve provides the minimum area for the flow within an internal combustion engine and hence the gas velocities generated by flow through the intake valve are at their highest. It has been shown that the intake jet velocity is proportional to the mean piston speed and thus it follows that in-cylinder flow velocities at different engine speeds also scale with mean piston speed (Heywood, 1988).

2.3.2 In-Cylinder Flow

The charge motion within the cylinder of a GDI engine exhibits a number of characteristics:

- Three-Dimensional
- Compressible
- Spatially and temporally varying
- Fully turbulent; anisotropic and non-homogeneous
- High levels of interaction with solid boundaries

In addition to this, the charge motion has a major influence on all of the processes that occur within the combustion chamber, including heat transfer, fuel injection, mixture preparation, near spark plug conditions at the point of ignition timing, the combustion event and subsequent pollutant formation. The in-cylinder charge motion can be loosely classified as either a bulk gas motion or small scale turbulence and both need characterisation. In-cylinder flow characteristics of significance are; the mean flow components, the stability of the mean flow, the temporal turbulence evolution during the compression stroke and the mean velocity in the vicinity of the spark plug around the point of ignition timing. In engines, the problem is further compounded by the impact of the moving geometry of valves and piston, changing the flow pattern throughout the engine cycle. In addition, the random nature of turbulent flows generate significant cyclic variability where large scale patterns may repeat but the small scale variations can cause significant changes in the flow field from one cycle to the next (Zhao, Lai & Harrington, 1999; Fansler & French, 1987; Rimmer, Long, Garner, *et al.*, 2009; Ozdor, Dulger & Sher, 1994).

As noted previously, the in-cylinder bulk gas flow motion is significantly impacted by the intake valve jets during the intake process and is a key factor in all subsequent in-cylinder flow processes.

Within the cylinder, a number of rotating flow structures exist and the instantaneous angle of inclination between the structures principal axis of rotation and the cylinder axis are often used to help describe the orientation of the flow structure. Structures which rotate parallel to the axis of the cylinder are commonly denoted as ‘swirl’ and structure which rotate perpendicular to the cylinder axis described as ‘tumble’. The magnitude of swirl and tumble flow components is highly dependent on intake port geometry and subsequent intake valve jets, and the in-cylinder flow field is often designed such that it provides characteristics that favour the chosen fuel injection and combustion strategy.

Tumble dominated flow fields tend to generate large-scale rotating structures that generate a significant amount of in-cylinder mixing. This flow structure therefore tends to favour homogeneous mixture formation. The rising piston compresses the rotating flow structures causing deformation and energy dissipation into smaller flow structures until high levels of turbulence are generated by TDC. Tumble flow structures are typically generated using pronounced intake port geometry to cause the intake jet to travel down the cylinder wall and back up the exhaust side of the combustion chamber. Tumble flow fields are therefore very

effective at generating high velocities in the near wall region for promoting increased rates of wall film evaporation in the event of spray plume impingement. Due to the break down of flow structures by the rising piston and subsequent increases in turbulence levels, tumble dominated flow fields tend to suffer from increased cyclic variability.

Swirl dominated flow fields are much less susceptible to degradation due to piston motion and hence flow structures are often preserved for longer into the compression stroke. This aspect can allow swirl dominated flow structures to better maintain mixture stratification later into the cycle. Swirl flow structures are seen to be much more engine speed dependent and this can lead to a limited region of adequate fuel-air mixing.

A third significant flow structure which should be discussed is squish. Squish flow progresses radially inwards near TDC and is initiated as a consequence of the significantly reduced volumes between the piston and outer areas of the combustion chamber causing the flow to be forced towards the centre of the combustion chamber. Squish only acts to intensify the bulk flow of swirl or tumble and does not become significant until near TDC. The amount of squish is often defined by the percentage squish area, i.e. the percentage of area where the piston closely approaches the cylinder head and its magnitude is also highly dependent on engine speed (Zhao, Lai & Harrington, 1999; Heywood, 1988; Ma, 2006).

In addition to the three large-scale flow structures discussed above, the final in-cylinder flow field can be a complex combination of each flow type, and the flow structure is both non-homogeneous (i.e. non-uniform) and anisotropic (i.e. highly directionally dependent). There is significant research available both experimental and numerical, that has reported on the large-scale flow structures within internal combustion engines and GDI variants including Auriemma, Corcione, Macchioni, *et al.* (1998), Binjuwair (2013), Chen (1994), Das (1996), Davis & Borgnakke (1982), Delhaye & Cousyn (1996), Fansler & French (1987), Faure, Sadler, Oversby, *et al.* (1998), Flowers, Aceves & Babajimopoulos (2006), Fukuda, Ghasemi, Barron, *et al.* (2012), Henson & Malalasekera (2000), Jarvis, Justham, Clarke, *et al.* (2006), Krishna, Mallikarjuna, Davinder, *et al.* (2013), Laget, Zaccardi, Gautrot, *et al.* (2013), Long (2010), Long, Rimmer, Justham, *et al.* (2008), Murad (2006), Osei-Owusu (2008), Ozdor, Dulger & Sher (1994), Rimmer (2011), Rimmer, Long, Garner, *et al.* (2009) and Gnana Sagaya Raj, Mallikarjuna & Venkitachalam (2013), but very few have attempted to quantitatively characterise the anisotropy present within the flow, including Petersen & Ghandhi (2010) and Lebrère & Dillies (1996).

Of particular interest are some of the flow variations apparent in the works by Justham (2010) that were measured in the GDI engine that will be the focus of this research. Figure 2.4 shows the flow past the intake valves generating a tumble motion down both intake and exhaust sides of the combustion chamber. The valve jet running down the intake side of the combustion chamber generates a counter clockwise tumble motion guided by the cylinder liner until it reaches the piston crown and a rotating vortex is generated. A clockwise tumble flow motion on the exhaust side of the combustion chamber is also present but due to the greater radial component of the flow structure, it reflects off the cylinder liner and creates another rotating vortex higher in the combustion chamber. These two flow structures act to create complex rotating flow structures within the combustion chamber interior that changes through the cycle as a consequence of the weakening valve jets and falling piston.

A number of smaller-scale rotating structures are also present in the swirl plane as seen in Figure 2.5. This is as a consequence of the radial component of the intake valve jet interacting with the combustion chamber wall and interaction with the valve jet from the adjacent intake valve. This example helps to illustrate the bulk motions as discussed above but also the complexity of the in-cylinder flow field where the flow in not limited to just a radial or axial flow component as is the case in typical diagrams showing either a ‘tumble’ or ‘swirl’ flow motion.

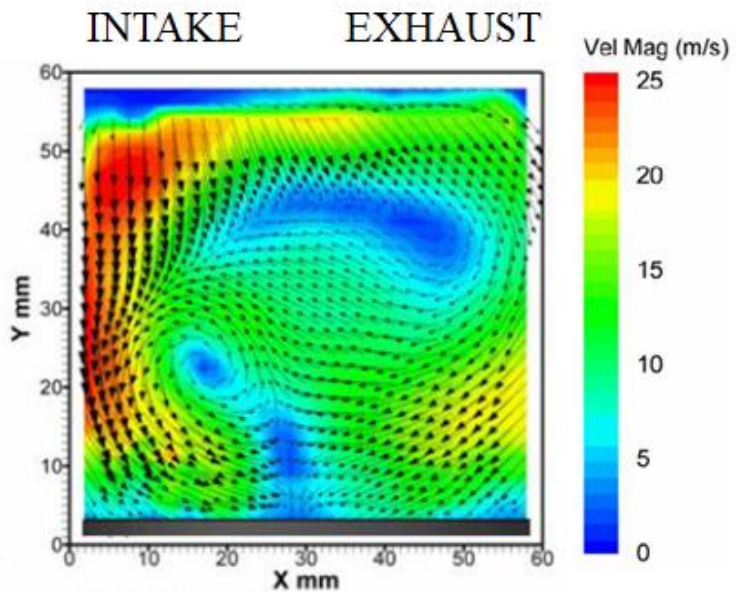

Figure 2.4 – Mean low frequency velocity magnitude contours along the bore centreline in the tumble plane at 92°ATDC reproduced from Justham (2010)

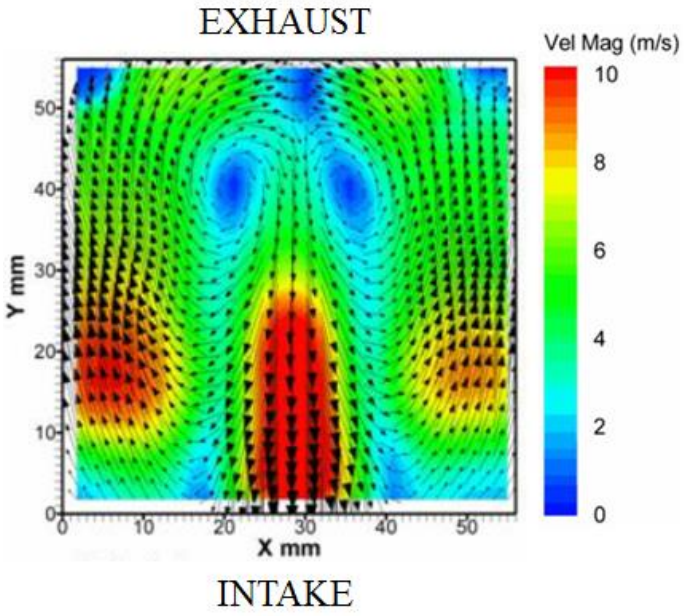

Figure 2.5 – Mean low frequency velocity magnitude contours 10mm below the peak piston height in the swirl plane at 112°ATDC reproduced from Justham (2010)

2.4 FUEL INJECTION

The fuel injection process in a GDI engine involves the injection of liquid fuel into the combustion chamber and subsequent disintegration mechanisms, which constitute a number of complex physical processes:

- Highly interacting two-phase flow
- Complex multi-component fuels with condition specific properties
- Highly transient in nozzle cavitation
- Impacted by both fuel injection system and in-cylinder aerodynamics
- Contains multiple break-up mechanisms
- Atomisation
- Droplet-to-droplet collisions and subsequent interactions
- Variety of impingement which vary dependent on local droplet, flow and surface conditions

- Liquid film formation and subsequent flow, evaporation and heat transfer processes

The following is a discussion of the physical processes occurring during fuel injection in a GDI engine and some of the typical numerical methods and sub-model used for making predictions in this area. Note: Additional detail is included for certain sub-models and physical processes that will be used to support analysis and discussion later in this thesis.

2.4.1 Fuel Spray Characteristics

At a macro level, fuel sprays are typically characterised by a number of defining parameters. The spray penetration is often split into two different characteristics. The first being the break-up length which defines the axial penetration of the liquid core from the injector tip into the gaseous medium. This is an important parameter for engine development due to it providing an indication of the rate of fuel-air mixing, which is important due to the limited timescales available during an engine cycle. The second is the spray tip penetration defining the maximum axial spray penetration including liquid droplets that have broken up from the liquid core. The spray angle is also often used to characterise the fuel spray plume. These quantities are depicted in Figure 2.6.

On a micro level, additional information is used to help characterise fuel sprays, including the mean droplet size and droplet size distribution.

The use of mean droplet size was standardised by Mugele & Evans (1951) and some common mean diameters used today in various applications include; arithmetic mean diameter D_{10}, surface mean diameter D_{20}, volume mean diameter D_{30} and the sauter mean diameter D_{32}. The sauter mean diameter (SMD) is the diameter of the droplet that has the same volume to surface area ratio as the entire spray. Due to the SMD relating the mean droplet diameter to the surface to volume ratio of the droplet, it is a commonly used measurement in engine sprays where the active surface area is an important characteristic in the breakup and atomisation processes.

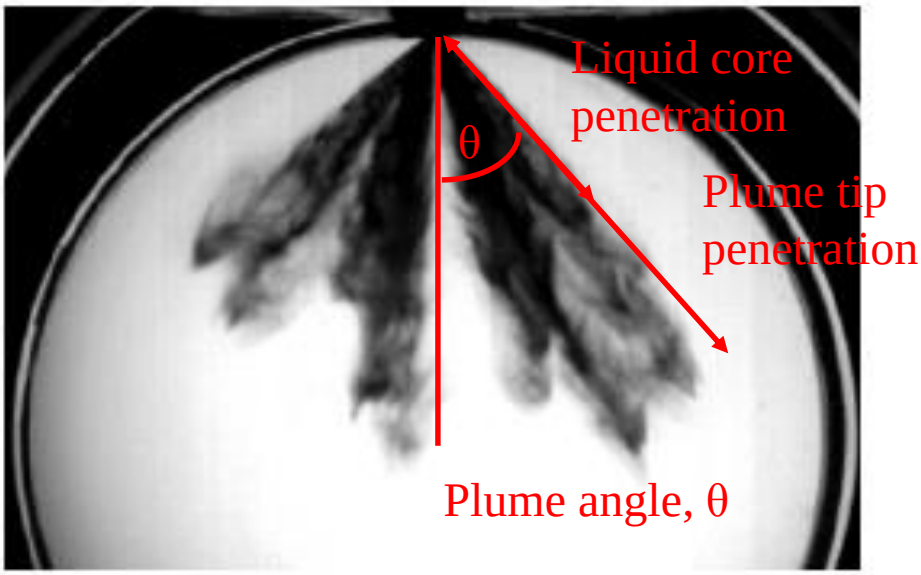

Figure 2.6 – Schematic of spray characterisation, spray image reproduced from van Romunde (2011)

Fuel injected ICE's present a particularly difficult challenge for numerical modelling due to the complex physical processes as outlined above. Models which explicitly treat the two-phase structure of the spray occur in two classes: continuum droplet models (CDM) and discrete droplet models (DDM).

A droplet is typically described by eight variables; three spatial components, three velocity components, temperature and radius. The CDM approach attempts to represent the motion of all droplets via an Eulerian partial differential probability equation for all eight variables across the hundreds of millions of droplets that constitute a typical fuel spray. Obviously this approach requires enormous computational requirements and has led to the widespread use of the Lagrangian approach of a DDM. A DDM solves the conservation equations of mass, momentum and energy for each element, with one of the first documented applications present in Bracco (1985). For the sake of brevity, the conservation equations of the dispersed-phased are not presented but can be found documented in CD-adapco (2014).

Due to the large number of droplets present in a realistic engine spray, a statistical approach is taken to reduce the computational expense where the total population of droplets is represented by a finite number of 'parcels', each of which represents a group of droplets with the same properties. Ensuring adequate statistical convergence must be considered, especially during mesh refinement, as illustrated in Figure 2.7. The idea of reaching statistical

convergence must be sought by seeking: cell size approaches zero and parcels per cell approaches infinity, though this increases the number of parcels and hence computational requirements. Merker, Schwarz & Teichmann (2012) suggests that fifty parcels per cell should be considered a reasonable number, i.e. if N cells of edge length Δl (in the spray direction) are found at the nozzle opening and the injection velocity is v, then 50*N parcels in time $\Delta t = \Delta l / v$ should be injected. Though ultimately, this requirement should be driven by the sub-models used and their individual need for statistical convergence. This is particularly true for inter-drop collision modelling.

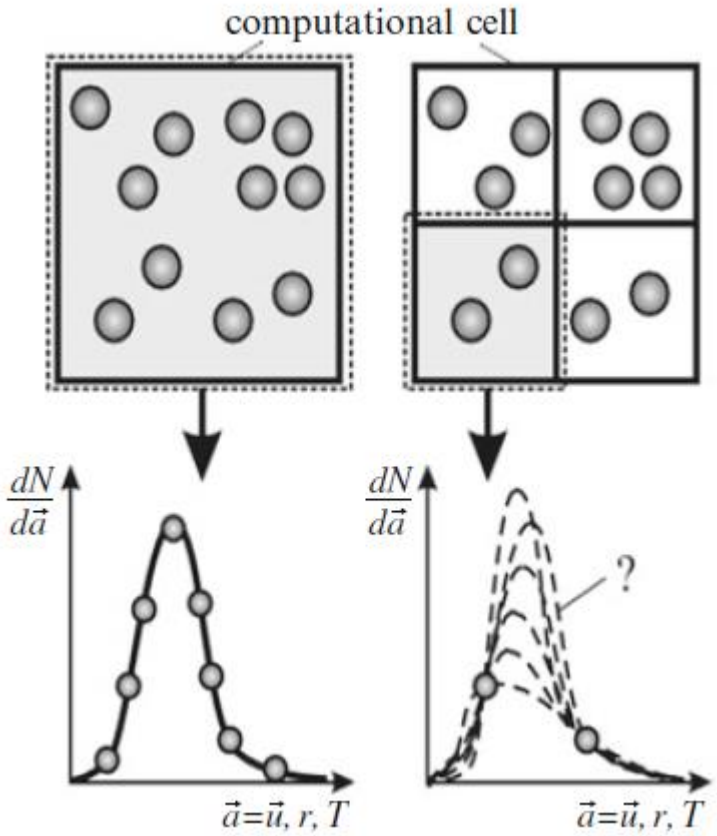

Figure 2.7 – Mesh refinement (parcel number remaining equal) leads to a diminishing number of parcels per cell and thus to poorer statistical resolution of the local droplet properties - taken from Merker, Schwarz & Teichmann (2012)

2.4.2 Primary Breakup

The break-up of liquid sprays is of fundamental importance to GDI engine. The impact on the spatially and temporally varying fuel-air mixture and subsequent combustion is significant and the complexity increased by the time and space constraints of a high speed automotive GDI engine.

The break-up process has been of significant interest for the past century and seen significant works including; Rayleigh mechanism, Weber theory, Castleman hypothesis, Ohnesorge criteria, Taylor mechanisms and instability theory (Sirignano & Mehring, 2000). The four forces acting on a liquid stream and that are important in break-up processes are summarised as:

- Gravity force, $\rho L^3 g$
- Inertia force, $\rho L^2 V^2$
- Surface tension force, σL
- Viscous force, $\mu L V$

From these four forces, three independent non-dimensional numbers can be derived:

- Reynolds number (ratio of inertia to viscous forces),

$$Re_l = \frac{\rho_l L V}{\mu_l} \tag{2.31}$$

- Weber number (ratio of inertia to surface tension forces),

$$We = \frac{\rho_l L V^2}{\sigma} \tag{2.32}$$

- Froude number (ratio of characteristic velocity to characteristic length),

$$Fr = \frac{V^2}{gL} \tag{2.33}$$

It was Ohnesorge in 1931 that first completed quantitative measurements to describe the liquid jet break-up process and found that the Reynolds number and Weber number could be combined to offer a description of the disintegration process including all the main fluid parameters and in so derived the Ohnesorge number Oh.

$$Oh = \frac{We^{0.5}}{Re} = \frac{\rho_l g L^2}{\sigma} \tag{2.34}$$

Where, ρ_l is the liquid density, σ is the surface tension coefficient, μ_l is the liquid dynamic viscosity, V the characteristic velocity and L the characteristic length. In addition to the forces acting on the liquid jet, there are equivalent forces acting on the surrounding gas (denoted with a g subscript) which influence the break-up process and are not described by the above equations. This results in four additional non-dimensional parameters being defined; gas-phase Reynolds number, gas-phase Weber number and gas-to-liquid density and viscosity ratios. The implication of this is that no single equation is able to characterise spray break-up behaviour and it is common to use a combination of the above parameters across a range of break-up behaviours.

Regimes of primary liquid break-up were identified by Reitz & Bracco (1982) and were superimposed on a log(Oh)-log(Re) plot as shown in Figure 2.8 as proposed by Lefebvre (1989).

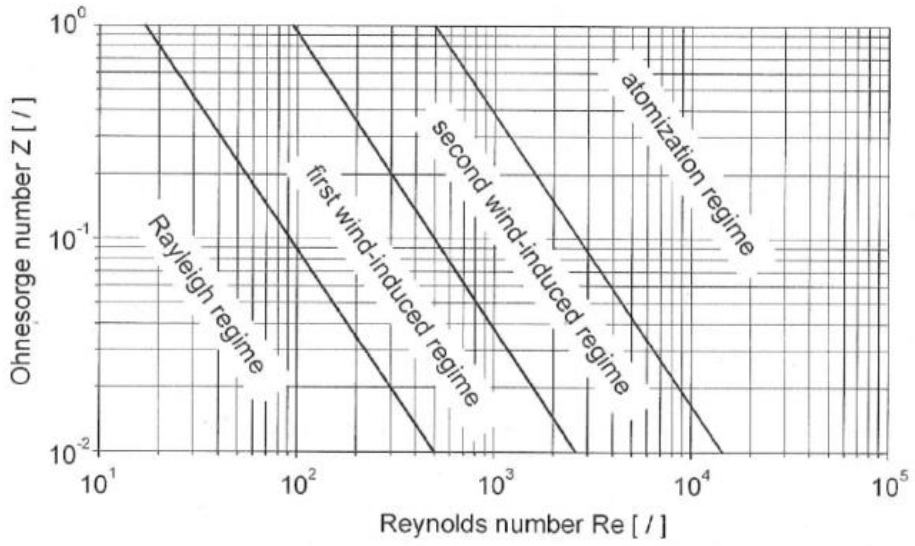

Figure 2.8 – Ohnesorge diagram with liquid breakup regimes identified by Reitz & Bracco (1982) superimposed, taken from Baumgarten (2006)

The first regime identified at low Re and Oh numbers was the Rayleigh capillary mechanism where aerodynamic interactions are less important and axisymmetric distortions occur as a result of hydrodynamic instabilities due to inertia and surface tension forces, with droplet

formation having radii of the same order as the radius of jet. With increasing Re and Oh number is the first wind induced regime where non-axisymmetric oscillations occur, again producing droplets of similar radii to the jet radius. There is an accompanying increase in both intact liquid jet length and jet break-up length. The third regime is the second wind induced regime where at higher Re numbers the flow becomes turbulent within the nozzle. The growth of shorter wavelength surface waves is initiated due to aerodynamic interactions with turbulence generated by the liquid-gas velocity gradient, producing droplets smaller than the jet radius. This regime sees a further increase in liquid jet length but a reduction in jet break-up length, with droplet formation now occurring closer to the nozzle exit. A further increase in Re number leads to an increasingly turbulent flow with chaotic break-up, droplet formation occurring at the nozzle exit and a reduction in liquid jet length. Images depicting the break-up regimes and the changes in liquid core length and break-up length are shown in Figure 2.9.

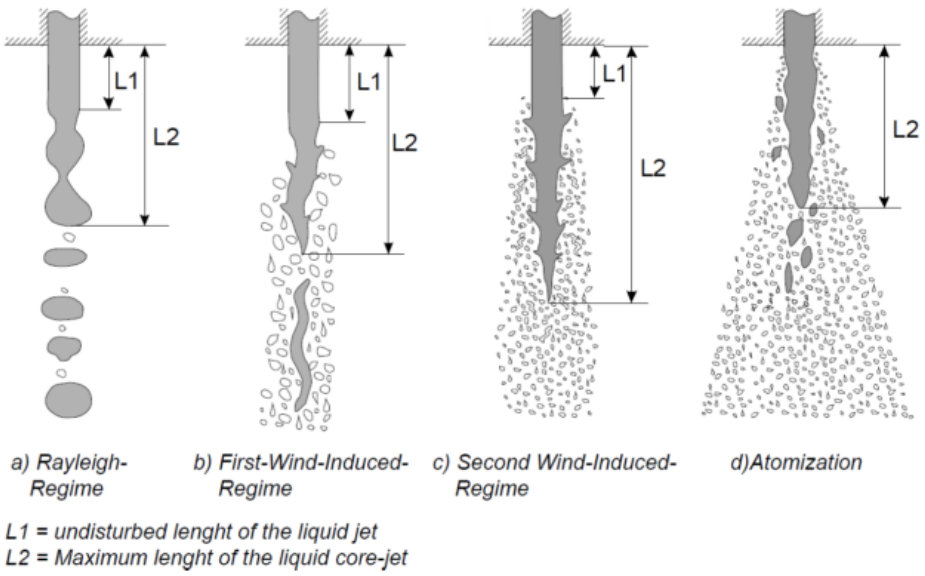

Figure 2.9 – Jet breakup for the four characteristic primary breakup regimes of Reitz & Bracco (1982)

Once the atomisation regime is reached, the concept of break-up length becomes complicated by the jet disintegration process, however attempts have been made to measure liquid penetration lengths within diesel sprays using macroscopic imaging. Changes in image gradient can provide an 'intact liquid surface length' which is shown to reduce with increasing jet velocity. Pertinent to GDI engines with small L/D nozzles and sprays within

the atomisation regime, whilst the liquid surface length may approach zero, the core length may actually increase due to the presence of large liquid fragments existing downstream of the nozzle. Due to being strongly influenced by in-nozzle conditions, this aspect of the atomisation regime is particularly difficult to define.

During the same works, a relationship called the dispersion equation was developed for low speed liquid jets. It was based around the linear theory of hydrodynamic stability of Taylor, and related the wave growth rate of an initial perturbation of infinitesimal amplitude to its wavelength. The solution to this equation provides the maximum growth rate of the Kelvin-Helmholtz wave that occurs at a particular wavelength. The maximum wave growth rate and the corresponding wavelength characterise the fastest growing waves on the liquid surface which are responsible for the liquid break-up.

Reitz & Bracco (1982) also investigated the driving mechanisms for the initiation of distortions and break-up characteristics at the surface of a liquid jet. The mechanisms included; boundary layer velocity profile relaxation, turbulence, cavitation and growth of surface waves due to aerodynamic forces, as depicted in Figure 2.10. Their findings showed that atomisation could occur irrespective of which mechanism was removed. They also concluded that the break-up mechanism was dependent on gas density but not gas pressure. Due to the complexity of the measurement, investigations on the impact of cavitation in turbulent liquid jet break-up in modern GDI injection systems is limited but a detailed example of such work is by Serras-Pereira, Aleiferis & Richardson (2012) where optical nozzles were used to characterise the fuel spray in the near nozzle region and investigate the impact of cavitation and flash boiling effects on primary break-up.

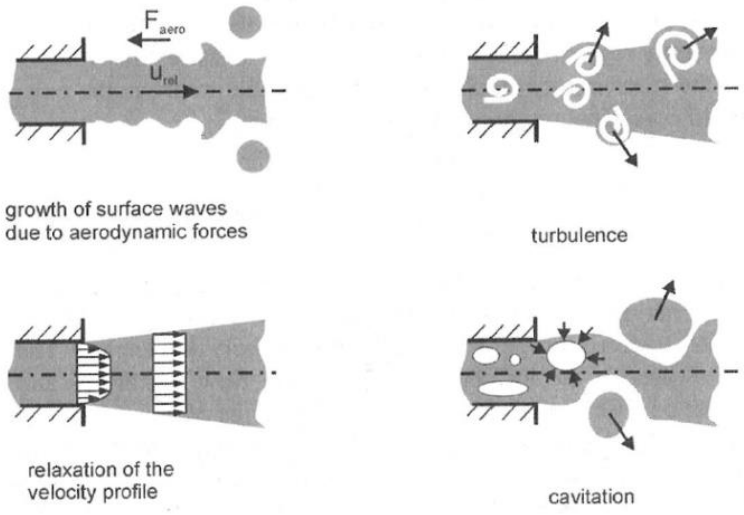

Figure 2.10 – Mechanisms of primary breakup, reproduced from Baumgarten (2006)

Due to the importance of nozzle effects on spray break-up characteristics, a number of efforts have been completed to provide dedicated sub-models to represent the primary break-up process occurring in the near-nozzle region.

The 'Huh' model in particular was created by Huh & Gosman (1991) and is based on the premise that the two most significant mechanisms in spray atomisation are the gas inertia and internal turbulence stresses generated in the nozzle. The assumption is that turbulence generated in the nozzle produces initial perturbations on the fuel jet surface as it exits the nozzle, which then grown exponentially via interaction with the surrounding gas (surface wave growth) until they detach from the jet as droplets. The model estimates the initial perturbations from an analysis of the flow through the hole and then uses Taylor wave growth theory to represent the atomisation process. Figure 2.11 taken from the paper by Som, Ramirez, Aggarwal, *et al.* (2009) in developing the KH-ACT model certainly suggested that for diesel sprays at low pressures (21MPa), cavitation effects were small compared to turbulence and aerodynamic effects. This is obviously not all encompassing since increases in fuel spray and ambient gas conditions or changes in nozzle geometry will impact the balance between driving break-up mechanism so one needs to bear this in mind when defining the most appropriate break-up model for their situation.

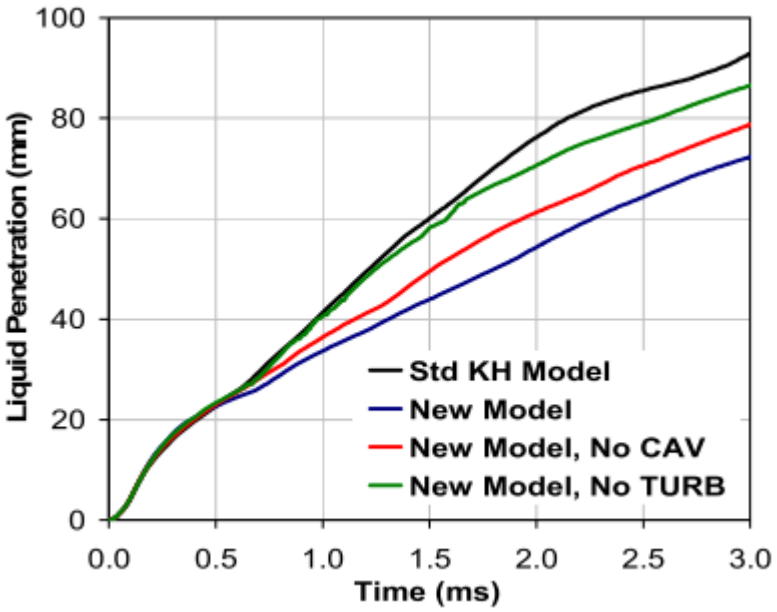

Figure 2.11 – Effect of different spray models on spray penetration for 21MPa rail pressure – taken from Som, Ramirez, Aggarwal, *et al.* (2009)

Campbell, Gosman, Hardy, *et al*. (2013) utilised the Huh primary break-up model with the Reitz-Diwakar break-up model for secondary break-up with grid refinement to model flame lift-off length in a multi-hole diesel injector at 150MPa (moderate injection pressures by today's standards). The author shows reasonable predictions of vapour penetration lengths but ultimately shows under-prediction of vapour lengths due to the "well known shortcoming of eddy viscosity turbulence models in free shear flow" when using the standard k-ε. Small improvements were seen with the RNG k-ε for a short period but ultimately the same under-prediction of penetration length was seen once the fuel spray was fully developed. The author concludes that considerable improvements could be made with improvements in turbulence predictions.

The Linearized Instability Sheet Atomization (LISA) model was created by Schmidt, Nouar, Senecal, *et al.* (1999) and utilises the experimental work by Senecal, Schmidt, Nouar, *et al.* (1999) that was undertaken at a similar time. The model was developed in response to the increasing use of hollow-cone pressure-swirl injectors being used in GDI engines. The model assumes little knowledge is known of the internal details of the injector, but instead utilises available observations of external spray characteristics and in particular, theories on liquid sheet break-up regimes. The author presents results showing favourable predictions of drop size and penetration length when compared with experimental data though does suggest that

further work is needed to improve the injector exit velocity prediction and validate the assumed aerodynamic break-up process.

The use of the KH model for primary break-up and KH-RT model for secondary break-up has been widely employed for diesel spray simulation due to it being computationally efficient and fairly effective at representing the global spray behaviour. However, this model does not account for the effects of cavitation and turbulence within the nozzle on the atomising spray, which has been shown to be significant in certain sprays. The work of Som, Ramirez, Aggarwal, *et al.* (2009) sought to modify the traditional KH model to include effect for nozzle turbulence and cavitation and was implemented in commercial code CONVERGE and called KH-ACT, an acronym for Kelvin Helmhotz-Aerodynamic Cavitation Turbulence. This, alongside subsequent reports by Som & Aggarwal (2010) and Som, D'Errico, Longman, *et al.* (2012), have shown this version of the model to show very reasonable improvements in ability to predict global spray structure of diesel sprays though as discussed previously, sprays with strong primary break-up characteristics would expect to be better modelled with more intensive modelling of the characteristics of the primary break-up regime.

Finally, mathematical correlations have also been used to define the droplet size distribution following the primary breakup process. Correlation types including, upper-limit, log-normal, squared, chi-squared and normal distributions have all been applied to droplet size distributions but the Rosin-Rammler distribution is the most commonly used. This method can provide very realistic predictions of droplet sizes and breakup processes but requires prior knowledge of the expected droplet size distribution, usually through experimental PDA data, to correctly specify the initial distribution characteristics at some location downstream of the nozzle exit.

2.4.3 Secondary Breakup

After the liquid jet has undergone the primary break-up into liquid ligaments and large droplets, it undergoes a process of secondary atomisation as a result of the aerodynamic forces between the droplet and surrounding gas. The aerodynamic forces act to flatten the droplets and ligaments resulting in an unstable growth of surface waves which eventually lead to disintegration.

Experimental investigations have found that the break-up modes can be broken down into a number of different mechanisms which can be classified by the gaseous Weber number of the droplet as summarised in Figure 2.12. The progression of research in this area has been summarised by Guildenbecher, López-Rivera & Sojka (2009), where the authors have attempted to resolve some of the discrepancies between Weber number transitions that exists in the literature. A summary of the physical processes involved in each deformation mechanism is now provided.

The first stage of all deformation mechanisms is the impact of aerodynamic forces on the droplet. Deformation is caused by an unequal static pressure distribution between the forward and rear of the drop periphery. This causes the drop to expand laterally and compress in the direction of motion. Vibrational breakup occurs when the aerodynamic forces are insufficient to overcome the droplet surface tension but cause the droplet to oscillate. If these oscillations are unstable then the droplet will break down into a few large fragments.

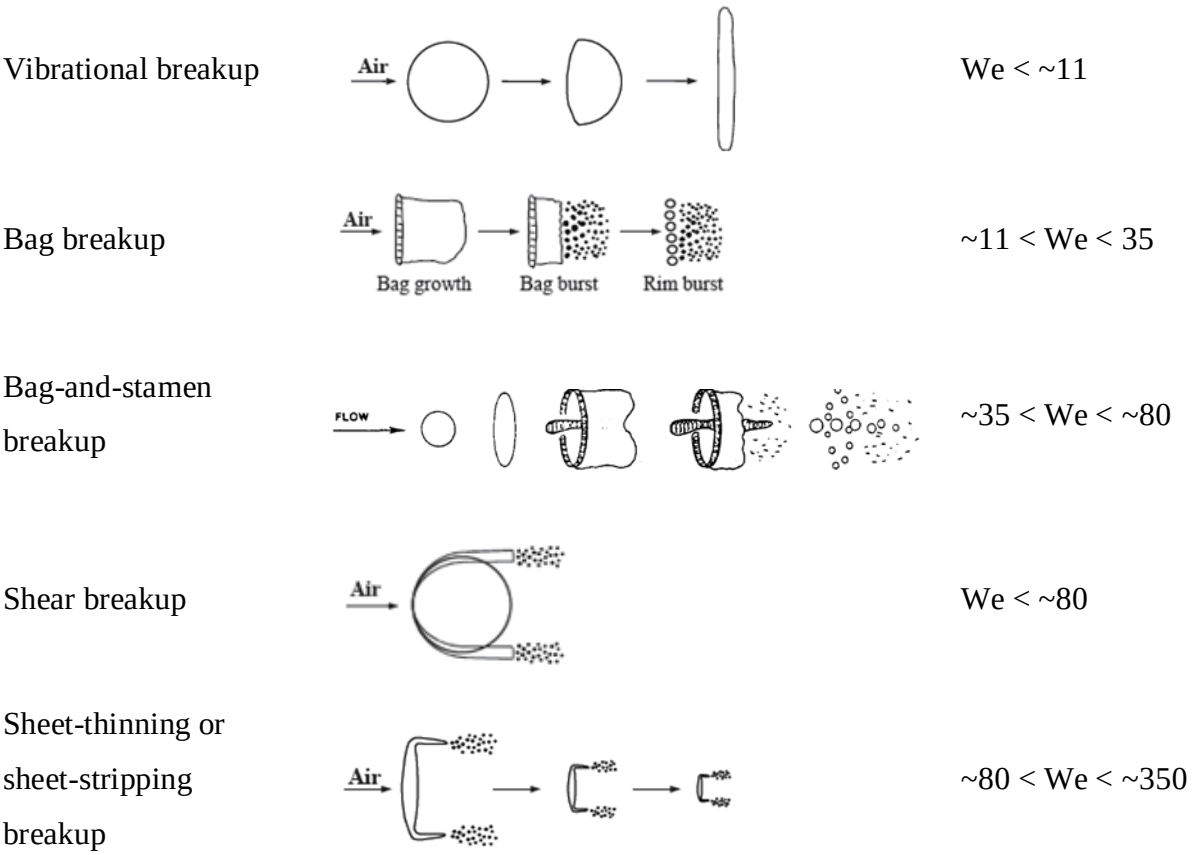

Wave crest stripping breakup		We > ~350
Catastrophic breakup	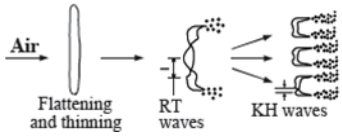	We > ~350

Figure 2.12 – Droplet secondary breakup mechanisms

The bag breakup mechanism occurs over four sub-stages; the evolution into an oblate spheroid due to aerodynamic deformation, bag growth where the centre of the drop gets blown downstream forming a hollow bag attached by a toroidal ring, breakup of the bag where the bag bursts forming a large number of small fragments, finally the toroidal ring breakup in which a number of larger fragments are formed. Due to the time (milliseconds) and length (micrometre) scales involved, experimental proof of this break-up mechanism is not yet available but Liu & Reitz (1993) have postulated that impurities within the droplet or disturbances in the flow field could be the initiation for bag breakup.

This transition between bag breakup and sheet-thinning breakup mechanisms is often subject to variation within the literature. Pilch & Erdman (1987) document a variation on the bag breakup regime called bag-and-stamen breakup where a toroidal ring and hollow bag are formed but column of liquid (stamen) is also formed along the droplet axis where the bag bursts first and rim and stamen disintegration follows. Hsiang & Faeth (1992) use the term multimode, and describe a breakup mechanism where both aerodynamic effects and shear effects are important. Two theories exist to describe this mechanism; the "combined Rayleigh-Taylor/aerodynamic drag" mechanism and the "internal flow" mechanism, though the latter has been shown to be a better fit to experimental and numerical evidence. The internal flow theory hypothesises that drop deformation leads to internal flow from the poles to the equator. This flow causes a pressure difference across the drop which tends to result in bag breakup, whilst the effect of the rapid deformation at the drop periphery tends to result in sheet-thinning breakup, hence a dual mode of breakup can exist. Ranger & Nicholls (1969) proposed an additional breakup mechanism called shear breakup where breakup is predominantly shear driven and thus happens at Weber numbers at the upper range of the bag-and-stamen or multimode regime.

Sheet thinning or stripping breakup occurs at much higher initial velocities. Initial deformation due to aerodynamic forces progresses as seen for vibrational breakup and bag breakup but following, due to the higher relative velocities, ligaments are stripped from the periphery where they break into smaller fragments. This continues until the droplet is completely fragmented or so small that aerodynamic forces become negligible (Liu & Reitz, 1997).

The catastrophic breakup regime occurs at the highest relative velocities between droplet and surrounding gas. In this breakup mechanism, the unstable surface waves grow rapidly with time and eventually penetrate the droplet leading to fragmentation. Liu & Reitz (1993) have noted that the wave growth may be described by either a Rayleigh-Taylor instability where instabilities occur when a density discontinuity is accelerated towards a lower density or Kelvin-Helmholtz instability where instabilities occur when high relative velocities exist at an interface though most authors have assumed that R-T instabilities dominate this mechanism due to the extremely high velocities seen by the droplets (Guildenbecher, López-Rivera & Sojka, 2009; Hwang, Liu & Reitz, 1996). Some researchers also include a wave crest stripping regime where the formation of small-wavelength surface waves (where catastrophic breakup would be initiated by long-wavelength surface waves) on the droplet surface allow the action of the flow field to strip the wave crests from the droplet surface.

In an in-cylinder application, spray momentum quickly reduces following primary break-up hence it is clear that high velocities necessary for effective secondary atomisation must be provided by the in-cylinder flow field. In dense diesel sprays with strong primary break-up regimes, secondary break-up regimes are of less significance whereas in GDI sprays, internal turbulence and cavitation are reduced and hence secondary break-up processes can be dominant (Merker, Schwarz & Teichmann, 2012), hence the secondary evaporation process is critical to the gaseous mixture formation around the spark plug and the rest of cylinder at the point of ignition, which has a subsequent impact on spark kernel development, flame propagation and pollutant formation.

A large number of models have been developed in support of modelling atomising fuel sprays.

One of the earliest model proposed by Reitz & Diwakar (1986) is very similar to that proposed by Dukowicz (1980) where the Weber number is used to define one of two break-up regimes, either ‘bag’ breakup or ‘stripping’ breakup, and dependent on the defined regime, the droplet radius is reduced by the rate of change equations. The model requires user input

through four constants, two to determine the onset of the breakup regime and two to determine the droplet characteristic timescale.

In 1987, O'Rourke & Amsden (1987) proposed an alternative break-up model called TAB, standing for Taylor Analogy Break-up, based on the earlier work of Taylor (1963). In this model, Taylors analogy between an oscillating and thus distorting drop is made to that of a spring-mass system with the gas aerodynamics, droplet surface tension, viscosity is suggested to be analogous to the external force acting on the mass, spring force and damping force respectively. The TAB model has been shown to predict well at low to moderate injection pressures but under predict penetration liquid and vapour penetration at higher injection pressures due to move to higher Weber number break-up regimes not being represented by the Taylor analogy (Habchi, Verhoeven, Huu, *et al.*, 1997).

The breakup model proposed by Pilch & Erdman (1987) was developed around an extensive database of experimental data on hydrodynamic fragmentation. From this data, Pilch and Erdman were able to generate correlations for the critical Weber numbers, the velocity history of accelerated droplets and droplet total breakup time, linked by a maximum stable diameter, which could be applied to create sub-models to characterise five breakup regimes: vibration, bag, bag-and-stamen, sheet stripping, wave crest stripping. This breakup model, whilst not explicitly modelling the KH-RT behaviour of high Weber number drops, benefits from having no user tuneable constants.

The WAVE break-up model is based on the work of Reitz & Diwakar (1987) and uses the theory of Kelvin-Helmholtz instability analysis as a consequence of pressure perturbations causing surface wave growth.

Habchi, Verhoeven, Huu, *et al.* (1997) attempted to resolve some of the short comings of the WAVE model by coupling this model with a new break-up model (FIPA) which is based on the work of Pilch & Erdman (1987). In this example, the model utilises the WAVE model for primary break-up of the liquid phase and the FIPA model for subsequent atomisation based on the Weber number and five subsequent break-up regimes. The authors reported good predictions of liquid and vapour penetrations against experimental data.

The KH-RT model proposed by Patterson & Reitz (1998) was a progression of the earlier model WAVE and considers both Kelvin-Helmholtz aerodynamic surface instabilities and Rayleigh-Taylor instabilities due to droplet deceleration as competing sub-models, with the

sub-model predicting droplet instability first determining the droplet breakup regime. This model again has four empirical constants, two for each sub-model. There are a number of examples in the literature of the KHRT model being applied to ICE sprays.

Wang, Reitz & Yao (2012) utilised the KH-RT model for making mixture, temperature and emissions predictions for a number of heavy duty diesel engines with multi-hole injectors and various multiple injection strategies. The author cites the simplicity and good predictive accuracy of the KH-RT break-up model but does not directly show results comparing predictions with experimental fuel spray data. The paper does show good predictions for global combustion parameters (pressure histories and rate of heat release) and presents a sensitivity analysis of the predictions to KH-RT model to model tuning constants. The authors also completed a parametric study on the model constants used in the KH-RT breakup model, indicating the need to provide good estimates of the model constants to yield accurate predictions for droplet breakup and all subsequent processes.

2.4.4 Impingement

The process of liquid impingement has been of interest to researchers in the internal combustion engine community since the identification that the injection of liquid fuel sprays in direct injection engines can result in impingement of liquid fuel on various in-cylinder surfaces. The effect of liquid fuel impingement in DI engines has been attributed to:

- Increases in fuel consumption and carbon dioxide production due to impinged fuel not contributing to effective piston work
- A key contributor to soot formation due to pool fires burning as an uncontrolled diffusion flame
- Increases in unburned hydrocarbons due film evaporation post flame extinction and gaseous hydrocarbons exiting the cylinder during scavenging

A number of researchers including Montanaro, Malaguti & Alfuso (2012), Montanaro, Allocca, Ettorre, *et al.* (2011), Luijten, Adomeit, Brunn, *et al.* (2013), Yang & Ghandhi (2007) and Drake, Fansler, Solomon, *et al.* (2003) have conducted experiments to investigate fuel spray impingement in direct injection engines and the impact of various factors on the fuel

impingement process including injection timing, injection pressure, fuel type, fuel temperature, gas temperature, surface temperature and surface roughness.

In GDI engines typical locations of potential fuel impingement are the intake valve, spark plug, cylinder liner and piston crown. Serras-Pereira (2010) operated a single cylinder optical GDI research engine over a number of injection timings and found that injection timing early in the intake stroke coincided with periods of high in-cylinder flow velocities and high intake valve lift which in turn caused significant intake valve impingement and adverse mixture preparation.

As part of a publication by Bai & Gosman (1995) (also including the formation of a modelling methodology), the authors conducted a literature survey of current research findings on single droplet impingement processes. Their findings were that a droplet may undergo different regimes dependent on the specific conditions at the point of impingement and are summarised in Figure 2.13 and described as follows.

1. 'Stick' or 'adhere' to the impingement surface in nearly spherical form. This occurs when the impact energy is low and the wall temperature is below the characteristic pure adhesion temperature.
2. 'Spread' to form a liquid film on the surface if impacted with moderate velocity onto a dry wall, or merge with a pre-existing liquid film on a wetted wall.
3. 'Rebound' where the droplet bounces off the wall after impact. This regime occurs under two conditions: on a dry wall when the wall temperature is greater than or equal to the characteristic pure rebound temperature where contact with the surface is prevented by the intervening vapour film, or on a wetted wall when the impact energy is low and the air film trapped between the impacting droplet and liquid film causes low energy loss and the droplet to rebound.
4. 'Rebound with breakup' where the wall temperature is less than the characteristic pure rebound temperature and bounces off the hot surface but is accompanied by the breakup of the droplet into two or three smaller droplets.
5. 'Boiling induced breakup' where the droplet breaks up due to rapid boiling on a hot wall with temperature near the Nukiyama temperature. This regime can exist even at very low impact energies.

6. 'Breakup' occurs when the wall temperature is greater than the pure rebound temperature and the droplet first undergoes a large deformation to form a radial film and then further liquid film fragmentation due to the thermo-induced instability.
7. 'Splash' when very high impact energies are present, a crown is formed, unstable jets develop on the periphery of the crown and breakup into many fragments.

The authors suggest that these regimes are governed by a number of characteristics that describe the impingement conditions: droplet velocity, size, temperature, incidence angle, fluid properties such as viscosity, surface tension, wall temperature surface roughness and if present, wall film thickness and gas boundary layer characteristics in the near-wall region.

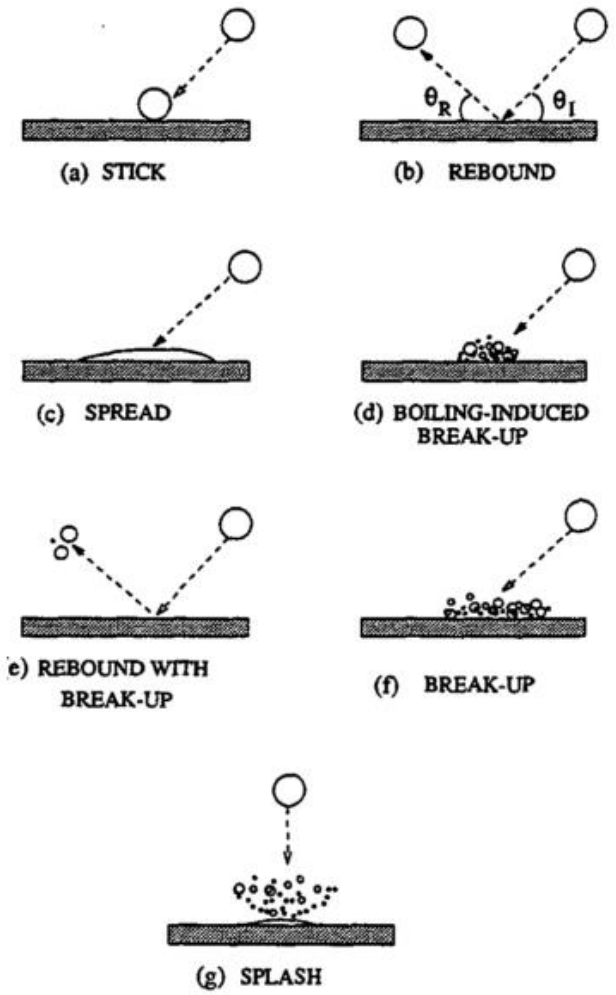

Figure 2.13 – Droplet impingement regimes as proposed by Bai & Gosman (1995)

In addition to Weber number (representing the relative importance of droplet kinetic energy to surface energy) as an important quantity in describing impinging flows, the authors also present the droplet Laplace number La, a measure of the relative importance of surface tension to viscous forces, as an important characteristic of impinging droplets. The Laplace number is shown in equation (2.35).

$$La = \frac{\rho_l \sigma L}{\mu^2} \tag{2.35}$$

The authors summarise the effect of Weber number and wall temperature on the droplet impingement regime in Figure 2.14 but note that the final outcome is a function of each of the parameters noted previously and multi-dimensional, and not two-dimensional as presented in Figure 2.14.

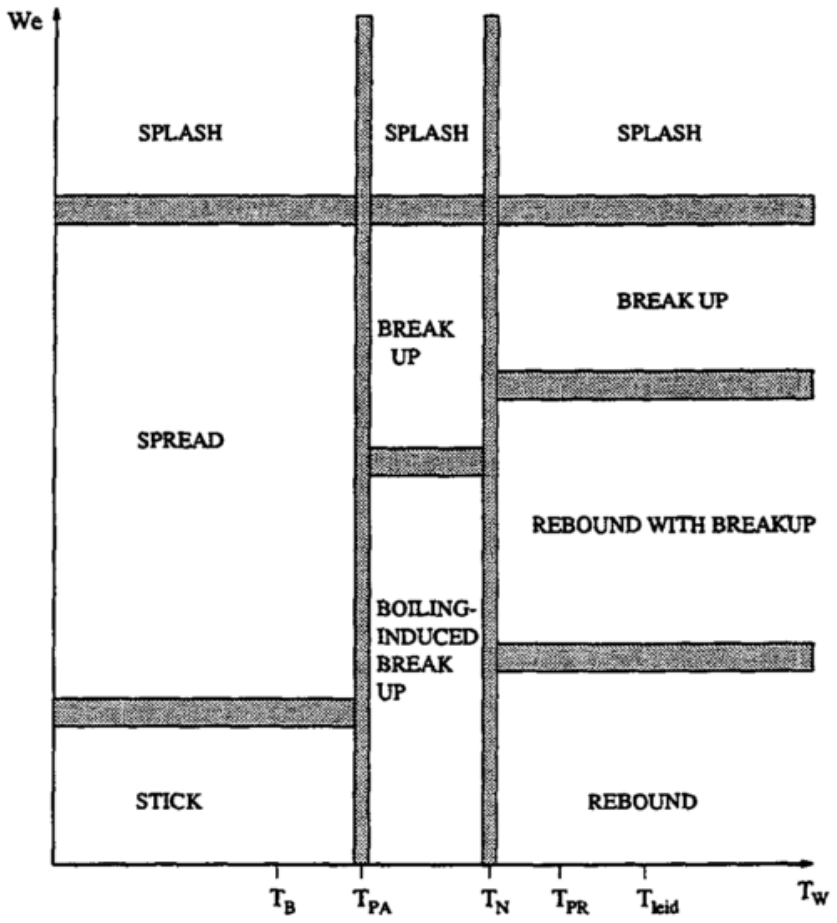

Figure 2.14 – Droplet impingement regimes and transition criteria as proposed by Bai & Gosman (1995)

The impingement model by Bai & Gosman (1995) utilises the results from their literature survey to develop a numerical model to represent the process. The model is based on mass, momentum and energy conservation constraints and the addition of a randomising procedure on the post-impingement characteristics to represent the stochastic nature of the impingement process. The model first evaluates whether the wall is 'wetted' or 'dry' and based on this determines the potential impingement and post-impingement regimes based on Weber number. The authors comment in several instances on the lack of available data to adequately characterise the influence of key parameters on the impingement regime, indicating the need for improvements. The model does have a number of limitations including conditions where wall temperatures are below the liquid boiling point and neglect the effects of neighbouring impinging droplets and the gas boundary layer on the impingement dynamics.

The work of Allocca, Andreassi & Ubertini (2007) compared the Bai & Gosman impingement model against a model by Lee & Ryou (2000) across a range of representative diesel like conditions. Their results suggested that whilst the Bai & Gosman model provided better predictions for secondary droplets due to the empirical relationship employed by the model from Lee & Ryou (2000), in their original form both models were inadequate of correctly predicting splash phenomena due to the number of secondary droplets generated by the spray-wall interactions and the tangential component of the splashed droplet velocity.

The modelling approach of Bai & Gosman (1995) has been furthered by a number of researchers in an attempt to improve the spray-wall interaction predictions.

The work by Rosa, Villedieu, Dewitte, *et al.* (2006) which only considers smooth dry walls but was based on a significant quantity of experimental data, was combined with the Bai & Gosman model described above to create the 'Bai-ONERA' model. Literature describing the predictive capability of this model under realistic operating conditions appears unavailable at this time.

Another significant development was through a series of works by Prof. Senda, including Senda & Fujimoto (1999), Senda, Kanda, Al-Roub, *et al.* (1997), Ashida, Takahashi, Tanaka, *et al.* (2000), Senda, Kobayashi, Iwashita, *et al.* (1994) and Matsuda & Senda (2003).

The results from these works are combined into a revised version of the original Bai & Gosman model with modifications made to the sub-models defining regime transition based on an extensive experimental dataset.

The model defines three regimes based on Temperature T^* which is defined by equation (2.36).

$$T^* = \frac{T_W - T_N}{T_L - T_N} \tag{2.36}$$

Where T_W is the wall temperature, T_L is the Leidenfrost temperature and T_N is the Nukiyama temperature and is defined by equation (2.37).

$$T_N = B_S T_{sat} \tag{2.37}$$

Where B_S is a user defined constant. T_{sat} is the liquid saturation temperature dependent on the liquid vapour pressure which can either be calculated via the Clausius-Clapeyron equation or by NIST tables, where the latter is used by the CFD code used in this research.

The three droplet impingement regimes are defined as follows:

Regime 1: Free convection and nucleate boiling regime, $T^* \leq 0.00$

This range is sub-divided into conditions for a dry surface and wetted surface, for which the following is a description of each sub-regime, and the free convection and nucleate boiling regime as a whole is summarised in Figure 2.15.

Dry Surface:

- Drop-drop interaction or deposition: $We \leq 400$

  In this regime the interaction between droplets during impingement affects their residence time on the surface, spreading, and droplet and film stability. After impact, droplet interactions are defined based on collision (including any coalescence) and secondary breakup models. Droplet deposition occurs until the surface coverage ratio is exceeded and a liquid film is formed – discussed further below (Senda & Fujimoto, 1999).

- Splash: $We > 400$

Wetted Surface:

- Drop-film interaction: $We \leq 300$

At low Weber numbers, three film breakup sub-regimes, 1) rim type, 2) cluster type, 3) column type, are defined from the experimental works of Al-Roub, Farrell & Senda (1996) and Al-Roub (1996) as a function of the non-dimensional film thickness (δ) and consequently define the child droplet diameter ratio and Weber number (Senda & Fujimoto, 1999).

- Deposition/joins existing film: $300 < We < We_{cr}$
- Splash: $We \geq We_{cr}$

The critical droplet Weber number, We_{cr} is defined by equation (2.38).

$$We_{cr} = (2164 + 7560\delta^{1.78})La^{-0.2} \quad (2.38)$$

Where δ is the non-dimensional film thickness defined by equation (2.39).

$$\delta = (2/3)/\beta^2 \quad (2.39)$$

Where β is the droplet spreading factor defined by equation (2.40).

$$\beta = 0.87(We/6 + 2)^{0.5} \quad (2.40)$$

The droplet spreading factor is used to relate the impinging droplet Weber number to the child droplet outgoing Weber number and diameter, and in the calculation of the critical Weber number for determining if a high Weber number impinging droplet is deposited into the film or splashes (Senda & Fujimoto, 1999).

Regime 2: Transition boiling regime, $0.00<T^{*}\leq 1.00$

- Rebound: $We \leq 200$
- Spread/deposition: $200 < We \leq We_{cr}$
- Splash: $We > We_{cr}$

Regime 3: Film boiling regime, $T^{*}>1.00$

- Rebound: $We \leq 100$
- Rebound and breakup: $100 < We \leq 200$
- Splash: $We > 200$

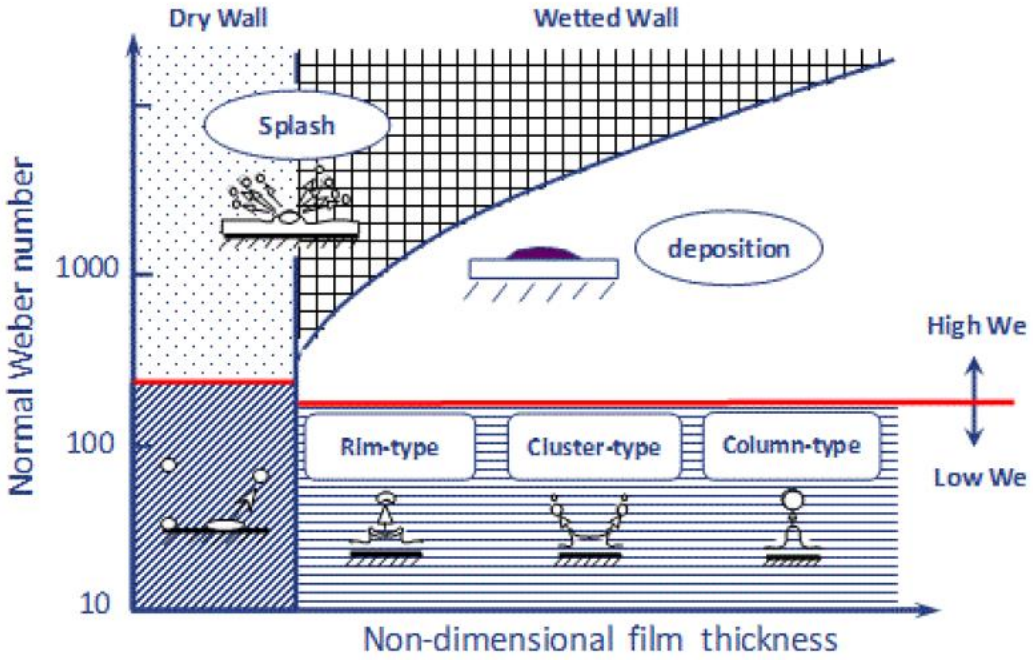

Figure 2.15 – Summary of Senda droplet-wall impingement model for regime 1, natural convection and nucleate boiling

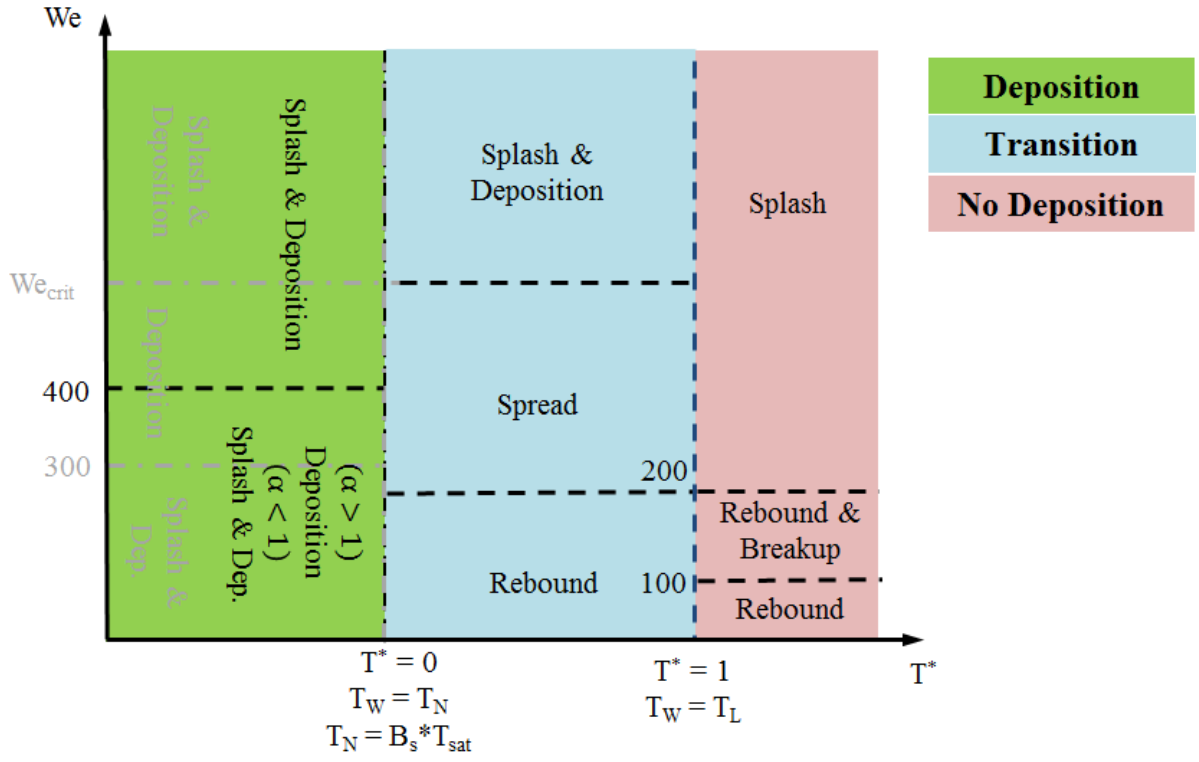

Figure 2.16 – Summary of all Senda droplet-wall impingement model regimes

This version of the Senda impingement model utilises the information and developments from each of the previously mentioned sources, and in particular provides a significant reduction in the number of user defined constants which is beneficial with limited experimental data for model validation.

In spite of the significance of liquid impingement in ICE's, its critical feature in fuel spray modelling and the numerous research efforts in this area, a general theory for impinging droplets on solid surfaces is still unavailable. The study of the interaction between impinging droplets and solid surfaces continues to be an area of active research in both experimental and numerical fields.

2.4.5 Liquid Films

A liquid film or droplet attached to a wall is subject to a number of physical phenomena, as listed below and depicted in Figure 2.17:

- Weight of the liquid film or droplet
- Surface tension
- Liquid-gas and wall-liquid shear stress
- Imparted momentum from impinging droplet and the surrounding gas phase and lost momentum due to splashing
- Flow separation and sheet breakup
- Heat transfer: convection to the surrounding gas, conduction to the solid surface
- Evaporation to the surrounding gas

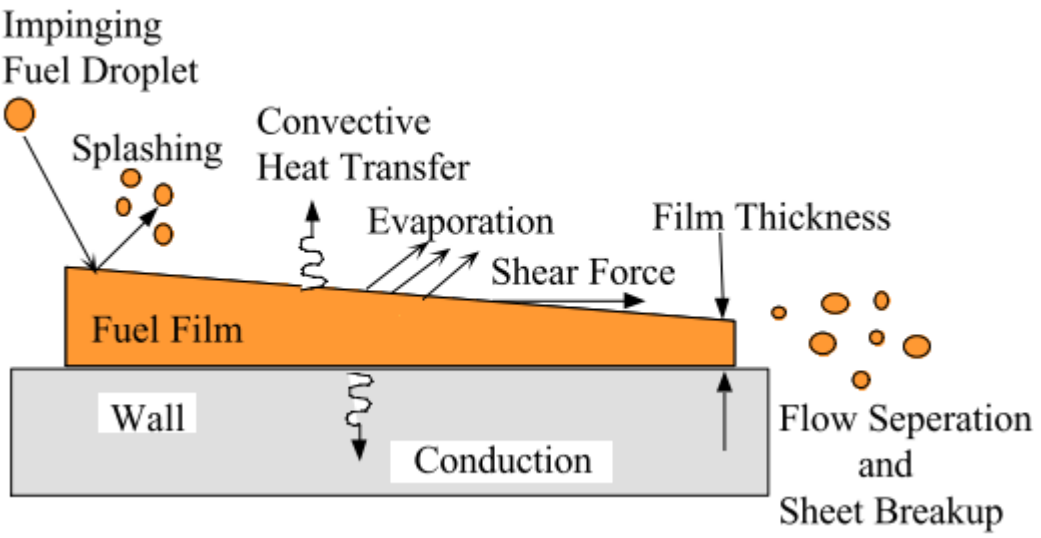

Figure 2.17 – Major Physical Phenomena Governing Film Flow – taken from (Stanton & Rutland, 1998)

In a subsequent work, Bai & Gosman (1996) also defined a methodology for modelling the characteristics of liquid films using an Eulerian approach, where transport equations for mass, momentum and energy for the wall film are solved in the boundary-layer framework.

This methodology is often furthered by considering a Lagrangian approach for individual impinged droplets up to a certain point, after which the code switches to the Eulerian approach as originally proposed by Bai & Gosman (1996).

A typical approach for defining the switch between Lagrangian and Eulerian approach is to use a surface coverage ratio limit. After a droplet has been determined to be deposited, it is assumed to spread into a cylindrical form with diameter D_s. The surface coverage ratio γ_c, defined by equation (2.41), is constantly evaluated as droplets impinge on the solid surface until exceeding a predefined value, after which the droplet parcels on the cell face merge into a liquid film and are subsequently treated under the Eulerian approach. A liquid film spreading into a new cell face will instantly absorb any individual impinged droplet parcels in the new cell face into the liquid film.

$$\gamma_c = \frac{\pi}{4A_C}\sum_i D_{s,i}^2 N_i \tag{2.41}$$

Where A_c is the area of the cell face where the droplet parcel is located, N_i is the number of droplets in the i^{th} parcel.

Film stripping has been investigated by a number of researchers (Maroteaux, Llory, Le Coz, *et al.*, 2002; Maroteaux, Llory, le Coz, *et al.*, 2003) and is defined by three different mechanisms:

- Stripping due to wave instability generated by adjacent flow
- Stripping due to body-force induced instability (e.g. gravity, piston acceleration)
- Breakup caused by flow over a sharp edge

The vaporisation rate of a liquid film is a function of both the wall temperature T_w, and the environmental gas pressure through a change in the vapour pressure of the liquid. Heat transfer from the solid surface to the liquid film is typically characterised by four regimes, separated by the saturation temperature T_{sat}, Nukiyama temperature T_N and Leidenfrost temperature T_L as characterised in the boiling curve and droplet evaporation curves shown in Figure 2.18 and described as follows:

Regime 1: Liquid film evaporation, $T_w < T_{sat}$

- The liquid film evaporates slowly and the evaporation rate is strongly dependent on the turbulence level within the surrounding gas.

Regime 2: Nucleate boiling, $T_{sat} < T_w < T_N$

- The liquid in the thermal boundary layer is overheated forming vapour cavities. The process of phase change consumes heat flux from the wall and prevents the temperature of the main film from exceeding the saturation temperature. This occurs until heat transfer from the wall to the liquid reaches a maximum at the Nukiyama temperature, often called the Critical Heat Flux (CHF).

Regime 3: Transition boiling, $T_N < T_w < T_L$

- Small vapour cavities coalesce to form larger vapour columns and pockets with an increasing amount of heat flux between wall and liquid being transferred through a vapour.

Regime 4: Film boiling or Leidenfrost, $T_w > T_L$

- Formation of a vapour cushion prevents direct contact between the liquid and wall, reducing heat flux from wall to liquid.

A typical method for modelling the film boiling characteristics is to use the pool boiling correlations from White (1988), where a graphical summary is shown in Figure 2.19.

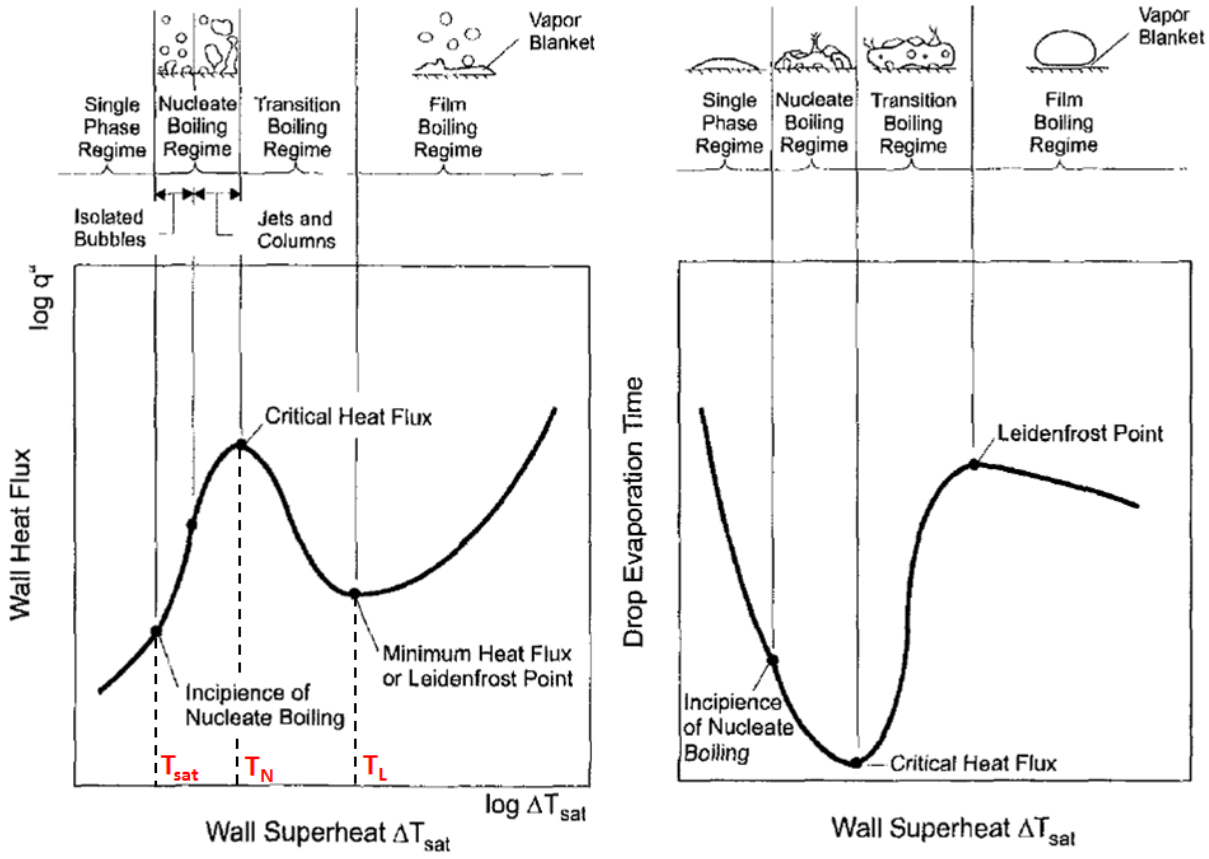

(a) (b)

Figure 2.18 – (a) Boiling curve and (b) Sessile droplet evaporation curve and schematics illustrating the regimes of boiling, reproduced from Bernardin & Mudawar (1999)

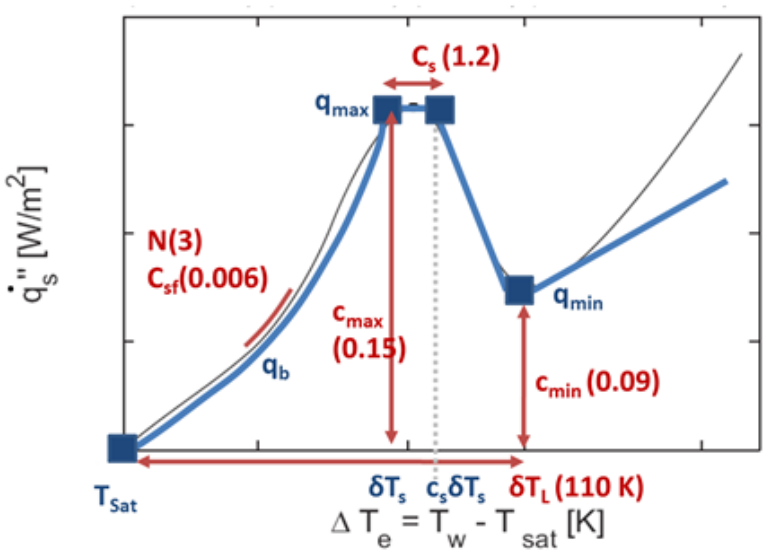

Figure 2.19 – Summary of the liquid film boiling model

2.4.6 Leidenfrost Temperature Determination

Imposing a reasonable estimate of the Leidenfrost temperature (which is difficult to measure experimentally) is critical for accurate predictions of high temperature wall-wetting and in particular, is used in the determination of the droplet impingement regime (equation (2.36)).

Habchi (2010) developed and validated a model for estimating the condition specific Leidenfrost temperature based on a number of experimental works and is defined by equation (2.42).

$$T_{cr} = T_{sat} + \Delta T \tag{2.42}$$

Where T_{cr} represents the pressure dependent Leidenfrost temperature T_L, and ΔT is defined by equation (2.43).

$$\Delta T = \begin{cases} T_{cr|1\,bar} - T_b & : if\ (p \leq 1\,bar) \\ \dfrac{(T_{cr|1\,bar} - T_b) - A}{T_c - T_b}(T_c - T_{sat}) + A & : if\ (p > 1\,bar) \end{cases} \tag{2.43}$$

Where $T_{cr|1\ bar}$ is the Leidenfrost temperature at 1 bar gas pressure, T_b is the normal boiling temperature of the liquid at 1 bar gas pressure, T_c is the critical temperature of the liquid and A is a constant calculated via: $A = \text{Max}(1, T_{cr|1\ bar} - T_c)$.

Hence the Habchi model assumes that the Leidenfrost temperature is static below atmospheric pressure, but at pressures greater than atmospheric it tends linearly towards A when the gas pressure tends towards the critical pressure.

As mentioned previously, determining the Leidenfrost temperature experimentally is difficult and a great deal of variation is seen in published data. Also, $T_{cr|1\ bar}$ across a variety of fuels (required to determine ΔT within equation (2.43)) may not be available.

Spiegler, Hopenfeld, Silberberg, *et al.* (1963) suggest that at conditions where the gas pressure is significantly less than the critical pressure, the result of $\frac{27}{32}T_c$ provides a good approximation of the foam limit and hence the minimum of the heat flux versus temperature curve at standard conditions. Thus, using the critical temperature T_c of the fuel (which is often well known), $T_{cr|1\ bar}$ can be approximated as defined by equation (2.44).

$$T_{L|1\ bar} = \frac{27}{32}T_c \tag{2.44}$$

Where in a CFD code T_c is typically determined from NIST tables for the fuel.

It is worth noting that in reality, the Leidenfrost temperature is a dynamic property also dependent on the impinging droplet conditions. This Leidenfrost temperature model is based on sessile droplets and does not account for the impact of droplet dynamics on Leidenfrost temperature.

2.4.7 Droplet-Droplet Collisions

In real developing sprays, droplets collide with each other and undergo subsequent processes. O'Rourke (1981) was the first to attempt to model inter-droplet collisions and the subsequent interactions, including coalescence, separation and bouncing. When separation or bouncing occurs only momentum is exchanged; in coalescence momentum, energy and mass are all

exchanged. The approach taken is statistical rather than deterministic to avoid significant computational cost.

Extensions to O'Rourke's model have come from Schmidt & Rutland (2000) via the use of a No-Time-Counter (NTC). The revised model evaluates the density of fuel drops within the cell to determine if a direct collision calculation via O'Rourke's method is cheaper than the NTC method and proceeds by the cheapest methodology, shown to both reduce computation time and improve accuracy of the original model.

Further revisions include addition of a coalescence time-step by Aamir & Watkins (1999), additional constraints for determining collision likelihood by Nordin (2001), and cell clustering routines that allows collisions between parcels in adjacent cells. This remains the standard methodology for inter-droplet collisions in fuel spray modelling but the difficultly and computational cost of trying to handle collision processes between parcels in a Lagrangian context has led some to believe that inter-droplet collisions should not be modelled at this time (Merker, Schwarz & Teichmann, 2012).

2.4.8 Droplet-Turbulence Interactions

The turbulent fluctuations within a high Reynolds number flow field mean a droplet experiences a randomly varying velocity field that affects all subsequent processes including its velocity, breakup, heat transfer and so on, i.e. the energy exchange from the continuous-phase flow field to the discrete-phase liquid droplets.

The droplet turbulence dispersion is typically modelled via a stochastic approach as proposed by Gosman & Ioannides (1983), whereby the droplet instantaneous velocity is equal to the sum of the mean velocity and the fluctuating velocity where it is assumed that the fluctuating velocity within an eddy is isotropic and follows a Gaussian probability density function (pdf) and that the interaction time is assumed sufficiently short that the fluid velocity in an eddy is effectively constant. The Gaussian pdf has a mean of zero and a standard deviation as defined by equation (2.45) where k is the turbulence kinetic energy.

$$\sigma = \sqrt{\frac{2}{3}k} \tag{2.45}$$

When using the RANS k-ε turbulence modelling approach, the mean velocity is taken from the time-averaged local flow velocity from the turbulence model and the turbulence kinetic energy is the modelled turbulence kinetic energy taken from the k-equation.

When using the LES turbulence modelling approach, the turbulent dispersion is used to represent turbulence effects at the SGS on the droplet position and velocity. Hence, in this context, the resultant droplet velocity uses the filter-velocity for the mean velocity component, and the standard deviation of the Gaussian pdf uses the SGS kinetic energy, either from a SGS kinetic energy equation (if it is present in the LES SGS model) or calculated from the SGS velocity. Thus the droplet relative velocity is now a function of the filtered-velocity and the turbulent fluctuations, imposed on the droplet from the continuous-phase as a function of the SGS velocity, including any anisotropic characteristics. Hence all droplet conservation equations (mass, momentum and energy) and subsequent sub-models (including break-up, droplet collision, impingement and liquid film) are also a function of both the filtered-velocity and the SGS velocity.

The above description considers the energy exchange from the continuous-phase to the dispersed phase but does not consider the converse where energy from the dispersed-phase is imparted on the continuous-phase. The droplets in this research have a diameter of the order of micrometres, whereas the smallest resolved scales of turbulence when using the LES approach are defined by the filter width, which is dependent on the cell size, hence are of the order of millimetres. Thus as the droplets lose momentum, much of their energy is transferred to the continuous-phase at the SGS. Since the SGS kinetic energy feeds back into the continuous-phase momentum equations and the droplet turbulent dispersion, modelling of this effect is of significance.

When using a LES SGS model that utilises a separate transport equation to calculate the SGS turbulence kinetic energy k_{sgs}, e.g. the k-equation or DSM SGS models, the dissipated turbulence kinetic energy from the droplets can be easily imparted on the continuous-phase via a source term. Bharadwaj, Rutland & Chang (2009) utilised a DSM and Lagrangian DDM both with and without the inclusion of a spray source term in the k_{sgs}-equation and found

that the absence of the source term had the effect of increasing the droplet turbulent dispersion and subsequently over predicting the liquid penetration length.

A methodology for the exchange of energy from the discrete-phase to the continuous-phase at the SGS when using a LES SGS model that does not include a turbulence kinetic energy transport equation, e.g. Smagorinsky, is not yet available. This infidelity will feed back into the continuous-phase momentum equations and the droplet turbulent dispersion and cause a subsequent increase in droplet kinetic energy, and hence will be an inherent limitation on the accuracy of the predictions.

2.5 CONCLUDING REMARKS

This literature review has provided:

- An overview of the physical processes within a GDI engine that are to be the subject of this research, specifically the in-cylinder flow field and fuel injection processes
- A discussion of the numerical approaches to modelling these physical processes, including additional detailed information that will be used when either deciding on the most appropriate sub-model, evaluating the competency of the sub-model, or when using the sub-model to investigate the physical process itself

The first section has focused on turbulence, starting with the characteristics of turbulence and how it is typically described, and following with a discussion on turbulence modelling approaches focusing on the RANS k-ε and LES modelling approaches.

The second section follows from the first section by discussing the resultant flow field characteristics in the intake port and cylinder, with additional discussion being made on the flow structures relevant to the GDI engine that is the subject of this research.

The final section has focused on the fuel injection process and numerical methods for modelling it. This includes discussion on the physical processes of: primary and secondary breakup, impingement and liquid films, Leidenfrost temperature, droplet collisions and droplet-turbulence interactions.

CHAPTER 3

THE ENGINE AND NUMERICAL MODEL

"It doesn't matter how beautiful your theory is, it doesn't matter how smart you are. If it doesn't agree with experiment, it's wrong."

– Richard P. Feynman

3.1 INTRODUCTION

This chapter is split into two main sections. The first section of the chapter introduces the experimental single cylinder optical research engine that was used in this research. Details of the engine configuration are presented including aspects of the experimental setup, fuel injection system and standardised operating condition.

The second part of this chapter introduces the numerical model and presents results from a number of validation exercises, proving their capability to adequately predict the physical phenomena occurring and that they are suitable to be used for further studies investigating the physical processes within a GDI engine.

First, section 3.3 starts by describing the computational domain and methodology.

Next the section will discuss the modelling of the in-cylinder flow field as a single-phase simulation via the use of two turbulence modelling approaches, namely the RANS and LES approaches. Sub-sections present a number of sensitivity studies, initial and boundary conditions, and the model validation results proving the capability of adequately modelling the in-cylinder flow field within their respective limitations.

The next section will provide a similar structure but this time with the focus around modelling the fuel injection event and a two-phase flow. Again, the section will be split-up into two sections, modelling the fuel injection event using the RANS turbulence modelling approach, and second using the LES approach. The sub-sections will summarise the sub-models used (described in detail previously in chapter 2), present the initial and boundary conditions used, sensitivity studies and finally results comparing model predictions to experimental results.

3.2 THE SINGLE CYLINDER OPTICAL RESEARCH ENGINE

3.2.1 Experimental Configuration

The experimental engine that was the subject of the numerical modelling in this research was that of a single cylinder optical research engine developed by Jaguar Cars and built by Ford Research Laboratories in Dearborn, USA. The engine was originally operated between the years of 2003 and 2007 for a project entitled ‘Combustion Concepts for Sustainable Premium Vehicles (CCSPV) as part of a four university consortium, with financial and technical input from Jaguar Cars and Shell Global Solutions, and financial input from the EPSRC (GR/S58836/01, GR/S858850/01, GR/S58843/01, GR/S58829/01), to investigate the characteristics of cycle-to-cycle variations in the in-cylinder flow field, fuel injection process and combustion event. It was during this time that the data used to validate the results within this research was collected.

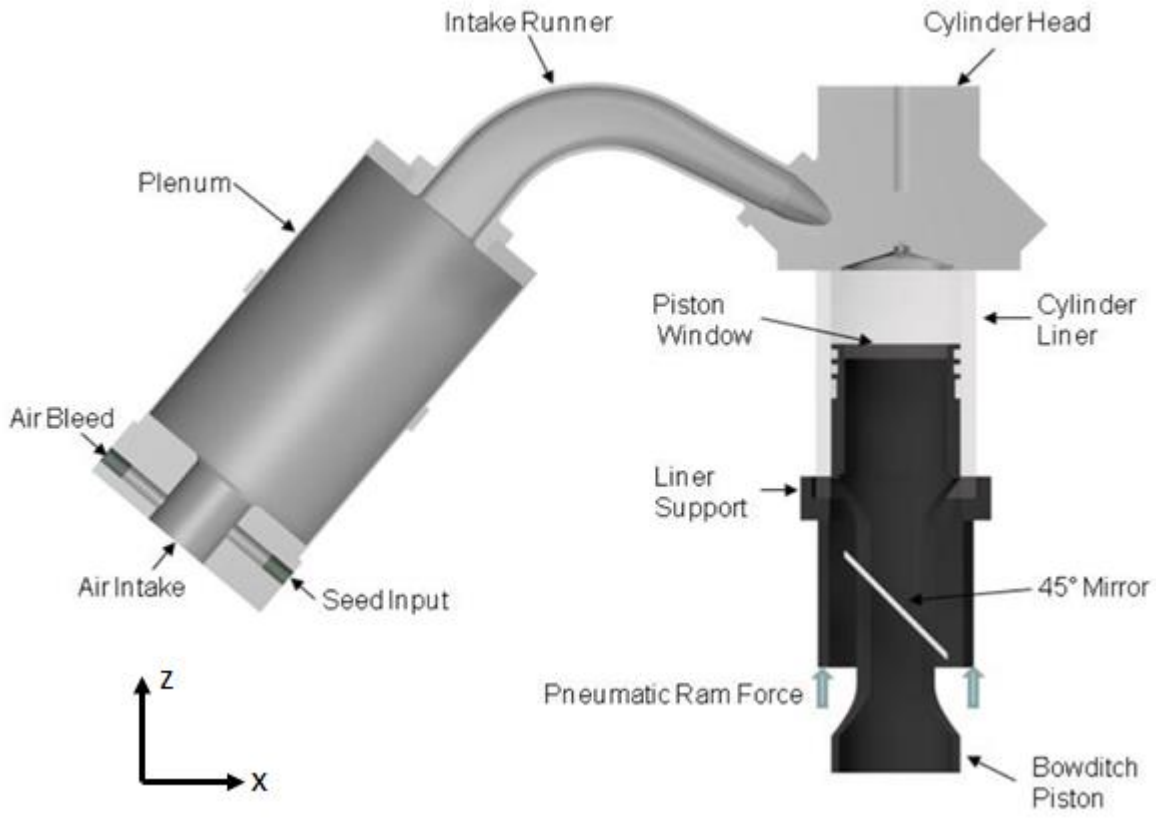

Figure 3.1 – Schematic drawing of the engine configuration taken from Justham (2010)

The engine crank case was developed based on an in-line three cylinder engine, utilising two balancer shafts to replace the missing two pistons. The cylinder head was designed to represent a Jaguar 4.5L V8 prototype GDI engine and was a pent-roof design with 4-valves, centrally mounted fuel injector and spark plug.

A schematic drawing of the engine is shown in Figure 3.1 and the in-cylinder layout is shown in Figure 3.2 and 3.3. The geometric parameters for the engine are summarised in Table 3.1.

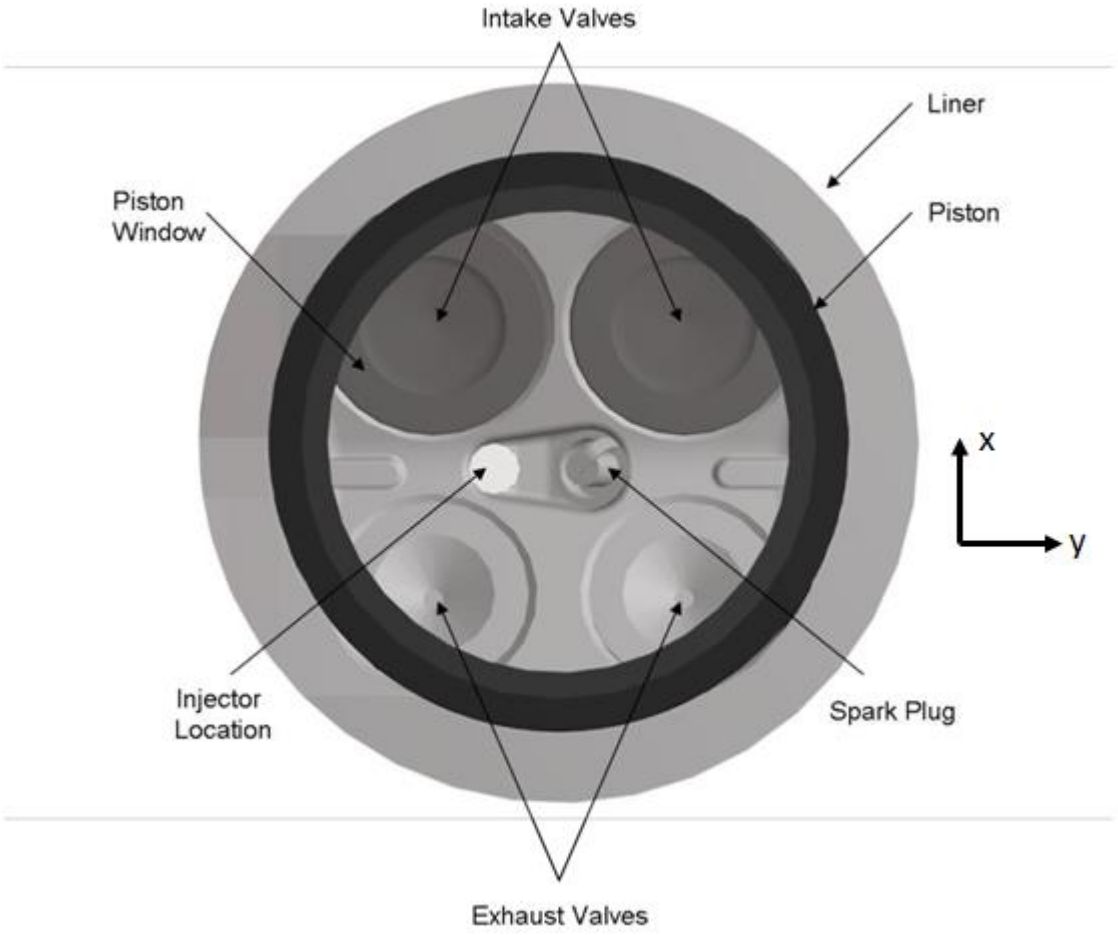

Figure 3.2 - View through bowditch piston up into the combustion chamber taken from Justham (2010)

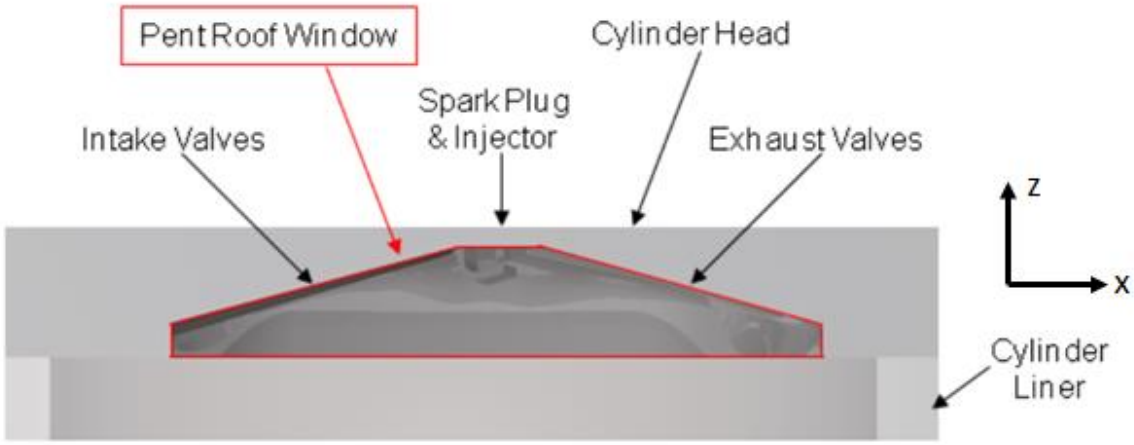

Figure 3.3 - View through the pent-roof access window taken from Justham (2010)

Table 3.1 – Experimental engine configuration (Jarvis, Justham, Clarke, *et al.*, 2006)

Bore	89 mm
Stroke	90.3 mm
Conrod length	148.97 mm
Capacity	0.562 l
Compression ratio	10.5:1 nominal
Piston bowl shape	Flat
Combustion chamber shape	Pent-roof
Fuel injection system	DI, centrally mounted, Bosch 6-hole VCO
Valves	2 Intake, 2 Exhaust
Intake valve diameter	34.9 mm
Exhaust valve diameter	29.0 mm
Intake valve max lift	10.53 mm
Exhaust valve max lift	9.36 mm
Intake valve cam opening	24 °ATDC
Intake valve cam closing	274 °ATDC
Exhaust valve cam opening	224 °ATDC
Exhaust valve cam closing	6 °ATDC

The engine was optically accessible via a number of features:

- Fused silica window in the pent-roof of the cylinder head
- Bowditch piston arrangement with flat fused silica piston crown and 45° mirror
- Full length fused silica liner
- Rapid prototype clear resin intake runner, polished to provide an optically acceptable finish

Figure 3.4 shows a photograph of the engine with the features providing optical access identified. The figure also shows the positioning of laser and camera to collect HSDPIV in the tumble plane.

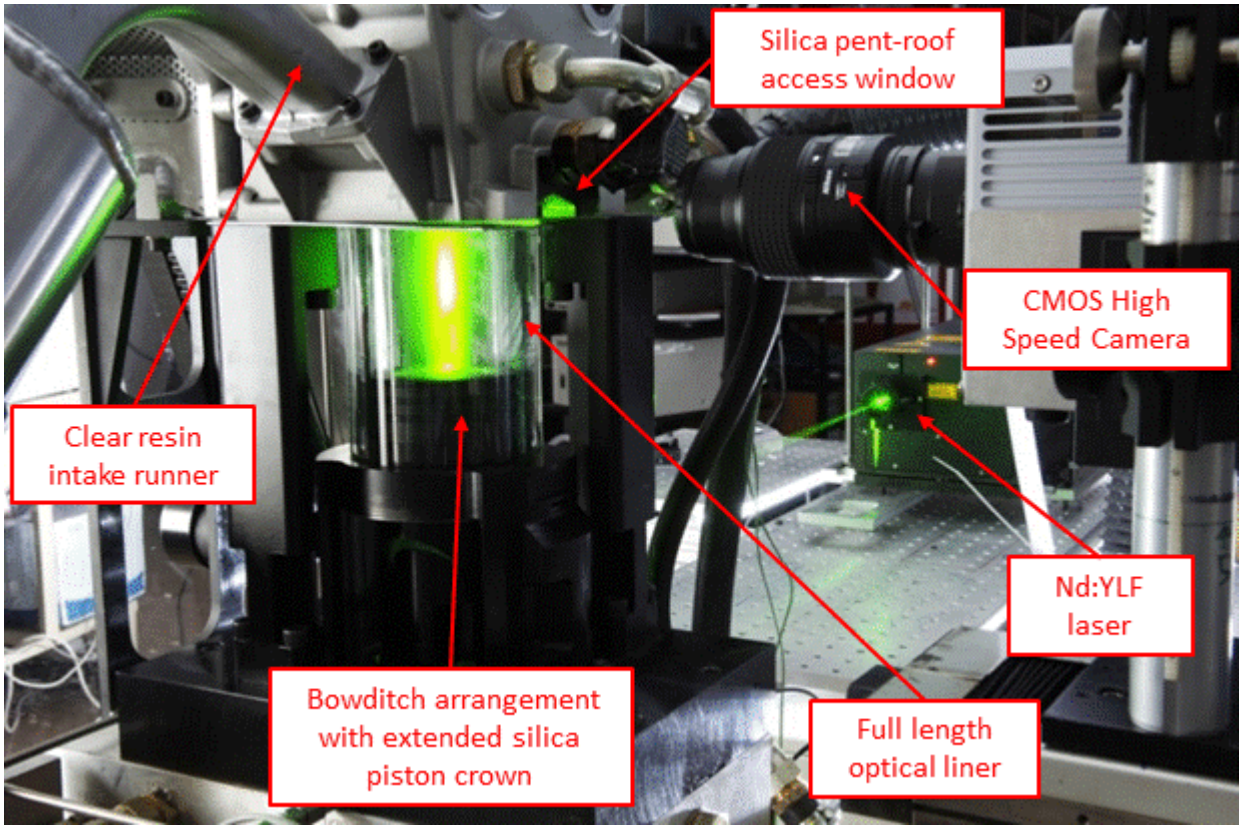

Figure 3.4 - Photo of the single cylinder optical research engine with PIV laser activated and generating a light sheet in the tumble plane

The in-cylinder pressure was measured using a piezo-capacitive pressure transducer mounted in the pent-roof of the cylinder head. A piezo-resistive pressure transducer was mounted towards the bottom of the cylinder liner and used as a reference pressure to adjust the dynamic relative pressure measurement of the in-cylinder pressure. A piezo-resistive pressure transducer was also used in the intake runner to monitor intake system pressure.

3.2.2 The World Wide Mapping Point

The operating condition used for the majority of the data collection in the previous experimental works was a standardised condition called the World Wide Mapping Point (WWMP) which corresponds to a typical low speed inner city driving condition and the equivalent engine conditions are summarised in Table 3.2.

Table 3.2 – Experimental operating condition (WWMP)

Engine Speed	1500 rpm
Engine Load / BMEP	2.6 bar
Injection timing	80°ATDC$_{intake}$
Spark timing	35°BTDC$_{firing}$
Fuel-air equivalence ratio	1
iEGR (internal via valve timing strategy)	~15%
Intake manifold pressure (abs)	0.5 bar
Intake air temperature	301 K
Exhaust back pressure (abs)	1.016 bar
Exhaust temperature	784 K
Coolant temperature	363 K

3.2.3 Valve Events

The valve lift profiles were derived by adjusting the valve cam profile to account for lash, due to thermal expansion and dimensional tolerances within the valvetrain system, using measured data provided by JLR. The intake valve lash was measured at the WWMP as 0.29mm. The exhaust valve lash was calculated as 0.225mm via the sum of the thermal expansion of exhaust valve and aluminium cylinder head at the WWMP and set clearance. Figure 3.5 shows the effective intake and exhaust valve lift profiles in relation to the cam lift profiles and Table 3.3 shows the key positions within the profiles.

Note, that the lift profiles are different to those published in previous CCSPV publications (e.g. Justham (2010), Rimmer (2011) and Serras-Pereira (2010)). At the point of publication of the previous studies, thermal expansion results were not available, thus valve opening and closing events were calculated based on the assumption that valve lift is zero during the opening and closing ramps of the cam profile. The adjustments made based on thermal expansion and set clearances should provide a much better estimation for effective valve lift and improve the quality of the numerical predictions.

When adjusting the cam profiles to provide effective valve lift, it is also becomes clear that whilst previous studies were under the impression that a degree of negative valve overlap was present under the current configuration (~18°c.a.), due to the actual valve lash being less than predicted previously, the current configuration actually produces neither negative nor positive valve overlap.

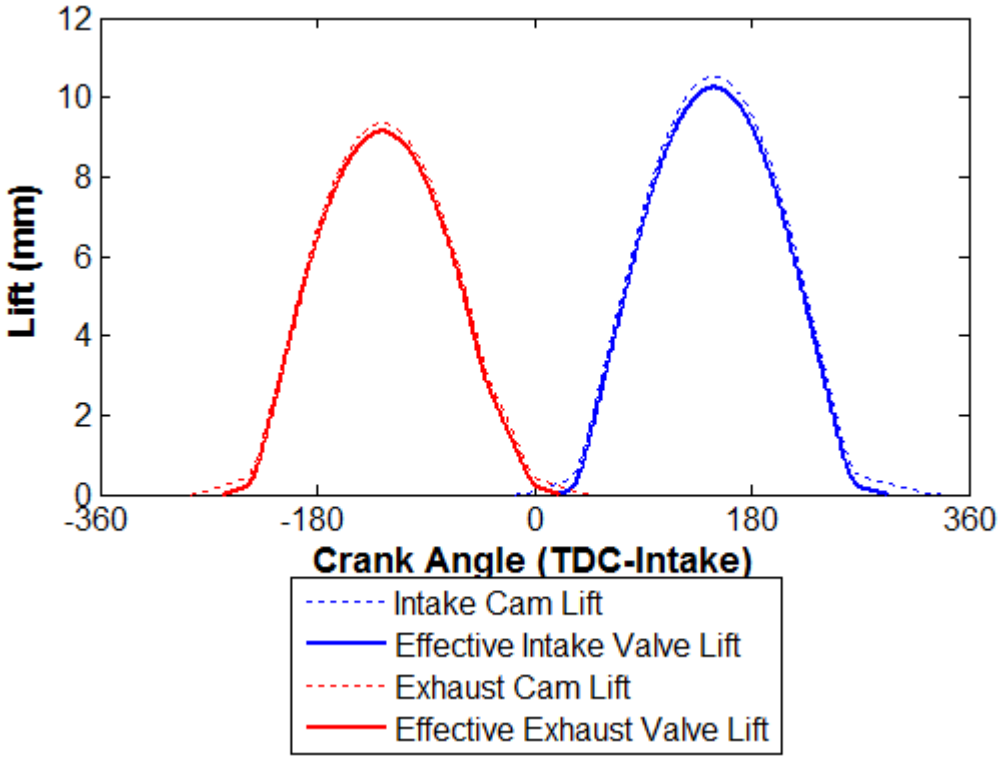

Figure 3.5 - Comparison of cam lift and effective valve lift profiles

Table 3.3 - Valve Events

Intake valve opening	20°ATDC
Intake valve max opening point	149°ATDC
Intake valve closing	293°ATDC
Exhaust valve opening	258°BTDC
Exhaust valve max opening point	126°BTDC
Exhaust valve closing	20°ATDC

3.2.4 Fuel Injection System

The injector was centrally mounted in the roof of the combustion chamber, in close proximity to the spark plug. The positioning of the spark plug, coupled with the designed spray angle, allows the engine to be operated in either an air-guided or spray-guided mixture control strategy. The spray plume orientation, as shown in Figure 3.6, was designed to be symmetric around the x-axis but asymmetric of the y-axis. Plumes 1/6 designed to penetrate around the spark plug at a shallower angle, avoiding impingement and subsequent wetting of the electrodes, but producing a rich mixture around the spark plug electrodes to avoid misfire and support stable combustion when utilising a spray-guided late injection strategy and stratified fuel-air mixture. Plumes 3/4 and 2/5 where designed with larger spray angles to penetrate further into the combustion chamber and be carried by a tumble flow motion generated by the intake port and runner geometry. The larger spray angles also prevent excessive liner impingement during early injection strategies. Whilst both early and late injection strategies were investigated in the previous experimental works, this research has focused on the WWMP which uses an early injection strategy, with injection at 80°ATDC. This strategy utilises the benefits of high turbulence levels and large length scales, particularly in the tumble x-z plane, to promote increased mixture homogeneity. The delay between the activation of the trigger signal and presence of first fuel at the injector tip consists of: the electrical delay between the activation of the trigger signal and the signal reaching the solenoid, the mechanical delay associated with the movement of the injector needle by the solenoid, and the hydraulic delay associated with the time for fuel to fill the injector sac volume and nozzles. This delay was found to be ~221.1μs, or 1.99°c.a. at 1500rpm, from spray tip penetration data taken in a constant-volume chamber (van Romunde, 2011). Table 3.4 characterises the key information pertinent to the fuel injection system.

Table 3.4 – Fuel injection system configuration

Injection timing (timing of electrical signal)	80°ATDC$_{intake}$
Delay to first fuel (including electrical and hydraulic delays within the injection system)	221.1 μs

Injection pressure	150 bar
Pulse Width	0.78 ms
Nozzle orifice outer diameter	0.5 mm
Nozzle orifice inner diameter	0.2 mm

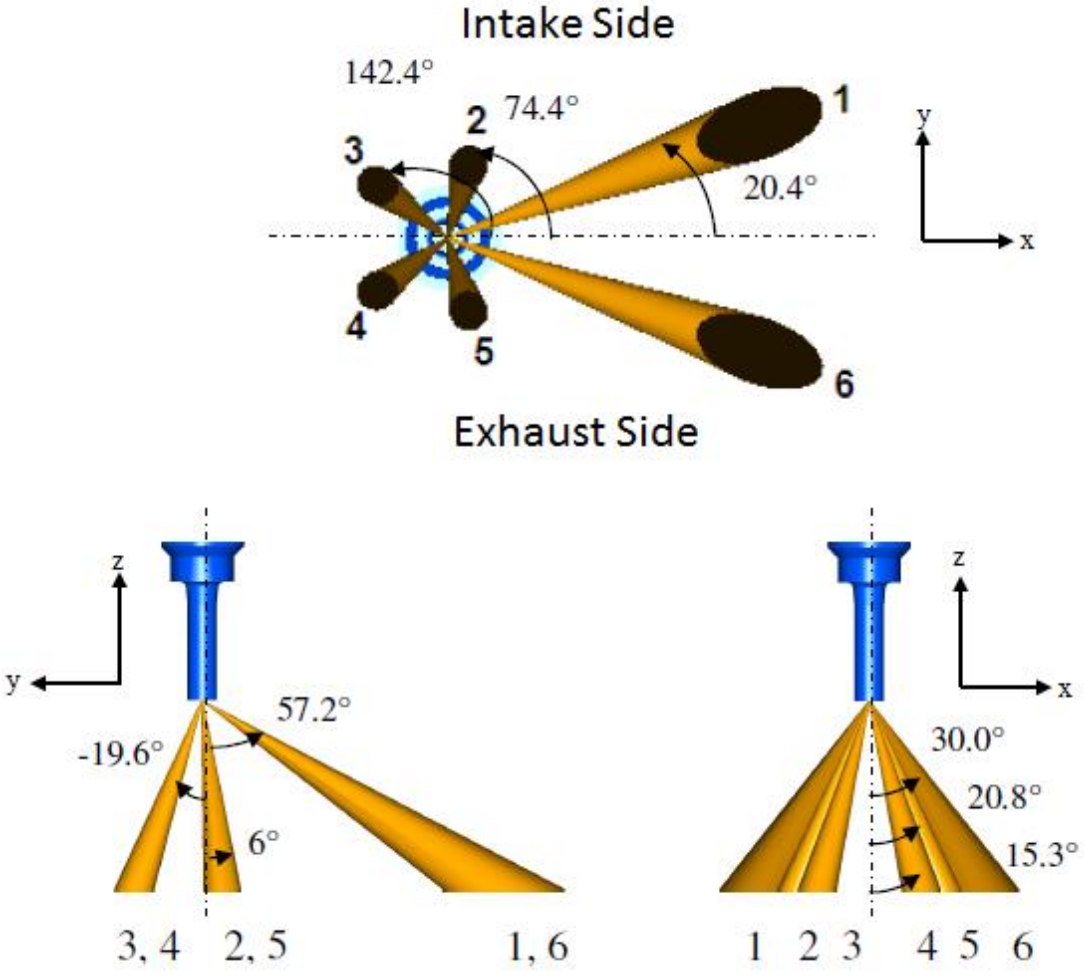

Figure 3.6 - Spray plume orientation, reproduced from van Romunde (2011)

3.2.5 Summary of In-Cylinder Events

A summary of the in-cylinder events is shown in Figure 3.7.

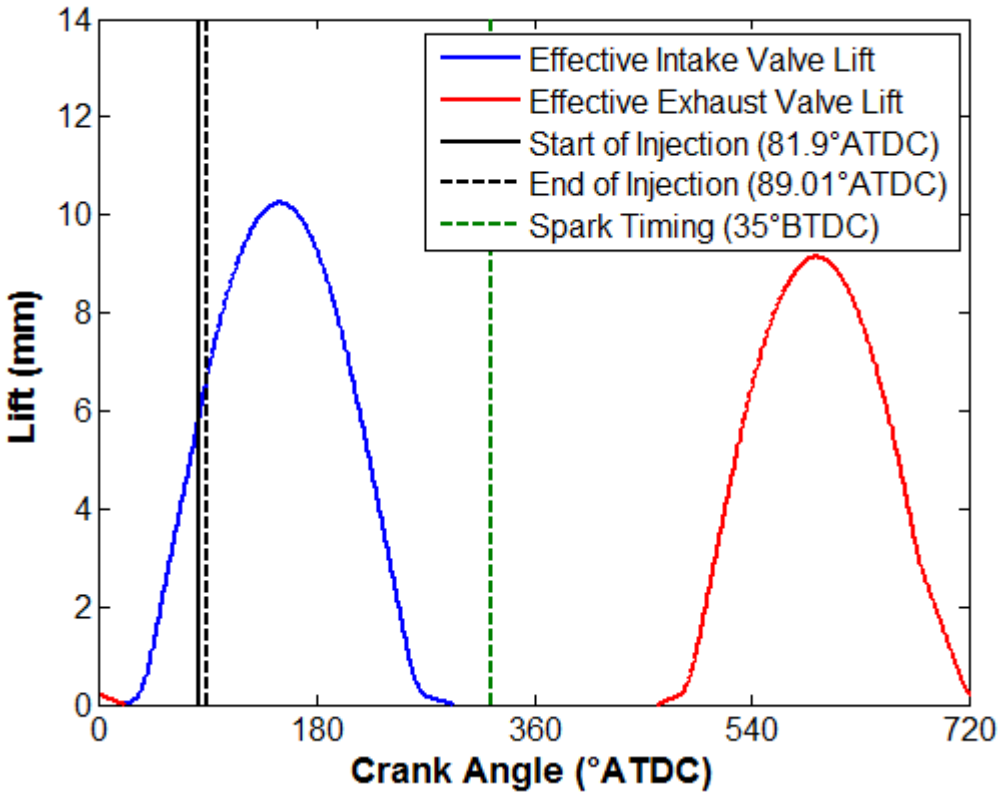

Figure 3.7 – Summary of in-cylinder events

3.3 THE NUMERICAL MODEL

3.3.1 The Computational Domain

A schematic of the computational domain is shown in Figure 3.8. The complete experimental geometry was included in the domain, including detailed meshing of the pent-roof access window, valve shrouds (that were significant on this engine due to the large exhaust valves) and spark plug electrodes. The intake plenum and intake runner were included to better model the dynamics of the intake system (discussed more in section 4.2.1.3). The exhaust runner was also included to ensure that there were no recirculation regions around the outflow that would cause solution instability.

The mesh was created using CD-adapco's purpose built 'es-ice' software. es-ice is a ICE specific meshing and model configuration software that allows configuring of a 3D mesh for an ICE, definition of all the events including cell addition and deletion around moving boundaries (e.g. valves, and piston), and set up of boundary and initial conditions.

The first stage of the mesh creation was to create a two-dimensional template as shown in Figure 3.9. The visual characteristics of the 2D template are as a consequence of the method used by the es-ice software to configure the moving mesh components. The typical cell size in the x-y plane of the cylinder interior was set at this point, primarily based on the number of cells used to mesh the valves. Particular attention was paid to minimising cell non-uniformity and orthogonality.

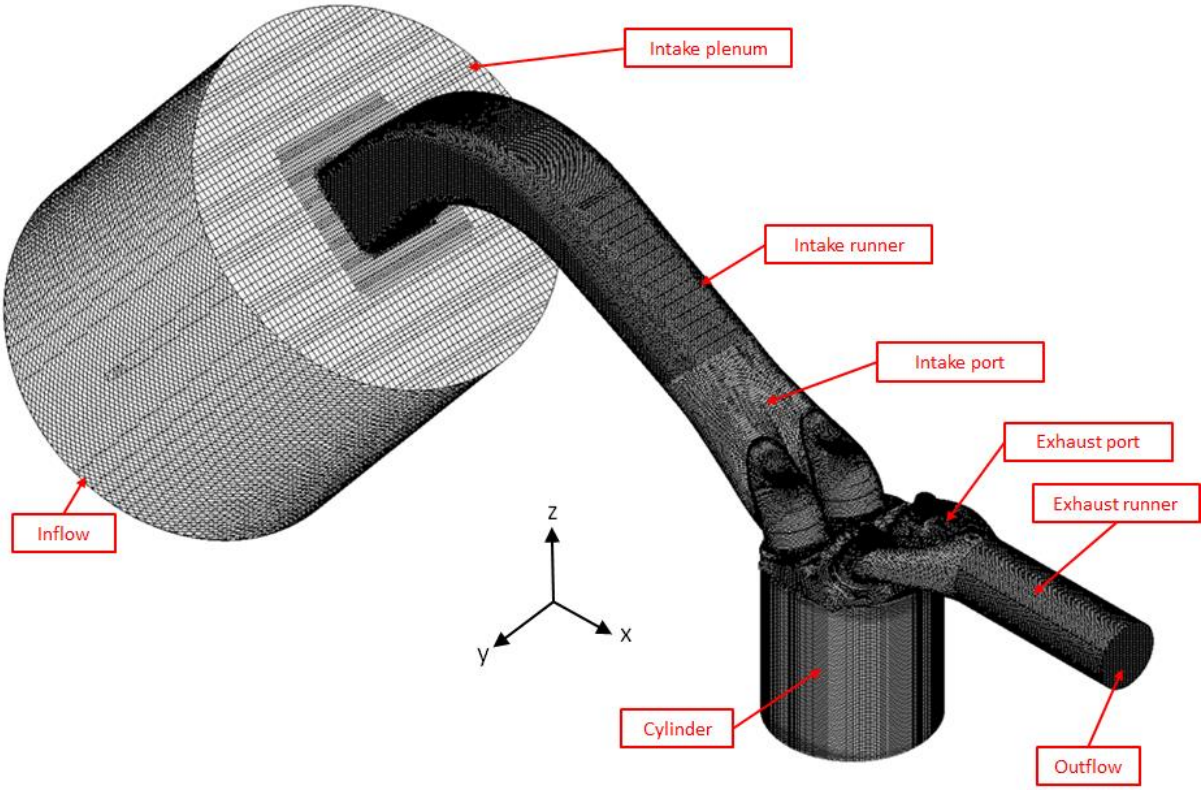

Figure 3.8 – The computational domain

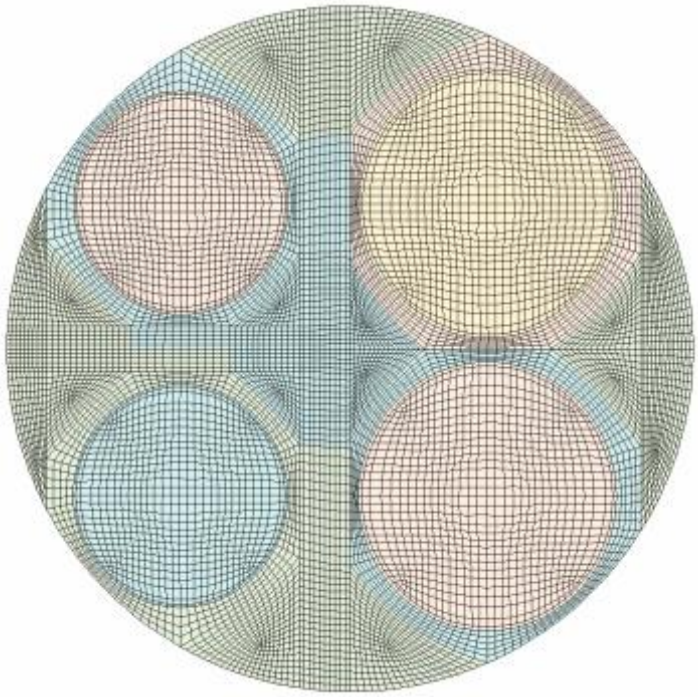

Figure 3.9 – A section view of the computational mesh in the x-y plane through the cylinder interior

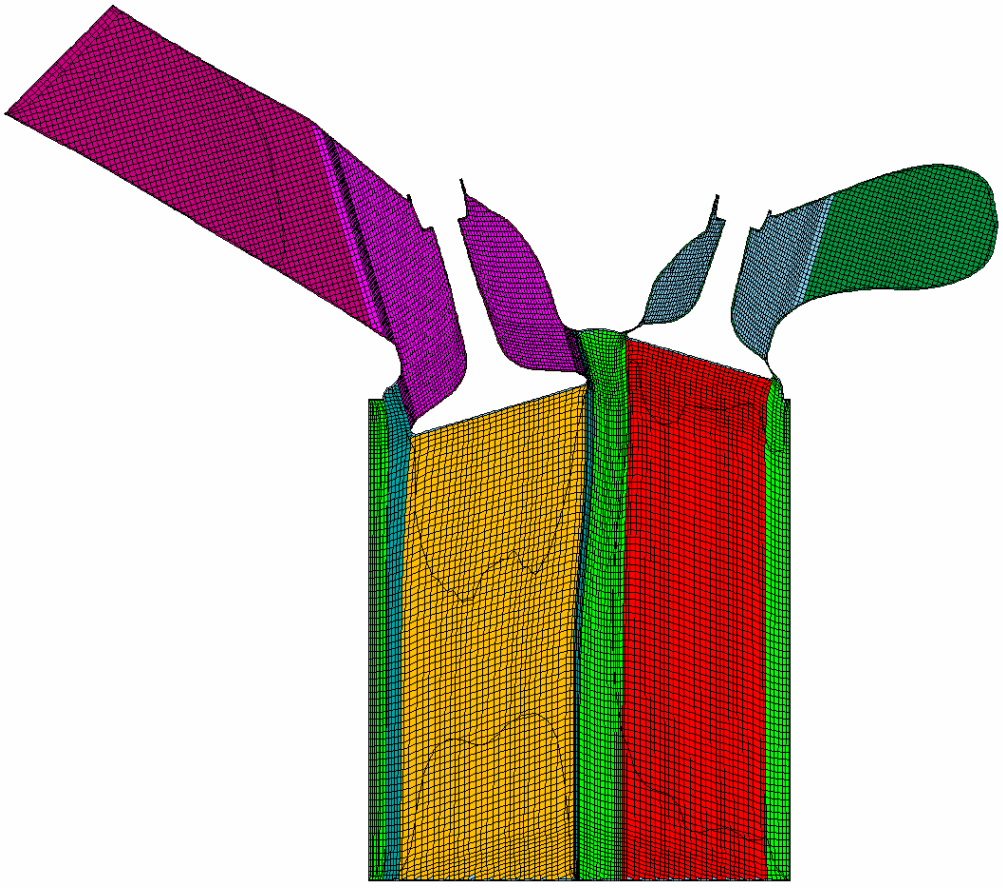

Figure 3.10 – A section view of the computational mesh, through the rear valves [0,-19,0], zoomed in on the cylinder at 180°ATDC (i.e. BDC) through a x-z plane

In the next stage, the 2D template was trimmed around the cylinder geometry and extrapolated to include the entire cylinder down to BDC. A section view of the mesh in the x-z plane through the rear valves is shown in Figure 3.10.

Figure 3.11 shows a section view of the mesh through the x-z plane along the bore centreline and in particular, the intake and exhaust system mesh. The prime purpose of the intake plenum and runner and exhaust runner is to provide the cylinder with accurate boundary conditions with the least computational expense possible. For this reason, the intake plenum, intake runner and exhaust runner were meshed separately in STAR-CCM+. This allowed increased control over the variation in cell size through the component, with significantly larger cells than used in the cylinder interior due to the simpler flow structures present requiring less cell density to adequately represent the flow structures.

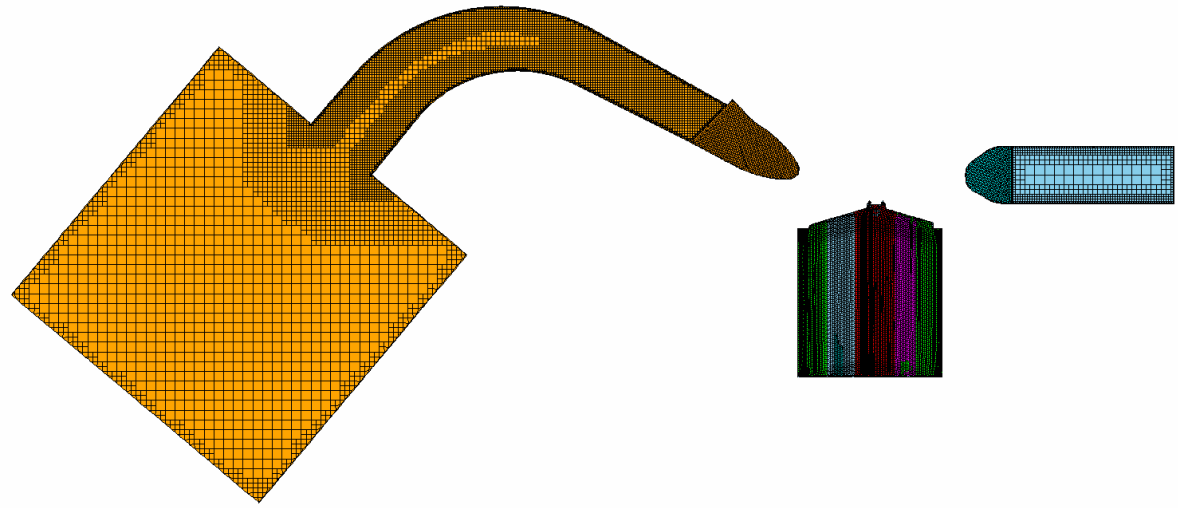

Figure 3.11 – A section view along the bore centreline of the computational mesh at 180°ATDC (i.e. BDC) through the x-z plane

The final mesh had a total of approximately 2.2 million cells at BDC with an approximate cell size of 0.7-0.8 mm^3 in the cylinder interior. Mesh size dependency studies were completed prior to flow field and spray model validation exercises to prove the mesh was acceptable for the requirements of this research. Results from these studies are discussed later.

3.3.2 The Computational Methodology

The CFD code used in this research, STAR-CD ver4.22, uses the finite-volume method where the computational domain is discretised into control volumes. The partial differential equations are then integrated over each individual control volume and then approximated in terms of the cell-centred nodal values. The implicit method is used to solve the algebraic finite-volume equations. Temporal discretisation is achieved using the fully-implicit Euler algorithm PISO, or Pressure Implicit with Splitting of Operator (Issa, 1986; Issa, Gosman & Watkins, 1986; Issa, Ahmadi Befrui, Beshay, *et al.*, 1991), which results in temporal accuracy of around second-order.

Spatial discretisation is achieved by a combination of second-order schemes, dependent on the discretised scalar. Second-order schemes were used here to preserve steep gradients, reducing numerical diffusion, but at the potential cost of increased solution instability due to numerical dispersion. Density was discretised using the Central Differencing (CD) scheme which interpolates linearly on the nearest neighbour value, is second-order accurate but can suffer numerical dispersion. Turbulence kinetic energy, dissipation and temperature were discretised using the Monotone Advection and Reconstruction Scheme (MARS), a blending scheme that can help to reduce numerical dispersion and is second-order accurate.

The computational timestep was set *a priori* based on ensuring adequate solution stability and an average Courant-Friedrichs-Lewy (CFL) number of less than one (Beavis, Ibrahim & Malalasekera, 2016).

3.3.3 The In-Cylinder Flow Field: Model and Validation

3.3.3.1 RANS Approach

Table 3.5 summarises the turbulence models and model constants used during when the RANS turbulence modelling approach was used for in-cylinder flow predictions.

Table 3.5 – Summary of turbulence sub-model and constants used during RANS approach

Turbulence (gas phase)	RNG k-ε (Yakhot & Orszag, 1986; Yakhot, Orszag, Thangam, *et al.*, 1992) [C_μ=0.085, $C_{\varepsilon 1}$=1.42, $C_{\varepsilon 2}$=1.68, $C_{\varepsilon 3}$=1.42, $C_{\varepsilon 4}$=-0.387, κ=0.4, β=0.012, η_0=4.38, σ_k=0.719, σ_ε=0.719, σ_h=0.9, σ_m=0.9]
Turbulence – Near Wall	Angelberger (Angelberger, Poinsot & Delhay, 1997) [y^+_{sw}=13.2, a_w=2.075, b_w=3.9]

3.3.3.1.1 Sensitivity Studies

Prior to model validation, a number of sensitivity studies were completed to understand the sensitivity of the model predictions to a number of key user inputs. Note: The sensitivity studies shown in this section were completed very early in the research and at an operating condition not the same as the WWMP (Table 3.2) used for model validation, hence the differences in peak pressure between Figure 3.13 and Figure 3.18, and Figure 3.23 and Figure 3.37.

Mesh Size

Two dependency studies were completed to examine the sensitivity of the model solution to the mesh size and initial conditions. First the cell size was evaluated across six different meshes as summarised in Table 3.6.

Table 3.6 – Different mesh sizes investigated in the mesh size dependency study

Case	Total number of cells at BDC [none]	Approximate cell size in the cylinder interior [mm^3]
1	1.25m	1.6-1.8
2	1.4m	1.5-1.7
3	1.55m	1.4-1.6
4	1.8m	1.1-1.3
5	2.15m	0.7-0.8
6	2.6m	0.6-0.7

Figure 3.12 shows a 2D section of the mesh for the smallest mesh size (1.25 million cells) and the largest mesh size (2.6 million cells), illustrating the increase in cell density. The mesh was also adjusted so that the cell length in the z-axis also reduced proportionally with increasing number of cells to maintain cell uniformity as best possible.

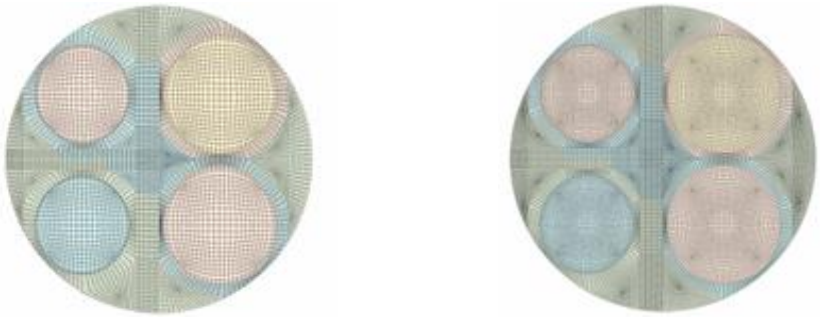

(a) (b)

Figure 3.12 – 2D slice of the mesh in the swirl plane for two different mesh sizes (a) 1.25 million cells, (b) 2.6 million cells

The results were first compared in terms of cylinder averaged values of pressure (Figure 3.13), temperature (Figure 3.14), turbulence kinetic energy (Figure 3.15) and turbulence dissipation (Figure 3.16). As can be seen from these cylinder averaged results, the predictions begin to become mesh independent for the 2.15 million and 2.6 million cell meshes.

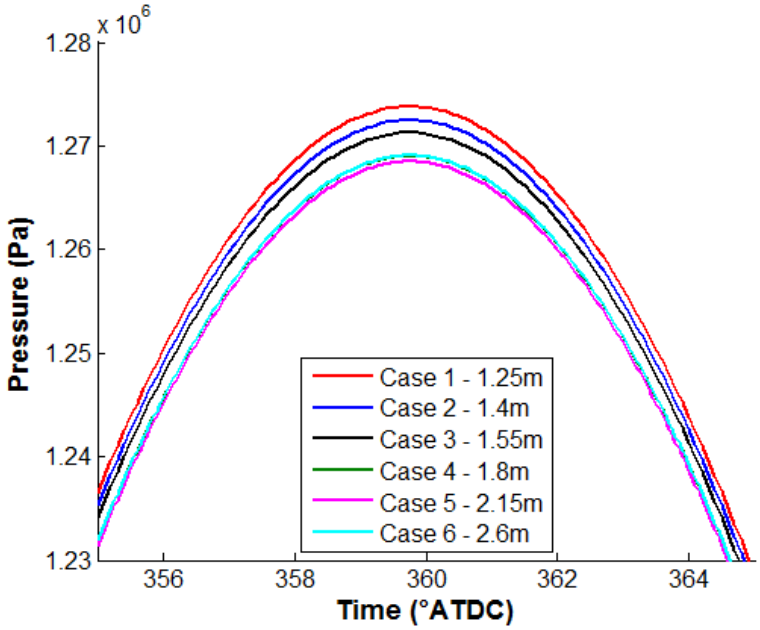

Figure 3.13 – In-cylinder pressure averaged across all cells in the cylinder as a function of crank angle but zoomed in around TDC and peak cylinder pressure, for each mesh size

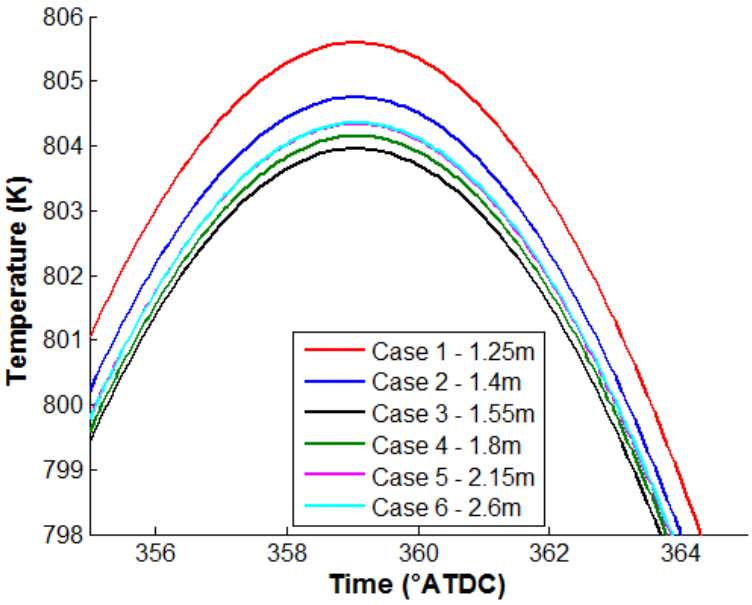

Figure 3.14 – In-cylinder temperature averaged across all cells in the cylinder as a function of crank angle but zoomed in around TDC and peak temperature, for each mesh size

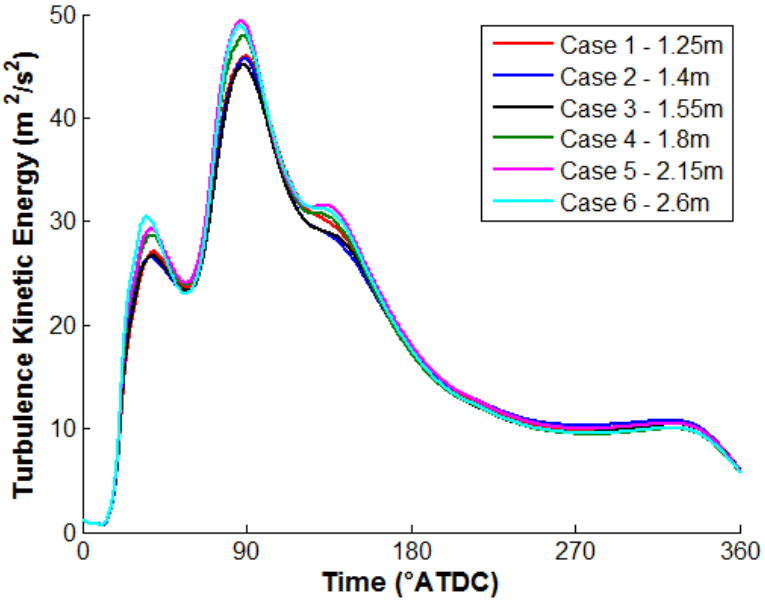

Figure 3.15 – Turbulence kinetic energy averaged across all cells in the cylinder as a function of crank angle through the intake and compression stroke, for each mesh size

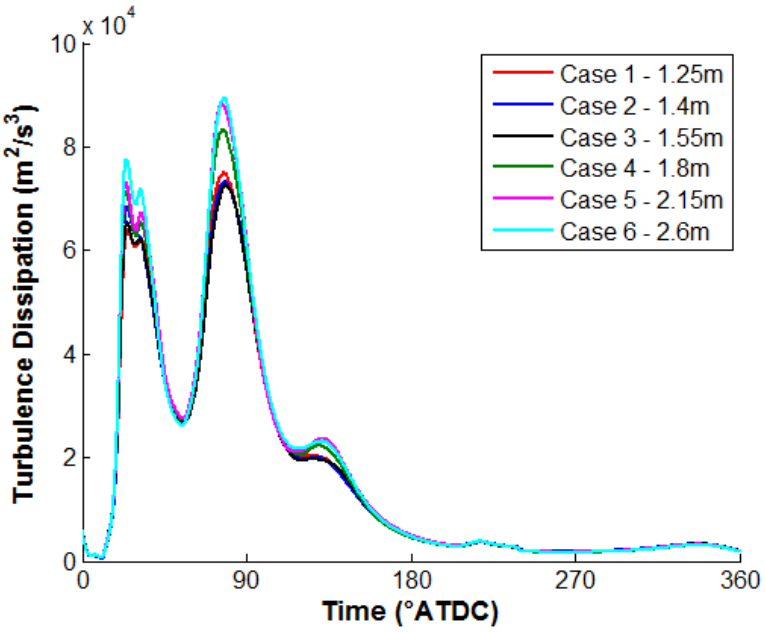

Figure 3.16 – Turbulence dissipation averaged across all cells in the cylinder as a function of crank angle through the intake and compression stroke, for each mesh size

To investigate the more subtle changes in model predictions with changes in cell size, contours of velocity magnitude were plotted across the tumble plane at 80°ATDC (~ half lift) as shown in Figure 3.17. Similarities are seen in flow structures in the 1.8, 2.15 and 2.2 million cell meshes, particularly in the velocity magnitude of the flow through the intake valve curtain between the cylinder head and valve head and in the flow structures within the intake port around the intake valve stem. This confirms the findings above of the solution being approximately cell size independent at 2.15 million cells.

The primary reason for the differences seen in Figure 3.13-Figure 3.17 is due to the differences in number of cells present in the intake valve curtain. As the number of cells changes, the trapped mass predicted by the model changes, affecting the pressure and temperature at TDC as seen in Figure 3.13and Figure 3.14, the resultant turbulence kinetic energy and turbulence dissipation as seen in Figure 3.15 and Figure 3.16, and the variation in the flow structures within the valve curtain and propagating valve jet as seen in Figure 3.17.

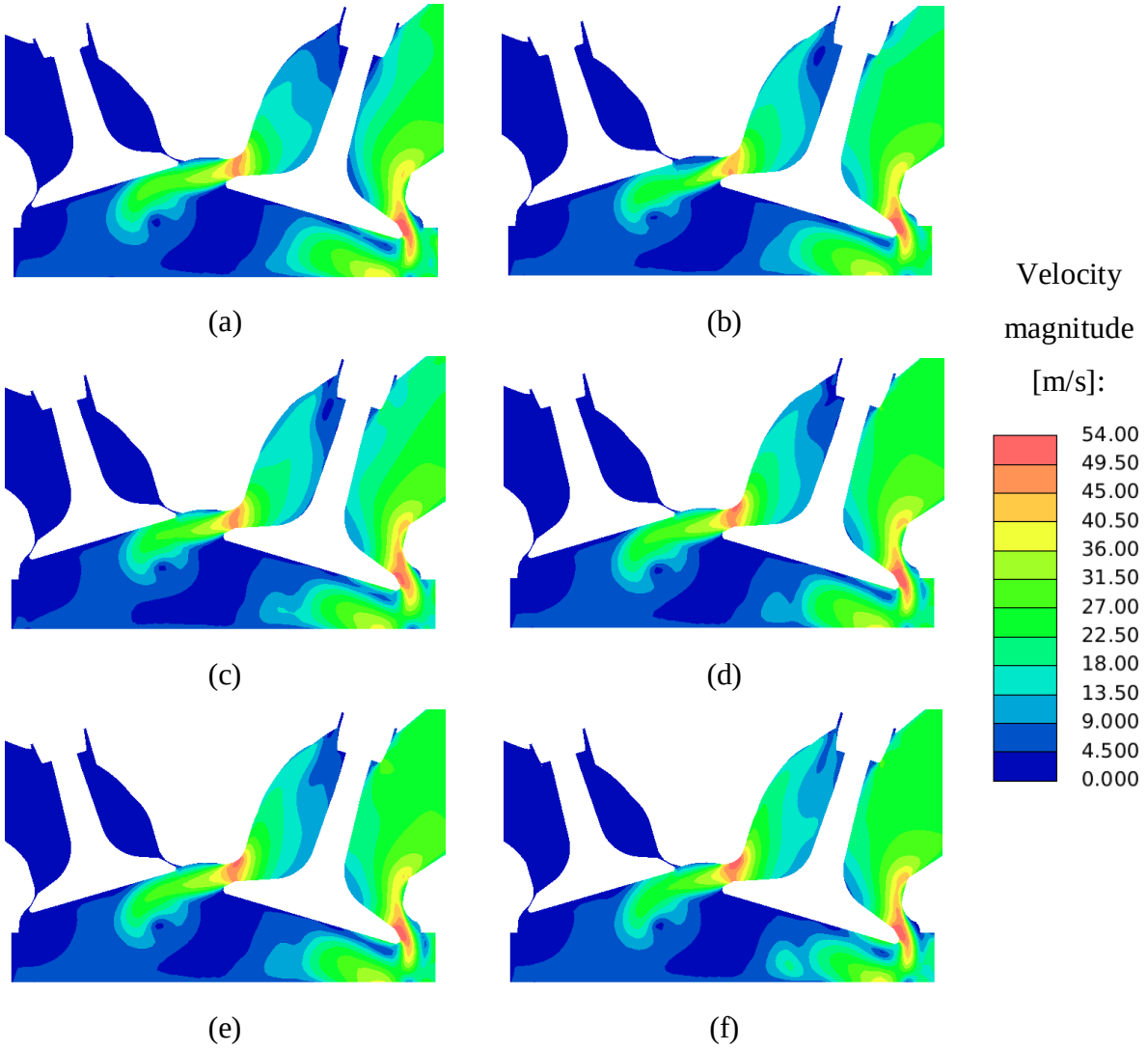

Figure 3.17 – Contours of velocity magnitude in the x-z tumble plane cutting through the intake and exhaust valves (y=19mm) at 80°ATDC for each mesh size (a) 1.25m cells, (b) 1.4m cells, (c) 1.55m cells, (d) 1.8m cells, (e) 2.15m cells, (f) 2.6m cells

When the computational expense is examined, shown in Table 3.7, a significant increase in computational expense is seen when moving from the 2.15 million cell mesh to the 2.6 million cell mesh. A reasonable jump in computational expense is also seen when the mesh size was increased from 1.55 million cells to 1.8 million cells due to the need to increase the pressure-correction under relaxation and reduce the size of the time step around the intake and exhaust opening and closing periods to maintain sufficient solution stability.

Table 3.7 – Computational expense in CPU-hrs for each of the meshes for a complete 720° cycle

Mesh Size	Computational Expense (CPU-hrs)
1.25m	967
1.4m	1086
1.55m	1100
1.8m	1689
2.15m	1730
2.6m	3068

Based on the results above, a mesh providing approximately 2.15 million cells, which provided an approximate cell size in the cylinder interior of $0.8mm^3$, was chosen as providing a solution that is approximately mesh size independent with acceptable computational expense.

Initialisation Conditions

The second dependency study was to evaluate the solution with respect to the initialisation conditions, and in particular the number of cycles needed to be completed to provide an initialisation condition independent solution.

Figure 3.18, Figure 3.19 and Figure 3.20 show the in-cylinder cell averaged pressure, temperature and turbulence kinetic energy respectively as a function of crank angle for four consecutive cycles, i.e. each cycle is initialised by the final conditions of the preceding cycle. Some comments on the findings:

- There appears little influence on the in-cylinder pressure with the exception of some effect during the intake stroke and around TDC-firing.
- Both cylinder averaged temperature and turbulence kinetic energy largely show independency on the initial conditions after the second cycle.

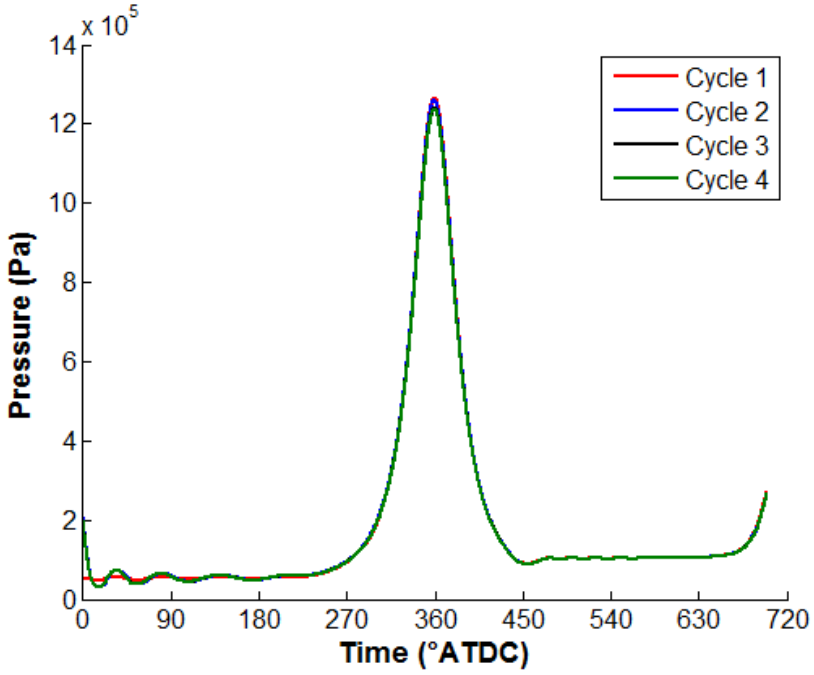

Figure 3.18 – In-cylinder pressure averaged across all cells in the cylinder as a function of crank angle, for four consecutive cycles

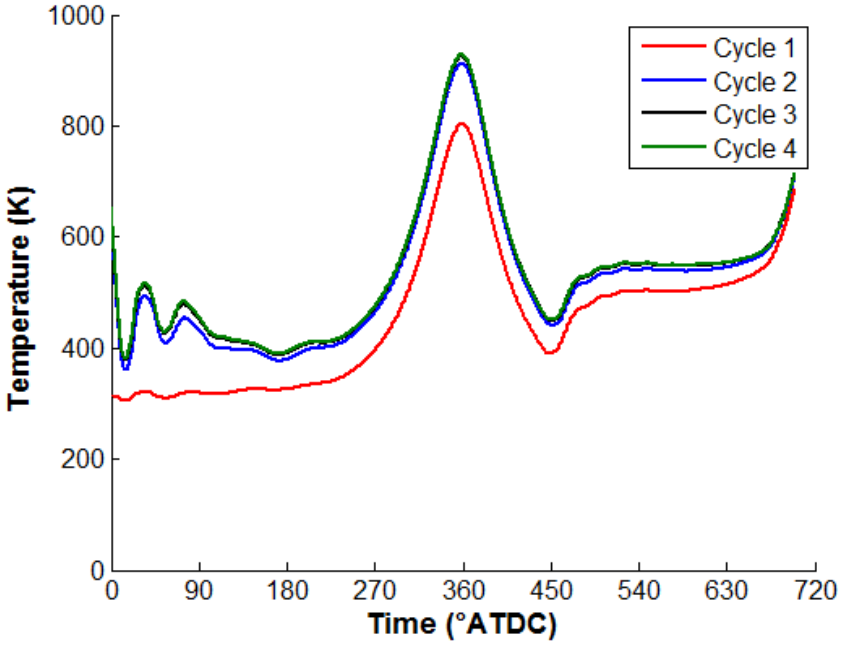

Figure 3.19 – In-cylinder temperature averaged across all cells in the cylinder as a function of crank angle, for four consecutive cycles

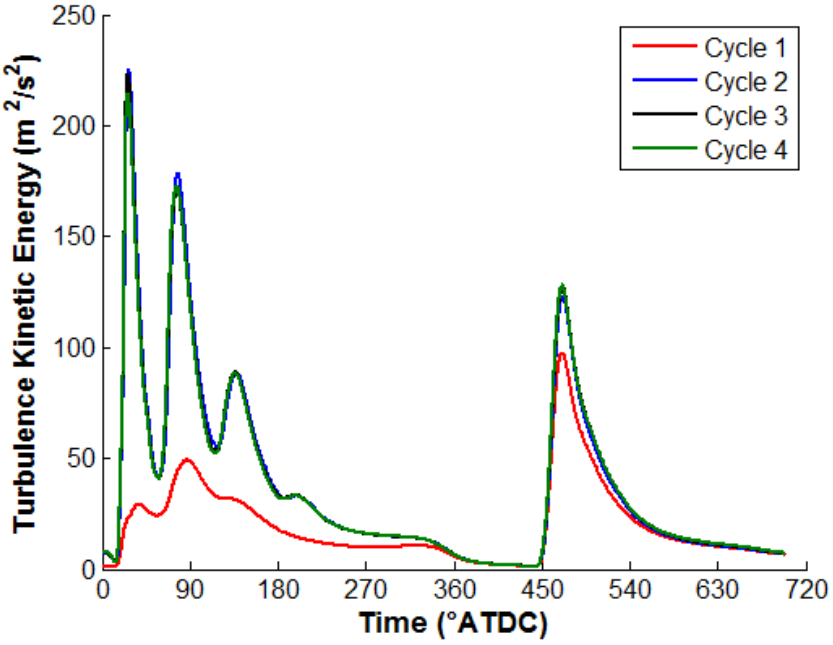

Figure 3.20 – In-cylinder turbulence kinetic energy averaged across all cells in the cylinder as a function of crank angle, for four consecutive cycles

Figure 3.21 shows the intake port pressure as a function of crank angle across four consecutive cycles. Similar to the in-cylinder results, cycle 1 is seen to be highly dependent on the initial conditions but cycles 2 onwards show independency, implying that a minimum of one cycle is required to be run to establish convergent intake system wave dynamics. This is largely driven by the intake system pressure fluctuations not being damped out by the end of the cycle hence have a large impact on the following intake valve opening (IVO) and induction event.

Figure 3.22 shows the exhaust port pressure as a function of crank angle across four consecutive cycles. Little initial condition dependency is seen in the results. This is due to any pressure fluctuations in the exhaust port that are created during the scavenging event having been dissipated by the point of the exhaust valve opening (422°ATDC) at the start of the next scavenging cycle. Thus whilst the pressure fluctuations oscillate at a much higher frequency than seen in the intake system, they also dissipate much more quickly in the exhaust port due to the significantly smaller runner length and volume between the port and boundary condition, when compared to the intake system.

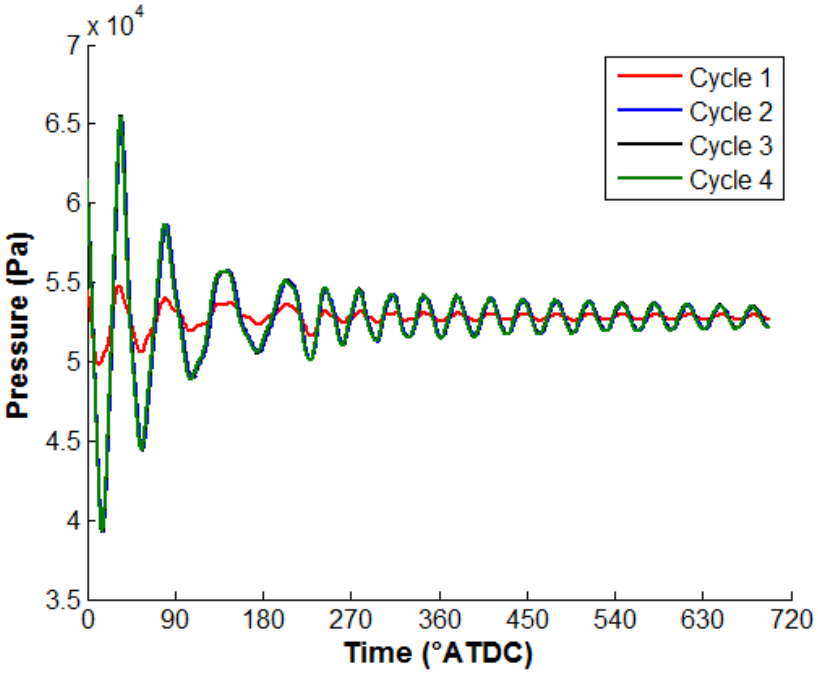

Figure 3.21 – Intake port pressure as a function of crank angle for four consecutive cycles

Thus in conclusion, it was established that a minimum of one complete cycle was needed to establish the correct initial conditions in the intake port and hence cylinder at the beginning of the cycle and hence provide an initial condition independent solution.

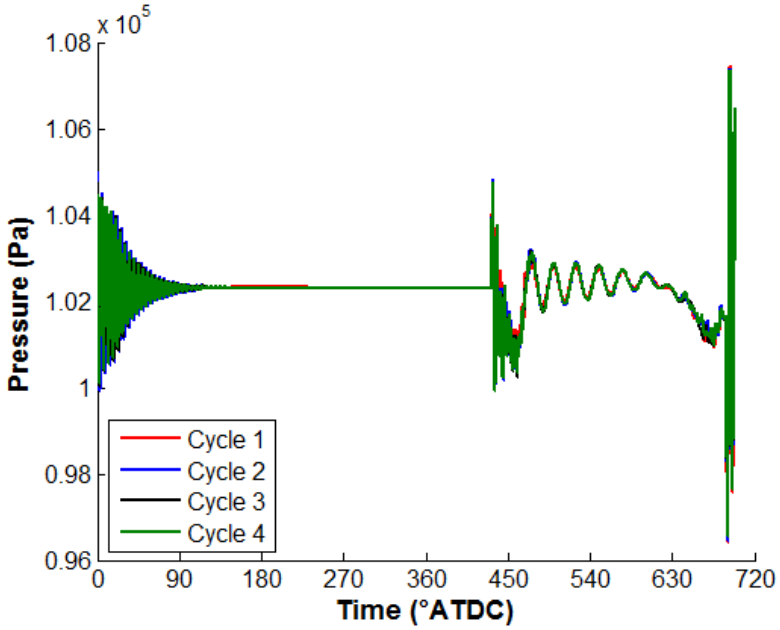

Figure 3.22 – Exhaust port pressure as a function of crank angle for four consecutive cycles

3.3.3.1.2 Initial and Boundary Conditions

The inflow at the intake plenum is specified as a constant-pressure constant-temperature environment in the absence of time varying experimental data. The inflow pressure was reduced by 7% from the experimental intake pressure to better match the in-cylinder intake stroke pressure-volume profile. The optical research engine had significant heat losses and blow-by past the piston rings due to the poor sealing of the piston rings against the quartz cylinder liner used to provide optical access. Hence reducing the inflow pressure in the numerical model acted to reduce the trapped mass and hence the pressure at TDC and provide a better prediction of the in-cylinder pressure in lieu of modelling the realities of high blow-by and wall heat transfer.

The outflow at the exhaust port-manifold interface was also specified as a constant-pressure constant-temperature boundary condition. In this instance, the pressure distribution profile from the domain interior is applied where the mean of this profile is equal to the supplied outflow pressure.

A turbulence intensity of 10% (0.1) was imposed at both the inflow and outflow and the turbulence length scale as 10% of the hydraulic diameter. The numerical boundary conditions are summarised in Table 3.8.

Table 3.8 – Numerical boundary conditions

Engine Speed	1500 (rpm)
Inflow Pressure	0.453 (bar)
Inflow Temperature	301 (K)
Inflow Turbulence	Intensity: 0.1 (none) Length scale: 0.0048 (m)
Outflow Pressure	1.023 (bar)
Outflow Temperature	784 (K)
Outflow Turbulence	Intensity: 0.1 (none) Length scale: 0.001 (m)
Wall Temperatures	Adiabatic

The model was run through one completed cycle and then used to initialise the second cycle before predictions were used for analysis to ensure the solution was independent of the initialisation settings.

3.3.3.1.3 Model Validation

The model is validated against published experimental data at a standardised motored condition also known as the WWMP (as shown earlier in Table 3.2).

Before beginning an in-depth evaluation of the predicted flow field, the model was compared against experimental indicating data, specifically pressure-crank angle (Figure 3.23) and pressure-volume (Figure 3.24).

One difference between experimental results and numerical predictions is the point of re-compression around TDC_{intake}, visible in the experimental results but not present within the numerical predictions. Due to this characteristic typically being very difficult to model accurately (due to the flow interactions during the negative valve overlap period) and the discrepancy not affecting the final flow predictions between intake valve closing and spark timing (which was the final purpose of this work), extensive efforts weren't spent trying to improve this further. Overall the model shows good agreement to experimental results.

The model was validated with respect to its ability to predict the conditions within the intake runner. This part of the model validation was performed at 700mbar intake manifold pressure, due to differences in the experimental operating conditions for this data set.

First the predicted intake runner velocity is compared against the available experimental velocity data at discrete crank angles as shown in Figure 3.25. Following this, the experimental intake runner momentum, calculated from the PIV profiles, was compared against model intake valve curtain flux, as shown in Figure 3.26. Whilst these two datasets are not directly comparable, a qualitative comparison provides useful insight into how accurately the model is predicting changes in flow momentum as a consequence of wave dynamics. Figure 3.25 and Figure 3.26 indicate that the model is well suited to predicting the intake system flow field.

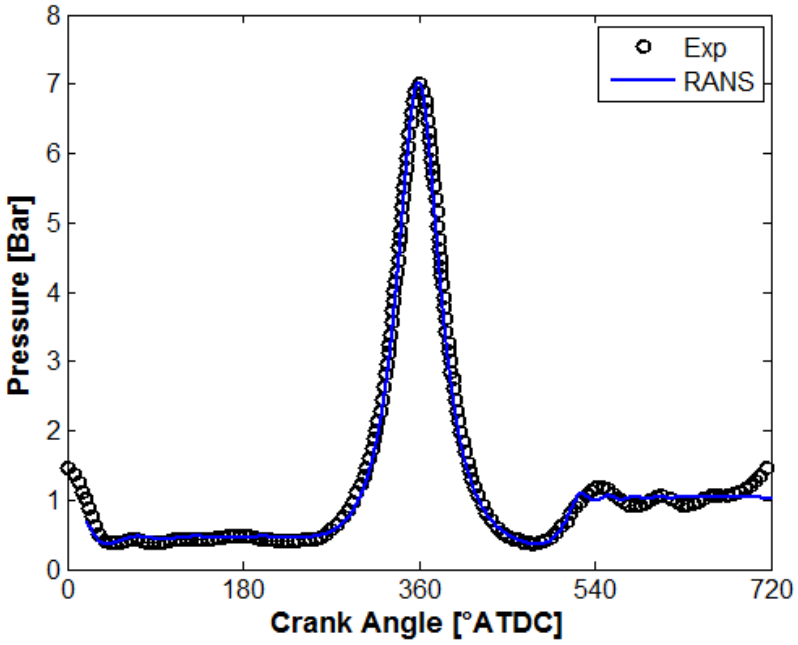

Figure 3.23 – In-cylinder pressure as a function of crank angle, comparing the RANS model and experimental data

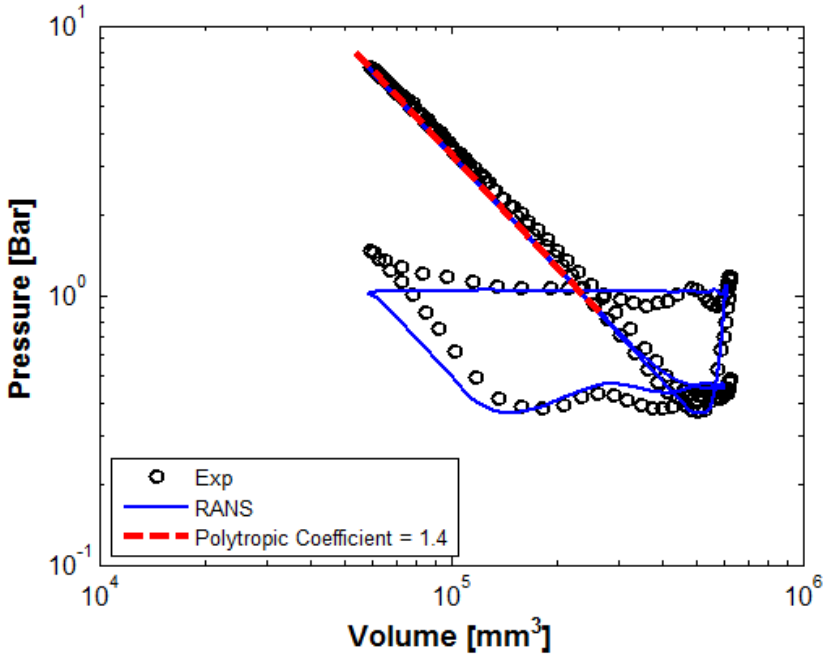

Figure 3.24 – In-cylinder pressure as a function of volume on a log-log scale, comparing the RANS model and experimental data, including a slope curve at n=-1.4

Both experimental datasets in Figure 3.25 and Figure 3.26 are taken from Justham, Jarvis, Garner, *et al*. (2006) where a complete description of the experimental setup and post-processing techniques used are given. Note that data was only available at four different crank angles within the intake stroke, hence the limited number of experimental data points presented in Figure 3.25.

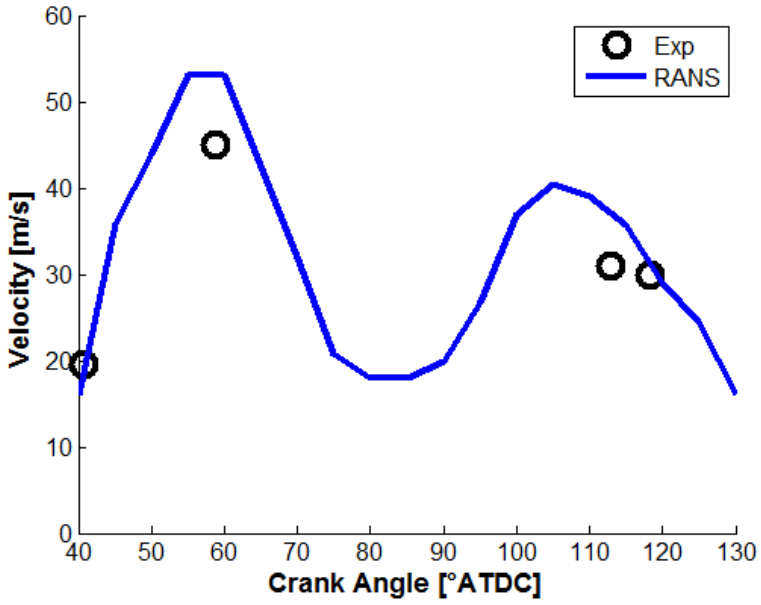

Figure 3.25 – Intake runner velocity as a function of crank angle, comparing the RANS model and experimental data (Justham, Jarvis, Garner, *et al.*, 2006)

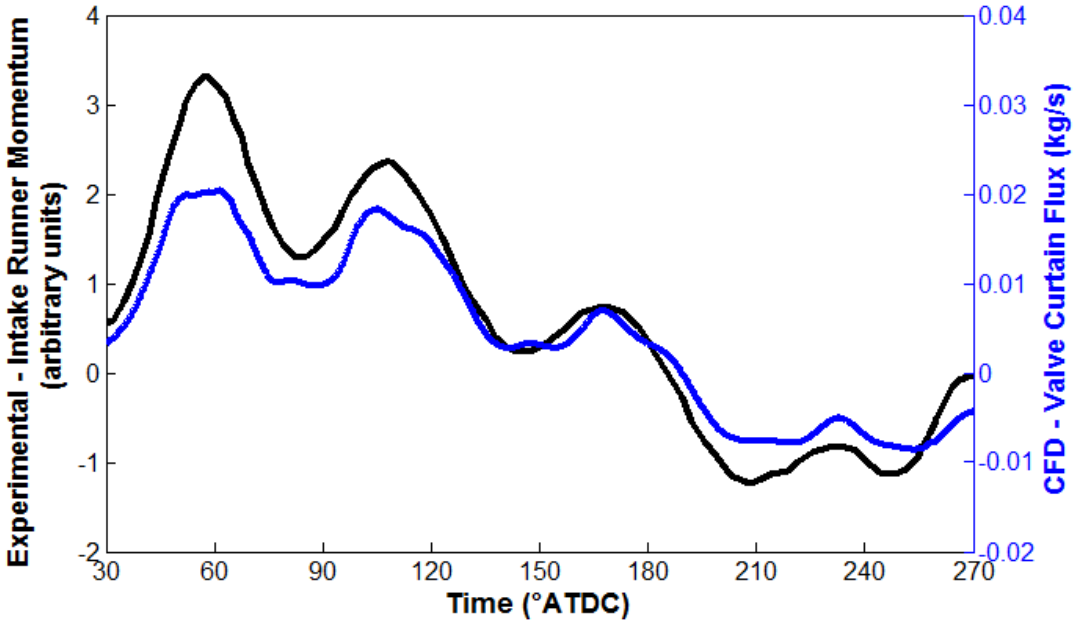

Figure 3.26 – Experimental intake runner momentum (Justham, Jarvis, Garner, *et al.*, 2006) and RANS model valve curtain mass flux as a function of crank angle

Next, experimental PIV data in the pent roof region focussed on the intake valve jet was used to validate the model flow field predictions for flow entering the cylinder past the intake valve. Experimental data was used from Justham (2010) and Justham & Jarvis (2006). A schematic of the measurement location within the combustion chamber is shown in Figure 3.27. Due to the large degree of cyclic variability seen in this flow structure, the experimental PIV data used to support model validation is a combination of both mean low frequency flow fields and raw flow field data. Whilst the mean low frequency flow fields offer a more direct comparison to RANS model predictions, the raw flow fields also provide details on some of the cycle-to-cycle variations in the flow field and offer the potential for providing insight into differences between predictions and experiments.

Figure 3.28 shows a comparison between the mean low frequency flow field from experimental data and the predicted flow field for the intake valve jet. The figures show that the flow field structure is well predicted, with the positioning of recirculation zones and valve jet angle well predicted. The velocity profile is reasonably well predicted over the crank angles shown with a slight over prediction of valve jet velocity later in the cycle as shown by the images at 100°ATDC.

Figure 3.29 provides a comparison of the model predictions against experimental data from a single cycle. The results also indicate that the model is predicting the valve jet well with respect to the overall structure and position of recirculation zones above and below the valve jet. Based on the velocity contour data, the model also appears predict the velocity magnitude well but due to the rather coarse scale used for the velocity magnitude early in the intake valve jet development period (circa 70°ATDC to 75°ATDC), it is difficult to say with confidence that the predicted velocities predicted at this part in the cycle are reasonable.

It can also be seen from Figure 3.29 and Figure 3.30 that the model predicts that the intake valve jet detaches from the cylinder head earlier in the cycle and at lower valve lifts than seen in the experimental data. This will act to drive differences between the predicted discharge coefficient and that of the experiments. It is well known that the valve discharge coefficient is intrinsically linked to the flow field past the valve and hence changes in flow field as a consequence of flow detaching from a particular surface, causes a subsequent change in discharge coefficient. In this case, the model predicts the valve jet to detach from the cylinder head earlier in the cycle thus it could be theorised that this will act to lower the discharge coefficient, reduce the effective flow area and cause an over prediction of valve jet velocity in

comparison to experimental data. Unfortunately, experimental data is not available to validate this theory.

Additional experimental data was reviewed from Justham & Jarvis (2006) (though not shown here) for a number of engine cycles at 70°ATDC and 97°ATDC. The data illustrates the difficulty of validating a CFD model using time-averaged turbulence modelling for highly unstable flow fields with strong shear flows that are present in the intake valve jet. The data indicates that a high degree of cyclic variability is present early in the intake valve jet development period with some cycles showing the valve jet still attached to the cylinder head whereas other cycles show varying levels of detachment. By 97°ATDC the data shows that the valve jet exhibits significantly less cycle-by-cycle variation in flow structure indicating that the valve jet is more stable by this point in the cycle.

The model predictions also appear to show the valve jet to be much more susceptible to the influence of wave dynamics in the intake system. Between 75°ATDC and 80°ATDC the model shows a clear weakening of the valve jet which can be linked with the drop in intake valve curtain flux (refer Figure 3.26).

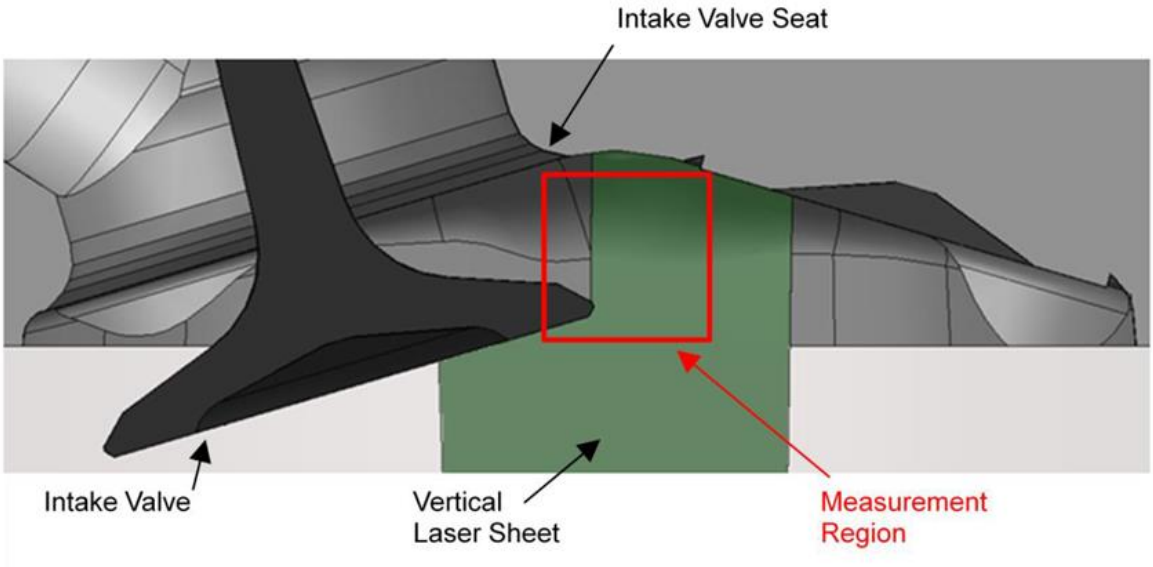

Figure 3.27 – Schematic showing the measurement location of the intake valve jet PIV velocity fields, taken from Justham (2010)

Experimental – Mean Low Frequency PIV Flow Fields

RANS – Velocity Magnitude Contours and Vectors

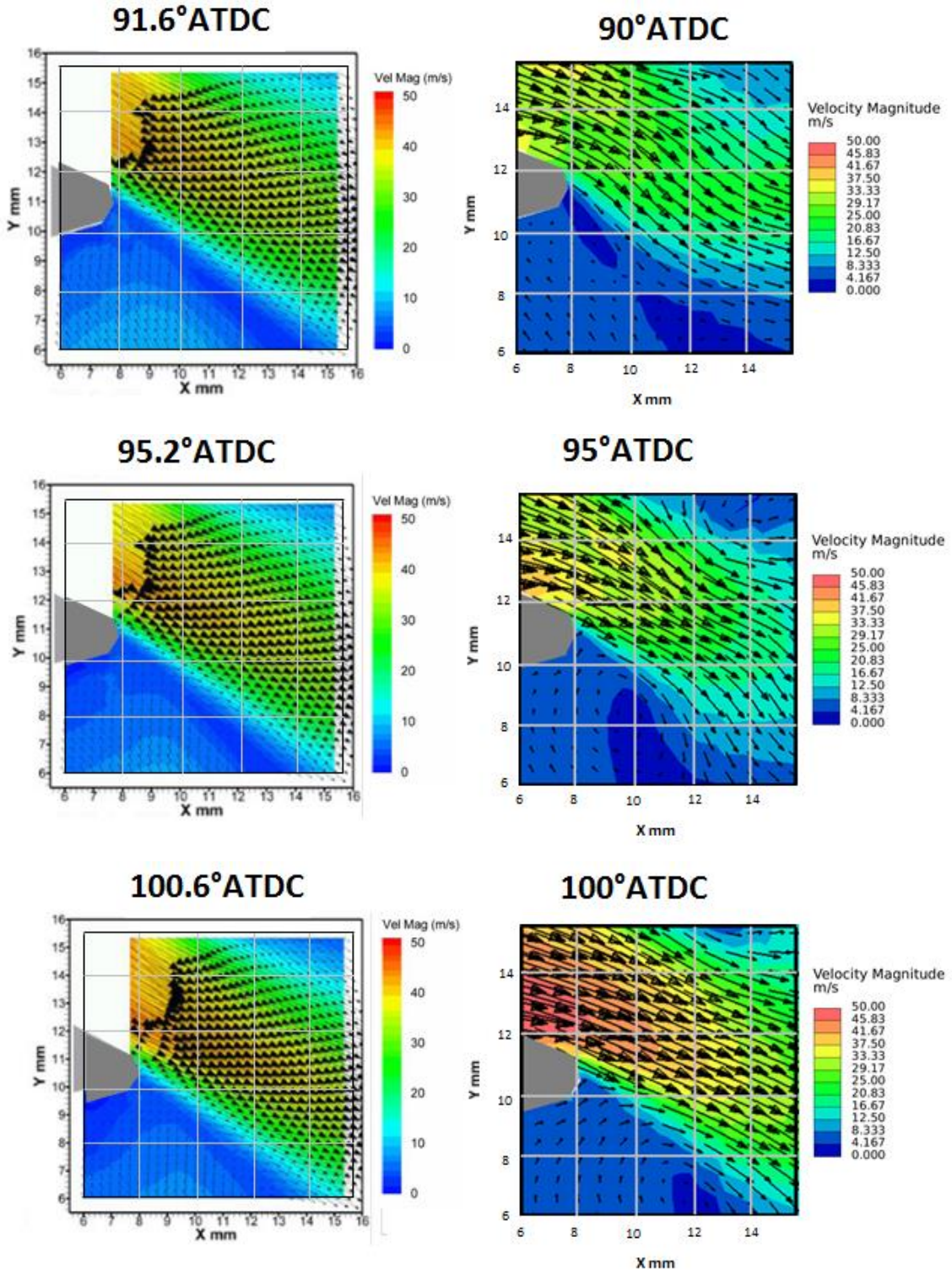

Figure 3.28 – A comparison of mean low frequency PIV flow fields (Justham, 2010) and CFD model predicted flow fields for the intake valve jet

Experimental – Raw PIV Flow Fields for One Arbitrary Cycle

RANS – Velocity Magnitude Contours and Vectors

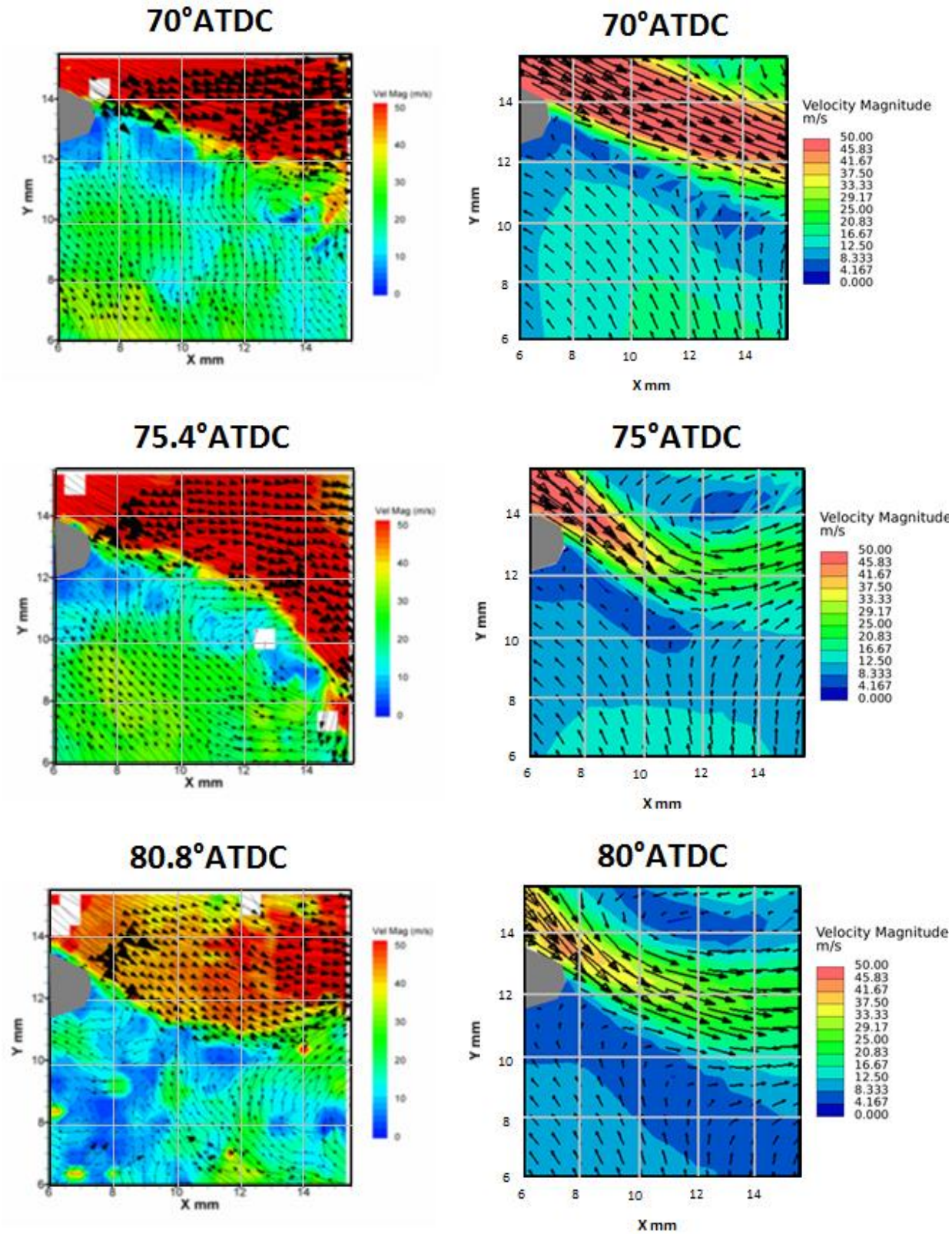

Figure 3.29 – A comparison of raw PIV flow fields for one arbitrary cycle (Justham & Jarvis, 2006) and CFD model predicted flow fields for the intake valve jet at 70, 75° and 80°ASOI

Experimental – Raw PIV Flow Fields for One Arbitrary Cycle

RANS – Velocity Magnitude Contours and Vectors

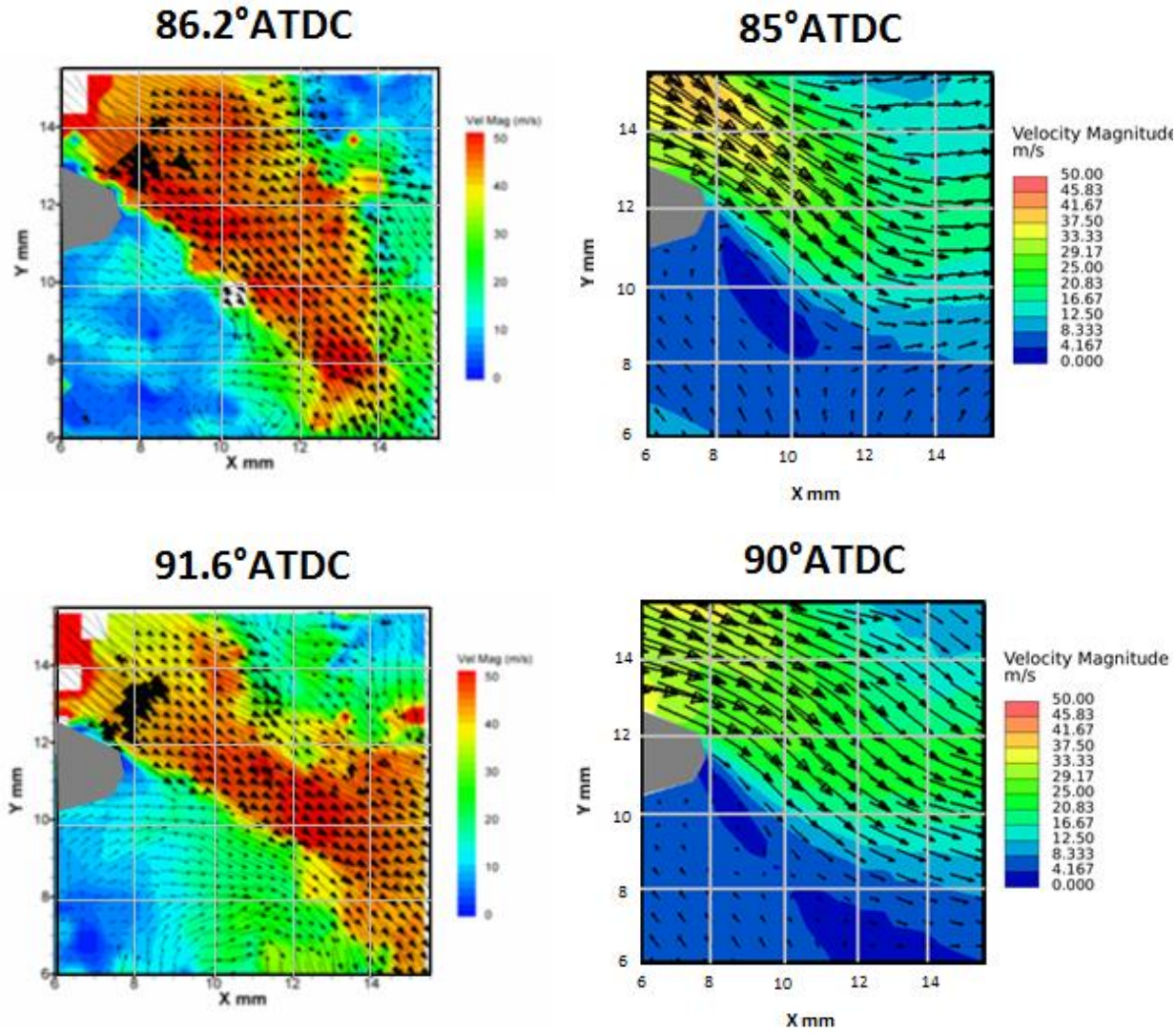

Figure 3.30 – A comparison of raw PIV flow fields for one arbitrary cycle (Justham & Jarvis, 2006) and CFD model predicted flow fields for the intake valve jet at 85° and 90°ASOI

The in-cylinder flow field was validated using experimental PIV data from Justham (2010) along the bore centreline in the tumble plane and comparative figures are presented in Figure 3.31 and Figure 3.32.

The engine presented here has a fairly weak tumble ratio due to the intake port and valve geometry and as a consequence, the flow structures generated by the flow past the intake valve and subsequent interactions with cylinder walls are also weaker in comparison to an engine with a strong tumble ratio and well defined tumble motion. Weaker flow structures are inherently more challenging to model due to being more susceptible to the influence of cyclic

variations in turbulence. This particular engine was also configured to exhibit higher than normal levels of cyclic variation (since this was the original objective of the experimental research project) which also makes predicting the in-cylinder flow structure difficult with a Reynolds averaged turbulence model.

It is clear from Figure 3.31 and Figure 3.32 that at 80°ATDC and 100°ATDC, the in-cylinder velocities are over predicted by the model when compared against the PIV data (note the difference in contour scales). As discussed previously, this is thought to be as a consequence of the over prediction of intake valve jet flow velocity due to differences in timing of flow detachment from the cylinder head. This is of particular note when modelling a homogeneous GDI engine where injection is early in the intake process, since the over predicted in-cylinder flow velocities have the potential to more strongly influence the fuel spray break-up and atomisation processes and mixture cloud distribution than would be expected in experiments.

That said, in general the flow structures are fairly well predicted by the model considering its complexity. There are clear similarities in predicted and measured recirculation regions, though the exact positioning within the cylinder is sometimes not perfectly predicted. The model provides a good basis for understanding the in-cylinder flow structures occurring within a single cylinder optical GDI research engine and for making deductions on the impact of the spatial and temporal development of the flow structure on other in-cylinder processes including injection, combustion and pollutant formation.

Experimental – Mean Low Frequency PIV Flow Fields **RANS – Velocity Magnitude Contours and Vectors**

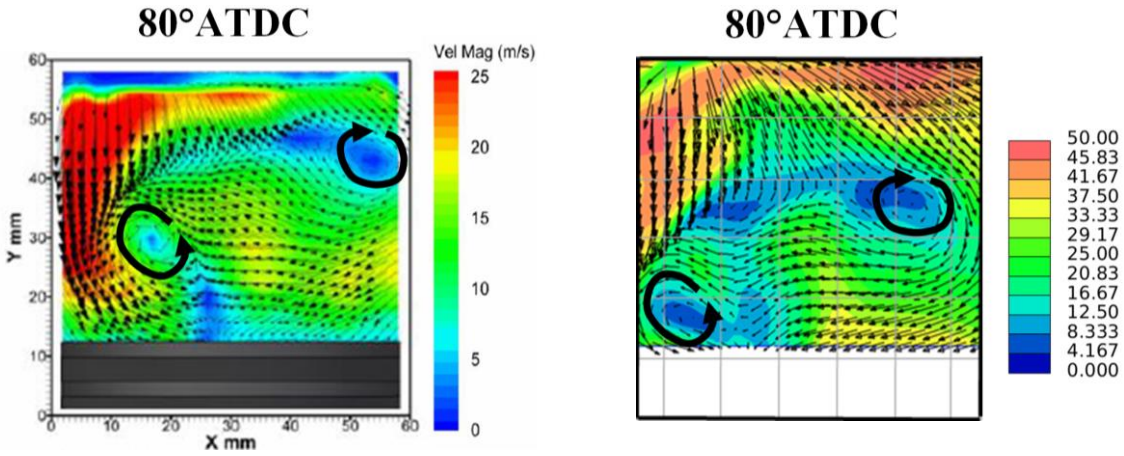

Figure 3.31 – Experimental PIV data (Justham, 2010) compared against CFD model predicted flow fields along the bore centre line in the tumble plane, with black arrows indicating similarities in flow structures between experiment and model at 80°ASOI

Experimental – Mean Low Frequency PIV Flow Fields

RANS – Velocity Magnitude Contours and Vectors

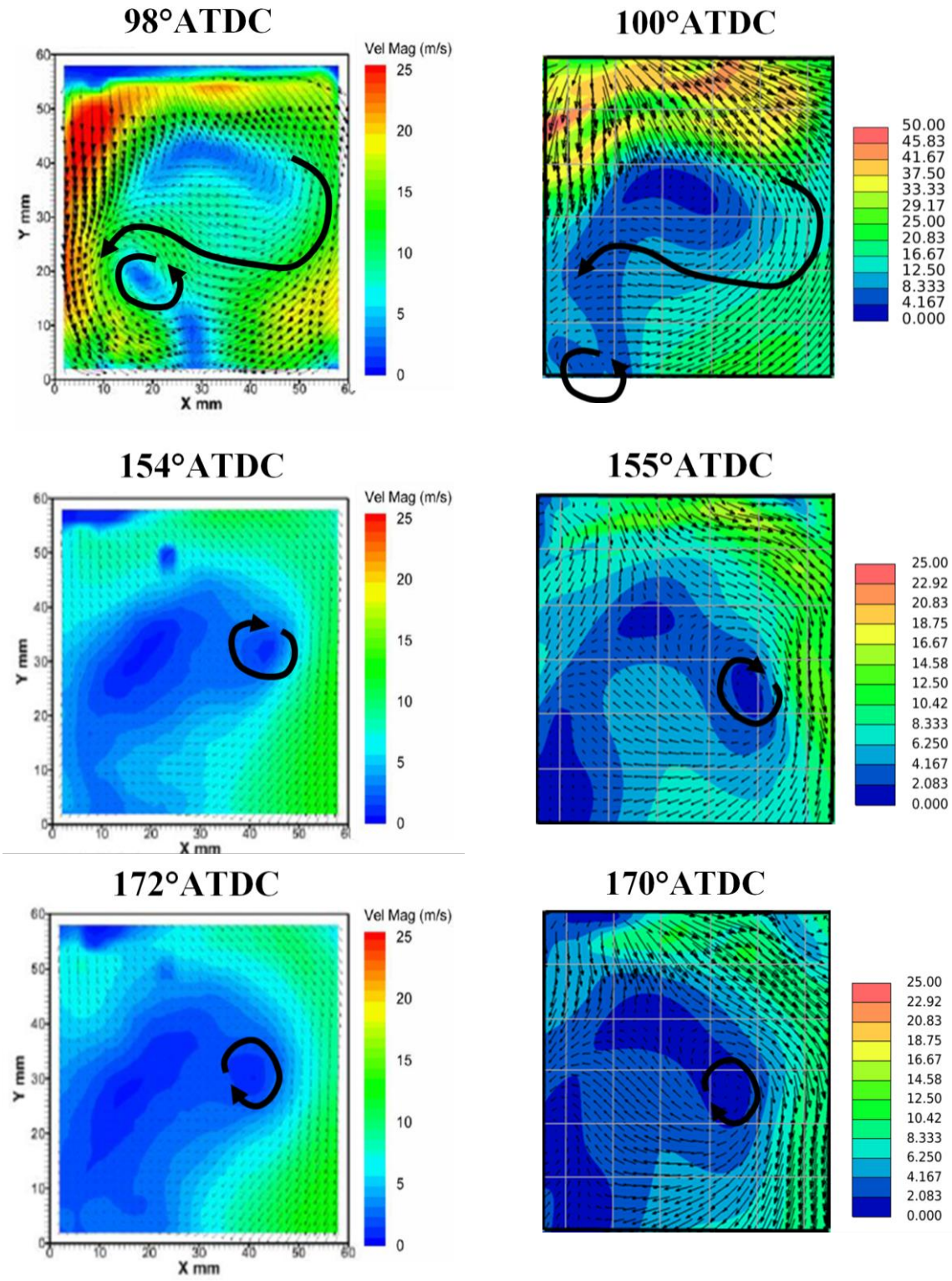

Figure 3.32 – Experimental PIV data (Justham, 2010) compared against CFD model predicted flow fields along the bore centre line in the tumble plane, with black arrows indicating similarities in flow structures between experiment and model at 100°, 155° and 170°ASOI

3.3.3.2 LES Approach

Table 3.9 summaries the turbulence models and model constants used during when the LES turbulence modelling approach was used for in-cylinder flow predictions.

Table 3.9 – Summary of turbulence sub-model and constants used during LES approach

Turbulence (gas phase)	Smagorinsky (1963) SGS model [C_S=0.02]
Turbulence – Near Wall	Angelberger, Poinsot & Delhay (1997) [y^+_{sw}=13.2, a_w=2.075, b_w=3.9]

3.3.3.2.1 Initial and Boundary Conditions

The boundary conditions used are the same as previously described for the RANS predictions in section 3.3.3.1.2 and summarised in Table 3.8.

Relevant to the unsteady nature of the LES approach, an unsteady turbulence perturbation at the inflow was not implemented in this particular study since it was considered that the inflow was sufficiently upstream of the cylinder for correct turbulence levels to form prior to the intake valves.

The influence of model initialisation was briefly investigated. Due to the unsteady nature of the LES approach, the methodology used for initialising the model has a large influence on the resultant flow field and a flow field solution that is only a function of a physically appropriate variation in the cycle initialisation is desired. To ensure this, the LES model was first initialised by a RANS cycle, primarily for solution stability and the resultant 30 cycles were inspected with respect to their variation in pressure history and relation to the other cycles. Figure 3.33 shows a zoomed in view around TDC of the in-cylinder pressure history for all the LES cycles. As can be seen, cycle 1 (highlighted in the figure) appears to be uncharacteristically high when compared to all other cycles and therefore was discarded, and the remaining 29 cycles used to form the ensemble-average and all subsequent analyses of the single-phase LES results.

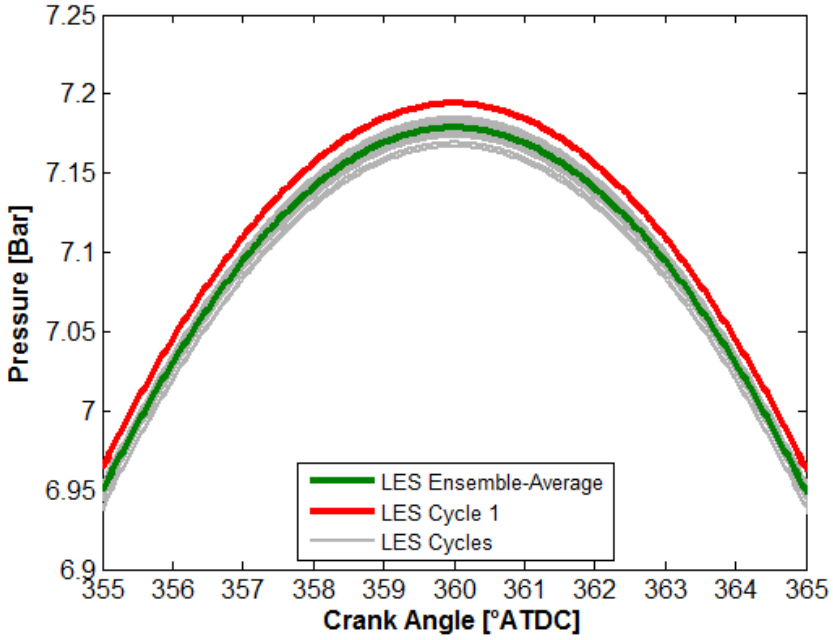

Figure 3.33 – In-cylinder pressure as a function of crank angle, comparing the LES predictions for the ensemble-average, cycle 1 and all other LES cycles

Note that in this research, each subsequent LES cycle is initiated from the final conditions of the previously computed cycle so that any variability in the initial conditions is retained and used to initiate cyclic variability in the following cycle.

3.3.3.2.2 Mesh Suitability

Since the solution is dependent on the filter width, the mesh suitability to capture the length scales present within the flow field, and hence a sufficient quantity of the flow turbulence kinetic energy, is not known *a priori* with a non-solution adaptive gridding approach. Thus, the suitability of the mesh previously defined as suitable for RANS simulations in section 3.3.3.1.1, was evaluated for its suitability for use in the LES studies using the turbulence resolution parameter. The turbulence resolution parameter, originally proposed by Pope (2000), evaluates the fraction of kinetic energy that is resolved k_{res}, against the fraction of kinetic energy that is modelled in the SGS k_{sgs} and is defined by equation (3.1).

$$M_{res}(x,t) = \frac{k_{res}(x,t)}{k_{res}(x,t) + k_{sgs}(x,t)} \tag{3.1}$$

Thus as $M_{res}(x,t)$ approaches zero the solution approaches that of RANS, and as $M_{res}(x,t)$ approaches one the solution approaches that of a direct numerical simulation (DNS). Values of $M_{res}(x,t) > 80\%$ are considered as a requirement to be deemed a 'Large' eddy simulation (Pope, 2004), whereas values between 60%-80% are considered a 'Very Large' eddy simulation (Fontanesi, Paltrinieri & D'Adamo, 2013).

In this research the turbulence resolution parameter has been evaluated at three different crank angles through the intake and compression strokes, along three swirl cutting planes (z-axis) with the results being shown in Figure 3.34-Figure 3.36.

The results show that generally turbulence resolution ($M(x,t)$) is greater than 80% with a small degree of deviation down to approximately 60% resolution at earlier crank angles due to insufficient resolution of the high shear regions around the intake valve jet. In the interests of maintaining a computational expense that is compatible within an engineering workflow, no further mesh refinement was completed.

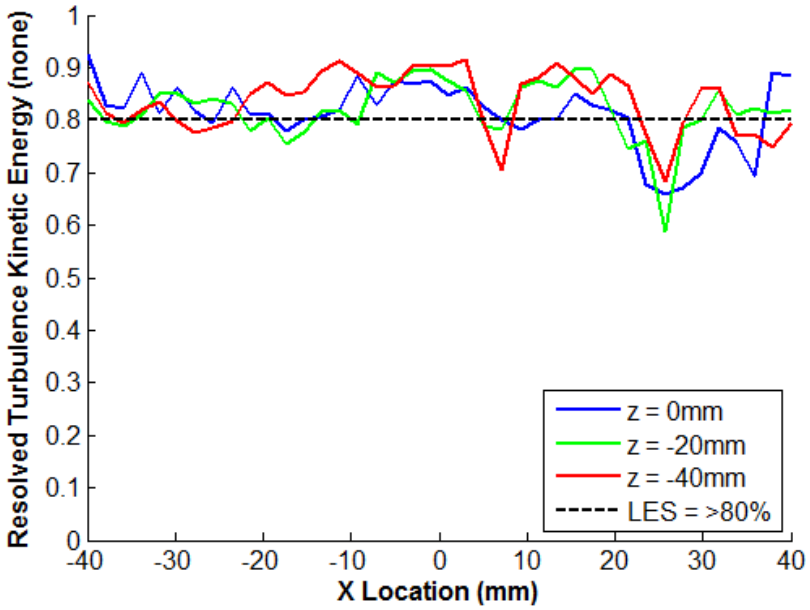

Figure 3.34 – Resolution of Turbulence Kinetic Energy as a function of X-axis Position at 150°ATDC (max lift)

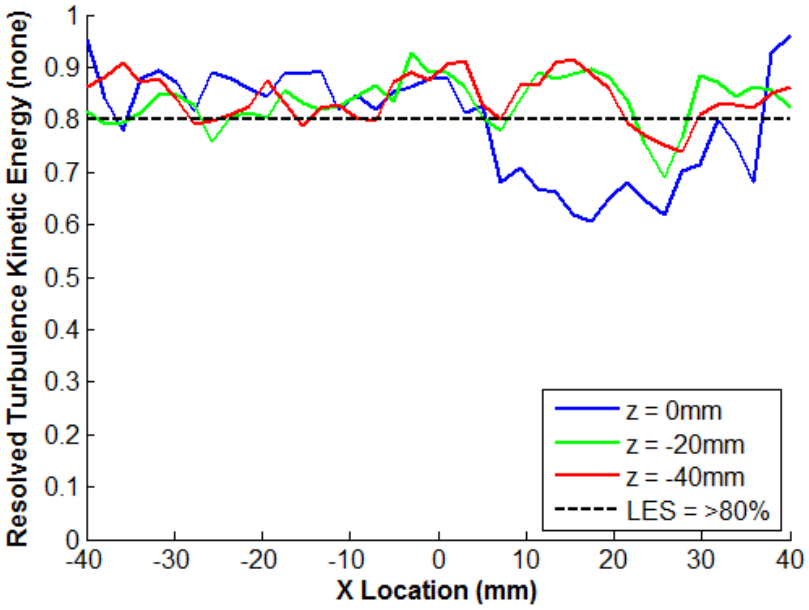

Figure 3.35 – Resolution of Turbulence Kinetic Energy as a function of X-axis Position at 180°ATDC (BDC)

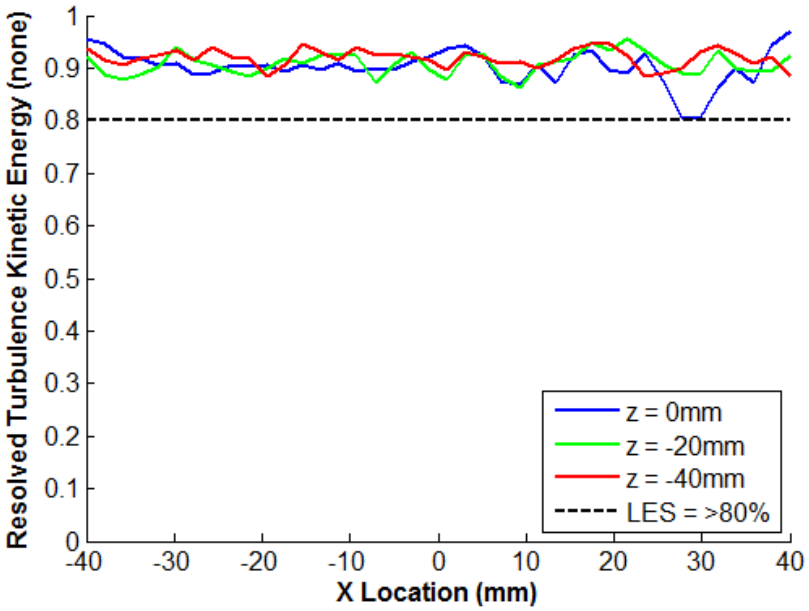

Figure 3.36 – Resolution of Turbulence Kinetic Energy as a function of X-axis Position at 270°ATDC (mid-compression)

As a caveat, it is known that the resolution of turbulence kinetic energy is dependent on both the filter width and the SGS model used. The Smagorinsky SGS model used in this research is a turbulent viscosity based approach and is well known for being overly dissipative of

kinetic energy, especially when used with a coarse mesh (Rutland, 2011). Hence results for turbulence resolution should be used with care since due to its dissipative nature and viscosity closure approach, the turbulence model can suggest that a greater amount of kinetic energy is being resolved than is reality.

3.3.3.2.3 Model Validation

As completed previously for the RANS predictions, first the in-cylinder pressure history from the LES predictions was compared against the experimental results with the pressure-crank angle curve shown in Figure 3.37 and the pressure-volume on a log-log scale is shown Figure 3.38. As can be seen, LES predictions follow the experimental in-cylinder pressure history well with the only notable differences along the compression stroke as seen and discussed previously in section 3.3.3.1.3 when comparing the RANS predictions.

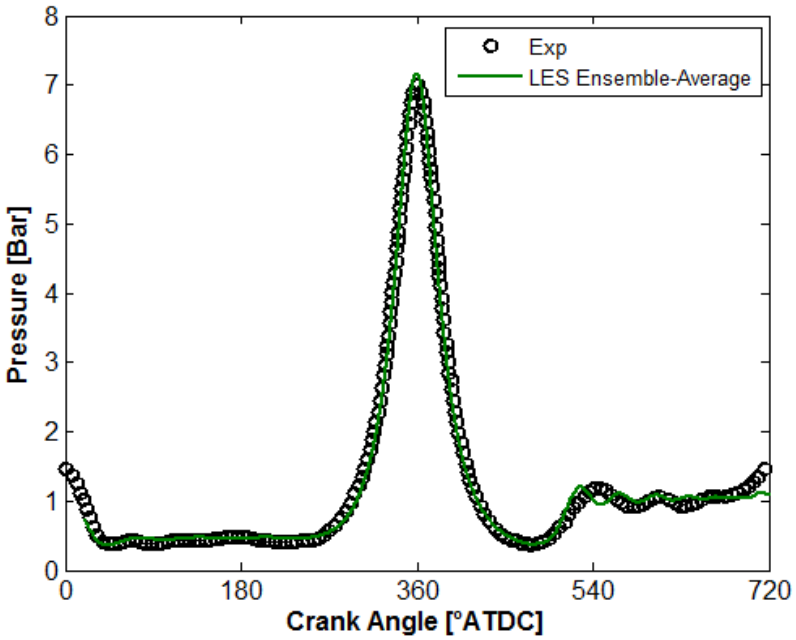

Figure 3.37 – In-cylinder pressure as a function of crank angle, comparing the LES model and experimental data

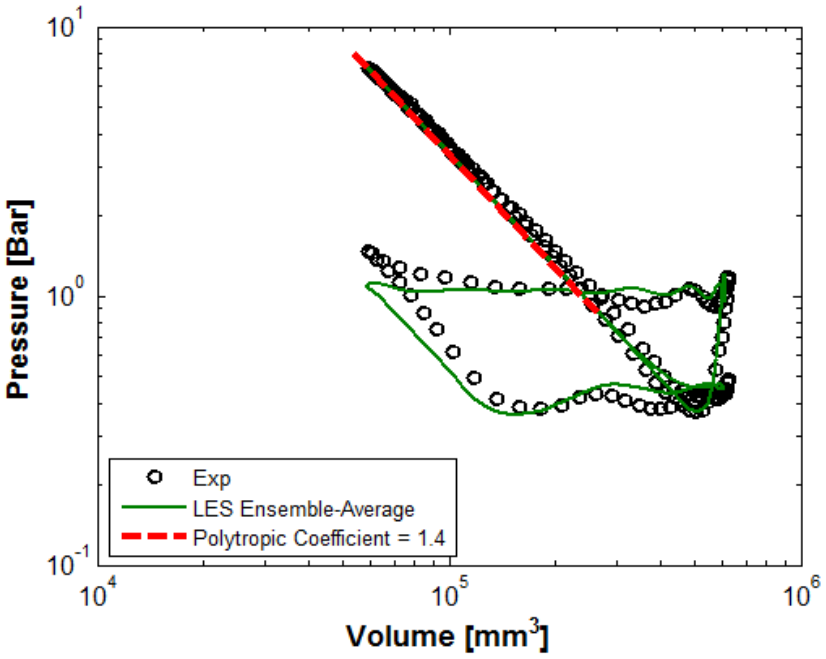

Figure 3.38 – In-cylinder pressure as a function of volume on a log-log scale, comparing the LES model and experimental data, including a slope curve at n=-1.4

The next part of the model validation was of the in-cylinder flow field. Due to a number of different methodologies being available in the literature for decomposing the instantaneous velocity field, first it is pertinent to review the definitions used in both the numerical and experimental works to ensure that the results are indeed comparable.

Typically the instantaneous velocity field is decomposed by one of two methodologies:

1. Ensemble-averaging – as used in the decomposition of the instantaneous velocity field for the LES predictions
2. Cyclic-averaging – as used in the decomposition of the instantaneous velocity field by experimental results

Ensemble-averaging is defined by equation (3.2).

$$U(\theta, c) = \overline{U_E}(\theta) + u'_E(\theta, c) \tag{3.2}$$

Where: U is the instantaneous velocity field, $\overline{U_E}$ is the ensemble-average velocity and defined by equation (3.3), u'_E is the fluctuating velocity or turbulence velocity, θ the crank angle and c the cycle number.

$$\overline{U_E}(\theta) = \frac{1}{n}\sum_{c=1}^{n} U(\theta, c) \tag{3.3}$$

Where n is the total number of cycles.

As can be seen, this methodology assumes that the mean cycle repeats each engine cycle, and the mean velocity or $\overline{U_E}$ includes all scales of turbulence, not just low frequency scales.

Cyclic-averaging can be shown generally in equation (3.4), decomposing the instantaneous flow velocity into the individual cycle mean velocity $\overline{U_C}$ and the individual cycle turbulence velocities u'_C.

$$U(\theta, c) = \overline{U_C}(\theta, c) + u'_C(\theta, c) \tag{3.4}$$

The decomposition is achieved by first transferring the instantaneous velocity into the frequency domain using a Fast Fourier Transform and then filtering each cycle using a filter frequency to separate the velocity signal into a low frequency or 'bulk flow' component U_{LF} and a high frequency or 'turbulent fluctuation' component U_{HF} as shown in equation (3.5).

$$U(\theta, c) = U_{LF}(\theta, c) + U_{HF}(\theta, c) \tag{3.5}$$

Here the low frequency component is typically further decomposed, as was the case of the experimental results in Justham (2010), into the mean cycle of the low frequency flow field $\overline{U_{LF}}$ (defined in equation (3.7)) and the low frequency cyclic variation U'_{LF} as shown in equation (3.6).

$$U_{LF}(\theta, c) = \overline{U_{LF}}(\theta) + U'_{LF} \tag{3.6}$$

$$\overline{U_{LF}}(\theta) = \frac{1}{n}\sum_{c=1}^{n} U_{LF}(\theta, c) \tag{3.7}$$

Whilst this technique does include the arguable advantage of the mean low frequency flow field $\overline{U_{LF}}$ not including the high frequency turbulent fluctuations due to the pre-filtering, it does introduce an arbitrariness since the division between high and low frequency turbulence is far from clear cut. For the experimental results presented here, the filter frequency was defined in Justham (2010) as follows: "based on the size of the recirculation structures expected to occur within the low frequency 'bulk' flow motion".

Thus as is clear, the choice of decomposition methodology has a large effect on the interpretation of the flow field. In this case:

- The ensemble-average velocity $\overline{U_E}$ (calculated via ensemble-averaging) was considered qualitatively similar enough to the low frequency flow field $\overline{U_{LF}}$ (calculated via cyclic averaging) such that a comparison between experimental and numerical predictions was made and is shown below.
- The fluctuating velocity u'_E from the LES predictions was not considered qualitatively similar enough to the low frequency cyclic variation U'_{LF} experimental results presented within the reference to provide a fair comparison and unfortunately results for the high frequency component U_{HF} were not available.

Thus, the LES predicted ensemble-average velocity ($\overline{U_E}$) is compared against experimental data extracted from Justham (2010) for 100 cycle averaged mean low frequency flow field $\overline{U_{LF}}$.

For the experimental results, the velocity magnitude data as a function of x-axis position had to be manually extracted from the velocity contour diagrams by importing them into MATLAB and relating the pixel intensity to velocity magnitude via the colour bar for discrete x-axis locations at the three z-axis planes, z = -8, -28 and -48mm. Note this methodology was used due unavailability of the raw PIV data and as such, whilst meticulous care was taken during the data extraction, the experimental results are expected to have a measurement uncertainty due to the extraction method of approximately ±1m/s.

The ensemble-average velocity predictions from the LES results were calculated over 29 individual LES cycles, with both the ensemble-average results shown as a bold black line series and individual cycle results shown in the background of the figures as light grey line series to illustrate the level of CCV present. Predictions using the RNG k-ε turbulence model are also shown for completeness.

The following is a discussion about the relative differences in mean velocity field between experimental results and LES predictions at the three crank angles investigated.

Figure 3.39 shows the velocity magnitude contours and velocity vectors for both experimental and LES results along the bore centreline at 80°ATDC and Figure 3.40 velocity magnitude as a function of x-axis position for the two z-axis cutting planes. Similarly to the RANS predictions shown earlier in Figure 3.31, the LES predictions do a good job of predicting the complex recirculation regions within the centre of the combustion chamber but does fail to correctly place them within the combustion chamber. A good example of this is shown by the red circles in either diagram; the experimental data shows a large recirculation region near -8mm>z>-20mm highlighted by the solid red circle, whereas in the LES predictions the same recirculation region is predicted to be lower in the cylinder around -20mm>z>-30mm and further into the centre of the combustion chamber (shown by the dashed red circle). This is also evident in Figure 3.40(a). Inspection of Figure 3.40(b) appears to show the model correctly predict a recirculation region at z=-28mm x=-15mm (purple circle) but upon inspection of the velocity magnitude contours, the equivalent recirculation region is again predicted lower in the cylinder around z=-45mm x=-5mm. Inspection of the valve jet velocity predictions in Figure 3.40(a) x=-25 suggests the LES model to over predict the valve jet velocities as seen in the RANS predictions but since the experimental results were extracted from the velocity magnitude contour plots and the maximum velocity contour is 25m/s, it is not possible to know if the valve jet predictions are in fact a reasonable prediction of the physical flow field.

Figure 3.41 shows the equivalent velocity magnitude contours for experimental and LES results at 100°ATDC and Figure 3.42 velocity magnitude as a function of x-axis position for the three z-axis cutting planes. Similarly to as seen at 80°ATDC, inspection of the velocity magnitude contours shows that, whilst the LES predictions correctly capture the flow structures within the combustion chamber, the positioning of the centre of the recirculation regions are not well captured. An examples of this is the large recirculation region shown in

the LES predictions in Figure 3.41(b) around z=-28mm, highlighted by a red circle, and the equivalent recirculation region in the experimental predictions is seen around z=-15mm; seen similarly is the recirculation region highlighted by the purple circles in each diagram.

Figure 3.43 shows the equivalent velocity magnitude contours for experimental and LES results at 150°ATDC and Figure 3.44 velocity magnitude as a function of x-axis position for the three z-axis cutting planes. Interestingly, later in the intake stroke the in-cylinder flow structures are much better predicted by the LES results with much better predictions of both the magnitude and positioning of the flow structures within the cylinder.

Despite these observed differences, it is felt that the LES model does a good job of correctly predicting the complex in-cylinder flow structures and their magnitude, and in most cases provides better agreement than the RANS predictions, thus is considered an acceptable model for further investigations into the physical processes of the in-cylinder flow field and turbulence induced CCV.

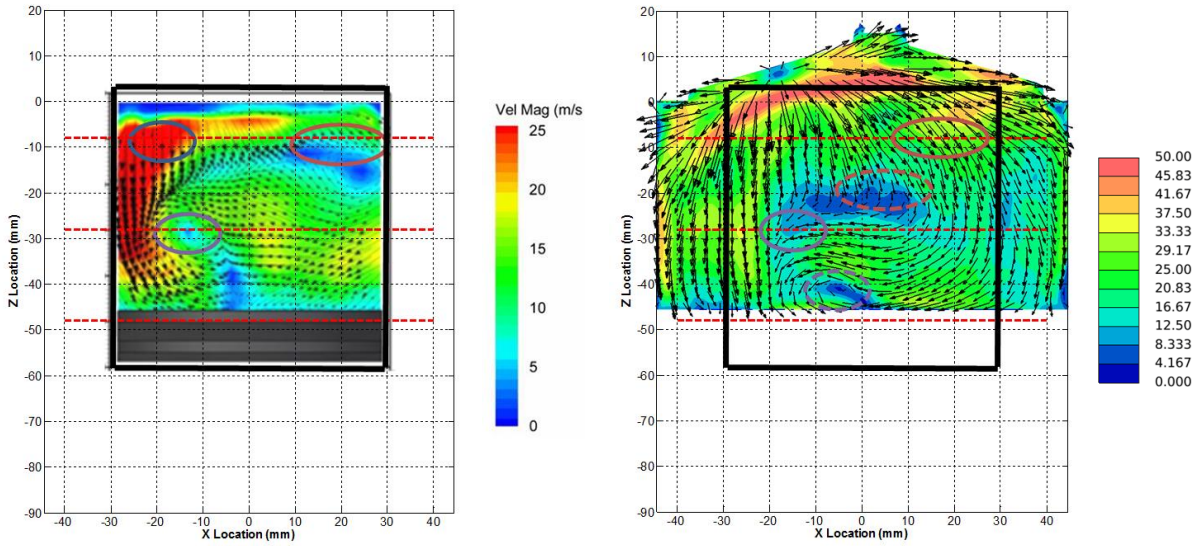

(a) (b)

Figure 3.39 – Velocity magnitude contours and vectors along the bore centreline at 80°ATDC for (a) Experiments (Justham, 2010) and (b) LES predictions

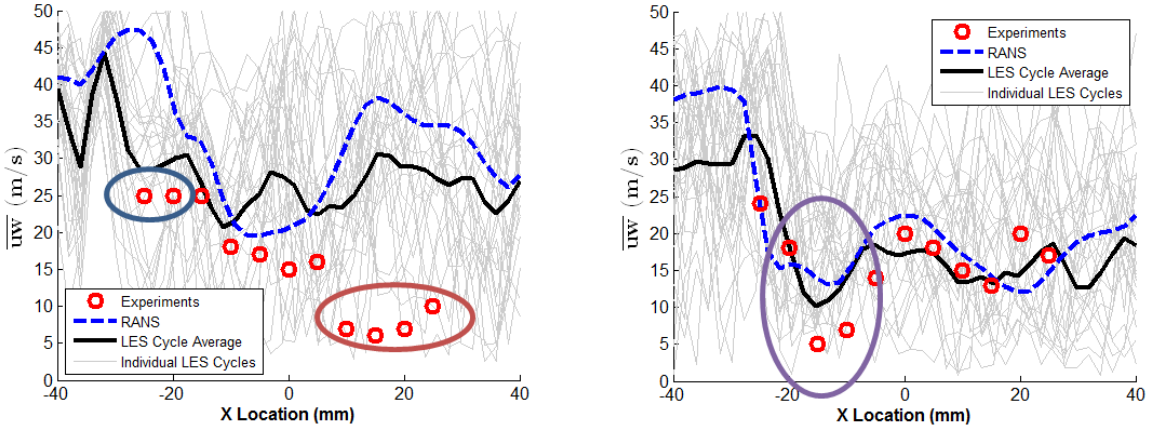

(a) (b)

Figure 3.40 – Ensemble-average velocity magnitude as a function of x-position for experimental (Justham, 2010) and LES results along the bore centreline at 80°ATDC, at two cutting planes (a) z=-8mm and (b) z=-28mm

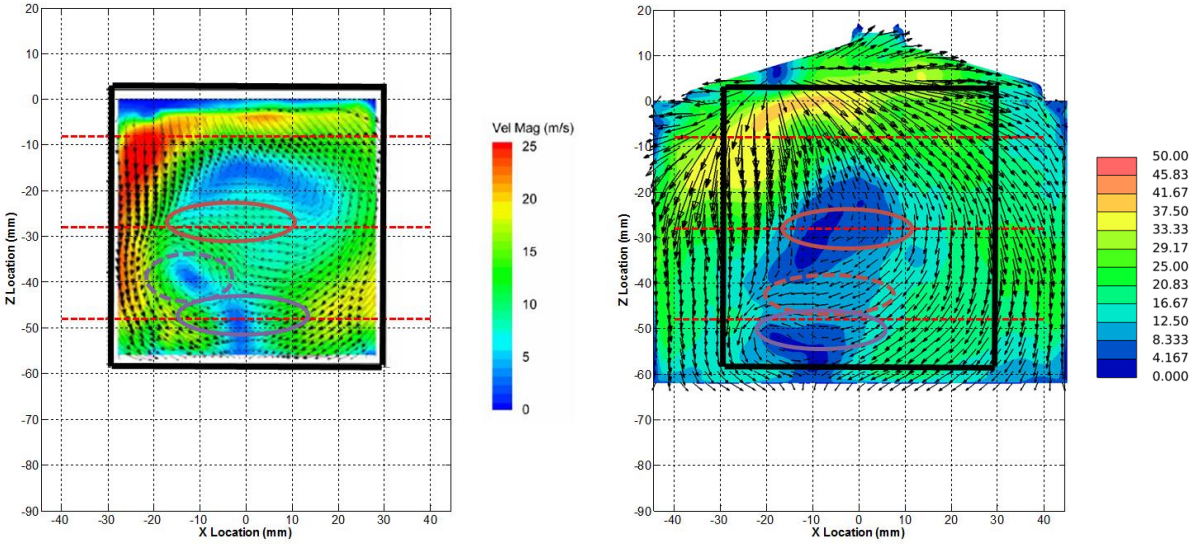

(a) (b)

Figure 3.41 – Velocity magnitude contours and vectors along the bore centreline at 100°ATDC for (a) Experiments (Justham, 2010) and (b) LES predictions

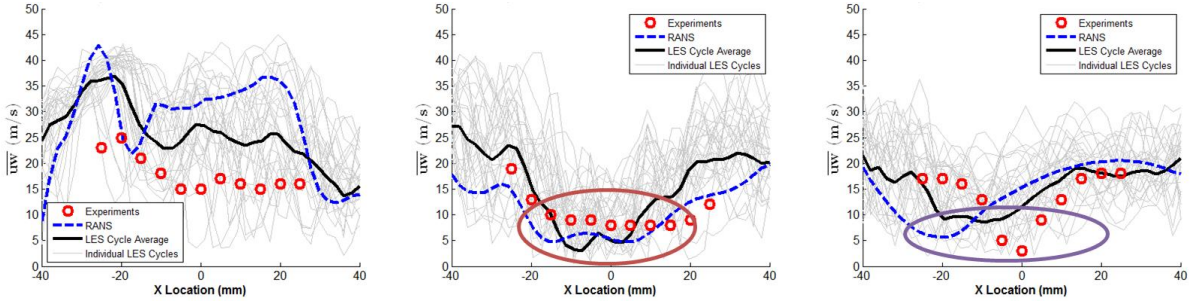

(a) (b) (b)

Figure 3.42 – Ensemble-average velocity magnitude as a function of x-position for experimental (Justham, 2010) and LES results along the bore centreline at 100°ATDC, at three cutting planes (a) z=-8mm, (b) z=-28mm and (c) z=-48mm

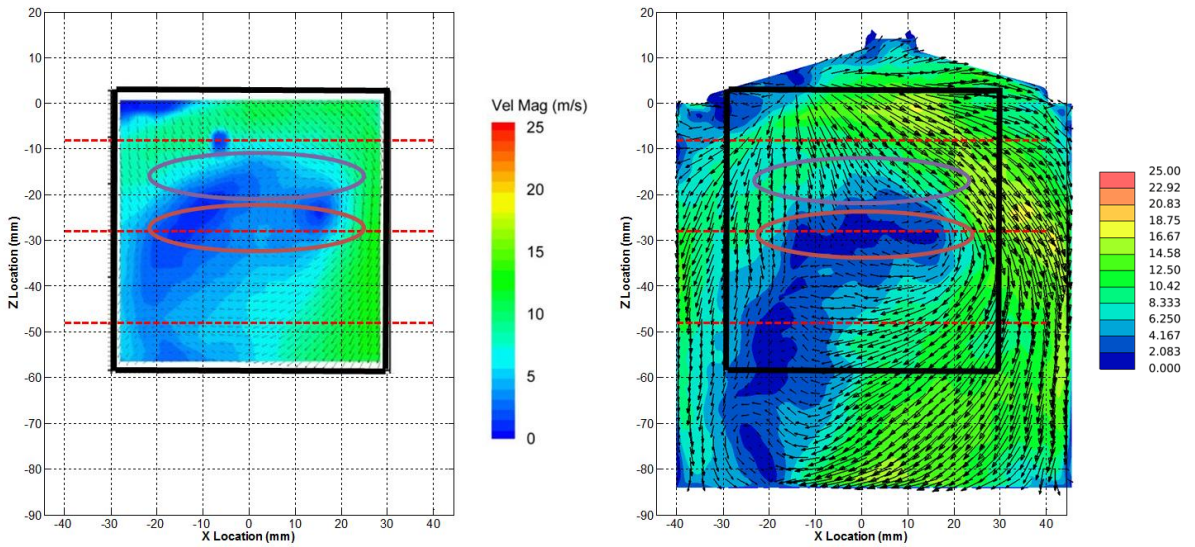

(a) (b)

Figure 3.43 – Velocity magnitude contours and vectors along the bore centreline at 150°ATDC for (a) Experiments (Justham, 2010) and (b) LES predictions

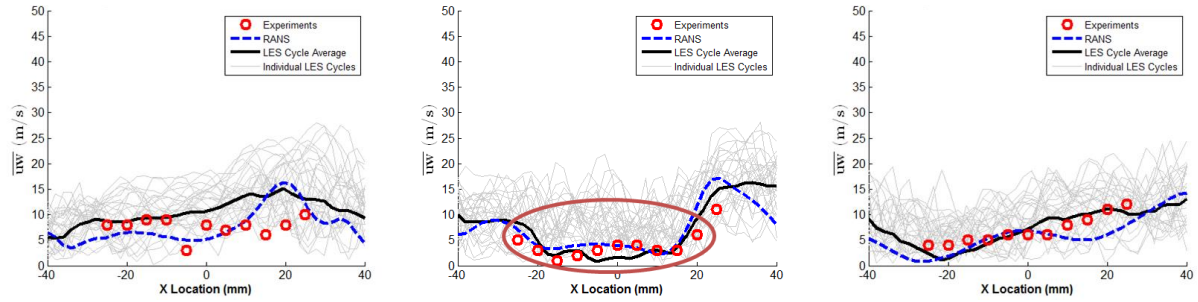

(a) (b) (c)

Figure 3.44 – Ensemble-average velocity magnitude as a function of x-position for experimental (Justham, 2010) and LES results along the bore centreline at 150°ATDC, at three cutting planes (a) z=-8mm, (b) z=-28mm and (c) z=-48mm

3.3.4 Fuel Injection: Model and Validation

3.3.4.1 RANS Approach

Table 3.10 summarises the fuel injection sub-models and model constants used for fuel injection predictions when the RANS turbulence modelling approach was used for in-cylinder flow.

Table 3.10 – Summary of fuel injection sub-models and constants used during LES approach

Turbulence Dispersion	Gaussian pdf (Gosman & Ioannides, 1983) where mean velocity is taken from the time-averaged local flow velocity and *k* is taken from the *k*-equation
Secondary Breakup Model	Pilch & Erdman (1987a) [B1=0.375, B2=0.2274]
Flash Boiling	None – see discussion below
Collision Model	O'Rourke (1981) (called 'Standard' in STAR-CD), with addition sub-models for algorithm speed-up (Schmidt & Rutland, 2000), automatic coalescence timestep adjustment (Aamir & Watkins, 1999) and additional geometric constraints (Nordin, 2001) [K_{rm}=1]
Droplet-Wall Interaction Model	Senda et al. (Senda & Fujimoto, 1999; Senda, Kanda, Al-Roub, *et al.*, 1997; Ashida, Takahashi, Tanaka, *et al.*, 2000; Senda, Kobayashi, Iwashita, *et al.*, 1994; Matsuda & Senda, 2003), Bai & Gosman (1995), Rosa, Villedieu, Dewitte, *et al.* (2006) [c_f=0.7]
Leidenfrost temperature determination	Habchi (2010) & Spiegler, Hopenfeld, Silberberg, *et al.* (1963)
Liquid Film Model	Bai & Gosman (1996) [γ_c=0.8]
Liquid Film Model – Boiling Model	White (1988) [C_{sf}=0.06, *n*=3, C_S=1.2, c_{max}=0.15, c_{min}=0.09]
Liquid Film Model – Film Stripping due to Flow Over Edge	Friedrich, Lan, Wegener, *et al.* (2008) [θ_{min}=45°, FR_c=1, c1=3.78, q=1.5]
Liquid Film Model – Film Stripping due to Wave & Body-Force Induced Instability	Foucart, Habchi, Coz, *et al.* (1998)
Liquid Film Model – Effect of Contact Angle	Foucart, Habchi, Coz, *et al.* (1998) [θ_c=35°, c=1]

Table 3.10 shows how a dedicated flash boiling model was not used during this research. The below is a short discussion of why this was considered an acceptable omission.

Flash boiling is a rapid evaporation of injected fuel at the nozzle exit occurring in direct injection engines as a consequence of a rapid reduction in the fuels boiling point as high pressure fuel is injected into the low pressure cylinder environment. The rapid evaporation associated with flash boiling typically causes significant distortion of the spray structure, with the in-cylinder flow field now able to easily influence the smaller fuel droplets and in many cases cause individual spray plumes to collapse towards each other, destroying any initial plume directionality initially imparted by the nozzle geometry (Serras-Pereira, 2010; van Romunde, 2011).

Application of the Clausius-Clapeyrun equation in the form as shown in equation (3.8), re-arranged to evaluate the fuel saturation temperature at the start and end of injection was applied to understand the degree of superheating of the fuel at the conditions present in this research.

$$ln\left(\frac{p_1}{p_2}\right) = \frac{\Delta H_{vap}}{R}\left(\frac{1}{T_2} - \frac{1}{T_1}\right) \tag{3.8}$$

Where, ΔH_{vap} is the enthalpy of vaporisation, R is the specific gas constant equal to 8.314J/K-mol.

Table 3.11 shows the change in saturation temperatures for each fuel component between the start and end of injection due to in-cylinder pressure change. The injected fuel temperature was T_f = 363K, thus showing that both iso-pentane and iso-octane fuel components are in a state of superheat and would exhibit characteristics of flash boiling upon entering the cylinder.

Table 3.11 – Saturation temperatures calculated for each fuel component at the start of injection (SOI) and end of injection (EOI) to determine the degree of superheating

	Iso-pentane		Iso-octane		n-decane	
	SOI	EOI	SOI	EOI	SOI	EOI
T_0 (T_b) [K]	301.1		372.2		447.2	
P_0 [Bar]	1		1		1	
P [bar]	0.474	0.450	0.474	0.450	0.474	0.450
ΔH_{vap} [kJ/mol]	25.0		35.1		47.4	
T (T_{sat}) [K]	**280.1**	**278.8**	**349.2**	**347.7**	**422.5**	**420.9**

In spite of this, no additional sub-model was used to model this phenomenon. Experimental results from Aleiferis & van Romunde (2013) for a constant-volume chamber at the same experimental conditions, show that both a single-component surrogate of iso-octane and a pump grade gasoline are only just beginning to show changes in plume structure at T_f = 363K and p = 0.5 bar. Figure 3.45 shows experimental spray images from a quiescent chamber for iso-octane and gasoline at 363K, showing that only a small amount of plume distortion is visible. Comparative images at 293K are also shown as an example where flash boiling would not be present in iso-octane and very mildly present in gasoline. In addition to this, results from the same publication shows almost negligible differences in plume tip penetration for iso-octane and gasoline at 293K and 363K. Thus it was felt that, whilst a separate sub-model to model the effects of flash boiling could improve the quality of the predictions, at 363K (the standardised condition for this research) a single-component surrogate fuel of iso-octane and multi-component surrogate containing fractions of iso-pentane, iso-octane and n-decane could be adequately modelled without the use of an additional flash boiling sub-model, whilst still capturing a considerable portion of the spray development process and not suffer additional increases in computation time.

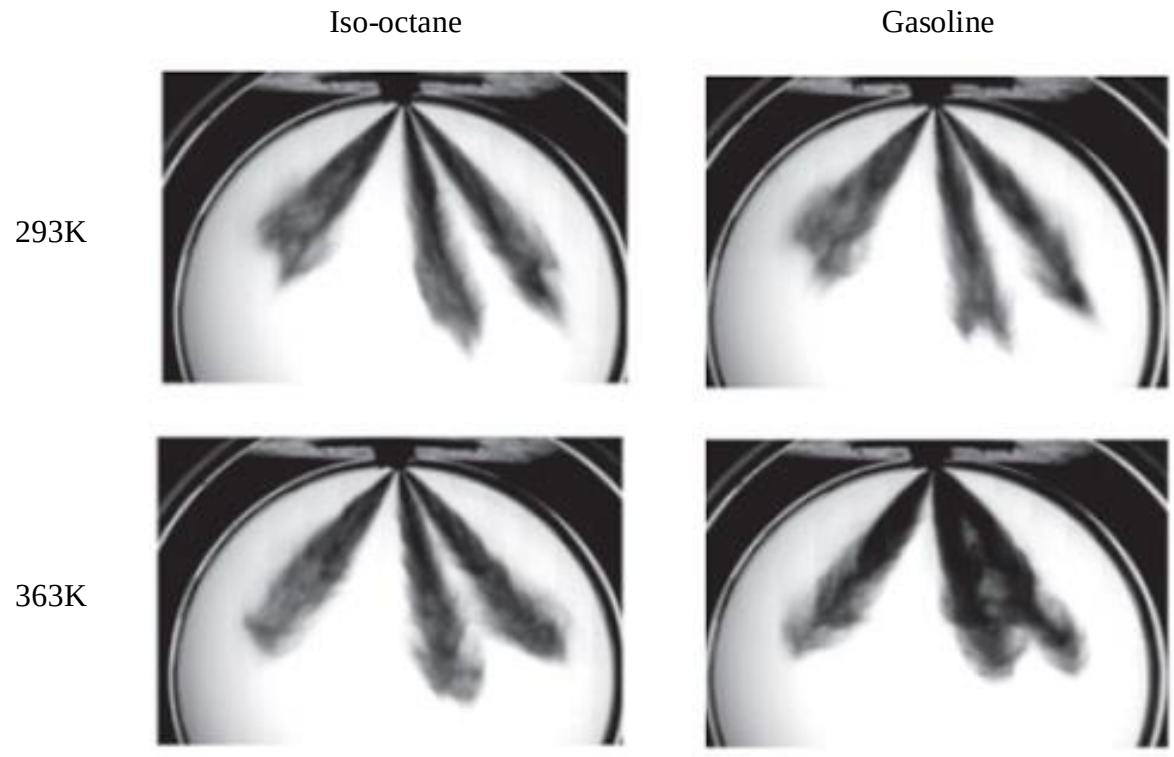

Figure 3.45 – Spray images from a quiescent chamber for iso-octane and gasoline at 777µs ASOI, reproduced from Aleiferis & van Romunde (2013)

3.3.4.1.1 Sensitivity Studies

Prior to model validation a number of sensitivity studies were completed to understand the sensitivity of the solution to the inputs chosen.

Mesh Size Dependency

For the mesh size dependency study, three different cases were investigated, with the total number of cells at BDC and the approximate cell size in the cylinder interior shown in Table 3.12. Case 2 represents the same mesh size as documented previously in section 4.2. A fourth mesh of 8.5m cells and an approximate cell size of 0.3-0.4mm^3 was developed but due to the meshing procedure and the cell addition and deletion method used to model boundary movement within the software, it was not possible to create a mesh that didn't suffer significant cell uniformity and orthogonality issues that then caused the solution to be unstable. Note: This study was completed with a total number of parcels per spray plume of 1'000'000. This was significantly more than was known to be needed for parcel number independency, which ensured that any effect that the number of parcels may have on the solution was minimised.

Table 3.12 – Different mesh sizes investigated in the mesh size dependency study

Case	Total number of cells at BDC [none]	Approximate cell size in the cylinder interior [mm^3]
1	1.7m	1.25-1.4
2	2.2m	0.7-0.8
3	3.6m	0.4-0.6

The plume tip penetration for plumes 2/5 and plumes 1/6 were investigated first. Figure 3.46 shows the spray plume numbering system used. The results are shown in Figure 3.47 and Figure 3.48. Whilst the difference in penetration between the three meshes is not significant, neither of the results appeared to show the results trending towards an insensitive solution with an increasing number of cells.

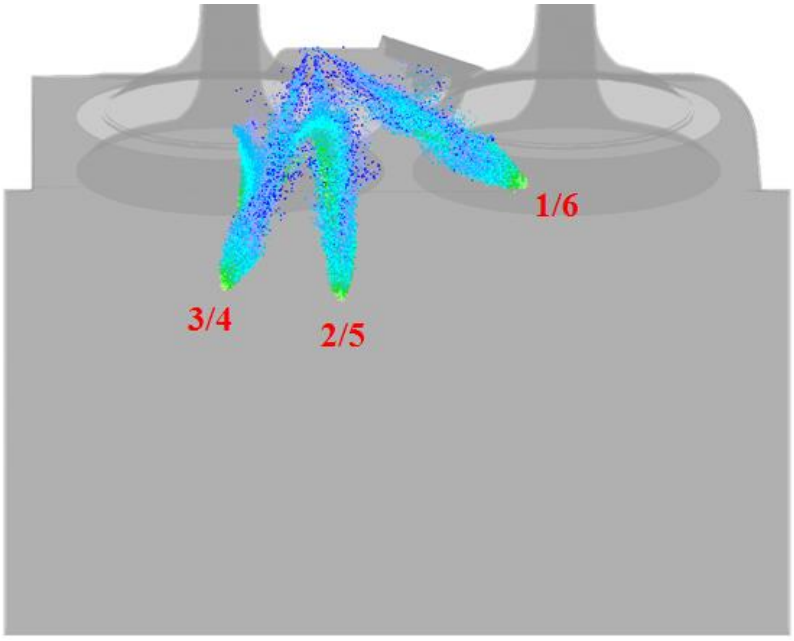

Figure 3.46 – Image of spray penetrating in y-z plane, indicating the spray plume numbering system

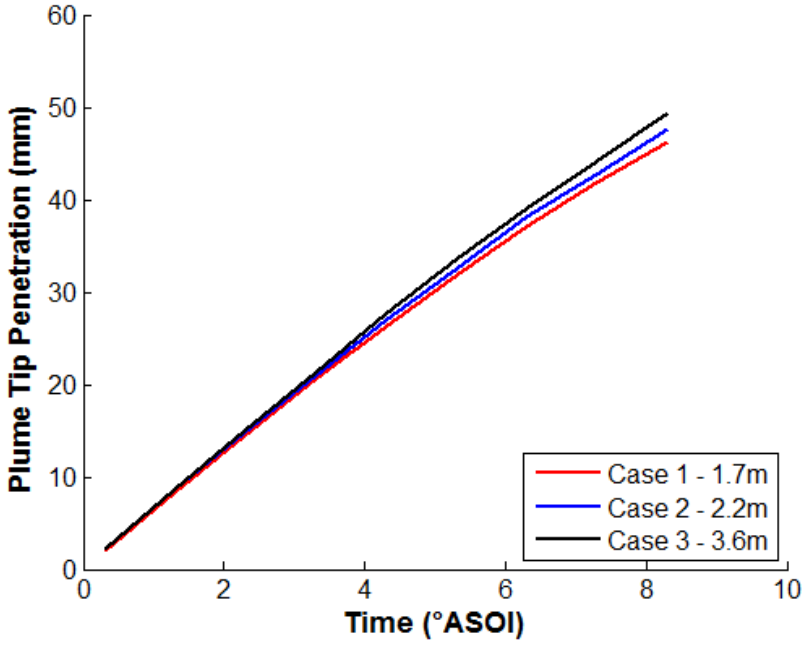

Figure 3.47 – Plume tip penetration for plumes 1/6 for three different mesh sizes

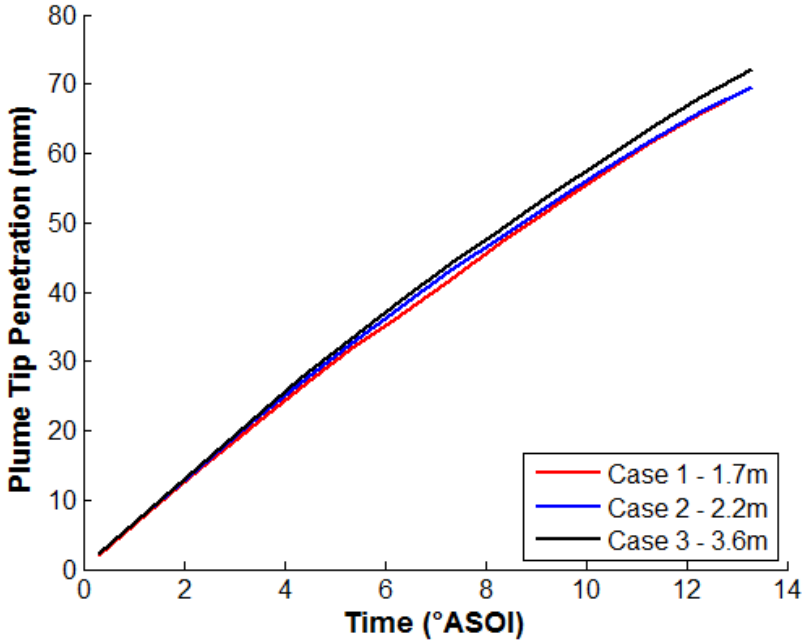

Figure 3.48 – Plume tip penetration for plumes 2/5 for three different mesh sizes

Next, Figure 3.49 shows contours of fuel mass fraction plotted in the tumble plane, intersecting plumes 2/5, for each mesh size to provide a qualitative comparison between cases.

The results indicate a number of differences particularly between the coarse mesh in case 1 and the finer meshes used in cases 2 and 3; whilst the magnitude of fuel mass fraction is similar between each of the meshes, the spatial variation in the fuel vapour cloud is quite different with the coarse mesh not depicting the correct shape of the plume head and trailing vapour cloud. In general, both case 2 (2.2m) and case 3 (3.6m) show similar spatial variations in the fuel mass fraction.

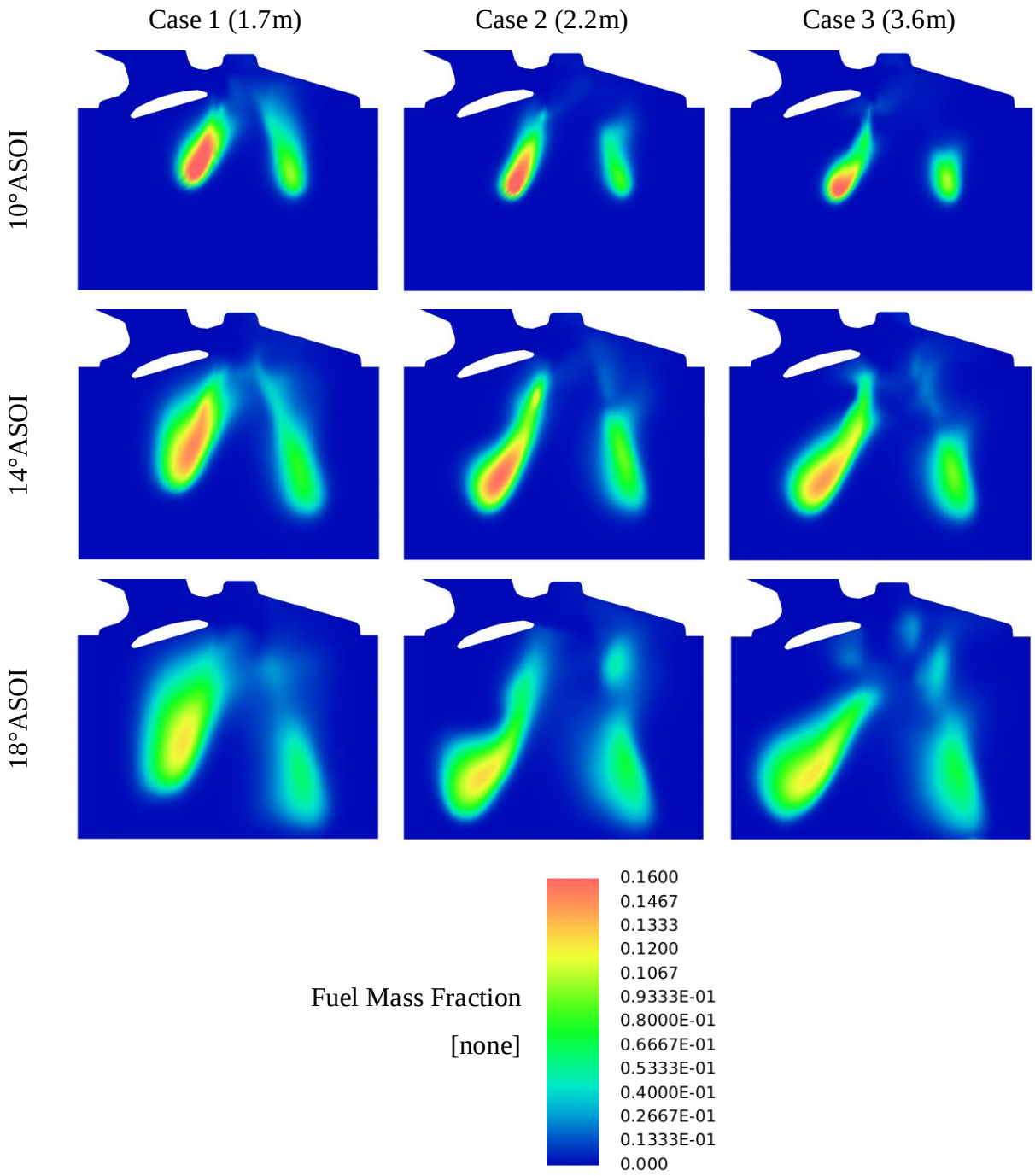

Figure 3.49 – Fuel mass fraction contours along the tumble plane intersecting plumes 2/5 for the three different mesh sizes

To provide a more quantitative comparison and to support the above fuel mass fraction result, fuel mass fraction as a function of x-plane position was plotted for different z-plane cutting planes at a specific y-plane location for four crank angles and the results are shown in Figure 3.50.

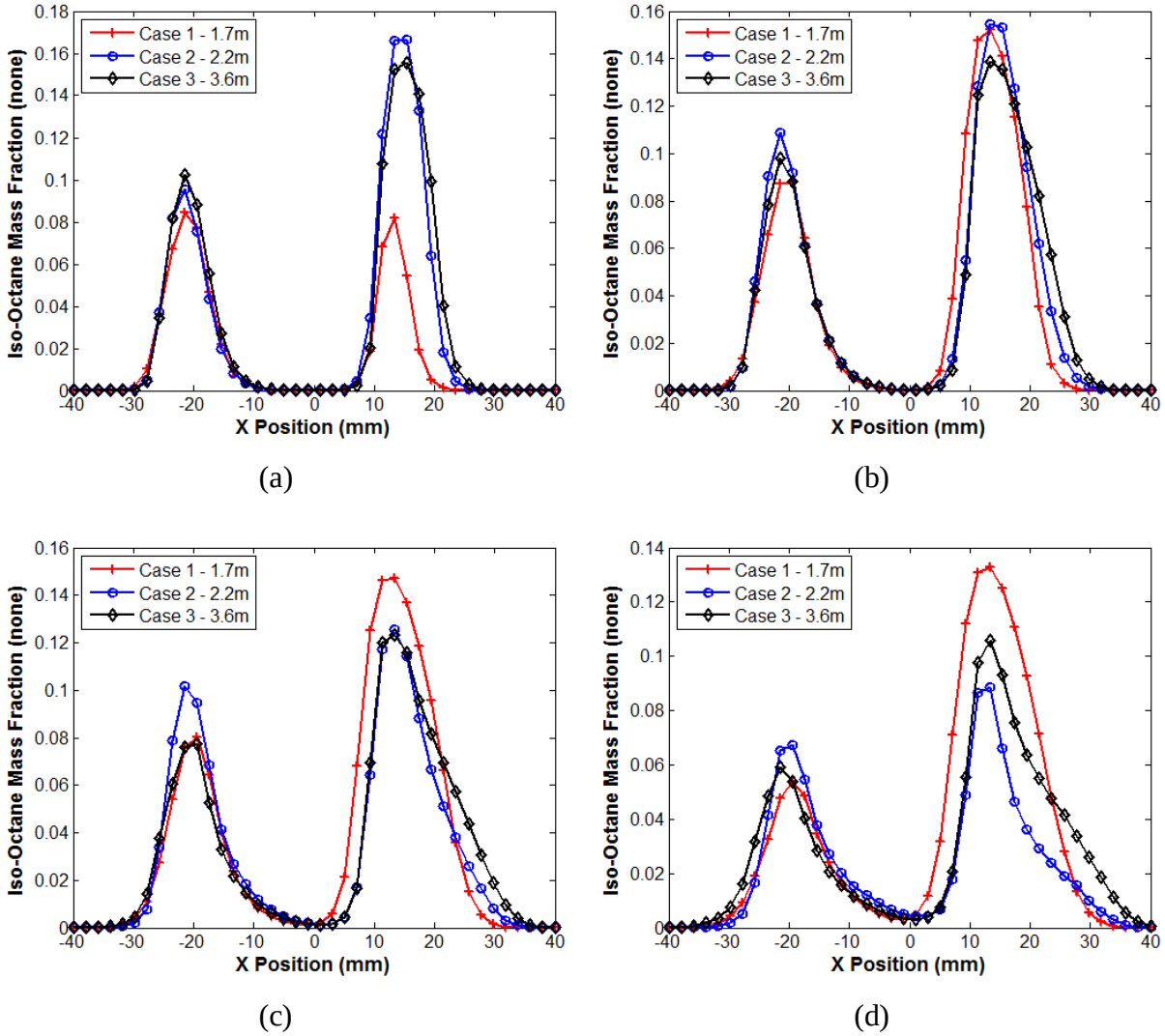

Figure 3.50 – Plots of fuel mass fraction as a function of x-plane position at y=4.57mm z=-30mm at four crank angles, (a) 12°ASOI, (b) 14°ASOI, (c) 16°ASOI, (d) 18°ASOI

Similarly to seen above in the fuel mass fraction contours, generally the predictions for case 2 (2.2m) and case 3 (3.6m) as comparatively similar, thus implying the predictions with respect to spatial and temporal variation in fuel mass fraction is relatively insensitive by 2.2m cells.

Finally, the distribution of droplet diameter calculated across the cylinder for each mesh size, was compared at 14°ASOI at three different z-plane cutting planes and the results are shown in Figure 3.51.

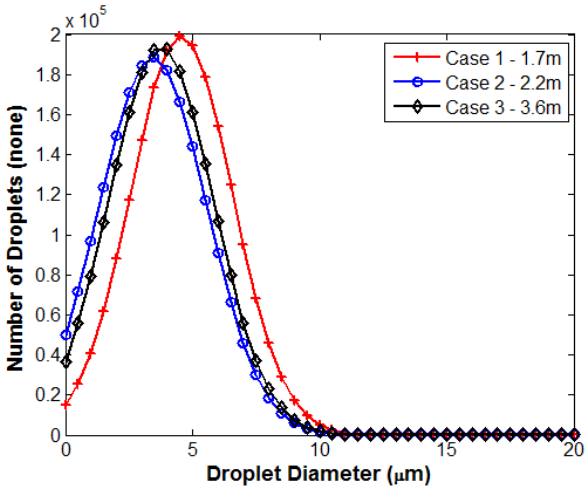

(a)

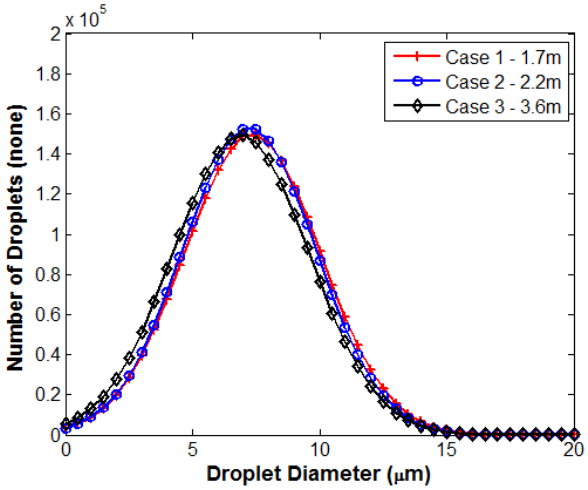

(b)

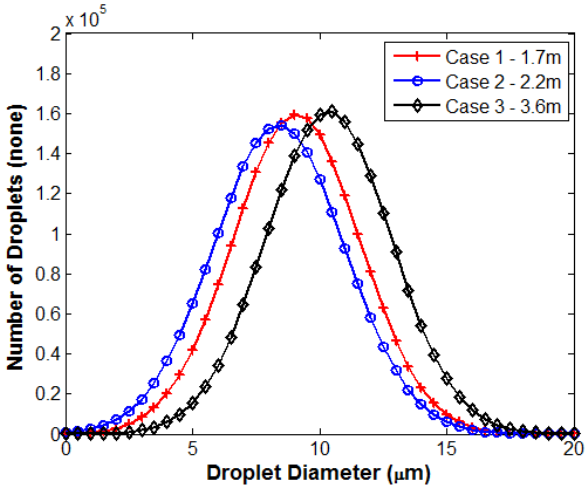

(c)

Figure 3.51 – A comparison of droplet diameter distribution across the cylinder for the three different mesh sizes at 14°ASOI for three separate z-plane cutting planes, (a) z=-10mm, (b) z=-30mm, (c) z=-50mm

Again, generally the predictions for case 2 (2.2m) and case 3 (3.6m) are comparatively similar, thus implying the predictions with respect to spatial and temporal variation in droplet size distribution is relatively insensitive by 2.2m cells.

Finally the computational expense between three mesh sizes was compared and the results for the number of CPU-hrs for a simulation between SOI and ASOI+20° are shown in Table 3.13. As is shown, a relatively large increase in computational expense is seen between case 2 (2.2m) and case 3 (3.6m).

Table 3.13 – A comparison of the sensitivity of computational expense with respect to the number of CPU-hrs required for a simulation between SOI and SOI+20° for the three mesh sizes

Case	Total number of cells at BDC [none]	CPU-hrs for SOI to ASOI+20° [CPU-hr]
1	1.7m	289
2	2.2m	328
3	3.6m	462

In conclusion, the mesh with 2.2m cells (case 2) was seen to provide predictions that are relatively insensitive to the size of mesh and chosen for the following reasons:

- Variation in plume tip penetration was small between all three cases though none appeared to suggest reaching the point of being insensitive
- Results for fuel vapour mass fraction and droplet size distribution both saw predictions becoming relatively insensitive to mesh size with case 2 (2.2m)
- The computational cost for each cycle was considered acceptable with the computing resources available to this research

Secondary Break-up Model

To assess the sensitivity of the earlier decision to use the Pilch & Erdman (1987) secondary break-up model, the variation in arithmetic mean or D_{10} droplet diameter was compared

against the Reitz & Diwakar (1986) and KHRT (Patterson & Reitz, 1998) breakup models for three separate z-plane cutting planes and the results are shown in Figure 3.52.

To understand the reason for the differences in average droplet D_{10} diameter between the three breakup models, the Reynolds number and Weber number at 18°ASOI was calculated for the droplets at two z-cutting planes, z=-5mm and z=-25mm, corresponding to a time and location of difference in droplet D_{10} diameters seen in Figure 3.52(a) and (c) and the results are presented in Table 3.14 and Table 3.15. Inspection of Figure 3.52(a) (z=-5mm) and Table 3.14 shows both the Reitz-Diwakar and KHRT models to have similar average Reynolds numbers and Weber numbers and the Pilch Erdman to have droplets with a comparatively lower average Reynolds number and Weber number. Similarly, in Figure 3.52(c) (z=-25mm) and Table 3.15, both the Reitz-Diwakar and Pilch and Erdman models have similar average Reynolds numbers and Weber numbers thus predict similar droplet D_{10} diameters.

Table 3.14 – A comparison of Reynolds number and Weber number for three secondary breakup models at 18°ASOI and z=-5mm

	Reitz-Diwakar	Pilch-Erdman	KHRT
Re [none]	178	154	172
We [none]	66	57	62

Table 3.15 – A comparison of Reynolds number and Weber number for three secondary breakup models at 18°ASOI and z=-25mm

	Reitz-Diwakar	Pilch-Erdman	KHRT
Re [none]	137	135	124
We [none]	76	74	70

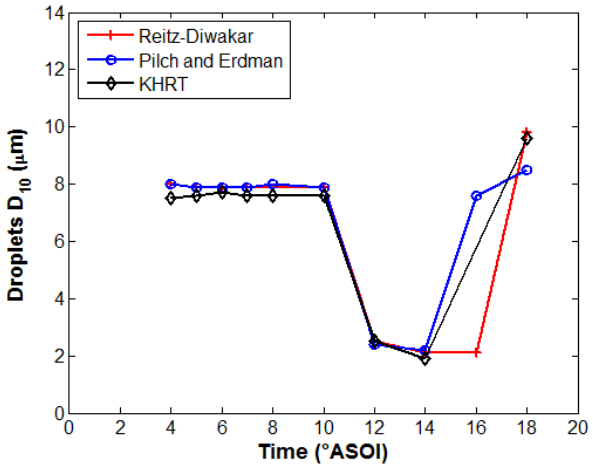

(a)

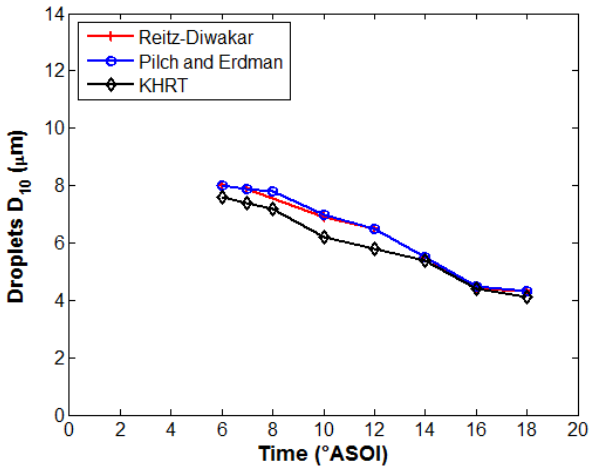

(b)

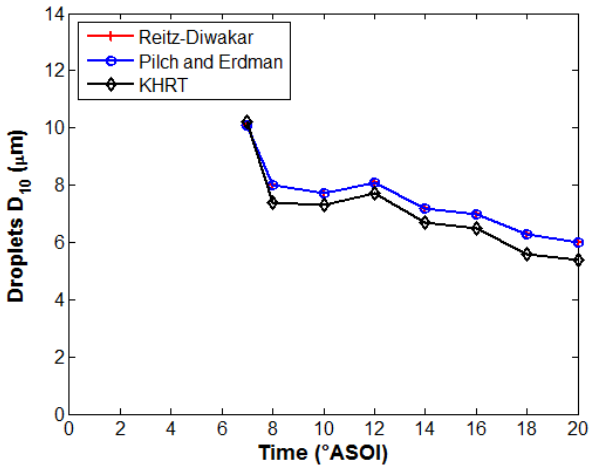

(c)

Figure 3.52 – A comparison of droplet D_{10} diameter for three different secondary break-up models at three different z-plane locations, (a) z=-5mm, (b) z=-15mm, (c) z=-25mm

In general though, the variation in D_{10} droplet diameter appears to vary little between the proposed breakup models, particularly between the Pilch and Erdman model and the Reitz-Diwakar model. The relative insensitivity is thought to be due to imposing a pre-defined droplet diameter distribution at the nozzle exit (via the Rosin Rammler distribution) to model the result of the primary breakup process, thus reducing the amount of droplet breakup performed by the secondary breakup model before droplet evaporation and hence the reduced prediction sensitivity to the imposed secondary breakup model. This insensitivity and the absence of empirical constants is the reason for this research using the Pilch and Erdman secondary breakup model.

Number of Injected Parcels

Once the mesh size was defined based on the above dependency study (due to the effect of the number of parcel within a given cell size), the dependency of the solution on the number of injected parcels was investigated via: plume tip penetration, cylinder averaged droplet sauter mean diameter (D_{32}) and computational expense.

Five different parcel number configurations were investigated as shown in Table 3.16.

Note: This study was completed on the mesh of 3.6m cells, i.e. the largest number of cells tested. This helped to ensure that any effect on the solution due to the size of mesh used was minimised.

Table 3.16 – Configurations tested in number of injected parcels sensitivity study

Case	Total number of parcels injected per jet/plume	Number of parcels injected per jet/plume per second
1	4’000	$5.13x10^6$
2	8’000	$1.01x10^7$
3	50’000	$6.41x10^7$
4	100’000	$1.28x10^8$
5	1’000’000	$1.28x10^9$

The plume tip penetration was first compared across each case for plumes 1/6 (Figure 3.53) and plumes 2/5 (Figure 3.54) and to provide a more quantitative comparison, the difference in plume tip penetration at 12.3°ASOI (i.e. close to the point of cylinder liner impingement) for plumes 2/5 between cases 1-4 and case 5, with the assumption that case 5 would provide a prediction that was least sensitive to the number of injected parcels due to the large number of parcels used, shown in Table 3.17. The results show that case 4 (100'000) and case 3 (50'000) predict an approximately 2% difference in plume tip penetration, and case 2 (8'000) and case 1 (4'000) predict an approximately 5% difference in plume tip penetration when compared to case 6 (1'000'000).

Table 3.17 – Percentage difference in plume tip penetration for plume 2/5 when compared to case 6 at 12.3°ASOI

Case	Total number of parcels injected per jet/plume	Plume 2/5 tip penetration at 12.3°ASOI [mm]	Percentage difference in penetration to case 5 [%]
1	4'000	67.1	5.4
2	8'000	67.7	4.6
3	50'000	69.6	1.8
4	100'000	69.7	1.7
5	1'000'000	70.9	-

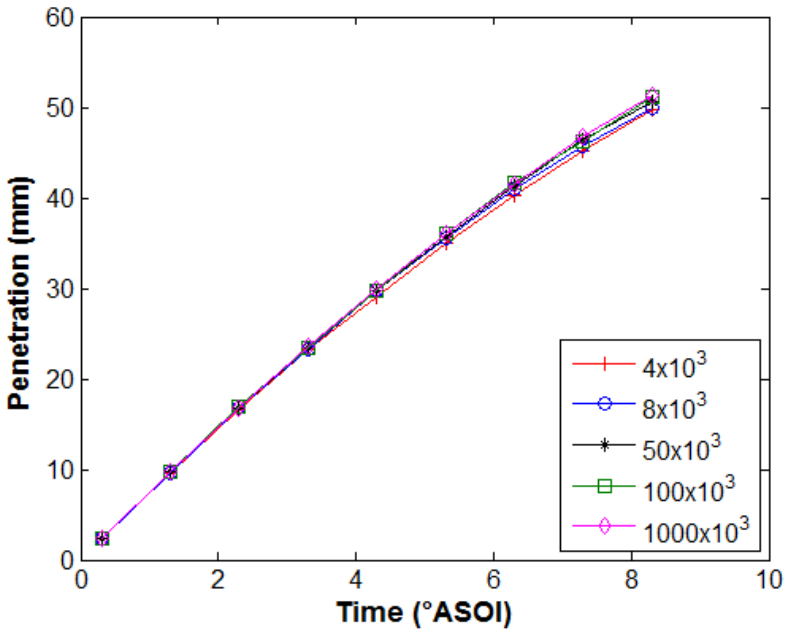

Figure 3.53 – Plume tip penetration for plumes 1/6 with a varying number of parcels injected per jet

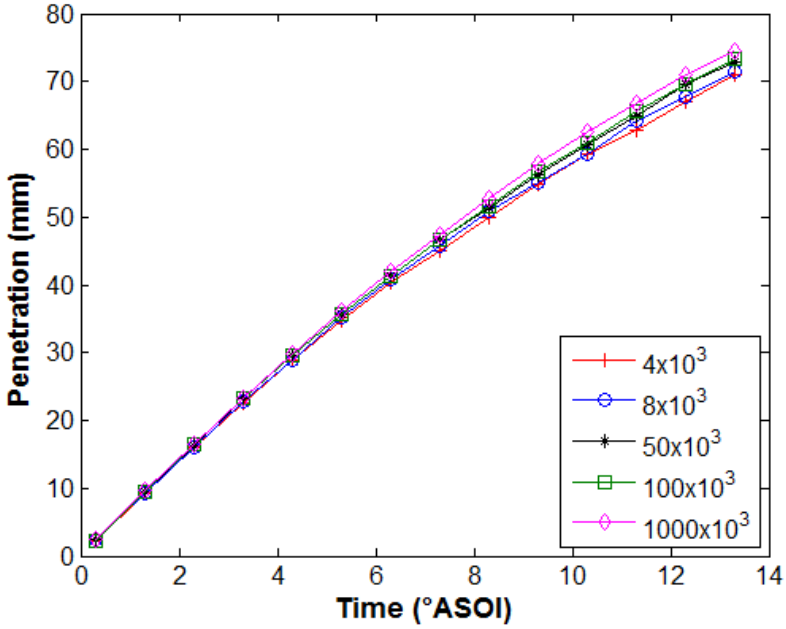

Figure 3.54 – Plume tip penetration for plumes 2/5 with a varying number of parcels injected per jet

The cylinder averaged droplet sauter mean diameter (D_{32}), as defined by equation (3.9), was next compared across the 6 cases and the result as a function of time shown in Figure 3.55.

$$D_{32} = \frac{\sum_i m_p d_p^3}{\sum_i m_p d_p^2} \tag{3.9}$$

Where m_p is the mass of the droplet parcel, d_p is the diameter of the droplet parcel and i is the total number of droplet parcels.

Figure 3.55 shows that cases with 50'000, 100'000 and 1'000'000 injected parcels per jet all have comparative trends of cylinder averaged D_{32} diameter with time, thus the cylinder averaged D_{32} diameter is considered relatively insensitive at 50'000 parcels.

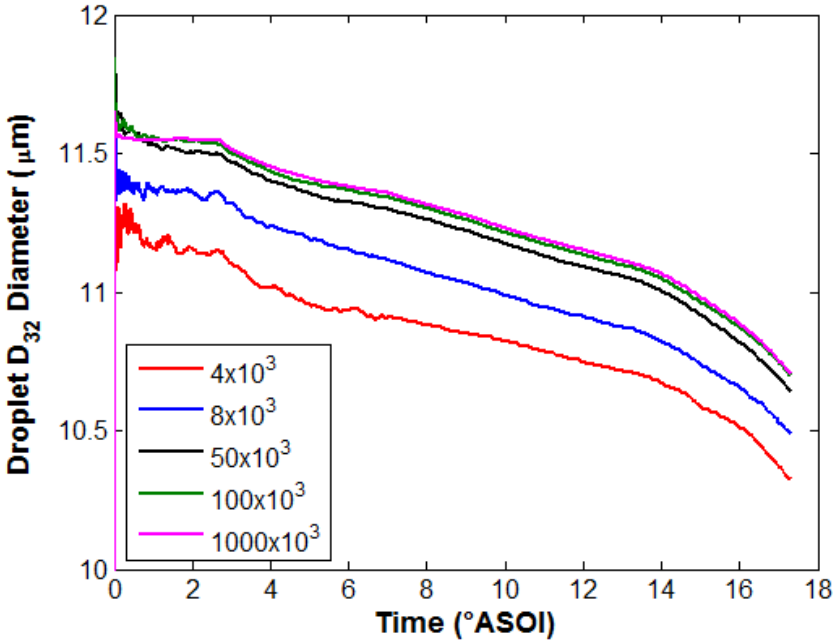

Figure 3.55 – Droplet D_{32} diameter as a function of time in °ASOI for the 6 cases in the number of injected parcels sensitivity study

Finally, the computational expense between each 6 cases was investigated by examining the variation in the average time taken for each timestep and CPU-hrs required to simulate between SOI and ASOI+20°. The result from this is shown in Figure 3.56 and summarised in Table 3.18, with a significant increase in the computational expense seen between case 4 (100'000) which has an average time per timestep of 12.5s, and case 5 (1'000'000) which has an average time per timestep of 316.5s. The difference between case 1 (4'000) and case 4 (100'000) is a very modest 6s.

Table 3.18 – A comparison of average time taken per timestep and CPU-hrs required for simulating between SOI and ASOI+20°

Case	Total number of parcels injected per jet/plume	Average time taken per timestep [s]	CPU-hrs for SOI to ASOI+20° [CPU-hr]
1	4'000	6.6	243
2	8'000	6.7	248
3	50'000	8.5	314
4	100'000	12.5	463
5	1'000'000	316.5	11693

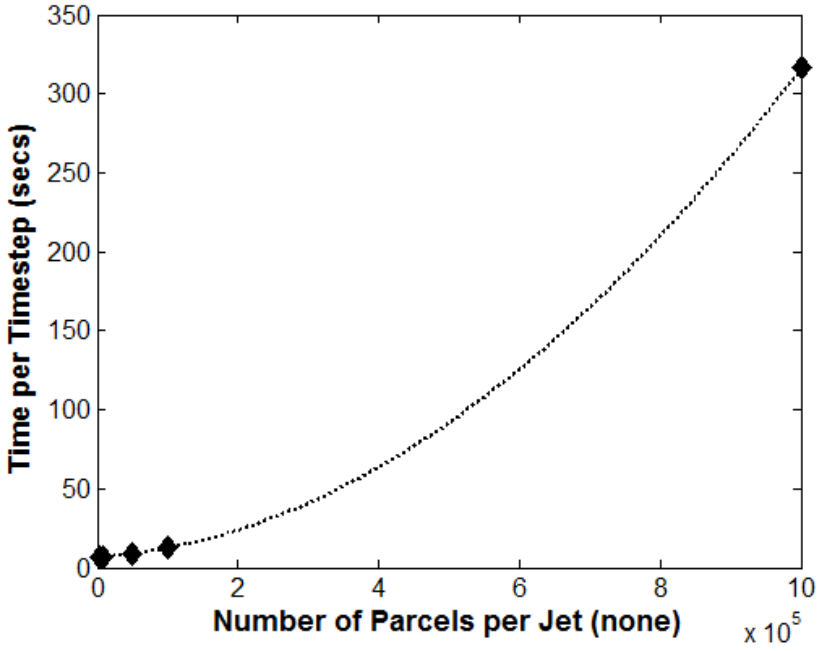

Figure 3.56 – A comparison of the time in seconds per timestep as a function of the number of injected parcels per jet

In conclusion, for this mesh size and physical sub-models, 50'000 parcels per jet was considered to provide a prediction that is mostly insensitive to the number of injected parcels for the following reasons:

- Penetration results showed little sensitivity above 50'000 injected parcels per jet.
- Average D_{32} drop diameter results showed little sensitivity above 50'000 injected parcels per jet.
- A computational expense of up to 12s/timestep during the injection process was acceptable with the computational resources available to this research.

Cell Clustering

An additional sub-model called 'Cell Clustering' is imposed within the droplet-droplet collision model of the CFD code where a pre-set number of 'levels' affects the ability of droplets to collide with droplets in adjacent cells. i.e. a 'cell clustering level' equal to zero means that droplets can only collide with other droplets within the same computational cell within a given timestep. A 'cell clustering level' equal to one means that droplets can collide

with other droplets within the same computational cell and droplets within adjacent computational cells within a given timestep. The theory being that it is possible that droplets could collide with droplets outside of a given cell within a given timestep, where this is particularly probable with large timesteps, small cell sizes and/or large droplet velocities.

Obviously, increasing the amount of cell clustering allows droplets to collide with a greater number of other droplets and in theory increases the ability of the collision model to represent the physical process. The disadvantage of this is the significant increase in computational expense required to compute the probability of a collision occurring.

To investigate this effect, cell clustering levels of zero, one and two were investigated with respect to the impact on plume tip penetration, D_{10} droplet diameter and computational expense. Negligible sensitivity was seen in the predictions of penetration and droplet diameter but significant increase in computational expense compared with zero clustering levels, with a 50% and 104% increase in CPU-hrs for one and two levels respectively. This result implies that the combined result of the timestep, cell size and droplet velocities sees only a very small number of droplet collisions outside of the same computational cell and thus no cell clustering is necessary in this example.

3.3.4.1.2 Initial and Boundary Conditions

The simulation was initialised at 80°ATDC using the results from a cold-flow single-phase simulation. Numerical wall temperatures were set based on the experimental conditions or approximated based on surrounding material and gas temperatures. The boundary conditions are summarised in Table 3.19.

A summary of the fuel injection model inputs is shown in Table 3.20 and items included within this table are discussed in more detail below.

Table 3.19 – Numerical boundary conditions for the fuel injection model specific predictions

Intake Plenum and Port Wall Temperatures	Adiabatic
Intake Valve Temperatures	323 K
Exhaust Valve Temperatures	363 K
Cylinder Head Temperature	363 K
Liner Temperature	293 K
Piston Temperature	301 K
Intake Gas Pressure	528 mbar
Intake Gas Temperature	301 K

Table 3.20 – Summary of the fuel injection model inputs

Droplet Distribution	Rosin-Rammler: $X = 14\times10^{-6}$ m, q = 2.3
Fuel Temperature	363 K
Number of Injected Parcels	50’000 parcels per jet
Droplet Initial Velocity	Shown in Figure 3.57
Injection Rate	Shown in Figure 3.57
Total Injected Fuel Mass	13.8 mg

A Rosin-Rammler distribution was used to provide an initial droplet size distribution for the injected parcels due to the required information to configure dedicated primary breakup sub-model not being available. The constant ‘q’ (the ‘shape’ parameter) was set to 2.3 based on the experimental works of Keller, Knorsch, Wensing, *et al.* (2015) which used a similar injector configuration and experimental conditions. The constant ‘X’ (the ‘scale’ parameter) was set to 14×10^{-6}m which provided the best match against experimental PDA droplet size data.

The steady-state injection mass flow rate was measured during a previous experimental study by Serras-Pereira, van Romunde, Aleiferis, *et al.* (2010) as 16.68g/s but the time varying mass flow rate profile for the injector was not available. To ensure a reasonable rate profile was supplied to the model, the opening and closing injection rate characteristics from a similar injector were combined with the known steady-state flow rate to create a realistic injection profile. The final profile is shown in Figure 3.57.

The droplet velocity at the injector nozzle was imposed via a time-dependent profile as shown in Figure 3.57, with an increase in initial droplet velocity used around the needle opening and closing to provide the best match against experimental plume tip velocity data – results shown below.

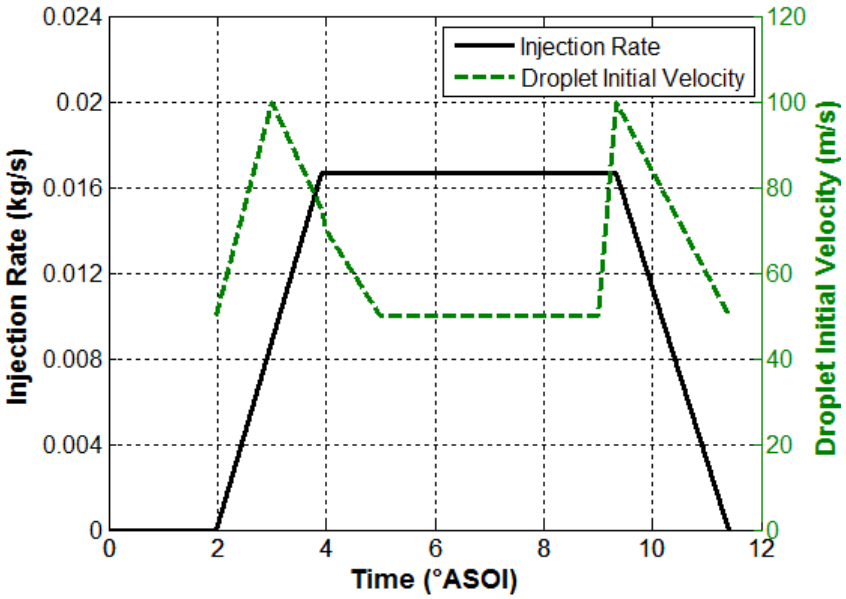

Figure 3.57 – Computational injection rate profile and initial droplet velocity

In this research both a single-component fuel and a multi-component fuel are modelled. The fuel component and respective initial mass fraction is defined in Table 3.21. The individual components of the multi-component fuel were chosen based on being a reasonable representation of the light, medium and heavy components of gasoline. The multi-component fuel is modelled as a miscible mixture where the evaporation of each component is dependent on the concentration and vapour pressure of the other components in the mixture. Since the

components modelled in this research have a similar molecular structure (i.e. are all Alkanes), the application of Raoult's law to obtain the vapour mole fraction at the droplet/liquid surface was deemed an acceptable approximation. A comparison of the vapour pressures for each fuel component and the multi-component fuel (calculated by the sum of the partial pressures for each component) against a typical gasoline fuel (Aleiferis & Van Romunde, 2013) is provided in Figure 3.58. All fuel properties required by the CFD code are extracted from NIST tables for the respective component but a sample of key fuel properties are shown in Table 3.22.

Table 3.21 – Mass fraction and boiling point of fuel components used within the single- and multi-component surrogate fuels used in this research

Single-Component Surrogate Fuel			Multi-Component Surrogate Fuel		
Component Fuel	Mass fraction	Boiling Point, T_b (K)	Component Fuel	Mass fraction	Boiling Point, T_b (K)
Iso-Octane	1	372.2	Iso-Pentane	0.33	301.1
			Iso-Octane	0.34	372.2
			n-Decane	0.33	447.2

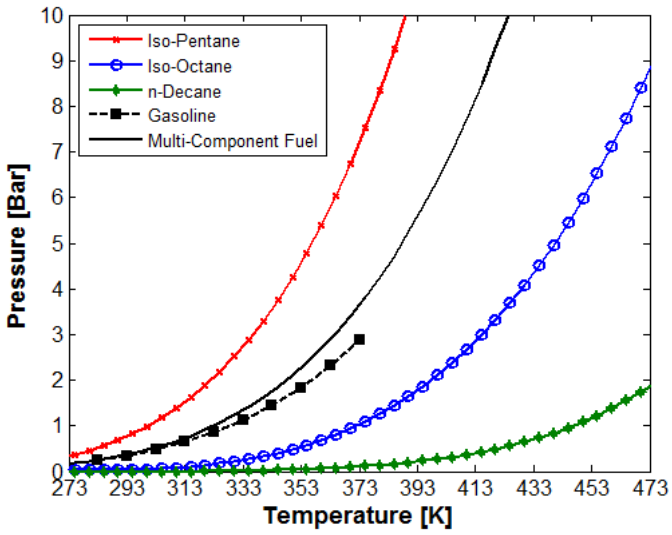

Figure 3.58 – Comparison of fuel vapour pressures, including the multi-component fuel against a typical gasoline fuel (Aleiferis & van Romunde, 2013)

Table 3.22 – Summary of properties for fuels used within this research

Fuel Property	Iso-Pentane	Iso-Octane	n-Decane	Gasoline
Density (20°C) [kg/m3]	616	691.9	730	719
Dynamic Viscosity (20°C) [g/m-s]	0.233	0.5	0.92	0.3-0.8
Surface Tension (20°C) [mN/m]	16.05	18.77	23.83	25.8
Boiling Point [K]	301.1	372.2	447.2	303-463
Critical Temperature [K]	460.4	543.9	617.7	544-562
Critical Pressure [Bar]	33.76	23.88	21.03	25.7-32.6
Enthalpy of Vaporisation [kJ/mol]	25.0	35.1	47.4	35.4-37.3

3.3.4.1.3 Model Validation

Experimental results to validate the fuel injection model were available in the form of plume tip penetration, plume tip velocity and D_{10} droplet diameter.

Plume tip penetration was extracted from Aleiferis & van Romunde (2013) and compared against the predicted plume tip penetration for iso-octane (single-component fuel) as shown in Figure 3.59, showing good agreement between experimental results and numerical predictions. Also of note is that when fuel is injected into a non-quiescent chamber, like that of an ICE, the spray will break up faster due to spray-flow interactions which will act to reduce plume tip penetration. Thus the slightly lower plume tip penetration predicted by the engine model when compared against the experimental bomb result, is very much in line with expectations of the actual process.

Spray plume tip velocity was calculated from the derivative of the plume tip penetration data presented previously and is shown in Figure 3.60. Numerical predictions show good agreement with experimental plume tip velocity and well capture the steep rise in plume tip velocity soon after the start of injection. As a consequence, this provides excellent agreement between experimental and numerical results for tip penetration during the early stages of injection.

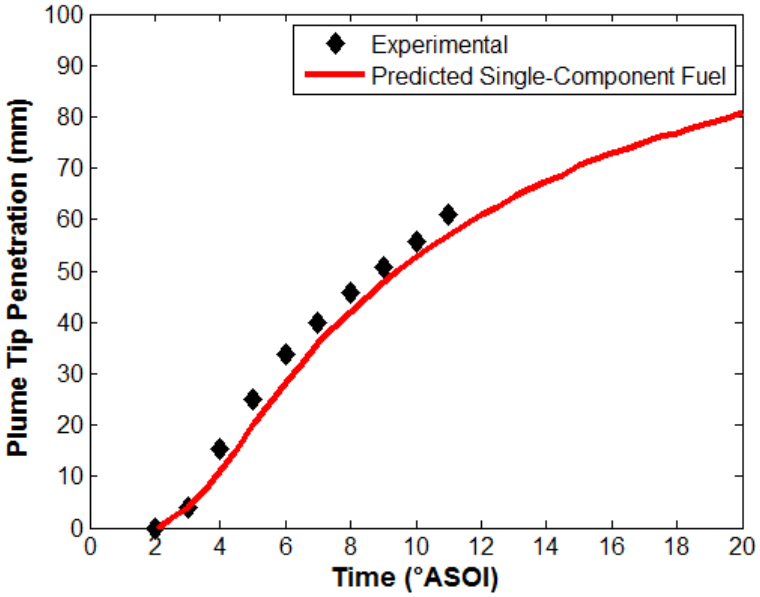

Figure 3.59 – A comparison of experimental and predicted plume tip penetration (Plume 1/6) for iso-octane with a RANS turbulence model

Experimental PDA data was extracted from Aleiferis & van Romunde (2013) where the D_{10} droplet diameter was measured in a quiescent chamber for plume 2 at z=-25mm from the injector nozzle tip across a range of temperature and pressure conditions and compared against the numerical results and is shown in Figure 3.61. Unfortunately, experimental results were not available at the standardised condition of T_f=363K and 0.5bar gas pressure but the results suggest that the droplet diameter is within the expected range and the change in droplet diameter over time closely matches the experimental results providing increased confidence in the capability of the droplet breakup model to satisfactorily predict the secondary breakup processes.

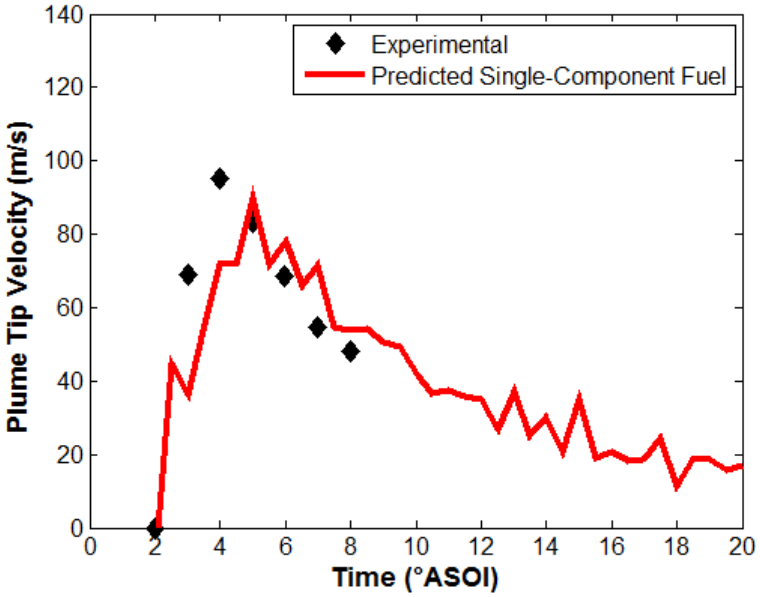

Figure 3.60 – A comparison of experimental and predicted plume tip velocity (Plume 1/6) for iso-octane

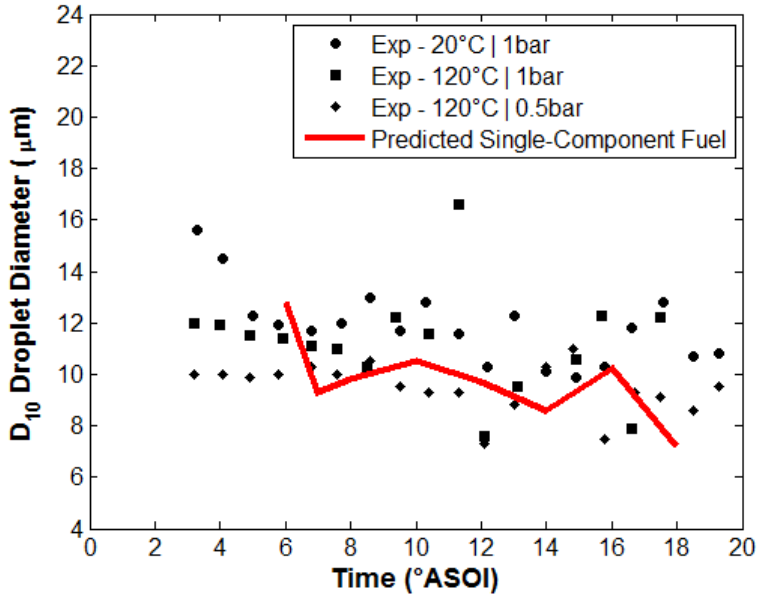

Figure 3.61 – A comparison of experimental and predicted D_{10} droplet diameter at z=-25mm from the injector tip for iso-octane

Of note are two caveats related to the comparison of these numerical predictions to the experimental results.

The first caveat exists in the differences between the experimental and numerical results with respect to the number of droplets and area over which the D_{10} droplet diameter is calculated.

The PDA measurement system is focused on a very small area in the centre of the spray plume with the elliptical volume having a long axis of approximately 2.7mm. Due to the exact location of the PDA laser interference volume within the spray not being known, it was not possible to validate the numerical predictions against the same area and location as the experimental results. This implies that the numerical results would include a significant number of smaller droplets at the periphery of the spray (lowering the D_{10} droplet diameter), that would not have been captured in the experimental PDA data. It was not possible to isolate plume 2 within the numerical results and perform a more comparative positional comparison to experimental data due to plume 2 being strongly distorted in the x-y (swirl) plane by the intake valve jet in the numerical engine model which is not present in the experimental data from the quiescent chamber.

The second caveat arises due to each plume pair having a different y-z axis injected plume angle. The average droplet diameter is seen to vary along the length of the plume, with the plume tip consisting of larger droplets with higher momentum and the tail of the spray plume consisting of smaller droplets with lower momentum. As mentioned previously, the D_{10} droplet diameter for the numerical results is calculated across all droplets at a fixed z-axis position, but due to the plume pairs having different plume angles, the averaging plane will intersect each plume pair at a different axial position, thus contributing to another source of variation of numerical D_{10} droplet diameter.

In spite of these caveats, the differences are not expected to be significant enough to indicate a false conclusion and are still likely within the variation and measurement uncertainty of experimental results.

As a means of validating the numerical predictions for spatial mixture variation, fuel-air equivalence ratio contours when using the single-component fuel at 60°BTDC (Figure 3.62) was compared against QPLIF results from Williams, Ewart, Wang, *et al*. (2010) (Figure 3.63).

Williams, Ewart, Wang, *et al.* (2010) used three different tracers to match the evaporation characteristics and hence track the light, medium and heavy components of a typical gasoline fuel:

- Acetone: designed to match the evaporation characteristics of the light fractions of gasoline, predominantly butanes and iso-pentanes fractions

- Toluene: designed to match the evaporation characteristics of the medium fractions of gasoline, predominantly iso-octane and n-octane fractions
- 1,2,4 Tri-methyl benzene (TMB): designed to match the evaporation characteristics of the heavy fractions of gasoline, predominantly iso-dodecane and n-decane fractions

As can be seen from Figure 3.63, some stratification is seen with a slightly richer mixture towards the exhaust side of the combustion chamber when using a toluene tracer and richer fuel-air mixture up either side of the combustion chamber when using the TMB tracer but neither of the tracers show a rich fuel-air mixture propagating up the intake side of the combustion chamber as seen in the numerical predictions, perhaps suggesting that the clockwise rotating vortex seen in the velocity field in the numerical predictions is more pronounced than seen in experiments.

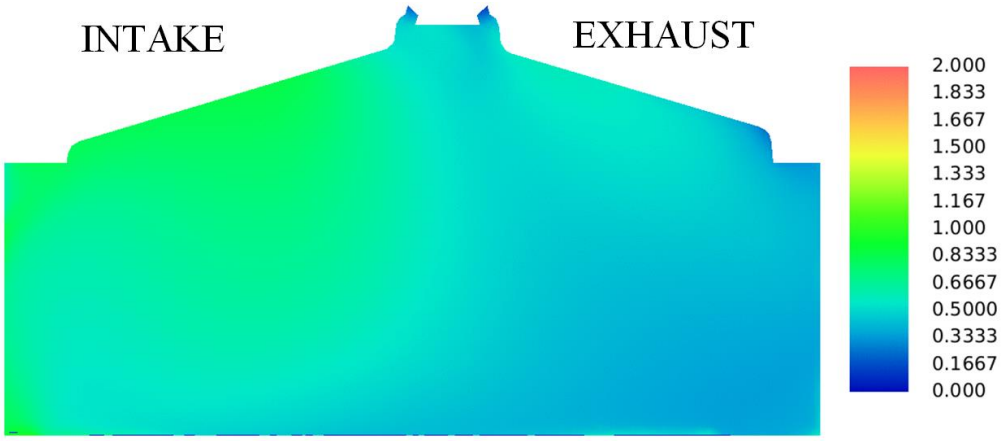

Figure 3.62 – Contours of fuel-air equivalence ratio for the single-component fuel surrogate and RANS turbulence modelling approach, along the bore centreline at 60°BTDC

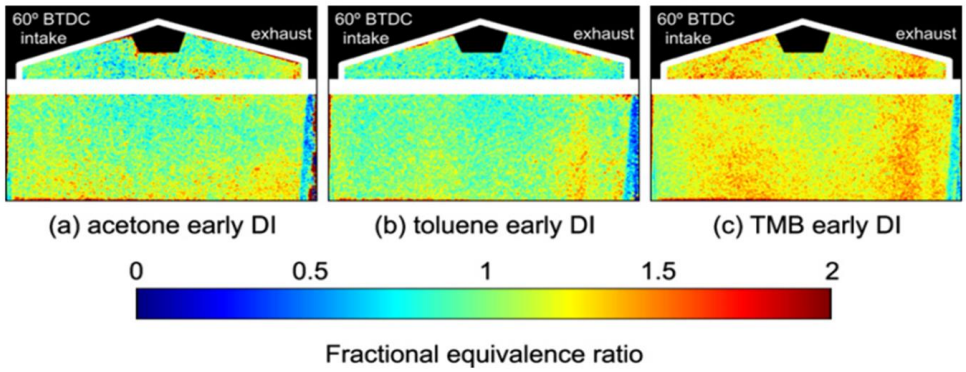

Figure 3.63 – Fractional equivalence ratio distribution along the bore centreline at 60°BTDC for three different tracers, QPLIF results taken from Williams, Ewart, Wang, *et al.* (2010)

To test this theory, experimental PIV data in both the tumble plane and swirl plane was compared to the predicted velocity field from the numerical model to see if any differences in flow structures were predicted that could help explain the differences in mixture field stratification between model and experiments.

When comparing the velocity fields in the tumble plane, the experimental results (Figure 3.64(a)) suggest a slightly more uniform upward flow field than seen in the numerical predictions (Figure 3.64(b)) but still a propensity to have higher flow velocities on the intake side of the combustion chamber as seen in the numerical predictions, due to large scale tumble motion. Also of note is the difference in gas velocities near the piston crown. A simple calculation of the instantaneous piston speed S_p at this crank angle can be completed using equation (3.10) and thus yielding an instantaneous piston speed of approximately 7.1m/s at this engine condition. It is expected that the gas velocity near the piston will be approximately equivalent to the instantaneous piston speed thus the experimental results are perhaps showing gas velocities slightly below reality and the numerical results showing gas velocities slightly higher than reality (expected to be due to the effect of the rising piston on the gas combining with the upward momentum generated due to the flow field rebounding off the piston crown).

$$S_p = \bar{S}_p \left\{ \frac{\pi}{2} \sin\theta \left[1 + \frac{\cos\theta}{(R^2 - \sin^2\theta)^{1/2}} \right] \right\} \tag{3.10}$$

Where $\bar{S}_p$ is the mean piston speed, θ is the crank angle and R is the ratio of connecting rod length to crank radius.

Inspection of the swirl plane velocity fields indicates some differences between experimental and predicted flow fields. The experimental results (Figure 3.65(a)) show two dominant flow structures moving from the intake side of the combustion chamber, generated as a consequence of the two intake valve jets that have tumbled down the exhaust side of the combustion chamber, reflected off the piston crown and the recirculated back up the intake side and across the top of the combustion chamber. The symmetrical flow features lending to increased homogeneity of the fuel-air mixture in the x-y plane. The numerical results (Figure 3.65(b)) show slow moving flow progressing from the intake to the exhaust side of the combustion chamber but being initiated by strong flow structures around the periphery of the combustion chamber, colliding on the intake side of the combustion chamber. The limited

field of view in the experimental results does not allow one to say for sure if similar rotating flow structures exist in reality but this could contribute to some of the observed differences in mixture stratification between experimental and numerical results observed above.

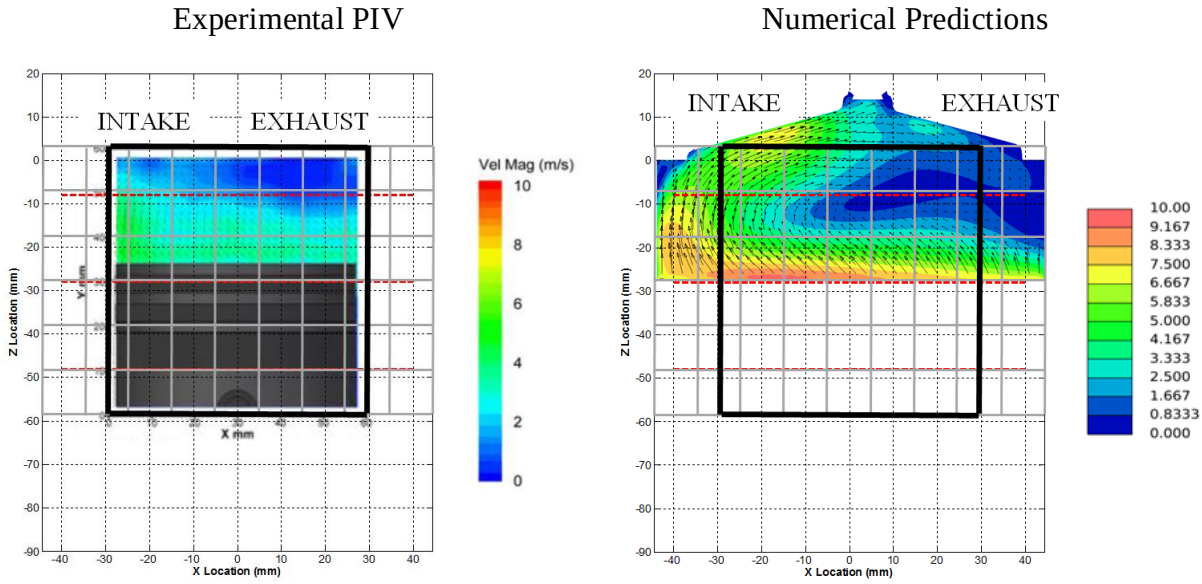

Figure 3.64 – (a) Experimental PIV (Justham, 2010) and (b) numerical velocity magnitude contours and vectors, in the tumble plane along the bore centreline at 60°BTDC

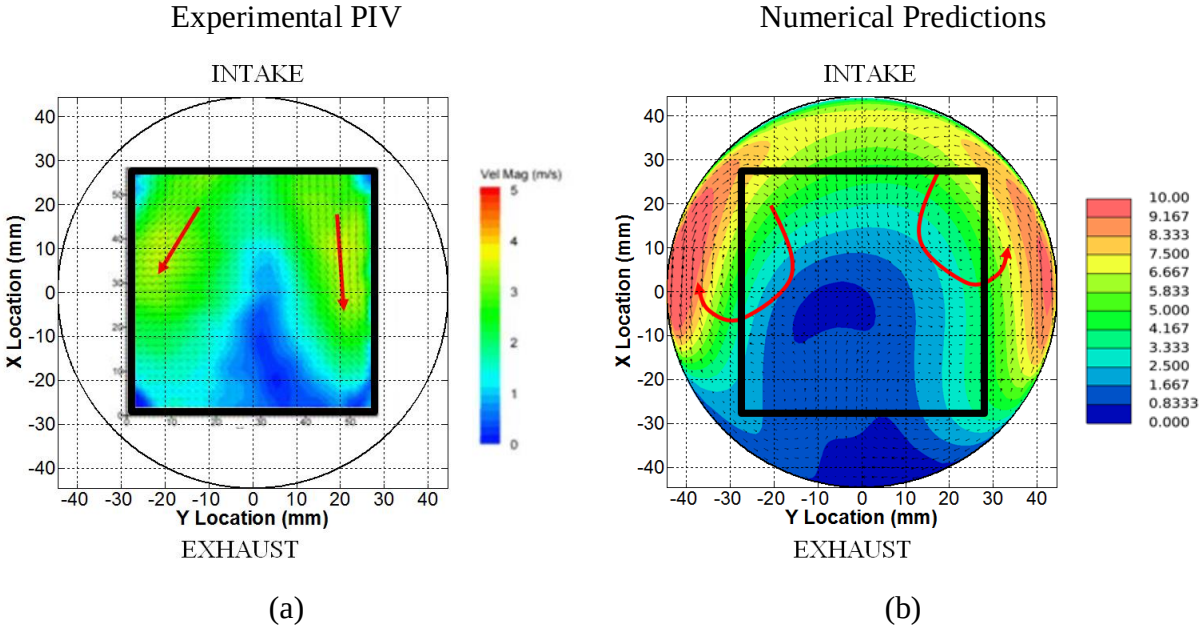

Figure 3.65 – (a) Experimental PIV (Justham, 2010) and (b) numerical velocity magnitude contours and vectors, in the swirl plane 10mm below peak height of the piston (~12mm below the head gasket plane) at 60°BTDC

Another consideration for the differences between experimental and numerical flow structures could also be attributed to the capability of a RANS turbulence modelling approach to accurately model the effects of turbulence within the flow field through both the intake and compression strokes.

3.3.4.2 LES Approach

The fuel injection sub-models used during the LES approach are the same as shown above in Table 3.10, with the exception of the turbulence dispersion sub-model which differs as shown in Table 3.23, thus meaning that the droplet relative velocity is now a function of the filtered-velocity and the modelled turbulent fluctuations. No model is included for energy exchange from the discrete-phase to the continuous phase, as discussed in earlier in section 2.4.8.

Table 3.23 – LES specific sub-models used in fuel injection sub-models

Turbulence Dispersion	Gaussian pdf (Gosman & Ioannides, 1983) where mean velocity is the sum of the local filtered-velocity velocity from the momentum equation and SGS velocity from SGS model, and *k* is calculated from the SGS velocity

3.3.4.2.1 Initial and Boundary Conditions and Model Configuration

The turbulence model and all associated boundary and initial conditions are the same as described previously in section 3.3.3.2.

Similarly to the single-phase LES model described in section 3.3.3.2, the model was first initialised by running a RANS cycle and a subsequent LES cycle that was discarded, before running a further 15 cycles. Again, each subsequent LES cycle was initiated from the final conditions of the previously computed cycle so that any variability in the initial conditions is retained and used to initiate cyclic variability in the following cycle.

The spray model, all associated sub-models (with exception of the differences noted above) and all boundary and initial conditions are the same as described previously in section 3.3.4.1 with the exception that only a single-component surrogate fuel was modelled with the LES turbulence model due to computational limitations.

3.3.4.2.2 Model Validation

First, Figure 3.66 shows the plume tip penetration compared against experimental results. Upon first inspection the LES plume tip penetration is clearly lower than both the RANS predictions and experimental results. The expectation would be for the droplet penetration to be greater due to the model not including a contribution of kinetic energy from the disperse phase to the SGS turbulence kinetic energy of the continuous phase as seen from the work on Banerjee, Liang, Rutland, *et al.* (2010). The likely cause of this is due to a difference in turbulence conditions. Banerjee et al. modelled a case in a quiescent chamber where the only turbulence generated was as a consequence of the dispersed-phase imparting energy on the continuous-phase. In the case simulated here, the fuel was injected into a highly turbulent combustion chamber, with a large range of length and velocity scales, hence the energy imparted from the continuous-phase on the dispersed phase is much more significant. Hence it would be expected that plume tip penetration could be either increased or reduced depending on the local flow conditions and flow-spray momentum exchange.

The increase in standard deviation with increasing penetration is also evident; as the spray momentum reduces with time due to drag and momentum exchange, it becomes more and more influenced by variations in the flow field.

The LES results were only ensemble-averaged up to 16°ASOI since beyond this time some cycles had already impinged on the piston crown and/or the plume tip had become so distorted by the in-cylinder flow field that the uncertainty of deducing the plume tip became excessively large. Encouragingly, the LES predictions still well capture the change in penetration profile during the early part of the injection process.

Whilst the LES predictions do not match the experimental predictions quite as accurately as seen in the RANS predictions, they are still believed to be representative and behaving in a

physically correct nature, and hence are sufficient to be used for further investigations into CCV and other fuel injection processes.

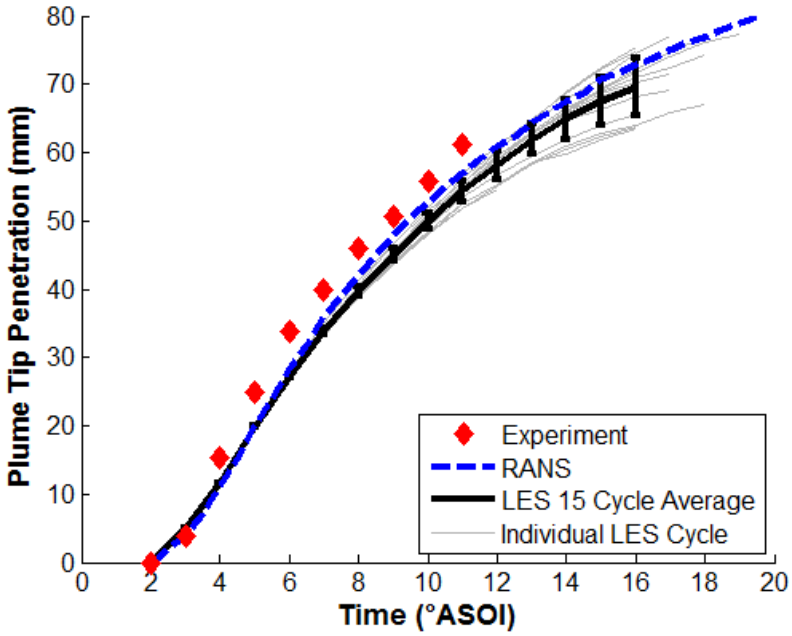

Figure 3.66 – A comparison of experimental and LES predicted plume tip penetration (Plume 1/6) for iso-octane, showing LES ensemble-average with error bars for cycle standard deviation, individual LES cycles and RANS predictions

It was also possible to plot the variation in plume tip position in the X-Z plane for both the RANS and LES cases as shown in Figure 3.67. The effect of flow field inhomogeneities on the injected droplets is apparent, with plumes 2 and 3 showing higher levels of CCV when compared with plumes 4 and 5 due to the CCV of the flow field.

Similarly to completed in section 4.3.1.3 the predicted plume tip velocity was calculated and compared against experimental results and is shown in Figure 3.68. Largely the LES predictions well match the RANS predictions and experimental results, again with an increase in CCV later during the cycle due to increased interaction with the in-cylinder flow field.

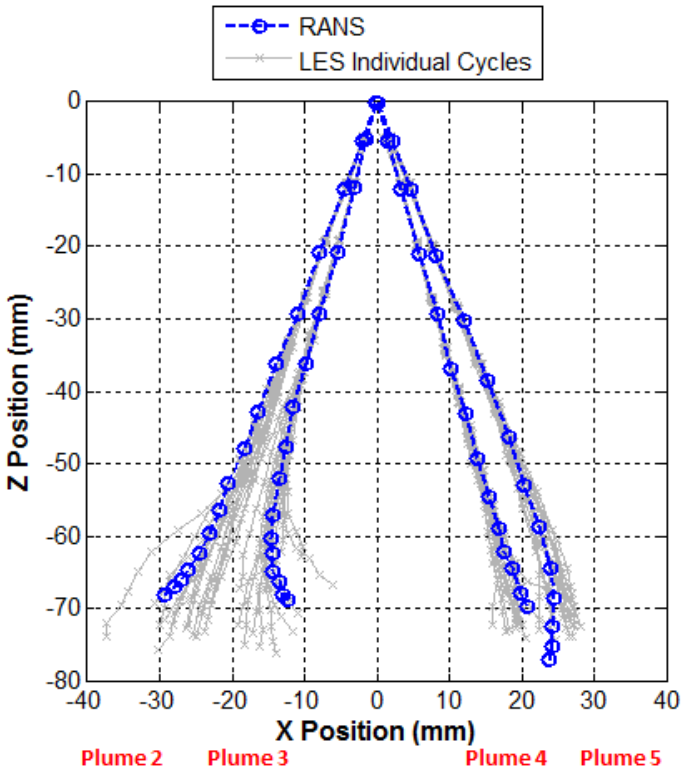

Figure 3.67 – Plume tip position as a function of z-axis and x-axis position from the injector tip for RANS and individual LES cycles, with each marker representing 2°c.a.

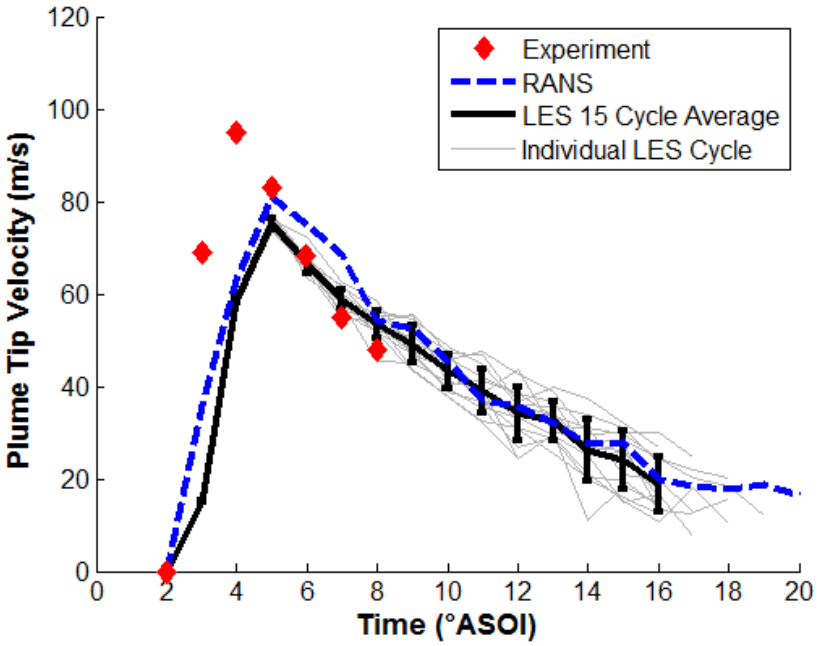

Figure 3.68 – A comparison of experimental and LES predicted plume tip velocity (Plume 1/6) for iso-octane, showing LES ensemble-average with error bars for cycle standard deviation, individual LES cycles and RANS predictions

The variation in droplet diameter as a function of time was also compared to the experimental PDA data as presented previously in section 3.3.4.1.3 and is shown in Figure 3.69. As seen previously with the RANS turbulence model, the predictions using the LES turbulence model fall within the range of experimental data available and hence it is believed the model is well predicting the change in droplet diameter due to breakup and atomisation processes.

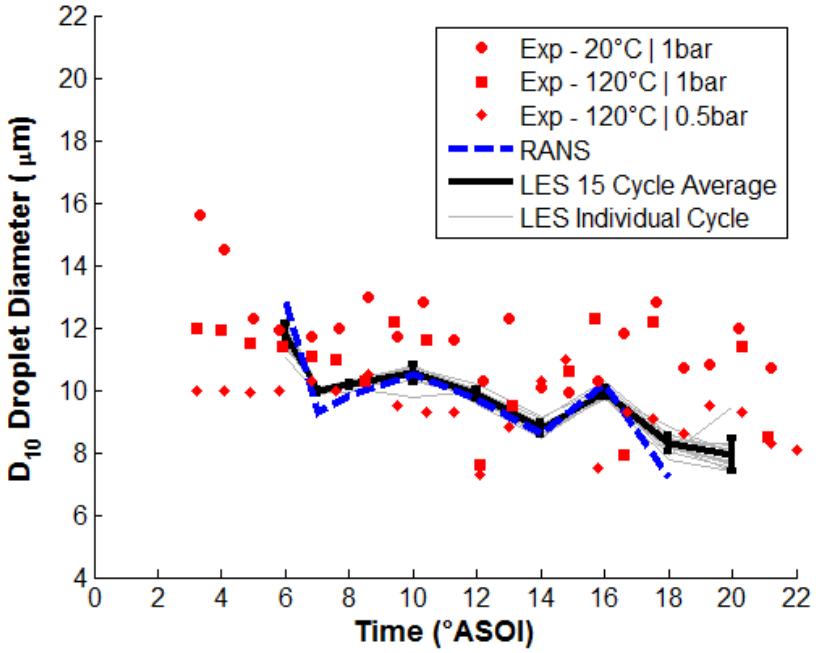

Figure 3.69 – A Comparison of experimental and LES predicted D_{10} droplet diameter at z=-25mm from the injector tip for iso-octane, showing LES ensemble-average with error bars for cycle standard deviation, individual LES cycles and RANS predictions

It is also interesting to investigate how the temporal variation in droplet diameter, with respect to cycle-to-cycle variations and crank angle-to-crank angle variations, vary with the turbulence modelling technique used. It was also decided to investigate the variation in droplet diameter at z=-50mm to investigate if the higher levels of CCV are present when further from the injector tip, the result of which is shown in Figure 3.70. Unfortunately experimental data on the cyclic variation of the droplet diameter was not available.

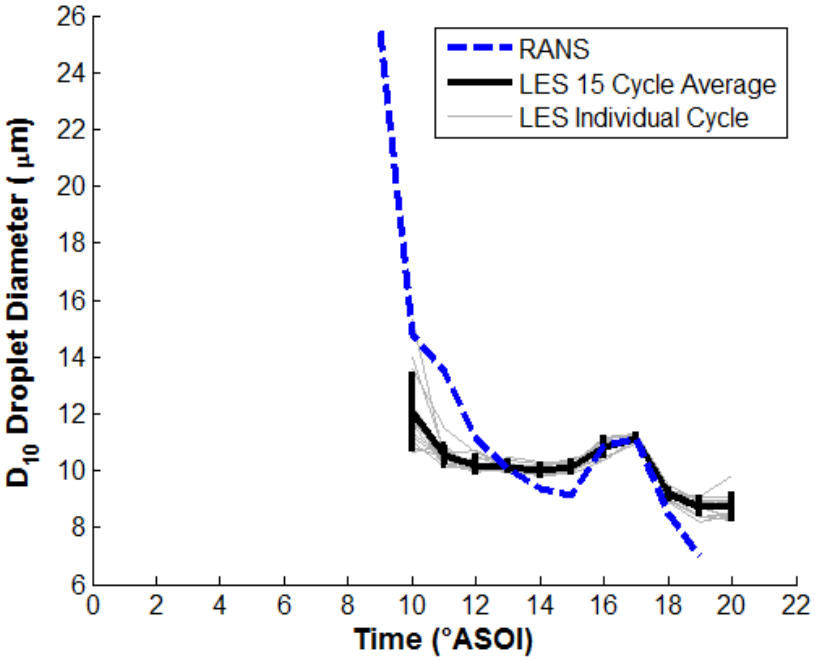

Figure 3.70 – A Comparison of LES and RANS predicted D_{10} droplet diameter at z=-50mm from the injector tip for iso-octane, including the LES ensemble-average with error bars for cycle standard deviation

First, examining the variation in D_{10} diameter through the crank angle range presented here (SOI to SOI+20°), shown in Figure 3.71 and Figure 3.72. The 'D_{10} standard deviation' is calculated as follows:

First, the arithmetic mean droplet diameter $\overline{D_c}$ is calculated for a given cycle:

$$D_{10,c} = \overline{D_c}(\theta, z) = \frac{1}{x}\sum_{i=1}^{x} D_i(\theta, z, c) \tag{3.11}$$

Where D is the droplet diameter, x is the total number of droplets, i individual droplets, at a θ crank angle, z cutting plane and cycle c.

Then obtain the ensemble-average arithmetic mean droplet diameter $\overline{D}$:

$$D_{10} = \overline{D}(\theta, z) = \frac{1}{n}\sum_{c=1}^{n} \overline{D_c}(\theta, z) \tag{3.12}$$

Where *n* is the total number of cycles.

Then the standard deviation of the cycle average droplet diameter *S* is defined below as the square root of the variance:

$$S(\theta,z) = \sqrt{\frac{1}{n}\sum_{c=1}^{n}[\overline{D_c}(\theta,z) - \overline{D}(\theta,z)]^2} \tag{3.13}$$

The CCV is seen to be small with the exception of 10°ASOI at z=-50mm (Figure 3.72). This is due to the plume tip just reaching the cutting plane at this crank angle. Thus there is a combined effect of significant droplet size stratification present in the plume head with variations in plume tip penetration and the positioning of the cutting plane through the plume head, causes a large variation in the mean droplet diameter.

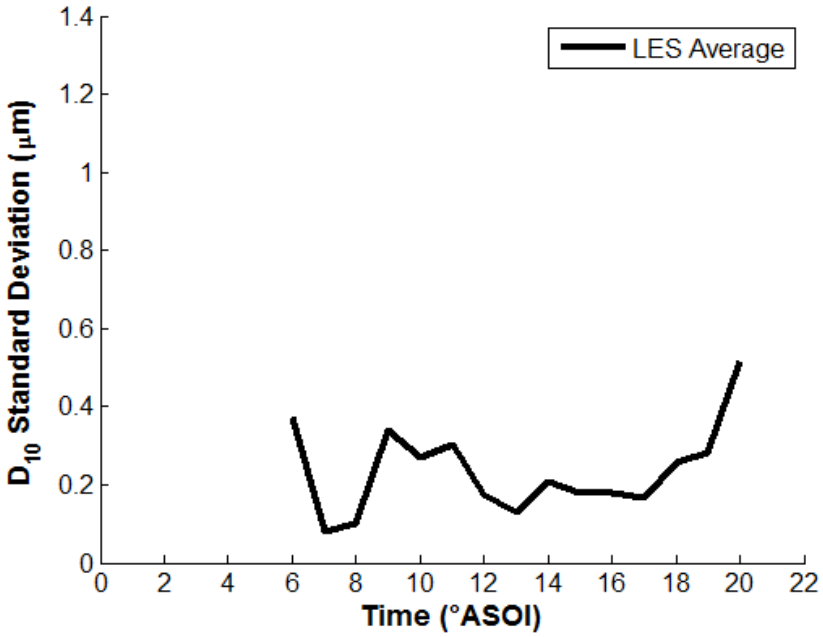

Figure 3.71 – Standard deviation of the droplet D_{10} diameter at z=-25mm across all LES cycles

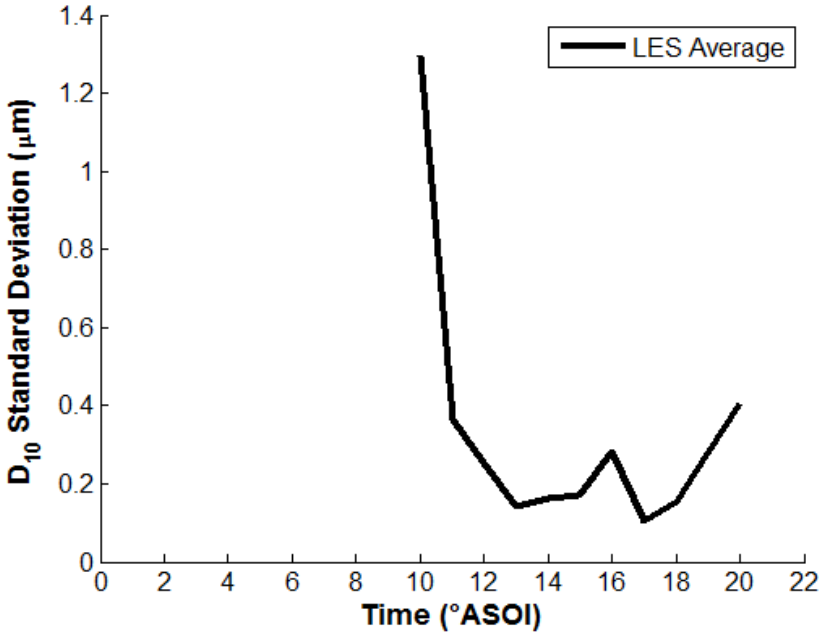

Figure 3.72 – Standard deviation of the droplet D_{10} diameter at z=-50mm across all LES cycles

Next, the variation in droplet diameter, for all droplets, rather than the variation in D_{10} diameter as shown above, on a cycle-by-cycle basis was investigated. The 'droplet diameter standard deviation' is defined as follows:

Here the standard deviation is not of the mean droplet diameter but the standard deviation of all droplets at the defined z-cutting plane and crank angle:

$$D_{10,c} = \overline{D_c}(\theta, z) = \frac{1}{x}\sum_{i=1}^{x} D_i(\theta, z, c) \tag{3.14}$$

Then calculate the standard deviation based on the cycle mean S_c:

$$S_c(\theta, z, c) = \sqrt{\frac{1}{x}\sum_{c=1}^{x}[D_n(\theta, z, c) - \overline{D_c}(\theta, z)]^2} \tag{3.15}$$

Where D is the droplet diameter, x is the total number of droplets, n individual droplets, at a θ crank angle, z cutting plane and cycle c.

The average of the standard deviation based on the cycle mean $\bar{S}$ is calculated via:

$$\bar{S}(\theta, z) =) = \frac{1}{n}\sum_{c=1}^{n} S_c(\theta, z, c) \tag{3.16}$$

When comparing the RANS and LES predictions (Figure 3.73 and Figure 3.74), it is seen that when using the RANS turbulence model a comparatively greater variation in droplet diameter is seen than when compared to the LES predictions – this is in spite of the droplet D_{10} diameter predictions being very similar between the RANS and LES predictions (Figure 3.69 and Figure 3.70), implying that the RANS turbulence model generates a greater spread of droplet diameters. It is also possible to deduce that not only is the LES cycle mean droplet diameter standard deviation lower (solid black series), but it is consistently lower on a cycle-by-cycle basis (grey series), hence it is reasonable to assume that this difference is driven by the inherent differences between a RANS time-filtered approach where flow anisotropic effects are not modelled and a LES space-filtered approach directly resolving a large proportion of the scales of turbulence.

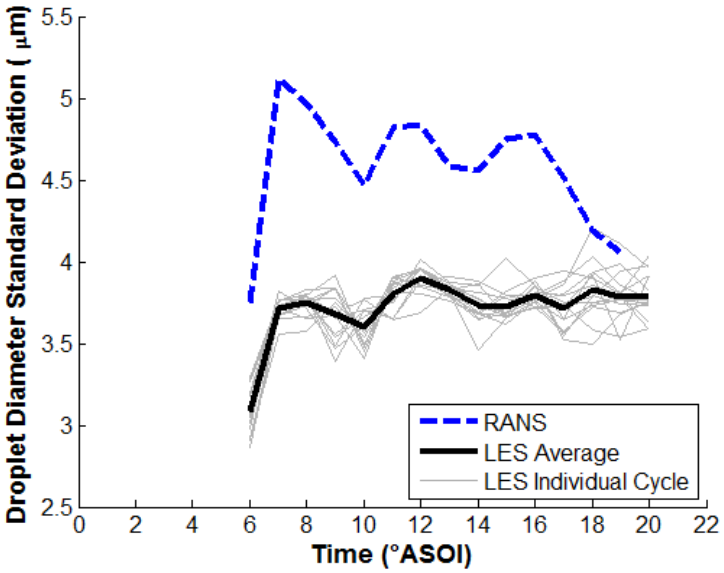

Figure 3.73 – Standard deviation of the diameter of all droplets at z=-25mm for each LES cycle, the LES mean and RANS

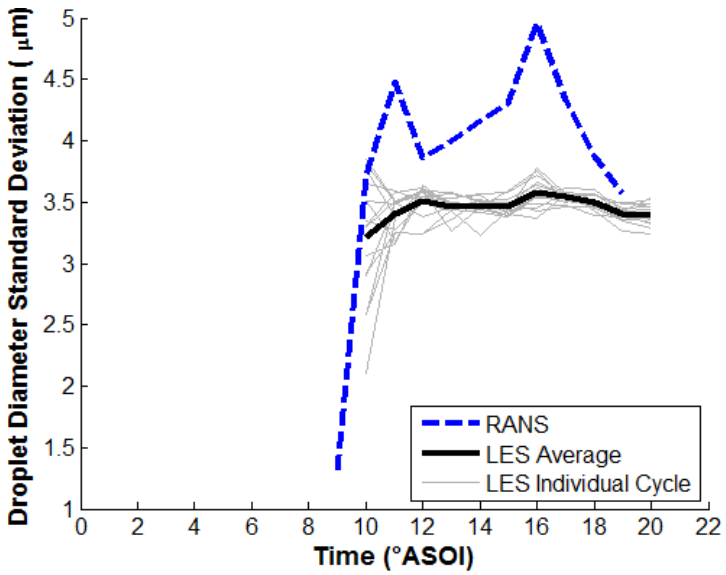

Figure 3.74 – Standard deviation of the diameter of all droplets at z=-50mm for each LES cycle, the LES mean and RANS

In the LES SGS model used in this research, whilst the droplet instantaneous velocity and turbulent dispersion are affected by the instantaneous velocity field (which is a function of both the resolved and model velocity field), the lack of a sink/source term in the SGS model to account for momentum transfer-to-from the dispersed-phase and the SGS velocity field will mean that droplets retain a higher amount of energy than is expected to be realistic which will influence droplet breakup and evaporation rates, and hence the variation in droplet diameter. Without further work to evaluate the impact of droplet energy dissipation on the SGS TKE, and the subsequent variation in droplet diameter, and additional experimental data for validation, it is unclear whether the variation in droplet diameter predicted by either the LES or RANS predictions are reasonable.

Finally, the fuel-air equivalence ratio was evaluated along the bore centreline at 60°BTDC, shown in Figure 3.75 for comparison against previously presented experimental results and RANS predictions. When compared to the RANS predictions (Figure 3.62) and experimental results (Figure 3.63), a significant reduction in the amount of stratification is seen. The degree of stratification on the intake side of the combustion chamber has reduced, and a greater quantity of fuel is present on the exhaust side which is not seen in the RANS predictions but is present in the toluene and TMB fractions of the experimental QPLIF results. Whilst it is not possible to quantitatively compare the numerical predictions to the experimental QPLIF results, the fuel-air equivalence ratio predictions with the LES SGS model show a qualitative improvement in the spatial distribution of fuel-air mixture.

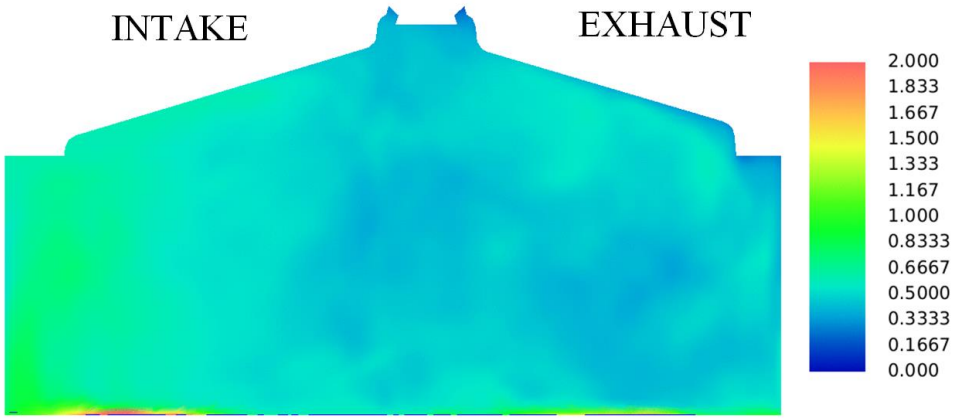

Figure 3.75 – Contours of ensemble-average fuel-air equivalence ratio with the LES turbulence modelling approach, along the bore centreline at 60°BTDC

3.4 CONCLUDING REMARKS

This chapter started by presenting the experimental test case that is the subject of the numerical modelling for this research. This has included details of the GDI single cylinder optical research engine configuration, the operating condition, valve events and the fuel injection system and strategy used by this engine.

Next this chapter presented the numerical models used within this research. The computational domain and methodology used was presented first. The rest of the chapter was largely split into two sections:

1. The description and validation of the model used to investigate the in-cylinder flow field using single-phase flow simulations;
2. The description and validation of the model used to investigate the fuel injection process of two-phase flow simulations using a Lagrangian DDM.

Within each of these two sections, they were further sub-divided into sections presenting the model using either the RANS or LES turbulence modelling approaches.

Conclusions from the sensitivity studies and model validation when using the RANS RNG k-ε turbulence model to model the in-cylinder flow field:

- Six different mesh sizes were investigated, ranging from 1.25m cells upto 2.6m cells and results from both cylinder averaged quantities and contours of turbulence kinetic

energy indicated that the solution was mostly independent of the mesh size with a mesh of 2.15million cells or a cell size of approximately 0.7-0.8mm^3 in the cylinder interior.

- An initialisation sensitivity study showed that a minimum of one cycle must be used to initialise a solution to ensure that intake system wave dynamics, and their effect on the resultant in-cylinder flow field, are adequately modelled.
- Model validation results showed that: the in-cylinder pressure history well matched the experimental results; intake system velocity and flow momentum were well matched to experiments; differences in the intake valve jet were seen with respect to the timing of jet detachment from the cylinder head acting to reduce the effective area and consequently caused valve jet velocities to be over predicted; comparison to experimental in-cylinder PIV velocity magnitude contours showed general flow structures to be well predicted but with some discrepancies in the location of certain recirculation regions.

Conclusions from the mesh suitability study and model validation when using the LES Smagorinsky SGS model run over 29 engine cycles to model the in-cylinder flow field:

- The mesh suitability was evaluated by the use of the turbulence resolution parameter which showed the mesh to generally allow over 80% of the turbulence kinetic energy to be resolved, with the exception of certain areas around the high shear regions of the intake valve jet where upward of 60% was resolved.
- When compared to experimental results: the in-cylinder pressure history was again well matched; velocity magnitude contours and ensemble-average velocity line charts at a number of cutting planes and crank angles were presented, and similarly to the RANS predictions, show the model to well represent the complex flow structures but mis-predict the location of certain recirculation regions; the LES results were also seen to generally provide better agreement than the RANS predictions.

Conclusions from the dependency studies and model validation when using the DDM model with a single-component surrogate of iso-octane to model the fuel injection process, with the RANS RNG k-ε turbulence model:

- A mesh size sensitivity study was completed using three different meshes ranging from 1.7m cells to 3.6m cells with respect to predictions of plume tip penetration, fuel

mass fraction and droplet diameter distribution profiles. The results showed that with respect to the parameters investigated here, the solution was largely insensitive to the mesh size by 2.2m cells.

- The effect of secondary breakup model on droplet D_{10} diameter was investigated at three separate z-plane positions and showed the predictions to be largely insensitive to the chosen breakup model, expected to be due to the use of a prescribed droplet diameter distribution as part of the model boundary conditions.
- The sensitivity of the prediction of plume tip penetration, cylinder averaged droplet diameter and computational expense due to the number of injected parcels was investigated and showed the predictions to be largely insensitive to the number of injected parcels per jet by 50'000 parcels, with an acceptable computational expense.
- The model was validated against plume tip penetration, plume tip velocity and droplet diameter and was seen to well match the experimental results. The predicted fuel-air equivalence ratio was also compared to experimental QPLIF results and showed additional stratification in the model predictions that does not appear present in the experimental results. Inspection of PIV data for flow field velocity magnitude suggested potential differences in flow feature symmetry between experimental and RANS predictions could be the cause of the additional mixture stratification in the RANS predictions but this will be a subject for further investigation in the following chapter.

Conclusions from the validation of the DDM model with a single-component surrogate of iso-octane to model the fuel injection process, when using the LES Smagorinsky SGS turbulence model run over 15 engine cycles:

- The model was validated against plume tip penetration, plume tip velocity and droplet diameter and similarly to the RANS predictions, was seen to well match the experimental results. Additional analysis was presented, investigating the variation in droplet diameter and comparisons against RANS predictions with a reduction in spatial variation of droplet diameter noted between predictions using the LES model when compared to the RANS model. The contours of the ensemble-average fuel-air equivalence ratio showed increased homogeneity and a qualitative improvement in the predicted spatial equivalence ratio variation when compared against experimental results.

CHAPTER 4

INVESTIGATIONS INTO THE IN-CYLINDER FLOW FIELD

"When written in Chinese, the word 'crisis' is composed of two characters – one represents danger, and the other represents opportunity."

– John F. Kennedy

4.1 INTRODUCTION

This chapter presents the results from a number of numerical analyses, looking at the physical processes of the in-cylinder flow field occurring inside the GDI engine under study in this research. The physical processes investigated use a combination of both the RANS and LES turbulence modelling approaches as described and validated in Chapter 4, where the modelling approach selected for a particular analysis was chosen based on the required outcome.

The first section investigates a number of different aspects of the in-cylinder flow field including: the identification of transient flow structures and the evolution of flow features due to the movement of solid boundaries within the combustion chamber, the effect of the pent-roof optical access geometry on the in-cylinder flow field, a look into flow three-dimensionality often not captured during experimental research and a phenomenon called intake valve jet flapping.

The second section investigates flow anisotropy within the combustion chamber by evaluating the fluctuating velocity component and turbulence intensity at a number of cutting planes and key crank angles within the intake and compression strokes up to the point of spark timing. This also includes a detailed look at the impact of turbulent fluctuations and CCV of the flow field in the near spark plug region with suggestions on the expected impact on initial kernel development and subsequent flame propagation.

The final section presents the use of POD as a method for decomposing the spatially and temporally (both through a cycle and cycle-by-cycle) varying flow field to quantify and characterise turbulent flow structures, assess the amount of small scale turbulence at the point of spark timing, quantify the level of cyclic variability within the flow field and assess the degree of statistical convergence of the ensemble-average based on the number of numerical cycles completed and cyclic variability present in the flow field.

4.2 IN-CYLINDER FLOW STRUCTURES

4.2.1 Identification of Transient Flow Structures

This section presents the results from a short analysis of a number of flow structures, underneath the intake valve and early in the intake stroke, as an introduction into the prevalent flow structures found within this experimental test case. The results presented in this section were generated using the RNG k-ε turbulence model and computational setup as defined in section 3.3.3.1.

As stated earlier, the engine under study here exhibits a relatively weak tumble flow structure (tumble ratio of approximately 0.5). Valve jets of similar velocity magnitude are formed down both the cylinder wall closest to the intake valve and down the opposite wall underneath the exhaust valve, as a consequence of the relatively straight intake port geometry.

Figure 4.1 shows the velocity magnitude contours and vectors at 70°ATDC and 80°ATDC in the tumble plane, cutting through one of the intake valves. Intake valve jets propagating from both the front and back of the valve head are visible, reflecting off the liner and piston crown

and meeting in the centre of the combustion chamber, where they generate a highly turbulent recirculating region. Due to prominent valve jets being formed on both sides of the intake valve, and the obvious axis asymmetry due to the intake valve being positioned on one side of the cylinder, a number of complex flow structures are generated through the intake and compression strokes.

One such flow structure is seen at 70°ATDC, where a small recirculation region on the liner wall is generated as a consequence the intake valve jet interacting with flow reflecting off the piston crown, which at this crank angle is still relatively high in the combustion chamber. By 85°ATDC the flow structure is largely dissipated due to the falling piston and weakening valve jet, illustrated by black annotations in Figure 4.1.

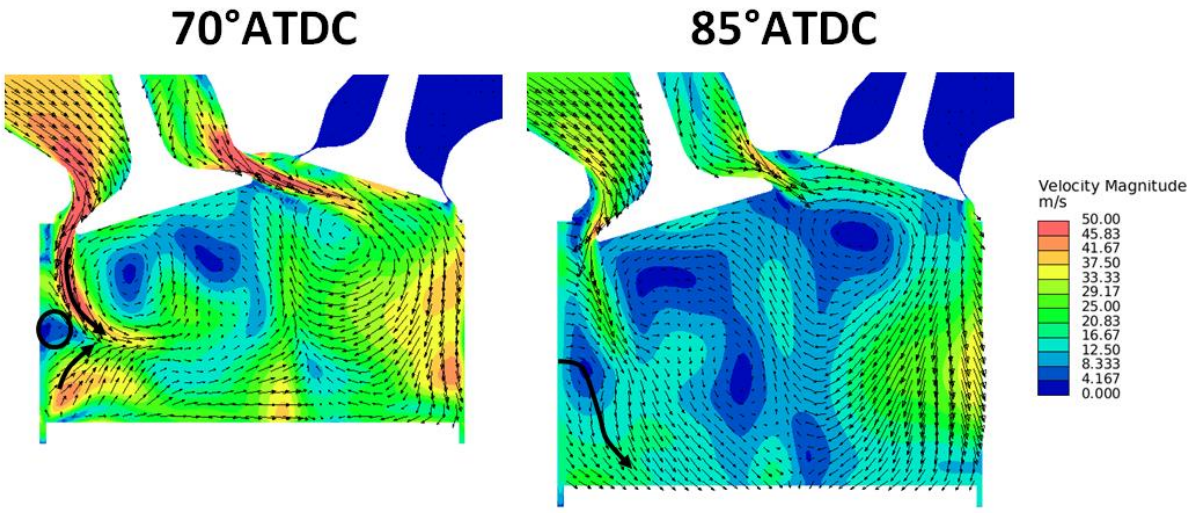

Figure 4.1 – Velocity magnitude contours and velocity vectors at 70°ATDC and 85°ATDC, illustrating the transient nature of a recirculation zone close to the cylinder wall

The reduced impact of the piston crown on in-cylinder flow structures later in the intake stroke is highlighted by Figure 4.2. Earlier in the cycle the flow field is heavily influenced by tumble flow rebounding off the piston crown as seen at 85°ATDC, in this case causing the rotating vortices formed underneath the intake valve to be displaced. By 110°ATDC the piston is significantly lower in the cylinder. This reduces the likelihood of flow reflecting off the piston surface and interacting with flow structures in the centre and upper portions of the combustion chamber, allowing more symmetrical recirculation regions to be formed underneath the intake valves.

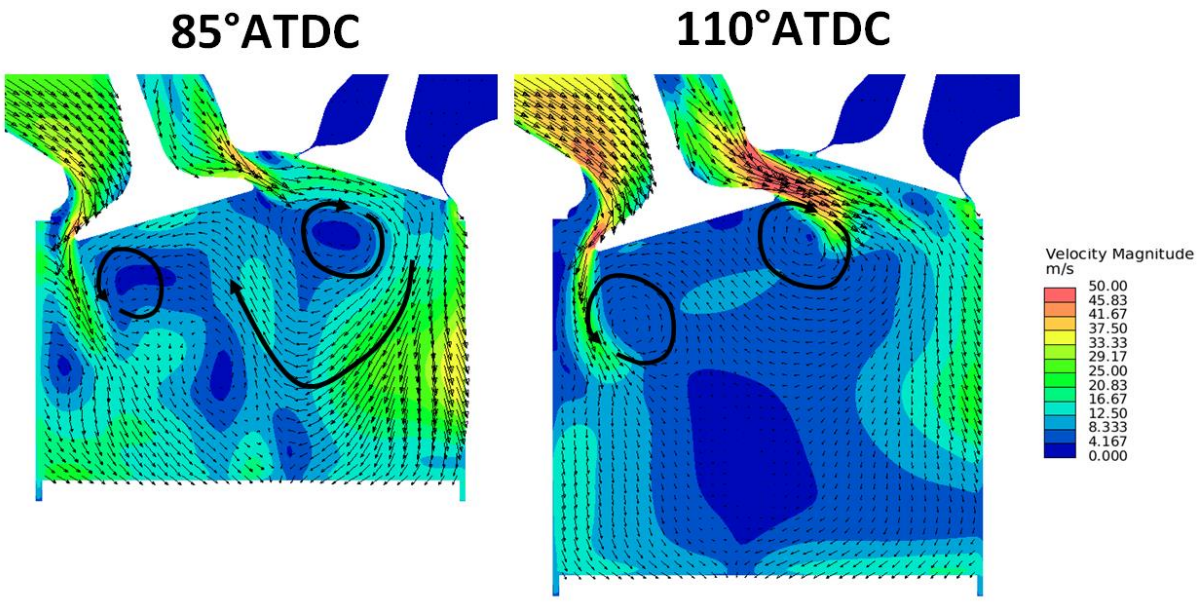

Figure 4.2 – Velocity magnitude contours and velocity vectors at 85°ATDC and 110°ATDC, illustrating the impact of solid boundaries on re-circulating flow structures at different points in the intake stroke

5.2.2 Effects of the Optical Access Window

This section presents the results from an analysis on the impact of the pent-roof optical access window on the in-cylinder flow field, including a number of considerations for experimentalists when using an optical access window of this type. The results presented in this section were generated using the RNG k-ε turbulence model and computational setup as defined in section 3.3.3.1.

Another appropriate use of this model is to study the impact of the pent-roof optical access window on the in-cylinder flow structures. This is of particular interest to experimentalists looking to compare experimental results from an optical research engine with pent-roof window against the results from an engine without optical access.

Figure 4.3 shows velocity magnitude contours and vectors along a swirl cutting plane in the pent-roof region, intersecting the optical access window. Immediately apparent is the presence of two additional turbulent eddies on the front side of the cylinder as a consequence of the abrupt geometry of the optical access window. This has the effect of generating flow asymmetry from front-to-rear of the combustion chamber.

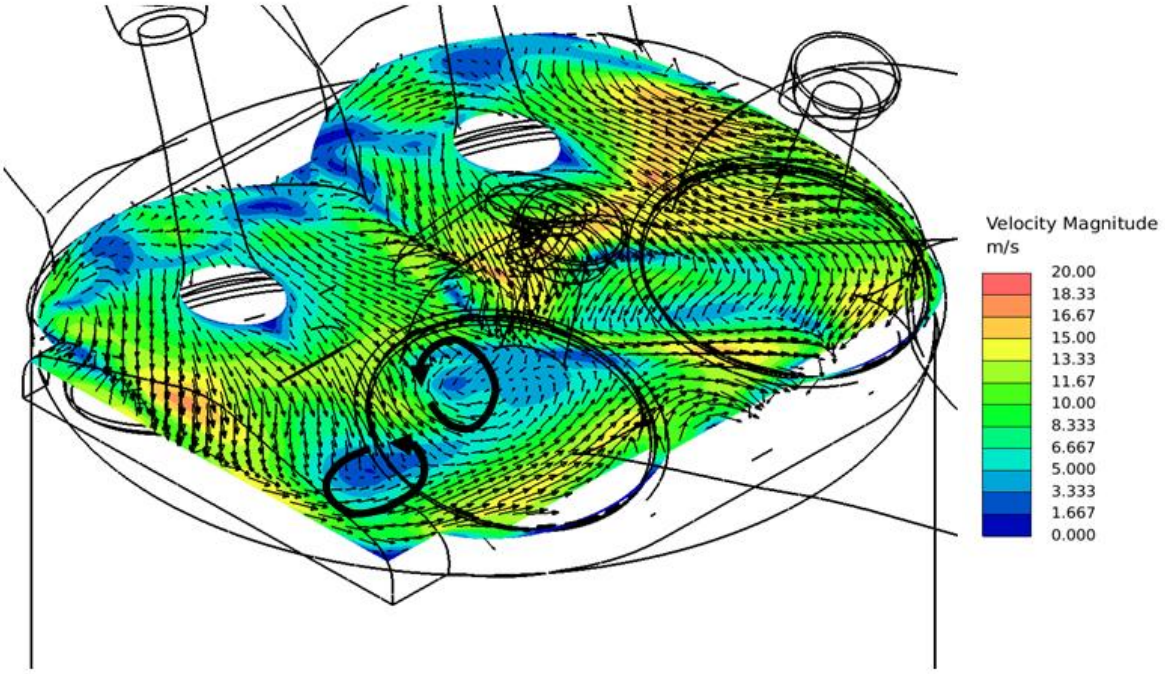

Figure 4.3 – Velocity magnitude contours and vectors along a swirl plane intersecting the optical access window, with black arrows indicating rotating vortices generated as a consequence of the optical access window

Figure 4.4 is in the head gasket plane and again illustrates flow asymmetry generated by the optical access window. The flow field from the rear of the combustion chamber is seen to be more dominant due to the rounded cylinder wall causing less obstruction than the optical access window at the front of the combustion chamber. The intersection of flow fields from front-to-rear of the combustion chamber also occurs in a different plane, generating additional recirculation regions highlighted by the annotated black arrows on the figure.

From these results, a number of considerations can be proposed for experimentalists using a pent-roof access window as a consequence of the predicted flow asymmetry:

- The flow field is less representative of the flow field generated in an engine without the pent-roof window
- The choice of experimental measurement location is of greater significance due to the added asymmetry
- There will potentially be an impact on fuel spray symmetry and fuel-air mixture in the near spark plug region at the point of ignition timing

Results suggest that the influence of the optical access window on the in-cylinder flow field is largely limited to the pent-roof region and does not appear to significantly influence the flow field within the cylinder interior.

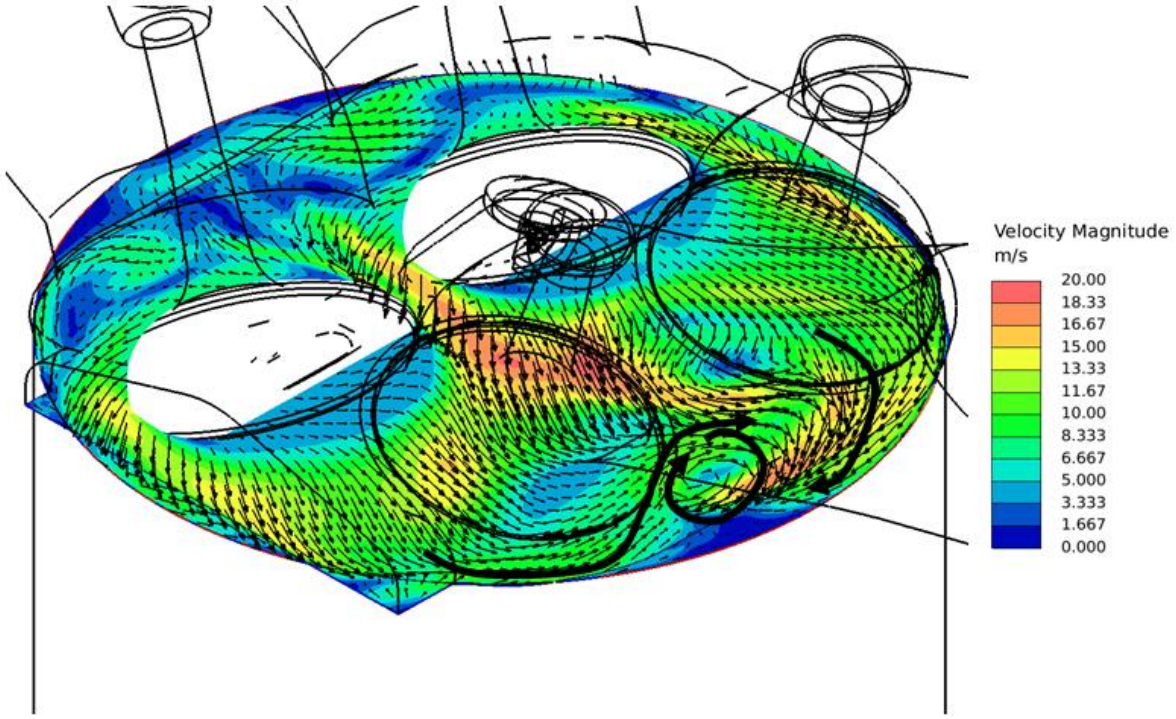

Figure 4.4 – Velocity magnitude contours and velocity vectors along the head gasket plane, with black arrows indicating flow asymmetry as a consequence of the optical access window

Figure 4.5 shows velocity magnitude contours and vectors across the surface of the combustion chamber with recirculation regions in the sharp corners of the optical access window clearly visible. The presence of these recirculation zones in the pent-roof window provides additional considerations including:

- An opportunity for increased mixture inhomogeneity which will influence flame front propagation and pollutant formation, particularly UHC and PM, in the optical access window
- An increased opportunity for end gas autoignition due to reduced flame speed in this region and the development of ignition sites or ‘hot-spots’ due to deposits

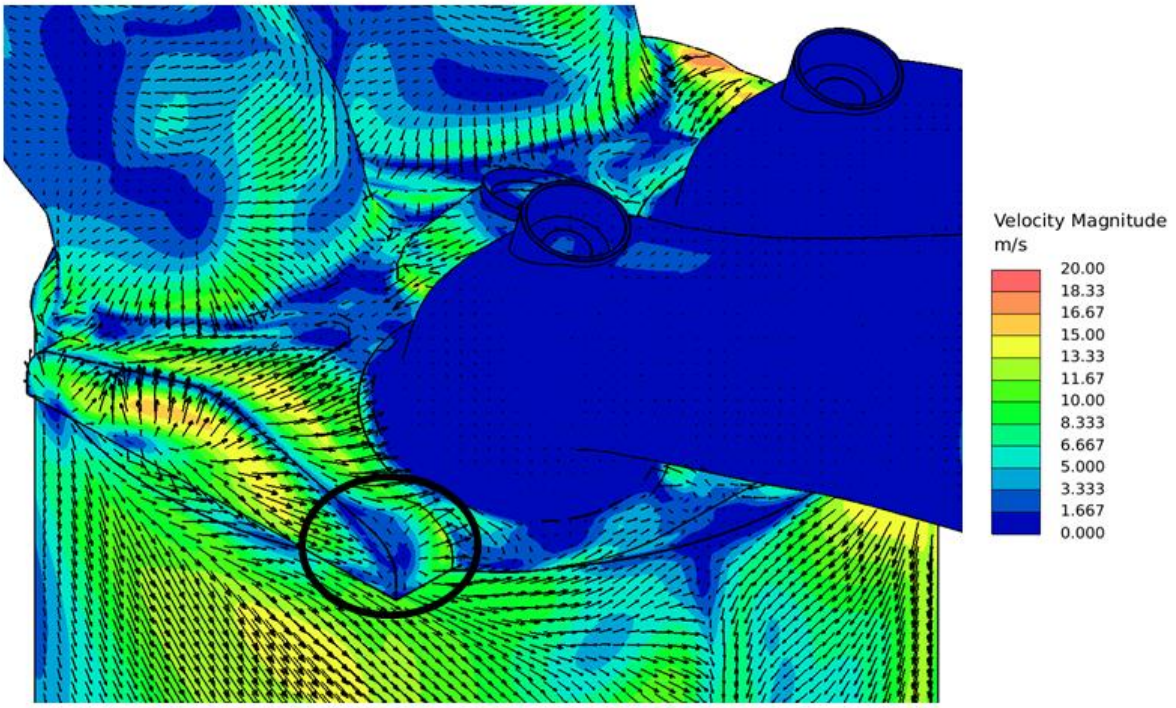

Figure 4.5 – Velocity magnitude contours and vectors across the surface of the domain focussed on the optical access window, with a black circle indicating the presence of a recirculation zone in the corner of the optical access window

4.2.3 Flow Three-Dimensionality

This section presents results investigating the three-dimensionality of the flow field. The results were generated using the Smagorinsky SGS model and computational setup as defined in section 3.3.3.2.

As discussed earlier in this thesis, the use of experimental techniques to measure flow fields in three-dimensions has limited examples in literature and even fewer when applied to ICE's. Numerical techniques, utilising the increases in computational resources over the past decades, offer a unique advantage to be able to provide detailed information on the in-cylinder flow field across all three planes. In this section, the three-dimensional nature of the flow field is investigated, with particular focus on the flow structures setup during the intake stroke.

The LES approach was used in preference to a RANS approach due to it providing an increased number of flow structures represented on the computational grid. This allows

additional insight into the characteristics of the flow structures present. This study has used the result from a single arbitrary cycle since, whilst it doesn't provide a representation of the average flow field (as is the case for an ensemble-average result), it does provide information on the actual flow field that occurred within a particular cycle.

First, velocity magnitude contours for four different cutting planes through the tumble plane (shown in Figure 4.6) were used to investigate the variation of in-cylinder flow field and intake valve jet through the combustion chamber at 70°ATDC, i.e. early in the induction process, and the results are shown in Figure 4.7.

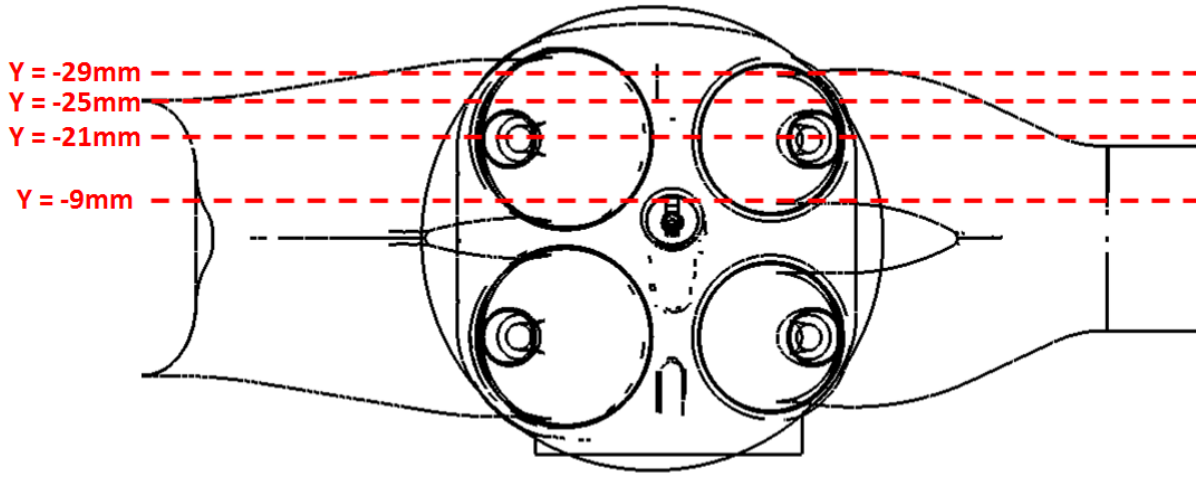

Figure 4.6 – Images shows cutting planes used for investigating three-dimensional nature of the intake valve jet

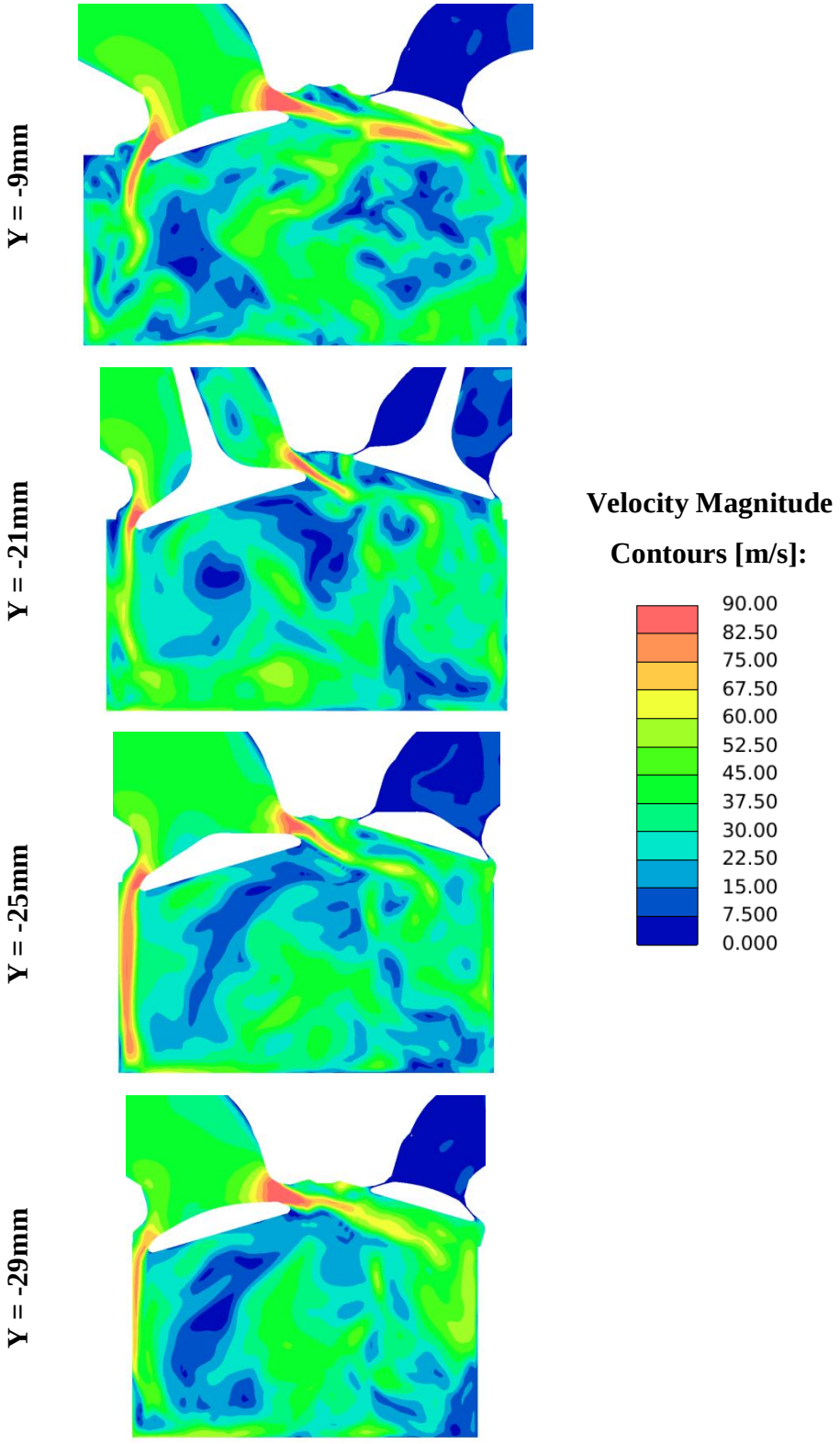

Figure 4.7 – Velocity magnitude contours for an arbitrary cycle at 70°ATDC, at successive cutting planes in the X-Z (tumble) plane, illustrating the variations in flow structures and intake valve jet through the combustion chamber

A variety of turbulent flow structures can be seen in the cylinder interior, with no one dominant flow direction, that varies across all four cutting planes.

The intake valve jet also is subject to variation across the combustion chamber. Inspection of the valve jet that propagates down the cylinder wall show the jet to penetrate almost to the piston crown in the y=-25mm cutting plane, but closer to the centre of the combustion chamber at y=-21mm and y=-9mm, the penetration is significantly reduced. This is thought to be as a consequence of its interaction with flow structures generated between the two valve jets. The valve jet that passes over the top of the valve head and across the top of the combustion chamber also varies in penetration depth and jet strength across the cutting planes shown here. At the periphery of the valve, at y=-9mm and y=-29mm, increased penetration is seen with the valve jet almost impinging the cylinder liner underneath the exhaust valve. Closer to the centre of the valve, at y=-21mm and y=-25mm, reduced jet penetration is seen and thought to as a consequence of the valve stem disrupting the flow as it travels past the valve and into the cylinder.

To further investigate the three-dimensional nature of the flow field the vorticity (ω), or 'curl' of the velocity vector field, was calculated as defined by equation (4.1). The vorticity defines the rotation of each cell's three-dimensional velocity vector and thus when plotted on a 2D contour plot, provides information on three-dimensional rotating flow structures or flow structures with movement in the hidden dimension.

$$\omega = \nabla \times u_i = \left(\frac{\partial u_z}{\partial y} - \frac{\partial u_y}{\partial z}\right)\boldsymbol{i} + \left(\frac{\partial u_x}{\partial z} - \frac{\partial u_z}{\partial x}\right)\boldsymbol{j} + \left(\frac{\partial u_y}{\partial x} - \frac{\partial u_x}{\partial y}\right)\boldsymbol{k} \qquad (4.1)$$

Figure 4.8 shows velocity magnitude and vorticity contours for two cutting planes at y=-1mm (approximately the centre of the combustion chamber) and y=-19mm (through the middle of the rear intake valve).

The following comments can be made on the flow structures observed in Figure 4.8:

- At y=-1mm, an area of high vorticity is present to the left of the centre of the combustion chamber in line with the intake valve, due to interactions between the two valve jets.
- High vorticity is present in areas of high shear. This effect is visible either side of the intake valve jet in the images at y=-19mm where the high velocity valve jet impinges

the slow moving flow of the cylinder interior, and in locations where high velocity flow meets a solid boundary, e.g. piston crown, combustion chamber and intake port wall, intake valve head, due to the velocity gradient between the freestream and the boundary layer.

- Areas of high vorticity are also visible within the cylinder interior, indicating regions of strongly rotating turbulent vortices.

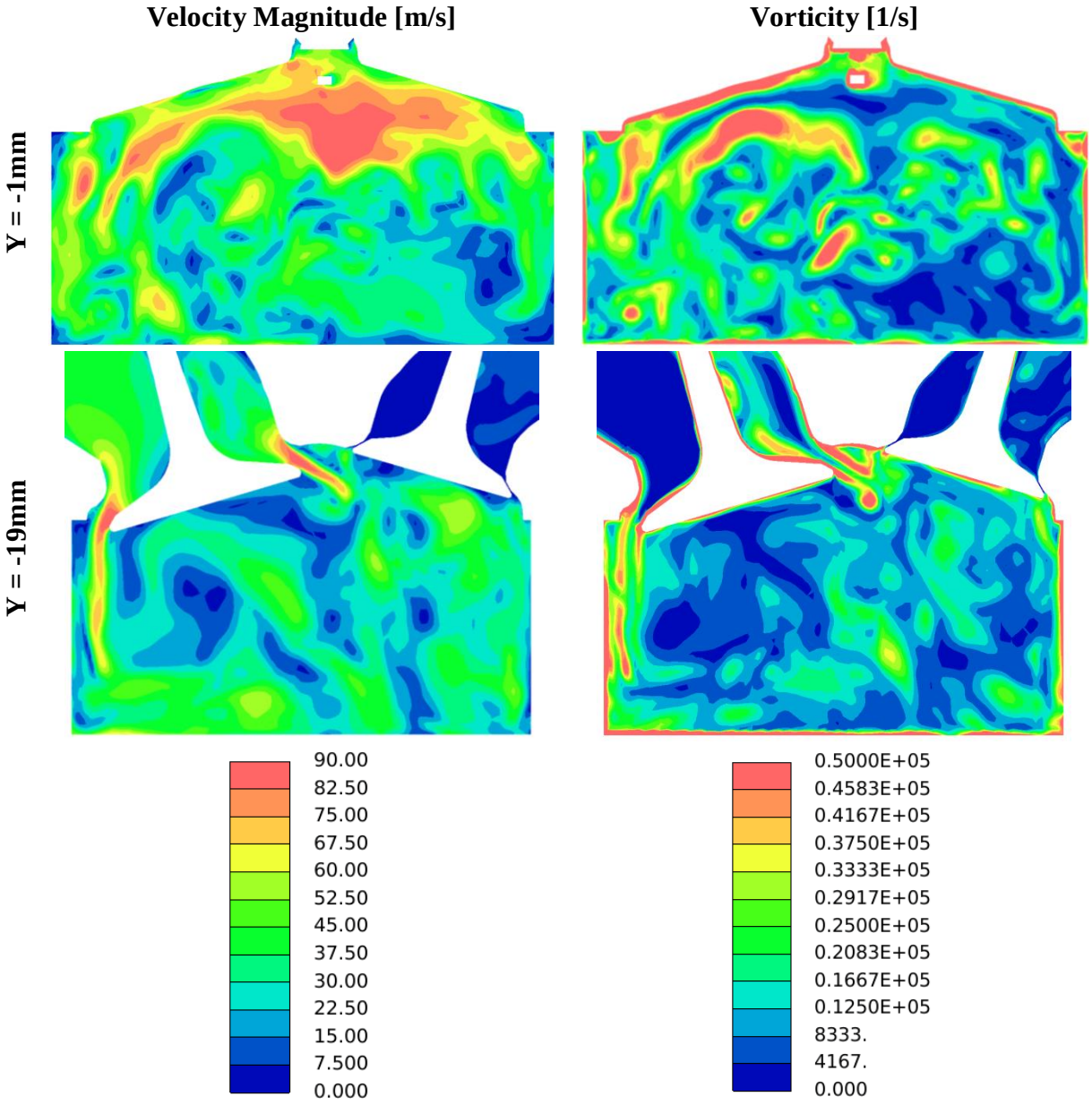

Figure 4.8 – Velocity magnitude contours and vorticity contours for an arbitrary cycle at 70°ATDC, at two cutting planes in the X-Z (tumble) plane

To investigate areas of high vorticity around the intake valve jet in more detail, Figure 4.9 provides a zoomed in view. Regions of high vorticity are clearly visible around the intake valve jet, across the top of the valve head and in the valve curtain where the flow detaches from the cylinder head, as a consequence of the high velocity valve jet causing regions of high shear as it moves past regions of lower velocity flow. A number of regions with high vorticity are also visible within the cylinder interior. This indicates turbulent flow structures in the dimension not plotted (i.e. into or out of the page) as a consequence of recirculating eddies generating highly three-dimensional flow structures.

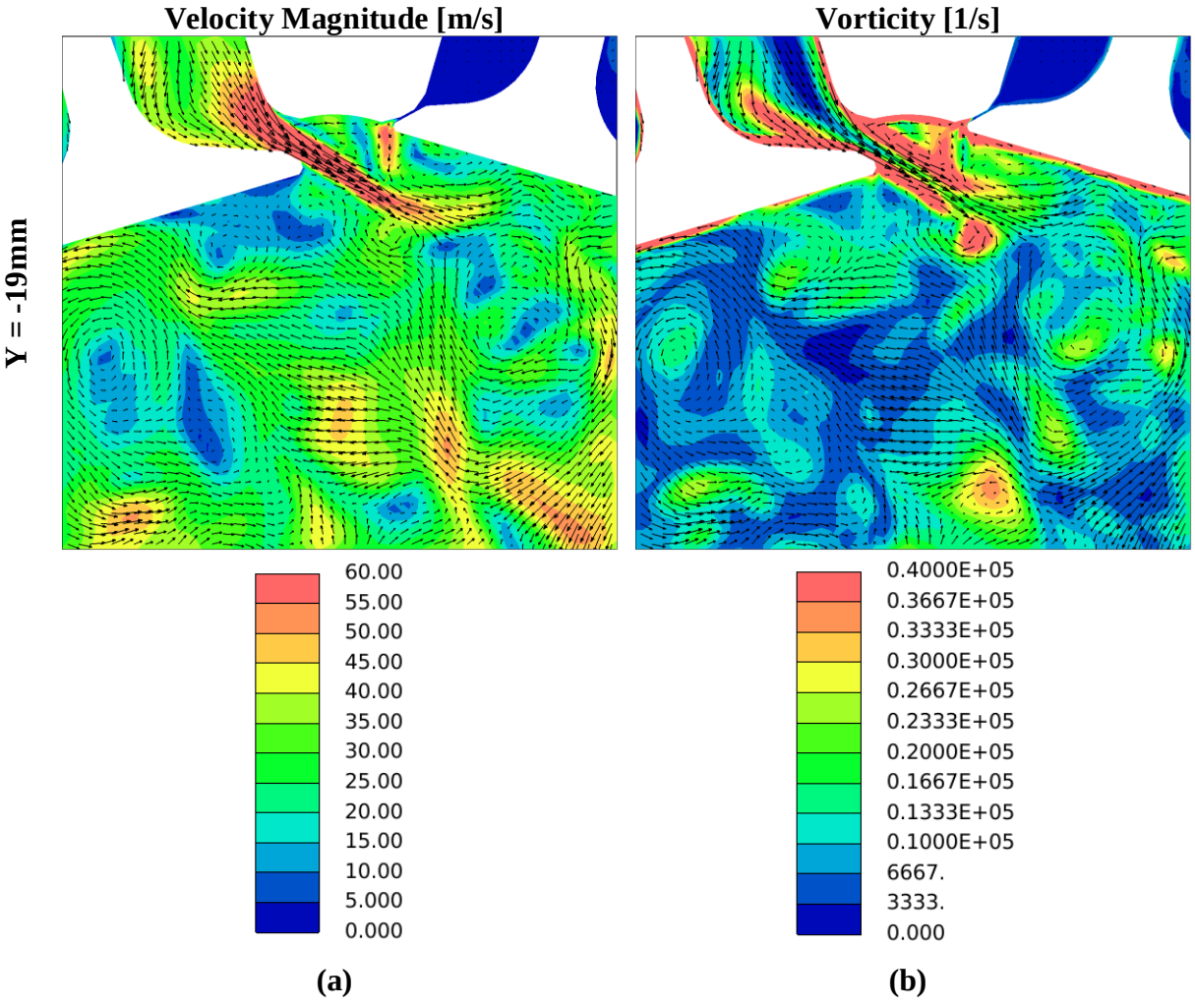

Figure 4.9 – (a) Velocity magnitude contours and vectors, (b) Vorticity contours and velocity vectors, zoomed in around the intake valve jet, for an arbitrary cycle at 70°ATDC, in the X-Z (tumble) plane

As observed above, areas of vorticity are generated due to either a shear induced flow field or a swirling flow field, thus vorticity cannot be used to distinguish between the two flow types.

4.2.4 Intake Valve Jet Flapping

In the previous section, interactions between the two intake valve jets were observed, particularly with respect to the generation of vorticity where the two jets collide in the region between the two valves. This section focuses on the interaction between the two valve jets and the specific phenomenon of intake valve jet instability or 'flapping'.

Intake valve jet flapping describes the sinusoidal flow motion generated between the two intake valves during the intake stroke where examples are given in Figure 4.10 and Figure 4.11. Jet flapping has been observed both experimentally and numerically in both detailed and simplified engine geometries (e.g. Hasse, Sohm & Durst (2009), Hasse (2016) and Borée, Maurel & Bazile (2002)) and suggested as a potential source of cycle-to-cycle variability, due to the instability of the flow structure leading to significant differences in the resultant large scale tumbling motion (Hasse, 2016; St Hill, Asadamongkon, Lee, *et al.*, 2000). In spite of this very little research exists where valve jet flapping has been characterised or attempts made to determine causality. This section aims to investigate the characteristics of intake valve jet flapping, establish causality and investigate the cyclic variability of this phenomenon.

The results in this section were generated using the Smagorinsky SGS model and computational setup as defined in section 3.3.3.2.

In the research presented here, individual cycles were investigated for evidence of intake valve jet flapping. Velocity magnitude contours at 5°CA intervals were used in the y-z cutting plane, intersecting through both intake valves. During early observations it became apparent that prior to an intake valve jet flapping event, a stronger velocity field was present in one of the intake valve curtains as a consequence of turbulent fluctuations. The difference in valve curtain flux between the two intake valves was compared to consecutive images of velocity magnitude contours and a relationship found between the temporal variation in valve

curtain mass flux and valve jet flapping. The results from cycle 10 are shown in Figure 4.12 and Figure 4.13 and the following is a supporting commentary.

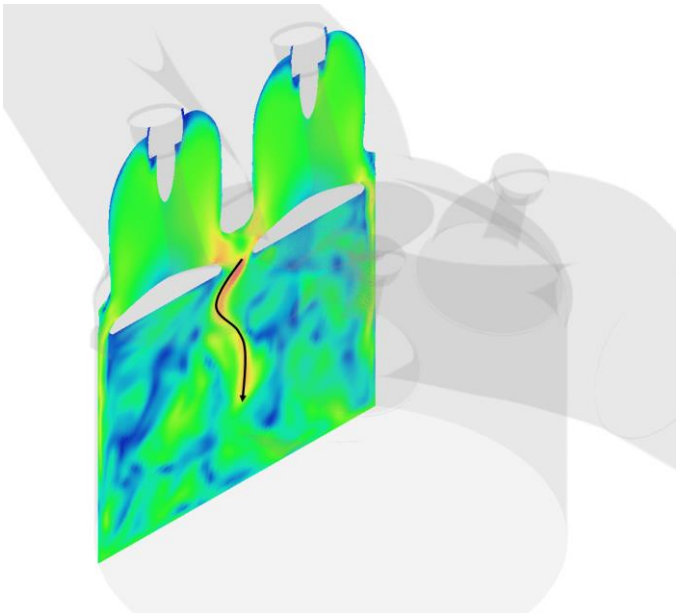

Figure 4.10 – Velocity magnitude contours illustrating of intake valve jet flapping in the cross-cylinder plane taken from results from this research

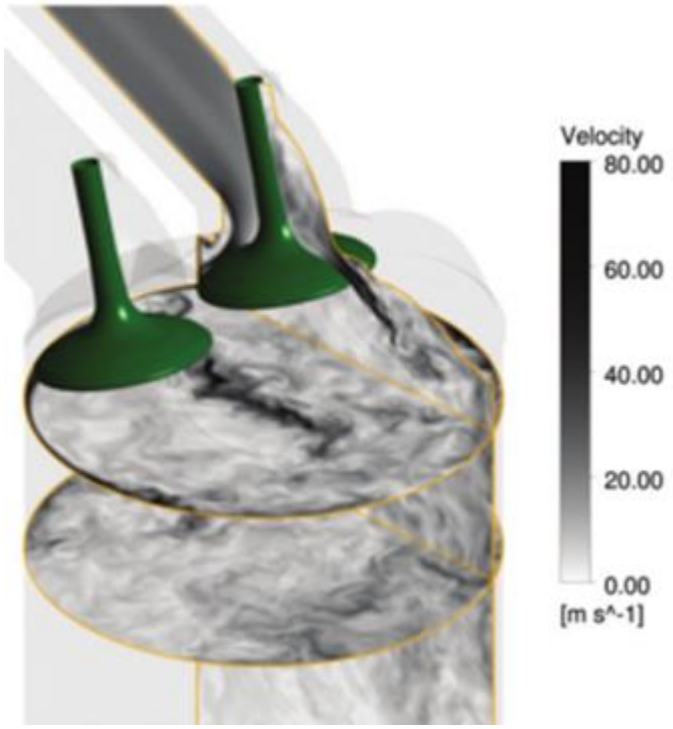

Figure 4.11 – Velocity magnitude contours providing an example of intake valve jet flapping in the swirl plane, taken from Hasse (2016)

Early in the intake stroke, between 30-70°ATDC, variations in mass flux past the intake valve curtains are small and this is reflected in a fairly constant jet propagating down the centre of the combustion chamber (Figure 4.13(a)).

At around 75°ATDC a significant variation in valve curtain mass flux occurs between the two intake valves, observed as a weakening of the flow through the left valve curtain (Figure 4.13(b)).

This imbalance in valve curtain flux causes a momentary strengthening of the valve jet from the right hand valve and a resultant instability in the combined vertical jet, causing it to propagate more diagonally under the left intake valve.

5°CA later at 80°ATDC, the difference in valve curtain flux has returned to similar values but this oscillation in the relative strength of each valve jet causes the resulting jet to begin to 'flap' in a sinusoidal motion (Figure 4.13(c)).

A further 5°CA later at 85°ATDC, since the valve curtain flux had stabilised 5°CA earlier, any flapping has been dissipated but a weakening of the flow past the left valve prompts the initiation of further valve jet flapping, which is visible at 90°ATDC (Figure 4.13(d) & Figure 4.13(e)).

This process continues until approximately 140°ATDC where any difference in valve curtain flux between the two intake valves is minimal as a consequence of much lower valve jet velocities at large valve lifts.

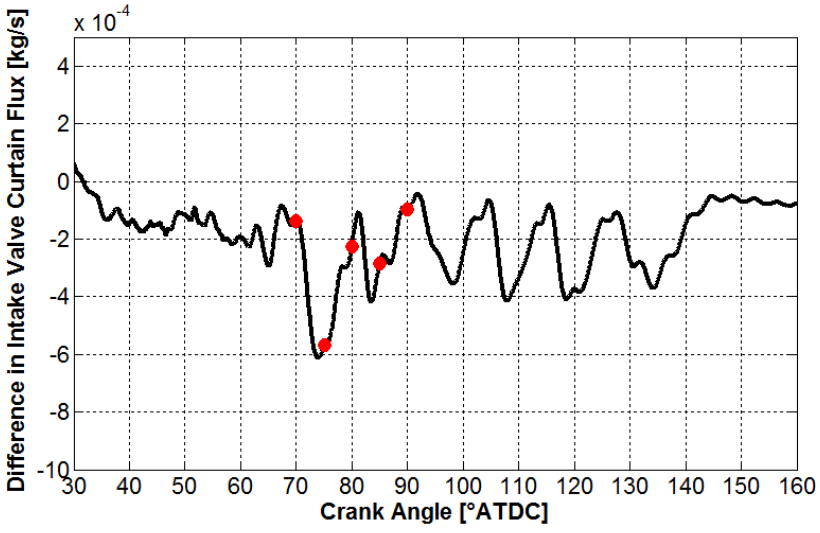

Figure 4.12 – Difference in valve curtain flux between the intake valves for cycle 10 with red markers used to highlight crank angles for images in Fig.4

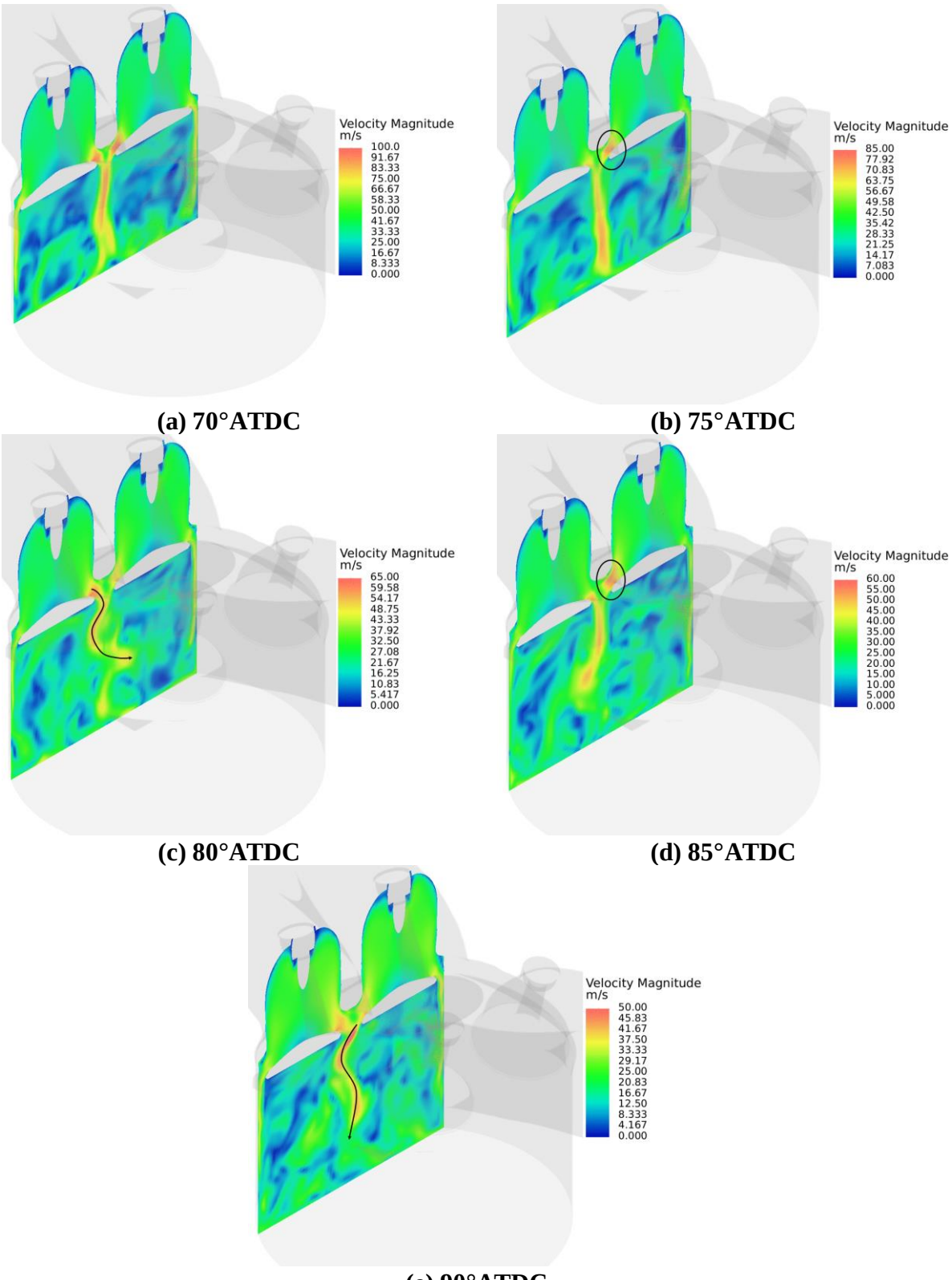

(a) 70°ATDC **(b) 75°ATDC**

(c) 80°ATDC **(d) 85°ATDC**

(e) 90°ATDC

Figure 4.13 – Velocity magnitude contours with black circles highlighting valve curtain flow imbalance and black arrows highlighting valve jet flapping

It has also been observed that all engine cycles show cycle-to-cycle variations in valve curtain flux through the intake stroke. As seen in Figure 4.14 where all engine cycles are overlaid, all cycles exhibit variation in the intake valve curtain flux with the magnitude and phasing of the variation changing on a cycle-by-cycle basis.

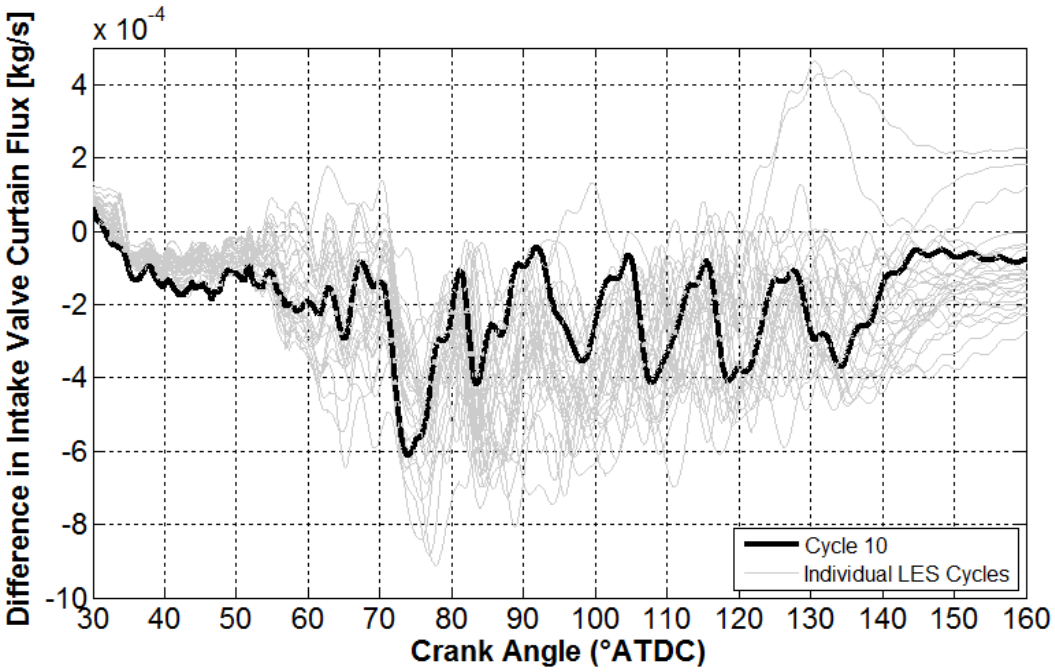

Figure 4.14 – Highlighting the variation in phase and magnitude of difference in intake valve curtain flux across all cycles

As an example of the cyclic variations present, Figure 4.15 shows the difference in intake valve curtain flux and velocity magnitude contours at 100°ATDC for cycle 23. Here the flapping intake valve jet can be seen to have lower penetration into combustion chamber but oscillate at a higher frequency when compared to cycle 10. Figure 4.16 shows results for cycle 12 at 75°ATDC where the flapping valve jet oscillates at a lower frequency but penetrates all the way to the piston crown surface.

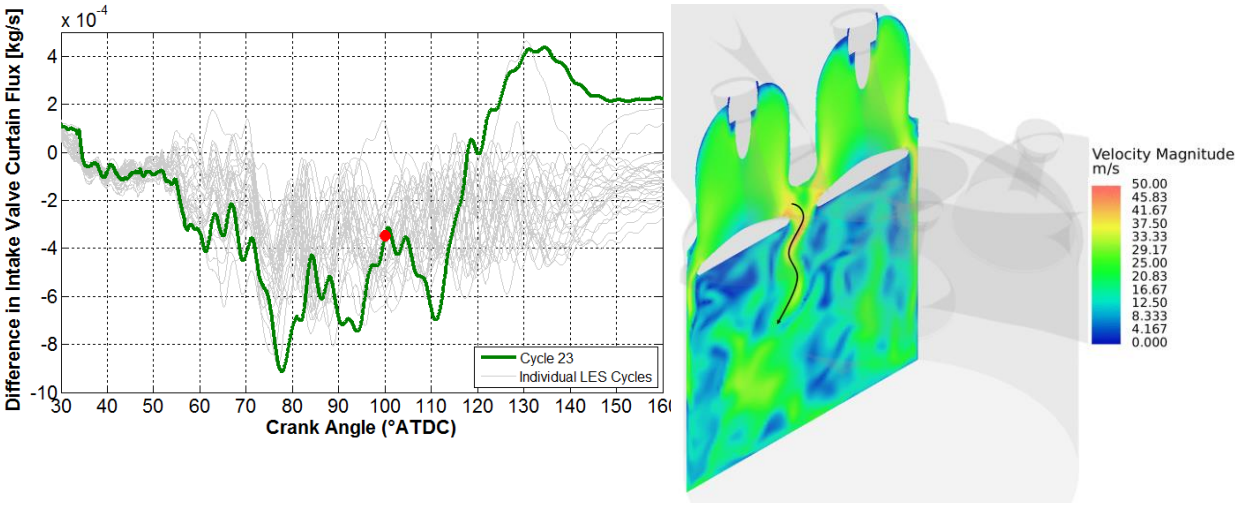

(a) **(b)**

Figure 4.15 – Cycle 23 (a) Difference in intake valve curtain flux, (b) Velocity magnitude contours at 100°ATDC

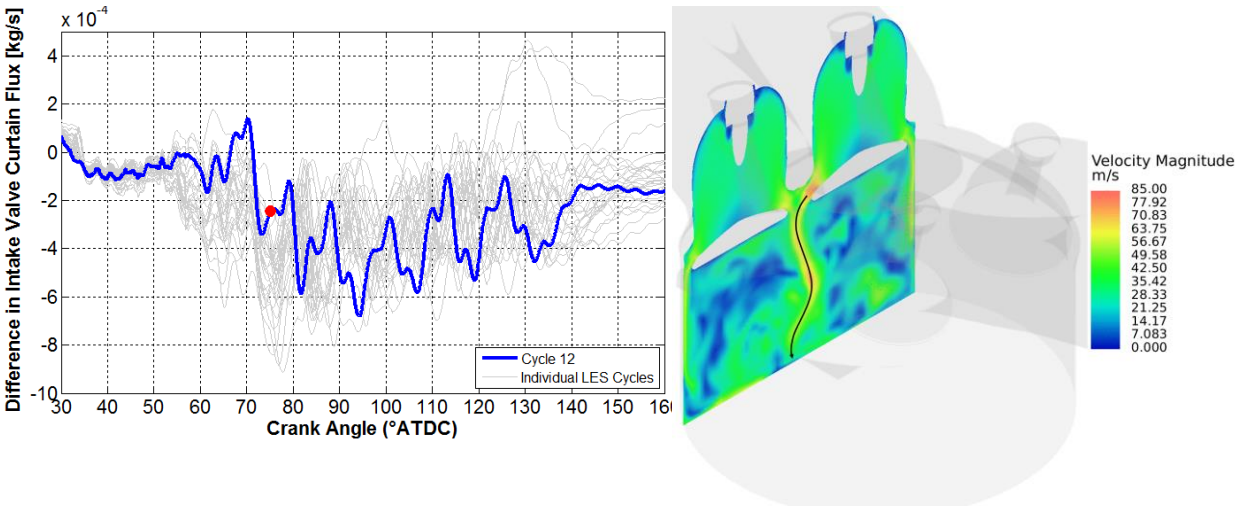

(a) **(b)**

Figure 4.16 – Cycle 12 (a) Difference in intake valve curtain flux, (b) Velocity magnitude contours at 75°ATDC

Due to the variation in magnitude and phase of the intake valve jet flapping that occurs on a cycle-by-cycle basis, when an ensemble-averaging process is applied to the velocity field, most of the information associated with jet flapping is lost and the results largely show a steady valve jet penetrating directly down into the combustion chamber, as shown by Figure 4.17(a). Interestingly, contrary to the findings of Hasse (2016), when compared to a RANS solution of the same geometry (using the RNG k-ε turbulence model and computational setup as defined in section 3.3.3.1), jet flapping is visible but due to the time-averaging of the N-S equations, does not capture any of the cyclic-variability present in the LES predictions,

Figure 4.17(b). This finding becomes clear when the difference in valve curtain mass flux is calculated for the LES ensemble-average and RANS results, shown in Figure 4.18. The averaging effect on the perturbation, and then on the resultant valve jet instability in the LES ensemble-average trace is clear with a significant reduction in amplitude of the oscillatory trend. The difference in valve curtain flux for the RANS simulation shows a similar trend to that of the previously presented LES cycle 10 (Figure 4.12) and explains the presence of valve jet flapping in the predicted velocity field in the RANS predictions.

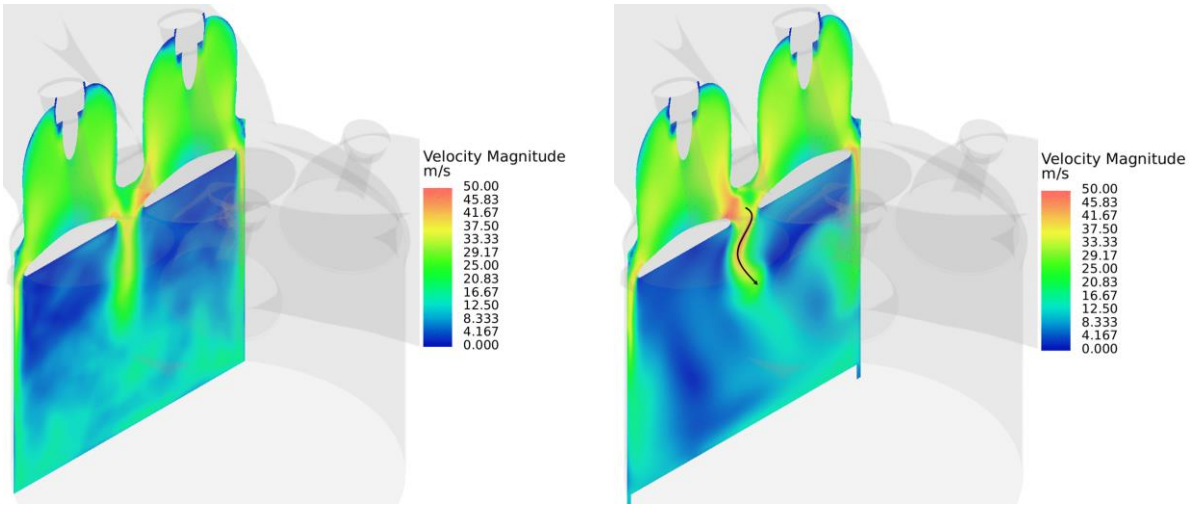

(a) LES Ensemble-Average **(b) RANS**

Figure 4.17 – Comparison of velocity magnitude contours at 100°ATDC for (a) LES 29 cycle ensemble-average and (b) RANS predictions

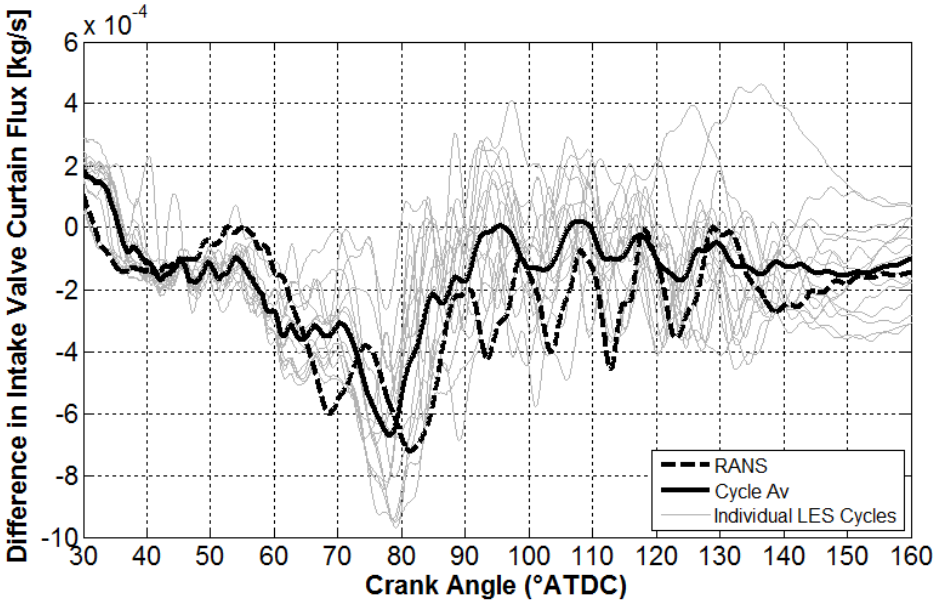

Figure 4.18 – Difference in valve curtain mass flux as a function of crank angle for the LES ensemble-average and for a RNG k-ε turbulence model

4.3 CHARACTERISATION OF FLOW ANISOTROPY

As discussed in section 3.3.1.1 on turbulence, the large turbulent eddies can be assumed to be independent of viscous forces (i.e. dominated by inertial effects) and predominantly defined by the mean flow characteristics. The length scales are related to the geometry of the system boundaries, boundary layer thickness and boundary surface roughness. Thus the structure of the largest eddies are highly anisotropic and characterising the flow field with respect to its anisotropic nature is of interest to engine researchers for improved understanding and to numerical modellers for improving turbulence modelling techniques and their application to ICE flows.

Whilst some examples of the application of experimental techniques for producing velocity field results in three-dimensions within an ICE are available, e.g. Peterson, Regaard, Heinemann, *et al.* (2012) and Peterson, Ding, Baum, *et al.* (2015), it is still very much emergent within the engine research community due to the difficultly of both the experimental technique and optical access into the combustion chamber. Due to computational limitations, traditional turbulence modelling techniques (to be discussed further below) have typically not allowed anisotropic affects to be accurately modelled, but the constant progression in computing resources is allowing the use of more computationally expensive turbulence modelling approaches, providing some unique opportunities to investigate the unique nature of flow anisotropy in ICE's.

This section begins with a brief discussion of turbulence modelling and relative advantages and disadvantages of RANS and LES turbulence modelling approaches with respect to modelling the anisotropic effects of the flow field. It will then follow with the methodology behind the results within this section and finish by presenting the findings from the evaluation of velocity fluctuations and turbulence intensity with respect to the overall flow field and characteristics of anisotropy in this single cylinder optical research engine. The LES predictions in this section were generated using the Smagorinsky SGS model and computational setup as defined in section 3.3.3.2, and the RANS predictions generated using the RNG k-ε turbulence model and computational setup as defined in section 3.3.3.1. Note that whilst the results are discussed with respect to a fuel injection event, this is a cold flow/single-phase analysis and an investigation into flow anisotropy when an injection event is simulated is presented in Chapter 6.

In a classical RANS formulation the viscous stresses are assumed to be proportional to the rate of deformation for a fluid element and thus the turbulence viscosity is assumed isotropic. Thus each of the fluctuating components are assumed to have an equal 1/3 contribution to the turbulence kinetic energy, making the Reynolds stresses equal in all directions, or isotropic. This is known to be highly inaccurate in even the simplest of turbulent flows.

When using the LES turbulence modelling approach, flow structures greater than the filter width, or the cell size as is the case in this research, are solved directly using the N-S equations and only the flow structures smaller than the filter width are modelled, thus resolving the anisotropic behaviour for a significant proportion of the flow field.

In this research, the fluctuating velocity component and turbulence intensity were evaluated across a number of cutting planes and at a number of crank angles through the intake and compression strokes up to the point of spark timing, using the LES turbulence modelling approach, in order to evaluate the anisotropic characteristics of the flow field. The equivalent results from a RANS RNG k-ε turbulence model were also calculated and compared.

The fluctuating or sub-grid velocity u_i', and turbulence intensity T_i for the LES results were calculated via the following methodology:

1. Calculate the ensemble-average velocity (or filtered-velocity) for each velocity component $\bar{u}_i$:

$$\bar{u}_i(\theta) = \frac{1}{n}\sum_{c=1}^{n} u_i(\theta, c) \tag{4.2}$$

Where c is cycle number, n is the total number of cycles and θ the crank angle

2. Calculate the fluctuating velocity component (or sub-grid velocity) u_i':

$$u_i'(\theta, c) = u_i(\theta, c) - \bar{u}_i(\theta) \tag{4.3}$$

Where u_i is the instantaneous velocity.

3. Calculate the RMS (or standard deviation) of each fluctuating velocity component $u_{i,rms}'$:

$$u'_{i,rms}(\theta) = \sqrt{\frac{1}{n}\sum_{c=1}^{n} u'_i(\theta, c)^2} \tag{4.4}$$

4. Calculate the turbulence intensity T_i:

$$T_i(\theta) = \frac{u'_{i,rms}(\theta)}{\bar{u}_i(\theta)} \tag{4.5}$$

When looking at the velocity fluctuations in isolation, whilst they provide an indication of the magnitude and relative anisotropy of the turbulent fluctuations, the result does not indicate the relative significance of the flow fluctuations in relation to the mean velocity. The turbulence intensity calculates the ratio of fluctuating component to the mean or ensemble-average flow field, thus providing a direct indication of their relative significance in comparison to the mean flow.

The fluctuating velocity component u'_i, and turbulence intensity T_i for the RANS results were calculated via the following methodology:

1. Starting with the equation for the extended Boussinesq assumption as shown earlier in equation (2.22), the normal stresses are calculated by setting $\delta_{ij} = 1$, $i = j$ and thus:

$$\overline{u_i u_j} = -\frac{\mu_t}{\rho}\left(\frac{\partial \bar{u}_i}{\partial x_j} + \frac{\partial \bar{u}_j}{\partial x_i}\right) - \frac{2}{3}\rho k \delta_{ij} = -\frac{2}{3}k \tag{4.6}$$

2. Thus the fluctuating velocity component can be calculated from the (modelled) turbulence kinetic energy via the following equation:

$$u'_i = \sqrt{\frac{2}{3}k} \tag{4.7}$$

3. The turbulence intensity T_i can be calculated via equation (4.5) as defined previously, but in the RANS context $\bar{u}_i$ is the mean velocity rather than the ensemble-average velocity.

The fluctuating velocity and turbulence intensity components were calculated:

- Across three separate tumble cutting planes; mid bore, through the centre of each intake valve (shown by red tumble cutting planes in Figure 4.19) in the x-z plane to evaluate differences in anisotropy as a consequence of the interactions between the intake valve jets and the rest of the in-cylinder flow field, and an additional cutting plane at spark timing in the y-z plane that cut through the spark plug to investigate anisotropy around the spark plug electrodes at the point of spark timing (shown by the blue cutting plane in Figure 4.19).
- For each x-z tumble plane, the fluctuating velocity and turbulence intensity was evaluated at different z-locations across the cylinder bore to capture differences in turbulence characteristics through the combustion chamber.
- Results were evaluated at 80°ATDC (point of fuel injection), 100°ATDC (10° after end of injection), 180°ATDC (BDC, start of compression), 90°BTDC (mid-compression), 35°BTDC (spark timing).

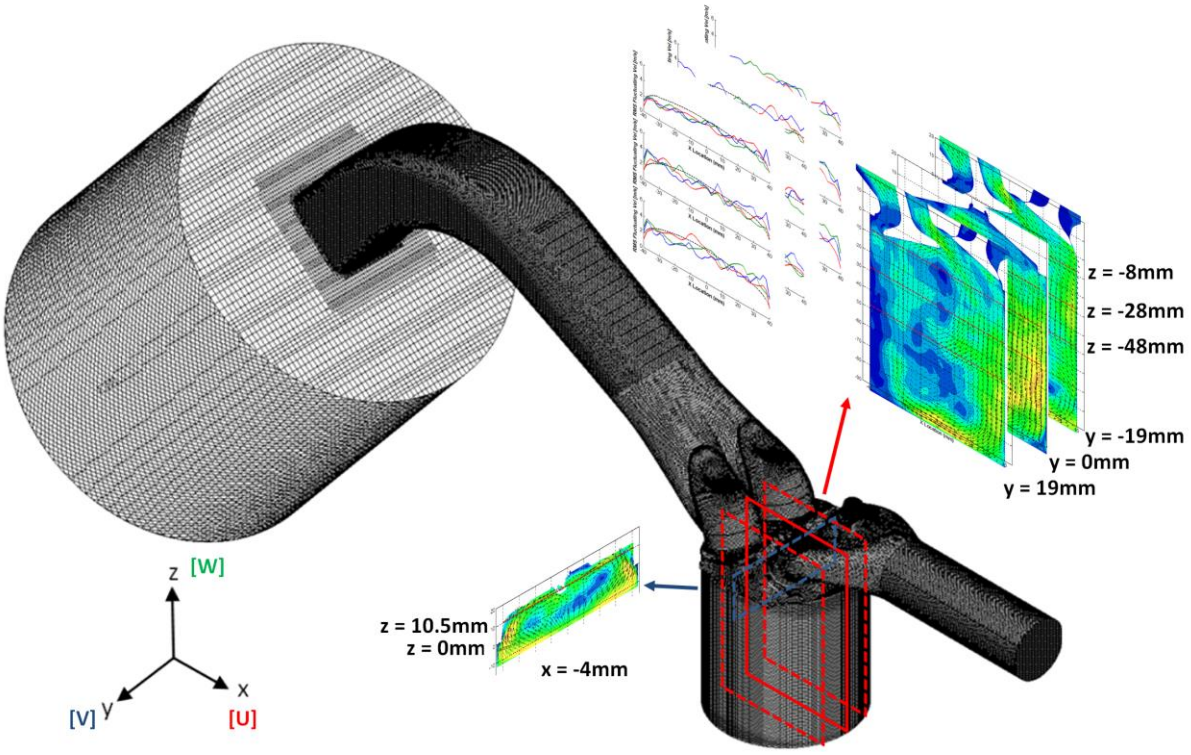

Figure 4.19 – Computational domain and a graphical representation of the cutting planes used for investigating flow anisotropy

The following is a discussion of the key findings from this analysis and the graphical results follow.

At 80°ATDC (Figure 4.20) the injection process is started, fuel is injected into the centre of the combustion chamber, close to the valve jets from both intake valves, which then propagates into the centre of the combustion chamber interior. Away from the stronger flow structures at the periphery of the combustion chamber and along the combustion chamber walls due, a number of weaker, highly three-dimensional, recirculation regions are present in the centre of the combustion chamber are visible in the velocity magnitude contour plots and also indicated by the more oscillatory nature of the fluctuating velocity components. A good example of this is the increase in x-plane velocity fluctuations (red line series) (relative to near the cylinder walls) around the centre of the combustion chamber (x=0mm) at z=-28mm for both y=-19mm and y=19mm cutting planes. The rise in fluctuations will act to increase normal and shear stresses which will help distort and diffuse the droplets and subsequent vapour cloud in this region.

By 100°ATDC (Figure 4.21) the injection process is complete and a significant portion of the early injected droplets will have been through the secondary breakup process and be contributing to a fuel-rich vapour cloud. One anisotropic characteristic of note is the relatively high y-plane velocity fluctuation (blue line series) in the y=0mm cutting plane at z=-8mm and around x=-30mm when compared to x- (red line series) and z-plane (green lines series) velocity fluctuations. This feature can be attributed to the intake valve jet flapping phenomenon where, whilst the mean flow direction is down and into the combustion chamber, due to CCV in the valve jet (as discussed earlier in Chapter 5.2.5), large velocity fluctuations are seen in the y-plane.

At 180°ATDC (BDC) (Figure 4.22) the flow field is least wall bounded allowing turbulent structures with the largest length scales to form. As is seen in this engine, the tumble motion generates a large recirculating flow structure around the periphery of the combustion chamber. Whilst the magnitude of the velocity fluctuations have reduced, it is not proportional to the reduction in mean flow velocities, thus an increase in the number of fluctuations in turbulence intensity is seen when compared to earlier in the cycle.

At 90°BTDC firing (mid-compression) (Figure 4.23) a significant anisotropic feature is seen in the z-plane velocity fluctuations (green line series) at y=-19mm, z=-28mm and z=-48mm around x=30mm (and to a lesser extent at y=19mm, z=-48mm, x=35mm). This rise in z-plane

velocity fluctuations and subsequent anisotropy is caused by the rising piston generating an upward flow that meets the clockwise rotating tumble flow set up by the intake system. This characteristic of the flow field is completely missed by the RANS predictions (dashed black line series) due to the use of the aforementioned Boussinesq mean-gradient assumption to solve the Reynolds stresses. Inspection of the velocity magnitude contour plots reveals that large differences in the mean flow structures now exist from the front to the rear of the combustion chamber that were not present through the intake stroke. The impact of the rising piston and subsequent compression of the turbulent length scales has increased the velocity fluctuations and mean flow in the y-plane (cross cylinder) creating additional rotating structures in the swirl plane and subsequent differences in the mean flow field across the cylinder. Also of note are the very low levels of turbulence intensity near the piston surface. This is due to the rising piston driving the flow upward, damping out turbulent fluctuations and thus reducing small scale turbulence close to the piston surface.

35°BTDC is the point of spark ignition at this operating condition and by this point in the compression stroke, the rising piston and reducing combustion chamber volume has caused most of the large scale structures to be dissipated into small scale turbulence (Figure 4.24). A strong clockwise rotating mean flow structure of between 5-8m/s is visible in all x-z planes which will act to convect the flame kernel primarily in the positive x-plane direction away from the intake valves and towards the exhaust valves. A RMS fluctuating velocity component of order 2.5m/s means the instantaneous velocity is expected to of the order 10m/s which is below the 15m/s suggested by (Heywood, 1988) as the point where increased restrike frequency occurs.

Inspection of the flow structure in the y-z plane (cutting through the spark plug electrodes) (Figure 4.25), shows strong counter rotating vortices that meet at the top of the combustion chamber by the spark plug electrodes. The x-plane fluctuating velocity component is seen to be large relative to y- and z-plane components in the near spark plug region as a consequence of variations in the strength of the counter-rotating vortices in the y-z plane and subsequent motion in the x-plane. Also of note is the rise in x-plane velocity fluctuations at y=-2.5mm due to the flow field interacting with the geometry of the spark plug electrodes. These turbulent fluctuations will cause variations in the degree of flame kernel stretch during the initial kernel development phase and contribute to the overall CCV of the combustion process. The turbulent fluctuations in the x- and y-planes are almost equal to 50% of the mean flow

velocity which also indicates that turbulence will be a significant contributor to CCV in the combustion process at this engine condition.

A general observation of the results through the intake and compression stroke, fluctuations in the y-plane turbulence intensity (blue line series) are generally seen to be more dominant than turbulence intensity fluctuations in the x- and z-planes; whilst the y-plane fluctuating velocity is seen to be of the same magnitude as the other fluctuating velocity components. This indicates that whilst velocity fluctuations are present in all planes, the mean flow field is not dominant in the y-plane. This is as expected since the intake runner and port geometry set up a dominant tumble flow structure but also that, whilst the bulk flow will generate significant momentum in the x-z (tumble) plane, the turbulent fluctuations in the y-plane (cross cylinder) will also act to promote diffusion and mixing across the cylinder; of particular significance for its impact on the fuel-air mixing process and minimising stratification within the cylinder.

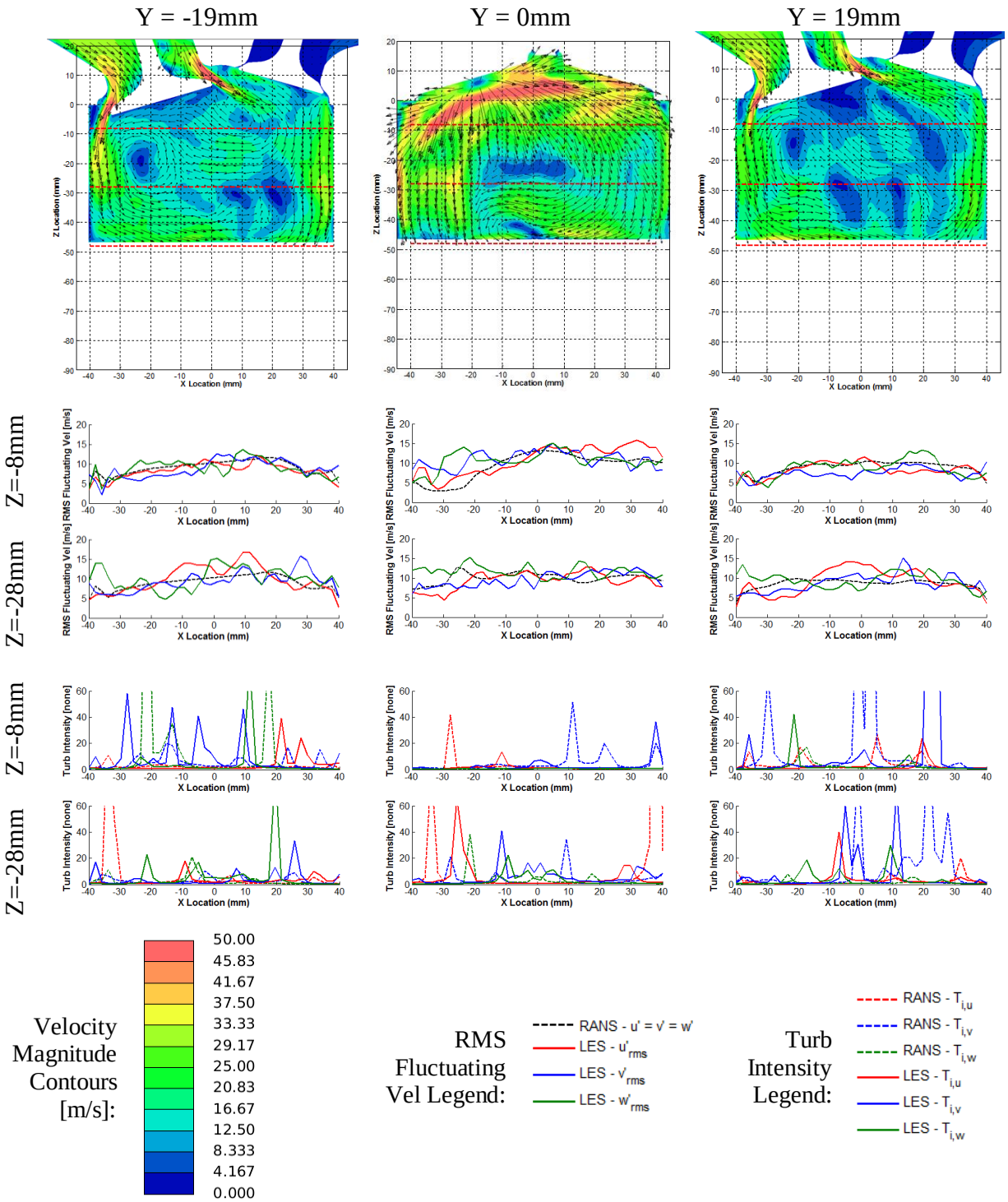

Figure 4.20 – 80°ATDC; top row are ensemble-averaged velocity magnitude contours and velocity vectors $\bar{u}$; middle row are $u'_{i,rms}$; bottom row are T_i

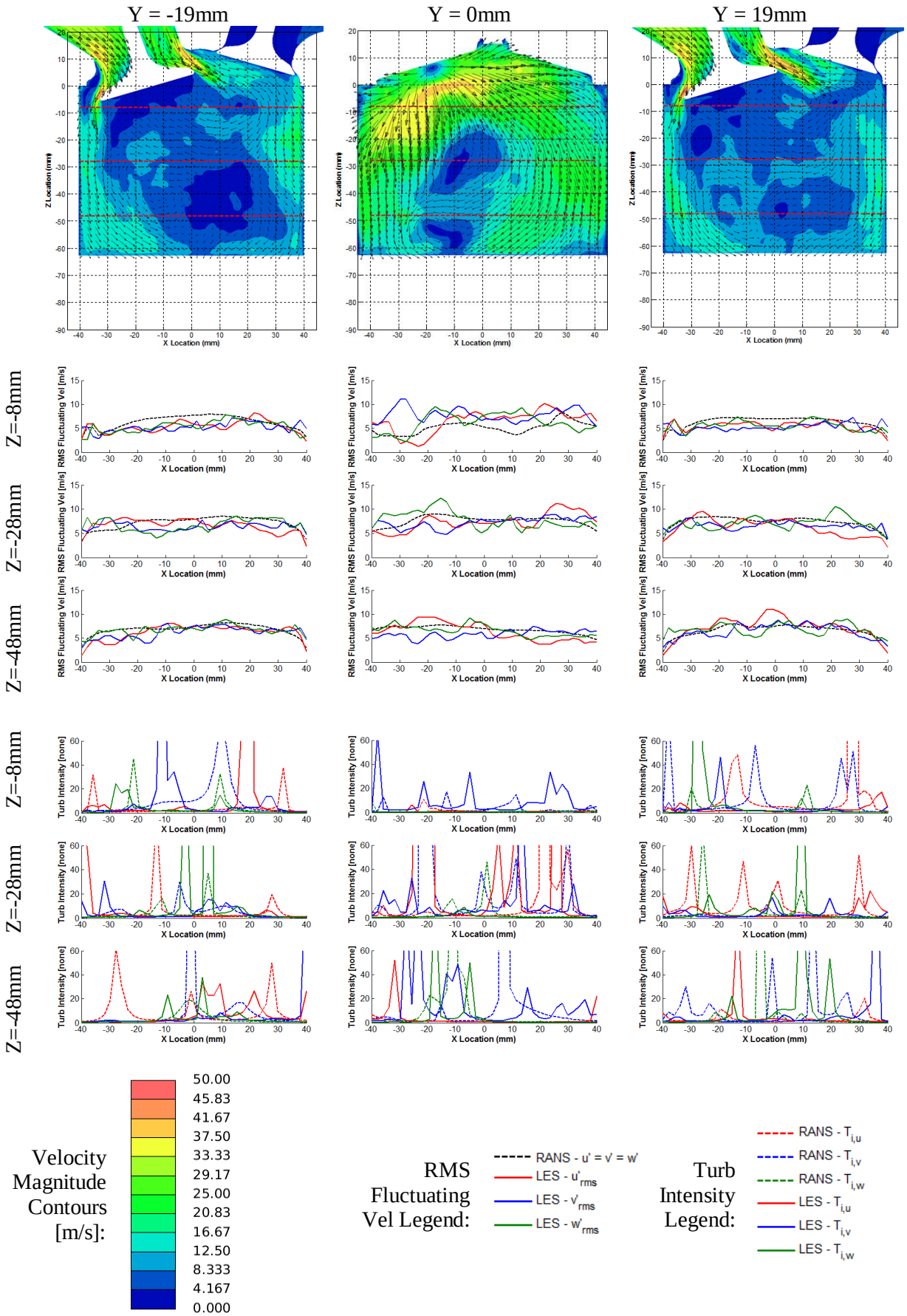

Figure 4.21 – 100°ATDC; top row are ensemble-averaged velocity magnitude contours and velocity vectors $\bar{u}$; middle row are $u'_{i,rms}$; bottom row are T_i

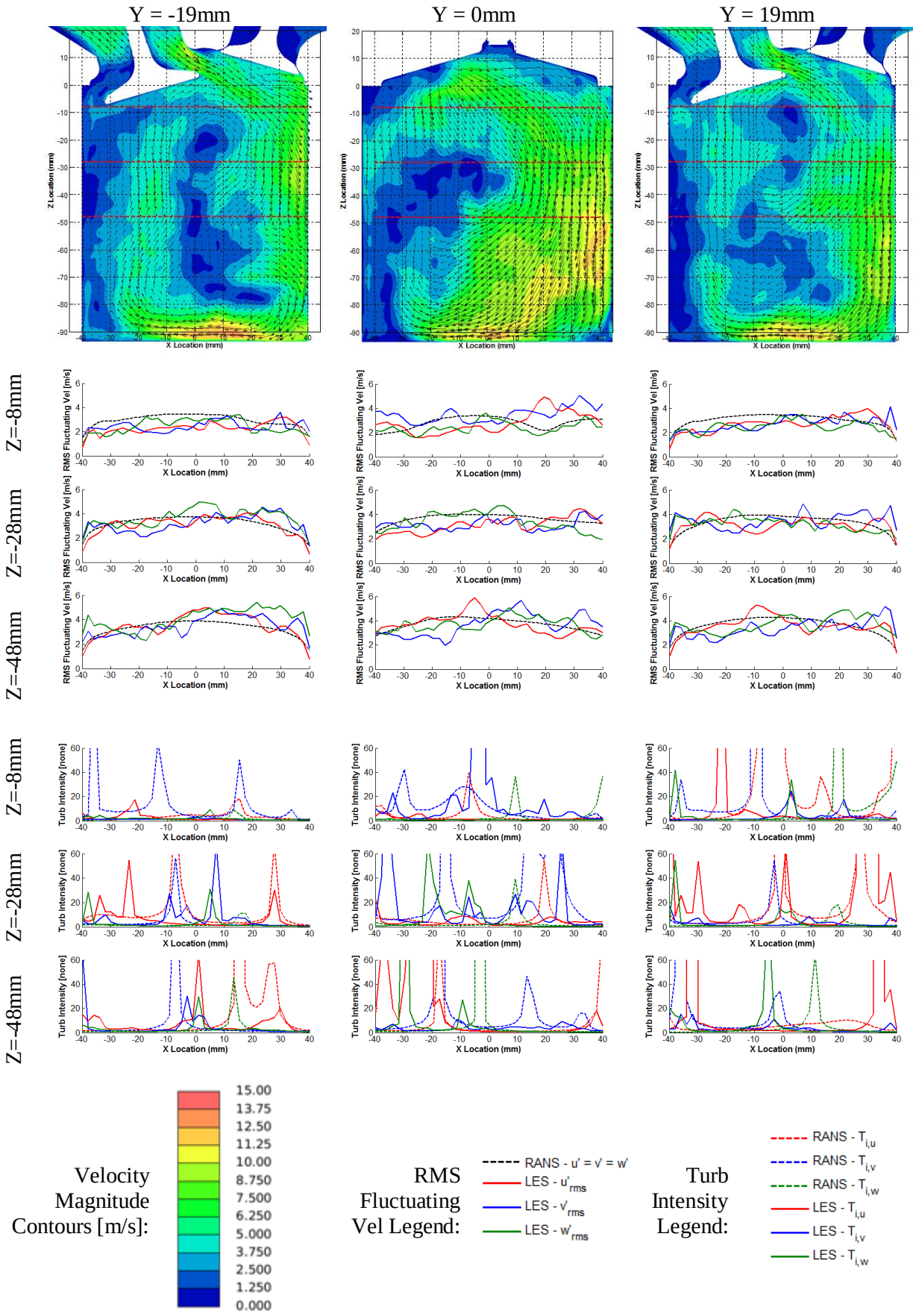

Figure 4.22 – 180°ATDC; top row are ensemble-averaged velocity magnitude contours and velocity vectors $\bar{u}$; middle row are $u'_{i,rms}$; bottom row are T_i

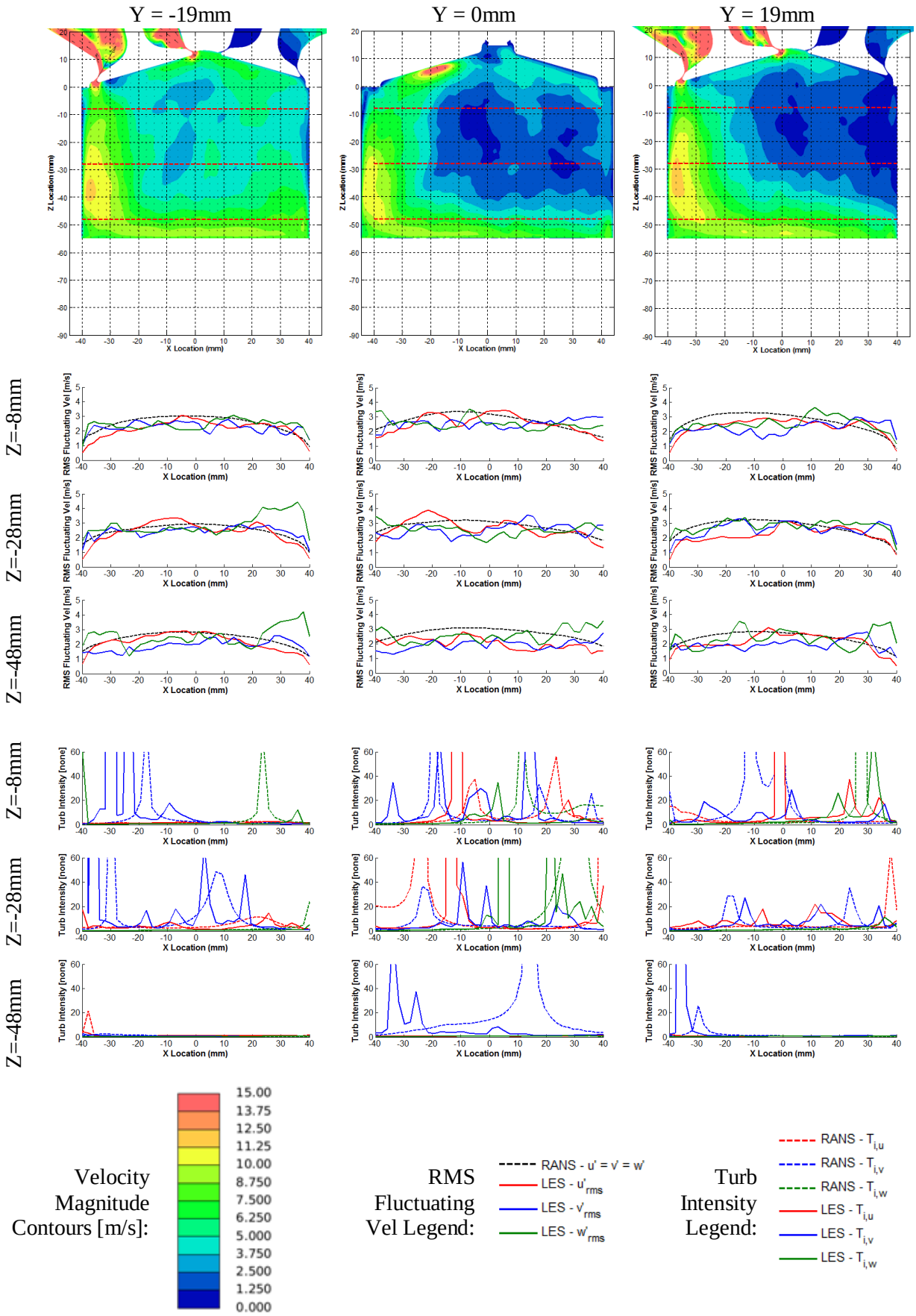

Figure 4.23 – 90°BTDC; top row are ensemble-averaged velocity magnitude contours and velocity vectors $\bar{u}$; middle row are $u'_{i,rms}$; bottom row are T_i

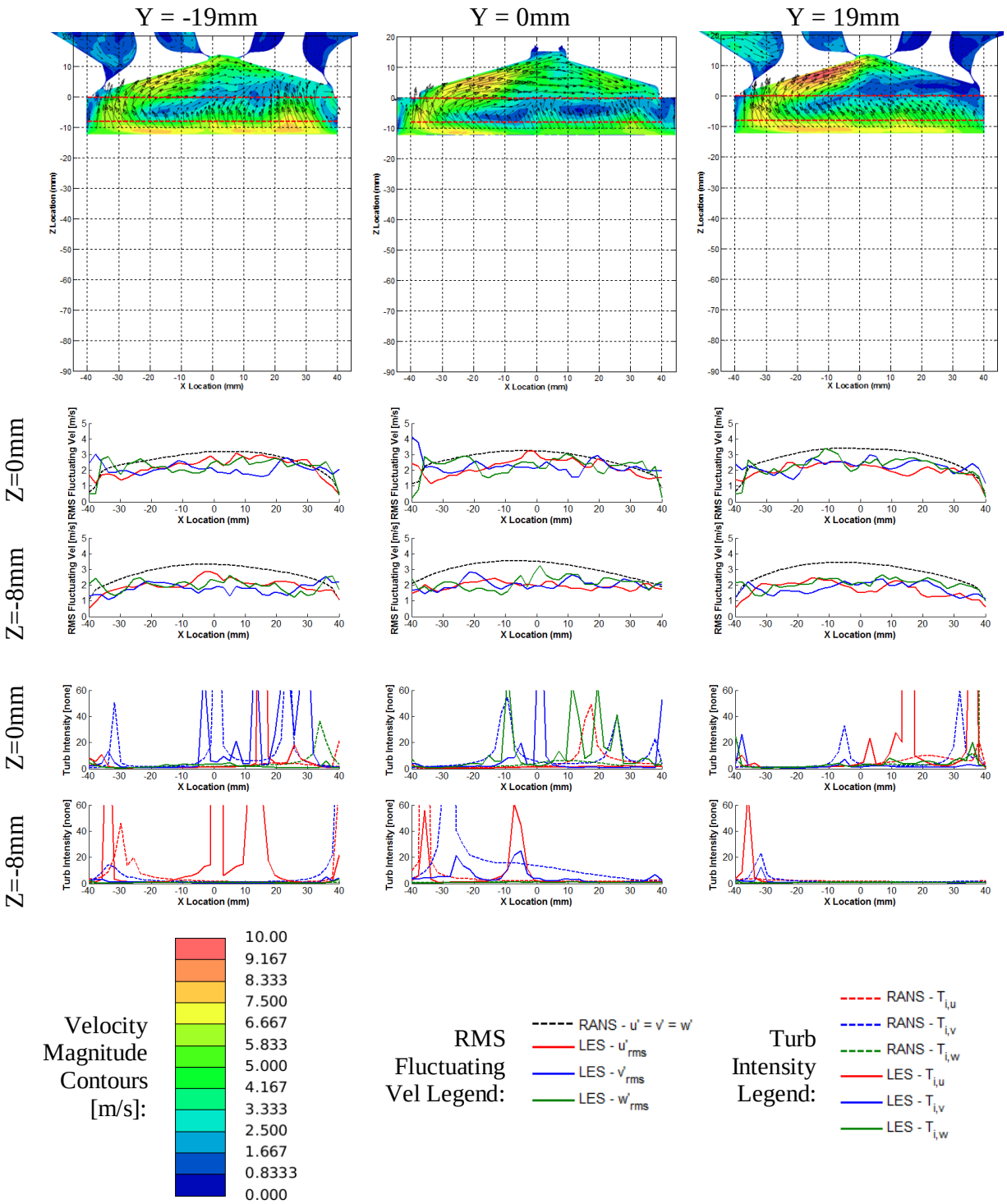

Figure 4.24 – 35°BTDC; top row are ensemble-averaged velocity magnitude contours and velocity vectors $\bar{u}$; middle row are $u'_{i,rms}$; bottom row are T_i

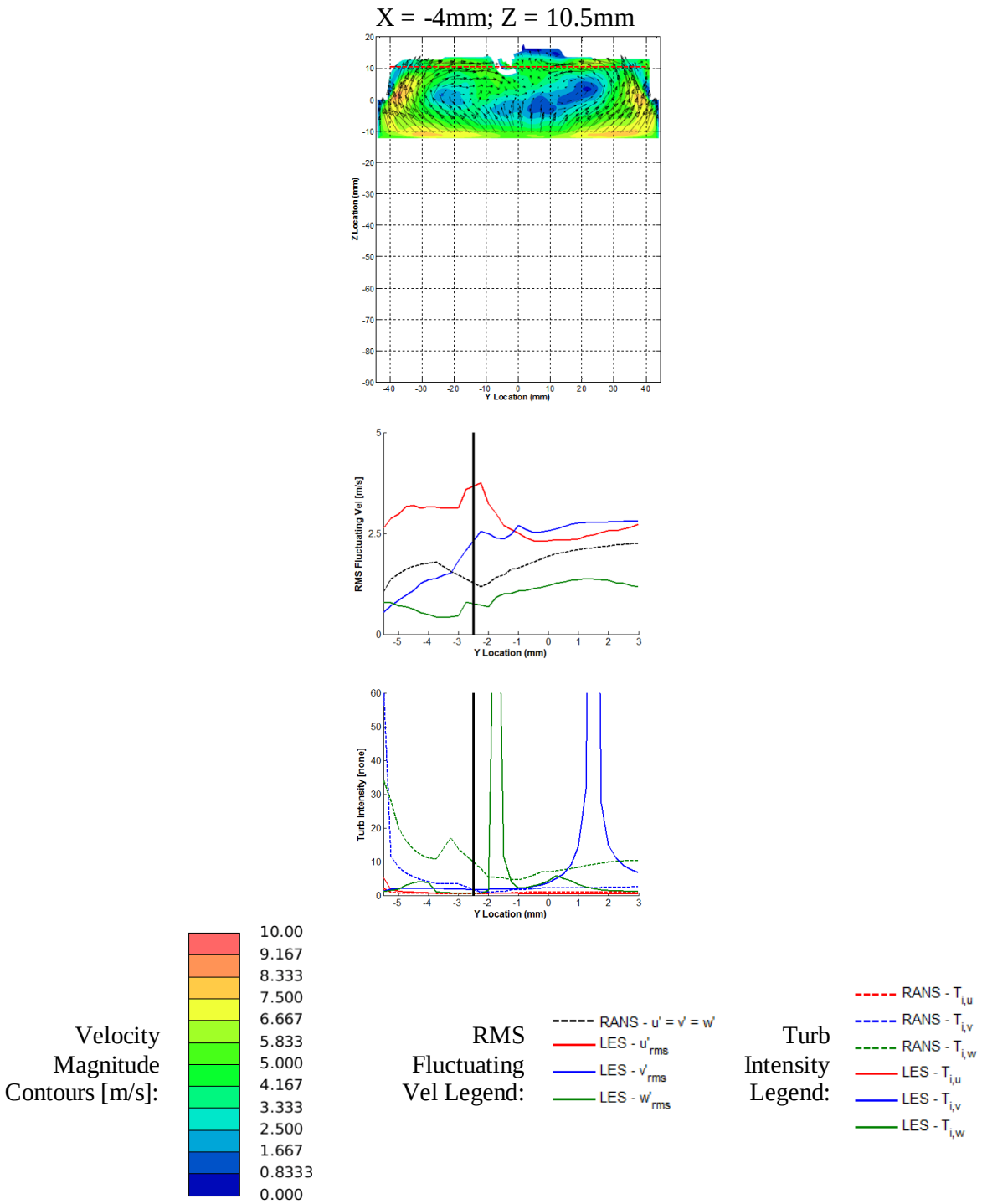

Figure 4.25 – 35°BTDC in the spark plug Y-Z plane; solid black line indicates spark plug y-location; top row are ensemble-averaged velocity magnitude contours and velocity vectors $\bar{u}$; middle row are $u'_{i,rms}$; bottom row are T_i

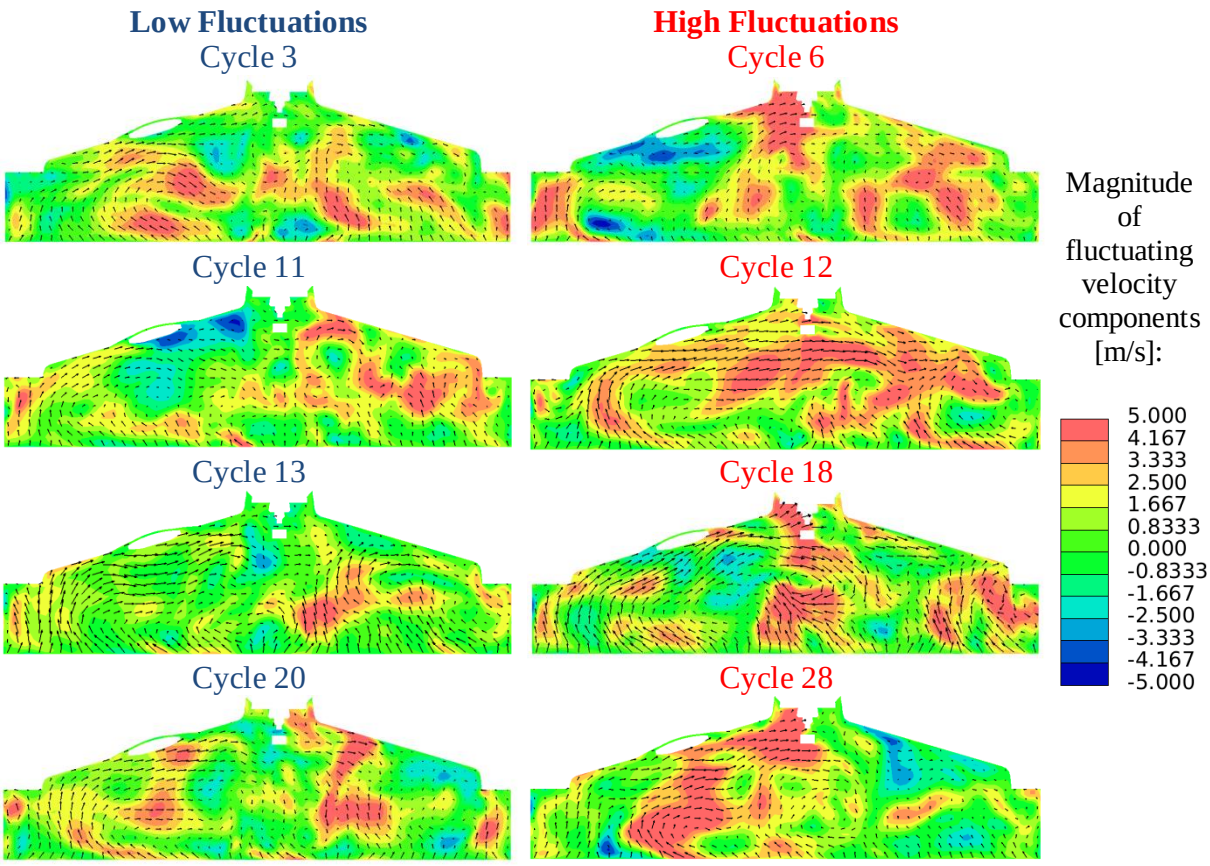

Figure 4.26 – Fluctuating velocity magnitude contours and fluctuating velocity vectors u', in the tumble plane, through the spark plug, at spark timing

To further investigate the CCV in the fluctuating velocity around the spark plug at the point of spark timing, contour plots of the magnitude of the fluctuating velocity components $\boldsymbol{u_i'}$, were plotted and cycles exhibiting low and high velocity fluctuations around the spark plug are shown in Figure 4.26. Based on these results a number of observations were made:

- Generally a clockwise rotating tumble motion remains from the intake event but significant spatial variability exists in the small scale flow structures.
- Significant small scale turbulence is visible in the vicinity of the spark plug electrodes as a consequence of the compression of turbulent length scales with the rising of the piston.
- Up 5 m/s variation in the fluctuating velocity from one cycle to the next which equates to an instantaneous velocity near the spark plug between 5-10m/s at the point of spark timing.
- Variations in the small scale flow structures near the spark plug will cause variations in the direction of the stretched flame kernel and the presence of small recirculation

regions on the exhaust (right) side of the spark plug electrodes will act to slow the propagating flame kernel. For example, cycle 11 shows a recirculation region that would divert the flame kernel up towards the roof of the combustion chamber and exhaust valves, increasing the distance for the flame to travel (and subsequently CCV) and suffer additional conduction from the flame kernel to the cylinder walls.

4.4 ANALYSIS USING PROPER ORTHOGONAL DECOMPOSITION

Traditionally, in both numerical and experimental analyses of ICE flows, results are often limited to ensemble-average and averaged-mean quantities. But as has already been seen through this chapter, the in-cylinder flow field is highly turbulent and a function of complex and highly dynamic phenomenon that vary on a cycle-by-cycle basis. Thus the use of ensemble-averaged or averaged-mean quantities, whilst convenient, does not provide a true representation of the in-cylinder flow field that occurs on a cycle-by-cycle basis and most of the information associated with cyclic variations is lost. Proper Orthogonal Decomposition (POD) has been suggested as tool for resolving the inherent problem of how to conveniently represent the data from many cycles of an in-cylinder flow field, whilst still preserving the information associated with cyclic phenomenon.

In this research, the POD technique is applied to the predicted velocity field from the LES results to:

- investigate the use of POD for quantitatively characterising the turbulent flow structures through the engine cycle,
- illustrate it as a method for quantifying the level of cyclic variability within the flow field,
- and as a means of assessing the level of statistical convergence of the ensemble-average solution based on the number of numerical cycles completed and cyclic variability present in the flow field.

The results in this section were generated using the Smagorinsky SGS model and computational setup as defined in section 3.3.3.2.

The POD methodology was first applied to turbulent flows by Lumley (1967) but the 'method of snapshots' was introduced later by Sirovich (1987) and was found to be less computationally expensive than other POD methods when applied in the context of ICE's. A brief summary of the 'method of snapshots' is now provided.

POD is the decomposition of a time dependent velocity field *u(x,t)* (or scalar distribution) into a linear combination of *M* spatial basis functions; POD modes denoted by $\psi^{(k)}(x)$ and time-dependent coefficients $a^{(k)}(t)$, as defined in equation (4.8).

$$u(\boldsymbol{x},t) = \sum_{k=1}^{M}\left(a^{(k)}(t)\cdot\psi^{(k)}(\boldsymbol{x})\right) \tag{4.8}$$

Where $k = 1, 2, \ldots, M$.

Using the 'method of snapshots', where *M* is the number of instantaneous velocity fields or snapshots (and equates to the total number of engine cycles in this case) and *N* is the spatial position within the domain, a matrix *C* can be formed as defined by equation (4.9).

$$C_{MN} = \begin{bmatrix} C_{11} & \ldots & C_{1N} \\ \vdots & \ddots & \vdots \\ C_{M1} & \ldots & C_{MN} \end{bmatrix} \tag{4.9}$$

A *M*x*M* the covariance matrix *C* is formed via $C = CC^T$. Thus the following eigenvalue equation can be solved:

$$C\cdot A^{(k)} = \lambda^{(k)}\cdot A^{(k)} \tag{4.10}$$

Equation (4.10) is solved for the *M* eigenvalues $\lambda^{(k)}$ and *M* eigenvectors $A^{(k)}$ and typically ordered in descending order to indicate the modes containing the largest fraction of the total flow field energy, where the energy content present in a particular mode is defined as the square of the modal eigenvalue.

Finally, *M* POD modes $\psi^{(k)}(x)$ are formed via equation (4.11), where each mode has the same structure as each of the snapshots of the original velocity field, and time-varying coefficients $a^{(k)}(t)$ are solved via equation (4.12).

$$\psi_d^{(k)}(x_n) = \sum_{k=1}^{M}\left(A_m^{(k)} \cdot \boldsymbol{u}_d^{(k)}(x_n)\right) \tag{4.11}$$

$$a^{(k)}(t) = \left(u^{(i)}, \psi^{(k)}\right) = \sum_{n=1}^{N}\left[\sum_{d=1}^{D}\left(u_d^{(i)}(x_n) \cdot \psi_d^{(j)}(x_n)\right)\right] \tag{4.12}$$

Where *d* is the number of dimensions and index *i* plays the role of the temporal index.

The eigenvalues (or kinetic energy) associated with each mode gives an indication of the structural complexity of the flow. When the modes are ordered by quantity of energy contained:

- A rapid decrease in eigenvalue magnitude where the majority of flow energy is contained within the first few modes characterises a flow field with large scale dominant flow structures
- A gradual decrease in eigenvalue magnitude where the majority of the flow energy is spread across many modes characterises a flow field with many weak and smaller scale flow structures.

Note that due to the temporal variation in computational domain size through an engine cycle, a 'phase-dependent' POD analysis has been applied in this research, where a new POD analysis is performed for each crank angle of interest. 'Phase-independent' POD analyses have been completed by Fogleman, Lumley, Rempfer, *et al.* (2004) but are not the subject of this study.

The POD 'method of snapshots' approach, as presented above, was applied across the 29 LES cycles through the intake and compression stroke, up to and including spark timing. Initially the number of modes required to capture 90% of the total kinetic energy is plotted for each velocity component at specific crank angles and shown in Figure 4.27.

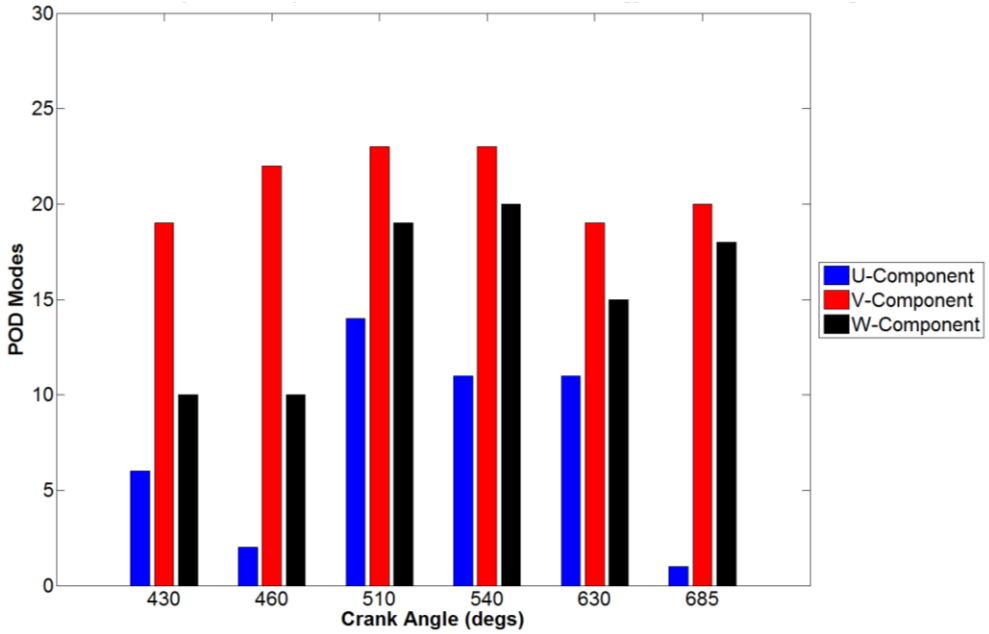

Figure 4.27 – Number of modes required to capture 90% of the flow kinetic energy for each velocity component at discrete crank angles

From Figure 4.27 it is clear that a significantly lower number of modes are required to capture the majority of the kinetic energy in the x-axis (u-velocity component); the intake port geometry and valve positioning generate a strong cross-cylinder flow field. Conversely, relatively weak flow structures are generated in the y-axis (v-velocity component) and consequently require a larger number of modes to capture the bulk of the kinetic energy. Early in the intake stroke a tumble charge motion is generated in the z-axis (w-velocity component) but this large scale flow motion is compressed and dissipated into smaller eddy length scales and less dominant flow structures during the compression stroke. Correspondingly, a lower number of modes are required to capture the majority of the kinetic energy for the W-velocity component during the intake stroke but increasing through the compression stroke up to spark timing.

In Figure 4.28, the energy captured against POD mode is shown in more detail. When examining the eigenvalue data in this manner, it is possible to deduce additional information about the structure of the in-cylinder flow field. When eigenvalue/energy data is examined in this format it is pertinent to evaluate the shape of the decay of eigenvalue/energy by POD mode; a steep gradient indicating that the majority of the energy is contained in the first mode and a strong or highly organised flow field is present, whereas a gradual gradient indicates

that the flow energy is spread across a number of modes and hence a weak or disorganised flow field is present. Based on this, it is possible to evaluate the previous conclusions with regard to strength of the flow field in each plane.

Based on Figure 4.27, it was suggested that the v-velocity component (y-axis) exhibited a weak and disorganised flow field throughout the intake and compression stroke due to the large number of modes required to capture the majority of the flow kinetic energy but upon inspection of Figure 4.28 it is clear that the flow field is perhaps more organised than originally suggested. Examining the v-component at 430°c.a. shows that whilst it does require a large number of modes to capture the majority of the flow energy, early in the intake stroke it still has a significant quantity of energy contained in the first mode, and only requires several more mode to capture 90% of the energy due to the following modes containing very little of the flow energy. Comparing the energy profile at 430°c.a. with that at 685°c.a. (spark timing), a very different energy profile can be seen. Significantly less energy is present in the first mode, with a greater quantity spread across the first seven modes. This observation suggests that the choice of fraction to define the majority of flow kinetic energy (90% in this research) can influence the conclusions drawn about the strength of the flow field and that additional information gleaned from review of the eigenvalue/energy data by mode is also useful for evaluating the in-cylinder flow field.

It is clear that the eigenvalue/energy data that is available from a POD analysis can be used to provide quantitative information about the characteristics of the in-cylinder flow field throughout the engine cycle and it is expected that this could be a useful method for quantitatively comparing an engine design:

- The expected level of charge mixing through large scale charge motion, i.e. high tumble levels could be deduced via a small number of modes to capture the majority of the flow energy and a steep drop in energy captured against POD for x- and z-axis velocity components
- The level of small scale turbulence present at the point of spark timing, i.e. high turbulence levels deduced via a large number of modes is required to capture the majority of the flow energy and gradual drop in energy capture against POD in all velocity components.

If it is assumed that at the limit where there is no CCV present in the original velocity field, the standard deviation of the time varying coefficients ($a^{(k)}(t)$) for each POD mode would

tend to zero. Hence the cycle-by-cycle variation of the time varying coefficients can be used to directly assess the CCV present within the in-cylinder flow structures.

First, the time coefficient results for velocity in the x-axis (u-velocity component) are examined, Figure 4.29(a) and (b). Early in the cycle the time coefficient for Mode 1 appears to have relatively high magnitude variation and with low standard deviation, but later in the compression stroke (around 600°c.a.) the time coefficients exhibits a significant rise in standard deviation. Mode 2 on the other hand shows significant magnitude and standard deviation most of the way through the intake stroke, rising quickly after TDC (360°c.a.) but damping out by BDC (540°c.a.) and then showing a small rise again through the mid portion of the compression stroke. Modes 3 and 4 show very similar characteristics where moderate levels of dispersion both early in the intake stroke and mid compression stroke are observed.

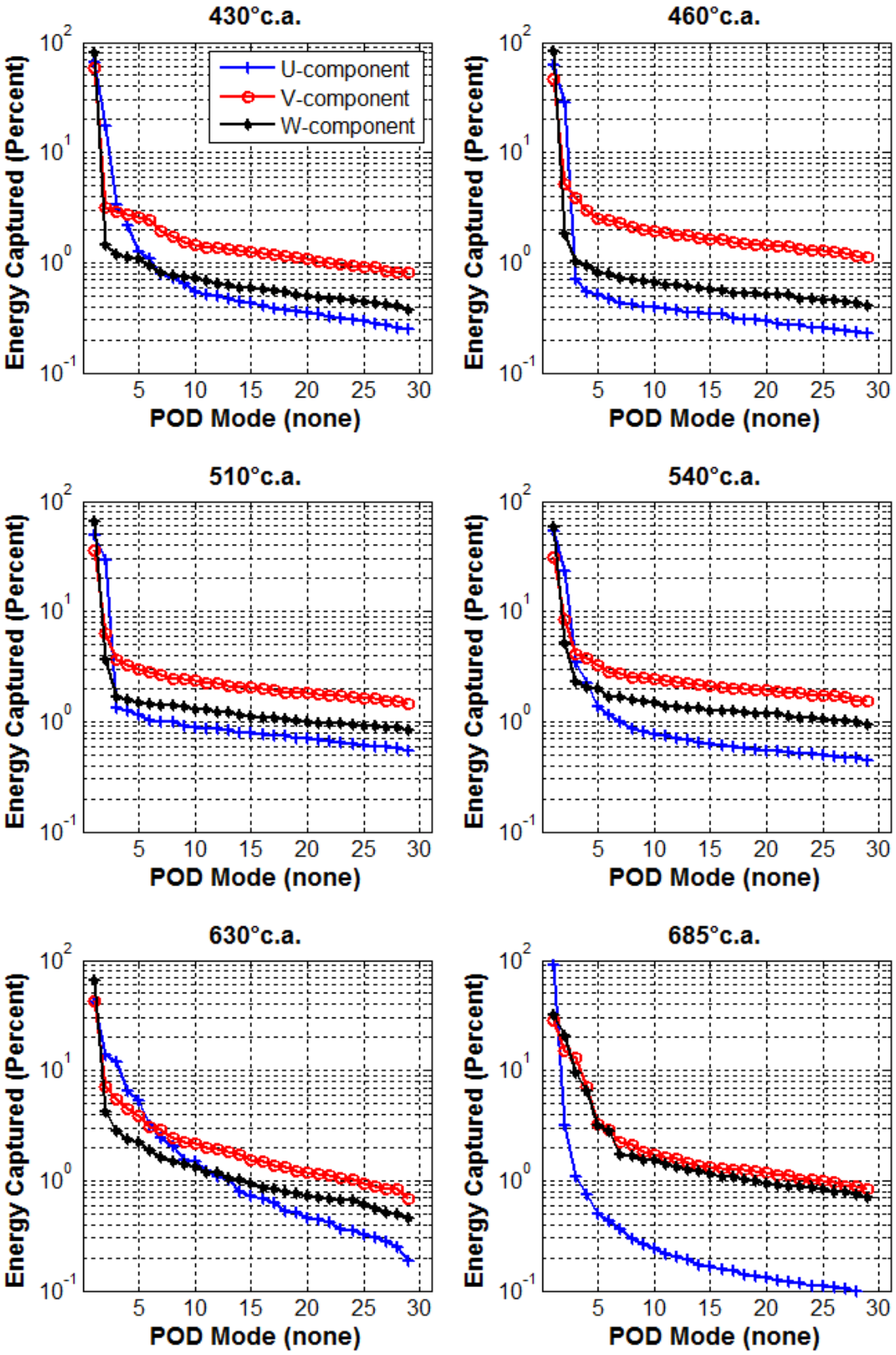

Figure 4.28 – Comparison of energy captured as a function of POD mode for each velocity component at discrete crank angles

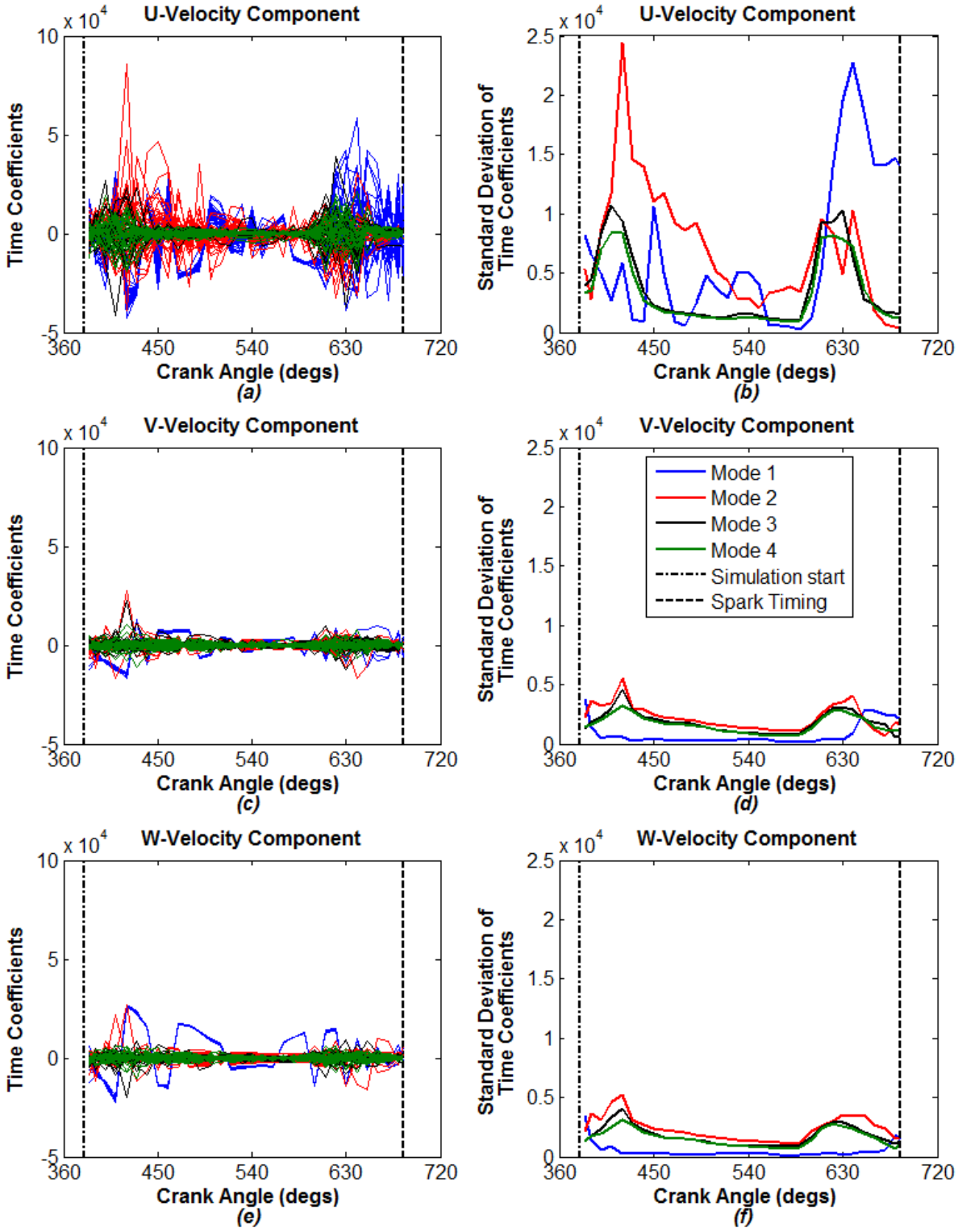

Figure 4.29 – Time varying coefficients for each velocity component: (a) (c) (e) showing the time varying coefficients, (b) (d) (f) showing the standard deviation of the time varying coefficients

When the intake valve lift profile is overlaid (shown in Figure 4.30), it is clear that that the intake valve opening and closing event is a significant driver for CCV. During the early opening period when the intake valve effective area is small, orifice discharge coefficient low and expansion ratio across the valve high, flow velocities rise quickly as the valve jet forms and begins to stabilise. As can be seen from the POD analysis, this generates significant CCV, particularly within the smaller and less dominant flow structures. This is evident from the dispersion within modes 2-4 being more significant than mode 1. During the intake valve closing period, high levels of CCV in the small scale structures becomes present again but a high level of dispersion, and hence CCV, is also seen in the larger scale flow structures (mode 1).

The coefficient dispersion in the v- (Figure 4.29 c-d) and w-velocity components (Figure 4.29 e-f) is seen to be of significantly smaller magnitude and in particular, coefficient dispersion of Mode 1 is seen to be lower than all other modes. Examining the energy content of each mode for v- and w-velocity components against crank angle (Figure 4.31 b-c), shows that mode 1 contains a significantly greater fraction of the energy content in the v- and w-velocity components than is seen in the u-velocity component (Figure 4.31 a). This agrees with previous discussions; higher modes are related to larger scale flow structures that will exhibit lower levels of CCV, hence a greater fraction of energy being present in mode 1 will contribute to overall lower levels of CCV.

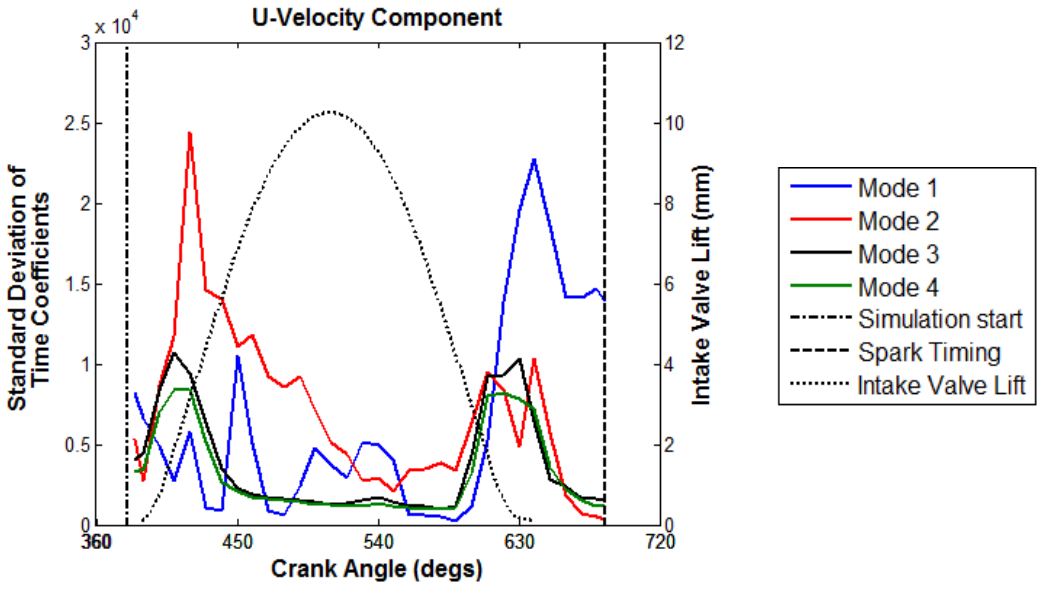

Figure 4.30 – Standard deviation of the time varying coefficients for U-velocity component with intake valve lift profile overlaid

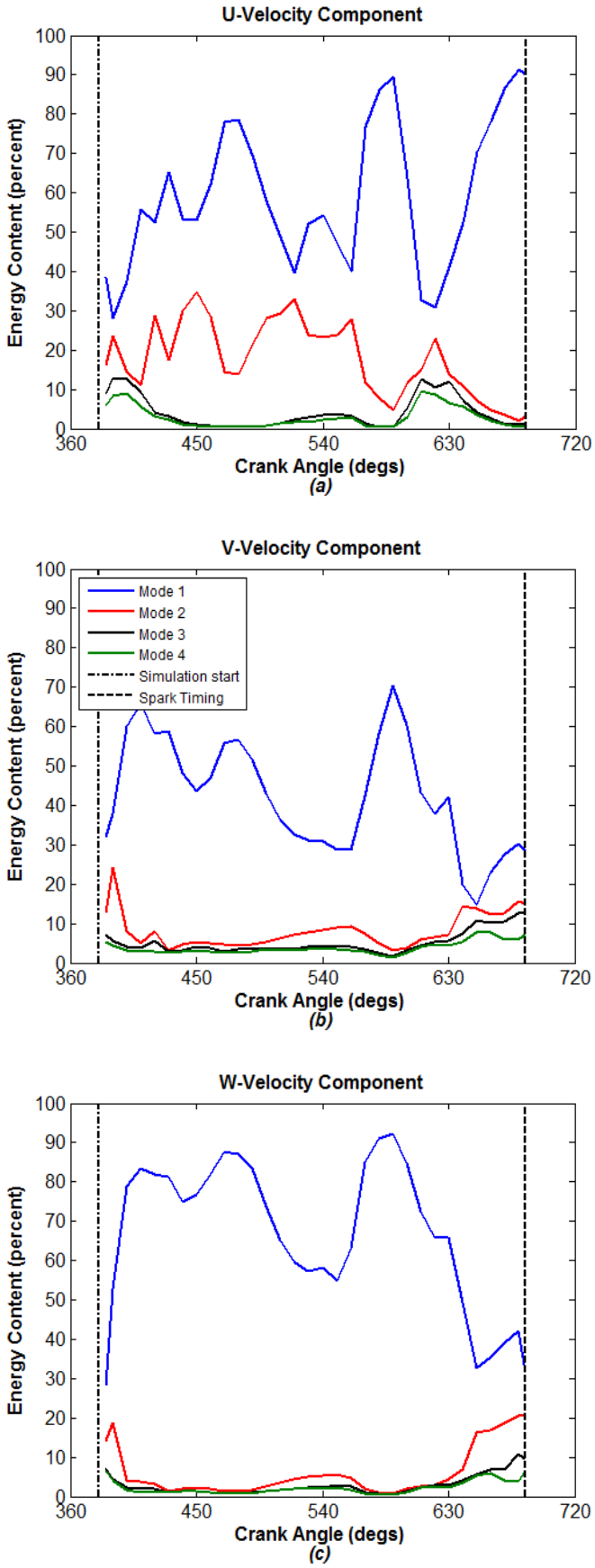

Figure 4.31 – Energy content as a function of crank angle for each velocity component

Using the time varying coefficients directly to assess the total level of CCV present must be done cautiously since the level of CCV present in each mode is a function of both the magnitude of time varying coefficient and the total fraction of energy present in that particular mode.

Fontanesi, Paltrinieri & Cantore (2014) proposed the use of the of a 'CCV RMS Index' as a method of examining the variation in CCV through an engine cycle by summing the root mean square of the energy weighted time varying coefficients. This approach has been applied to the data presented here and the method used for calculating individual modes '$CCV_{index\_rms,M}$' and the overall '$CCV_{index\_rms,Overall}$' is shown in equations (4.13) and (4.14), the results of which are shown for each velocity component in Figure 4.32.

$$CCV_{index_{rms,M}} = \sqrt{\frac{1}{k}\sum_{k=1}^{M}(a^{(k)}(t) - \langle a^{(k)}(t)\rangle)^2} \cdot \frac{\lambda^{(k)}}{\sum_{k=1}^{M}\lambda^{(k)}} \tag{4.13}$$

$$CCV_{index_{rms,Overall}} = \sum_{k=1}^{M}\left[\sqrt{\frac{1}{k}\sum_{k=1}^{M}(a^{(k)}(t) - \langle a^{(k)}(t)\rangle)^2} \cdot \frac{\lambda^{(k)}}{\sum_{k=1}^{M}\lambda^{(k)}}\right] \tag{4.14}$$

The results again indicate that a greater level of CCV is present in the u-velocity component (x-axis) and, similarly to previous findings and expectation:

- CCV is highest around TDC when length scales are most wall bounded and during the intake valve opening and closing event when large changes in effective flow area generate valve jet CCV
- CCV is lowest around BDC when flow structures are least wall bounded and large scale structure less susceptible to CCV are able to form

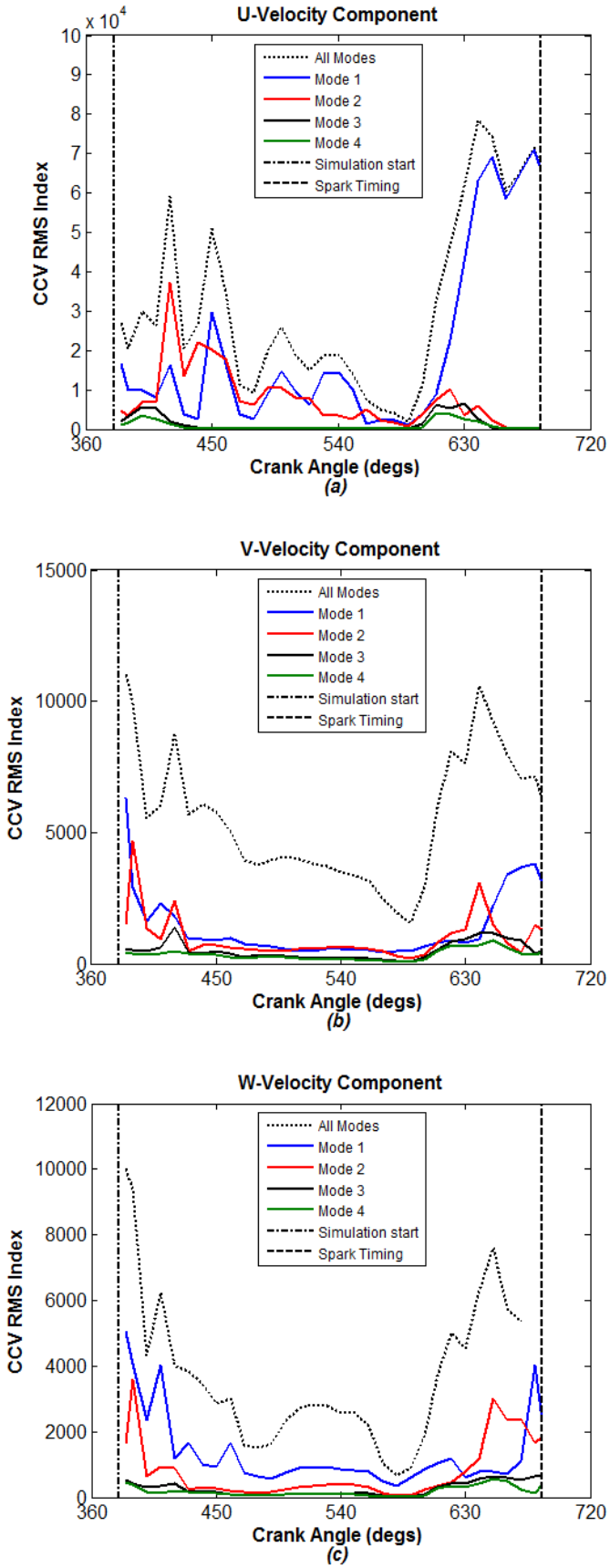

Figure 4.32 – CCV RMS index as a function of crank angle for each velocity component. Note: different y-axis scales used to improve figure clarity

In Liu & Haworth (2011) it was proposed that the eigenvalue/energy data could be used as a means to deduce the level of statistical convergence of the ensemble-average solution by comparing the eigenvalue/energy content by mode for a varying number of snapshots. Once the curves for a certain number of snapshots overlaid, it could be deduced that there were sufficient snapshots/cycles to provide a statistically representative ensemble-average of the in-cylinder flow field. This approach has been applied in this research at:

- 460°c.a. – intake stroke, many large scale turbulent structures, less CCV present
- 685°c.a. - spark timing, predominantly small scale structures, high CCV present

As seen in Figure 4.33, the results indicate that the dominant flow structures present in the x-axis (u-velocity component) require a smaller number of cycles to achieve statistical convergence, with 25 and 29 snapshots having effectively converged at both crank angles examined here. Due to the weaker and smaller length scale structures present in the y- and z-axes, greater dispersion is present between the series and none appear to converge for the number of snapshots presented here. This is not surprising since the engine in question was known to exhibit high levels of CCV and the experimental procedure typically included capturing 100-120 engine cycles to better ensure statistical convergence, and other experimental studies have even indicated the need for 600-1200 cycles to capture the full range of the CCV.

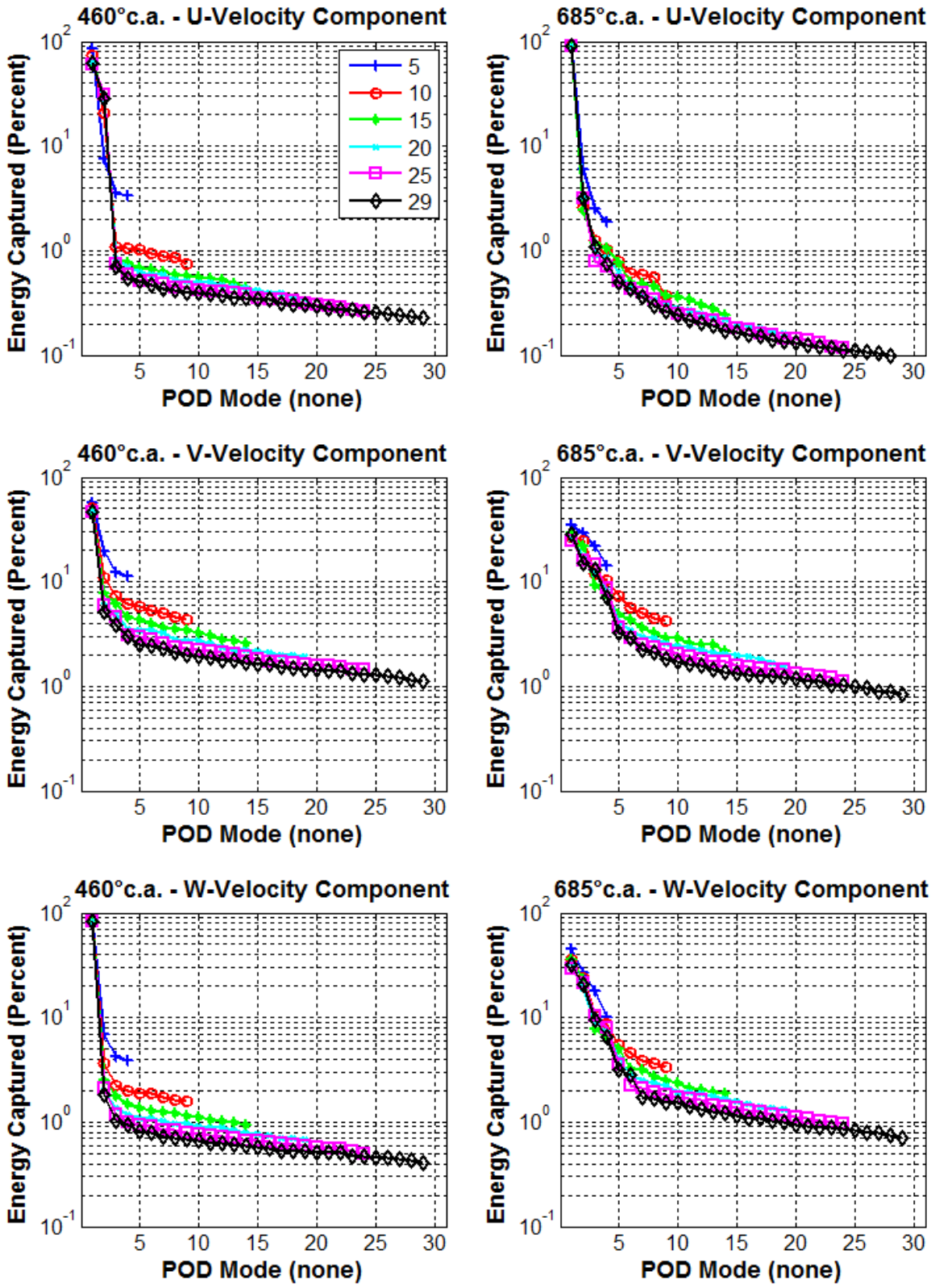

Figure 4.33 – Comparison of energy captured as a function of POD mode with a varying number of snapshots for each velocity component at 460°c.a. and 685°c.a.

4.5 CONCLUDING REMARKS

This chapter has presented the results from a number of numerical investigations into the physical processes occurring in the in-cylinder flow field in the single cylinder optical research engine, using both the RANS and LES turbulence modelling techniques.

The chapter begins by presenting the identification of a number of in-cylinder flow structures present within the intake stroke that are highly transient and heavily influenced by their interaction with the moving solid boundaries within the combustion chamber.

Following this was the investigation of the effect of the pent-roof optical access window on the in-cylinder flow field. A number of flow asymmetries and the presence of additional recirculation zones were identified as a consequence of the geometry, and considerations presented for the use of a pent-roof optical access window in experimental research.

The highly three-dimensional nature of the in-cylinder flow field was investigated via the use of multiple cutting planes and vorticity contours. The intake valve jet was found to spatially vary significantly, with variations in penetration and velocity at different points in the combustion chamber. Areas of highly three-dimensional flow were also identified via areas of high vorticity; within the cylinder interior due to swirling flow structures, and around the intake valve jets and solid boundaries due to shear flows.

Intake valve jet flapping was investigated and found to be due to a transient valve curtain mass flux imbalance that initiates valve jet instability and the subsequent sinusoidal motion called flapping. Significant cyclic variability was observed in both the magnitude and phasing of the valve curtain mass flux imbalance, which results in variations in both frequency and penetration of the resultant flapping valve jet. Due to the significant cyclic variability, the impact of using an ensemble-averaging procedure was seen to cause most of the information associated with the phenomenon to be lost. A RANS solution was shown to capture the phenomenon, but due to the time-averaging process used in the RANS turbulence modelling approach, all cyclic variability associated with the phenomenon is lost.

The fluctuating velocity and turbulence intensity was compared to the mean flow field at multiple cutting planes through the intake and compression strokes up to the point of spark

timing, to investigate the development of the flow field and turbulence characteristics. A number of anisotropic effects were observed from the turbulent fluctuations, including:

- Comparatively high fluctuations in the y-plane as a consequence of intake valve jet flapping
- Increased fluctuations in the z-plane close to the piston crown due to the rising piston crown causing flow to impinge on a tumbling flow structure setup by the preceding intake event
- A rise in turbulent fluctuations as a consequence of the spark plug electrode geometry was observed which is expected to be a contributor to the overall CCV of the combustion process.

Turbulence intensity was used due to it providing information on the relative significance of the turbulent fluctuations in relation to the mean flow field. In particular, whilst the mean flow in the y-plane was small in comparison to the x- and z-planes due to the predominant tumble motion, fluctuations in all three planes produces areas of turbulence intensity in the y-plane that would also promote diffusion and mixing across the cylinder.

Proper Orthogonal Decomposition was applied to the velocity field to investigate its ability to quantitatively characterise the turbulent flow field. The energy spread across modes was seen to be capable of providing details of the characteristics of the flow structures, relative dominance of flow structures in each plane and thus their susceptibility to CCV. The modal energy data was combined with the time-dependent coefficients and found as a very effective method of quantitatively evaluating CCV through the engine cycle and the intake valve opening and closing event was seen as a key driver for CCV. It was also seen how the number of snapshots could be varied as a means of evaluating the level of statistical convergence of the ensemble-average result, based on the number of cycles compared and level of CCV present within the flow field.

CHAPTER 5

INVESTIGATIONS INTO THE FUEL INJECTION PROCESS

"I am not discouraged, because every wrong attempt discarded is another step forward."

–Thomas A. Edison

5.1 INTRODUCTION

This chapter presents the results from a number of numerical analyses investigating the fuel injection process. The analyses use a combination of both the RANS and LES turbulence modelling approaches, and the use of single- and multi-component fuel surrogates, as described earlier and validated in Chapter 3.

The first section shows results for the fuel impingement and liquid film development processes for the impingement of the intake valve, cylinder liner and piston crown, including analyses into the cycle-to-cycle variations.

The second section shows results for the characteristics of the fuel-air mixture field, focusing on the evolution through the intake and compression strokes up to the point of spark timing, differences in the predicted mixture field when modelling either a single- and multi-component surrogate fuel, CCV of the mixture field at spark timing and potential causes for

the variability, and intake valve jet flapping as a precursor to CCV of the mixture field at spark timing.

In the final section, results on the interactions between the fuel injection event and the in-cylinder turbulence characteristics are presented and discussed, showing the impact of the fuel injection event on in-cylinder turbulence characteristics and limitations of using the Boussinesq assumption for correctly predicting turbulence characteristics up to spark timing..

5.2 FUEL IMPINGEMENT AND LIQUID FILM DEVELOPMENT

The impingement of liquid fuel on solid surfaces in ICE's is an important research interest due to its effect on the resultant mixture characteristics, and hence combustion efficiency and pollutant formation. In port fuel injected (PFI) gasoline engines, research has focused on the impingement of the liquid fuel on the intake port and back of the intake valve head, particularly with respect to the transient control of the combustion system (Stanton & Rutland, 1998; O'Rourke & Amsden, 1996). In direct injection diesel engines, high fuel injection pressures to improve fuel atomisation can lead to high levels of impingement and the formation of liquid films on the piston and cylinder wall, leading to reduced efficiency and increased emissions, particularly during cold start conditions (Senda, Kobayashi, Iwashita, *et al.*, 1994; Senda & Fujimoto, 1999; Yang & Ghandhi, 2007). The increasing use of GDI engines over PFI engines for improvements in efficiency, pollutant formation and transient control, has led to further research in this area. Similarly due to its important role in pollutant formation in the form of PM and UHC, but also due to its influence on the spatial and temporal variation in the mixture field evolution which becomes increasingly important as the complexity of mixture control strategies increases, with stratified mixtures within GDI engines being pursued for further improvements in engine efficiency and reduced pollutants (Serras-pereira, Aleiferis, Richardson, *et al.*, 2007; Malaguti, Cantore, Fontanesi, *et al.*, 2009; Drake, Fansler, Solomon, *et al.*, 2003; Schulz, Schmidt, Kufferath, *et al.*, 2014; Stevens & Steeper, 2001). But due to the differences in injection pressures, spray patterns and fuel atomisation characteristics between diesel engines and GDI engines, further research is required to characterise the impingement process in GDI engines so that improvements in

engine design can be realised to eliminate or mitigate the negative consequences of liquid fuel impingement.

The section presents results for: (1) impingement characteristics and liquid film development and (2) the CCV of impingement and film formation.

5.2.1 Impingement and Liquid Film Development

Through the experimental studies of Serras-pereira, Aleiferis, Richardson, *et al.* (2007), Serras-Pereira, Aleiferis & Richardson (2012) and Rimmer (2011) and the current research, three spray impingement locations have been identified for the engine that is the subject of this research: intake valve, cylinder liner and piston crown, as shown by Figure 5.1.

.

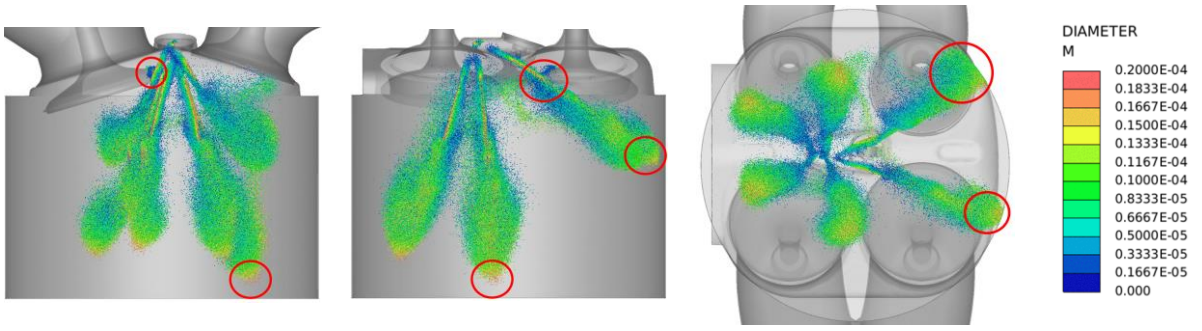

(a) (b) (c)

Figure 5.1 – Predicted spray plumes at 14°ASOI in (a) tumble plane (x-z), (b) front-to-rear plane (y-z), (c) swirl plane (x-y), with droplets coloured by diameter and intake valve, cylinder liner and piston crown impingement locations highlighted by red circles

In this section, two instances of impingement are discussed in detail; impingement of plume 1 on the intake valve and impingement of plume 6 on the cylinder liner. Before evaluating each impingement location in detail, it is useful to evaluate the expected impingement regime within the impingement model.

The regime within the impingement model is defined based on parameter T^* (equation (4.18)), which was calculated for the different fuel components and surfaces within the combustion chamber and shown in Table 5.1.

Table 5.1 – Calculated values of T* for each fuel component impinging on the different solid surfaces within the combustion chamber

Fuel component	T_W [K]	T^*	T_W [K]	T^*	T_W [K]	T^*	T_W [K]	T^*
Iso-Pentane	363 (Exhaust Valve and Head)	0.953	323 (Intake Valve)	0.485	301 (Piston)	0.228	293 (Cylinder Liner)	0.134
Iso-Octane		0.141		-0.32		-0.574		-0.666
n-Decane		-0.809		-1.338		-1.629		-1.735

Upon inspection of Table 5.1, it is clear that for a single-component fuel of iso-octane, droplets will be in the free convection and nucleate boiling regime ($T^*<0$) for impingement on the intake valve and cylinder liner (surface temperatures, Tw of 323K and 293K respectively).

For the multi-component fuel the situation is more complex since each droplet is made up of a fraction of three components. Unfortunately, due to restrictions in the code used, there is no method for determining the instantaneous fraction of a given component in each droplet and hence deduce the T* value of impinging droplets. That being said, it is expected that by 6°ASOI (the point of intake valve impingement) a significant fraction of iso-pentane will have evaporated from the injected droplets, and since the iso-pentane fraction accounts for only 1/3 of the total mass fraction at the inception of each injected droplet, the majority of the droplets impinging on the intake valve will also fall within the free convection and nucleate boiling regime ($T^*<0$). Impingement on the cylinder liner is far later in the injection process hence an even smaller quantity of the iso-pentane fraction is expected to remain and the majority of impinging droplets will also be within the free convection and nucleate boiling regime ($T^*<0$).

Based on the range of values for T*, it is clear that no droplet in either the single- or multi-component fuel cases will impinge in the film boiling range ($T^*>1$).

5.2.1.1 Intake Valve Impingement

From results shown in Figure 5.2 and using equations 4.20, 4.21 and 4.22, it is possible to calculate the critical Weber number (We_{cr}) at a number of key points within the impingement process, shown in Table 5.2. Due to the impinging droplets covering a range of Weber numbers and Laplace numbers, the critical Weber number was calculated at approximate upper and lower values to provide an expected range of We_{cr}.

Table 5.2 – Table shows the range of droplet Weber and Laplace numbers and calculated We_{cr} through the intake valve impingement process for droplets from the multi-component surrogate

Time [°ASOI]	Comments	We		La		We_{cr}	
		Upper	Lower	Upper	Lower	Upper	Lower
5	Pre-impingement	5000		1200		524	
6	Immediately post initial impingement	3000	2000	1000	500	624	544
9	Immediately prior to film formation	1200	600	900	600	602	555
10	First crank angle of film formation	1000	600	800	400	653	569
13	Splitting of plume due to impingement on top of valve head	1200	600	700	400	653	584

Figure 5.2 shows the spatial development of plume 1 impingement on the intake valve with the multi-component fuel surrogate and the following is a discussion of the observations made.

At 5° and 6°ASOI the Weber number of the impinging droplets are all significantly greater than the Weber number needed for the generation of a liquid film ($We \leqslant 400$) hence splash off the surface.

By 9°ASOI, the Weber number of the impinging droplets has reduced considerably. The table above shows a lower Weber number of 600 but based on a velocity of 50m/s, any droplet of ~4μm or less will have a Weber number less than 400 and hence be deposited on the surface.

By 10°ASOI there are sufficient deposited droplets that the surface coverage ratio is exceeded and a liquid film has formed. Once a film has formed, the regime for splashing or deposition is defined based on the critical Weber number We_{cr} which, based on Table 5.2, will be in the region of $570<We_{cr}<650$. Thus once a liquid film has formed, it will quickly grow due to the larger Weber number criteria and greater proportion of smaller, lower Weber number droplets.

At 13°ASOI the descending intake valve causes the plume to be split by the edge of the valve head and droplets be deflected beneath and above onto the top surface of the valve head. As a consequence of the sudden reduction in velocity of droplets impinging the top surface, a liquid film is rapidly formed. Movement of the film across the surface also occurs due to imparted momentum by the spray.

There is evidence of a large number of droplets being stripped from the liquid film due to charge motion over the valve head edge, indicated by the large slow moving droplets shown in Figure 5.3 at 19°ASOI. This process is of significance due to the size and velocity of the new droplets; most in the region of 100-300μm but some >500μm. Figure 5.4 shows droplets still being stripped from the intake valve head much later in the cycle at 115°BTDC, i.e. late into the compression stroke which, due to the reducing turbulence, will take a significant period of time to evaporate and likely become a source of UHC and PM emissions.

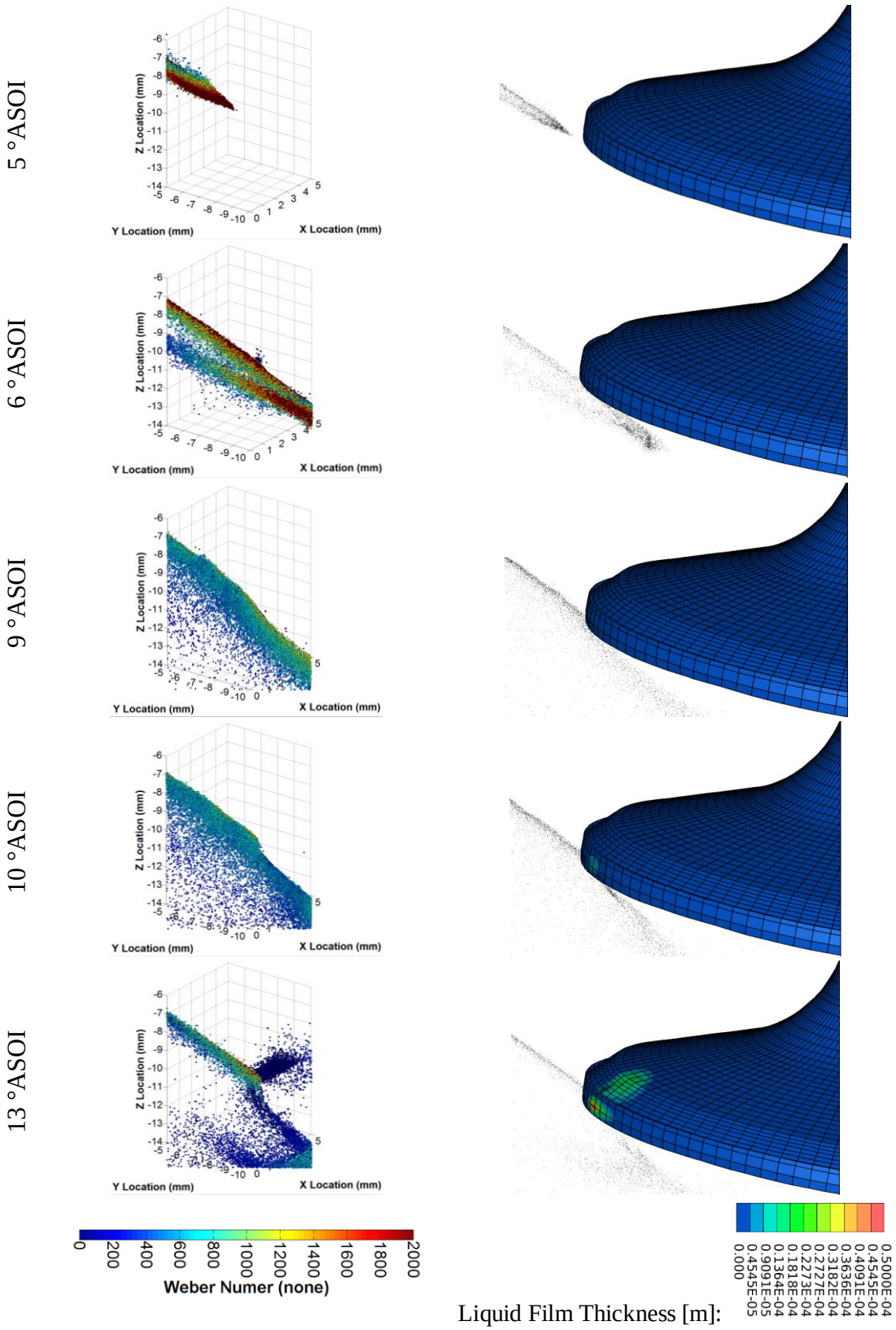

(a) (b)

Figure 5.2 – Spatial development of plume 1 intake valve impingement with the multi-component surrogate, (a) Droplets coloured by droplet Weber number and the intake valve geometry is not shown for clarity, (b) Contours of liquid film thickness with the droplet size significantly reduced to improve clarity

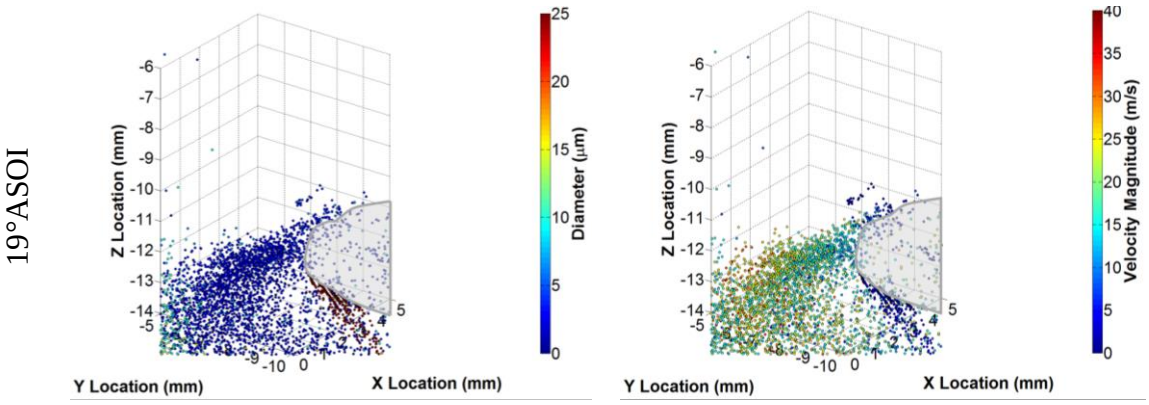

Figure 5.3 – Images illustrate the presence of very large and slow moving droplets formed underneath the valve head due to film stripping over the sharp edge of the intake valve head at 19°ASOI with multi-component surrogate. Droplets in (a) are coloured by droplet diameter and in (b) are coloured by droplet velocity magnitude with the valve head outline shown in grey

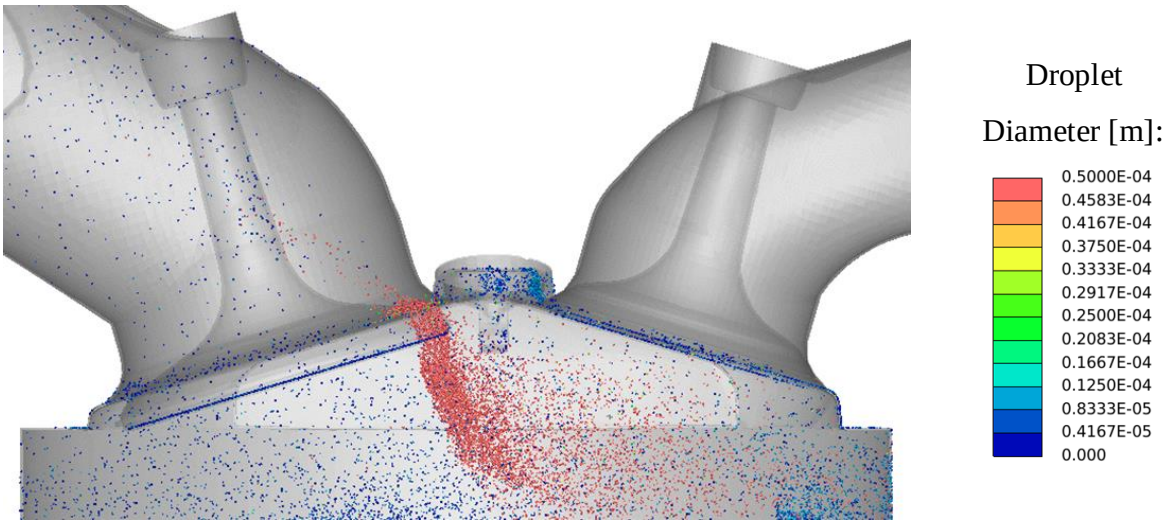

Figure 5.4 – Image illustrates droplets being formed due to film stripping from the intake valve head in the compression stroke at 115°BTDC for the multi-component surrogate, droplets coloured by droplet diameter

When comparing predictions between the single- and multi-component fuel predictions, a difference of note is the larger predicted film thickness for the multi-component fuel case. As shown in Figure 5.5 at 14°ASOI, the film thickness formed on the side of the intake valve in the single-component fuel case is predicted to be ~20 microns but is predicted to be ~50 microns with the multi-component fuel. This is due to the presence of the heavier n-decane

fraction in the multi-component fuel reducing the number of droplets that have evaporated prior to impingement, thus increasing the number of droplets reaching and impinging on the intake valve and available to contribute to the liquid film.

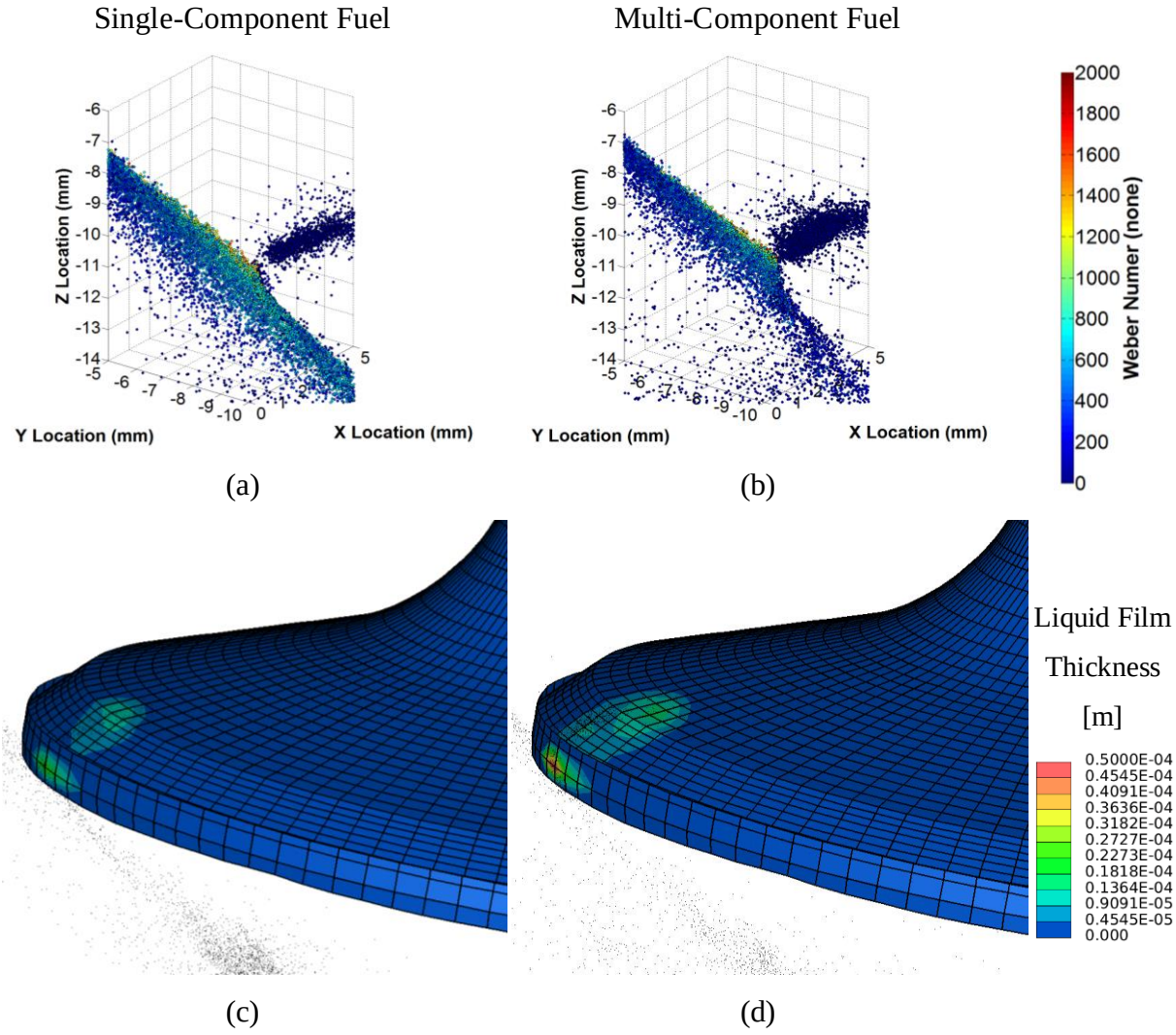

Figure 5.5 – Figure compares the intake valve impingement location and liquid film thickness for single- and multi-component fuel at 14°ASOI. In upper images droplets are coloured by droplet Weber number and lower images show contours of liquid film thickness

Another observed difference between the predictions for the multi- and single-component fuel cases is the location of impingement. Figure 5.5(a) and (b) compare the impinging droplets at 14°ASOI. Recall Figure 5.2 at 6°ASOI for the multi-component fuel, the spray plume enters the visualised domain at approximately z=-7.2mm whereas by 14°ASOI (Figure 5.5(b)) the plume enters the domain at approximately z=-6.8mm, displaced towards the

cylinder head by the in-cylinder charge motion. This is thought to be due to the presence of the lighter iso-pentane fraction within the multi-component fuel, allowing the droplets to be more easily influenced by the momentum of the in-cylinder flow field. The single-component fuel (Figure 5.5(a)) in contrast, due to only containing a single component of iso-octane, is less influenced by charge motion. The onset from this is that towards the end of injection process the multi-component fuel predicts a greater proportion of fuel to be injected directly onto the back on the intake valve head, causing a difference in film formation between the two cases. Figure 5.5(c) and (d) show the film thickness for single- and multi-component fuels. It is clear that in the case of the multi-component fuel, a larger and thicker liquid film is formed on the top of the valve head compared with the single-component fuel. Thus the prevalent film stripping and child droplet formation processes will be different for the single- and multi-component fuel cases; predominantly stripping over a sharp edge for the single-component fuel and a greater number of child droplets formed via flow induced wave instabilities over the valve head surface for the multi-component fuel. This impacts the droplet size distribution and subsequent fuel-air mixture through the remainder of the intake and compression strokes.

5.2.1.2 Cylinder Liner and Piston Crown Impingement

Prior to investigating the cylinder liner liquid film development, an additional validation exercise was completed on the cylinder liner impingement process.

Three different pieces of experimental data were used to support this validation exercise: (1) quantitative data from a heat flux sensor study and (2) qualitative mean spray images were used to validate the timing and location of impingement, and (3) a high resolution instantaneous spray image was used to help validate the subsequent plume tip motion following liner impingement.

Figure 5.6 reproduces the pertinent results from the heat flux sensor study by Serras-pereira, Aleiferis, Richardson, *et al.* (2007) where a heat flux sensor was placed at consecutive positions around the periphery of the cylinder bore at approximately 17mm below the head gasket plane. The resultant data from the heat flux sensor provides information on the predominant impingement location and timing for plume 6. Upon inspection of these

experimental results, it is clear that with iso-octane and for a fuel temperature (T_f) of both 363K and 293K, plume 6 predominantly impinges the liner between 30°-50° to the horizontal and at approximately 15°ASOI.

Note: Data at T_f=293K was included in Figure 5.6 since it indicates that the impingement location and timing varies little between T_f=293K and T_f=363K which allows comparison of the predicted results with the second and third experimental images with more confidence, since these images are only available at T_f=293K.

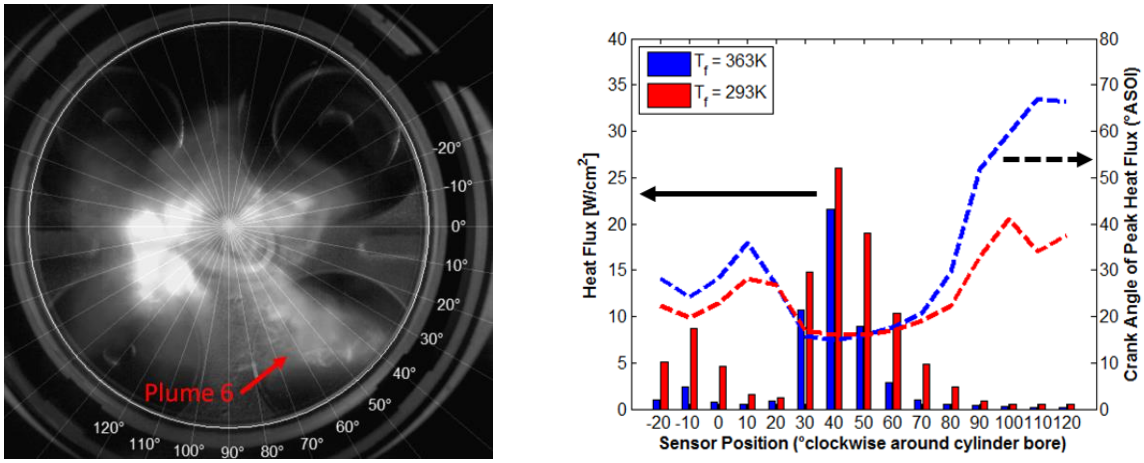

(a) (b)

Figure 5.6 – (a) Indicates the peripheral sensor locations for the heat flux sensor taken from4 (b) Shows peak heat flux and the equivalent crank angle at various peripheral locations for iso-octane and T_f=363K and T_f=293K, reproduced using results from Serras-pereira, Aleiferis, Richardson, *et al.* (2007).

The second piece of experimental data taken from Serras-Pereira, Aleiferis & Richardson (2012) used to support model validation is shown in Figure 5.7(a & c) and are the mean spray images along the swirl plane at z=-15mm from the head gasket plane, at 13°ASOI (identified as the timing of first impingement) and 15°ASOI. Figure 5.7(b & d) show results from the numerical simulations for single-component fuel iso-octane at the same crank angles and cutting plane. The numerical results are shown to agree well with experimental data sets in Figure 5.6 and Figure 5.7 (a & c), correctly predicting plume 6 to impinge the cylinder liner at 30° to 50° to the horizontal and having just impinged the liner by 13°ASOI.

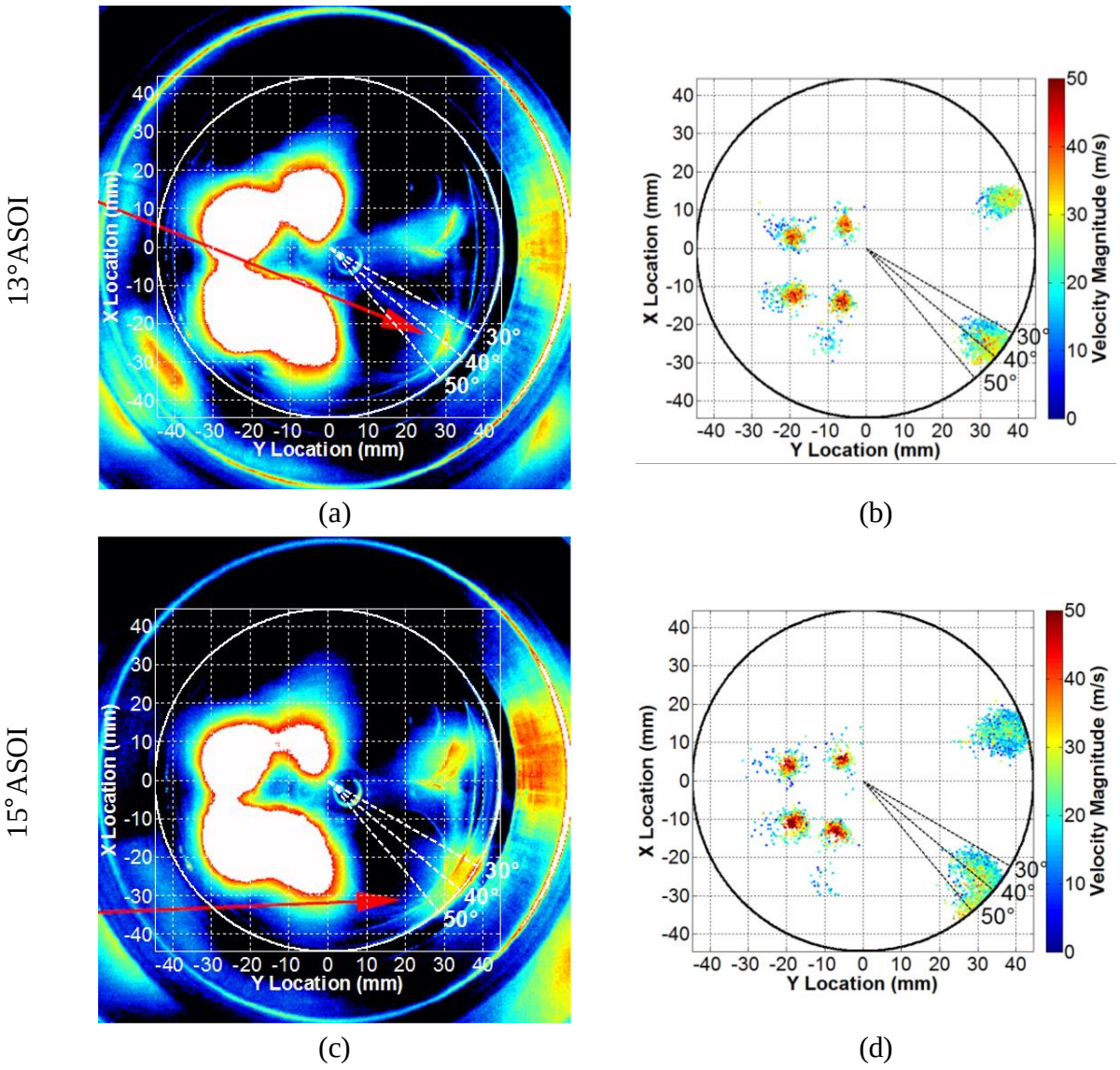

Figure 5.7 – Figure compares the location of liner impingement for plume 6 with iso-octane. (a & c) Experimental images (Serras-Pereira, Aleiferis & Richardson, 2012) show mean (60 cycle ensemble-average) spray development with iso-octane at T_f=293K, 0.5bar intake pressure, 1500rpm, illuminated by an applied laser sheet due to Mie-scattering and the pixel intensity coloured for improved visualisation. An overlay is applied to more easily compare the impingement locations with numerical results. Red arrows in the experimental images indicate the spray plume crossing the laser sheet and impingement on the liner. (b & d) Predicted droplets for the single-component fuel, coloured by droplet velocity magnitude and the cylinder liner indicated by a black circle

The third piece of experimental data is extracted from Serras-Pereira, Aleiferis & Richardson (2012) and shown in Figure 5.8. Here a comparison is made between an instantaneous swirl plane experimental image and the single-component fuel predictions to evaluate the post impingement droplet trajectory. This comparison also indicates good representation of the

impingement characteristics of the spray and subsequent circumferential motion of the spray around the liner.

More complex impingement regimes were also identified in the experimental data, including multiple roll up vortices of order 5mm diameter interacting with the spray just behind the plume tip. Predicted results were found not to capture the spray dynamics at this level of detail and would need very high resolution of the turbulent flow structures only possible with significant localised mesh refinement.

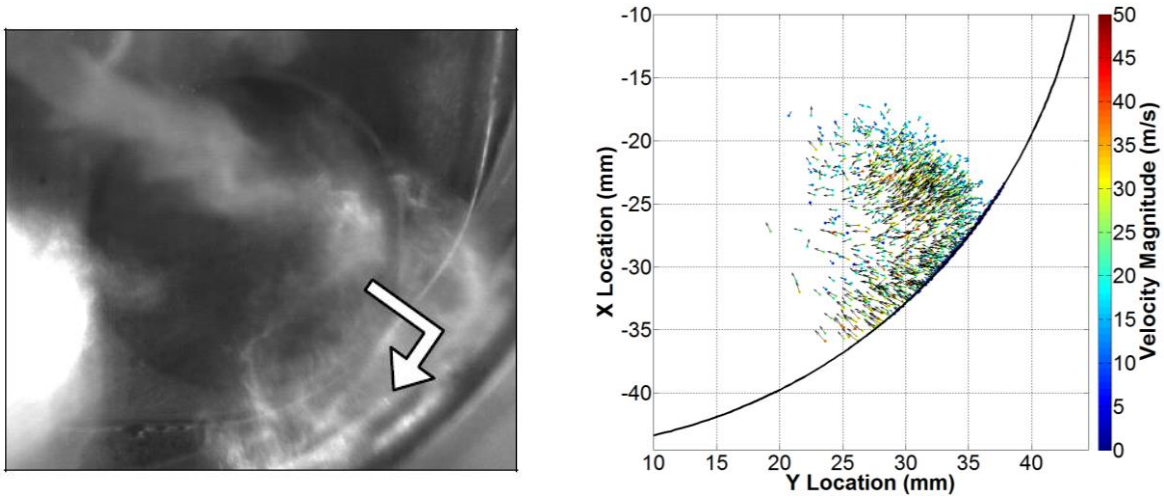

(a) (b)

Figure 5.8 – Figure compares liner impingement dynamics for plume 6 at 15°ASOI. (a) Experimental image (Serras-Pereira, Aleiferis & Richardson, 2012) is an instantaneous spray image for iso-octane at T_f=293K, 0.5bar intake pressure, 1500rpm, illuminated by an applied laser sheet due to Mie-scattering, indicating radial droplet motion post-liner impingement (b) Predicted droplets for the single-component fuel, coloured by droplet velocity magnitude and with x-y plane velocity vector arrows, the cylinder liner indicated by a black circle. Note: images are not of equal scale

Very similar impingement timing and location was seen between the single- and multi-component fuels hence the remainder of the analysis on cylinder liner impingement will be using the results from the multi-component fuel.

Figure 5.9 illustrates the development of a fuel film on the liner surface between 18 and 19°ASOI for the multi-component fuel. Performing the same analysis as completed for the intake valve impingement, the droplet Weber number and Laplace number can be calculated and compared against the critical Weber number for film formation within the free convection and nucleate boiling regime of the impingement model. The results are shown in Table 5.3 and it is clear that most impinging droplets upto 18°ASOI are above the critical

Weber number for deposition but by 19°ASOI the Weber number of impinging droplets has reduced sufficiently that a large proportion of impinging droplets are beneath the critical Weber number and are deposited, with the coverage ratio limit quickly exceeded and a liquid film formed.

The predictions indicate that a film thickness of the order of 5µm is formed on the liner surface. Drake, Fansler, Solomon, *et al.* (2003) completed a number of experimental tests using a refractive-index-matching approach to evaluate continuous cycle-by-cycle piston film development using both a pressure-swirl and multi-hole fuel injector. Their results for the multi-hole injector showed an area-averaged film height of up to 1µm, with images indicating a peak film thickness of 1-2.5µm, providing additional confidence that the liquid film predictions presented here are of the correct magnitude.

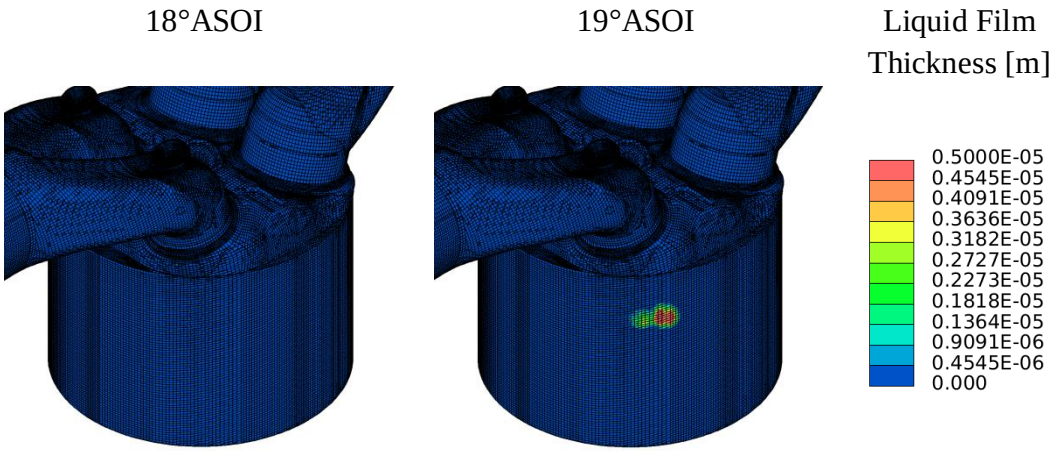

Figure 5.9 – Development of a liquid film on the cylinder liner as a consequence of spray impingement with a multi-component fuel at 18° and 19°ASOI

Table 5.3 – The range of droplet Weber and Laplace numbers and calculated We_{cr} for two crank angles at the point of liner liquid film formation for the multi-component fuel

Time [°ASOI]	Comments	We		La		We_{cr}	
		Upper	Lower	Upper	Lower	Upper	Lower
18	Pre-liquid film formation	1600	400	1000	500	544	625
19	Immediately post initial film formation	800	300	500	300	625	693

As seen during liquid film formation in intake valve impingement, a thicker liquid film is predicted with the multi-component fuel due to less droplets having evaporated prior to the spray reaching the cylinder liner. Figure 5.10 shows droplets coloured by the wall fuel mass-fraction later in the cycle at 35°ASOI or 65°BBDC, allowing one to deduce the differences in impingement location and relative differences in quantity of fuel impinged between the either the single-component surrogate or for each component of the multi-component surrogate. The following observations were made:

- Both fuel surrogates see significant piston crown impingement of the medium fraction iso-octane in plume 5 (1), but due to the reduced quantity of fuel in the multi-component surrogate, the total quantity impinged at this location is smaller with the multi-component surrogate.
- The multi-component surrogate fuel sees a greater percentage of its drops impinge on the cylinder liner than is seen when using the iso-octane single-component surrogate. This is visible in the quantity of lighter fraction C_5H_{12} of plume 6 (2) and plume 2 (3) and of the heavy fraction $C_{10}H_{22}$ in plume 6 (4).
- Plume one cylinder liner impingement (5) is seen to be more significant when using the single-component surrogate than in the case of the multi-component surrogate.

The use of a multi-component surrogate provides improved predictions of droplet evaporation and liquid film formation and evaporation. This is particularly true when modelling firing cycles, where the elevated wall temperatures would still be below the saturation temperature of the heavier components of a multi-component fuel allowing deposition, whereas the wall temperatures would be above the saturation temperature of a typical single component surrogate like iso-octane, thus not providing realistic liquid film predictions. This will also allow improvements in the modelling of subsequent processes such as pool-fires, oil dilution and entrainment of large particles that can contribute to UHC and PM emissions.

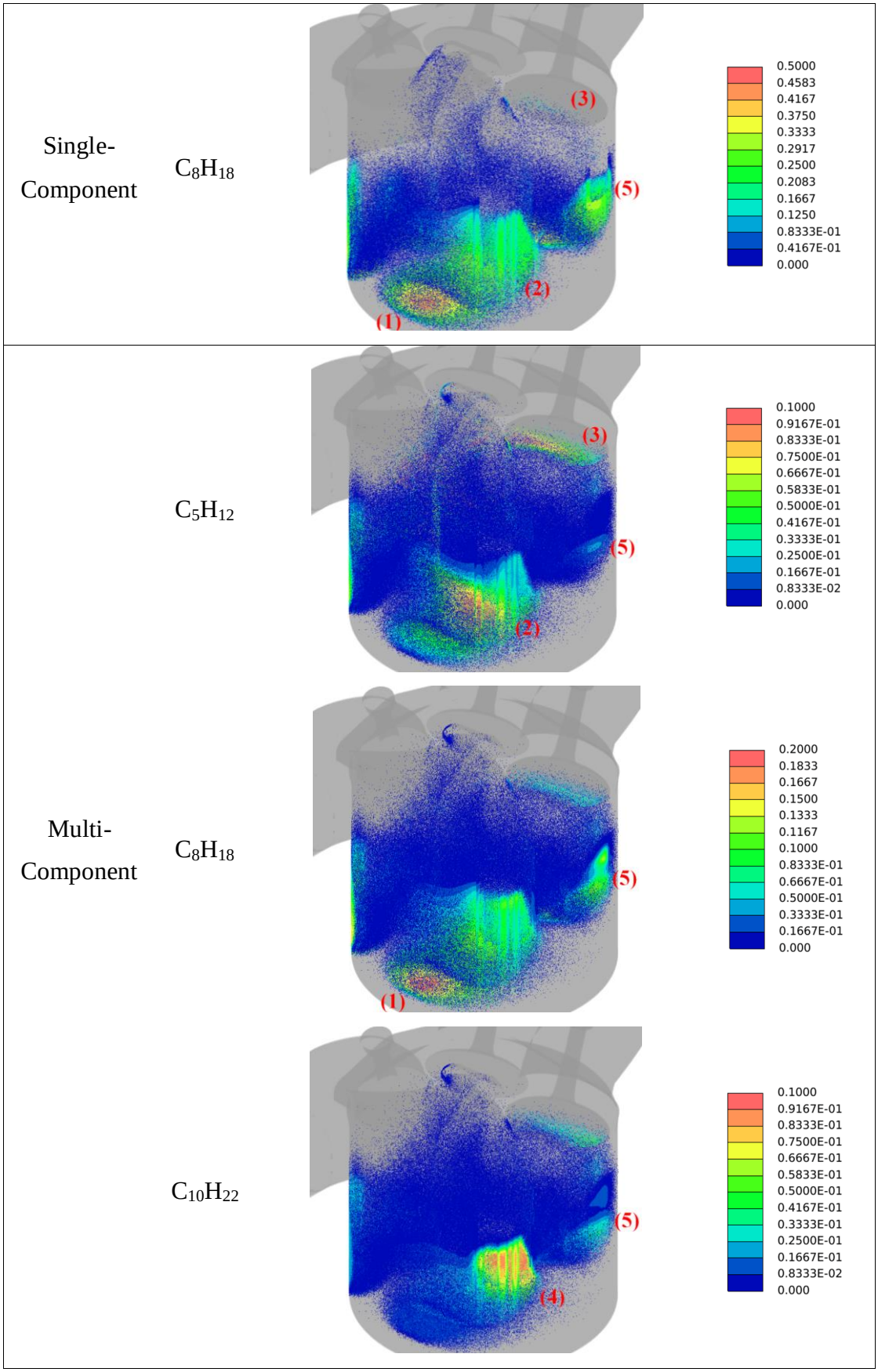

Figure 5.10 – Droplets coloured by wall fuel mass-fraction indicating the quantity of fuel impinging a solid surface and the relative differences in impingement locations between the single-component and multi-component fuel surrogates at 35°ASOI

5.2.2 Cycle-to-Cycle Variations of the Impingement Process

Whilst the previous section has focused on characterising the process of liquid fuel impingement and the subsequent development of a liquid film on the intake valve, cylinder liner and piston crown using a time-averaged RANS based approach to turbulence modelling, this section will use the LES approach to turbulence modelling to investigate the cyclic variations in the impingement process on the internal surfaces of the combustion chamber. First the section will look at the CCV of plume 1 impinging on the intake valve head, identifying variations in total film mass and film thickness and establishing causality. The second part of this section will look into CCV of plume impingement on the cylinder liner and piston crown, again with a view to identifying variations in total film mass and establishing causality, but in particular the quantity and location of any remaining film at the point of spark timing, thus allowing one to deduce the impact of cyclic variations in the impingement process on the subsequent combustion process.

5.2.2.1 Cyclic Variability of Intake Valve Impingement

The variation in liquid film mass present on the intake valve was used as a means of differentiating between anomalous cycles and is presented in Figure 5.11 with cycles identified as either ‘high’ or ‘low’ separately coloured and all other engine cycles coloured in grey. Cycle 1 was identified as a characteristically ‘low’ cycle and cycle 7 identified as a characteristically ‘high’ cycle and both were investigated in further detail by reviewing the droplet trajectories and liquid film formed due to plume 1 impingement.

Inspection of Figure 5.12(a) for cycle 1 shows a thinner film formed on the top surface of the intake valve head when compared to cycle 7 in Figure 5.13(a) and a corresponding increase in liquid film formed on the side and underside of the valve head in cycle 1 when compared to cycle 7 as shown in Figure 5.12(b) and 6.13(b) respectively.

Figure 5.12(c) and Figure 5.13(c) show droplets coloured by Weber number impinging the intake valve for cycles 1 and 7 respectively. Figure 5.12(c) for cycle 1 shows a clear increase in the number of droplets deflected over the top surface rather than contribute to film

formation on the top surface of the valve head when compared to cycle 7. Conversely, cycle 7 in Figure 5.13(c) shows an increase in the number of droplets being deflected underneath the valve head rather than contribute to film formation on the side and underneath the valve head. This implies that cycle-by-cycle variations in the flow field can have subtle differences in the droplet impingement location, impinging droplet Weber number and flow field surrounding the intake valve head. Note that it is fair to assume that momentum transfer has occurred from the droplets to the continuous-phase, rather than the opposite way around, since the impinging droplet velocity is approximately 50-75m/s and the valve jet velocity is of the order 25-50m/s based on findings from the in-cylinder flow field investigations in Chapter 4.

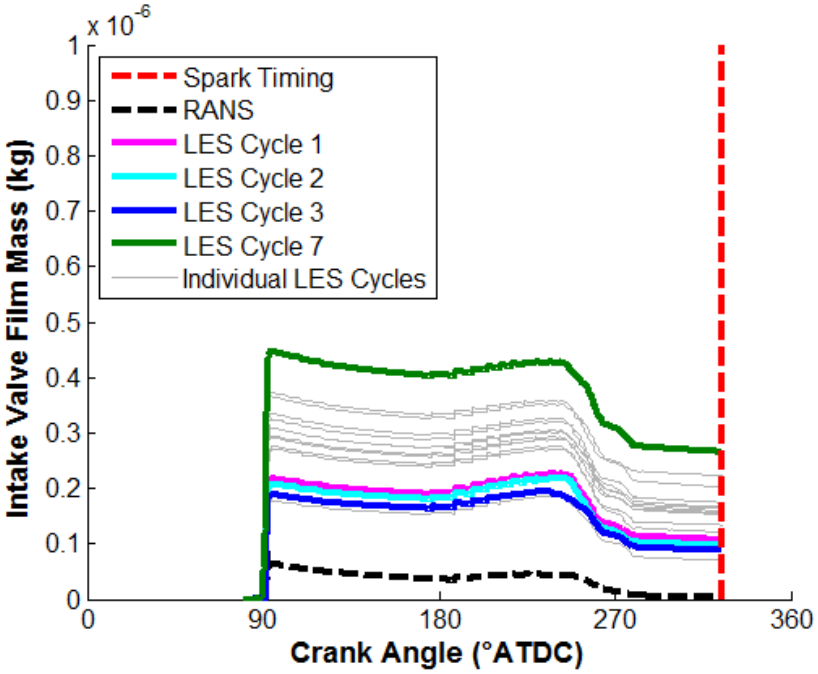

Figure 5.11 – Intake valve film mass as a function of crank angle from SOI (80°ATDC) to spark timing (325°ATDC)

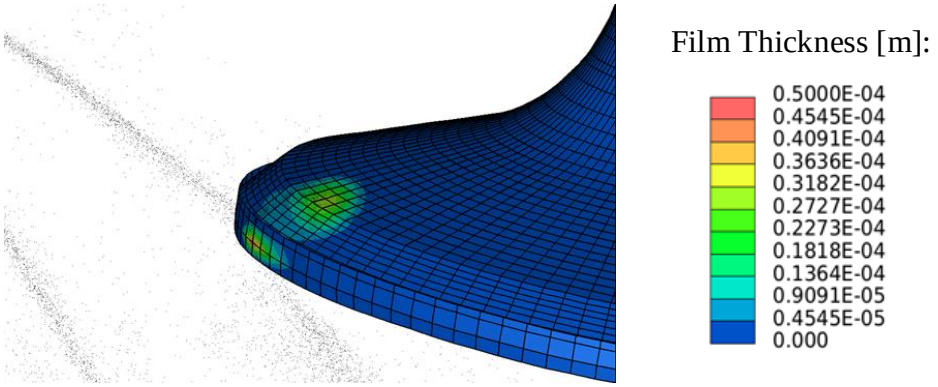

(a)

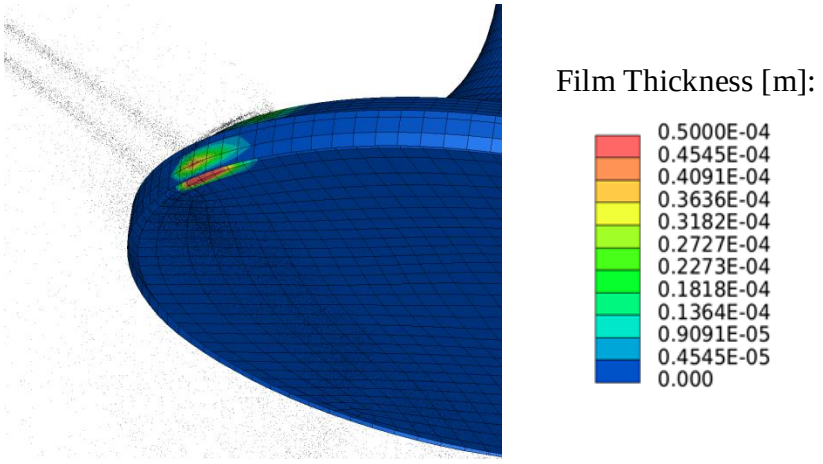

(b)

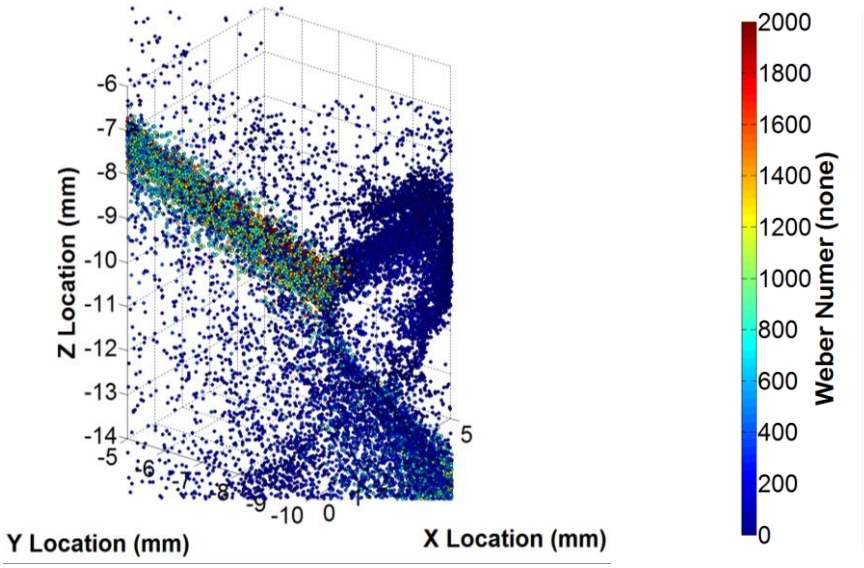

(c)

Figure 5.12 – LES Cycle 1 predictions at 13°ASOI, (a) Droplets impinging the top surface of the intake valve head with colour scale indicating liquid film thickness, (b) Droplets impinging the bottom surface of the intake valve head with colour scale indicating liquid film thickness, (c) Droplets coloured by Weber number impinging the intake valve head with the valve head geometry hidden to improve visibility of the impinging and rebounding droplets

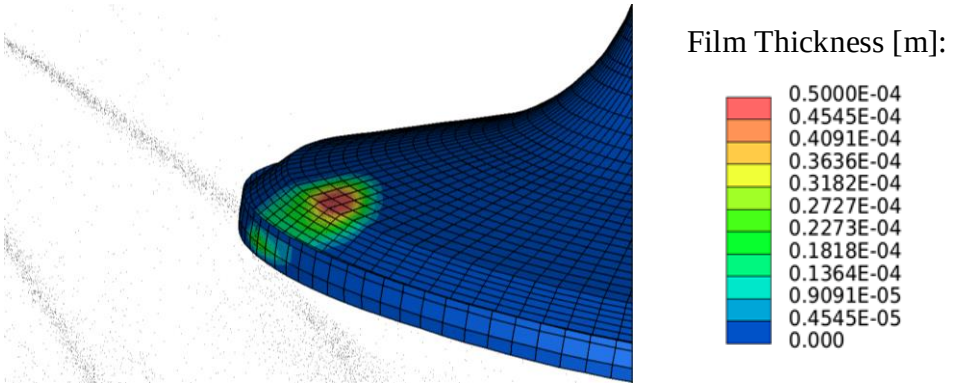

(a)

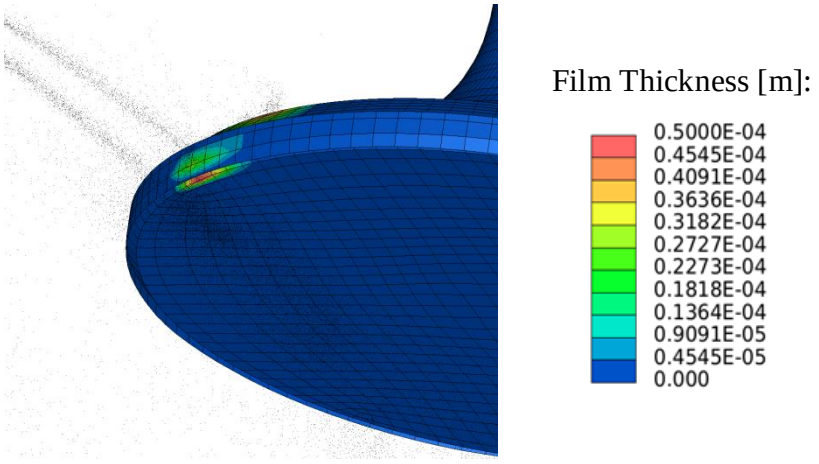

(b)

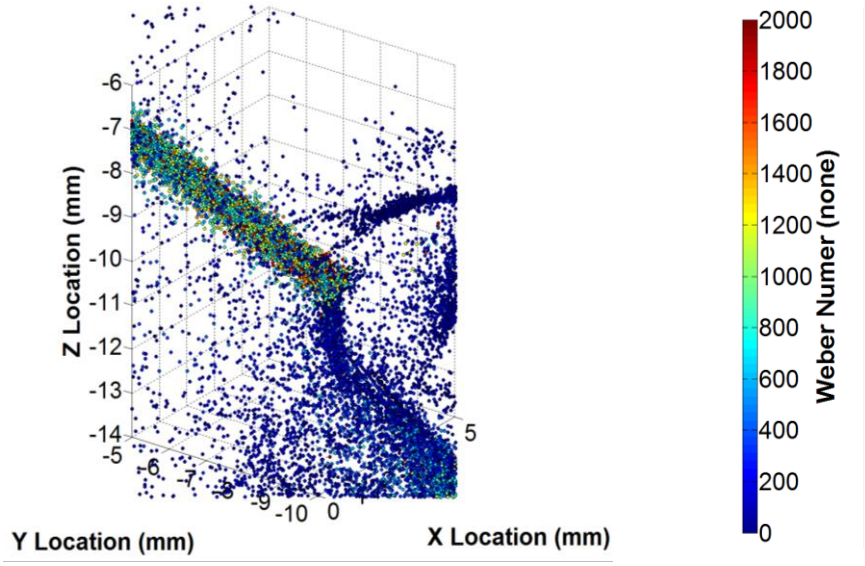

(c)

Figure 5.13 – LES Cycle 7 predictions at 13°ASOI, (a) Droplets impinging the top surface of the intake valve head with colour scale indicating liquid film thickness, (b) Droplets impinging the bottom surface of the intake valve head with colour scale indicating liquid film thickness, (c) Droplets coloured by Weber number impinging the intake valve head with the valve head geometry hidden to improve visibility of the impinging and rebounding droplets

Upon inspection of the variation in the intake valve peak film thickness with time as shown in Figure 5.14, a difference in the variation of peak film thickness with time is visible; cycle 7 showing an initially high peak film thickness that reduces with time, cycle 1 shows a similar maximum peak film thickness but with its peak one crank angle degree later. This difference is characteristic of a difference in impingement mechanism; cycle 1 and 2 generating their peak film thickness on the underside of the valve head and all other cycles generating their peak film thickness on the top of the valve head, due to cycle-by-cycle differences in the in-cylinder flow field as discussed above. Cycle 3 is highlighted as an example of a cycle that has a low total film mass similar to cycle 1 and 2 but with an impingement mechanism similar to the cycle 7.

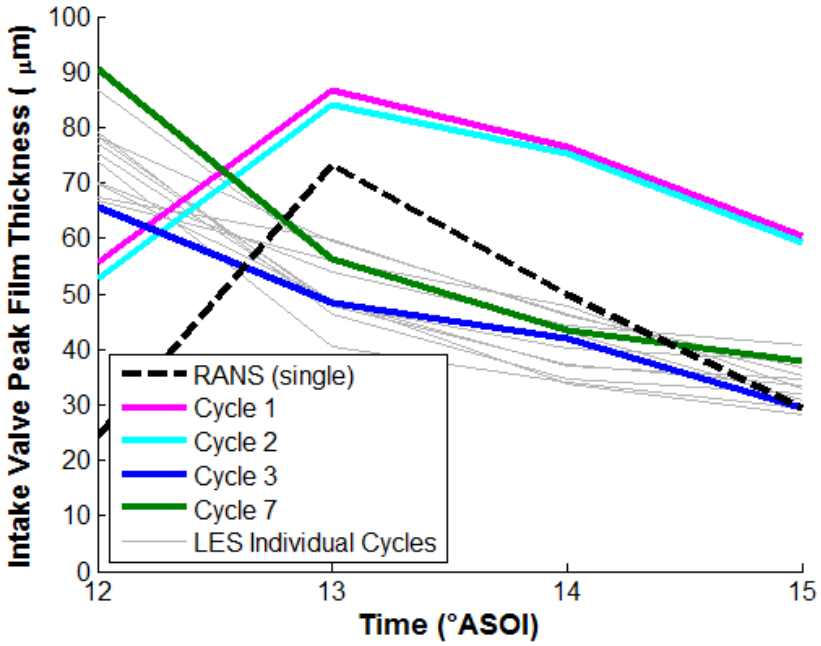

Figure 5.14 – Intake valve peak film thickness as a function of time

This result also indicates that whilst the total mass of fuel impinged in cycle 7 is over twice that seen in cycle 1 (Figure 5.11), both cycle 1 and cycle 7 have similar peak film thicknesses. When the cycle-to-cycle variability of total mass of impinged fuel is combined with the cyclic differences in the predominant location of the deposited fuel (i.e. cycle 7 predominantly on the top surface of the valve head and cycle 1 on the side and underside of

the valve head), cyclic variations will also be seen in the secondary droplets formed and resultant vapour cloud due to film evaporation:

- Secondary droplets stripped from a film formed on the top surface of the valve head will include droplets formed due to wave induced instability and droplets formed due to stripping over a sharp edge, whereas a film formed on the side of the valve head and underneath the valve head will predominantly see secondary droplets formed due to film stripping over a sharp edge.
- Fuel vapour formation due to liquid film evaporation will vary as a function of the quantity of liquid film formed (which as presented above, is a function of flow field affects) and heat transfer to the wall and continuous-phase throughout the cycle.

Both effects contributing to the overall CCV of the in-cylinder fuel-air mixture at the point of spark timing, and resultant combustion and pollutant formation processes.

One suggestion for the differences in impingement mechanism between cycles 1 and 2 and the following cycles would be due to the simulation initialisation method. Typically the first cycle and sometimes up to the first five LES cycles (Fontanesi, Paltrinieri & Cantore, 2014) are discarded prior to analysis of results to avoid dependency of the solution on the initialisation conditions. In this research, the model was initialised using a RANS cycle and then a single LES cycle (which was discarded) before using the results for the following 15 cycles. A single LES cycle was considered sufficient upon analysis of the in-cylinder pressure trace which showed the following cycles within the general population (Figure 4.27) but it is conceivable that more subtle uncharacteristic variations in the in-cylinder flow field are still present within the first few LES cycles, thus making the differences in impingement characteristics seen here in cycles 1 and 2 as a consequence of the numerics rather than the physical process itself. To better understand whether the variation in impingement characteristics is a function of the numerics or a reality of the CCV in the physical process would either require additional cycles to be simulated or experimental results to be gathered and would form further work from this research.

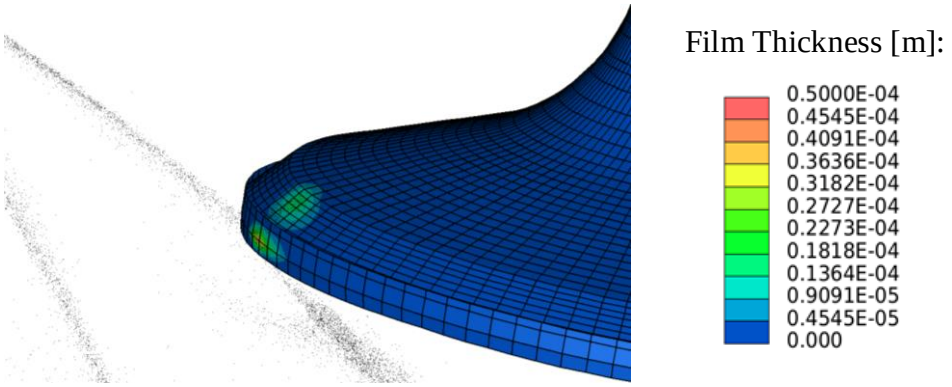

(a)

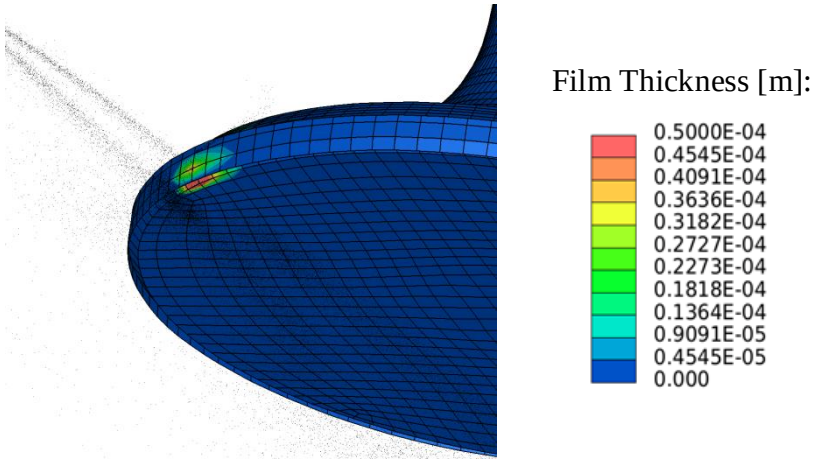

(b)

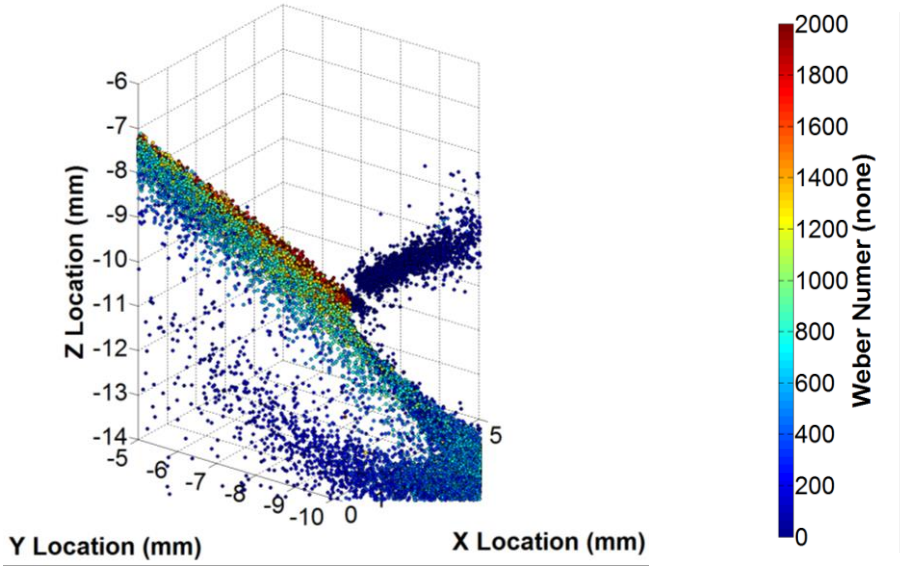

(c)

Figure 5.15 – RANS predictions at 13°ASOI for the single-component surrogate, (a) Droplets impinging the top surface of the intake valve head with colour scale indicating liquid film thickness, (b) Droplets impinging the bottom surface of the intake valve head with colour scale indicating liquid film thickness, (c) Droplets coloured by Weber number impinging the intake valve head with the valve head geometry hidden to improve visibility of the impinging and rebounding droplets

Of final note are the observed differences in impingement characteristics predicted using a RANS RNG k-ε turbulence model and a LES Smagorinsky SGS turbulence model. Figure 5.15 shows the equivalent impingement images when using the RNG k-ε turbulence model and a similar impingement mechanism is predicted as seen in cycle 1 and 2 of the LES predictions where plume 1 impingement predominantly causes a liquid film to be formed on the side and underside of the valve head. Contrary to the LES predictions, a smaller peak film thickness is predicted as shown in Figure 5.14, and a significant reduction in total film mass is predicted as seen in Figure 5.11.

Interrogation of Figure 5.15(c) suggests that when using the RNG k-ε turbulence model, the droplets impinge at significantly higher velocity and hence Weber number, thus significantly more droplets rebound from the valve surface rather than stick or deposit, reducing the total amount of liquid film formed. The results from Figure 3.68 confirm that the LES turbulence model does not modify the droplet D_{10} diameter considerably in comparison to the RANS predictions, thus the difference in Weber number can predominantly be attributed to a reduction in the impingement velocity. The implication from this observation is that there has been increased momentum transfer between the droplets and the continuous-phase when using the LES SGS turbulence model, thus reducing the droplet velocity and hence Weber number prior to impingement.

A greater number of droplets within the cylinder interior and a reduced liquid film on the intake valve head (as is the case in the RANS predictions when compared with the LES predictions) will act to cause differences in the spatial distribution of fuel vapour through the cylinder and temporally through the engine cycle.

5.2.2.2 Cyclic Variability of Cylinder Liner and Piston Crown Impingement

When comparing the impingement locations for the LES predictions in the same manner as completed previously in Figure 5.10, due to the additional turbulent structures predicted by the LES model, a significant increase in the amount of plume distortion and movement of the droplets is visible. A comparative example is shown in Figure 5.16. The onset from this is that it is much more difficult to discern the CCV in impingement positions via this method.

As a consequence, the impinged liquid film mass as a function of time for both the cylinder liner and piston crown were evaluated to identify anomalous cycles and then film thickness contours used to investigate the causes of such anomalous cycles.

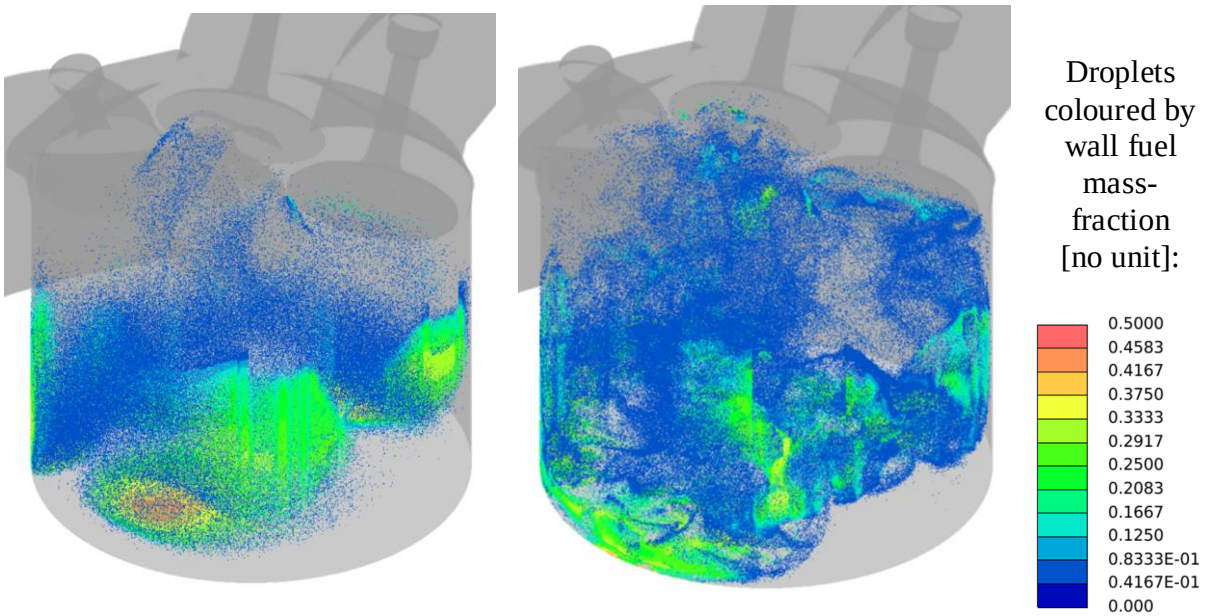

(a) (b)

Figure 5.16 – Droplets coloured by wall fuel mass-fraction indicating the quantity of fuel impinging a solid surface within the combustion chamber at 35°ASOI for (a) RANS, (b) LES Cycle 5

Figure 5.17 and Figure 5.18 show the piston crown film mass and the cylinder liner film mass respectively as a function of crank angle between the start of injection and spark timing with cycles of interest coloured separately for further discussion. From inspection, there is almost 100% variation across the maximum and minimum cycles in both piston and liner film mass:

- At 110°ATDC or 30°ASOI, piston liquid film mass ranges from 1×10^{-6}kg for cycle 15 with a peak film thickness of approximately 7µm, to 1.8×10^{-6}kg for cycle 2 with a peak film thickness of 25µm
- At 110°ATDC or 30°ASOI, cylinder liner film mass ranges from 0.85×10^{-6}kg for cycle 15 with a peak film thickness of approximately 1µm, to 1.5×10^{-6}kg for cycle 5 with a peak film thickness of 1µm

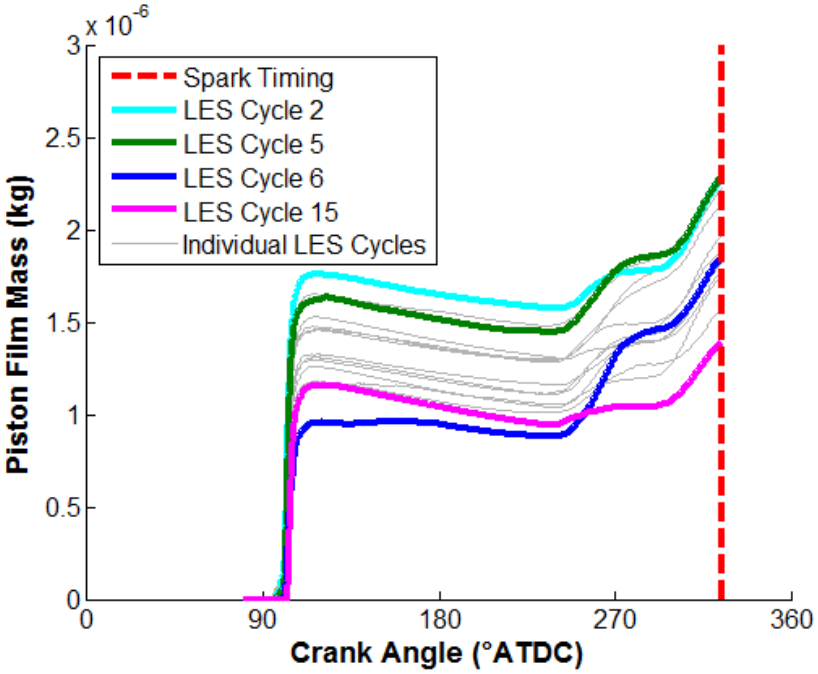

Figure 5.17 – Piston crown film mass as a function of crank angle from SOI (80°ATDC) to spark timing (325°ATDC)

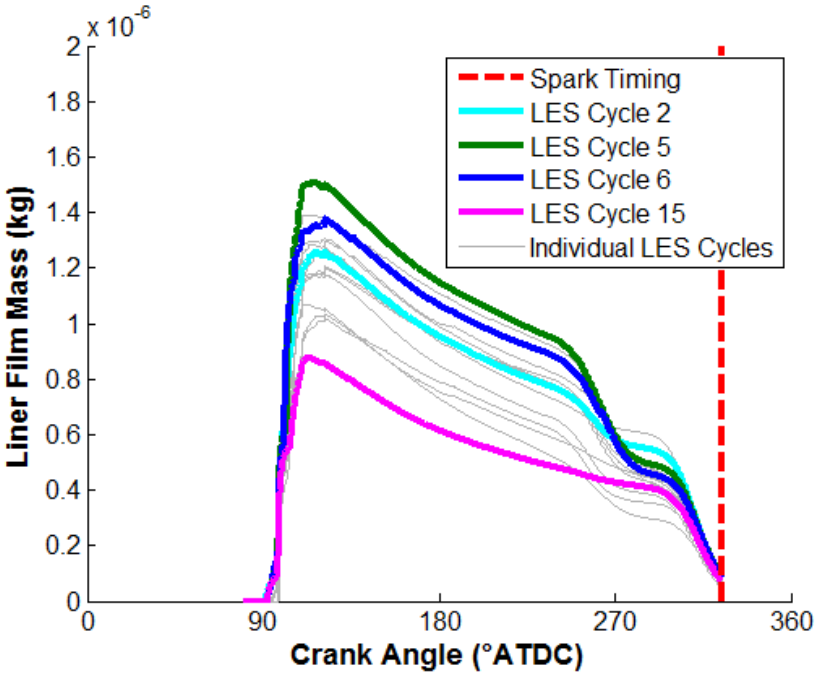

Figure 5.18 – Cylinder liner film mass as a function of crank angle from SOI (80°ATDC) to spark timing (325°ATDC)

Figure 5.19 shows contours of liquid film thickness for the cylinder liner and piston crown impingement locations for cycle 2 at 110°ATDC, indicating significant impingement of plumes 2/3/4/5 on the piston crown when compared to the same impingement locations for cycle 15 in Figure 5.20. The cause of this can be seen when comparing plume tip penetration in Figure 5.23 for plume 3 and Figure 5.24 for plume 5, where cycle 15 shows reduced plume penetration compared with cycle 2 leading to reduced quantities of fuel impinging on the piston crown. This is as a consequence of variations in the in-cylinder flow field causing increased interaction between the droplets and the continuous-phase, creating greater momentum exchange and slowing the rate of plume tip penetration. Reduced penetration rate allows more time for droplet breakup and evaporation and hence less fuel available to contribute to a liquid film once the plume impinges on a solid surface. It also means that a greater number of droplets don't penetrate far enough to even reach the solid surface.

Also of interest is a comparison between cylinder liner impingement characteristics between cycles 15 and 5. As noted above, whilst both cycles have very similar peak film thickness, they have significantly different total film masses. Inspection of the liquid film thickness contours for cycle 5 in Figure 5.21 shows that due to continuous-phase interactions with the plume tip, plume tips 3 and 4 suffer increased displacement towards the cylinder liner when compared to other cycles and thus impinge more significantly on the cylinder liner first, before reaching the piston crown, increasing the total film mass on the cylinder liner for that particular cycle. This characteristic is also present in cycle 6, as seen in Figure 5.22 where most of plume 3 and 4 impinge on the cylinder liner and not the piston crown causing comparatively low piston film mass but the rising of the piston later in the compression stroke scrapes the film off the cylinder liner and onto the piston surface, contributing to the large change in piston film mass during the compression stroke as seen in Figure 5.17.

Figure 5.25 shows plume tip penetration as a function of time for plumes 1/6, with far less CCV visible in tip penetration. This is due to the smaller distances travelled by plumes 1/6 before they impinge on the cylinder liner and as a consequence there is less time available for interaction with the continuous-phase and hence exhibit lower CCV. This is evident in the images of film thickness contours for plumes 1/6 which show very similar film thickness contour characteristics across all cycles.

All the cycles show a quantity of liquid film remaining on the piston surface up to the point of spark timing which would burn as uncontrolled diffusion flames or 'pool-fires' on the

piston surface and are known as a large source of PM and UHC emissions when found within GDI engines (Drake, Fansler, Solomon, *et al.*, 2003).

The computational domain in this research did not include the top land of the ring pack due to the very small cells required to adequately resolve the gas flow and provide sufficient solution stability that in turn would create a model that was too computationally expensive for the number of cycles intended to be run. Thus whilst in this numerical model, the rising piston scrapes any remaining film on the cylinder liner onto the piston crown, in reality any liquid film remaining on the cylinder liner would be forced into the ring pack and be a potential cause of a number of concerns including:

- Ring pack coking: increased temperatures during the compression stroke causing pyrolysis of the fuel trapped in the ring pack, which can lead to premature ring breakage and a mechanism for the release of solid carbon particles which can create spikes in engine out PM or act as ignition sites for autoignition events.
- Increased UHC's: trapped fuel being released from the ring pack as the cylinder depressurises during scavenging, increasing engine out UHC.
- Oil dilution: trapped fuel being absorbed into the oil film leading to a need for reduced oil change intervals and increased engine wear.

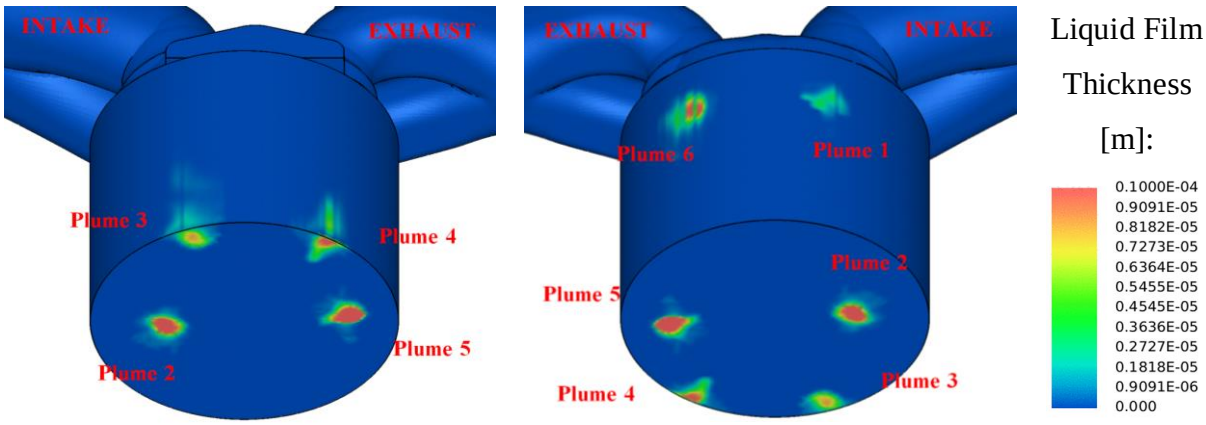

(a) (b)

Figure 5.19 – Contours of liquid film thickness for cycle 2 at 30°ASOI or 110°ATDC for (a) front of the combustion chamber and (b) rear of the combustion chamber

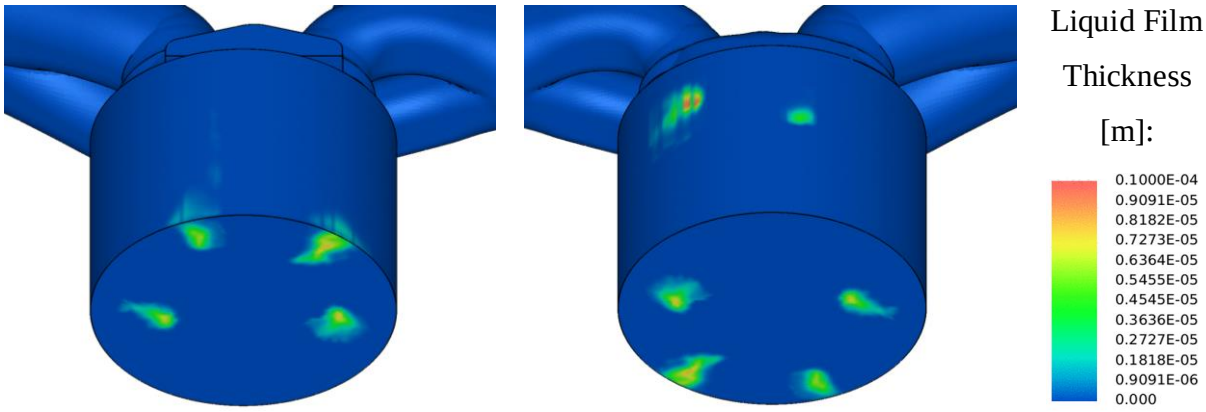

(a) (b)

Figure 5.20 – Contours of liquid film thickness for cycle 15 at 30°ASOI or 110°ATDC for (a) front of the combustion chamber and (b) rear of the combustion chamber

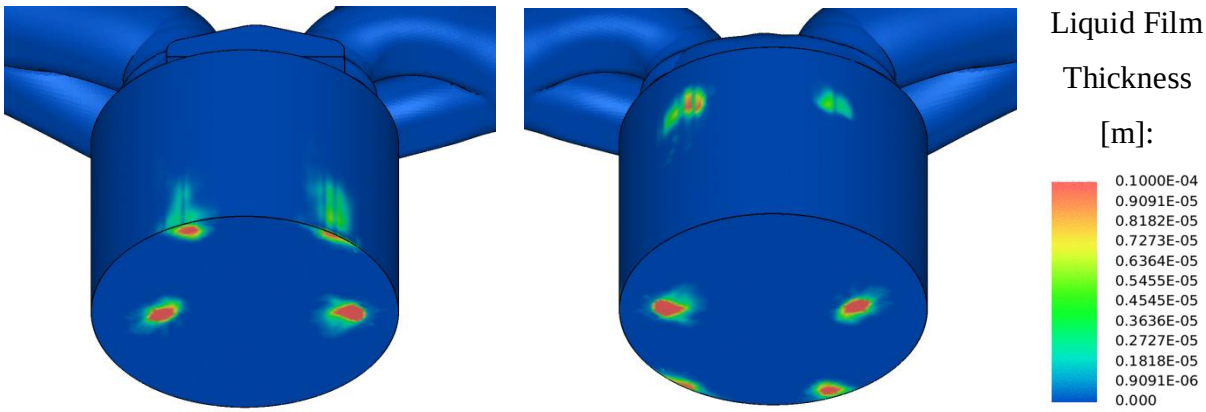

(a) (b)

Figure 5.21 – Contours of liquid film thickness for cycle 5 at 30°ASOI or 110°ATDC for (a) front of the combustion chamber and (b) rear of the combustion chamber

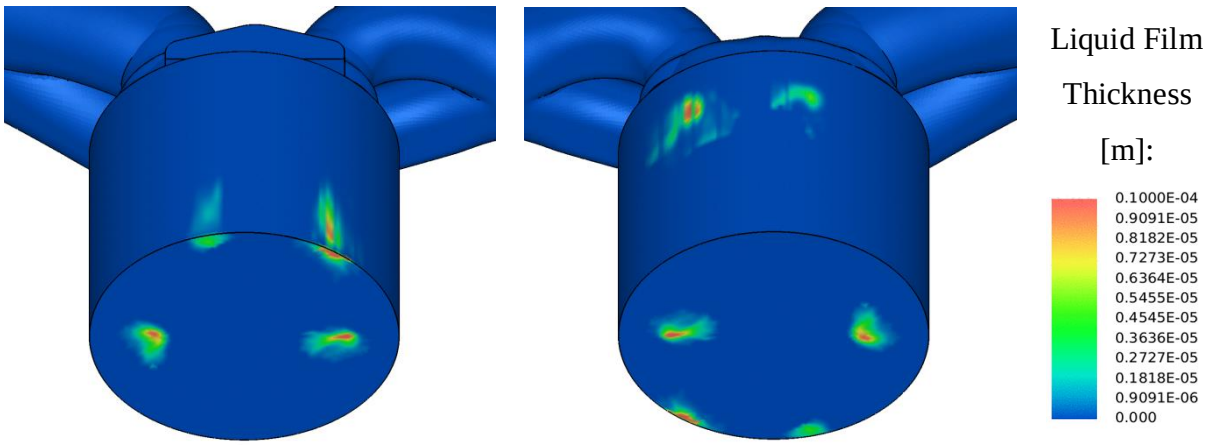

(a) (b)

Figure 5.22 – Contours of liquid film thickness for cycle 6 at 30°ASOI or 110°ATDC for (a) front of the combustion chamber and (b) rear of the combustion chamber

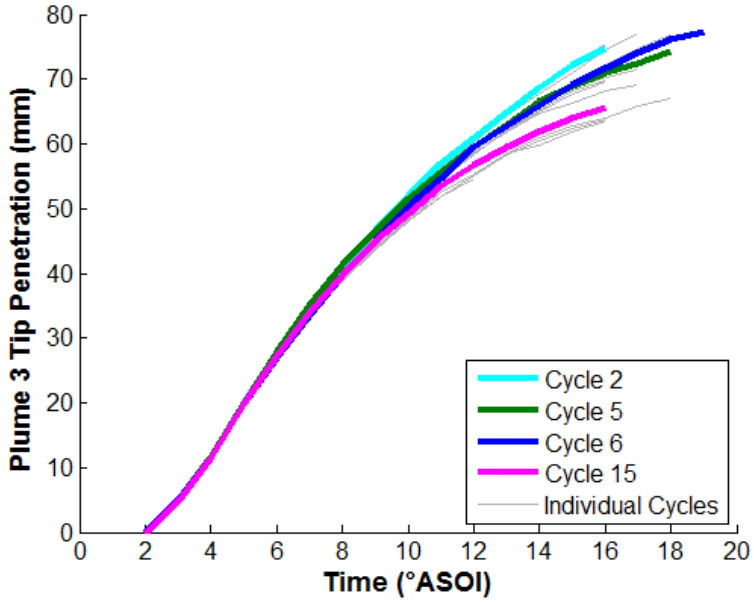

Figure 5.23 – Plume 3 tip penetration, for all LES cycles but highlighting the cycles of interest

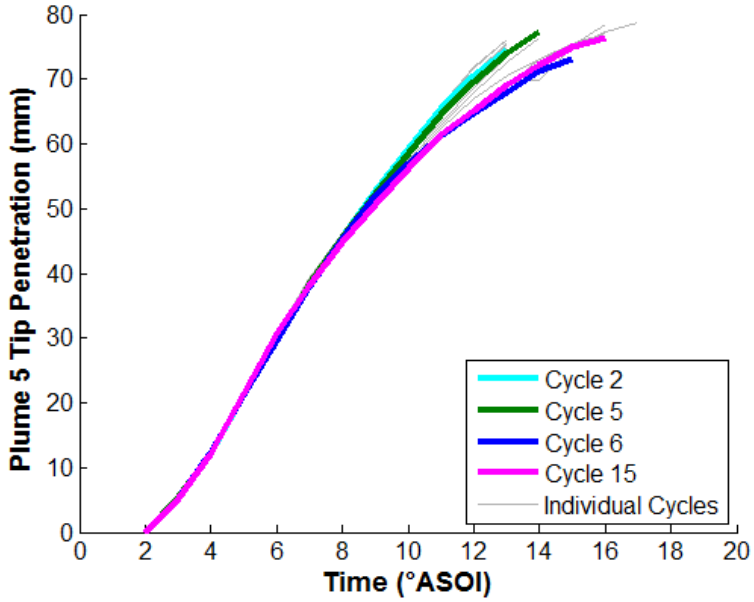

Figure 5.24 – Plume 5 tip penetration, for all LES cycles but highlighting the cycles of interest

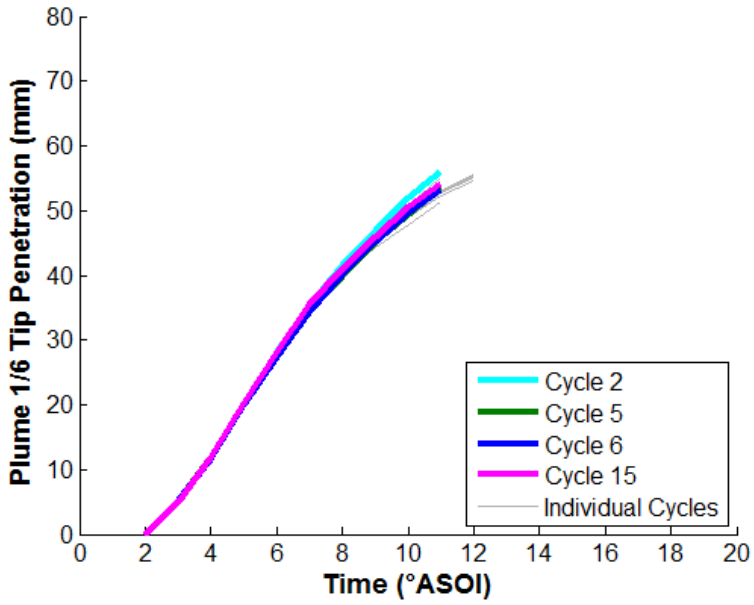

Figure 5.25 – Plume 1/6 tip penetration, for all LES cycles but highlighting the cycles of interest

5.3 MIXTURE FIELD CHARACTERISTICS

Precise control of the fuel-air mixture in ICE's is fundamental to all subsequent processes within the combustion chamber, including desirable affects such as stable kernel development and flame front propagation, and undesirable affects such as abnormal combustion regimes (e.g. knock phenomena, pool fires), hydrocarbon absorption into crevice volumes and oil films, and the subsequent impact on pollutant formation. For a GDI engine utilising an early injection homogeneous charge strategy, perfect mixing and avoiding excessive fuel impingement on internal surfaces is sought, whereas accurate control of a rich fuel-air mixture around the spark plug at the point of spark timing is the primary objective with a late injection stratified charge strategy. This is particularly challenging in a commercial context where product life cycle variability and robustness further increase the design solution complexity.

The use of detailed numerical techniques to model the fuel injection and subsequent mixing process has been common place for a number of year but studies typically utilise a single-component surrogate fuel to represent the reality of a complex multi-fractional fuel, largely

due to computational restrictions. Advantages to modelling multiple components of the fuel include: improvements in the modelling of droplet evaporation due to it being dependent on the different volatilities of the individual components within the fuel, and the ability to evaluate the variation in mixing between the charge and different fuel fractions.

This section aims to complete a number of investigations into the mixture field characteristics of the GDI engine that is the subject of this research:

- Understand the physical processes involved in generating the spatial and temporal mixture field evolution within this GDI engine.
- Investigate differences in the predicted mixture field evolution when using a single-component surrogate and a multi-component surrogate.
- Explore the CCV of the mixture field at spark timing, and look for causality.
- Continuing from the research in section 5.2.4, consider if intake valve jet flapping can be attributed as a source of mixture field variation at spark timing.

5.3.1 Mixture Field Development

5.3.1.1 Mixture Field Evolution

Upon inspection of the in-cylinder fuel-air equivalence ratio at spark timing (35°BTDC), shown in Figure 5.26, it is apparent that despite using an early injection strategy to promote relatively high levels of mixture homogeneity, the predicted mixture field still contains a fair degree of stratification at this engine conditions.

The following is a discussion and evidence for the evolution of the aforementioned mixture inhomogeneity. Figure 5.28 presents contours of the fuel-air equivalence ratio and velocity magnitude at three crank angles: 115°ATDC (approximately 25°AEOI), 5°ABDC (early compression) and 35°BTDC (spark timing), in a cutting plane intersecting plumes 2 and 5, as shown in Figure 5.27.

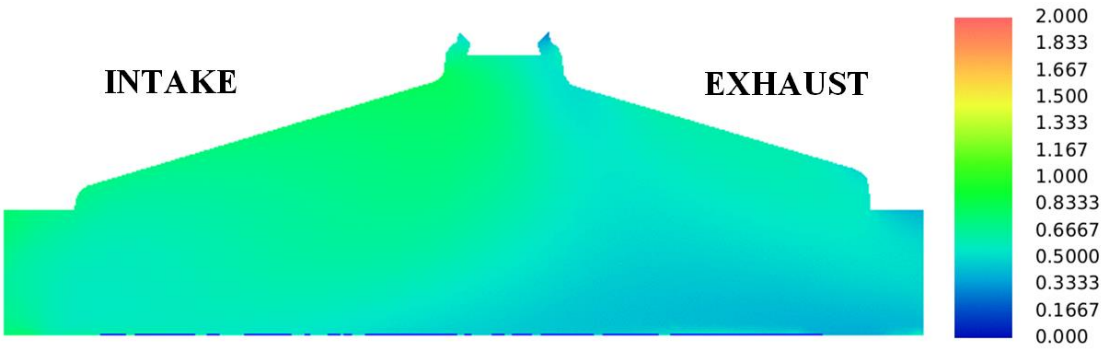

Figure 5.26 – Contours of fuel-air equivalence ratio for the single-component fuel surrogate, along the bore centreline at 35°BTDC (spark timing)

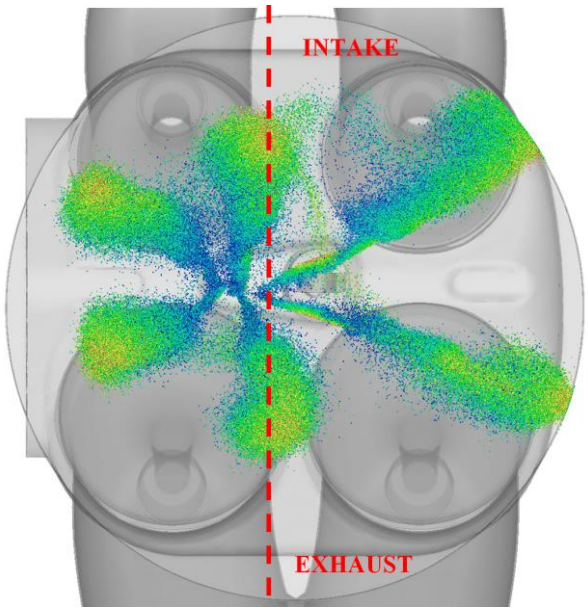

Figure 5.27 – Tumble cutting plane in the x-z plane that intersects plume 2 and 5, plane coordinates:[0,5,0]

Shortly after the end of the injection event at 115°ATDC (Figure 5.28(a & b)), due to the relative strength of the intake flow and valve jets, the mixture cloud is moved and distorted by the valve jets, pushing the atomised fuel cloud either side of the jet, forming a rich mixture in the centre of the combustion chamber and underneath the intake valve head.

By 5°ABDC (Figure 5.28(c & d)), the dominant counter-clockwise tumble motion has driven a significant portion of the mixture towards the bottom of the intake side of the combustion chamber. Due to the recirculation region formed at the piston-liner interface on the exhaust side of the combustion chamber, some of the fuel-air mixture is also forced against the piston crown, a precursor for liquid film formation on the piston crown.

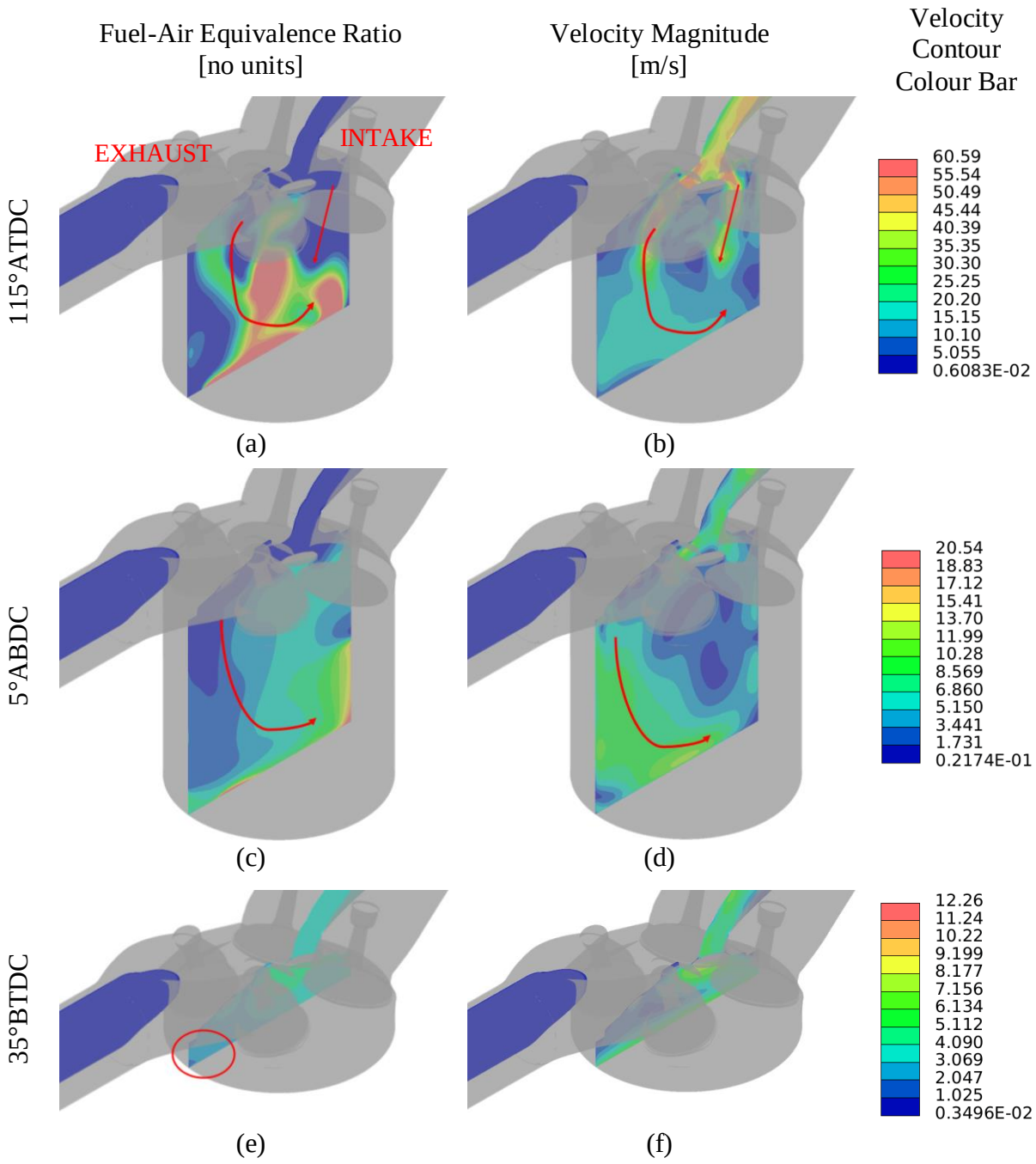

Figure 5.28 – Diagram shows contour plots of (a) fuel-air equivalence ratio using the single-component fuel surrogate (see Figure 5.26 for colour bar), and (b) velocity magnitude (colour bar provided), in the plume 2-5 cutting plane, to illustrate the impact of the dominant flow structures on the final equivalence ratio at spark timing

The rising piston acts to maintain the counter-clockwise tumble motion and carry the rich fuel-air mixture up the intake side of the combustion chamber to form the stratified mixture distribution of richer mixture under the intake valve head and weaker mixture at the piston-liner intersection on the exhaust side of the combustion chamber seen at spark timing (Figure 5.28(e & f)).

But as seen previously in the preceding chapter, the in-cylinder flow field is fully turbulent and highly three-dimensional thus one would also expect any mixture stratification to also exist across all planes. Figure 5.29 shows the cylinder geometry and an iso-surface of fuel-air equivalence ratio Φ=0.8 at spark timing, indicating that substantial mixture stratification exists through the cylinder with a preference for a rich mixture cloud to be concentrated near the front of the combustion chamber.

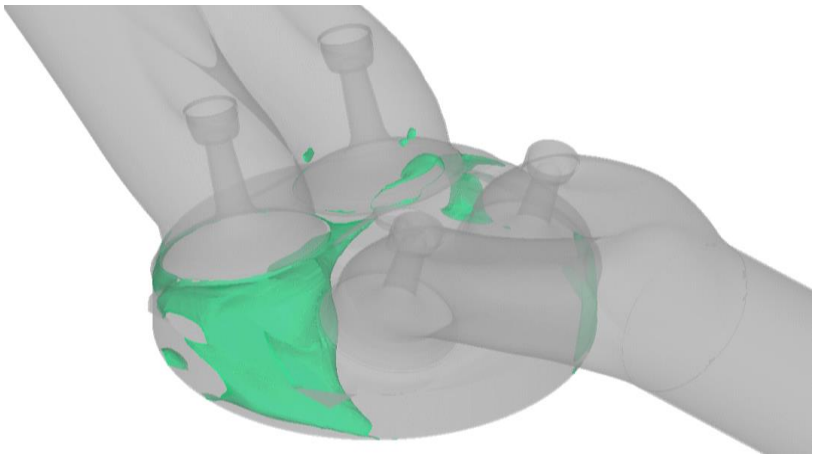

Figure 5.29 – Iso-surface of fuel-air equivalence ratio at Φ=0.8 illustrating mixture stratification through the cylinder at spark timing (35°BDTC) for the single-component fuel

The following is a commentary of the evolution of this mixture cloud structure due to the in-cylinder flow field.

Figure 5.30 shows an iso-surface at a fuel-air equivalence ratio Φ=0.8, soon after the end of the injection process. At 95°ATDC (~5°AEOI), the droplet trajectory is dominated by its inertia, imparted from the pressure difference across the injector nozzle, and is sufficiently high that the penetrating droplets and surrounding vapour cloud largely follow the shape of the intended shape of the spray plume geometry (Figure 5.30(a)). This is with the exception of any droplets or fuel-air mixture that intersect the intake valve jet which has sufficiently high momentum to deflect the passing spray plume, as seen earlier in Figure 5.28(a).

By 105°ATDC (~15°AEOI) (Figure 5.30(b)) the drag due to the surrounding environment is beginning to dissipate the droplet momentum initially imparted by the injector such that the droplets and resultant vapour cloud begin to be more heavily influenced by the in-cylinder flow field, visible by the more distorted equivalence ratio iso-surface.

By 115°ATDC (~25°AEOI) (Figure 5.31(a & b)) most of the initial droplet momentum has been dissipated to the surrounding gas and the influence of the flow field is much more pronounced with flow structures around the cylinder periphery seen to be shaping and moving the vapour cloud.

Upon inspection of the velocity field at the periphery of the combustion chamber close to BDC (shown at 15°BBDC in Figure 5.31(d)), two counter rotating vortices in the swirl plane can be seen to collide and be driven downwards towards the piston crown due to the tumble motion set up by the intake system. As the cycle progresses, a preferential direction of rotation is found (likely due to a difference in velocity magnitude of a particular flow structure) and a clockwise rotating vortex is formed close to the combustion chamber wall and piston crown (Figure 5.31(f)), creating a semi-circular profile of the fuel-air equivalence ratio iso-surface (Figure 5.31(e)). The clockwise rotating vortex contains upward momentum due to it being reflected off the liner and piston crown with its earlier tumble motion and due to the momentum imparted from the rising piston crown. The onset from this is a helical flow structure formed around the cylinder periphery, generating the fuel-air equivalence ratio iso-surface with the equivalent structure.

The resultant flow structure causes fuel vapour to be directed up towards the open intake valve (IVC is 67°BTDC due to a relatively late IVC strategy) at the rear of the cylinder where fuel vapour enters the intake port. This will lead to atomised fuel vapour being a fraction of the fresh air entering the cylinder for the next cycle and the potential for increases in UHC. The formation of the large scale clockwise rotating flow structure seen in Figure 5.31(f) is seen to be the dominant mechanism for the rich fuel-air mixture being formed towards the front of the combustion chamber at spark timing as seen earlier in Figure 5.29.

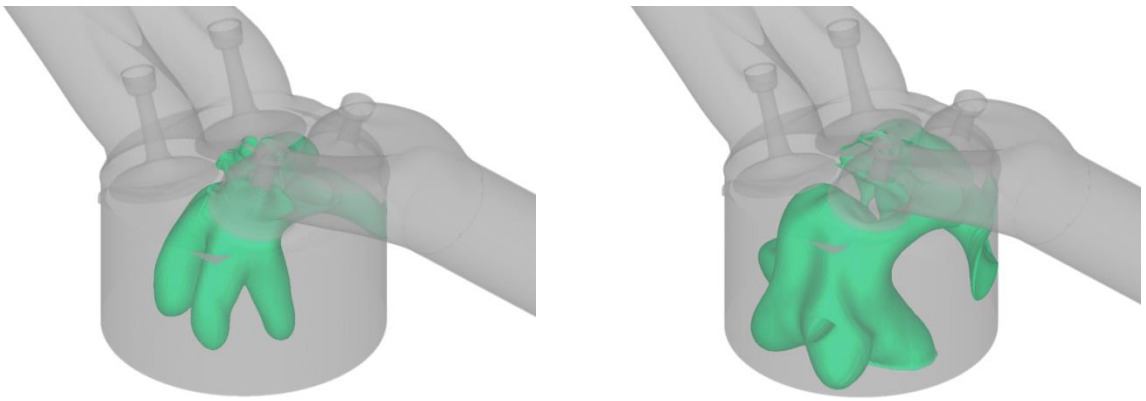

(a) 95°ATDC/~5°AEOI (b) 105°ATDC/~15°AEOI

Figure 5.30 – Iso-surface of fuel-air equivalence ratio at Φ=0.8, at 95° and 105°ATDC

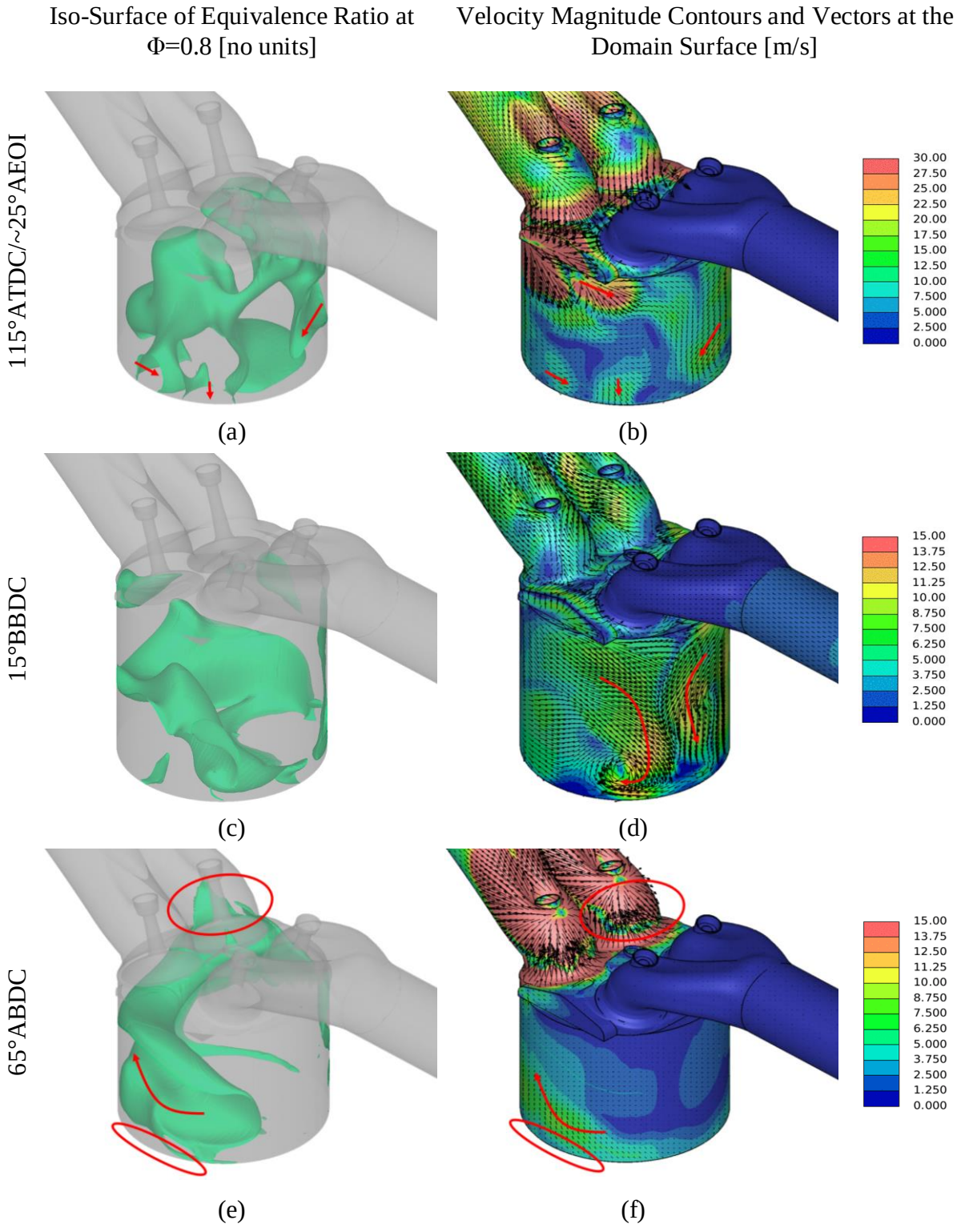

Figure 5.31 – (a,c,e) Fuel-air equivalence ratio iso-surface at Φ=0.8 and (b,d,f) Surface velocity magnitude contours and vectors

5.3.1.2 Differences in Mixture Field Evolution when using a Single- and Multi-Component Fuel Surrogate

The following section presents the observed differences in mixture field evolution between numerical predictions when using a single- and multi-component fuel surrogate, with explanation for the observed differences and some of the implications for subsequent processes including combustion.

First, the spatial differences between single- and multi-component surrogate are investigated by figures of fuel component mass fraction, fuel droplets and charge motion at four different crank angles between the start of injection (SOI) and 18°ASOI in the x-z (tumble) plane intersecting the plume pair of 2/5 (Figure 5.27); plume 2 is injected into the intake side of the cylinder and plume 5 the exhaust side of the cylinder. Figure 5.32 shows the spatial progression of the mixture fraction for each fuel component in both single- and multi-component fuel cases. Different colour bar scales have been used for each fuel component to allow easier analysis of the results. Figure 5.33 shows the liquid droplets coloured by diameter and contours of velocity magnitude.

Examination of the multi-component fuel case shows faster breakup of the lighter iso-pentane fraction with the majority of the vapour fraction situated in the upper portion of the combustion chamber. Delayed breakup of the heavier fractions of iso-octane and n-decane is also apparent with increased penetration into the combustion chamber.

It is also interesting to compare the difference in mixture fraction predicted for iso-octane between the single- and multi-component cases. In the single-component surrogate predictions, a greater quantity of the mixture fraction remains in the upper portion of the combustion chamber near the spark plug whereas it is more detached and penetrates further into the combustion chamber in the multi-component fuel predictions, see Figure 5.32(m & o). This is due to the impact of the iso-pentane and n-decane fractions within the droplets on the evaporation rate of the iso-octane fraction. Slower breakup is also supported by the presence of a greater number of droplets in the near spark plug region that have yet to breakup and contribute to the vapour mass fraction, see Figure 5.33(m & o). The presence of a larger number of droplets is also visible in the velocity field plot Figure 5.33(p), where higher velocities in the region indicate an increased contribution from droplet momentum.

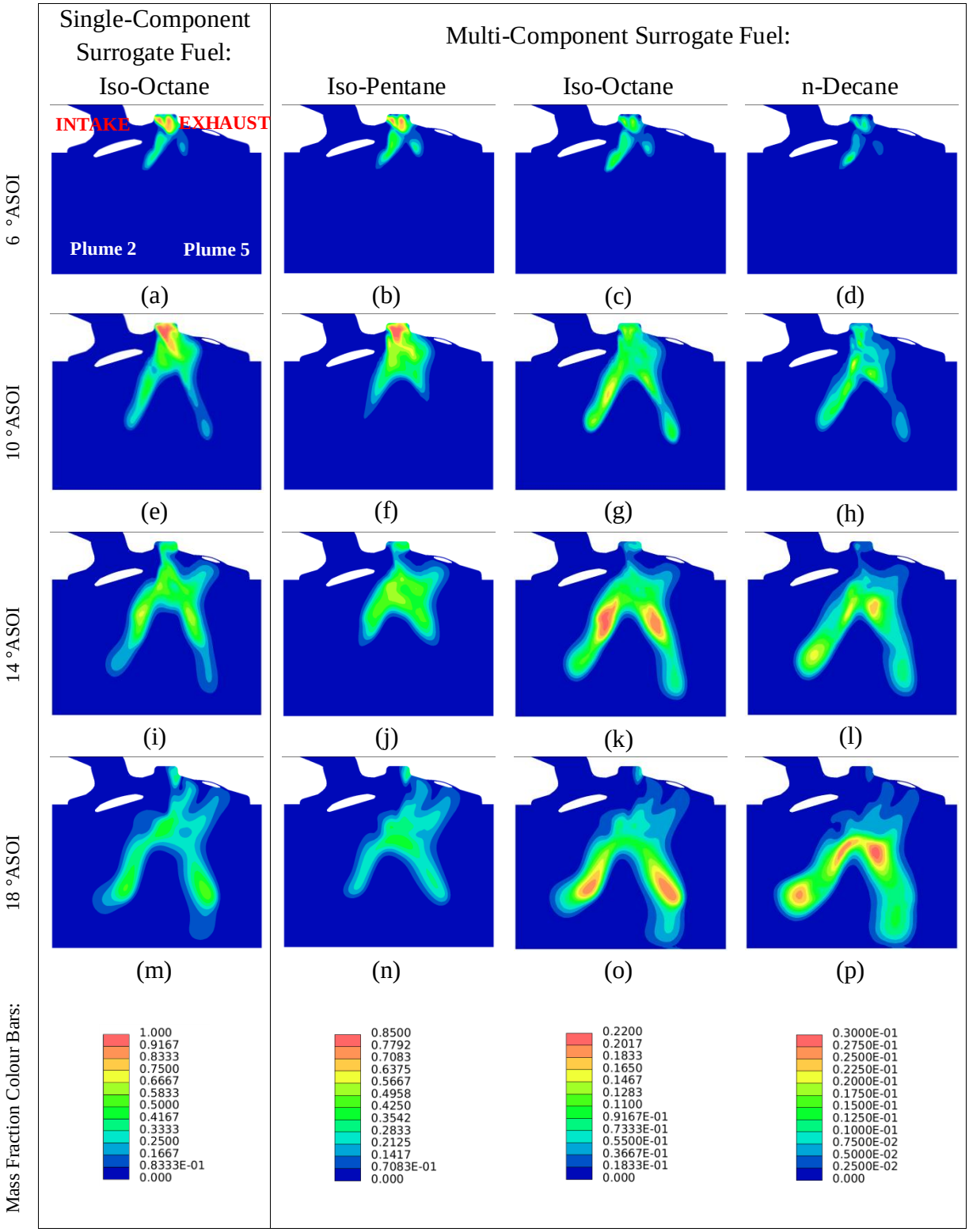

Figure 5.32 – A comparison of the fuel mass fraction for the single- and multi-component surrogate fuels in the tumble plane intersecting plume 2 and 5

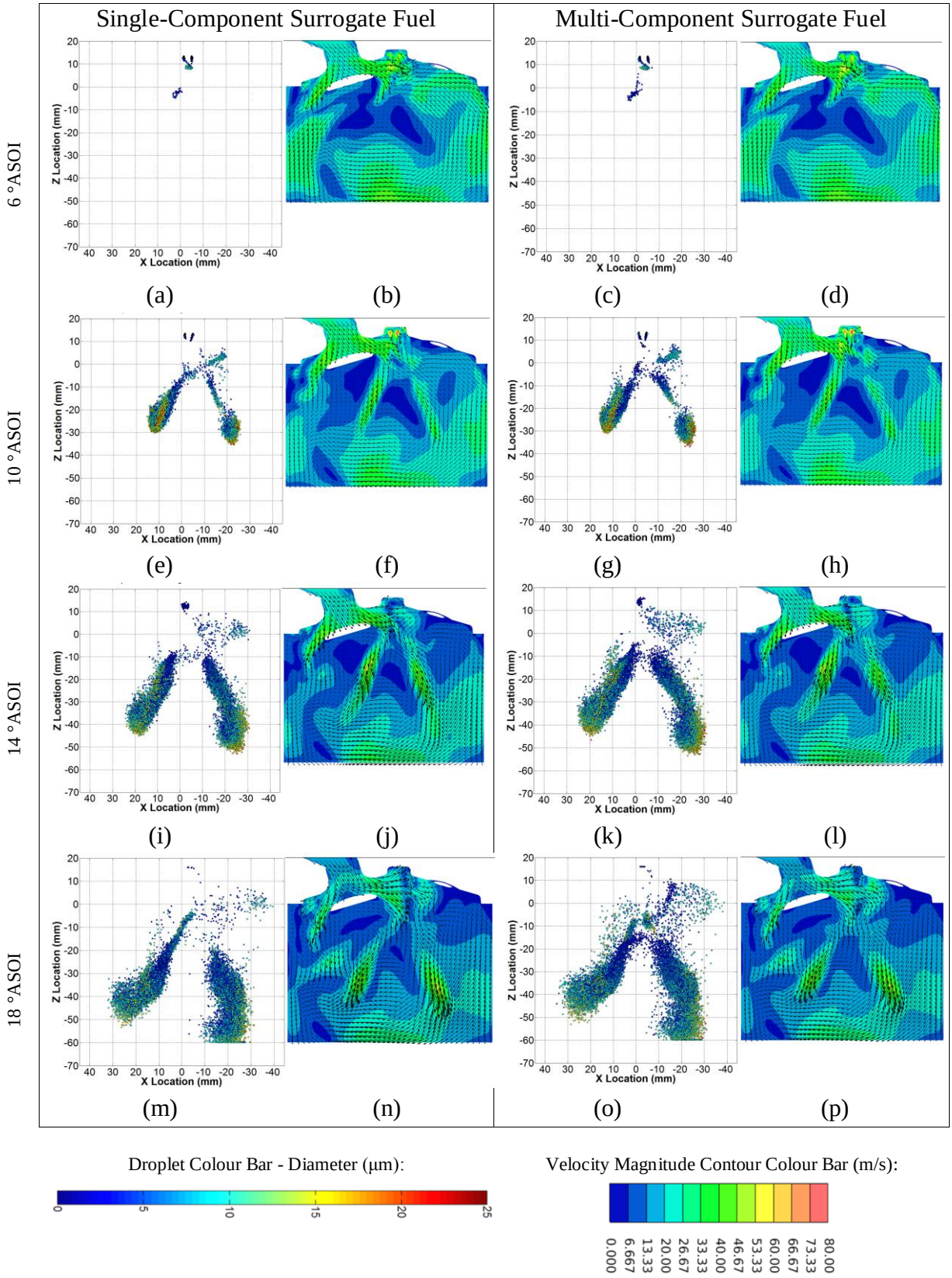

Figure 5.33 – A comparison of the droplet and velocity field for the single- and multi-component surrogate fuels in the tumble plane intersecting plume 2 and 5

When comparing the differences in spatial positioning of the droplets within the combustion chamber between single- and multi-component surrogate cases (Figure 5.33), it is apparent that an increased number of smaller droplets remain in the upper part of the combustion chamber with the multi-component surrogate. The lighter iso-pentane component may cause some droplets with a higher iso-pentane fraction to have reduced momentum and thus be more easily influenced by charge motion. This increases the probability for droplets to impinge onto hard surfaces; visible in Figure 5.33(m & o) where a larger number of droplets have impinged and stuck on the upper part of the combustion chamber in the multi-component fuel case than in the single-component fuel case. This effect also causes an increase in plume dispersion, evident with the multi-component fuel. This is particularly noticeable in plume 2 at 14°ASOI (Figure 5.33(i & k)) and 18°ASOI (Figure 5.33(m & o)).

It is clear from the velocity magnitude images that the charge motion is strongly influenced by the spray momentum; the charge motion follows the trajectory of the spray plumes with higher spray induced charge velocities around the plume tips as a consequence of the plume tip containing larger droplets that better maintain their momentum across the combustion chamber.

The next stage of the investigation was to review the differences in mixture field predicted by a single- and multi-component surrogate fuel at spark timing, and establish causality for any observed differences.

Upon inspection of the iso-surface diagrams at spark timing (35°BTDC) and slightly earlier (85°BTDC) as shown in Figure 5.34, a characteristic difference in the predictions with the multi-component surrogate is the increased quantity of fuel vapour present in the rear intake port when compared to predictions using a single-component surrogate. This is not attributable to differences in the in-cylinder flow field, thus must be due to differences in the relative evaporation rates between the two surrogate fuels.

Figure 5.36 shows the fuel-air equivalence ratio contours in the tumble plane, cutting through the rear intake valve (see Figure 5.35 for orientation of cutting plane), illustrating a key difference in the spatial distribution of fuel vapour between the two fuel surrogates. In the multi-component case, a large quantity of fuel is situated around the top of the combustion chamber underneath the open intake valve whereas in case of the single-component surrogate, an additional pocket of rich mixture has remained on the exhaust side of the combustion chamber, coinciding with the evaporation of a liquid film formed from the impingement of

plume 6. A rich pocket of mixture is also visible along the back of the combustion chamber, coinciding with the evaporation of the liquid film formed from the impingement of plume 1, visible in Figure 5.34(a).

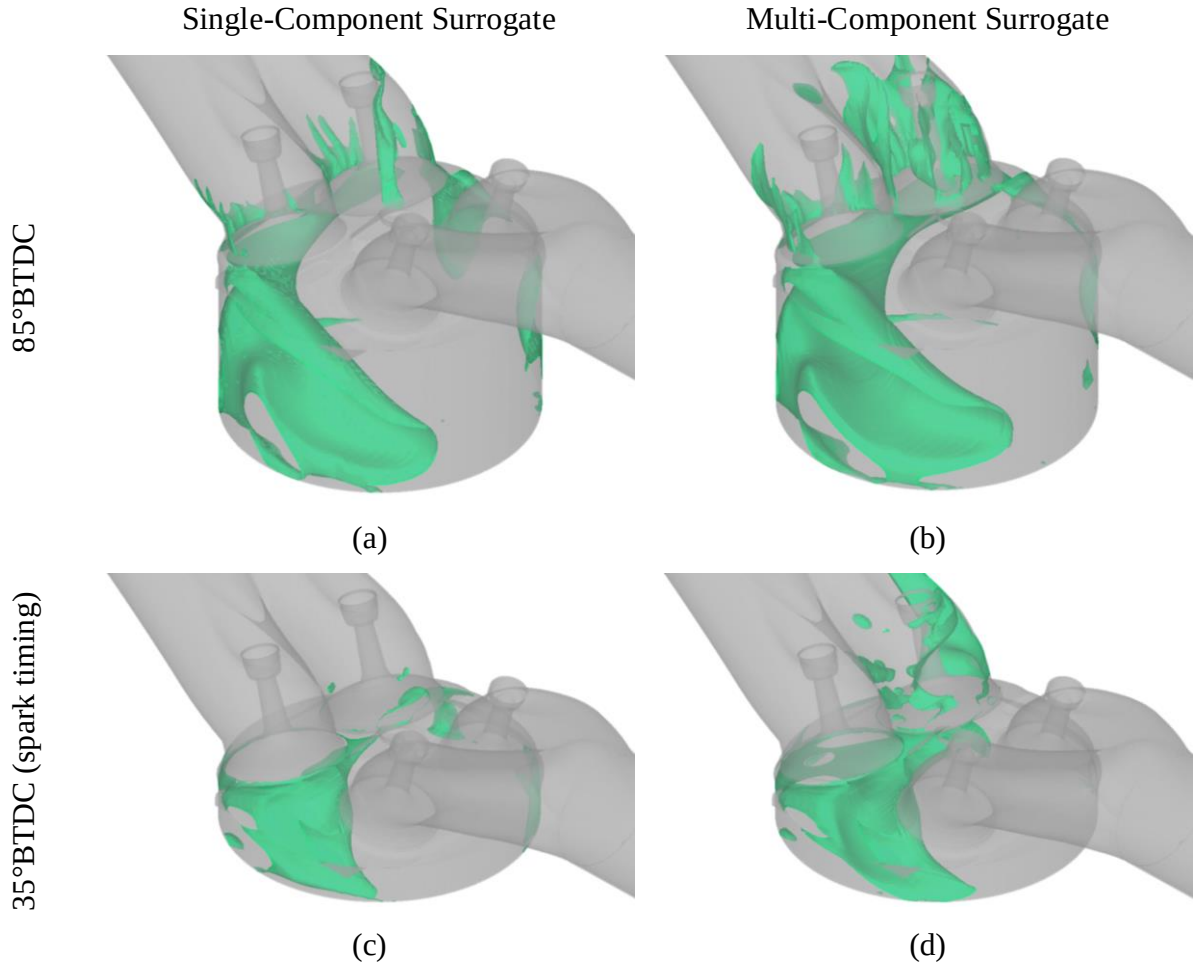

Figure 5.34 – Fuel-air equivalence ratio iso-surface at Φ=0.8 for (a) single-component fuel surrogate at 85°BTDC, (b) multi-component fuel surrogate at 85°BTDC, (c) single-component fuel surrogate at 35°BTDC and (d) multi-component fuel surrogate at 35°BTDC

Figure 5.37 shows the liquid fuel droplets coloured by wall film thickness, hence any droplets indicating a film thickness greater than zero have impinged a solid surface and are contributing to a liquid film. Inspection of Figure 5.37(a) for the single-component surrogate shows that earlier in the cycle a significant quantity of fuel has contributed to liquid film formation on the rear of the cylinder, corresponding to liner impingement from plumes 1 and 6, which are later available to evaporate and be entrained into the flow field, generating the rich mixture pockets seen in the equivalent locations on the iso-surface plot (Figure 5.34(a)) and equivalence ratio contour plot (Figure 5.36(c)).

The equivalent figure for the multi-component fuel surrogate (Figure 5.37(b) and Figure 5.37 (d)) shows that a smaller quantity of the fuel that impinges the cylinder liner forms a liquid film thus a greater quantity of liquid fuel will be available to atomise and be carried by the dominant flow structures to contribute to the rich pockets of fuel vapour found at the top of the combustion chamber and in the intake port at the point of spark timing.

The differences noted above indicate the potential inaccuracies associated with using a single-component surrogate when trying to predict the mixture field of a real fuel, when compared to a multi-component surrogate.

In the case of the multi-component surrogate predictions, less fuel is available in the cylinder at the point of spark timing to contribute to useful work due to more fuel being trapped in the intake ports. The fuel trapped in the intake port will be available to enter the cylinder on the next induction cycle but, unlike injected fuel where the resultant mixture field can be controlled by the design of the injector nozzle and timing of the injector event, it will be entirely governed by the in-cylinder flow field from the point of the intake valve opening.

When using a single-component fuel, increased liquid film mass would see a greater number of large droplets remaining in the cylinder at the point of spark timing due to the film stripping process, contributing to increases in PM and UHC pollutant formation.

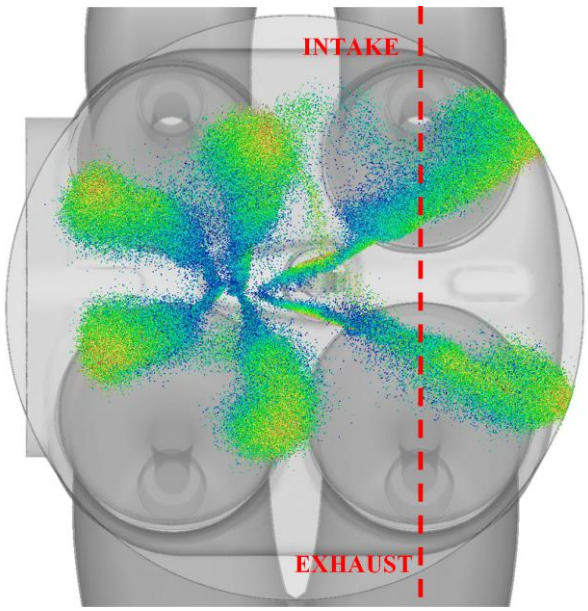

Figure 5.35 – Tumble cutting plane in the x-z plane that intersects the rear valves, plane coordinates:[0,-17.5,0]

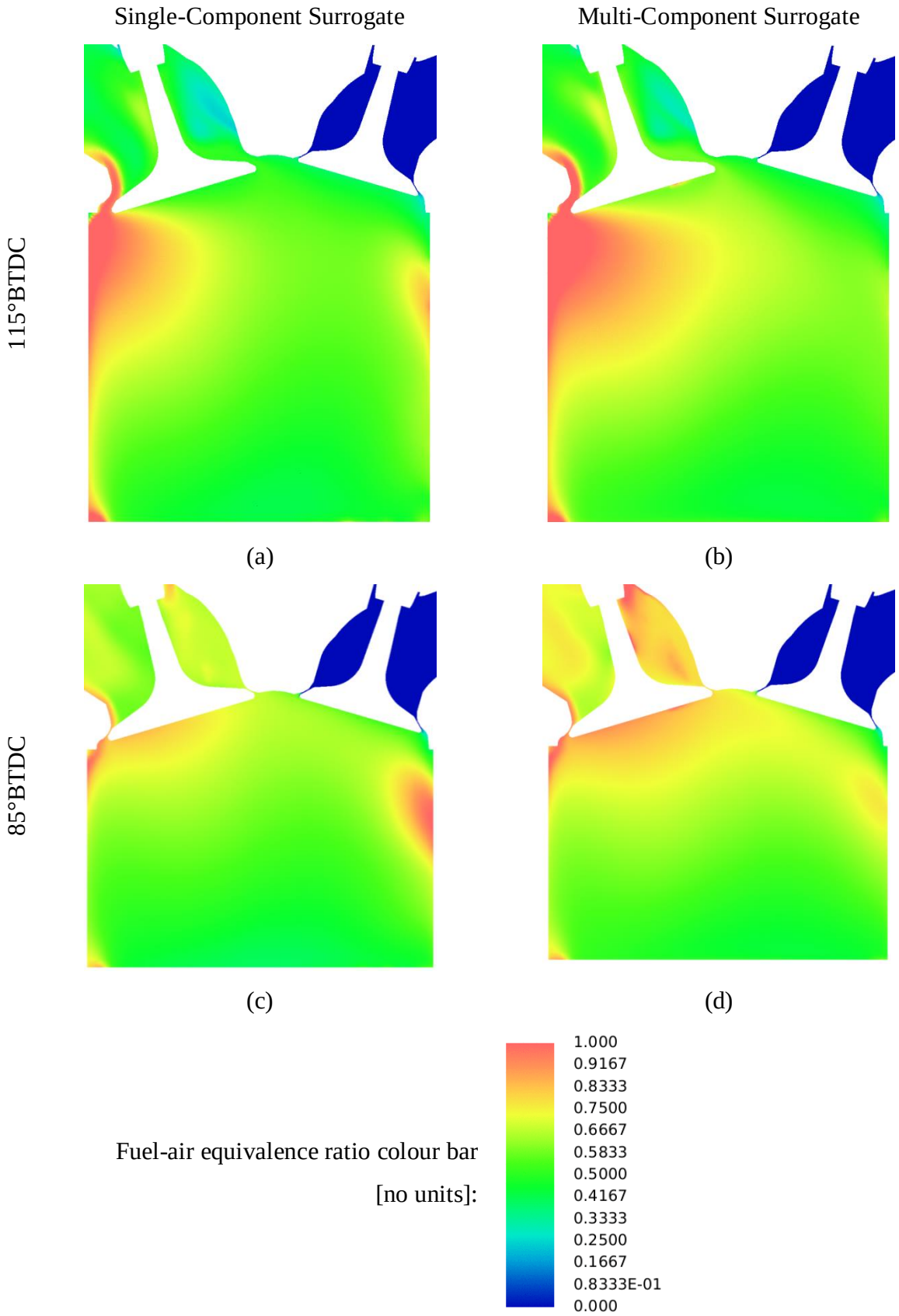

Figure 5.36 – Contours of equivalent fuel-air equivalence ratio, in the tumble plane through the rear intake valve, for (a) single-component fuel surrogate at 115°BTDC, (b) multi-component fuel surrogate at 115°BTDC, (c) single-component fuel surrogate at 85°BTDC and (d) multi-component fuel surrogate at 85°BTDC

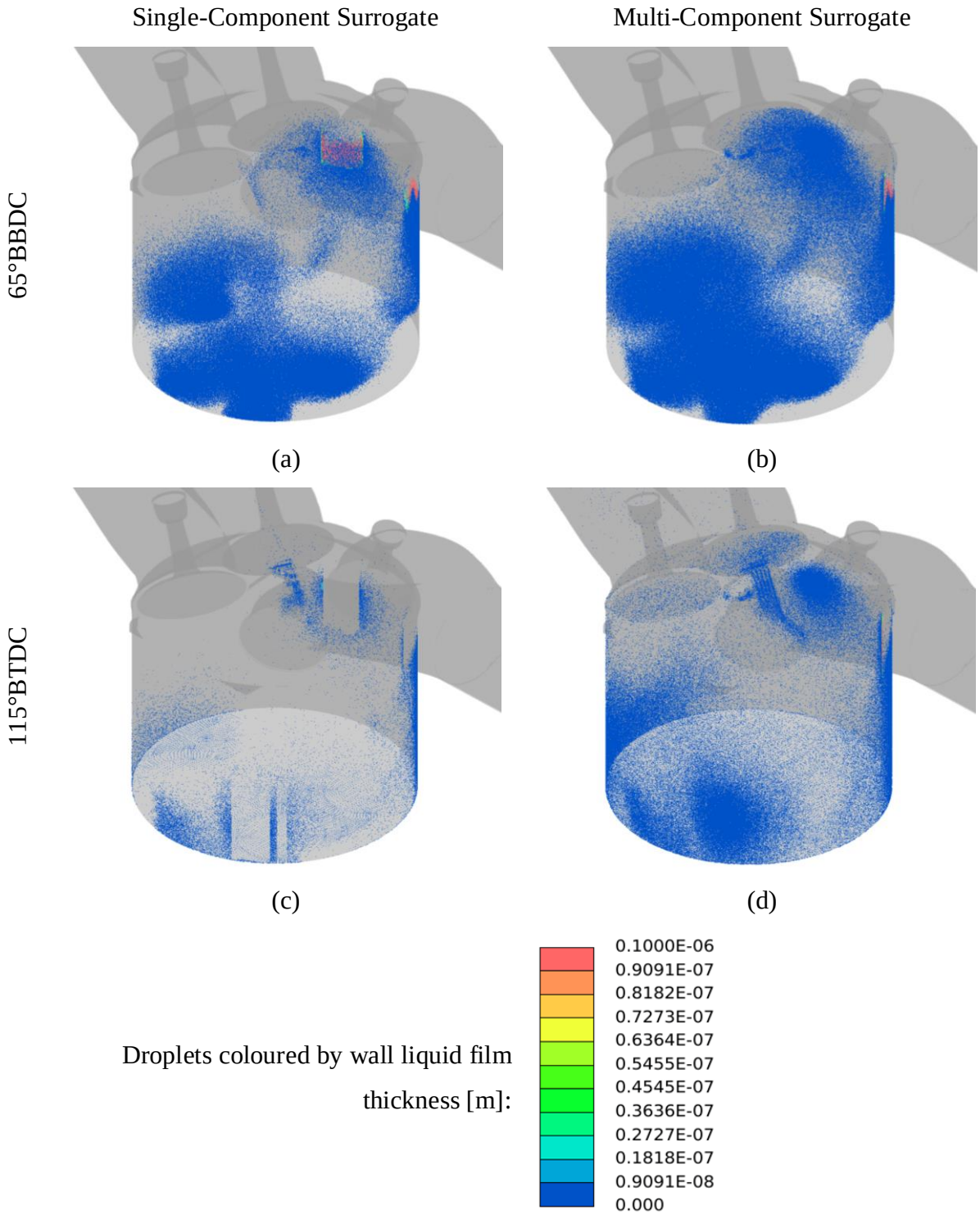

Figure 5.37 – Figure show droplets coloured by liquid film thickness for (a) single-component fuel surrogate at 115°BTDC, (b) multi-component fuel surrogate at 115°BTDC, (c) single-component fuel surrogate at 85°BTDC and (d) multi-component fuel surrogate at 85°BTDC

Thus correctly predicting and hence understanding the evolution of the fuel-air mixture is important for making improvements in engine design. E.g. in this case, the degree of late

intake valve closure and acceptable quantity of mixture trapped in the intake port at the end of the cycle, and its potential contribution to fuel mass in the following cycle and increased pollutants (UHC and PM), could be understood and mitigated as necessary.

In addition to the findings above related to fuel-air mixture transport into the intake port, the additional fuel situated towards the top of the combustion chamber in the multi-component surrogate predictions acts to create a richer mixture around the spark plug at spark timing. Figure 5.39 shows the fuel-air equivalence ratio for both the single-component surrogate and the multi-component surrogate at spark timing in the y-z plane spark plug cutting plane (see Figure 5.38 for orientation of cutting plane), with a richer mixture present around the spark plug in the multi-component surrogate predictions whereas a greater quantity of fuel is situated at the periphery of the combustion chamber close to the piston crown in the single-component surrogate case, which will impact the laminar flame speed and hence any subsequent predictions of the combustion process.

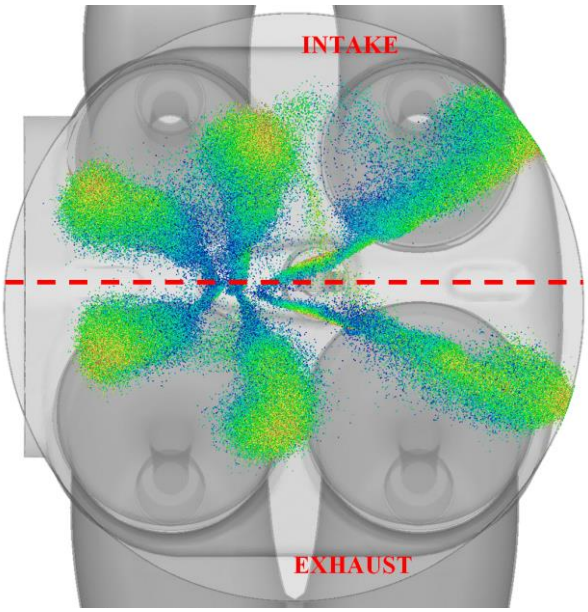

Figure 5.38 – Spark plug cutting plane in the y-z plane, plane coordinates:[-4,0,0]

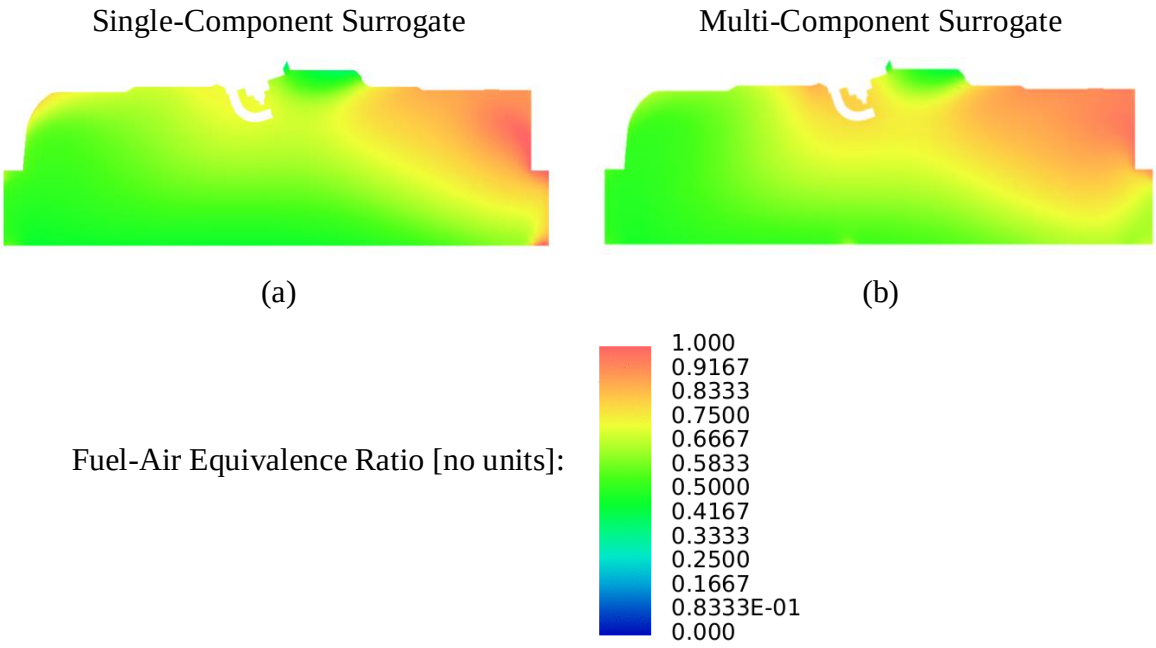

Figure 5.39 – Contours of fuel-air equivalence ratio along the spark plug cutting plane at 35°BTDC (spark timing) for (a) single-component surrogate, (b) multi-component surrogate

5.3.2 Spray and Mixture Field CCV at Spark Timing

The cycle-to-cycle variations of the mixture field at spark timing are known to have a large effect on the resultant combustion process, including variations in laminar flame speed, pollutant formation and abnormal combustion phenomenon including misfire and knocking events. The following section looks at the CCV in the mixture field at spark timing, both spatially and temporally, identifying both 'high' and 'low' cycles and their potential causes via the coefficient of variance of the fuel-air equivalence ratio.

The coefficient of variance (CoV) of the fuel-air equivalence ratio, effectively defining the degree of homogeneity of the mixture, was calculated at spark timing to identify cycles with comparatively high or low mixture stratification using the following methodology:

1) Calculate the mean fuel-air equivalence ratio $\bar{\phi}$:

$$\bar{\phi}(\theta, c) = \frac{1}{N}\sum_{i=1}^{N} \phi(\theta, c, i) \tag{5.1}$$

2) Calculate the standard deviation of the fuel-air equivalence ratio ϕ_{SD}:

$$\phi_{SD}(\theta, c) = \sqrt{\frac{1}{N}\sum_{i=1}^{N}[\phi(\theta, c, i) - \bar{\phi}(\theta, c)]^2} \tag{5.2}$$

3) Calculate the coefficient of variance of the fuel-air equivalence ratio ϕ_{CoV}:

$$\phi_{CoV}(\theta, c) = \frac{\phi_{SD}(\theta, c)}{\bar{\phi}(\theta, c)} \tag{5.3}$$

Where: N is the total number of cells in the domain, i is the cell number, θ is the crank angle and c is the cycle number.

Figure 5.40 shows the CoV of fuel-air equivalence ratio as a function of engine cycle at spark timing, and identifies cycles 3 and 6 with comparatively high CoV and cycle 12 with comparatively low CoV.

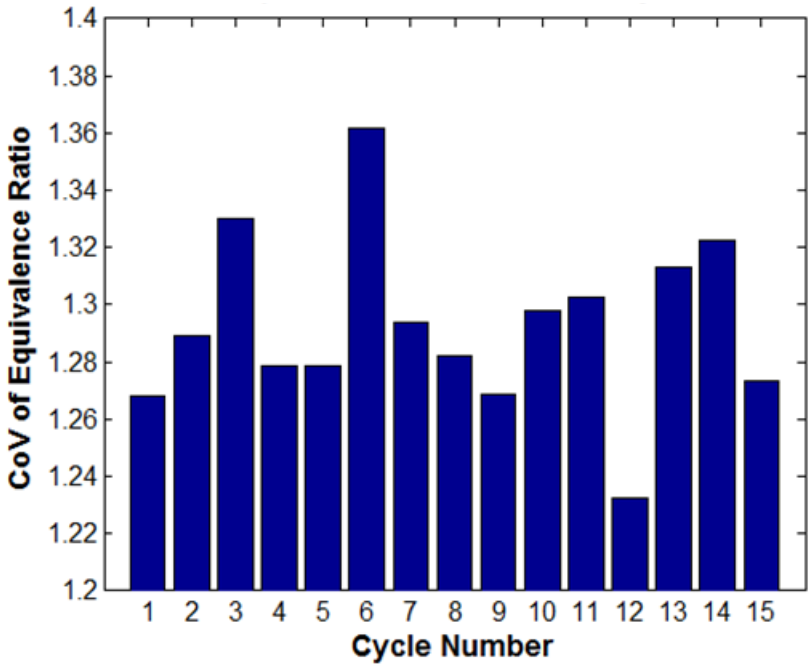

Figure 5.40 – CoV of equivalence ratio as a function of cycle number at 35°BTDC (spark timing)

To analyse the spatial variation of the fuel-air equivalence ratio for cycles 3, 6 and 12, the fluctuating equivalence ratio (ϕ'), standard deviation of the equivalence ratio (ϕ_{SD}) and coefficient of variance of the equivalence ratio (ϕ_{CoV}), were calculated via the following methodology and then plotted as contour plots in the y-z plane intersecting the spark plug electrodes (see Figure 5.38 for orientation of cutting plane).

1) Calculate the ensemble-average of the fuel-air equivalence ratio $\bar{\phi}$:

$$\bar{\phi}(\theta) = \frac{1}{n}\sum_{c=1}^{n} \phi(\theta, c) \tag{5.4}$$

2) By applying the Reynolds decomposition to the variation in equivalence ratio, the fluctuating equivalence ratio ϕ'can be found:

$$\phi'(\theta, c) = \phi(\theta, c) - \bar{\phi}(\theta) \tag{5.5}$$

3) Calculate the standard deviation of the equivalence ratio ϕ_{SD}:

$$\phi_{SD}(\theta) = \sqrt{\frac{1}{n}\sum_{c=1}^{n}[\phi(\theta, c) - \bar{\phi}(\theta)]^2} = \sqrt{\frac{1}{n}\sum_{c=1}^{n}\phi'(\theta, c)^2} \tag{5.6}$$

4) Calculate the coefficient of variance of the fuel-air equivalence ratio ϕ_{CoV}:

$$\phi_{CoV}(\theta) = \frac{\phi_{SD}(\theta)}{\bar{\phi}(\theta)} \tag{5.7}$$

Where: n is the total number of cycles, c is the cycle number and θ is the crank angle.

Figure 5.41(a) (c) (e) show the fuel-air equivalence ratio and Figure 5.41(b) (d) (f) show contours of the fluctuating equivalence ratio, indicating spatially where the cycles of interest (cycles 3, 6 and 12) differ from the ensemble-average spatial variation in equivalence ratio shown in Figure 5.42(a).

In cycles 3 and 6, a number of rich pockets of fuel-air mixture are identifiable when compared to the ensemble-average result, particularly around the periphery of the combustion chamber. This is due to either, poorer mixing through the intake and compression stroke due to differences in turbulence levels, or higher quantities of fuel impinged on the liner and piston that evaporate late in the compression stroke due to the elevated temperatures but do not mix sufficiently with the remaining charge due to the lower turbulence levels available. These variable pockets of rich fuel mixture will contribute to CCV towards the end of the combustion event due to the variation in equivalence ratio impacting the laminar flame speed. Interestingly, the RANS predicted equivalence ratio (Figure 5.42(b)) shows a similarly rich region along the front of the combustion chamber (to the right in the images) but does not capture the rich mixture at the rear of the combustion chamber (to the left in the images) as identified in the LES ensemble-average, indicating the impact of differences in predicted flow structures on the transport and diffusion of the fuel-air vapour cloud both temporally through the cycle and spatially through the cylinder.

Cycle 12, previously identified with low equivalence ratio CoV in Figure 5.40, i.e. higher homogeneity, does not exhibit the same pockets of rich mixture around the periphery suggesting either a variation in in-cylinder flow structures and/or turbulence levels that have improved mixing, or a lower quantity of impinged fuel on the liner and piston crown again due to a variation in in-cylinder flow structures.

Figure 5.43 shows the standard deviation of the fuel-air equivalence ratio ϕ_{SD} and the CoV of the fuel-air equivalence ratio ϕ_{CoV} along the same cutting plane and Figure 5.44 shows an iso-surface of the coefficient of variance of equivalence ratio at ϕ_{CoV}=0.5, thus indicating areas of high variability in mixture homogeneity, effectively providing a graphical representation of areas within the combustion chamber that see high levels of CCV of the fuel-air equivalence ratio. From these figures it is possible to identify areas of high equivalence ratio CCV around the front of the combustion chamber and in the rear intake valve port, both expected to be due to variations in the resultant strength and direction of the tumble flow structures through the end of the intake stroke and compression stroke. The CoV of the velocity magnitude $u_{i,CoV}$, was calculated using the same procedure as documented for equivalence ratio above and an iso-surface plotted shown in Figure 5.45. A large area of high CCV flow is visible on the exhaust side of the combustion chamber between the two exhaust valves as a consequence of variability of the recirculation regions and tumble flow structures

(as observed previously in Figure 5.24), a driver for the observed CoV of equivalence ratio. Also of note from Figure 5.45 is the significant CCV present in the flow in the intake ports as a consequence of the high velocity, and as a consequence highly turbulent, flow generated during the intake valve closing event that occurred 33°c.a. earlier.

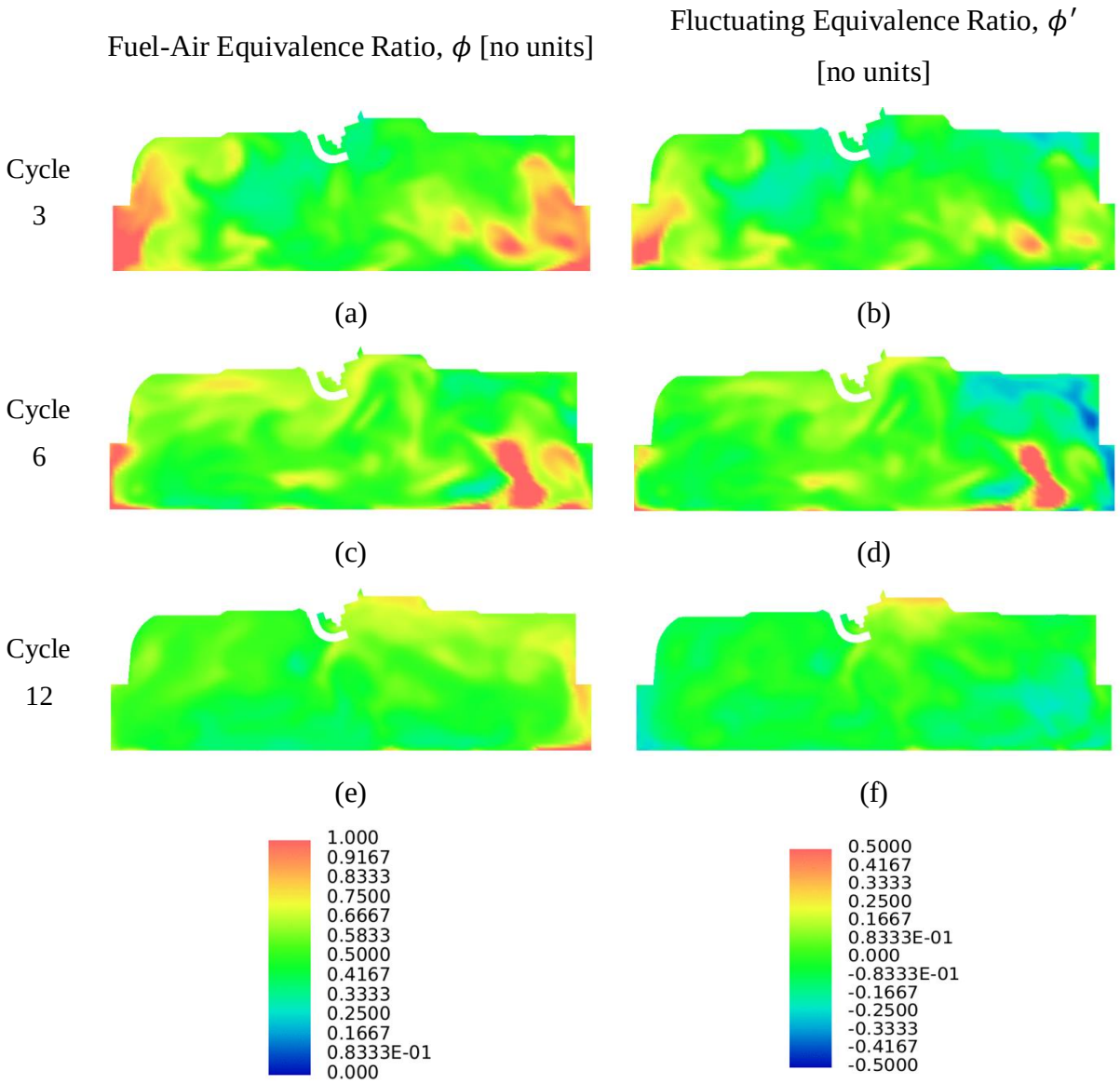

Figure 5.41 – (a) (c) (e) Contours of fuel-air equivalence ratio ϕ, (b) (d) (f) Contours of fluctuating equivalence ratio ϕ', for cycles 3, 6 and 12 along the spark plug cutting plane

Figure 5.43(b) does identify a region of increased equivalence ratio variability in the pent-roof close to the spark plug which will act to increase CCV of the combustion process during the earlier stages of kernel development, a critical time for CCV of the overall process but based inspection of both Figure 5.43 and Figure 5.44, ϕ_{CoV} is mostly less than 0.5 throughout

the cylinder interior which will contribute to lower levels of CCV through the majority of the turbulent flame propagation phase.

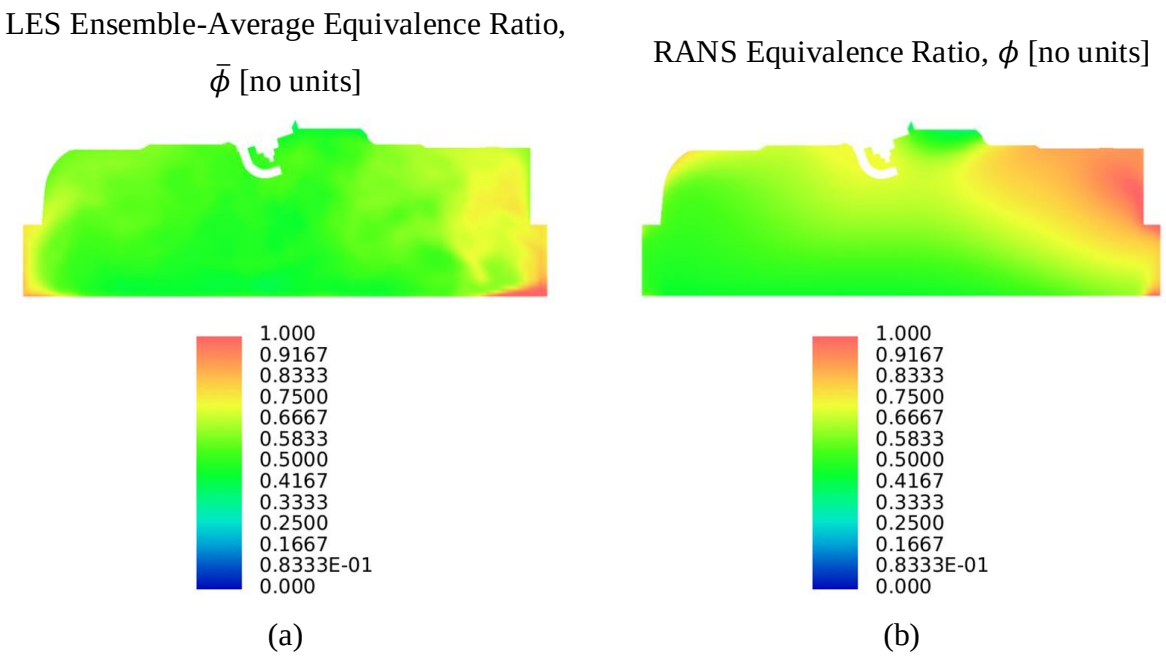

Figure 5.42 – Contours of fuel-air equivalence ratio along the spark plug cutting plane for (a) LES ensemble-average, (b) RANS

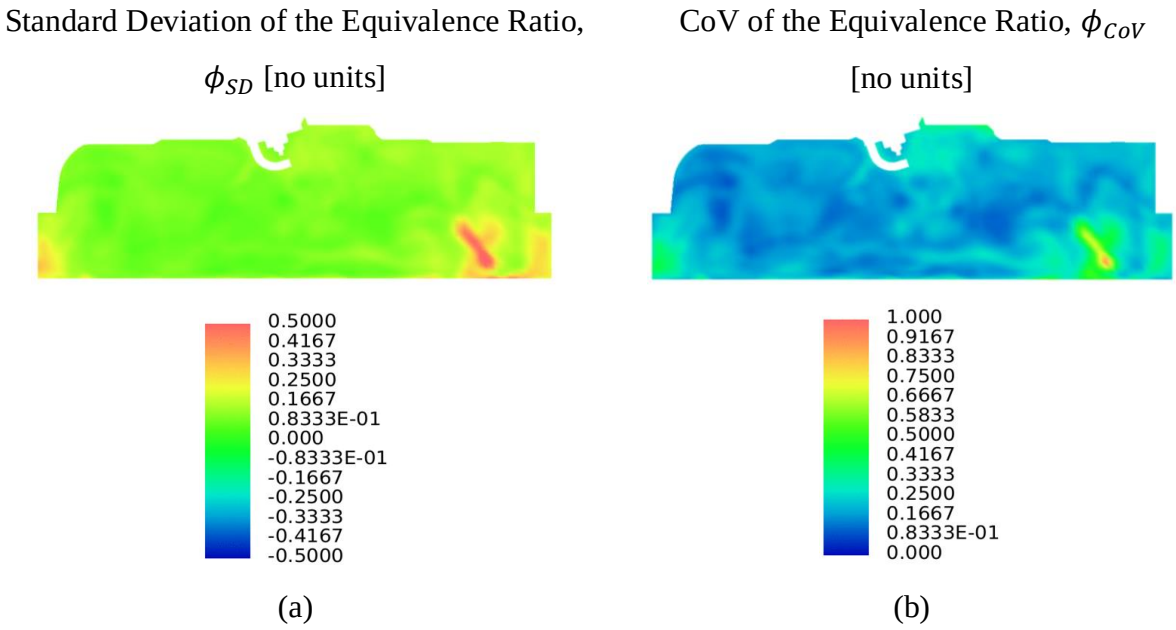

Figure 5.43 – (a) Contours of standard deviation of the equivalence ratio ϕ_{SD} and (b) coefficient of variance of equivalence ratio ϕ_{CoV}, along the spark plug cutting plane

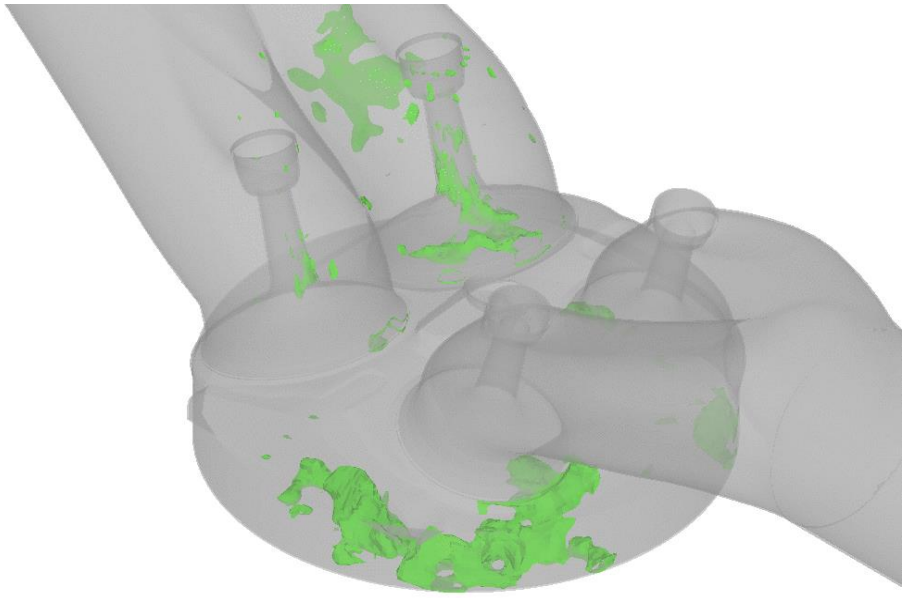

Figure 5.44 – Iso-surface of the coefficient of variance of the equivalence ratio ϕ_{CoV}=0.5, indicating areas of high equivalence ratio CCV in the cylinder and intake ports at 35°BTDC (spark timing)

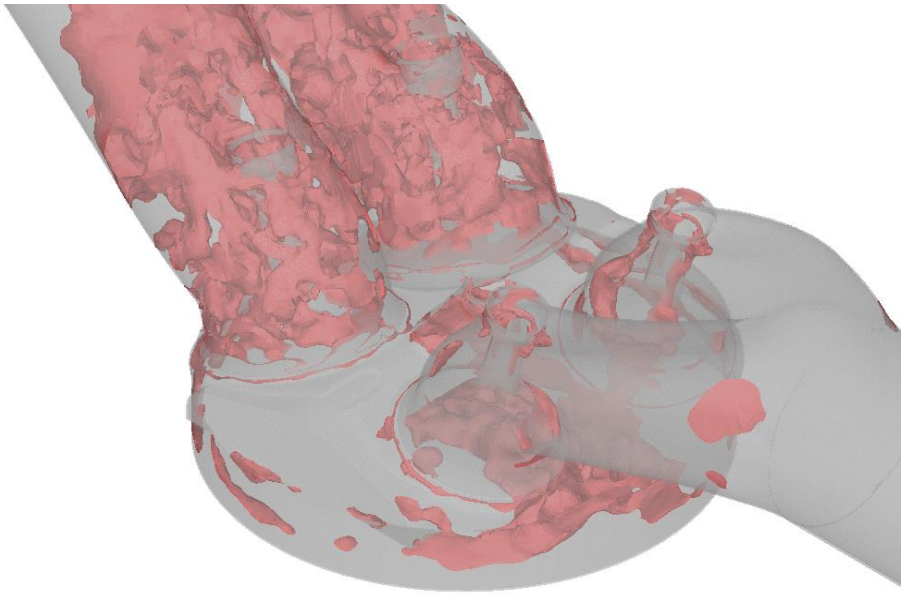

Figure 5.45 – Iso-surface of the coefficient of variance of the velocity magnitude at $u_{i,CoV}$=2, indicating areas of high velocity magnitude CCV in the cylinder and intake ports at 35°BTDC (spark timing)

5.3.3 The Effect of Intake Valve Jet Flapping on Mixture Field Development

As discussed earlier in section 4.2.4, intake valve jet flapping has been suggested as a potential source of CCV of the large scale flow structures within the intake and compression strokes. Thus it follows that the phenomenon has the potential to cause CCV in the spatial variation of fuel-air equivalence ratio at spark timing and resultant combustion process. The purpose of this section is to investigate the potential of intake valve jet flapping as a source of fuel-air equivalence ratio variation at spark timing. The results in this section were generated using the Smagorinsky SGS model and computational setup as defined in section 3.3.4.2.

First, velocity magnitude contours for an arbitrary cycle exhibiting valve jet flapping are examined in conjunction with images showing fuel-air equivalence ratio contours along the same cutting plane to establish if the influence jet flapping on the mixture field evolution is evident.

Figure 5.46(a) shows velocity magnitude contours in a cutting plane intersecting the two intake valves at 105°ATDC and intake valve jet flapping is seen to be present. In Figure 5.46(b) fuel-air equivalence ratio contours are shown along the same cutting plane. At this crank angle it is only approximately 15°AEOI and as can be seen, much of the fuel-air mixture is still within the centre of the combustion chamber (note, mixture in this plane almost entirely air) and hence is not significantly affected by valve jet instability. This is seen to be the case up until approximately 130°ATDC.

At 130°ATDC the fuel-air mixture has begun to diffuse across the cylinder sufficiently that the flapping valve jet is able to begin to influence the mixture variation. In Figure 5.47(b) it is possible to see the valve jet flapping between the two intake valves beginning to influence and displace the fuel-air mixture cloud. Due to this occurring later in the intake event, the flapping valve jet is propagating at lower velocity and hence has a relatively small influence on the vapour cloud.

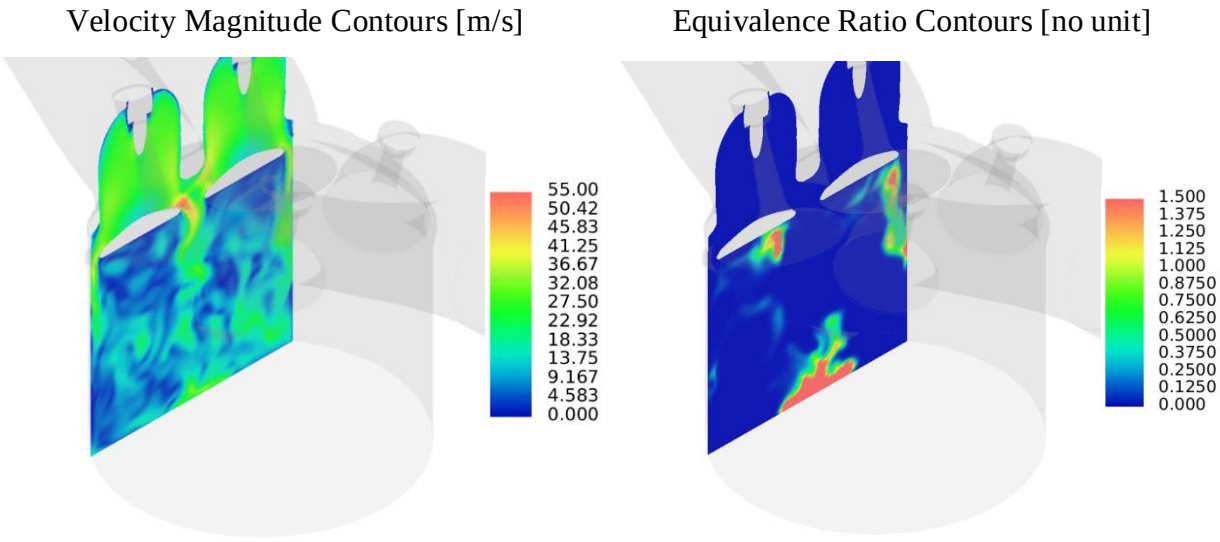

(a) (b)

Figure 5.46 – (a) Velocity magnitude contours and (b) fuel-air equivalence ratio contours, intersecting both intake valves at 105°ATDC

Upon inspection of the difference in valve curtain mass flux as a function of crank angle, a difference is seen between the profile when the cycle includes an injection event (Figure 5.48) and during a single-phase analysis as previously presented in section 4.2.4 (Figure 5.49). After the injection event (SOI=80°ATDC) the difference in intake valve curtain mass flux rises much more significantly than seen in a cold flow analysis. This acts to reduce the magnitude of fluctuation in valve curtain mass flux between the two valves and hence the amplitude of the resultant flapping valve jet. The change in intake valve mass flux after fuel injection is believed to be due to changes in the in-cylinder flow field (due to momentum imparted on the flow field from the injected fuel droplets) effecting the valve jet and hence mass flux through each valve.

Also of note from Figure 5.48 is that results from both RANS and LES show the same change in profile thus indicating that the influence of the injection event on the flow entering the cylinder is seen regardless of whether a time-filtered or space-filtered turbulence modelling approach is used.

The impact of the vapour cloud on the intake valve jet is also evident upon inspection of the velocity magnitude contours later in the cycle. Figure 5.50 shows the velocity magnitude contours at 150°ATDC, where the jet velocities are reduced due to the intake valve being at

maximum lift (149°ATDC) and the increased density of the in-cylinder charge due to the entrainment of atomised fuel, causes any jet flapping to be dissipated.

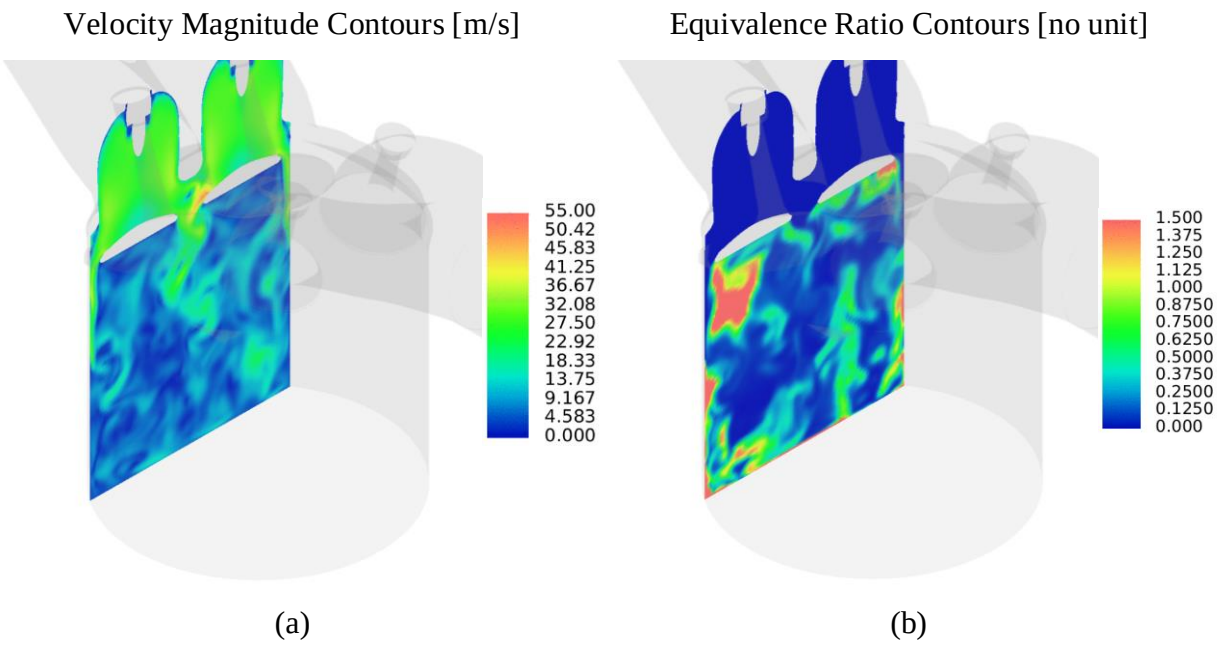

Figure 5.47 – (a) Velocity magnitude contours and (b) fuel-air equivalence ratio contours, intersecting both intake valves at 130°ATDC

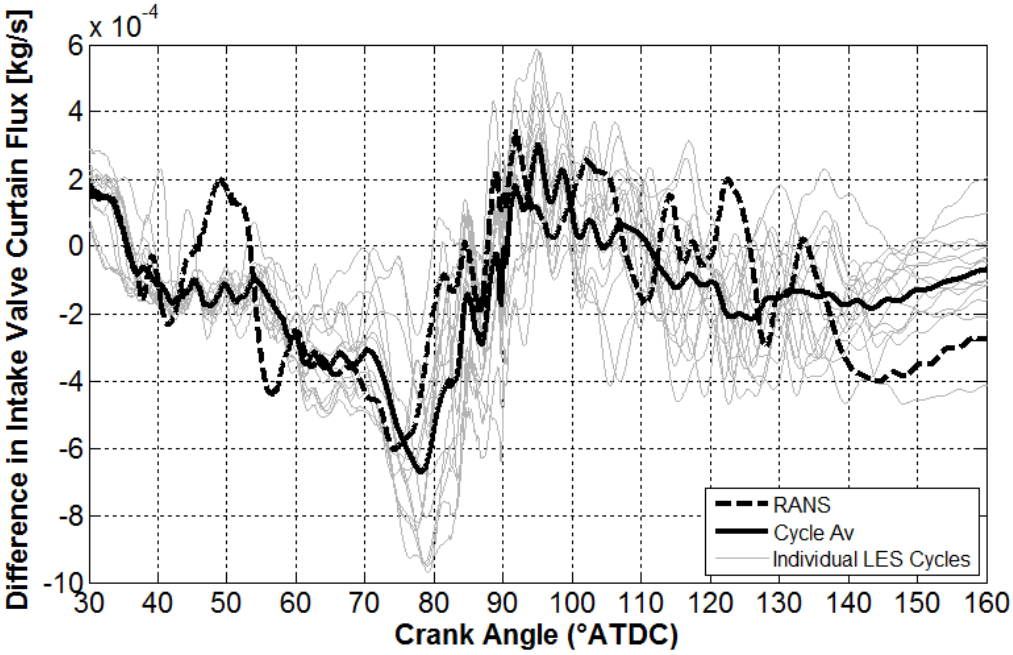

Figure 5.48 – Difference in intake valve curtain mass flux as a function of crank angle for LES and RANS two-phase simulations including an early injection event at 80°ATDC

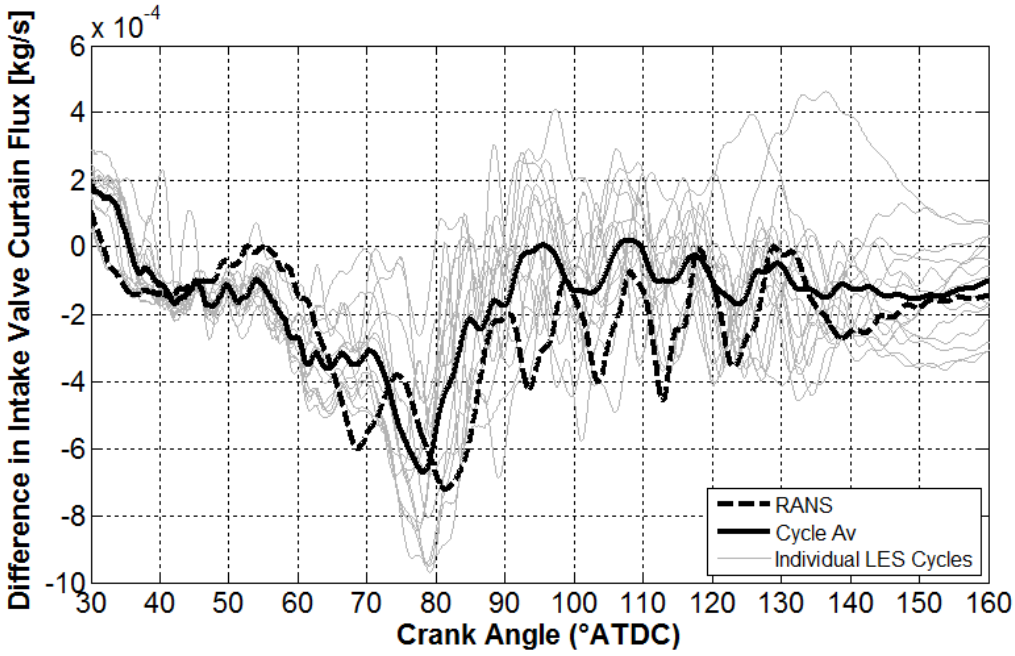

Figure 5.49 – Difference in intake valve curtain mass flux as a function of crank angle for LES and RANS single-phase/cold flow simulations (Figure 4.18, reprinted for convenience)

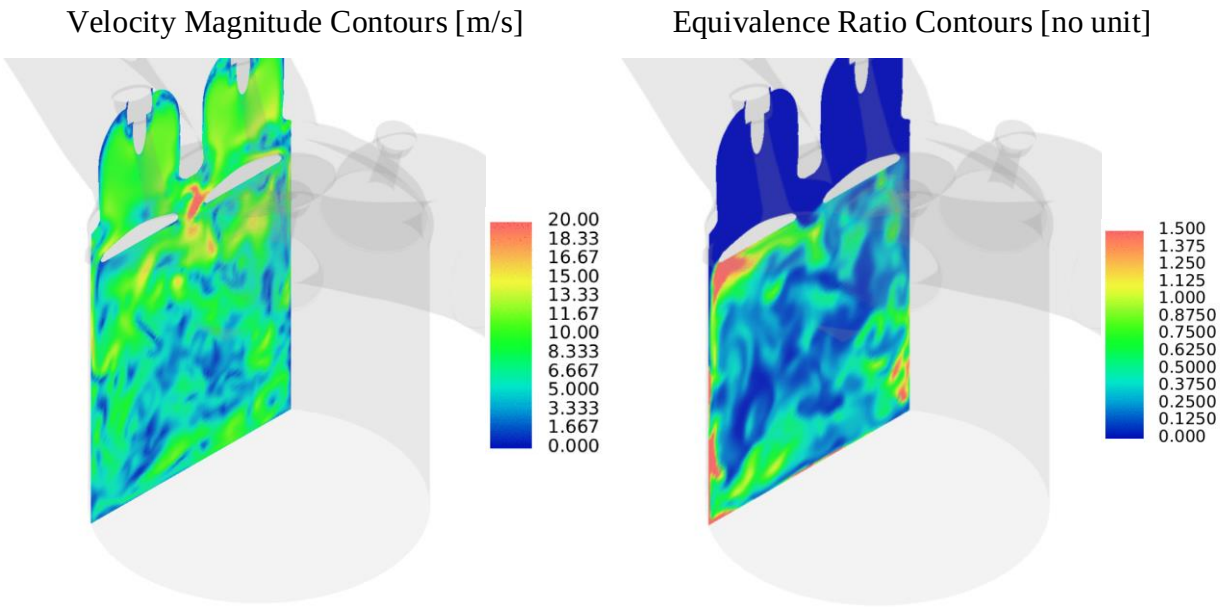

(a) (b)

Figure 5.50 – (a) Velocity magnitude contours and (b) fuel-air equivalence ratio contours, intersecting both intake valves at 150°ATDC

The above analysis was constrained to one two-dimensional cutting plane and it was considered feasible that intake valve jet instability could also be occurring in other planes (e.g. the swirl plane as identified in Hasse (2016)) and its CCV having a greater impact on the fuel-air equivalence ratio than observed.

As previously identified in Figure 5.40, cycle 3 and 6 were identified as cycles with comparatively high CoV and cycle 12 with comparatively low CoV.

To investigate if the observed CoV in the high and low cycles had occurred earlier in the cycle around the point when intake valve jet flapping is prominent, the CoV of the fuel-air equivalence ratio was calculated across the range of 80°ATDC to 160°ATDC where intake valve jet flapping had previously been identified to be present. Figure 5.51 shows the CoV of equivalence ratio at 90°ATDC (or 1°AEOI) and 160°ATDC (or approximately 70°AEOI). A clear increase in CoV is visible earlier in the cycle as expected due to the reduced time available for mixing but cycles 3 and 6 are not seen to have comparatively high CoV, nor cycle 12 seen to have comparatively low CoV, thus suggesting that the variability seen at spark timing cannot be entirely attributed to variability in the flow field earlier in the cycle due to intake valve jet flapping.

In addition to the two crank angles presented here, the change in CoV as a function of crank angle from 100°ATDC to 160°ATDC was also investigated to see if any particular cycles showed a significant difference in how the CoV reduced with time but the data did not provide evidence as such.

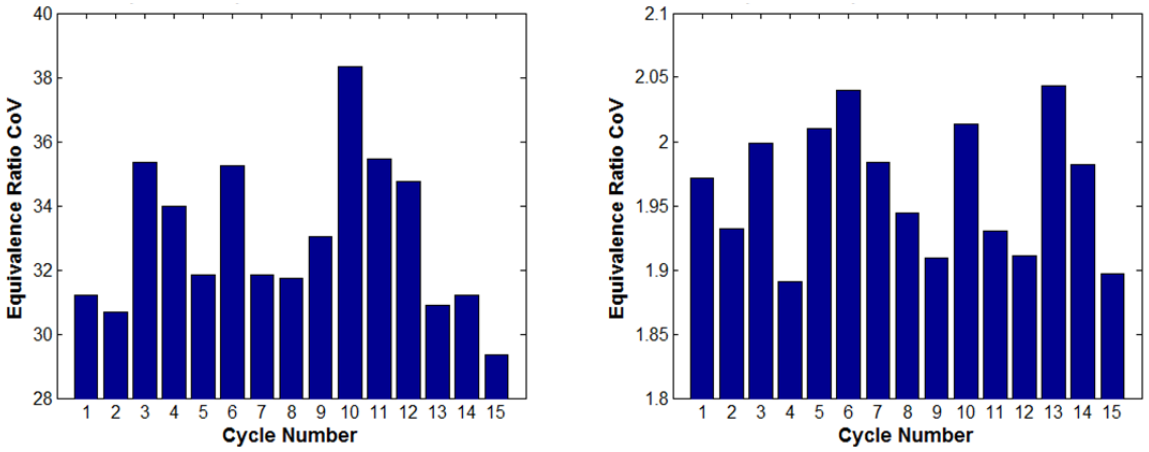

(a) (b)

Figure 5.51 – CoV of equivalence ratio as a function of cycle number at (a) 90°ATDC/1°AEOI and (b) 160°ATDC/~70°AEOI

The difference in intake valve curtain mass flux for cycles 3, 6 and 12 were also compared to the population, shown in Figure 5.52, to see if any differences existed between those cycles and the rest of the population that could be used to infer a difference in the resultant valve jet flapping and hence CoV of equivalence ratio at spark timing, but neither of the cycles identified appear as significant outliers that could be used to derive a conclusion that intake valve jet flapping has a significant influence on equivalence ratio CoV at spark timing.

It could be hypothesised that since the magnitude of the jet flapping is more significant in the absence of a fuel injection event (as seen when comparing the single-phase and two-phase results described above), an injection event later in the intake stroke or even in the compression stroke, as used in a stratified mixture control strategy, would allow CCV of the intake valve jet flapping process more time to influence, and generate CCV in, the bulk flow structures and subsequently be a larger contributor to CCV of the final fuel-air equivalence ratio but to prove or disprove this hypothesis would require further numerical effort and is beyond the scope of this current research.

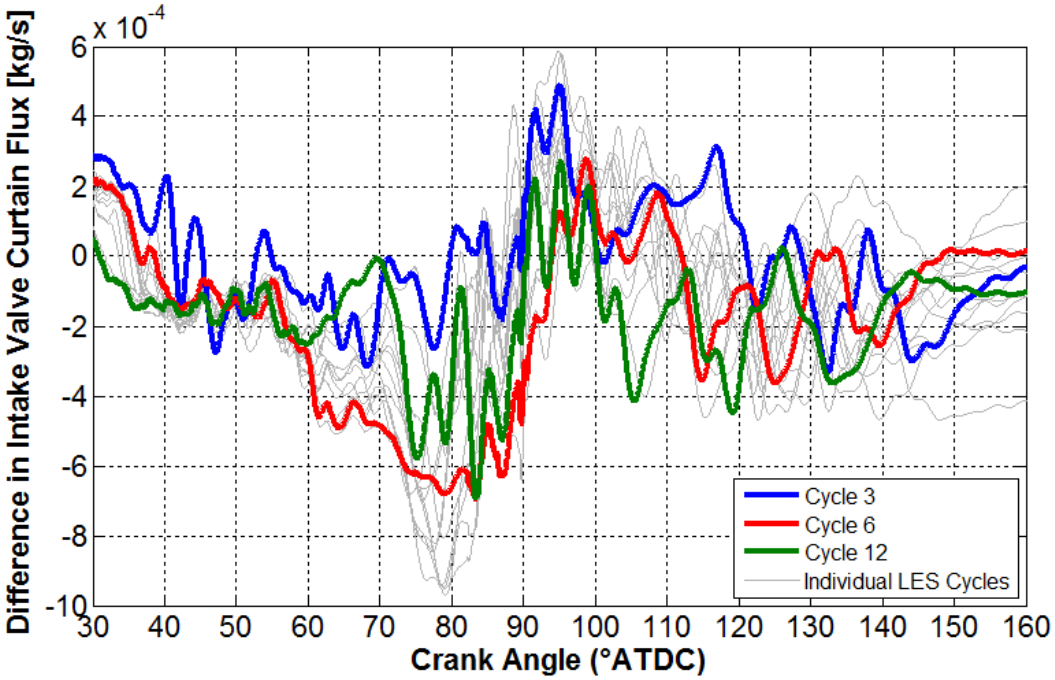

Figure 5.52 – Difference in intake valve curtain mass flux as a function of crank angle for all LES cycles with cycles 3, 6 and 12 highlighted

5.4 INTERACTIONS BETWEEN IN-CYLINDER TURBULENCE AND THE FUEL INJECTION EVENT

The previous sections within this thesis have investigated both the in-cylinder flow structures of the continuous-phase and the processes of the liquid-phase injection event. The purpose of the following section is to further investigate the interactions between the liquid-phase of the fuel injection event and the turbulent continuous-phase.

5.4.1 Turbulence Characteristics Before Fuel Injection

Before making comparisons of the turbulence characteristics between injecting (two-phase) and non-injecting cold flow (single-phase) cases, it is first pertinent to check that the turbulence characteristics prior to injection when only 15 cycles were simulated are similar to those at the equivalent point when 29 cycles were simulated, ensuring that any differences in turbulence characteristics post injection are due to the injection event and not due to differences in the total number of cycles.

Figure 5.53 shows ensemble-average and RMS fluctuating velocity results (as calculated using the methodology presented in section 4.3) for the 29 cycle single-phase model as described in section 3.3.3.2 at 80°ATDC or 0°ASOI (i.e. the point of fuel injection), and Figure 5.54 presents equivalent results for the 15 cycle two-phase model as described in section 3.3.4.2.

Comparing the fluctuating velocity components between the two cases shows very similar turbulence characteristics across the cylinder, picking up similar anisotropic characteristics as noted previously in section 5.3, e.g. increases in z-plane w'_{rms} when compared to the other components at y=-19mm and y=0mm z=-28 x=-40mm and y=0mm z=-8mm x=-30mm.

Note: cutting planes used in this section are the same as used in section 4.3 and shown previously in Figure 4.19.

There appears to be a slightly larger anisotropy predicted across the cylinder in the 15 cycle two-phase case at y=0mm z=-8mm when compared to the 29 cycle single-phase case; this is as a consequence of the more turbulent flow structures and less well defined recirculation regions present due to the reduced number of cycles available for averaging. Nevertheless, the predictions from both models are considered sufficiently similar and thus it deemed acceptable to compare the turbulence characteristics between 29 cycle single-phase results with the 15 cycle two-phase results to understand the interactions between the injection process and the continuous-phase turbulence.

5.4.2 Comparison of Turbulence Characteristics between Single-Phase and Two-Phase Predictions

The next stage of the analysis was a comparison of the predicted turbulence characteristics between the single-phase and two-phase results to understand the impact of the injection event on in-cylinder turbulence levels.

Figure 5.55 compares results from the continuous-phase only model over 29 cycles (model described in section 3.3.3.2) against two-phase results over 15 cycles (model described in section 3.3.4.2) in the tumble plane along the bore centreline at 100°ATDC or 20°ASOI, which intersects plumes 2 and 5 towards the bottom of the combustion chamber. The momentum exchange between spray plumes and continuous-phase is apparent in both the velocity magnitude contour plots and ensemble-average line charts, with an increase in z-plane velocity magnitude, and to a lesser extent x-plane velocity magnitude. Inspection of the RMS fluctuating velocity line charts shows an increase in local anisotropy around the spray plumes, particularly noticeable in the z-plane component towards the bottom of the combustion chamber at z=-48mm where spikes in w'_{rms} are present at x=-20mm and x=25mm due to the penetrating spray plumes. A small rise in x-plane fluctuations is also visible due to the trajectory imposed by the injector nozzle geometry on the spray plumes generating localised variations in anisotropy.

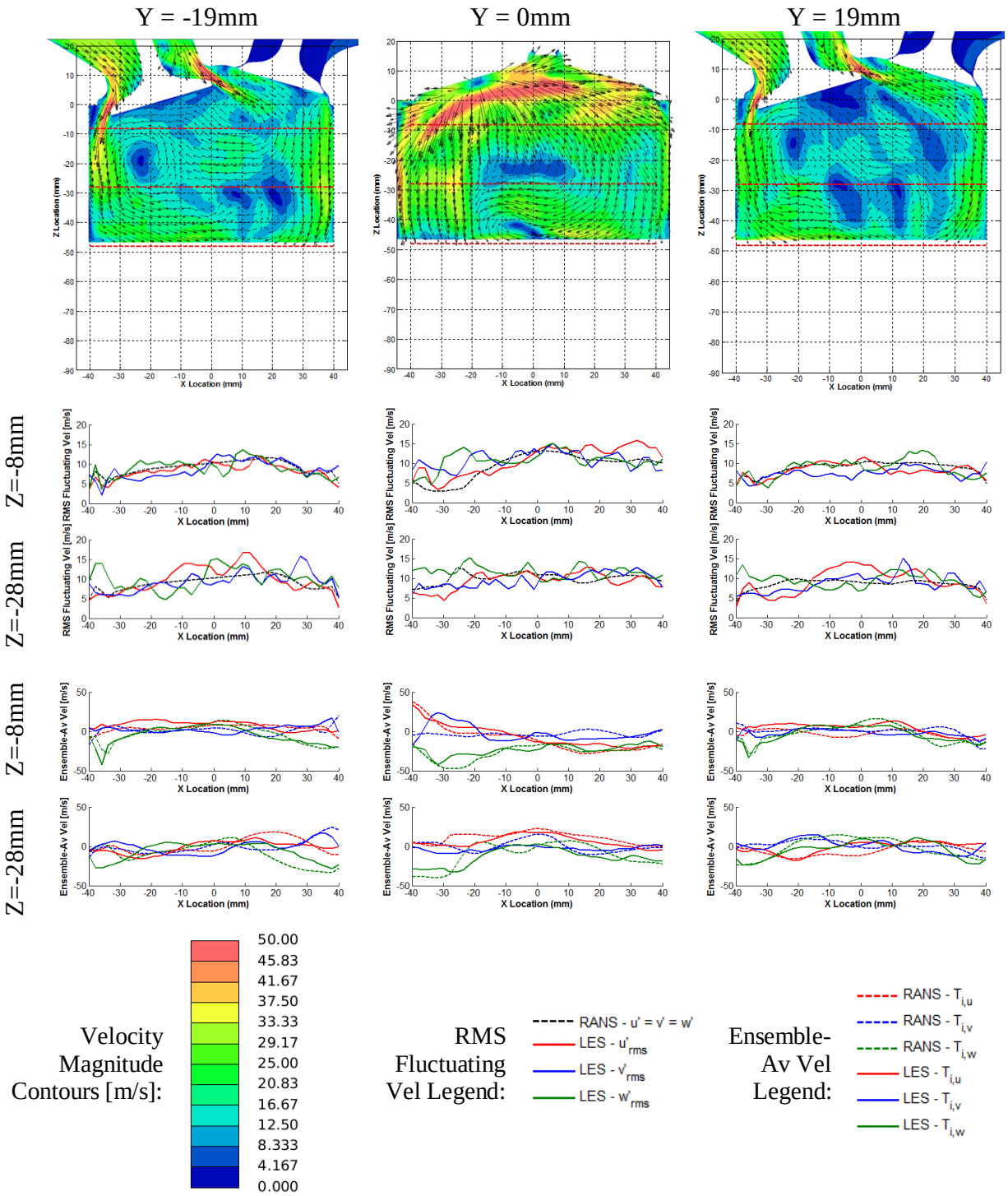

Figure 5.53 – 29 Cycle single-phase; 80°ATDC/0°ASOI; top row are ensemble-averaged velocity magnitude contours and velocity vectors $\bar{u}$; middle row are fluctuating velocity $u'_{i,rms}$; bottom row are ensemble-average velocity $\bar{u}_i$

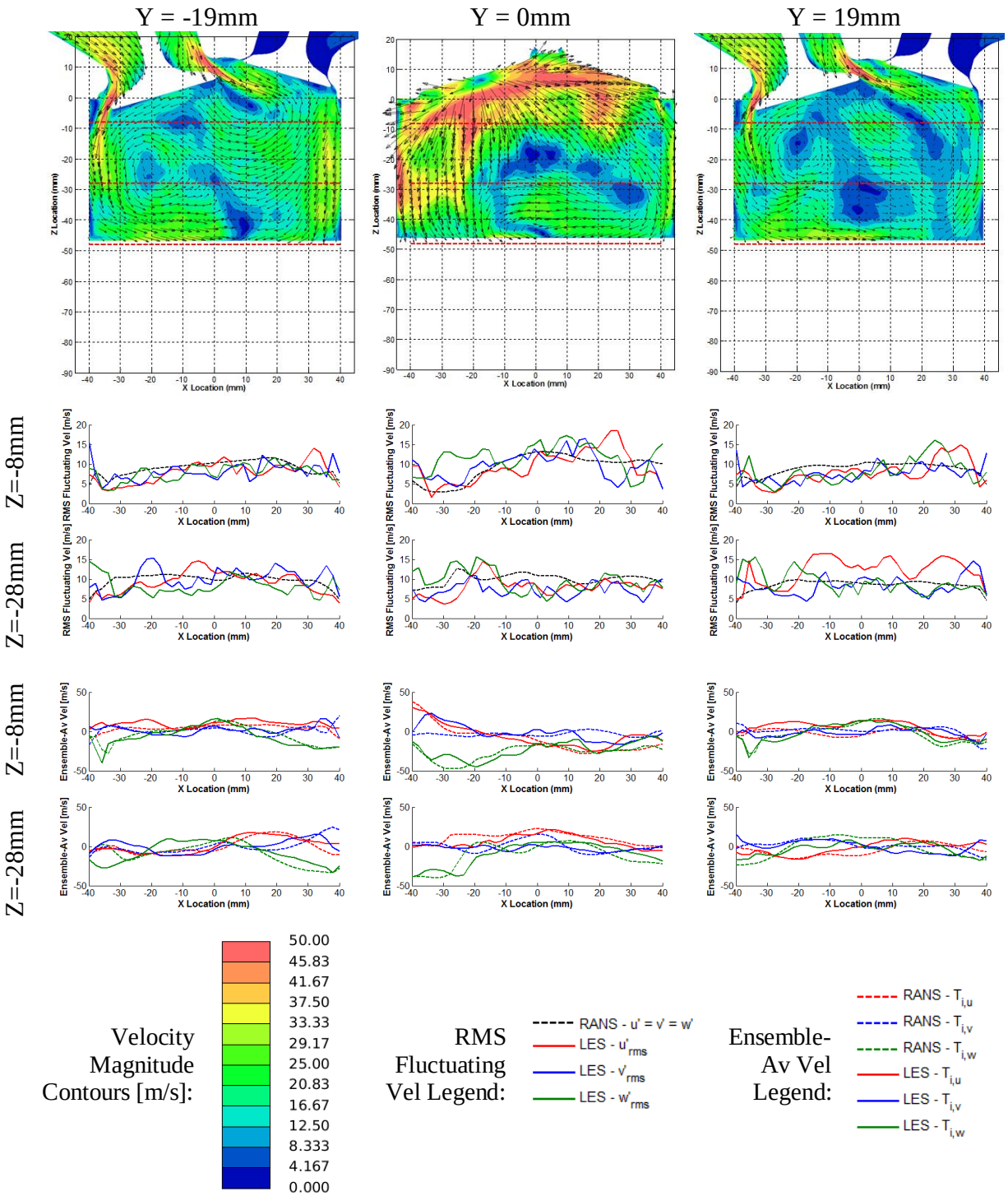

Figure 5.54 – 15 Cycle two-phase; 80°ATDC/0°ASOI; top row are ensemble-averaged velocity magnitude contours and velocity vectors $\bar{u}$; middle row are fluctuating velocity $u'_{i,rms}$; bottom row are ensemble-average velocity $\bar{u}_i$

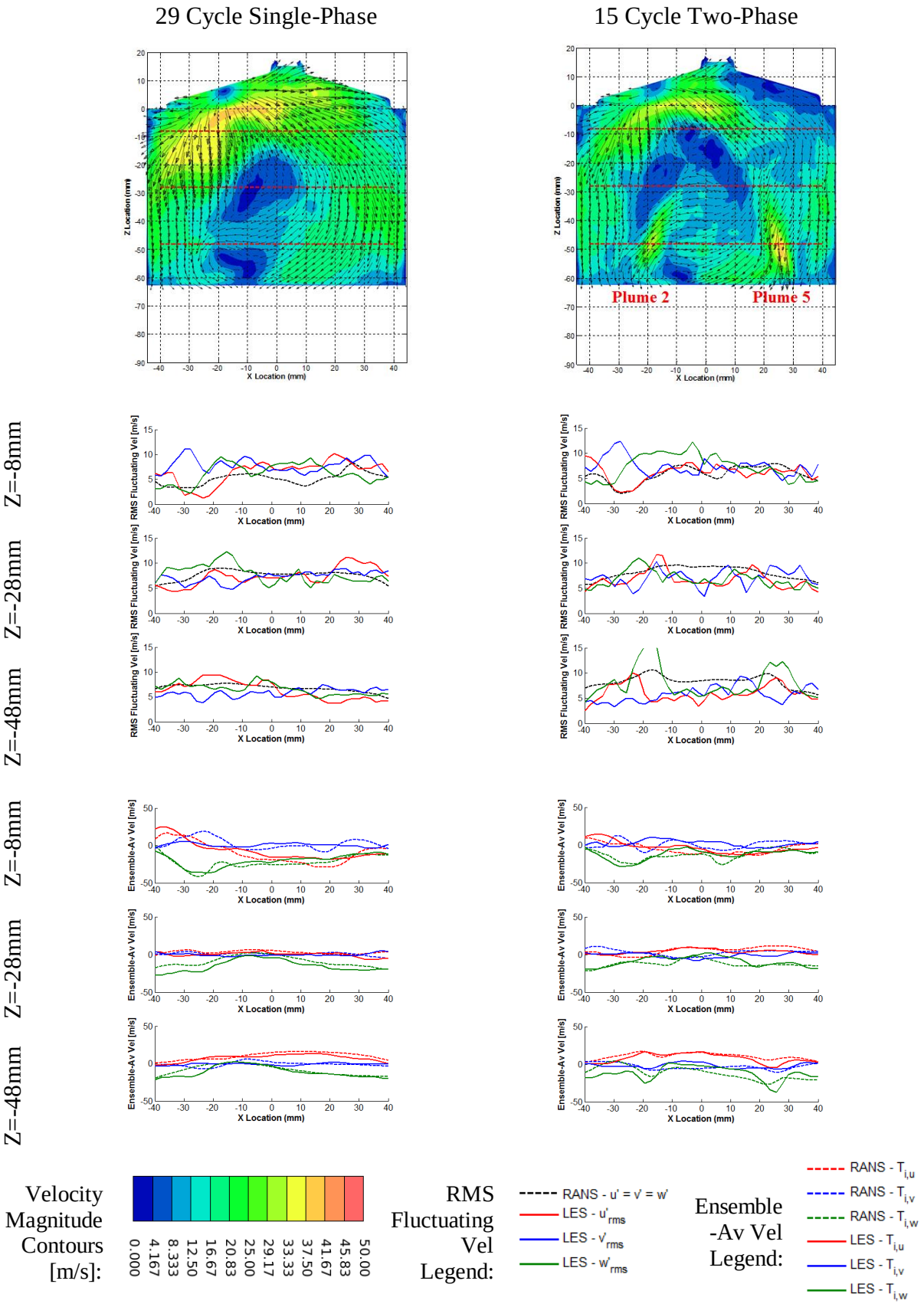

Figure 5.55 – Comparing single-phase and two-phase turbulence characteristics at 100°ATDC/20°ASOI at y=0mm (bore centreline) in the tumble plane; top row are ensemble-averaged velocity magnitude contours and velocity vectors $\bar{u}$; middle row are fluctuating velocity $u'_{i,rms}$; bottom row are ensemble-average velocity $\bar{u}_i$

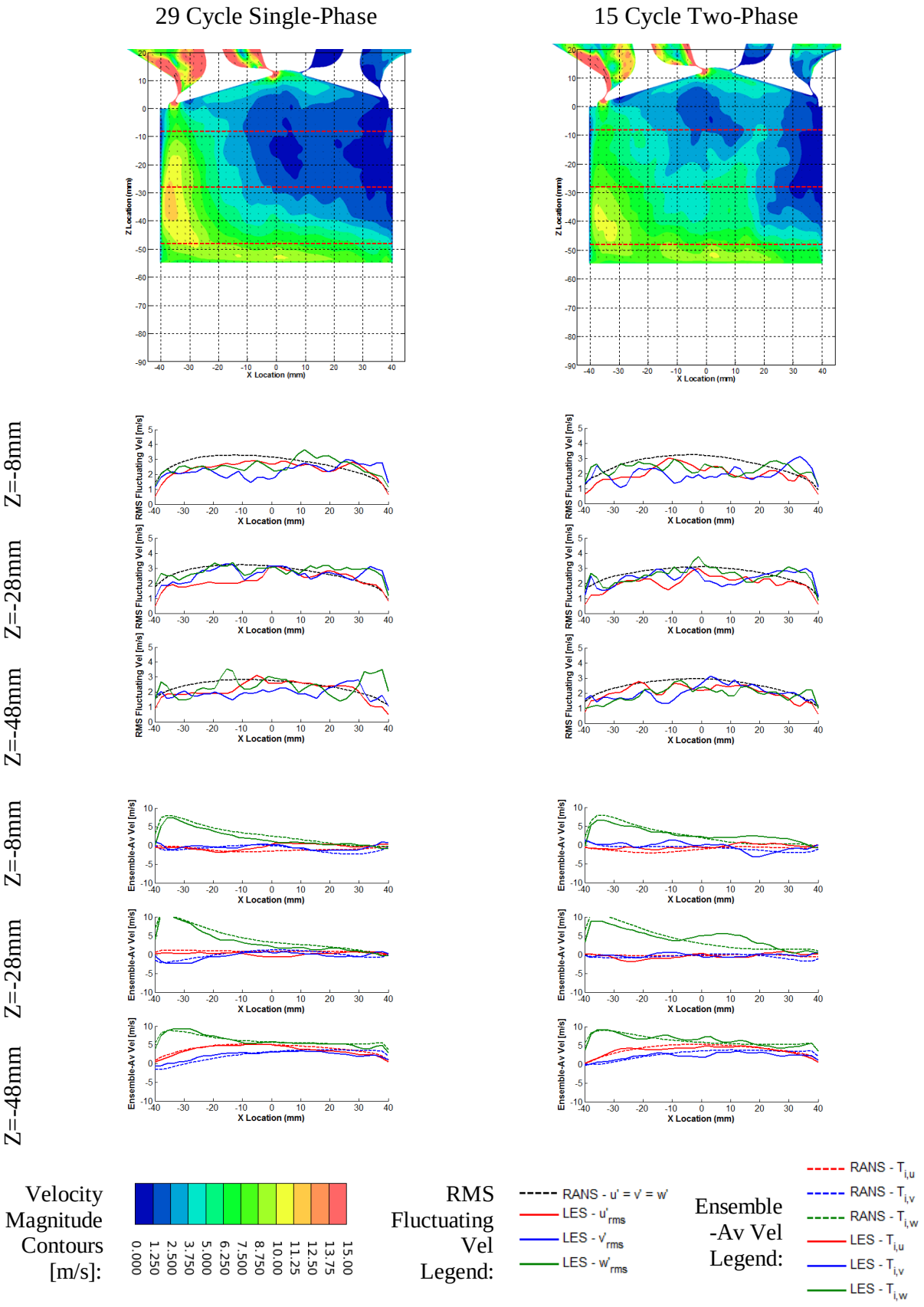

Figure 5.56 – Comparing single-phase and two-phase turbulence characteristics at 90°BTDC/190°ASOI at y=19mm in the tumble plane; top row are ensemble-averaged velocity magnitude contours and velocity vectors $\bar{u}$; middle row are fluctuating velocity $u'_{i,rms}$; bottom row are ensemble-average velocity $\bar{u}_i$

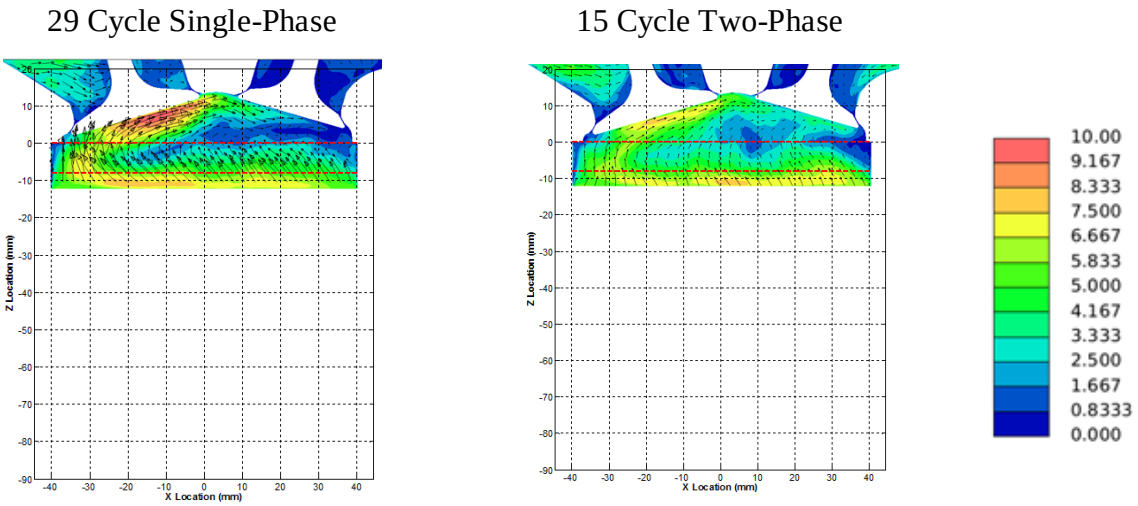

(a) (b)

Figure 5.57 – Comparing single-phase and two-phase results at 35°BTDC/spark timing at y=19mm in the tumble plane, ensemble-averaged velocity magnitude contours and velocity vectors $\bar{u}$

Comparison of the velocity magnitude contour plots also shows the modified flow field due to penetrating spray plumes has changed the bulk flow tumble motion travelling down both sides of the combustion chamber, modifying and reducing the large scale tumble motion. Thus it can be concluded that the injection event acts to modify the mean flow structures present during the induction event and generate localised anisotropy that is otherwise not present.

Figure 5.56 provides the same graphical comparison but at 90°BTDC and y=19mm (tumble cutting plane intersecting the front intake valve), to investigate the impact of the injection event on the in-cylinder flow field much later in the cycle during the compression stroke. An interesting variation is the increase in y-plane ensemble-average velocity at z=-28mm x=10mm in the two-phase case, that is clearly visible in the velocity magnitude contour plots as an area of gas with increased velocity moving up towards the roof of the combustion chamber towards the exhaust side of the combustion chamber. This is due to the presence of higher density fuel vapour in the centre of the combustion chamber being forced upwards by the rising piston. Figure 5.60(c) shows the equivalent cutting plane but with fuel mass fraction contours and the annotated arrow illustrating the increased fuel mass fraction corresponding to an increase in gas velocity at this location.

Also of note from the velocity magnitude contours in Figure 5.56 are the noticeably lower gas velocities of the large scale tumble motion propagating upwards on the intake side of the combustion chamber due to momentum exchange between droplets and the continuous-phase.

The impact of reduced mean flow velocities becomes of greater significance when considering the flow field at spark timing. Figure 5.57 shows velocity magnitude contours in the y=19mm tumble plane for both single-phase and two-phase results, similar to the findings at 90°BTDC, due to spray-flow momentum exchange, the two-phase results show a reduction in strength of the clockwise rotating tumble motion, accompanied by a weakening and subsequent increase in velocity magnitude of the recirculation regions. As seen in Figure 5.58, the y-z plane intersecting the spark plug electrodes, the weakened clockwise tumble motion results in lower velocity flow on one side of the spark plug electrodes. This suggests that without modelling of the momentum exchange between droplets and continuous-phase, there will be an over prediction of the mean velocity near the spark plug at the point of spark timing, affecting any subsequent modelling of the discharge channel deformation and initial kernel stretching due to the mean flow field. Whilst the mean flow field is lower, the fluctuating velocity components are of similar magnitude between both single-phase and two-phase predictions, indicating that turbulent fluctuations, and thus CCV of the instantaneous flow field, are more significant near the spark plug electrodes at the point of spark timing in the two-phase predictions.

Next, the predicted turbulence characteristics from a two-phase RANS simulation, were compared with the predictions from a two-phase LES simulation (which allows anisotropic turbulence) as a means of identifying the limitations of the assumptions made in the RANS turbulence model.

One such example is seen in Figure 5.55 at 100°ATDC or 20°ASOI, where in the LES predictions a large rise in z-plane fluctuating velocity is seen at z=-48mm due to the penetrating spray plume. In comparison to the RANS prediction (dashed black line), a small rise in fluctuating velocity is seen at the same location but since fluctuations are equal in all directions, not only is the magnitude of turbulent fluctuation in the z-plane under predicted but the fluctuations in the x- and y-planes are over predicted which will lead to inaccurate momentum transfer between droplets and the continuous-phase, and inaccurate diffusion of the fuel-air vapour cloud across plane. Figure 5.59 shows images of contours of fuel mass fraction in both the tumble plane and swirl plane illustrating how the impact of differences in

momentum transfer between droplets and the continuous-phase causes large differences in the distortion and movement of the spray plumes as they penetrate into the combustion chamber. Figure 5.59(e) and (f) shows iso-surfaces of fuel mass fraction for the LES and RANS predictions respectively and a rather different profile is seen, with lower energy dissipation and hence increased turbulence energy present in a LES simulation acting to increase the rate at which fuel is atomised and mixed with the surrounding air.

Figure 5.60 compares velocity magnitude contours and fuel mass fraction contours between the LES and RANS predictions at mid-compression 90°BTDC in the y=19mm tumble plane. The presence of rising flow towards the exhaust side of the combustion chamber in the LES two-phase results that is not present in the LES single-phase (Figure 5.56), is also not present in the RANS predictions, with Figure 5.60(b) showing a much more dominant clockwise rotating tumble flow and the fuel-air mixture predominantly being transported around the periphery as a consequence Figure 5.60(d). This indicates that the more uniform, less tumble dominated, flow feature in the LES two-phase results (Figure 5.60(a)) is only captured when modelling the injection event with a non-time-averaged turbulence modelling approach and based on findings from section 4.3.2 where the numerical predictions of the mixture field are compared against experimental QPLIF results, there is evidence to believe that this flow structure is a better match to reality due to it creating a more homogeneous mixture as a consequence.

Comparison between the RANS and LES two-phase predictions at spark timing as shown in Figure 5.58 indicates the RANS turbulence model to predict higher mean velocities, particularly in the x-plane. This will increase the convection of the flame kernel towards the exhaust side of the combustion chamber to a greater extent than would be seen when using the LES model. RMS fluctuating velocities from the RANS and LES predictions are of similar magnitude but obviously the RANS predictions do not capture the anisotropy present, thus would not capture the cyclic variations in kernel stretching during the early stages of combustion due to flow turbulence fluctuations.

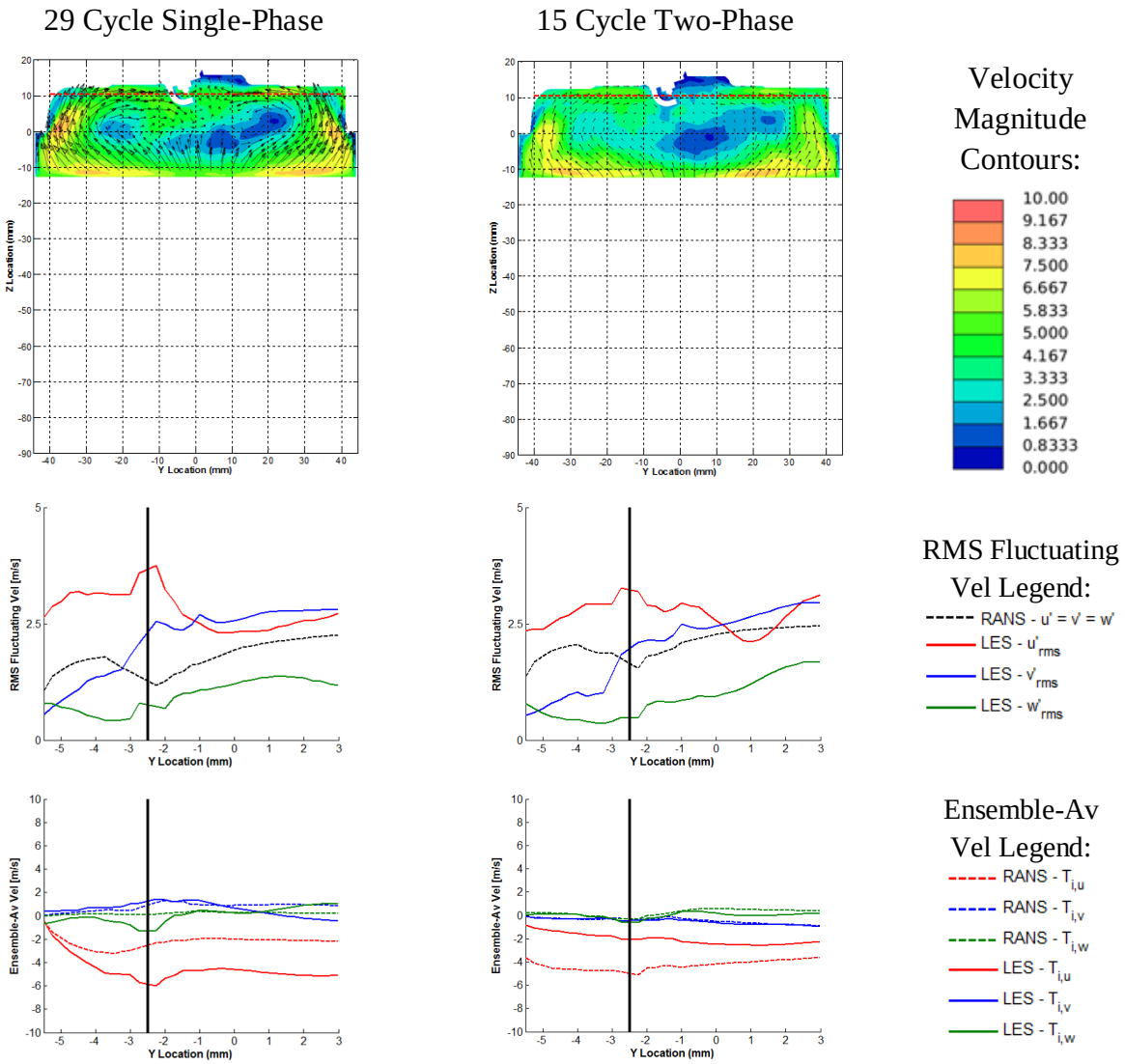

Figure 5.58 – Comparing single-phase and two-phase turbulence characteristics at 35°BTDC/spark timing in the y-z plane intersecting the spark plug; top row are ensemble-averaged velocity magnitude contours and velocity vectors $\bar{u}$; middle row are fluctuating velocity $u'_{i,rms}$; bottom row are ensemble-average velocity $\bar{u}_i$

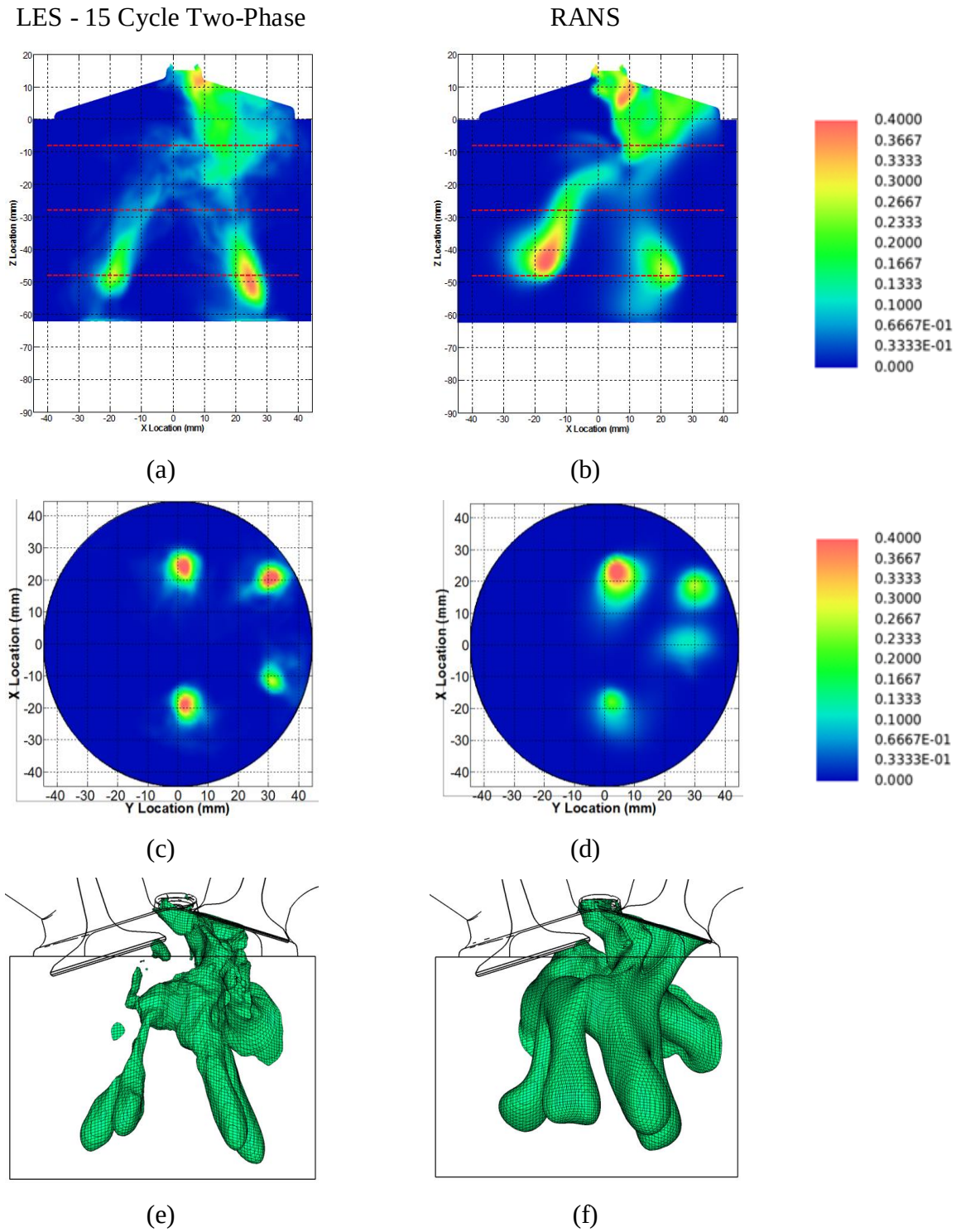

Figure 5.59 – Comparing LES ensemble-average and RANS results at 100°ATDC/20°ASOI; top row fuel mass fraction contours in the tumble plane along the bore centreline for (a) LES (b) RANS; middle row fuel mass fraction contours in the swirl plane at z=-48mm for (c) LES (d) RANS; iso-surfaces of fuel mass fraction at 0.15 in the tumble plane for (e) LES and (f) RANS

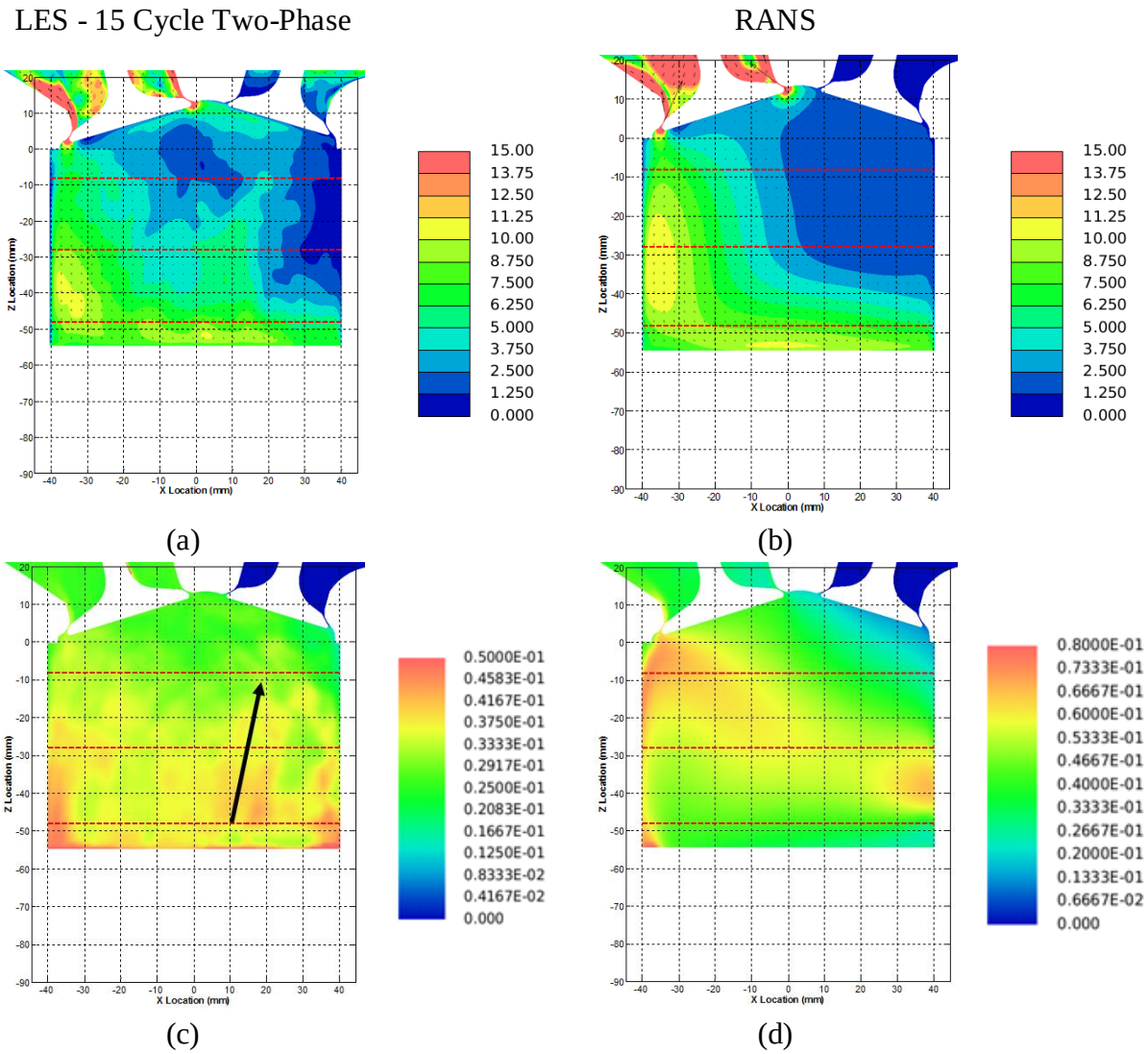

Figure 5.60 – Comparison of velocity magnitude contours for (a) LES and (b) RANS and fuel mass fraction for (c) LES and (d) RANS, at 90°BTDC at y=19mm, both two-phase simulations

5.5 CONCLUDING REMARKS

This chapter presented the numerical results from a number of investigations looking into the fuel injection processes occurring within a GDI single cylinder optical research engine using both RANS and LES turbulence modelling techniques, and the use of both a single- and multi-component fuel surrogate.

The chapter starts by investigating the impingement process and subsequent formation of liquid films on the solid surfaces inside the combustion chamber.

Examination of the fuel properties, wall surface temperatures and droplet properties allowed the calculation of key dimensionless droplet properties and the prediction of the droplet impingement regime and the onset of liquid film formation, with both single- and multi-component surrogates predominantly impinging within the free convection and nucleate boiling regime of the impingement model.

Evidence of film stripping was seen from the lower surface of the valve head with ejected droplets having very large diameters (100-500μm) and slow velocities. The stripping process was seen to continue through the intake stroke and into the compression stroke, ensuring that a number of large slow moving droplets will remain present up to spark timing, and be expected to form a source of UHC and PM emissions.

The influence of the in-cylinder flow field on the spray plumes was seen to be significant. Greater plume distortion was seen when using the multi-component surrogate due to the lighter components within the fuel, acting to vary the intake valve head impingement location and subsequent film formation, film stripping and child droplet formation processes when compared to a single-component surrogate. Increased plume distortion was also seen when using a LES Smagorinsky SGS turbulence model than when using a RANS RNG k-ε model, with up to 100% variation in total intake valve film mass noted across the 15 LES cycles completed in this research. Similar to the differences in impingement location between single- and multi-component surrogates with a RANS model, CCV of the intake valve head impingement location also showed cycle-by-cycle variations in the quantity of fuel deposited on either the top surface or side and underside of the valve head, expected to contribute to differences in the secondary droplets and resultant vapour cloud due to film evaporation.

Study of the cylinder liner and piston crown impingement process also showed significant cyclic variability in the total mass of fuel contributing to a liquid film. Variations in spray plume tip penetration due to variations in the in-cylinder flow field were linked with differences in total liquid film mass and film thickness for plumes 2/3/4/5. Due to the reduced penetration distances and subsequent reduced time available for the flow field to influence the spray plume, film formation due to plumes 1/6 cylinder liner impingement showed far less CCV in film thickness. At this operating condition, liquid films formed on the piston crown were seen to remain up to the point of spark timing, a precursor for pool-fires on the piston surface and scraping of liquid films remaining on the cylinder liner by the rising piston was prevalent which would contribute to ring pack coking, increased UHCs and oil dilution.

The second part of this chapter looked into the predicted mixture field characteristics.

First, the mixture field evolution has been investigated through the intake and compression strokes up to the point of spark timing. Non-symmetrical flow features have been identified, including a large scale swirling vortex during the compression stroke, as the cause for the mixture stratification present within the cylinder. Differences in the mixture field when using a single- or multi-component surrogate were also presented and discussed. Variations in atomisation rate and fuel impingement were found to drive a richer fuel-air mixture in the roof of the combustion chamber at spark timing with the multi-component surrogate.

The CCV of the mixture field at spark timing was quantified and investigated through the coefficient of variance of the fuel-air equivalence ratio, with cycles 3 and 6 identified as 'high' cycles and cycle 12 identified as a 'low' cycle. Contour plots of fuel-air equivalence ratio CoV and iso-surfaces of fuel-air equivalence ratio and velocity magnitude CoV were used to identify regions of high CCV and attribute the variation to variations in the in-cylinder flow structure and spray plume impingement.

Using the findings from the previous chapter, the potential for CCV in the intake valve jet flapping process to influence CCV of the final mixture field was also investigated. The effect of the fuel injection event reducing the magnitude of valve jet flapping and the injector nozzle geometry meaning the spray plumes did not pass close to the valve jet during flapping, meant that no relation was found between valve jet CCV and CCV of the mixture field at spark timing.

The final part of this chapter discussed the interactions between the in-cylinder flow field and the fuel injection event. Increased anisotropy identified around the penetrating spray plumes. The consequence of momentum transfer between the continuous-phase and the liquid-phase was seen with reduced in-cylinder velocities and modified flow structures around the spark plug at spark timing visible. The limitations of the Boussinesq assumption in the RANS RNG k-ε turbulence model were discussed and increased mixing was observed in mixture field due to the lower dissipation of the LES model.

CHAPTER 6

REGIMES OF TURBULENT PREMIXED COMBUSTION

"If we all did the things we are capable of doing, we would literally astound ourselves."

– Thomas A. Edison

6.1 INTRODUCTION

The results discussed thus far provide a large amount of information about the flow turbulence characteristics and in particular at the point of spark timing. This is of particular interest for the resultant premixed turbulent combustion process due to the impact of local turbulent flow on the propagation of the flame front. By using turbulent premixed combustion diagrams as proposed by Abraham, Williams & Bracco (1985) and Peters (1999), these diagrams can be used to indicate the nature of the flame front; whether the flows contains flamelets (thin reaction zones), pockets or distributed reaction zones.

In this section, the turbulent flow characteristics in the cylinder at the point of spark timing derived in the previous section are used to examine the:

- Characteristics of the subsequent flame front,
- Differences in predicted combustion regime when using turbulence results from either the RANS or LES model,

- CCV of the position on a combustion regime diagram using the predictions from the LES model, and the implied differences in combustion regime and flame structure that could ensue as a consequence.

6.2 BACKGROUND AND METHODOLOGY

To identify the regimes of the in-cylinder premixed turbulent combustion using combustion regime diagrams, the Damköhler and the turbulence Reynolds numbers are require to be calculated.

Since in most flames the Prandtl number (the ratio between kinematic viscosity and thermal diffusion) is close to unity, and the flame diffusivity is equal to flame thickness δ_l multiplied by the laminar burning velocity u_l, the kinematic viscosity can be replaced and allows the turbulence Reynolds number to be a function of the combustion event as shown in equation (6.1).

$$Re_T = \frac{u' l_l}{v} = \frac{u' l_t}{u_l \delta_l} \tag{6.1}$$

This equation now represents the ratio of inertia of turbulence to the inertia of the propagating flame. The flame inertia has a dissipative effect on turbulent eddies and so represents a viscous action acting on the turbulence.

The Damköhler number is the ratio of the characteristic flow time or characteristic eddy turnover time τ_T, to the characteristic chemical time of reaction or laminar burning time τ_l and defined in equation (6.2) (Heywood, 1988).

$$Da = \frac{\tau_T}{\tau_l} = \frac{{l_t}/{u'}}{{\delta_l}/{u_l}} = \left(\frac{l_t}{\delta_l}\right)\left(\frac{u_l}{u'}\right) \tag{6.2}$$

Where the ratio of u'/u_l is a measure of the relative strength of the turbulence.

Thus the key variables to be obtained are:

- Laminar flame thickness, δ_l
- Laminar burning velocity, u_l
- Turbulence intensity, u'
- Integral length scale of turbulence, l_t

The laminar flame thickness was obtained from a number of published experimental results at 0.2mm, which was considered a reasonable assumption for premixed combustion in a GDI engine (Peters, 1999; Poinsot & Veynante, 2005; Peters, 1991).

The laminar burning velocity was approximated as 0.37m/s from the experimental works of Metghalchi & Keck (1982) and Marshall, Taylor, Stone, *et al.* (2011) for iso-octane at representative pressures, temperatures and equivalence ratio.

The turbulence intensity was extracted from the numerical predictions, using the modelled kinetic energy in the case of the RANS RNG k-ε model, and using the sum of the resolved and SGS turbulence kinetic energy for the LES approach, using equation (6.3):

$$u' = \sqrt{\frac{2}{3}k} \tag{6.3}$$

The integral length scale was first estimated via the predicted turbulence dissipation rate, based on the assumption that the rate of dissipation is related to the rate of turbulence production, which can be related to the largest length scales, the integral length scale, as shown in equation (6.4).

$$l_t \approx \frac{u'^3}{\varepsilon} \tag{6.4}$$

It was also of interest to calculate the Karlovitz number which is similar to the Damköhler number but is the inverse and uses the Kolmogorov time scale instead of the integral time scale, since calculation of δ_l/l_k provides a measure on the impact of the smaller scales on the flame front due to flame stretch as defined by equation (6.5).

$$Ka = \frac{\tau_l}{\tau_k} = \frac{{\delta_l}/{u_l}}{{l_k}/{u'}} = \left(\frac{u'}{l_k}\right)\left(\frac{\delta_l}{u_l}\right) \tag{6.5}$$

Both the Damköhler number and Karlovitz number can be related to the turbulent Reynolds number through the integral length scale and kinematic viscosity as shown by equation (6.6).

$$Re_T = \frac{u' l_t}{v} = \left(\frac{u'}{u_l}\right)\left(\frac{l_t}{\delta_l}\right) = Da^2 Ka^2 \tag{6.6}$$

Re-arranging the turbulence Reynolds number in equation (6.6) to calculate the Karlovitz number and then re-arranging the equation for Karlovitz number in equation (6.5), the Kolmogorov length scale l_k can be found.

A caveat here is that the characteristic velocity in the Karlovitz number should be defined by the turbulence intensity at the Kolmogorov scale, i.e. $u'(l_k)$, whereas the turbulence intensity here was approximated from the kinetic energy which is a function of all the scales of turbulence, thus meaning the Kolmogorov length scales calculated will be subject to an additional degree of inaccuracy.

6.3 RESULTS AND DISCUSSION

The turbulence characteristics for the LES and RANS model after an injection event and at the point of spark timing, were calculated and are summarised in Table 6.1 and plotted on both the Da-Re_T diagram proposed by Abraham, Williams & Bracco (1985) in Figure 6.1 and the modified turbulent premixed combustion regimes diagram as proposed by Peters (1999) in Figure 6.2.

Table 6.1 – In-cylinder turbulence characteristics at spark timing (35°BTDC) with the integral length scale estimated from dissipation rate

		u' [m/s]	ε [m^2/s^3]	l_t [mm]	Da [none]	Re_T [none]	$\frac{u'}{u_l}$	$\frac{l_t}{\delta_l}$	Ka [none]	l_k [mm]	$\frac{l_k}{\delta_l}$
RANS		2.6	3138	5.4	3.9	190	7	27	3.5	0.4	2.0
LES Cycle	1	5.42	1110	143.4	48.9	10500	15	717	2.1	1.4	7.0
	2	4.48	1128	99.4	38.1	6477	13	497	2.1	1.2	6.2
	3	8.18	904	605.7	137.0	66973	22	3029	1.9	2.3	11.7
	4	7.89	1513	324.8	76.1	34641	21	1624	2.4	1.7	8.7
	5	7.89	946	519.4	121.8	55388	21	2597	1.9	2.2	11.0
	6	5.65	1287	140.2	45.9	10705	15	701	2.3	1.4	6.8
	7	5.83	1513	130.9	41.6	10312	16	655	2.4	1.3	6.4
	8	8.37	967	607.1	134.1	68708	23	3036	2.0	2.3	11.6
	9	8.91	1336	529.1	109.9	63686	24	2645	2.3	2.1	10.5
	10	7.23	1069	353.9	90.5	34588	20	1769	2.1	1.9	9.5
	11	6.25	1227	199.12	58.9	16827	17	996	2.2	1.5	7.7
	12	5.29	1263	117.1	41.0	8369	14	586	2.2	1.3	6.4
	13	5.34	1034	147.6	51.1	10662	14	738	2.0	1.4	7.1
	14	7.14	1424	256.0	66.3	24717	19	1280	2.4	1.6	8.1
	15	5.14	1235	109.9	39.6	7631	14	549	2.2	1.3	6.3
LES Ensemble-Average		6.62	1197	242.8	67.	21740	18	1214	2.2	1.6	8.8

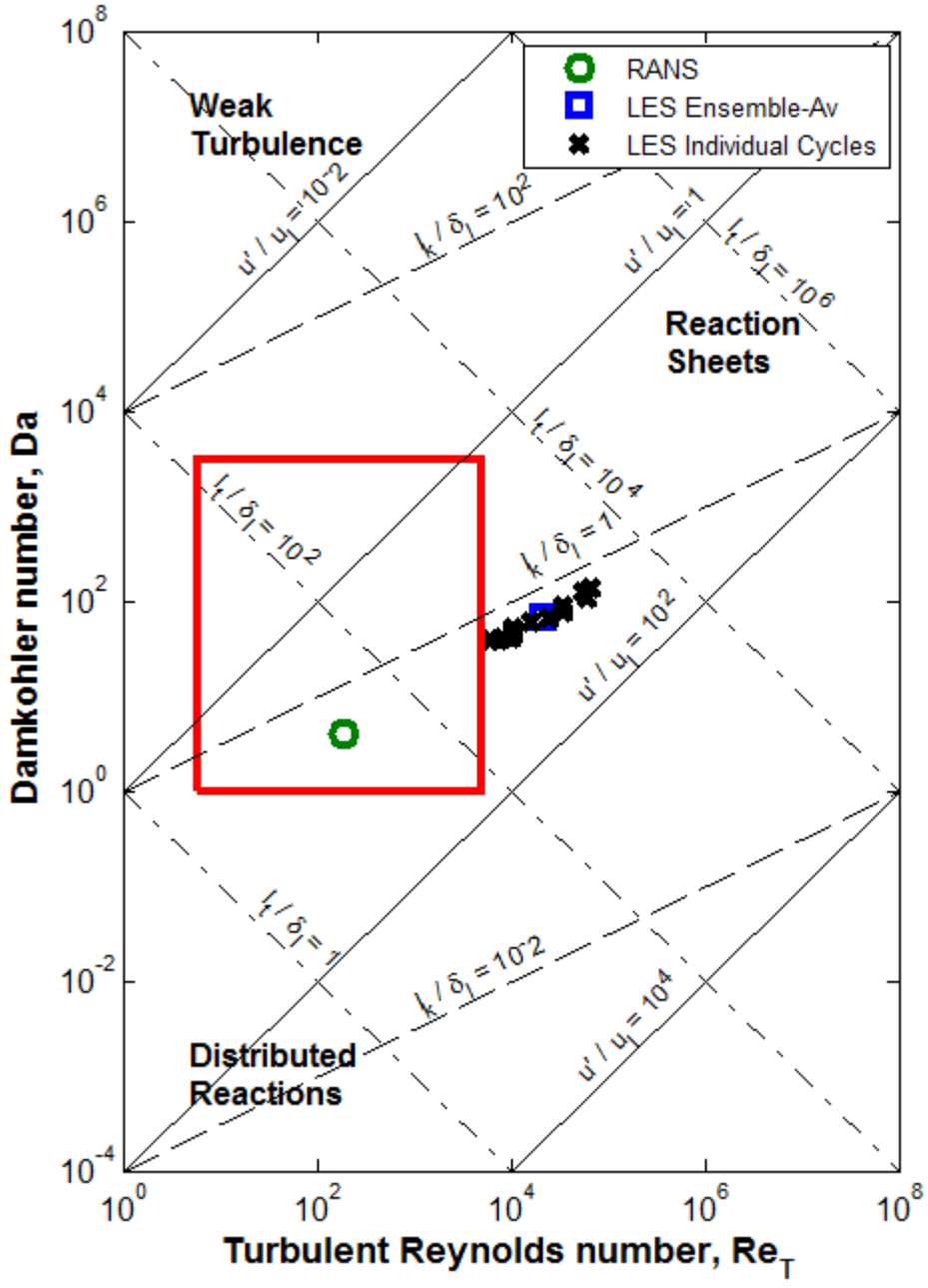

Figure 6.1 – Da-Re$_T$ diagram (Abraham, Williams & Bracco, 1985), with results added using turbulence characteristics from both LES and RANS predictions with LES integral length scale estimated from dissipation rate

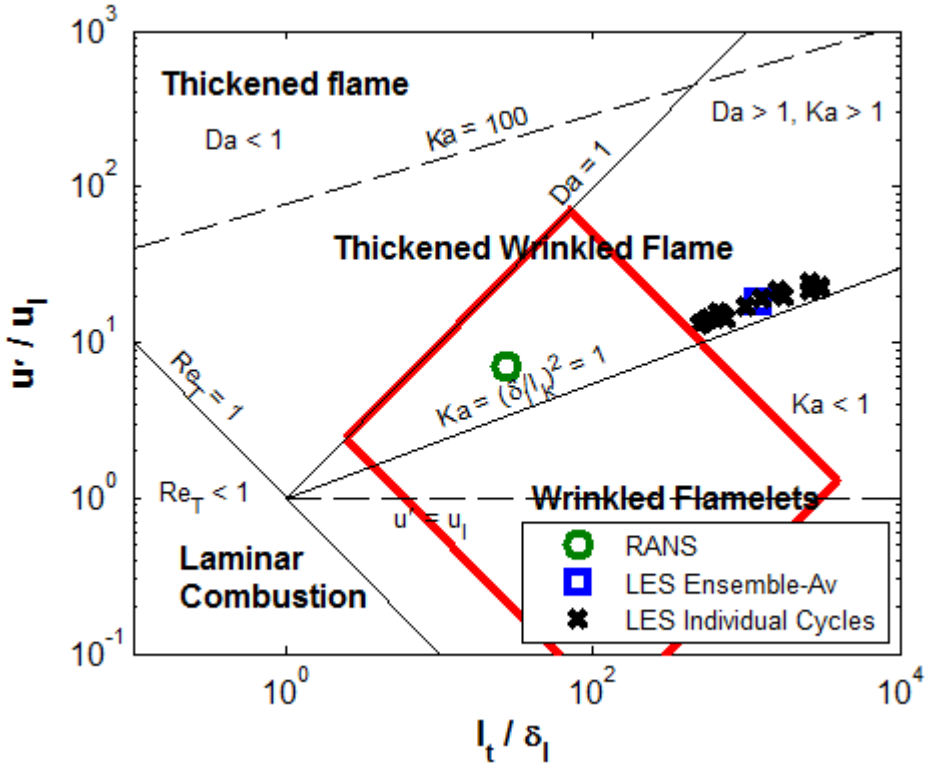

Figure 6.2 – Modified turbulent combustion regimes diagram (Peters, 1999), with results added using turbulence characteristics from both LES and RANS predictions with LES integral length scale estimated from dissipation rate

As can be seen from both combustion regime diagrams, a fair difference is seen between the LES and RANS turbulence characteristics at spark timing; LES predictions suggesting that both Damköhler number and turbulent Reynolds number are orders of magnitude greater than the RANS predictions but with a similar Karlovitz number. Both turbulence models predict the combustion regime to be within the 'distributed reaction regime' or 'thickened wrinkled flame' regime where the integral time scale is larger than the chemical time scale but the Kolmogorov scales are smaller than the flame thickness (i.e. $l_k/\delta_l < 1$ on the Da-Re_T diagram) and are able to modify the inner flame structure but in the case of the LES predictions, both Da and Re_T are greater still, indicating that the level of distortion of the flame front would potentially lead to distributed reaction zones of fresh charge and burnt gases.

These differences could be attributed to differences in the origins of certain parameters used to calculate the turbulence characteristics between the LES and RANS models:

- First lies in the definition of the turbulence intensity, u'. The RANS model calculates the turbulence intensity via the modelled turbulence kinetic energy from the k-equation of the k-ε model and the Boussinesq assumption. The LES model calculates the turbulence intensity via the sum of the resolved kinetic energy (directly from the N-S equations) and the SGS kinetic energy (modelled via an eddy-viscosity closure approach). Thus, due to being less dissipative that a RANS model, the LES approach resolves a much greater quantity of turbulence kinetic energy and hence the calculated turbulence intensity and therefore turbulent Reynolds number and velocity scale are much greater in the LES case.
- Second lies in the calculation of the integral length scale. Here the integral length scale has been approximated from the dissipation rate. Since the LES turbulence model is less dissipative than the RANS turbulence model due to using a smaller turbulent viscosity, the rate of dissipation is much lower in the LES model. Thus a smaller dissipation rate and greater turbulence intensity equates to a greater estimated integral length scale.

Abraham, Williams & Bracco (1985) approximated the integral length scales based on equation (6.7).

$$l_t \approx 0.21h \tag{6.7}$$

Where h is the clearance height of the combustion chamber and stated that this would be equivalent to the length scale predictions from a RANS k-ε turbulence model. This approximation was based on a pancake combustion chamber with flat piston crown and cylinder head profile thus its application to a pent-roof combustion chamber is less obvious but the clearance height from the piston crown to the top of the pent-roof at the point of spark timing is ~30mm, thus equating to an integral length scale of 6.3mm, very similar to the integral length scale of 5.4mm for the RANS predictions calculated via the dissipation rate.

The turbulence characteristics for the LES model were re-calculated using an integral length scale approximated from equation (6.7) and summarised in Table 6.2 and re-plotted on both the Da-Re_T diagram in Figure 6.3 and the modified turbulent combustion regimes diagram in Figure 6.4.

Figure 6.3 and 6.64 now show the LES results lying within the expecting operating range for ICE's, though still with a higher turbulent Reynolds number than the RANS predictions, thus the turbulence characteristics from the LES predictions suggest a more wrinkled and convoluted flame front than predicted by the RANS turbulence characteristics. This becomes a serious consideration for the modelling of the subsequent combustion process since the differences in turbulence characteristics predicted by the different turbulence modelling techniques of either a RANS or LES approach, will drive quite different combustion modelling approaches to accurately model the impact of turbulence on the rate of flame propagation.

Whilst the above estimation of the integral length scale was identified as the most likely contributor to error in the positioning on the combustion regime diagrams, a caveat exits with respect to the turbulence kinetic energy and hence the turbulence intensity estimation. The apparent turbulent kinetic energy is not well defined, except when far from the influence of the flame front. In experiments, the turbulent kinetic energy is the RMS velocity in the fresh gases, with an implicit assumption between combustion speeds and RMS velocity. In numerical results, turbulent kinetic energy is a localised quantity thus using this value to obtain a turbulent scale is not the same as used to form the combustion regimes as presented in combustion regime diagrams. Nor do turbulence models take account of density variations induced by the flame front and the subsequent impact on local velocity fluctuations. Thus whilst using predicted turbulence characteristics to estimate the subsequent combustion regime provides an interesting application for the numerical results, differences in the assumptions used between experimental and numerical methodologies provides an element of uncertainty to the accuracy of the results (Poinsot & Veynante, 2005).

Another application of the results is to inspect the variation in the position on the combustion regime diagram from cycle-to-cycle and the potential impact on CCV of the flame structure. When the integral length scale is estimated using the dissipation rate and turbulence intensity (Figure 6.1 and 6.62), the turbulent Reynolds number shows an order of magnitude variation across all cycles, whereas the Damköhler number shows less than one order of magnitude variation. This indicates that the CCV in the ratio of turbulence time scale to chemical time scale, and hence the predominant combustion regime, is not significant. By comparison, when the integral length scale is approximated based on the combustion chamber clearance height (Figure 6.3 and 6.64), the predicted CCV in turbulence characteristics, and hence combustion regime, is far smaller and almost negligible. Since the turbulence intensity is

equal between the two cases and the length scale constant, the outcome implies that the predicted rate of energy dissipation is a dominant factor in determining the magnitude of predicted CCV in turbulence characteristics and hence resultant combustion regime.

Table 6.2 – In-cylinder turbulence characteristics at spark timing (35°BTDC) with the LES integral length scale estimated based on clearance height

		u' [m/s]	ε [m^2/s^3]	l_t [mm]	Da [none]	Re_T [none]	$\frac{u'}{u_l}$	$\frac{l_t}{\delta_l}$	Ka [none]	l_k [mm]	$\frac{l_k}{\delta_l}$
RANS		2.6	3138	5.4	3.9	190	7	27	3.5	0.4	2.0
LES Cycle	1	5.42	1110	6.3	2.2	461	15	32	10.0	0.3	1.5
	2	4.48	1128	6.3	2.4	411	13	32	8.4	0.3	1.6
	3	8.18	904	6.3	1.4	697	22	32	18.5	0.3	1.2
	4	7.89	1513	6.3	1.5	672	21	32	17.6	0.3	1.2
	5	7.89	946	6.3	1.5	672	21	32	17.6	0.3	1.2
	6	5.65	1287	6.3	2.1	481	15	32	10.6	0.3	1.4
	7	5.83	1513	6.3	2.0	496	16	32	11.1	0.3	1.4
	8	8.37	967	6.3	1.4	713	23	32	19.2	0.3	1.2
	9	8.91	1336	6.3	1.3	758	24	32	21.0	0.3	1.1
	10	7.23	1069	6.3	1.6	616	20	32	15.4	0.3	1.3
	11	6.25	1227	6.3	1.9	532	17	32	12.4	0.3	1.4
	12	5.29	1263	6.3	2.2	450	14	32	9.6	0.3	1.5
	13	5.34	1034	6.3	2.2	455	14	32	9.8	0.3	1.5
	14	7.14	1424	6.3	1.6	608	19	32	15.1	0.3	1.3
	15	5.14	1235	6.3	2.3	437	14	32	9.2	0.3	1.5
LES Ensemble-Average		6.62	1197	6.3	1.8	564	18	32	13.5	0.3	1.3

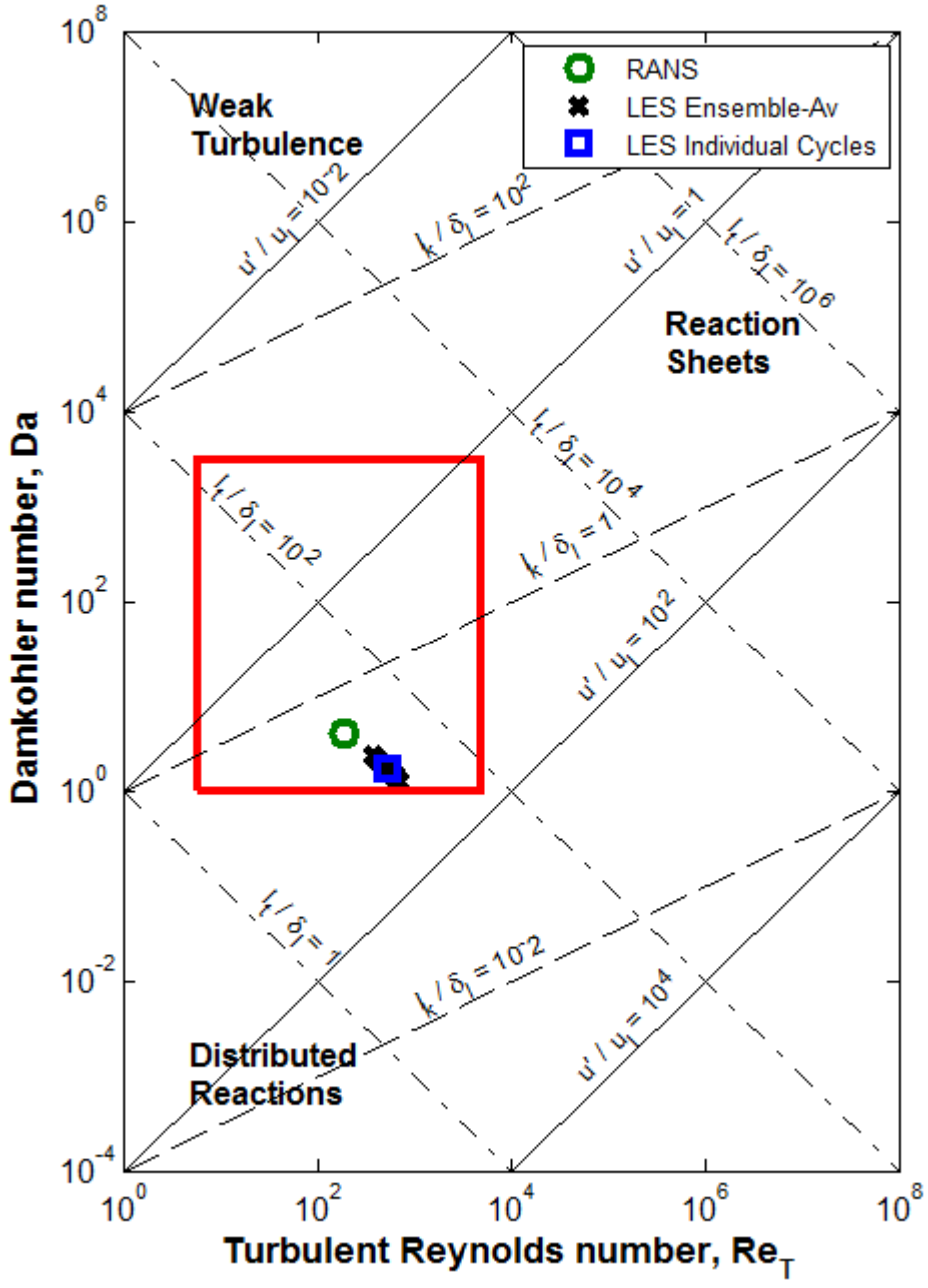

Figure 6.3 – Da-Re_T diagram (Abraham, Williams & Bracco, 1985), with results added using turbulence characteristics from both LES and RANS predictions with LES integral length scale estimated based on clearance height

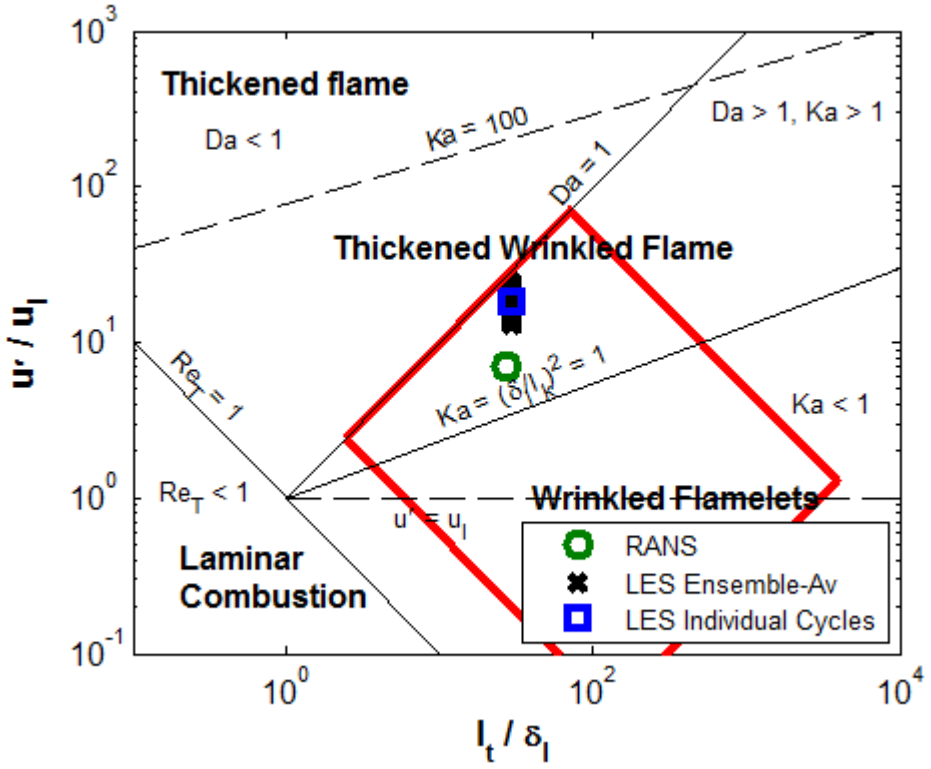

Figure 6.4 – Modified turbulent combustion regimes diagram (Peters, 1999), with results added using turbulence characteristics from both LES and RANS predictions with LES integral length scale estimated based on clearance height

6.5 CONCLUDING REMARKS

This chapter has presented the use of predicted in-cylinder flow characteristics at spark timing to determine the regime of turbulent premixed combustion using combustion regime diagrams.

Differences in the predicted combustion regime were seen when using turbulence predictions from RANS and LES approaches due to:

- The definitions for turbulence intensity are different in both RANS and LES contexts, coming from the turbulence kinetic energy in the Boussinesq assumption in RANS predictions and from the sum of the resolved and SGS kinetic energy in LES predictions.

- The use of turbulence dissipation to estimate the integral length scale produces large differences in integral length scale predictions due to large differences in the levels of turbulence dissipation between turbulence modelling approaches. The use of an approximation for integral length scale as proposed by Abraham, Williams & Bracco (1985) provided combustion regimes more in line with expectation.

The position on the combustion regime diagrams for each LES cycle was also plotted to provide an indication of the expected CCV of the combustion regime. The predictions suggest that CCV of the turbulence characteristics only has a small effect on the overall combustion regime but this obviously neglects localised variations through the cylinder which have the potential to be more significant as the flame progresses from spark plug to the far cylinder walls.

CHAPTER 7

CONCLUSIONS AND RECOMMENDATIONS

"The idea is to try to give all the information to help others to judge the value of your contribution; not just the information that leads to judgment in one particular direction or another."

– Richard P. Feynman

The Gasoline Direct Injection (GDI) engine has a number of practical advantages over the more traditional port-fuel injection strategy. These include eliminated transient dwell time, improved fuel metering for reduced unburned hydrocarbon (UHC) emissions, reduced knock propensity due to the charge cooling effect and the potential for significant fuel economy improvements with stratified charge combustion strategies. However, since the sustained interest in GDI technology in the early 1990's, a number of challenges remain the subject of continued research in an attempt to fully exploit the potential of GDI engines.

Cycle-to-cycle variability (CCV) in SI engines has long been a topic of research interest with a number of studies conducted to better understand the factors influencing CCV and its origins. Abnormal combustion phenomenon is of particular interest to GDI engine researchers with the increased activity in downsizing and heavily boosted engines, and the increasing prevalence of super-knock. The reduced time available for mixing due to direct injection means GDI engines suffer from higher particulate matter (PM) formation than seen previously in port-fuel injected engines, particularly with increasingly stringent particle

number legislations meaning that many current GDI engines are incapable of meeting the new legislation. The use of mixture stratification for fuel consumption improvements was pursued from some of the earliest GDI engines but a number of challenges still remain before the advantages of this strategy can be fully realised, including reductions in PM and UHC emissions and acceptable combustion stability across all operating conditions through reductions in solid surface impingement and more accurate spatial mixture control at the point of spark timing.

The internal combustion engine (ICE) is a hostile and difficult to access environment and although significant effort has been applied into the research and development of experimental methods, the use of computational techniques (validated by experimental data and direct numerical simulations) remains an integral part of research and development activities. This research has focused on the use of detailed 3D-CFD techniques for investigating physical phenomena of the in-cylinder flow field and fuel injection processes, contributing to the current scientific knowledge in this area and in support of continual progress towards solution of these engineering challenges.

7.1 CONCLUSIONS

The conclusions from this thesis are presented in the following three sections: the numerical model, and the three chapters investigating the physical processes of the in-cylinder flow field, fuel injection process and regimes of combustion.

7.1.1 The Numerical Model

Conclusions from the numerical model characterisation and validation using the RANS approach for modelling the in-cylinder flow field:

- A mesh dependency study was completed with the RANS RNG k-ε turbulence model and a mesh size of 2.15million cells, or a cell size of approximately 0.7-0.8mm^3 in the cylinder interior, was found to largely provide a solution independent of cell size.

- An initialisation dependency study showed the need to run at least one complete cycle for the solution to be independent of the initialisation conditions, highlighting the importance of supplying the cylinder with appropriate intake port boundary conditions.
- The model predictions were validated against available experimental results of the in-cylinder pressure history and intake plenum, intake valve jet and in-cylinder PIV data and generally well matched the experimental results.

Conclusions from the numerical model characterisation and validation, using the LES approach run over 30 engine cycles, for modelling the in-cylinder flow field:

- A turbulence resolution parameter was used to evaluate the mesh suitability for the in-cylinder flow conditions and showed the mesh to generally resolve upward of 80% of the flow kinetic energy.
- The model predictions using the Smagorinsky SGS turbulence model were validated against experimental results and showed the model to well represent the complex flow structures in the cylinder interior and generally provide better agreement than when using the RANS RNG k-ε turbulence model. This provides another example of the Smagorinsky SGS model applied to ICE flows, in a detailed engine geometry that has not yet been published in the literature.

Conclusions from the numerical model characterisation and validation, using a Lagrangian DDM, single-component fuel surrogate of iso-octane and the RANS approach, for modelling the fuel injection process:

- A number of sensitivity studies were completed to assess the sensitivity of the solution to the choice of sub-models and boundary conditions including mesh size, secondary breakup model, number of injected parcels and cell clustering, and the model solution was shown to be largely insensitive.
- The model was validated against experimental results for: plume tip penetration, plume tip velocity and droplet diameter and showed to well match the experimental results. The predicted fuel-air equivalence ratio was also compared to experimental QPLIF results and showed additional stratification in the model predictions that does not appear present in the experimental results. This provides another example of a DDM validated in detail against experimental results. In particular, the use of the Pilch and Erdman secondary breakup model and details of appropriate user constants

for a Rosin-Rammler droplet size distribution with a production like GDI injector, both of which have limited validation in the literature.

Conclusions from the numerical model characterisation and validation, using a Lagrangian DDM, single-component fuel surrogate of iso-octane and the LES approach run over 15 engine cycles, for modelling the fuel injection process:

- The differences in interactions between the LES SGS model and the DDM were presented, with the largest limitation of the current approach being noted as the absence of a source term in the LES SGS model to account for the transfer of energy from the droplets to the continuous-phase at the SGS level.
- The model was again validated against experimental results for: plume tip penetration, plume tip velocity and droplet diameter and showed to well match the experimental results. Model predictions for fuel-air equivalence ratio showed increased homogeneity and a qualitative improvement over the RANS predictions when compared to experimental QPLIF results. This provides another example of a DDM with LES SGS model validated against detailed experimental results, which are currently very limited within the published literature.

7.1.2 Investigations into the In-Cylinder Flow Field

Chapter 4 presented numerical results from a number of investigations looking into the in-cylinder flow field using both RANS and LES turbulence modelling techniques.

- The influence of the solid boundaries on the in-cylinder flow structures was first investigated. The moving boundary of the piston was seen to influence the temporal development of the flow structures through the intake stroke and the presence of the pent-roof optical access window was seen to generate flow asymmetries within the flow field in the roof of the combustion chamber.
- The three-dimensional nature of the in-cylinder flow field was investigated via a series of cutting planes and the use of velocity magnitude and vorticity contours. Significant three-dimensionality was seen in the intake valve jet with respect to

penetration and velocity through the combustion chamber and the flow field surrounding the valve jet as a consequence of the high shear flows.

- Intake valve jet flapping was observed and seen to be as a consequence of valve curtain mass flux imbalance. CCV in the valve curtain mass flux for each valve was seen to cause subsequent CCV in the valve jet flapping process in terms of both flapping frequency and jet penetration. The cyclic variation in the process meant that use of an ensemble-averaging process caused most of the information associated with the phenomenon to be lost. Whilst there are examples of flapping flows within the literature, there is very little published work on intake valve jet flapping in ICE's, and even less on the characterisation and potential causality, thus this research has contributed to the scientific knowledge within this area.
- The fluctuating velocity and turbulence intensity were used to investigate the characteristics of flow anisotropy through the intake and compression strokes, up to the point of spark timing. Intake valve jet flapping during the intake stroke, the rising piston during the compression stroke and the spark plug electrode geometry at the point of spark timing were all observed to increase flow anisotropy.
- Proper Orthogonal Decomposition was applied to the velocity field and it was shown how it can be used to quantitatively analyse the turbulent in-cylinder flow field. The modal energy data was combined with the time-dependent coefficients and found as a very effective method of quantitatively evaluating CCV through the engine cycle and the intake valve opening and closing event was seen as a key driver for CCV.

7.1.3 Investigations into the Fuel Injection Process

Chapter 5 presented the numerical results from a number of investigations looking into the fuel injection process using both RANS and LES turbulence modelling techniques, and with both a single- and multi-component fuel surrogate.

- The characteristics of the impingement process of fuel onto the intake valve, cylinder liner and piston crown were investigated, using Weber number and Laplace number to approximate the change in dominant impingement regime and onset of liquid film formation.

- Film stripping was observed from the intake valve head producing large slow moving droplets that persisted late into the compression stroke.
- When compared to a single-component surrogate fuel, the effect of multiple fuel components with varying density in the multi-component surrogate showed greater plume distortion, evident due to greater interactions with the in-cylinder flow field, acting to change the impingement location and subsequent film formation and film stripping processes. The use of multi-component fuel surrogates for modelling direct injection sprays in GDI engines is still relatively emergent hence this thesis will contribute to scientific understanding of the differences in numerical predictions when using a single- or multi-component surrogate fuel.
- Increased plume distortion was seen when using the Smagorinsky SGS turbulence model with up to 100% variation seen in the total intake valve film mass. Significant CCV was also seen in the total film mass on both cylinder liner and piston crown surfaces, associated with the variation in plume tip penetration from cycle-to-cycle due to cyclic variations in the in-cylinder flow field. To the author's knowledge, an example of CCV of impingement and liquid film formation in a GDI engine using numerical methods has yet to be published.
- At this operating condition, liquid films on the piston crown were seen to persist up to the point of spark timing, a known precursor for pool-fires. Scraping of liquid films remaining on the cylinder liner by the rising piston was also prevalent, which would contribute to ring pack coking, increased UHCs and oil dilution.
- Investigations into the mixture field identified a large asymmetrical swirling vortex during the compression stroke as the cause for the greater than expected fuel-air mixture stratification present at the point of spark timing. Differences in spatial and temporal mixture field development were also seen between single- and multi-component surrogate fuels as a consequence of differences in atomisation rates and the fuel impingement process.
- CCV of the mixture field at spark timing was quantified and investigated through the coefficient of variance (CoV) of the fuel-air equivalence ratio. Contour plots of fuel-air equivalence ratio CoV and iso-surfaces of fuel-air equivalence ratio and velocity magnitude CoV were used to identify regions of high CCV and attribute it to variations in the in-cylinder flow structure and spray plume impingement.

- The potential for CCV in intake valve jet flapping as a driver for CCV in the mixture field at spark timing was also investigated. A combined effect of the fuel injection event reducing the magnitude of valve curtain mass flux imbalance and geometry of the spray plumes meant that in this example, no relation was observed between valve jet CCV and the CCV of the mixture field at spark timing.
- The influence of the liquid-phase on continuous-phase turbulence was investigated, with increased anisotropy identified around the penetrating spray plumes and modified flow structures around the spark plug at spark timing visible. The quantification of flow anisotropy in ICE's in all three dimensions is very limited in the literature due to the difficulty of experimental measurement in three planes and the computational expense of using turbulence models that directly resolve the large scale flow motions. The results presented in this thesis act to publish information on flow anisotropy through the intake and compression strokes, and also on the influence of the in-cylinder fuel injection event on flow anisotropy, both of which are limited within the current literature.

7.1.4 Regimes of Turbulent Premixed Combustion

Chapter 6 presented the application of predictions of the in-cylinder turbulence at spark timing, to predicting the turbulence premixed combustion regime using combustion regime diagrams.

Differences in predicted combustion regime between when using a RANS and LES models were identified due to primary differences in the methodology by which turbulence is modelled.

The predicted CCV of turbulence characteristics at the spark plug appeared to have little effect on the characteristics of the predicted overall flame structure but this neglects the potentially larger variations through the cylinder over the course of the flame history.

7.2 PRESENT CONTRIBUTIONS

The following bullet points describe the main contributions from the research presented above:

- A detailed validation of the model against available experimental data is presented with all necessary input information to help the author correctly interpret and use the validation results, providing another reference point for modellers looking to correctly model GDI engines using 3D-CFD techniques but who do not have the luxury of highly sought after experimental optical engine results.
- The validation of Large Eddy Simulation (LES) turbulence models against experimental PIV results are still often limited to simplified geometries, e.g. Morse, Whitelaw & Yianneskis (1979), or already well documented optical geometries, e.g. the TCC-III engine of the University of Michigan (Schiffmann, Gupta, Reuss, *et al.*, 2016). Thus this research provides another experimental geometry and data point for the validation of a particular LES Sub Grid Scale (SGS) model and contributes to the growing literature in this area, used to support the development of best practices for the application of LES to ICE flows.
- Validation of the spray event against a number of experimental results including penetration, plume tip velocity and Phase Doppler Anemometry (PDA) results for droplet arithmetic mean diameter, allowed the boundary conditions for the injection model, including droplet initial velocity and droplet diameter distribution, to be validated with confidence and provide an additional reference for appropriate 'shape' and 'scale' parameters for a Rosin-Rammler distribution of the droplet diameter for a typical GDI injector of this era.
- The secondary breakup model selected for use in this research was that of Pilch & Erdman (1987) where, whilst it is formed from a significant quantity of experimental research and has the benefit of not using user adjustable constants, has seen very few applications to engine sprays. Thus the validation presented in this research provides evidence of its validity for use in a GDI injection context with relatively low injection pressures.
- The use of a LES SGS model for turbulence modelling with Lagrangian parcel tracking for modelling fuel injection in ICE's is still emerging. The framework for

correctly modelling the interaction between turbulence modelled by the SGS model and the injected parcels is still incomplete and often based on a Reynolds Averaged Navier-Stokes (RANS) methodology. There are also a limited number of publications present in the literature documenting the validation of different LES SGS models with a DDM. In this research, a relatively simple SGS model, as originally proposed by Smagorinsky (1963), is applied with a DDM to model the fuel injection process, and validated against experimental results and RANS predictions. The limitations of the modelling approach used here are discussed with respect to the models ability to correctly represent the physical processes present, but the reduced complexity of the SGS model and coupling to the DDM, means that investigations into the cyclic variability of the fuel injection process due to turbulence, is possible with reduced computational expense and instability (when compared with turbulence models using additional filtering or transport equations) and readily available in most commercial CFD codes used in industry.

- Through the course of this research a highly transient sinusoidal flow motion was observed between the two intake valves. It was identified through the literature as valve jet flapping but very little published results were found on the phenomenon in ICE's, particularly with respect to intake valve jet flapping and its potential impact on cyclic variability. Thus results presented here provide evidence of its existence in ICE's, causality, CCV and the apparent negligible effect on the resultant mixture field in an early injection GDI engine.
- A detailed investigation of spray plume impingement on the intake valve, cylinder liner and piston crown is provided, using an understanding of the impingement model to show how the impingement regime varies from a predominantly splash regime at high Weber numbers when the spray plume first impacts a surface, and transitions to a deposition regime and subsequent liquid film formation as impinging droplet velocities, and hence Weber numbers, reduce – within the literature, a study of this type, in this level of detail, is very limited within GDI engines.
- The comparison of predictions when using either a single-component or multi-component fuel surrogate provides additional information on the limitations in prediction fidelity due to using a single-component fuel to represent a complex multi-component fuel, and provide information to support the results from other researchers

suggesting that between three and five components provides a good compromise between accuracy and computational cost.

- The use of a LES turbulence model and DDM to investigate the cyclic variability of the impingement process and liquid film formation in a GDI engine due to continuous-phase turbulence is, to the best of the author's knowledge, the first example to be published.
- The quantification of turbulence characteristics in ICE's has been a research interest for a number of decades but due to the limitations of typically only measuring in two-dimensions and the limited number of data points in experimental works, and the loss of data associated with cyclic variability in time-averaged RANS numerical approaches, the quantification of flow anisotropy in ICE's is still very limited. In this research, a LES SGS turbulence model is used to provide information on the anisotropic nature of the flow field through the intake and compression stroke up to the point of spark timing. This research also acts to further currently emerging research on the interactions between the continuous-phase (flow field) and discrete-phase (fuel injection event), and resultant anisotropy within the flow.
- An example is provided showing how the numerical predictions of the flow turbulence characteristics can be used to evaluate the resultant premixed turbulent combustion process using combustion regime diagrams, of which, to the best of the authors knowledge, is not present within the current literature.

7.3 RECOMMENDATIONS FOR FUTURE WORK

The following recommendations for future work are based around either: additional investigations into in-cylinder processes using the model presented here, or numerical sub-models identified through this work that would benefit from additional effort to improve their predictive capability:

- This thesis has included studies into cycle-to-cycle variability of both the in-cylinder flow field and the fuel injection process up to the point of spark timing. The next logical stage would be to simulate the combustion event. This would allow direct links to be made between variations in both large and small scale flow structures,

mixture field development, spray plume impingement and liquid film formation, and the subsequent CCV of the combustion process. In particular, through the use of a detailed ignition model, investigations into how the flow fluctuations at spark timing (already presented) effect the initial kernel development and subsequent flame propagation phase. Careful consideration would also need to be paid to the integration between combustion model and the LES SGS model which is of prime significance for correctly modelling turbulent flame propagation.

- Through the course of this research, efforts were made to link cycles with high or low flow characteristics at the point of spark timing with certain flow characteristics earlier in the cycle in an attempt to establish causality for flow variations at spark timing, but none were found. Additional effort, potentially with the use of more statistical techniques, should be made to help draw conclusions around the precursors for high or low flow field CCV at spark timing.
- The CCV of the injection event observed in the research presented here is only a function of the variations in the continuous-phase. In reality, there are also variations in the fuel injection pressure, timing, velocity and angle due to variations in fuel injection system pressure due to pressure fluctuations and wave dynamics, variations in turbulence and cavitation within the injector nozzle and variations in electrical signal supplied to the injector needle solenoid. An interesting, but challenging, subsequent step would be to experimentally characterise the CCV variations in the fuel injection event due to the injector and injector system only and then impose these variations within the same model, either as individual effects or as a stochastic approach scaled by the variation seen in experiments, to investigate the relative magnitude of contribution between CCV of the fuel injection system and in-cylinder turbulence on the overall CCV of the fuel injection process.
- In section 5.3.3, it was seen that the effect of the fuel injection event early in the intake stroke acted to reduce the variation in valve curtain mass flux between the two intake valves and hence reduce the magnitude of the resultant valve jet flapping event. This was seen to be part of the reason why CCV in valve jet flapping had no discernible impact on the CCV of the mixture field at spark timing. It was hypothesised that since the magnitude of the jet flapping is more significant in the absence of a fuel injection event, an injection event later in the intake stroke or even in the compression stroke, as used in a stratified mixture control strategy, would allow

CCV of the intake valve jet flapping process more time to influence, and generate CCV in, the bulk flow structures and subsequently be a larger contributor to CCV of the final fuel-air equivalence ratio. It would be interesting to test this hypothesis by completing additional analyses across a range of fuel injection timings, to see if under certain conditions intake valve jet flapping can be attributed to a significant cause of CCV of the mixture field at spark timing.

- The use of the Lagrangian DDM and LES SGS models for modelling sprays in ICE's is still very much emerging, with most of the research being led by academic institutions and industry looking for guidance on best practices within this area before integration within their workflows. An area with very little information thus far is around the sensitivity of the choice of sub-model(s) used within the DDM (e.g. droplet breakup, droplet-droplet interactions, solid surface impingement, liquid films) and the LES SGS model used. An understanding of the dependency of the solution to user input is critical for defining best practices within this area.
- The use of a combined Eulerian-Lagrangian approach for modelling the fuel spray liquid core and dispersed droplets respectively, coupled with a LES SGS turbulence model would also allow additional information to be gathered with respect to the influence of the in-cylinder flow field on the fuel spray and the subsequent CCV, and again be an interesting progression of the current research.
- As discussed in section 2.4.8, one of the limitations of the research presented here is the absence of a source term in the LES SGS model to account for the transfer of energy from the dispersed-phase to the continuous-phase at a SGS level. The more complex SGS models of the k-equation and dynamic structure models include the use of an additional transport equation for kinetic energy, where the addition of a droplet source term is easily applied. Additional analyses with a SGS model of this type would allow interesting comparisons into the relative effect of the absence of this feature. The absence of additional kinetic energy transport equation in the Smagorinsky SGS model used here, means accounting for energy transfer from the dispersed-phase to the continuous-phase is less straightforward but determining a method of achieving this would prove a useful avenue of research, allowing simpler LES SGS models (where an additional kinetic energy transport equation is not present) to be used and still incorporate this aspect of physical modelling.

- The models used for determining the Nukiyama and Leidenfrost temperatures (used as critical inputs into the models for film boiling and impingement regimes), are predominantly based on experimental results for sessile droplets though it is known that they are both a dynamic property also dependent on the droplet impingement characteristics. Yao & Cai (1988) proposed a model to determine the Leidenfrost temperature of impinging droplets as a function of the droplet impingement angle but the study had a number of limitations; the study was conducted with large water droplets, the model contained four user tuneable coefficients and was a function of saturation temperature rather than a corrected Leidenfrost temperature, as used in Habchi's model. Further model developments in this area, including supporting experimental studies to investigate the sensitivity of Leidenfrost temperature to dynamic impingement conditions relevant to impinging sprays in engines, would further improve the accuracy of impingement and liquid film predictions in direct injection engines.
-

REFERENCES

Aamir, M. A. & Watkins, A. P. (1999) Dense propane spray analysis with a modified collision model. In: *ILASS-Europe'99, Toulouse, France, 5-7 July 1999*.

Abraham, J., Williams, F. A. & Bracco, F. V. (1985) A Discussion of Turbulent Flame Structure in Premixed Charges. SAE Technical Paper 850345.

Aleiferis, P. G. & van Romunde, Z. R. (2013) An analysis of spray development with iso-octane, n-pentane, gasoline, ethanol and n-butanol from a multi-hole injector under hot fuel conditions. Fuel. 105, 143-168. Available from: http://dx.doi.org/10.1016/j.fuel.2012.07.044.

Aleiferis, P. G., Serras-Pereira, J., van Romunde, Z., Richardson, D., et al. (2007) Optical studies of spray development in a quiescent chamber and in a direct-injection spark-ignition engine. *In: International Conference on Internal Combustion Engines: Performance, Fuel Economy and Emissions: IMechE, 11-12 December 2007, London, UK*. pp. 3–13. Available from: http://eprints.ucl.ac.uk/116996/.

Allocca, L., Andreassi, L. & Ubertini, S. (2007) Enhanced Splash Models for High Pressure Diesel Spray. *Journal of Engineering for Gas Turbines and Power*. 129 (2), 609-621. Available from: doi:10.1115/1.2432891.

Al-Roub, M. (1996) *Hydrodynamics And Heat Transfer Of Multiple Droplet Impingement*. Thesis, (PhD). University of Wisconsin-Madison.

Al-Roub, M., Farrell, P. V. & Senda, J. (1996) Near Wall Interaction in Spray Impingement. SAE Technical Paper 960863.

ARB (2012) *Laws and Regulations > California Air Resources Board*. Available from: http://www.arb.ca.gov/html/lawsregs.htm.

Ashida, K., Takahashi, T., Tanaka, T., Yeom, J. -K., et al. (2000) Spray-Wall Interaction Model Considering Superheating Degree of the Wall Surface. In: *Eighth International Conference on Liquid Atomization and Spray Systems, July 2000, Pasadena, CA, USA*.

Auriemma, M., Corcione, F. E., Macchioni, R. & Valentino, G. (1998) Interpretation of Air Motion in Reentrant Bowl in-Piston Engine by Estimating Reynolds Stresses. SAE Technical Paper 980483.

Bai, C. & Gosman, A.D. (1995) Development of Methodology for Spray Impingement Simulation. SAE Technical Paper 950283.

Bai, C. & Gosman, A. D. (1996) Mathematical Modelling of Wall Films Formed by Impinging Sprays. SAE Technical Paper 960626.

Banerjee, S., Liang, T., Rutland, C. J. & Hu, B. (2010) Validation of an LES Multi Mode Combustion Model for Diesel Combustion. SAE Technical Paper 2010-01-0361.

Baum, E., Peterson, B., Böhm, B. & Dreizler, A. (2014) On the validation of les applied to internal combustion engine flows: Part 1: Comprehensive experimental database. *Flow, Turbulence and Combustion*. 92 (1-2), 269–297. Available from: doi:10.1007/s10494-013-9468-6.

Baumgarten, C. (2006) *Mixture formation in internal combustion engines*. Berlin, Springer Verlag.

Beau, P. A. (2006) *Modelisation de l'atomisation d'un jet liquide - Application aux sprays diesel*. Thesis, (PhD). University of Rouen.

Beavis, N. J., Ibrahim, S. S. & Malalasekera, W. (2016) Numerical Simulations of a GDI Engine Flow Using LES and POD. SAE Technical Paper 2016-01-0598.

Bella, G., De Maio, A. & Grimaldi, C. N. (2003) Flow Characterization of a High Performance S.I. Engine Intake System - Part 2 : Numerical Analysis. SAE Technical Paper 2003-01-0632.

Bernardin, J.D. & Mudawar, I. (1999) The Leidenfrost Point : Experimental Study and Assessment of Existing Models. *Journal of Heat Transfer*. 121 (4), 894–903.

Berndorfer, A., Breuer, S., Piock, W. & Von Bacho, P. (2013) Diffusion Combustion Phenomena in GDi Engines caused by Injection Process. SAE Technical Paper 2013-01-0261.

Bharadwaj, N., Rutland, C. J. & Chang, S. (2009) Large eddy simulation modelling of spray-induced turbulence effects. *International Journal of Engine Research*. 10, 97-119. Available from: doi:10.1243/14680874JER02309.

Binjuwair, S. & Ibrahim, S. (2013) Numerical Analysis of Flow Structure inside a Single Cylinder of a 4 Valve Head under Steady-State Condition. SAE Technical Paper 2013-24-0186.

Binjuwair, S. A. (2013) *Characterisation of Flow Structures Inside an Engine Cylinder Under Steady State Condition*. Thesis, (PhD). Loughborough University.

Blokkeel, G., Barbeau, B. & Borghi, R. (2003) A 3D Eulerian Model to Improve the Primary Breakup of Atomizing Jet. SAE Technical Paper 2003-01-0005.

Borée, J., Maurel, S. & Bazile, R. (2002) Disruption of a compressed vortex. *Physics of Fluids*. 14 (7), 2543–2556. Available from: doi:10.1063/1.1472505.

Borghi, R. (1985) On the Structure and Morphology of Turbulent Premixed Flames. In: *Recent Advances in the Aerospace Sciences*. pp. 117–138.

Bracco, F. V. (1985) Modeling of Engine Sprays. SAE Technical Paper 850394.

Brandt, A. R., Millard-Ball, A., Ganser, M. & Gorelick, S. M. (2013) Peak oil demand: the role of fuel efficiency and alternative fuels in a global oil production decline. *Environmental science & technology*. 47 (14), 8031–8041. Available from: doi:10.1021/es401419t.

Campbell, J. W., Gosman, A. D., Hardy, G. & Ag, I. M. (2013) Analysis of Premix Flame and Lift-Off in Diesel Spray Combustion using Multi-Dimensional CFD. *SAE Int. J. Engines*. 1 (1), 571–590.

Cavina, N., Corti, E., Poggio, L. & Zecchetti, D. (2011) Development of a Multi-Spark Ignition System for Reducing Fuel Consumption and Exhaust Emissions of a High Performance GDI Engine. SAE Technical Paper 2011-01-1419.

CD-adapco (2014) *Methodology STAR-CD Version 4.22*.

Chen, A. (1994) *Application of Computational Fluid Dynamics to the Analysis of Inlet Port Design in Internal Combustion Engines*. Thesis, (PhD). Loughborough University of Technology.

Cheng, W. K., Hamrin, D., Heywood, J. B., Hochgreb, S., et al. (1993) An Overview of Hydrocarbon Emissions Mechanisms in Spark-Ignition Engines. SAE Technical Paper 932708.

Chiari, L. & Zecca, A. (2011) Constraints of fossil fuels depletion on global warming projections. *Energy Policy*. 39 (9), 5026–5034. Available from: doi:10.1016/j.enpol.2011.06.011.

Choi, W., Choi, B. -C., Park, H. -K., Joo, K. -J., et al. (2003) In-Cylinder Flow Field Analysis of a Single Cylinder Dl Diesel Engine Using PIV and CFD. SAE Technical Paper 2003-01-1846. 2003

Chumakov, S. G. & Rutland, C. J. (2005) Dynamic structure subgrid-scale models for large eddy simulation. *Int. J. Numer. Methods Fluids*. 47 (8-9), 911–923.

Colin, O., Ducros, F., Veynante, D. & Poinsot, T. (2000) A thickened flame model for large eddy simulations of turbulent premixed combustion. *Physics of Fluids*. 12 (7), 1843-1863. Available from: doi:10.1063/1.870436.

Craft, T. J., Launder, B. E. & Suga, K. (1996) Development and application of a cubic eddy-viscosity model of turbulence. *International Journal of Heat and Fluid Flow*. 17 (2), 108–115.

Damkohler, G. (1947) The Effect of Turbulence on the Flame Velocity in Gas Mixtures. *Zeitschrift Electrochem (English translation, NACA Tech. Memo. No. 112)*. 46601.

Das, S. (1996) *Computational Fluid Dynamic Modelling of Flow and Combustion in Spark Ignition Engines*. Thesis, (PhD). Loughborough University.

Davis, G. C. & Borgnakke, C. (1982) The Effect of In-Cylinder Flow Processes (Swirl, Squish and Turbulence Intensity) on Engine Efficiency - Model Predictions. SAE Technical Paper 820045.

Delhaye, B. & Cousyn, B. (1996) Computation of Flow and Combustion in Spark Ignition Engine and Comparison with Experiment. SAE Technical Paper 961960.

Desportes, A., Zellat, M., Desoutter, G., Abouri, D., et al. (2010a) Validation and Application of the Eulerian-Lagrangian spray atomization (ELSA) model for the Diesel injection

simulation. In: *20th International Multidimensional Engine User's Meeting at the SAE Congress 2010, 14 April 2010, Detroit, USA*. pp. 1–10.

Desportes, A., Zellat, M., Desoutter, G., Liang, Y., et al. (2010b) Application of the Eulerian-Lagrangian spray atomization (ELSA) model for the Diesel injection simulation. In: *Proc. THIESEL 2010, 14-17 September 2010, Valencia, Spain*. pp. 139-150

DieselNet (2007) *Emissions Standards > DieselNet*. [Online]. Available from: http://www.dieselnet.com/standards/.

Drake, M. C., Fansler, T. D., Solomon, A. S. & Szekely, G. A. (2003) Piston Fuel Films as a Source of Smoke and Hydrocarbon Emissions from a Wall-Controlled Spark-Ignited Direct-Injection Engine. SAE Technical Paper 2003-01-0547.

Drake, M. C. & Haworth, D. C. (2007) Advanced gasoline engine development using optical diagnostics and numerical modeling. *Proceedings of the Combustion Institute*. 31 (1), 99–124. Available from: doi:10.1016/j.proci.2006.08.120.

Dugue, V., Gauchet, N. & Veynante, D. (2006) Applicability of Large Eddy Simulation to the Fluid Mechanics in a Real Engine Configuration by Means of an Industrial Code. SAE Technical Paper 2006-01-1194.

Dukowicz, J. K. (1980) A Particle-Fluid Numerical Model for Liquid Sprays. *Journal of Computational Physics*. 35, 229–253.

EC (2014) *Road Transport: Reducing CO2 emissions from Vehicles > European Commission*. [Online]. Available from: http://ec.europa.eu/clima/policies/transport/vehicles/index_en.htm.

Eckbreth, A. C. (1988) Laser Diagnostics for Combustion Temperature and Species Measurements. *NASA Center for AeroSpace Information (CASI)*. 305–364.

Efthymiou, P., Davy, M. H., Garner, C. P., Hargrave, G. K., et al. (2013) Insights into Cold-Start DISI Combustion in an Optical Engine Operating at −7°C. *SAE Int. J. Engines*. 6 (2), 1059–1074. Available from: doi:10.4271/2013-01-1309.

Enaux, B., Granet, V., Vermorel, O., Lacour, C., et al. (2011) LES study of cycle-to-cycle variations in a spark ignition engine. *Proceedings of the Combustion Institute*. 33 (2), 3115–3122. Available from: doi:10.1016/j.proci.2010.07.038.

EPA (2014a) *Fuel Economy Regulations > EPA*. [Online]. Available from: http://www.epa.gov/fueleconomy/regulations.htm.

EPA (2014b) *Health > Particulate Matter (PM) > U.S. EPA*. [Online]. Available from: http://www.epa.gov/pm/health.html.

Fansler, T. D. & French, D. T. (1987) Swirl, Squish and Turbulence in Stratified-Charge Engines: Laser-Velocimetry Measurements and Implications for Combustion. SAE Technical Paper 870371.

Faure, M. A., Sadler, M., Oversby, K. K. & Stokes, J. (1998) Application of Lda And Piv Techniques to the Validation of a Cfd Model of a Direct Injection Gasoline Engine. SAE Technical Paper 982705.

Fenimore (1979) Studies of fuel-nitrogen in rich-flame gases. In: *17th Symp Comb, The Combustion Institute, Philadelphia, 1979*.

Ferrante, A. & Elghobashi, S. E. (2004) A robust method for generating inflow conditions for direct simulations of spatially-developing turbulent boundary layers. *Journal of Computational Physics*. 198, 372–387. Available from: doi:10.1016/j.jcp.2004.01.016.

Flowers, D. L., Aceves, S. M. & Babajimopoulos, A. (2006) Effect of Charge Non-uniformity on Heat Release and Emissions in PCCI Engine Combustion. SAE Technical Paper 2006-01-1363.

Fogleman, M., Lumley, J., Rempfer, D. & Haworth, D. (2004) Application of the proper orthogonal decomposition to datasets of internal combustion engine flows. *Journal of Turbulence*. 5 (23). Available from: doi:10.1088/1468-5248/5/1/023.

Fontanesi, S., Paltrinieri, S. & Cantore, G. (2014) LES Analysis of Cyclic Variability in a GDI Engine. SAE Technical Paper 2014-01-1148.

Fontanesi, S., Paltrinieri, S. & D'Adamo, A. (2013) Analysis of cyclic variability in a turbocharged GDI engine using LES. In: *International Multidimensional Engine User's Meeting at the SAE Congress, 15 April 2013, Detroit, USA*. Available from: https://imem.cray.com/2013/Meeting-2013/6-Emilia-Fontanesi-cyclic-LES.pdf [Accessed: 26 May 2014].

Foucart, H., Habchi, C., Coz, J. F. Le & Baritaud, T. (1998) Development of a Three Dimensional Model of Wall Fuel Liquid Film for Internal Combustion Engines. SAE Technical Paper 980133.

Friedrich, M. A., Lan, H., Wegener, J. L., Drallmeier, J. A., et al. (2008) A Separation Criterion With Experimental Validation for Shear-Driven Films in Separated Flows. *Journal of Fluids Engineering*. 130, 1-9. Available from: doi:10.1115/1.2907405.

Fukuda, K., Ghasemi, A., Barron, R. & Balachandar, R. (2012) An Open Cycle Simulation of DI Diesel Engine Flow Field Effect on Spray Processes. SAE Technical Paper 2012-01-0696.

Germano, M., Piomelli, U., Moin, P. & Cabot, W. H. (1991) A dynamic subgrid-scale eddy viscosity model. *Physics of Fluids A: Fluid Dynamics*. 7 (3), 1760–1765.

Gibson, M. M. & Launder, B. E. (1978) Ground effects on pressure fluctuations in the atmospheric boundary layer. *Journal of Fluid Mechanics*. 86 (03), 491–511. Available from: doi:10.1017/S0022112078001251.

Gnana Sagaya Raj, A., Mallikarjuna, J. M. & Venkitachalam, G. (2013) Analysis of In-Cylinder Air Motion in a DI Diesel Engine with Four Different Piston Bowl Configuration - A CFD and PIV Comparison. *SAE Int. J. Engines*. 6 (4), 1978–1983. Available from: doi:10.4271/2013-01-2786.

Gosman, A. D. (2012) Progress on Engine LES Using STAR-CD. In: *STAR Japanese Conference, 27-28 November, 2012, Yokohama, Japan*. Available from: http://www.cd-adapco.com/sites/default/files/Presentation/19 Japan 2012_David Gosman_Progress on Engine LES.pdf.

Gosman, A. D. & Ioannides, S. I. (1983) Aspects of computer simulation of liquid-fuelled combustors. *AIAA, J. Energy*. 7 (6), 482–490.

Gosman, A. D. & Johns, R. J. R. (1978) Development of a Predictive Tool for In-Cylinder Gas Motion in Engines. SAE Technical Paper 780315.

Gosman, A. D., Tsui, Y. Y. & Watkins, A. P. (1984) Calculation of Three Dimensional Air Motion in Model Engines. SAE Technical Paper 840229.

Guildenbecher, D. R., López-Rivera, C. & Sojka, P. E. (2009) Secondary atomization. *Experiments in Fluids*. 46 (3), 371–402. Available from: doi:10.1007/s00348-008-0593-2.

Habchi, C. (2010) A Comprehensive Model for Liquid Film Boiling in Internal Combustion Engines. *Oil & Gas Science and Technology – Revue de l'Institut Français du Pétrole*. 65 (2), 331–343. Available from: doi:10.2516/ogst/2009062.

Habchi, C., Devassy, B. M. & Kumar, R. (2014) LES of in-nozzle flows and liquid jet atomization using a two-surfaces density model. In: *LES for Internal Combustion Engine Flows [LES4ICE], 4-5 December 2014, Paris, France*. IFP Energies Nouvelles. Available from: http://www.rs-les4ice.com/Projet/jcms/c_408109/fr/friday-5-december.

Habchi, C., Verhoeven, D., Huu, C. H., Lambert, L., et al. (1997) Modeling Atomization and Break Up in High-Pressure Diesel Sprays. SAE Technical Paper 970881.

Hartmann, G. (2007) *Les moteurs et aeroplanes Antoinette*. [Online]. 2007. Available from: http://www.hydroretro.net/etudegh/antoinette.pdf.

Hasse, C. (2016) Scale-resolving simulations in engine combustion process design based on a systematic approach for model development. *International Journal of Engine Research*. 17 (1), 44–62. Available from: doi:10.1177/1468087415597842.

Hasse, C., Sohm, V. & Durst, B. (2009) Detached eddy simulation of cyclic large scale fluctuations in a simplified engine setup. *International Journal of Heat and Fluid Flow*. 30 (1), 32–43. Available from: doi:10.1016/j.ijheatfluidflow.2008.10.001.

Henson, J. C. & Malalasekera, W. (2000) Full-cycle firing simulation of a pent-roof spark-ignition engine with visualization of the flow structure, flame propagation and radiative heat flux. *Proceedings of the Institution of Mechanical Engineers, Part D: Journal of Automobile Engineering*. 214 (Part D), 957–971.

Heywood, J. B. (1988). *Internal Combustion Engine Fundamentals*. New York, McGraw-Hill.

Höök, M. & Tang, X. (2013) Depletion of fossil fuels and anthropogenic climate change—A review. *Energy Policy*. 52, 797–809. Available from: doi:10.1016/j.enpol.2012.10.046.

Hsiang, L. -P. & Faeth, G. M. (1992) Near-limit drop deformation and secondary breakup. *International Journal of Multiphase Flow*. 18 (5), 635–652. Available from: doi:10.1016/0301-9322(92)90036-G.

Huh, K. Y. & Gosman, A. D. (1991) A phenomenological model of Diesel spray atomisation. In: *Proc. Int. Conf. on Multiphase Flows (ICMF '91), 24-27 September 1991, Tsukuba, Japan*.

Hwang, S. S., Liu, Z. & Reitz, R. D. (1996) Breakup Mechanisms and Drag Coefficients of High Speed Vaporizing Liquid Drops. *Atomization and Sprays*. 6, 353–376.

IMechE (2013) *When will oil run out?* [Online]. 2013. Available from: http://www.imeche.org/knowledge/themes/energy/energy-supply/fossil-energy/when-will-oil-run-out.

Issa, R. I. (1986) Solution of the implicitly discretised fluid flow equations by operator-splitting. *J. Comp. Phys*. 62, 40–65.

Issa, R. I., Ahmadi Befrui, B., Beshay, K. & Gosman, A.D. (1991) Solution of the implicitly discretised reacting flow equations by operator-splitting. *J. Comp. Phys*. 93, 388–410.

Issa, R. I., Gosman, A. D. & Watkins, A. P. (1986) The computation of compressible and incompressible recirculating flows by a non-iterative implicit scheme. *J. Comp. Phys*. 62, 66–82.

Iwamoto, Y., Noma, K., Nakayama, O., Yamauchi, T., et al. (1997) Development of Gasoline Direct Injection Engine. SAE Technical Paper 970541.

Jarrin, N., Benhamadouche, S., Laurence, D. & Prosser, R. (2006) A synthetic-eddy-method for generating inflow conditions for large-eddy simulations. *International Journal of Heat and Fluid Flow*. 27, 585–593. Available from: doi:10.1016/j.ijheatfluidflow.2006.02.006.

Jarvis, S., Justham, T., Clarke, A., Garner, C. P., et al. (2006) Motored SI IC Engine In-Cylinder Flow Field Measurement Using Time Resolved Digital PIV for Characterisation of Cyclic Variation. SAE Technical Paper 2006-01-1044.

Justham, T. (2010) *Cyclic Variation in the Flow Field Behaviour within a Direct Injection Spark Ignition Engine: A High Speed Digital Particle Image Velocimetry Study*. Thesis, (PhD). Loughborough University.

Justham, T. & Jarvis, S. (2006) *EPSRC Research Report - Combustion Concepts for Sustainable Premium Vehicles - Loughborough Research Report Year 3*. EPSRC, UK.

Justham, T., Jarvis, S., Clarke, A, Garner, C. P., et al. (2006) Simultaneous Study of Intake and In-Cylinder IC Engine Flow Fields to Provide an Insight into Intake Induced Cyclic Variations. *Journal of Physics: Conference Series*. 45, 146–153. Available from: doi:10.1088/1742-6596/45/1/019.

Justham, T., Jarvis, S., Garner, C. P., Hargrave, G. K., et al. (2006) Single Cylinder Motored SI IC Engine Intake Runner Flow Measurement Using Time Resolved Digital Particle Image Velocimetry. SAE Technical Paper 2006-01-1043.

Keller, P., Knorsch, T., Wensing, M. & Hasse, C. (2015) Experimental and numerical analysis of iso-octane/ethanol sprays under gasoline engine conditions. *International Journal of Heat and Mass Transfer*. 84, 497–510. Available from: doi:10.1016/j.ijheatmasstransfer.2015.01.011.

Kim, W. -W. & Menon, S. (1995) A new dynamic one-equation subgrid scale model for large-eddy simulations. AIAA Paper 95-0356.

Klein, M., Sadiki, A. & Janicka, J. (2003) A digital filter based generation of inflow data for spatially developing direct numerical or large eddy simulations. *Journal of Computational Physics*. 186, 652–665. Available from: doi:10.1016/S0021-9991(03)00090-1.

Koban, W., Schorr, J. & Schulz, C. (2002) Oxygen-distribution imaging with a novel two-tracer laser-induced fluorescence technique. *Applied Physics B: Lasers and Optics*. 74 (1), 111–114. Available from: doi:10.1007/s003400100769.

Kolmogorov, A. N. (1941) The Local Structure of Turbulence in Incompressible Viscous Fluid for Very Large Reynolds Number. *Dokl. Akad. Nauk SSSR*. 30, 299–303.

Komiyama, K. & Heywood, J. B. (1973) Predicting NOx Emissions and Effects of Exhuast Gas Recirculation in Spark-ignition Engines. SAE Technical Paper 730475.

Krishna, A. S., Mallikarjuna, J. M., Davinder, K. & Ramachandra Babu, Y. (2013) In-Cylinder Flow Analysis in a Two-Stroke Engine - A Comparison of Different Turbulence Models Using CFD. SAE Technical Paper 2013-01-1085.

Laget, O., Zaccardi, J. M., Gautrot, X. & Cotte, E. (2013) Establishing New Correlations Between In-Cylinder Charge Motion and Combustion Process in Gasoline Engines Through a Numerical DOE. *SAE Int. J. Engines*. 3 (1), 183–201.

Lake, T., Stokes, J., Murphy, R., Osborne, R., et al. (2004) Turbocharging Concepts for Downsized DI Gasoline Engines. SAE Technical Paper 2004-01-0036.

Launder, B. E., Reece, G. J. & Rodi, W. (1975) Progress in the development of a Reynolds-stress turbulence closure. *Journal of Fluid Mechanics*. 68 (3), 537–566. Available from: doi:10.1017/S0022112075001814.

Launder, B. E. & Spalding, D. B. (1974) The Numerical Computation of Turbulent Flows. *Comput. Methods Appl. Mech. Eng*. 3, 269–289.

Lavoie, G. A., Heywood, J. B. & Keck, J. C. (1970) Experimental and Theoretical Study of Nitric Oxide Formation in Internal Combustion Engines. *Combustion Science and Technology*. 1, 313–326.

Lebas, R. (2007) *Modelisation Eulerienne de l'Atomisaton haute pression -Influences sur la vaporisation et la combustion induite*. Thesis, (PhD). University of Rouen.

Lebrère, L. & Dillies, B. (1996) Engine Flow Calculations Using a Reynolds Stress Model in the Kiva-II Code. SAE Technical Paper 960636.

Leder, F. & Shapiro, J. N. (2008) This time it's different. *Energy Policy*. 36 (8), 2850–2852. Available from: doi:10.1016/j.enpol.2008.04.015.

Lee, D. W. (1939) *A study of air flow in engine cylinders*. NACA Report No 653.

Lee, S. H. & Ryou, H. S. (2000) Development of a new spray/wall interaction model. International *Journal of Multiphase Flow*. 26, 1209–1234. Available from: doi:10.1016/S0301-9322(99)00080-4.

Lefebvre, A. H. (1989) *Atomization and Sprays*. New York, Hemisphere Publishing Company.

Lindh, B. -E. (1992) *Scania fordonshistoria 1891-1991 (Scania: vehicle history 1891-1991)*. Streiffert.

Liu, A. D. & Reitz, R. D. (1993) Mechanisms of air-assisted liquid atomization. *Atomization and Sprays*. 3, 55–75.

Liu, K. & Haworth, D. C. (2011) Development and assessment of POD for analysis of turbulent flow in piston engines. SAE Technical Paper 2011-01-0830.

Liu, Z. & Reitz, R. D. (1997) An analysis of the distortion and breakup mechanisms of high speed liquid drops. *International Journal of Multiphase Flow*. 23 (4), 631–650. Available from: doi:10.1016/S0301-9322(96)00086-9.

Long, E. J. (2010) *The Influence of Reactant Flow Structure on Flame Front Propagation*. Thesis, (PhD), Loughborough University.

Long, E. J., Rimmer, J. E. T., Justham, T., Garner, C. P., et al. (2008) The Influence of In-Cylinder Turbulence upon Engine Performance within a Direct Injection IC Engine. In: *Proceedings of the Seventh International Conference on Modeling and Diagnostics for Advanced Engine Systems, COMODIA 2008, 28-31 July 2008, Sapporo, Japan*. Japan, JSME. pp. 213–220.

De Luca, M., Vallet, A. & Borghi, R. (2009) Pesticide atomization modeling for hollow-cone nozzle. *Atomization and Sprays*. 19 (8), 741–753.

Luijten, B., Adomeit, P., Brunn, A. & Somers, B. (2013) Experimental Investigation of In-Cylinder Wall Wetting in GDI Engines Using a Shadowgraphy Method. SAE Technical Paper 2013-01-1604.

Lumley, J. L. (1967) The Structure of Inhomogeneous Turbulent Flows. In: *Atmospheric Turbulence and Radio Wave, 1967, Nauka, Moscow*. pp. 166–178.

Lund, T. S., Wu, X. & Squires, K. D. (1998) Generation of Turbulent Inflow Data for Spatially-Developing Boundary Layer Simulations. *Journal of Computational Physics*. 140, 233–258. Available from: doi:10.1006/jcph.1998.5882.

Ma, H. (2006) *Optical Diagnostics and Combustion Analysis in a Gasoline Direct Injection Engine*. Thesis, (PhD). University of Oxford.

Ma, H., Stevens, R. & Stone, R. (2006) In-Cylinder Temperature Estimation from an Optical Spray- Guided DISI Engine with Color-Ratio Pyrometry (CRP). SAE Technical Paper 2006-01-1198.

Malaguti, S., Cantore, G., Fontanesi, S., Lupi, R., et al. (2009) CFD Investigation of Wall Wetting in a GDI Engine under Low Temperature Cranking Operations. SAE Technical Paper 2009-01-0704.

Mantzaras, J., Felton, P. G. & Bracco, F. V. (1988) Three-Dimensional Visualization of Engine Flames : Islands of Reactants and Products ; Fractal Dimensions ; and Homogeneity. SAE Technical Paper 881635.

Maricq, M. M., Podsiadlik, D. H., Brehob, D. D. & Haghgooie, M. (1999) Particulate Emissions from a Direct-Injection Spark-Ignition (DISI) Engine. SAE Technical Paper 1999-01-1530.

Maroteaux, F., Llory, D., Le Coz, J. -F. & Habchi, C. (2002) Liquid Film Atomization on Wall Edges - Separation Criterion and Droplets Formation Model. *Journal of Fluids Engineering*. 124, 565–575. Available from: doi:10.1115/1.1493811.

Maroteaux, F., Llory, D., le Coz, J. -F. & Habchi, C. (2003) Potential of inertial instabilities for fuel film separation in port fuel injection engine conditions. *International Journal of Engine Research*. 4 (1), 11–26. Available from: doi:10.1177/146808740300400102.

Marshall, S. P., Taylor, S., Stone, C. R., Davies, T. J., et al. (2011) Laminar burning velocity measurements of liquid fuels at elevated pressures and temperatures with combustion residuals. *Combustion and Flame*. 158 (10), 1920–1932. Available from: doi:10.1016/j.combustflame.2011.02.016.

Matsuda, T. & Senda, J. (2003) Modeling on Spray-Wall Interaction for Direct Gasoline Injection Engines. *Journal of JSME*. 69 (688), 2698–2705. Available from: doi:http://doi.org/10.1299/kikaib.69.2698.

McDonald, P. W. (1971) The Computation of Transonic Flow through TwoDimensional Gas Turbine Cascades. ASME Paper 71-GT-89.

Merker, G. P., Schwarz, C. & Teichmann, R. (2012) *Combustion Engines Development*. Fourth. Berlin, Springer-Verlag.

Metghalchi, M. & Keck, J. C. (1982) Burning velocities of mixtures of air with methanol, isooctane, and indolene at high pressure and temperature. *Combustion and Flame*. 48, 191–210. Available from: doi:10.1016/0010-2180(82)90127-4.

Montanaro, A., Allocca, L., Ettorre, D., Lucchini, T., et al. (2011) Experimental Characterization of High-Pressure Impinging Sprays for CFD Modeling of GDI Engines. *SAE Int. J. Engines*. 4 (1), 747–763. Available from: doi:10.4271/2011-01-0685.

Montanaro, A., Malaguti, S. & Alfuso, S. (2012) Wall Impingement Process of a Multi-Hole GDI Spray: Experimental and Numerical Investigation. SAE Technical Paper 2012-01-1266.

Morse, A. P., Whitelaw, J. H. & Yianneskis, M. (1979) Turbulent Flow Measurements by Laser-Doppler Anemometry in Motored Piston-Cylinder Assemblies. *Journal of Fluids Engineering, Transactions of the ASME*. 101 (2), 208–216. Available from: doi:10.1115/1.3448937.

Moureau, V. (2004) Simulation aux grandes échelles de l'aérodynamique interne des moteurs à piston. Thesis, (PhD). Ecole Centrale Paris, Institut Français du Pétrole.

Mugele, R. A. & Evans, H. D. (1951) Droplet Size Distributions in Sprays. *Ind. Eng. Chem*. 43 (6), 1317–1324.

Murad, A. E. M. A. (2006) Flow and Combustion in Disc and Pent-Roof SI Engines. Thesis, (Phd). University of Leeds.

Namazian, M., Hansen, S., Lyford-Pike, E., Sanchez-Barsse, J., et al. (1980) Schlieren Visualization of the Flow and Density Fields in the Cylinder of a Spark-Ignition Engine. SAE Technical Paper 800044.

NHTSA (2011) *President Obama Announces Historic 54.5 mpg Fuel Efficiency Standard*. [Online]. Available from: http://www.nhtsa.gov/About+NHTSA/Press+Releases/2011/President+Obama+Announces+Historic+54.5+mpg+Fuel+Efficiency+Standard.

Ning, W., Reitz, R. D., Diwakar, R. & Lippert, A. M. (2009) An Eulerian-Lagrangian spray and atomization model with improved turbulence modeling. *Atomization and Sprays*. 19 (8), 727–739.

Nohira, H. (1997) Development of Toyota's direct injection gasoline engine. In: *Proceedings of 27th International AVL Conference 'Engine and Environment', 1997, Graz, Austria.* AVL LIST GmbH. pp. 239–249.

Nordin, N. (2001) Complex Chemistry Modelling of Diesel Spray Combustion. Chalmers University of Technology.

O'Rourke, P. J. (1981) *Collective Drop Effects on Vaporising Liquid Sprays*. Thesis, (PhD). University of Princeton.

O'Rourke, P. J. & Amsden, A. (1987) The Tab Method for Numerical Calculation of Spray Droplet Breakup. SAE Technical Paper 872089.

O'Rourke, P. J. & Amsden, A. (1996) A Particle Numerical Model for Wall Film Dynamics in Port-Injected Engines. SAE Technical Paper 961961.

Olsson, C. (1987) *Volvo – Lastbilarna igår och idag (Volvo – the trucks yesterday and today)*. Norden.

Osei-Owusu, P. (2008) *Numerical Studies of Charge Mixture Preparation for HCCI Engines*. Thesis, (PhD). Loughborough University.

Ozdor, N., Dulger, M. & Sher, E. (1994) Cyclic Variability in Spark Ignition Engines A Literature Survey. SAE Technical Paper 940987.

Patterson, M. A. & Reitz, R. D. (1998) Modeling the Effects of Fuel Spray Characteristics on Diesel Engine Combustion and Emission. SAE Technical Paper 980131.

Payri, F., Benajes, J., Margot, X. & Gil, A. (2004) CFD modeling of the in-cylinder flow in direct-injection Diesel engines. *Computers & Fluids*. 33 (8), 995–1021. Available from: doi:10.1016/j.compfluid.2003.09.003.

Peery, K. M. (1975) *The Heintz Straticharge Engine: modifications I through V*. Department of Mechanical Engineering, Stanford University.

Peters, N. (1986) Laminar flamelet concepts in turbulent combustion. In: *Twenty-First Symposium (International) on Combustion/The Combustion Institute, 1986, Munich, West Germany*. pp. 1231–1250. Available from: doi:10.1016/S0082-0784(88)80355-2.

Peters, N. (1991) Length Scales in Laminar and Turbulent Flames. *Numerical Approaches to Combustion Modeling*. 135, 611–629.

Peters, N. (1999) The turbulent burning velocity for large-scale and small-scale turbulence. *Journal of Fluid Mechanics*. 384, 107–132. Available from: doi:10.1017/S0022112098004212.

Peters, N. (2000) *Turbulent Combustion*. Cambridge, Cambridge University Press.

Petersen, B. R. & Ghandhi, J. B. (2010) High Resolution Scalar Dissipation and Turbulence Length Scale Measurements in an Internal Combustion Engine. *SAE Int. J. Engines*. 3 (1), 65–83. Available from: doi:10.4271/2010-01-0185.

Peterson, B., Ding, C. -P., Baum, E., Michaelis, D., et al. (2015) Influence of direct-injection on the volumetric flow field in a gasoline engine captured by tomographic PIV. In: *12th International Congress, Engine Combustion Processes, Current Problems and Modern Technologies, 12-13 March 2015, Ludwigsburg, Germany*. Erlangen, ESYTEC GmbH. pp. 1–12.

Peterson, K., Regaard, B., Heinemann, S. & Sick, V. (2012) Single-camera, three-dimensional particle track-ing velocimetry. *Optics Express*. 20 (8), 9031–9037.

Pilch, M. & Erdman, C. A. (1987) Use of Breakup Time Data and Velocity History Data to Predict the Maximum Size of Stable Fragments for Acceleration-Induced Breakup of a Liquid Drop. *International Journal of Multiphase Flow*. 13 (6), 741–757.

Pischinger, F. F. & Klocker, K. J. (1974) Single-Cylinder Study of Stratified Charge Process with Prechamber-Injection. SAE Technical Paper 741162.

Pischinger, S. & Heywood, J. B. (1990) How Heat Losses to the Spark Plug Electrodes Affect Flame Kernel Development in an SI-Engine. SAE Technical Paper 900021.

Poinsot, T. & Veynante, D. (2005) *Theoretical and Numerical Combustion*. USA, Edwards.

Pomraning, E. & Rutland, C. J. (2002) Dynamic one-equation nonviscosity large-eddy simulation model. *AIAA, J*. 40 (4), 689–701.

Pope, S. B. (2004) Ten questions concerning the large-eddy simulation of turbulent flows. *New Journal of Physics*. 6 (35), 1-9. Available from: doi:10.1088/1367-2630/6/1/035.

Pope, S. B. (2000) *Turbulent Flows*. Cambridge, Cambridge University Press.

Price, P. (2009) *Direct Injection Gasoline Engine Particulate Emissions*. Thesis, (PhD). University of Oxford.

Price, P., Stone, R., Collier, T. & Davies, M. (2014) Particulate Matter and Hydrocarbon Emissions Measurements : Comparing First and Second Generation DISI with PFI in Single Cylinder Optical Engines. SAE Technical Paper 2006-01-1263.

Pulkrabek, W. W. (1997) *Engineering Fundamentals of the Internal Combustion Engine*. Upper Saddle River, N.J., Prentice Hall.

Ranger, A. A. & Nicholls, J. A. (1969) The Aerodynamic shattering of Liquid Drops. *AIAA, J*. 7, 285–290.

Reitz, R. D. (2013) Directions in internal combustion engine research. *Combustion and Flame*. 160 (1), 1–8. Available from: doi:10.1016/j.combustflame.2012.11.002.

Reitz, R. D. & Bracco, F. V. (1982) Mechanism of atomization of a liquid jet. *Physics of Fluids*. 25, 1730–1742. Available from: doi:10.1063/1.863650.

Reitz, R. D. & Diwakar, R. (1986) Effect of Drop Breakup on Fuel Sprays. SAE Technical Paper 860469.

Reitz, R. D. & Diwakar, R. (1987) Structure of High-Pressure Fuel Sprays. SAE Technical Paper 870598.

Reuss, D. L., Adrian, R. J. & Landreth, C. C. (1989) Instantaneous Planar Measurements of Velocity and Large-Scale Vorticity and Strain Rate in an Engine Using Particle-Image Velocimetry. SAE Technical Paper 890616.

Richard, S., Colin, O., Vermorel, O., Benkenida, A., et al. (2007) Towards large eddy simulation of combustion in spark ignition engines. *Proceedings of the Combustion Institute*. 31 (2), 3059–3066. Available from: doi:10.1016/j.proci.2006.07.086.

Rimmer, J. E. T. (2011) *An Optical Investigation into the Effect of Fuel Spray, Turbulent Flow and Flame Propagation on DISI Engine Performance*. Thesis, (PhD). Loughborough University.

Rimmer, J. E. T., Long, E. J., Garner, C. P., Hargrave, G. K., et al. (2009) The Influence of Single and Multiple Injection Strategies on In-Cylinder Flow and Combustion within a DISI Engine. SAE Technical Paper 2009-01-0660.

Rodi, W. (1979) Influence of buoyancy and rotation on equations for the turbulent length scale. In: *Proc. 2nd Symp. on Turbulent Shear Flows, 1979*.

Rosa, N. G., Villedieu, P., Dewitte, J. & Lavergne, G. (2006) A New Droplet-Wall Interaction Model. In: *PAPER ID ICLASS06-167, ICLASS-2006, 27 August – 1 September 2006, Kyoto, Japan*.

Rothrock, A. M. & Spencer, R. C. (1939) *The influence of directed air flow on combustion in a spark ignition engine*. NACA Report No 657.

Rutland, C. J. (2011) Large-eddy simulations for internal combustion engines - a review. *International Journal of Engine Research*. 12 (5), 421–451. Available from: doi:10.1177/1468087411407248

Schiffmann, P., Gupta, S., Reuss, D., Sick, V., et al. (2016) TCC-III Engine Benchmark for Large-Eddy Simulation of IC Engine Flows. *Oil & Gas Science and Technology – Revue d'IFP Energies nouvelles*. 71 (3), 1–27. Available from: doi:10.2516/ogst/2015028.

Schlichting, H. (1968) *Boundary-layer Theory*. 6th Ed. New York, McGraw-Hill.

Schmidt, D. P., Nouar, I., Senecal, P. K., Rutland, C. J., et al. (1999) Pressure-Swirl Atomization in the Near Field. SAE Technical Paper 1999-01-0496.

Schmidt, D. P. & Rutland, C. J. (2000) A New Droplet Collision Algorithm. *Journal of Computational Physics*. 164, 62–80. Available from: doi:10.1006/jcph.2000.6568.

Schulz, F., Schmidt, J., Kufferath, A. & Samenfink, W. (2014) Gasoline Wall Films and Spray/Wall Interaction Analyzed by Infrared Thermography. *SAE Int. J. Engines*. 7 (1), 1165–1177. Available from: doi:10.4271/2014-01-1446.

Senda, J. & Fujimoto, H.G. (1999) Multidimensional Modeling of Impinging Sprays on the Wall in Diesel Engines. *Applied Mechanics Reviews*. 52 (4), 119–138. Available from: doi:10.1115/1.3098930.

Senda, J., Kanda, T., Al-Roub, M., Farrell, P. V., et al. (1997) Modeling spray impingement considering fuel film formation on the wall. SAE Technical Paper 970047.

Senda, J., Kobayashi, M., Iwashita, S. & Fujimoto, H. G. (1994) Modeling of diesel spray impinging on flat wall. In: *Proceedings of the Third International Symposium on Diagnostics and Modelling of Combustion in Internal Combustion Engines, COMODIA 94, 11-14 July 1994, Yokohama, Japan*. pp. 411–416.

Senecal, P. K., Schmidt, D. P., Nouar, I., Rutland, C. J., et al. (1999) Modeling high-speed viscous liquid sheet atomization. *International Journal of Multiphase Flow*. 25, 1073–1097. Available from: doi:10.1016/S0301-9322(99)00057-9.

Serras-Pereira, J. (2010) *Spray Formation and Combustion of Alcohols and Gasoline in a Direct-Injection Spark-Ignition Engine*. Thesis, (PhD). University College London.

Serras-Pereira, J., Aleiferis, P. G., Richardson, D. & Wallace, S. (2007) Spray Development in a Direct-Injection Spark-Ignition Engine. SAE Technical Paper 2007-01-2712.

Serras-Pereira, J., Aleiferis, P. G. & Richardson, D. (2012) Imaging and heat flux measurements of wall impinging sprays of hydrocarbons and alcohols in a direct-injection spark-ignition engine. *Fuel*. 91 (1), 264–297. Available from: doi:10.1016/j.fuel.2011.07.037.

Serras-Pereira, J., Aleiferis, P. G., Richardson, D. & Wallace, S. (2007) Mixture Preparation and Combustion Variability in a Spray-Guided DISI Engine. SAE Technical Paper 2007-01-4033.

Serras-Pereira, J., van Romunde, Z., Aleiferis, P. G., Richardson, D., et al. (2010) Cavitation, primary break-up and flash boiling of gasoline, iso-octane and n-pentane with a real-size optical direct-injection nozzle. *Fuel*. 89 (9), 2592–2607. Available from: doi:10.1016/j.fuel.2010.03.030.

Shih, T. -H., Liou, W. W., Sabbir, A., Yang, Z., et al. (1994) *A New k-e Eddy Viscosity Model for High Reynolds Number Turbulent Flows-Model Development and Validation*. NASA Technical Memorandum 106721.

Simonini, S., Elston, S. J. & Stone, C. R. (2001) Soot temperature and concentration measurements from colour charge coupled device camera images using a three-colour method. *Proceedings of the Institution of Mechanical Engineers, Part C: Journal of Mechanical Engineering Science*. 215 (9), 1041–1052. Available from: doi:10.1177/095440620121500905.

Sirignano, W.. & Mehring, C. (2000) Review of theory of distortion and disintegration of liquid streams. *Progress in Energy and Combustion Science*. 26 (4-6), 609–655. Available from: doi:10.1016/S0360-1285(00)00014-9.

Sirovich, L. (1987) Turbulence and the Dynamics of Coherent Structures. *Quarterly of Applied Mathematics*. 45, 561–590.

Smagorinsky, J. (1963) General circulation experiments with the primitive equations. I. The basic experiment. *Mon. Weather Rev*. 91 (3), 99–164.

Som, S. & Aggarwal, S. K. (2010) Effects of primary breakup modeling on spray and combustion characteristics of compression ignition engines. *Combustion and Flame*. 157 (6), 1179–1193. Available from: doi:10.1016/j.combustflame.2010.02.018.

Som, S., D'Errico, G., Longman, D. & Lucchini, T. (2012) Comparison and Standardization of Numerical Approaches for the Prediction of Non-reacting and Reacting Diesel Sprays. SAE Technical Paper 2012-01-1263.

Som, S. & Longman, D. (2012) Multi-Dimensional Modeling- High-Fidelity Large Eddy Simulation (LES). Available from: http://www.transportation.anl.gov/engines/multi_dim_model_les.html.

Som, S., Ramirez, A. I., Aggarwal, S. K., Kastengren, A. L., et al. (2009) Development and Validation of a Primary Breakup Model for Diesel Engine Applications. SAE Technical Paper 2009-01-0838.

Sorrell, S., Speirs, J., Bentley, R., Brandt, A., et al. (2010) Global oil depletion: A review of the evidence. *Energy Policy*. 38 (9), 5290–5295. Available from: doi:10.1016/j.enpol.2010.04.046.

Sorrell, S., Speirs, J., Bentley, R., Miller, R., et al. (2012) Shaping the global oil peak: A review of the evidence on field sizes, reserve growth, decline rates and depletion rates. *Energy*. 37 (1), 709–724. Available from: doi:10.1016/j.energy.2011.10.010.

Speziale, C. G., Sarkar, S. & Gatski, T. B. (1991) Modelling the pressure-strain correlation of turbulence : an invariant dynamical systems approach. *Journal of Fluid Mechanics*. 227, 245–272.

Spiegler, P., Hopenfeld, J., Silberberg, M., Bumpus, C. F., et al. (1963) Onset of stable film boiling and the foam limit. *International Journal of Heat and Mass Transfer*. 6 (11), 987–989. Available from: doi:10.1016/0017-9310(63)90053-X.

St Hill, N., Asadamongkon, P., Lee, K. C. & Yianneskis, M. (2000) On the turbulence and cyclic variation levels in internal combustion engine cylinders. In: *Proceedings of the 10th International Symposium on Applications of Laser Techniques to Fluid Mechanics, 10-13 July, 2000, Lisbon, Portugal*.

Stanton, D. W. & Rutland, C. J. (1998) Multi-Dimensional Modeling of Heat and Mass Transfer of Fuel Films Resulting from Impinging Sprays. SAE Technical Paper 980132.

Stevens, E. & Steeper, R. (2001) Piston wetting in an optical DISI engine: fuel films, pool fires, and soot generation. SAE Technical Paper 2001-01-1203.

Tatschl, R., Bogensperger, M., Pavlovic, Z., Priesching, P., et al. (2013) LES Simulation of Flame Propagation in a Direct-Injection SI-Engine to Identify the Causes of Cycle-to-Cycle Combustion Variations. SAE Technical Paper 2013-01-1084.

Taylor, G. I. (1963) *The Shape and Acceleration of a Drop in a High Speed Air Stream*. *The Scientific Papers of G. I. Taylor*. Cambridge, University Press Cambridge.

TheAA (2014) *Fuel Price Report Fuel Price Report*. [Online]. Available from: http://www.theaa.com/resources/Documents/pdf/motoring-advice/fuel-reports/february2014.pdf.

Time (1979) Detroit's Total Revolution. *Time magazine*. [Online]. Available from: http://content.time.com/time/magazine/article/0,9171,947023-4,00.html.

TransportPolicy.net (2016) *EU: Light-duty: Emissions*. [Online]. Available from: http://www.transportpolicy.net/index.php?title=EU:_Light-duty:_Emissions.

Tsoskounoglou, M., Ayerides, G. & Tritopoulou, E. (2008) The end of cheap oil: Current status and prospects. *Energy Policy*. 36 (10), 3797–3806. Available from: doi:10.1016/j.enpol.2008.05.011.

Turner, M. J., Clough, R. W., Martin, H. C. & Topp, L. J. (1956) Stiffness and Deflection Analysis of Complex Structures. *Journal of the Aeronautical Sciences (Institute of the Aeronautical Sciences)*. 23 (9), 805–823. Available from: doi:10.2514/8.3664.

USGPO (2014a) *Part 600 CFR40 Fuel Economy and Greenhouse Gas Exhaust Emissions of Motor Vehicles > Electronic Code of Federal Regulations > U.S. Government Printing Office*. [Online] Available from: http://www.ecfr.gov/cgi-bin/text-

idx?c=ecfr&SID=15aa2dd04f0ede89f963d0dcffb2b2b2&rgn=div5&view=text&node=40:31.0.1.4.43&idno=40.

USGPO (2014b) *Part 86 CFR40 Control of Emissions from New and In-Use Highway Vehicles and Engines*. [Online] Available from: http://www.ecfr.gov/cgi-bin/text-idx?c=ecfr&sid=b49b7f5bd81fb8b345dc29ef8a54f385&rgn=div5&view=text&node=40:20.0.1.1.1&idno=40#40:20.0.1.1.1.13.

Vallet, A., Burluka, A. A. & Borghi, R. (2001) Development of a Eulerian model for the atomization of a liquid jet. *Atomization and Sprays*. 11, 619–642.

Van Romunde, R. Z. (2011) *Factors Affecting the Development of Sprays Produced by Multihole Injectors for Direct-Injection Engine Applications*. Thesis, (PhD). University College London.

Van Romunde, Z. & Aleiferis, P. G. (2009) Effect of Operating Conditions and Fuel Volatility on Development and Variability of Sprays from Gasoline Direct-Injection Multihole Injectors. *Atomization and Sprays*. 19, 207–234.

Van Romunde, Z., Aleiferis, P. G., Cracknell, R. F., Walmsley, H. L., et al. (2007) Effect of Fuel Properties on Spray Development from a Multi-Hole DISI Engine Injector. SAE Technical Paper 2007-01-4032.

Vermorel, O., Richard, S., Colin, O., Angelberger, C., et al. (2009) Towards the understanding of cyclic variability in a spark ignited engine using multi-cycle LES. *Combustion and Flame*. 156 (8), 1525–1541. Available from: doi:10.1016/j.combustflame.2009.04.007.

Versteeg, H. K. & Malalasekera, W. (2007) *An Introduction to Computational Fluid Dynamics*. New Jersey, Pearson Education Limited.

Wang, H., Reitz, R. D. & Yao, M. (2012) Comparison of Diesel Combustion CFD Models and Evaluation of the Effects of Model Constants. SAE Technical Paper 2012-01-0134.

Weiss, M. F. (1979) *Design and Prototype Evaluation of a Fuel Control System for the Stratícharge 6 Engine*. Department of Mechanical Engineering, Stanford University. Available from:

http://books.google.co.uk/books?id=HTAEAAAAIAAJ&q=1973+AMC+Hornet&dq=1973+AMC+Hornet&hl=en&redir_esc=y.

Whitaker, P., Kapus, P., Ogris, M. & Hollerer, P. (2011) Measures to Reduce Particulate Emissions from Gasoline DI engines. *SAE Int. J. Engines*. 4 (1), 1498–1512. Available from: doi:10.4271/2011-01-1219.

White, F. M. (1988) *Mass and Heat Transfer*. Prentice Hall.

Williams, B., Ewart, P., Stone, R., Ma, H., et al. (2008) Multi-Component Quantitative PLIF: Robust Engineering Measurements of Cyclic Variation in a Firing Spray-Guided Gasoline Direct Injection Engine. SAE Technical Paper 2008-01-1073.

Williams, B., Ewart, P., Wang, X., Stone, R., et al. (2010) Quantitative planar laser-induced fluorescence imaging of multi-component fuel / air mixing in a firing gasoline-direct-injection engine : Effects of residual exhaust gas on quantitative PLIF. *Combustion and Flame*. 157 (10), 1866–1878. Available from: doi:10.1016/j.combustflame.2010.06.004.

Williams, B., Wang, X., Ewart, P., Stone, R., et al. (2007) Full bore imaging of combustion and quantitative AFR PLIF with a multi-component fuel and co- evaporating tracers. In: *Internal Combustion Engines: Performance, Fuel Economy and Emissions IMechE Conference, 11-12 December 2007, London, UK.*

Williams, F. A. (1958) Spray combustion and atomization. *Phys Fluids*. 541–544.

Winklhofer, E., Hirsch, A., Kapus, P., Kortschak, M., et al. (2009) TC GDI Engines at Very High Power Density – Irregular Combustion and Thermal Risk. SAE Technical Paper 2009-24-0056.

Withrow, L. & Rassweiler, G. M. (1938) Studying engine combustion by physical methods a review. *J. Appl. Phys*. 9, 363–372.

Xie, Z. -T. & Castro, I. P. (2008) Efficient Generation of Inflow Conditions for Large Eddy Simulation of Street-Scale Flows. *Flow, Turbulence and Combustion*. 81, 449–470. Available from: doi:10.1007/s10494-008-9151-5.

Yakhot, V. & Orszag, S. A. (1986) Renormalization group analysis of turbulence. I. Basic theory. *Journal of Scientific Computing*. 1 (1), 3–51. Available from: doi:10.1007/BF01061452.

Yakhot, V., Orszag, S. A., Thangam, S., Gatski, T. B., et al. (1992) Development of turbulence models for shear flows by a double expansion technique. *Physics of Fluids A: Fluid Dynamics*. 4 (7), 1510–1520. Available from: doi:10.1063/1.858424.

Yang, B. & Ghandhi, J. (2007) Measurement of Diesel Spray Impingement and Fuel Film Characteristics Using Refractive Index Matching Method. SAE Technical Paper 2007-01-0485.

Yao, S. C. & Cai, K. Y. (1988) The dynamics and leidenfrost temperature of drops impacting on a hot surface at small angles. *Experimental Thermal and Fluid Science*. 1 (4), 363–371. Available from: doi:10.1016/0894-1777(88)90016-7.

Yoshizawa, A. & Horiuti, K. (1985) A statistically-derived subgrid-scale kinetic energy model for the large eddy simulation of turbulent flows. *J. Phys. Soc. Japan*. 54 (8), 2834–2839.

Zeldovich, Y. B., Sadovnikov, P. Y. & Frank-Kamenetskii, D. A. (1947) *Oxidation of Nitrogen in Combustion*. Academy of Sciences of USSR, Institute of Chemical Physics.

Zhao, F., Lai, M. -C. & Harrington, D. (1999) Automotive spark-ignited direct-injection gasoline engines. *Progress in Energy and Combustion Science*. 25 (5), 437–562. Available from: doi:10.1016/S0360-1285(99)00004-0.